Development, deformation style, and seismic hazard of large normal faults

Michael Hodge

School of Earth and Ocean Sciences

Cardiff University

Submitted in partial fulfilment of the requirements for the degree of

Doctor of Philosophy

June 2018

ABSTRACT

Young rifts such as the Malawi Rift System, located at the southern end of the East African Rift System, are a natural laboratory for how continents begin to break apart. Extension is typically accommodated by earthquakes within the upper crust. However, where extension occurs at a slow rate, the small number of historically recorded earthquakes likely provides an incomplete view of the potential magnitude range of events, limiting seismic hazard knowledge and the understanding of rift dynamics. Geological and geomorphological studies of faults scarps may help understand how faults develop, structurally evolve and accommodate displacement. Thus, in this thesis, using field and satellite observations of fault scarps, alongside numerical models, I develop a number of new methodologies in order to better understand young rift evolution.

I show that the coseismic stress change between two active parallel faults influences whether the faults link, and the linkage style is determined by the distance between the faults. I also show that the orientation of a major border fault in a young rift can be influenced by local stresses and/or weakness at depth, forming faults oblique to what is expected by the regional stress field. Lastly, I identify segmentation on several Malawi Rift System faults from variations in scarp height and steps in the fault traces, and show that the morphology of each can be used to infer the number of prehistoric earthquake events.

My work may suggest that large, normal faults in young rifts develop through a specific growth model, and that they can host earthquakes larger in magnitude than historically recorded. This research can help better understand rift evolution and earthquake hazard in the Malawi Rift System, as well as other regions where normal faults have the potential to cause large magnitude earthquakes, such as the Rukwa rift, Baikal rift and the Basin and Range Province.

Declaration

This work has not been submitted in substance for any other degree or award at this or any other university or place of learning, nor is being submitted concurrently in candidature for any degree or other award.

Signed ______________________________ (candidate) Date: ____________

STATEMENT 1

This thesis is being submitted in partial fulfilment of the requirements for the degree of PhD.

Signed ______________________________ (candidate) Date: ____________

STATEMENT 2

This thesis is the result of my own independent work/investigation, except where otherwise stated. Other sources are acknowledged by explicit references. The views expressed are my own.

Signed ______________________________ (candidate) Date: ____________

STATEMENT 3

I hereby give consent for my thesis, if accepted, to be available online in the University's Open Access repository and for inter-library loan, and for the title and summary to be made available to outside organisations.

Signed ______________________________ (candidate) Date: ____________

Michael Hodge
June 2018

Acknowledgements

I've thoroughly enjoyed the past three and a half years I've spent undertaking this PhD. I've learned many skills you'd expect of a PhD student, including how to conduct independent research and present my work at international conferences, but I've also learned a great deal about myself too. The experiences of personal losses over the past few years have weighed heavy on my mind whilst conducting this research. This, alongside periods of depression, anxiety attacks and panic attacks, meant that I came close to quitting on a number of occasions. I'm glad I didn't. My advice to those PhD students who are struggling with anything at all is that you will always find someone willing to help, but first you must learn to ask.

Alas, whilst it is my name on the front of this thesis, this is a pseudonym for those that have helped me along my journey. As a result, brevity is excused.

First and foremost I would like to thank my supervisory duo of Dr Åke Fagereng and Dr Juliet Biggs whom have been constantly supportive of my work and exemplary researchers. I am grateful for their patience and empathy in dealing with any - and there were many - complex problems (both personally and academically) I have thrown at them. It goes without saying, without both of their help and support, I would not have been able to achieve this. I have learned so much from them, and can only hope this research was as rewarding and gratifying for them as it was for me.

My research was primarily sponsored by the Natural Environment Research Council (NERC) Great Western Four+ Doctoral Training Partnership and for that I owe NERC a huge thank you for supporting this research. Their sponsorship allowed me to undertake fieldwork in Malawi, purchase satellite data, and attend various workshops and conferences. The DTP also allowed me to meet a great number of interesting and enthusiastic students and academics, all whom I've had the pleasure of getting to know over several events.

I'd like to thank the wider academic research groups that I am part of: Tectonics Studies Group (TSG), and the Centre for Observation and Modelling of Tectonics and Volcanoes (COMET). The feedback I have received from annual conferences and meetings has been vital in shaping my work. I'd also like to thank COMET for providing financial support for the purchase of satellite data; without that data this research could have not been completed. A special thanks go to Dr Austin Elliott of the University of Oxford, who helped me process satellite data and provided invaluable comments on the final chapters in this thesis.

Within the School of Earth and Ocean Sciences at Cardiff University I owe a big thank you to all the administrative staff who've helped me and other students over the years, in particular Mrs Christine Williams. My thanks also go to all the academics who have provided me with invaluable technical and laboratory assistance. Of course, I owe a huge amount of gratitude to my PhD and Post-Doc friends, past and present. A number of these have been subjected to my emotional outbursts over these past few years, and I apologise for any harm done. I hope you all have rewarding and happy careers. In addition, I would like to acknowledge the imagination of my fellow PhD students, whom helped create a game called *T-ball*; whilst it sounds silly, this game provided me with a cathartic break from research for nearly three years.

Outside of academia I owe a great deal of thanks to my good friends for helping me maintain my mental stability and providing me with a sense of grounding. They have provided me with decades of joy and laughter. Whilst we are all growing up, moving away, getting married, having children, finding careers and settling down, knowing that our friendship won't change is important to me.

To my family, I can scarcely believe that the day has come that I am handing in this, my PhD thesis. As a result, I am struggling to know what to say here. I am eternally thankful to my parents for all their hard work and support they've given me and my brother, David. Mum, from you I learned how to be compassionate, kind, loving and polite; as I grow up I realise how similar we are, and those around me who have benefited from my humility have done so because of you. Dad, from you I learned how to be responsible, courageous, disciplined and how to persevere (which has been vital in this PhD); over the past few years you've helped me talk about my emotions, and I am so grateful for that. And to my brother, David, whilst we now live in different cities and are building our own families, I will always reminisce of my wonderful childhood, which was shaped by you.

And lastly, to my wife, Annie. My personal debt to you is the greatest of all. For over a decade now you've helped me through some really, really shit times. You inspired me to undertake this PhD, and encouraged me to find the strength to complete it. So many people are so fortunate to have you in their lives, and none more so than me. Whatever we do in life, I take so much comfort in the knowledge that we can overcome anything, together. *"I will love you forever; whatever happens. Till I die and after I die, and when I find my way out of the land of the dead, I'll drift about forever, all my atoms, till I find you again..."*.

Am Zach . . .

Ac yno yn y dyffryn tawel mi glywaf gân yn swn yr awel.

TABLE OF CONTENTS

LIST OF FIGURES

List of tables

Chapter 1

Introduction

Young continental rifts provide a rare natural laboratory for observing normal fault development and growth, and associated seismicity. However, such rifts typically experience slow/low strain rates, which may lead to relatively short instrumental catalogues compared to earthquake repeat times. Thus, the catalogue may provide an incomplete range of potential earthquake magnitudes, making quantifying seismic hazard challenging (e.g., Hodge et al., 2015; Murru et al., 2016; Ullah et al., 2015). An example of a young rift extending under a slow strain rate is the Malawi Rift System (MRS) at the southern end of the East African Rift System (EARS). The earliest historically recorded earthquakes on the MRS occurred around 100 years ago, and the instrumental catalogue is only complete above M_W 4.5 since *ca.* 1965. To date, earthquakes along the MRS have been moderate in magnitude, such as the 1989 M_W 6.3 Salima earthquake (Jackson and Blenkinsop, 1993) and four M_W 5.4$\sim$5.9 events in the 2009 Karonga earthquake sequence (Biggs et al., 2010). A complete rupture of one of the many large, normal border faults that the rift hosts (e.g., Flannery and Rosendahl, 1990; Hodge et al., 2015; Jackson and Blenkinsop, 1997; Rosendahl, 1987), however, could cause an earthquake greater in magnitude than the largest recorded earthquake along the entire EARS, the M_W 7.3 1910 Rukwa event (Ambraseys and Adams, 1991). Such an event would be devastating, especially for a country that is consistently in the lowest 10th percentile of world development indicators.

In this thesis I aim to use an array of field and satellite observations, and develop numerical models, in order to gain an insight into the evolution and deformation style of normal faults in early-stage continental rift settings. In addition, I shall develop new methodologies for calculating surface offsets formed by prehistoric earthquake ruptures. The new techniques are applied to a case study of southern Malawi, and I consider how the results can provide new insights to normal fault development and seismic hazard in slow strain rate rifts in general.

1.1 Continental rift systems

Divergent plate boundaries (also known as constructive plate margins) occur when two or more plates move apart from one another. This extensional movement in the oceans creates mid-ocean ridges, such as the Mid-Atlantic Ridge and the East Pacific Rise, whilst on continents it leads to continental drift, which in-turn may eventually mature into a mid-ocean ridge (Ebinger, 2005). Examples of young, early-stage continental rifts are the Gulf of Corinth rift in central Greece and the Malawi Rift System (MRS) at the southern end of the East African Rift System (EARS; fig. 1.1a). The Gulf of Corinth initiated rifting at around 5 Ma (Ori, 1989) and the MRS at around 8 Ma (Ebinger et al., 1989). The thickness of the lithosphere - the region comprising the crust and upper mantle - for most continental regions of the world, including young rifts such as the MRS and Gulf of Corinth, is typically around 100 km (e.g., Foster et al., 1997; Le Pichon and Angelier, 1981; Pollack and Chapman, 1977); however, rifting causes the lithosphere to thin. For example, for the more mature Baikal rift in southeastern Russian, which initiated rifting around 25 Ma (Mats, 1993), the lithosphere is around 40 to 80 km thick (Petit and Deverchere, 2006; Zorin et al., 1989).

As rifts continue to mature, the lithosphere undergoes further thinning, as seen in the Ethiopian rift at the northern end of the EARS and the Basin and Range Province in western USA; thinning of the lithosphere, and the ascent of magma, can lead to increased volcanic activity (fig. 1.1b). Continued rifting may result in seafloor spreading as seen in parts of the Red Sea rift, and eventually result in the passive margins observed around the Atlantic (fig. 1.1c,d). Where continental breakup and the creation of new oceanic lithosphere is achieved it is done so over multiple phases of lithospheric extension, with each phase occurring over tens of millions of years and comprising distinct structural, petrological and sedimentary processes (Naliboff and Buiter, 2015). An example of a multi-phase rift system is the Red Sea rift, whose first (lower Eocene-early Oligocene) and second (late Miocene-Holocene) phases of rifting were separated by a 30 Ma period of uplift and denudation (Girdler and Styles, 1974).

Not all rifts succeed in forming new oceanic lithosphere though, continental rifting may slow down and eventually stop, as seen on the Can-Hang failed rift in southeastern China (Goode et al., 1991), or slow down and stop at even more mature stages, such as the North Sea rift (Rattey and Hayward, 1993). Rifts where extension has halted, however, do not imply regions of seismic inactivity. Reactivation of pre-existing faults and structures continues to occur within the North Sea rift (e.g., Phillips et al., 2016; Whipp et al., 2014), resulting in a M 6 earthquake every few hundred years (Musson, 1996). Furthermore, the slow down of extension on the North Sea rift coincided with rift initiation in the North Atlantic (e.g., Ziegler, 1975). Rift-related processes therefore vary within the same rift zone throughout time and space, and rift evolution can be influenced by earlier phases of tectonic activity. As such, early-stage rifts provide an exciting and prosperous opportunity to understand rift evolution.

The initial extensional movement and lithospheric thinning of rift margins has been suggested to occur in response to far-field plate forces (e.g., McKenzie, 1978), such as slab pull and ridge push, but these forces alone may be insufficient to rupture normal continental lithosphere (Forsyth, 1975; Hayward and Ebinger, 1996). Gradients of gravitational potential energy (GPE) originating from mantle plumes (Lithgow-Bertelloni and Silver, 1998; Stamps et al., 2015) and tractions at the lithosphere-asthenosphere boundary induced by mantle convection and flow may play a role (e.g., Ebinger, 2005; Ebinger et al., 2013, fig. 1.1). However, joint numerical models incorporating mantle convection and deviatoric stress tensors show that GPE nor tractions alone can explain rift development and style of faulting in many of the deformation zones of the Earth's surface (Ghosh et al., 2008), including the EARS (Kendall and Lithgow-Bertelloni, 2016). Analogue models of continental rifting suggest that magma plays an important role in enhancing lithospheric stretching and strain localization in mature rifts (Buck, 2006), but the degree of magmatism is variable between rifts, as explained below.

Following their initiation, many of the rifts systems described above (EARS, Gulf of Corinth, Basin and Range Province) display similar evolutionary characteristics: (i) initiation and growth of a distributed conjugate fault network; (ii) segment growth and linkage; (iii) early development of rift-scale dip domains, where opposing-dipping faults occur in sections along the rift; (iv) changes in fault activity, new faults developing and some dying, associated with: (v) progressive evolution of rift asymmetry with development of a border fault system; and (vi) rapid linkage and localization of deformation onto the border fault system (Bell et al., 2009; Gawthorpe et al., 2017; Nixon et al., 2016). However, when looking more closely at areas of continental extension it becomes apparent that not all rifts are the same. Rifted margins are considerably variable in terms of their crustal architecture, amount of magmatism and sedimentation patterns (Brune et al., 2017). There are wide rifts, narrow rifts, magma-rich rifts, magma-poor rifts, and many other classifications one can assign to a rift system. Below, we briefly explain the differences between these types of rifts using reference to a few case study examples.

The difference between narrow rifts and wide rifts is the width of the rift compared to the thickness of the lithosphere they reside within (Buck et al., 1999). For a rift to be defined as a narrow rift, its width must be less than its lithospheric thickness. As mentioned above, a typical global lithospheric thickness is around 100 km (Pollack and Chapman, 1977). Many of the rifts listed above are narrow rifts, including: the MRS, Gulf of Corinth, and Baikal rift. For example, the Gulf of Corinth rift comprises several E-W to NW-SE trending basins along a zone 115 km long and 30 km wide (Beckers et al., 2015; Stefatos et al., 2002). In comparison, the Basin and Range Province is an example of a wide rift, comprising a width of around 800 km (Thatcher et al., 1999). Each type of rift displays a distinctive structural architecture. Whereas wide rifts are characterised by tilted blocks at high strain rates and horst and grabens at low strain rate (Tirel et al., 2006), narrow rifts typically form asymmetrical half grabens (Buck, 1991). However, this simplistic difference may not be true in nature; for example, the distribution and polarity of faults in the Gulf of Corinth produce a more complex basin structure than can be described by a simple half graben (e.g., Bell et al., 2008; Stefatos et al., 2002).

The processes that form either wide or narrow rifts has been postulated for some time (e.g., England, 1983). The formation of wide rifts was initially suggested to occur due to slow strain rates, which locally increase the yield strength of the lithosphere (England, 1983; Sonder and England, 1989); for example, extension within the Basin and Range interior is likely less than 3 mm per year (although the western boundary may deform at around 11$\pm$1 mm per year; e.g., Dixon et al., 2000) compared to the rapidly extending Gulf of Corinth rift, whose extension rate is between 5 and 15 mm per year (e.g., Avallone et al., 2004; McKenzie, 1972; Roberts and Jackson, 1991). However, numerical models of rift formation (e.g., Buck, 1991) do not support this prediction because some wide rifts extended at faster velocities than some narrow rifts did. Furthermore, narrow rifts such as the MRS extend at very slow extension rates of less than 2 mm per year (Ebinger et al., 2013; Saria et al., 2014). Other studies have suggested that viscous effects may lead to wide rifting (Bassi, 1991), or that the buoyancy forces resulting from local (crustal) isostasy (Buck, 1991) could produce wide regions of extension. Although strain rate does not directly correlate to rift width, we can arbitrarily classify rifts by their strain rate: rifts such as the Gulf of Corinth are considered fast strain rate rifts, and the MRS and Basin and Range Province are examples of slow strain rate rifts. Considering strain rate is important as it directly relates to the timescales in which deformation occurs within rifts. For comparison and completeness, the Baikal rift extends at around 4 to 5 mm per year (Calais et al., 1998).

As well as wide or narrow, and/or slow or fast strain rate, rifts can also be referred to as magma-rich or magma-poor/amagmatic (e.g., Brun, 1999; Buck, 1991). The difference between magma-rich and magma-poor rifts is when the onset of melt production occurs during continental break-up. Magma-poor margins are characterised by continental lithosphere thinning through multiple tectonic events, with little or no magmatic supply. However, the rise of the asthenosphere progressively produces magma that infiltrates the overlying continental lithospheric mantle (Picazo et al., 2016); this results in a combined tectonic and thermal

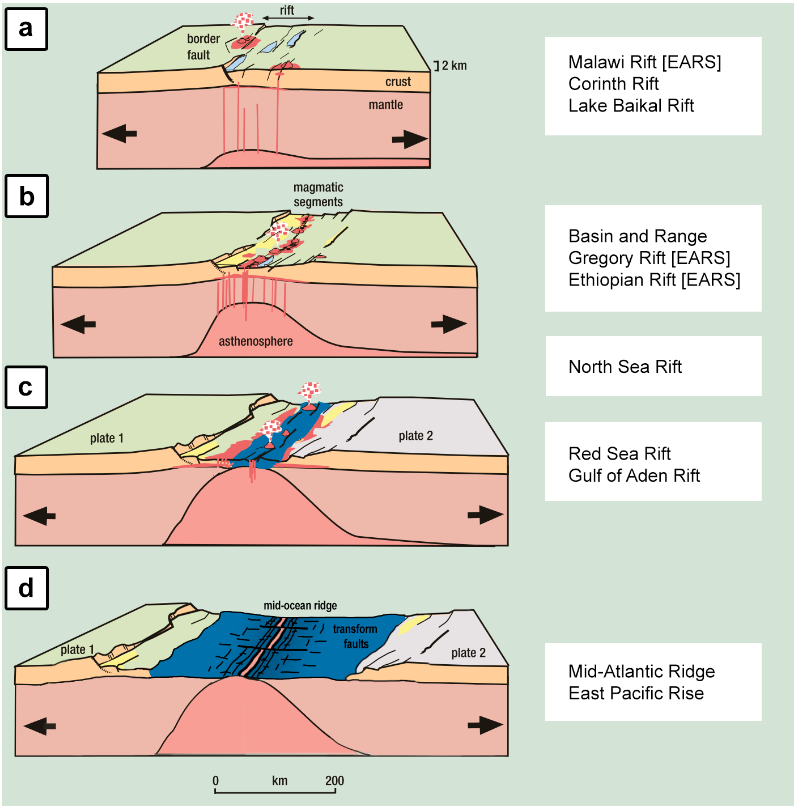

Fig. 1.1 The three-stage model for continental break-up (drift) for narrow rifts, as proposed by Ebinger (2005). a) 0 - 5 Myr after the onset of rifting, the lithosphere begins to thin through brittle and plastic deformation. The asthenosphere rises to replace the thinning lithosphere, transferring heat, causing some decompression melting. Some melt may reach shallow crustal levels and form volcanoes. Magmatic fluids modify and melt rocks at the base of the lithospheric mantle. Deformation in the brittle crust occurs via slip along rift border faults. The characteristic asymmetry develops. Examples of this early-stage of rifting are the Malawi rift (southern EARS), Corinth rift and Baikal rift. b) After $\sim$ 10 - 15 Myr, and with increasing time and strain, the lithosphere continues to thin by faulting and plastic deformation. The asthenosphere rises towards the surface, leading to more melting. This melt rises through the heated and weakened mantle lithosphere in cracks parallel to the faults at the subsurface. Strain begins to localise to a narrow zone marked by magmatic intrusions into the crust. The magma injection accommodates strain at lower tectonic stresses than faulting. Large, detachment faults become inactive. The Ethiopian rift is an example of this more mature rift phase. Some rifts continue to mature to the next phase, whilst others may fail. c) The seafloor spreading stage, as observed in the Read Sea and Gulf of Aden rifts. The tectonically and magnetically thinned lithosphere then ruptures in the heavily intruded zones, and creates new oceanic lithosphere. The thick piles of lava in the magmatic segments load the weak plate, flexing it towards the new ocean basin to form seaward-dipping lavas. The passive margin subsides as heat transferred from the asthenosphere dissipates. d) Continued extension leads to the formation of a complete mid-ocean ridge, such as the Mid-Atlantic Ridge or the East Pacific Rise. Mid-ocean ridges are characterised by long normal faults offset by transform faults. Figure modified after Ebinger et al. (2013).

thinning of the lithosphere (Gillard et al., 2017), which marks the onset of the lithospheric breakup. While for magma-rich margins magma production and extraction may be sufficient to directly rupture the lithosphere, continued tectonic processes (e.g. faulting) accommodates extension in the absence of a magma-driven system (Jagoutz et al., 2007; Péron-Pinvidic et al., 2007). An example of a magma-rich rift is the Red Sea, a mature rift that displays a tectonically active transition from continental rifting to incipient seafloor spreading (Keir et al., 2013). Geochronological constraints in Ethiopia suggest rifting began around 30 Ma on the western Afar margin (e.g., Ayalew et al., 2006; Wolfenden et al., 2005), but it has been suggested that magma intrusion has only dominated extension for the past $\sim$ 2 Ma (Daly et al., 2008; Keranen et al., 2004). The Gulf of Corinth rift, MRS and Baikal rift are examples of magma-poor, or amagmatic, rifts. For the Baikal rift, deformation in the rift is localised, forming a narrow rift zone around 40 km wide (Allemand and Brun, 1991). Rift-related magmatism is observed outside the rift centre, but not along the rift axis (Yang et al., 2018). Whilst a number of end-member models have been proposed for how magma-rich and magma-poor margins form (e.g., Brun, 1999; Doré and Lundin, 2015), most rifts display a gradual transition between these extreme cases (Brune et al., 2017). Furthermore, rifts such as the Black Sea have shown abrupt transitions from magma-poor to magma-rich rifting, indicating that end-member models may not encapsulate the complexities of rift evolution (Shillington et al., 2009). In addition, many models of rifting assume homogeneity of the lithosphere, however, the distribution of the plate boundary deformation and magnetism can also be influenced by the heterogeneities in pre-existing lithospheric thickness, strength and composition, as strain and/or magmatism are preferentially localised to pre-rift tectonic boundaries (Petit and Ebinger, 2000).

Models of rifting have been developed largely from interpretations of time-averaged deformation patterns (Ebinger et al., 2013). Many of the observed surface and subsurface structures associated with rifts, such as fault zones and dyke intrusions, however, develop through discrete rifting periods of 10^2 to 10^5 years (e.g., Machette et al., 1991; Wright et al., 2006). This timescale is termed the rifting cycle. As described in fig. 1.3, a magma-poor rifting cycle (as observed in early-stage rifts such as the MRS, Gulf of Corinth rift and Baikal rift) is made up of a series of earthquake cycles, that over 10^1 to 10^3 years help create the observable rift-zone architecture in continental rift regions. The earthquake cycle initiates with tectonic stress buildup over decades to millenia (the interseismic period), followed by seismogenic failure (the coseismic period), which occurs on a much shorter timescale (seconds). After stress release there is a period of viscoelastic relaxation and plastic creep in the lower crust and/or mantle lithosphere, this happens over years and decades, and is known as the postseismic period. After

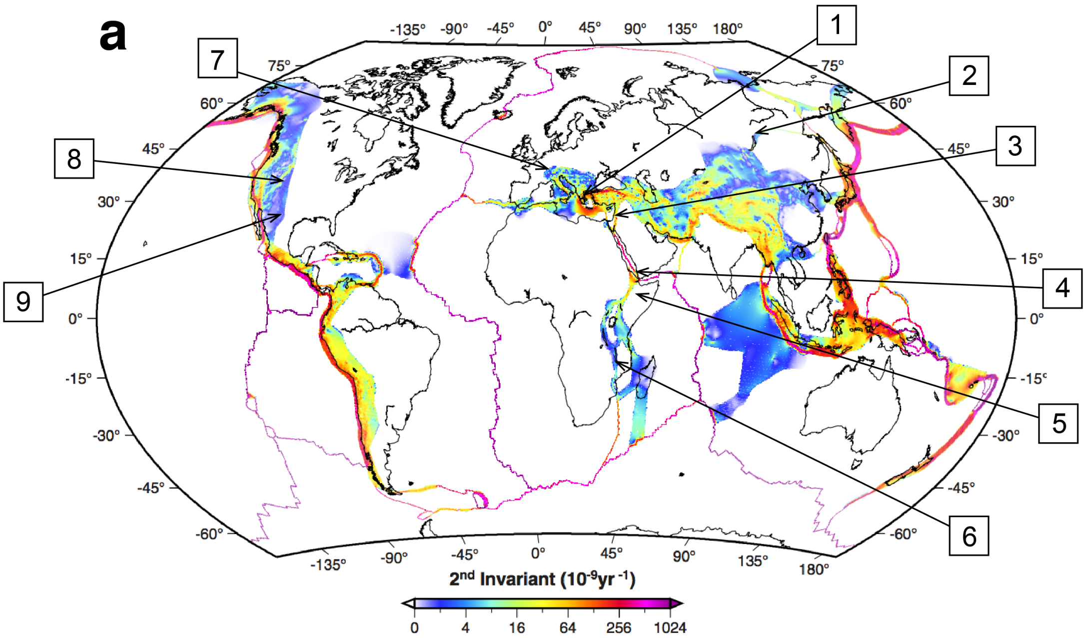

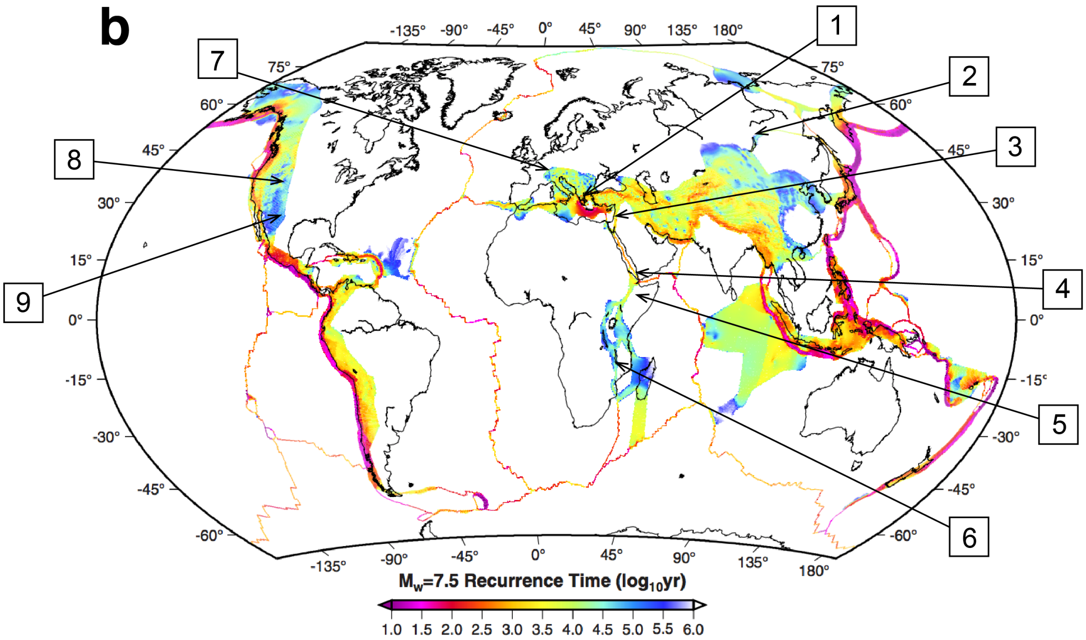

Fig. 1.2 a) Contours of the second invariant of the model strain rate field, used to represent strain 'magnitude'. b) Log_{10} of the recurrence interval T_R of a M_W = 7.5 earthquake, when the geodetic moment is released by a single (characteristic) event. Numbers relate to rifts: 1) Gulf of Corinth rift; 2) Baikal rift; 3) Dead Sea rift; 4) Red Sea rift; 5) Main Ethiopian Rift; 6) Malawi Rift System; 7) Lower Rhine Graben; 8) Basin and Range Province; and 9) Rio Grande rift. Figure modified after Kreemer et al. (2014).

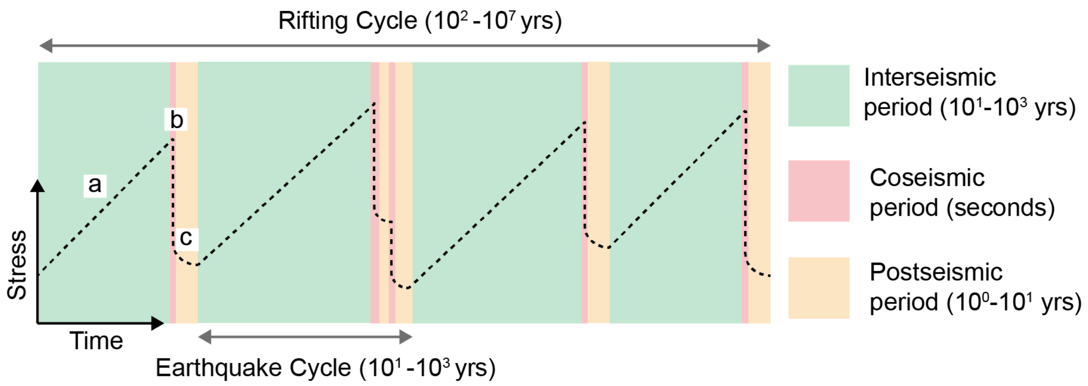

Fig. 1.3 A fault-related rifting cycle depicted as a series of earthquake cycles. Each earthquake cycle is made up of interseismic, coseismic and postseismic periods. a) The earthquake cycle initiates with a period of stress build-up, the interseismic period, which occurs over decades to millenia. b) Stress build-up is then released rapidly (seconds) by seismogenic failure (earthquakes), known as the coseismic period. c) Following the stress release there is a period of viscoelastic relaxation and ductile creep in the lower crust and/or mantle lithosphere, this stage is called the postseismic period.

the postseismic period, stress build up begins on an interseismic period to initiate a new earthquake cycle. In magma-rich rifts such as the Ethiopian rift, the rifting cycle is also modulated by the magmatic supply cycle, which may have time periods of years to centuries (Ebinger et al., 2013). Little is known about the nature of the transition between fault-controlled and dyke-controlled extension or about the processes in an intermediate setting (Biggs et al., 2009). Magmatic and seismicity events are likely entwined, however, such as the seismic swarms preceding the 2001 Mount Etna eruption (Patane et al., 2002) and earthquakes preceding the 2007 Northern Tanzania dyke intrusions (Biggs et al., 2009). Geodetic data and field observations from Iceland and Afar also demonstrate that the emplacement of dykes in volcanic rift zones frequently generates normal faulting (Rubin and Pollard, 1988). Thus, earthquake cycles in magma-rich rift settings are likely influenced by magmatic events. The exact length of an earthquake cycle depends on a number of physical and mechanical factors, such as the strain rate (Fialko, 2006; Gomberg, 1996). Lower strain rate environments typically have longer earthquake cycles (fig. 1.2).

1.1.1 Faulting and earthquakes

Both brittle and plastic deformation are important in thinning the crust as required for lithospheric stretching and rift initiation. Brittle deformation is the process of fracturing rocks usually along sub-planar surfaces that separate zones of coherent material. This can either be as extension fractures, or shear fractures, depending on the relative motion of the rock across the fracture plane. Fractures are surfaces along which a rock has broken, creating void space between the surfaces, whereas a fault is defined as a shear fracture along which there is a visible shear offset (Davis and Reynolds, 1996; Kolyukhin and Torabi, 2012). Whereas brittle deformation involves the breaking of rocks, there is no loss of cohesion with plastic deformation. For clarity, we define plastic deformation here according to Fossen (2016): "plastic deformation is ... the permanent change in shape or size of a body without fracture, produced by a sustained stress beyond the elastic limit of the material due to dislocation movement". Structures such as folds, foliations and lineations are the results of plastic deformation, which we can consider by measuring the amount of strain. Several factors, including the rheology, rock mechanics and pressure-temperature state in which the rock exists will affect whether a rock will undergo brittle or plastic deformation (e.g., Scholz, 2002). For example, under the low temperature and pressure conditions of the Earth's upper lithosphere, silicate rocks typically respond to stress and strains through brittle fracturing. Whereas, at higher temperatures and pressures, rocks can also fold or flow when subjected to stresses that exceed their plastic strength. This pressure-temperature control on rock strength and mineral-scale deformation mechanism is important as the geothermal gradient is not constant across all rifts. We explore this concept in Section 1.1.2.

Fundamental to rock mechanics and behaviour is the magnitude and orientation of the stresses imposed on the rock, i.e. the stress field. The stress acting on a plane with any orientation can be resolved into two components: a normal stress (σ_n), acting perpendicular to the surface, and a shear stress (τ_s), acting parallel to the surface (fig. 1.4). Furthermore, the stress tensor at a point can be divided into three orthogonal components, the maximum, intermediate and minimum principal stresses, known as σ_1, σ_2 and σ_3, respectively. These principal stresses act normal to planes of zero shear stress, and we define σ_1 as the greatest compressive stress. The presence of stresses on a rock can lead to strain, resulting in the change of shape or size of the rock, translation and/or rotation, the combination of which is know as deformation. It is important to note that whilst deformation (including strain, but also rotation/translation) can be observed and quantified through measurements by including assumptions of initial state, stresses can only be inferred.

The relative displacement along a fault is defined by its slip vector and is categorised as either: (i) dip slip, where the slip vector in the plane of the fault is perpendicular to the strike of the fault; (ii) strike slip, where the slip vector in the plane of the fault is parallel to the strike of the fault; or (iii) oblique slip, where slip vector is oblique to the fault strike. We subdivide faults further in terms of the relative movement, or shear sense, along them. For dip slip, if the hanging wall moves down relative to the footwall, it is referred to as a normal fault, and if

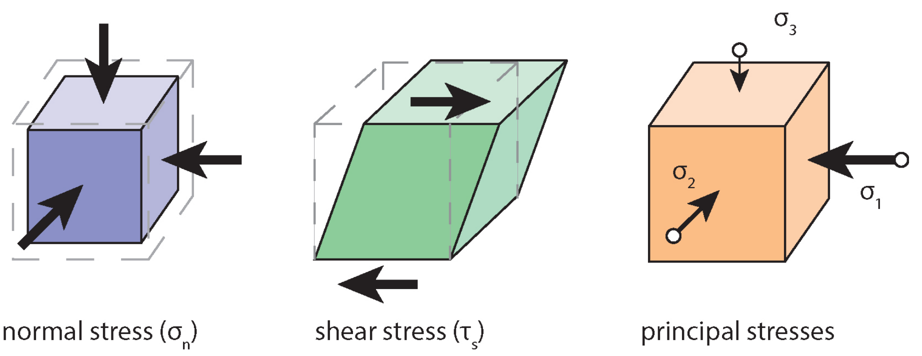

Fig. 1.4 Diagram of the normal stress component (σ_n), shear stress component (τ_s) and the three orthogonal principal stresses (the minimum principal stress σ_1, intermediate principal stress σ_2, and maximum principal stress σ_3). For the principal stresses we define them to be positive in compression.

upwards, a thrust fault (or reverse fault, if the dip is $\geq 45°$). For strike-slip, left lateral relative movement is called sinistral, and right lateral relative movement, dextral.

By assuming the following we can infer the geometry of the principal stresses based on the type of faulting: (i) that rocks can be considered isotropic; (ii) that slip is accommodated on a fault plane when the stress state satisfies a Coulomb failure criterion; and (iii) that the Earth's free surface is not acted on by shear stresses, and requires a principal stress direction to be vertical (Célérier, 2008). These assumptions give rise to the Andersonian theory of faulting (Anderson, 1905). In a pure Andersonian stress regime, normal faults form when σ_1 is vertical, thrust faults when σ_3 is vertical, and strike-slip faults when σ_2 is vertical. In rift environments, the greatest principal stress σ_1 is ideally vertical, under plane strain conditions, and as a result the most common type of faults are normal faults. As most rocks have an angle of internal friction of $\sim 30°$ (Byerlee, 1978), Andersonian theory also suggests that normal faults should dip around $\sim 60°$ and strike parallel to σ_2.

Although beneficial for clarity, and in order to briefly introduce the concepts of faulting, Section 1.1 may allude to the view that the lithosphere comprises a strong brittle layer overlying a weaker, more ductile layer, but this is overly simplified. Likewise, earthquake mechanics are more complicated than presented in this general introduction; earthquakes seldom occur by the sudden appearance and propagation of a new shear crack (Scholz, 1998). Instead a more precise understanding of earthquake mechanics suggests that they occur by sudden slippage along a pre-existing fault or other planar zone of weakness. Therefore, earthquakes are a frictional, rather than a fracture, phenomenon, where brittle fracturing plays a secondary role in lengthening faults, rather than generating them (e.g., Scholz, 2002).

1.1.2 Seismogenic thickness

The seismogenic thickness (T_s) indicates the transition from brittle faulting to plastic flow in the crust and is the indicative maximum depth to which an elastic deformation occurs as unstable frictional sliding (Scholz, 2002; Watts and Burov, 2003). In layman's terms, the seismogenic thickness represents the maximum depth at which an earthquake may nucleate (Scholz, 1998). A typical T_s for continental regions is $\sim$ 20 km (Mckenzie et al., 2005), such as the Gulf of Corinth (e.g., Roberts and Jackson, 1991); however, some regions such as the EARS and Tien Shan may have T_s up to $\sim$ 40 km (fig. 1.5a; Jackson and Blenkinsop, 1993; Mckenzie et al., 2005; Nyblade and Langston, 1995). Rifted regions characterised by a large seismogenic thickness may produce wide basins and extremely long faults (Jackson, 2001; Jackson and White, 1989; Scholz, 1998).

There are a number of proposals for why some regions have increased T_s relative to others (fig. 1.5). It has been suggested that in areas where deeper earthquakes occur (extending into the brittle part of the lithospheric mantle, 50 to 60 km), two seismogenic layers may exist with an aseismic layer in between, called the jelly sandwich model (Brace and Kohlstedt, 1980; Watts and Burov, 2003). However, the depth distribution of continental earthquakes may also imply that most of the lithospheric strength resides in the upper crust with a softer upper mantle in comparison to the lower crust, called the crème brûlée model (Jackson, 2002; Maggi et al., 2000). Both model conclusions have been extrapolated from scarce amounts of continental mantle earthquakes and correlations between effective elastic thickness T_e and seismogenic thickness, which may differ for various continental areas (Jackson and Blenkinsop, 1997). Elastic thickness can be described as the integrated brittle, elastic and ductile strength of the lithosphere (Watts and Burov, 2003). In terms of depth, T_e may incorporate the slowly deforming ductile region, which may or may not be part of seismogenic thickness. Lithospheric differences may also be a factor of different compositions and tectonothermal histories, leading to different rheological properties (Afonso and Ranalli, 2004). For example, whereas the upper crust is hydrated, and can be best approximated as wet quartzite, the composition of the lower crust is less constrained, being mainly inferred from seismic data and comparisons with experimental data (Afonso and Ranalli, 2004). Seismic velocities for the majority of the continental lower crust typically is compatible with mafic composition (e.g., Christensen and Mooney, 1995), but more felsic compositions may fit particular regions such as East China (e.g., Gao et al., 1998) and central Russia (e.g., Brown et al., 2003). Furthermore, as seismicity is an ambiguous indicator of strength, earthquakes may be a manifestation of transient mechanical instability within shear zones (Handy and Brun, 2004).

Regions of large seismogenic thickness may relate to the rheology of the lower crust. Old, cold, anhydrous, strong materials have been suggested to lead to thick seismogenic layers (e.g., Craig et al., 2011; Jackson et al., 2004; Jackson and Blenkinsop, 1993). The depth distribution of seismicity may also be affected by the presence of mafic material in the lower crust (Albaric et al., 2009), and high heat production in the upper crust compared to the lower crust (Nyblade and Langston, 1995). The presence of fluids has also been suggested, which would reduce the brittle strength, but would also lower the ductile strength (Watts and Burov, 2003).

1.1.3 Earthquake magnitude and scaling laws

There has been a substantial amount of work undertaken to determine scaling laws for earthquakes using fault attributes (e.g., Childs et al., 2009; Faulkner et al., 2011; Gudmundsson, 2004; Kanamori and Anderson, 1975; Kim and Sanderson, 2005; Savage and Brodsky, 2011; Scholz, 1982; Scholz et al., 1986; Schultz et al., 2008; van Der Zee et al., 2008; Wells and Coppersmith, 1994; Wibberley et al., 2008). Understanding the relationship between these attributes is important for a wide range of purposes in geology, including estimating strain distribution in a region (e.g., Walsh and Watterson, 1991), developing models for fault growth (e.g., Cartwright et al., 1995; Cowie and Scholz, 1992a; Walsh et al., 2002; Walsh and Watterson, 1988) and forecasting spatial distribution of faults (e.g., Torabi and Berg, 2011). Some of these scaling laws relate rupture slip u, the relative movement of formerly adjacent points on opposite sides of a fault in a single earthquake, or seismic moment M_0, a measure of earthquake size, to the dimensions (i.e. length L, width W, depth) of a fault or rupture (e.g., Anders and Schlische, 1994; Kolyukhin and Torabi, 2012).

Seismic moment M_0 can be calculated using $M_0 = GA\bar{u}$ (Aki, 1967), where G is the modulus of rigidity, A is the fault area (L^2 to L^3 depending on earthquake size, as described below) and $\bar{u}$ is the average slip across the fault surface. Where the coseismic slip is unknown, the slip-length ratio α may be used to infer what the average slip in a characteristic earthquake may be. The slip-length ratio α is assumed to be between 10^{-5} and 10^{-4} (Scholz, 2002; Wells and Coppersmith, 1994), whereby slip $\bar{u}$ has a constant scaling relationship with fault length L (assuming a constant stress drop). Fault width W also scales linearly with slip $\bar{u}$ (Gillespie et al., 1992; Walsh and Watterson, 1988). Seismic moment can then be used to calculate the moment magnitude M_W using $M_W = \frac{2}{3}\log M_0 - 6.05$ (Hanks and Kanamori, 1979).

For small earthquakes the seismic moment is suggested to follow $M_0 \propto L^3$, whereas for large earthquakes the relationship is $M_0 \propto L^2$, where L is the fault (rupture) length (Scholz, 1982; Shimazaki, 1986). Here, large earthquakes are defined as those that rupture approximately the entire thickness of the seismogenic zone (Scholz, 1998). More recent studies have suggested that for $M < 5$ earthquakes $M_0 \propto L^3$ is applicable, but for $M > \sim 5$ earthquakes $M_0 \propto L^{2.5}$ applies (e.g., Leonard, 2010).

As fault slip $\bar{u}$, length L and width W are proportional to M_0 and thus M_W, they are important fault characteristics in seismic hazard assessment. For example, fault lengths of up to 35 km may occur in the Gulf of Corinth rift (Micarelli et al., 2003), resulting in an estimated maximum earthquake magnitude of around M_W 7 (e.g., Avallone et al., 2004; McKenzie, 1972; Roberts and Jackson, 1991), whereas in the Baikal rift the length of the major faults can be up to 80 km (Sherman, 1992), meaning earthquakes with magnitudes greater than 7 can occur (Doser, 1991). The thicker seismogenic layer of the Baikal rift, at around 30 km (Déverchere et al., 2001), when compared to the Gulf of Corinth, may explain why it can produce larger faults and larger earthquakes. The short fault lengths within the Gulf of Corinth rift may also be because the applied strain has reached a certain value capable of producing constant spacing distributions for the normal fault population, which evolves with accumulation of fault displacement rather than fault lengthening (Poulimenos, 2000).

The correlation between seismogenic thickness and fault length is not absolute, however. The Basin and Range Province has a seismogenic thickness typical for a continental environment (10 to 15 km; Zoback et al., 1981), but still produces long, normal faults. Fault lengths can grow to 100 km (DePolo et al., 1991), and as a result, the Basin and Range Province is capable of large earthquakes, as shown by the 1887 M_W 7.5 Sonora and the 1872 M_W 7.7 Owens Valley earthquakes, both of which had a rupture length of around 100 km (Herd and McMasters, 1982; Wallace, 1984b). The lengths of faults are therefore not only determined by the mechanical properties of the lithosphere they reside within, but also due to other processes such as fault interaction and linkage; we explore these concepts later in Section 1.1.7.

Despite some anomalies to the relationship between fault length and seismogenic thickness, as down-dip width is inherently proportionally to the seismogenic thickness (e.g., Jackson, 2001; Shaw and Scholz, 2001), the maximum rupture width is proportional to the seismogenic thickness. As a result, rifts with thick seismogenic layers comprise faults whose width W, and thus rupture area A for earthquakes, is potentially larger than typical for continental settings, which subsequently increases the potential seismic hazard according to the scaling laws above. For example, the Baikal rift, which shows morphological evidence for several prehistoric earthquakes between M_W 7.5 and 8 (Chipizubov et al., 2007), may produce larger events than regions with a small seismogenic thickness, such as the Basin and Range Province.

Fault area also influences the recurrence interval between earthquakes, which is found by dividing slip u by slip rate r. As fault rupture area A is proportional to seismogenic thickness, and maximum u is proportional to A, the maximum recurrence interval is therefore proportional to seismogenic thickness. As such, regions with large seismogenic thicknesses may have longer recurrence interval for events than regions with smaller seismogenic thicknesses, which may explain why several large $M_W > 7$ events have been recorded on in the Basin and Range Province (e.g., Herd and McMasters, 1982; Wallace, 1984b) but not along the Baikal rift. Of course, this also relates to the strain rate within the regions, as mentioned earlier in Section 1.1.

Faulting is a complex process, which may be influenced by numerous factors such as pre-existing structures (see Section 1.1.4), rheology and heterogeneity; therefore, values obtained from scaling relationships such as those presented above should not be considered absolute. Errors and uncertainties, and variations in time and space, should also be considered.

1.1.4 The influence of pre-existing structures

So far we have focused on characteristics of the lithosphere (and assumed homogeneity) such as its thickness and mechanical behaviour; however, other controlling parameters such as fault reactivation and strain localization on pre-existing structures have been shown to be important when studying fault development and deformation (Bellahsen and Daniel, 2005). These pre-existing structures are often defined as faults, folds, shear zones, dykes and gneissic foliations that are attributed to earlier orogenies (Ebinger et al., 1987), but may also be weak, thin, and/or warm lithospheric blocks that localise strain in the mantle and lower crust (e.g., Tommasi and Vauchez, 2001). The influence of pre-existing structures and strain localization has been used to explain why rifts such as the Recôncavo-Tucano rift in northeast Brazil (e.g., Destro et al., 2003) and the Gulf of Aden rift (e.g., Withjack and Jamison, 1986) strike orthogonal to the direction of far-field tectonic forces.

Strain localization above pre-existing faults has been hypothesised from several reactivated fault systems (e.g., Morley et al., 2004; Walsh et al., 2002). It is typically thought that the EARS reactivates numerous pre-existing structures within the basement, formed from previous tectonic events (e.g., Chorowicz, 2005; Ebinger et al., 1987; Ring, 1994). Using satellite imagery, airborne magnetic, radiometric and gravity data, faults in the Albertine and Rhino grabens in Uganda have been shown to follow well-oriented pre-existing structures (Katumwehe et al., 2015), suggesting such structures may indeed localise strain over the scale of entire rifts. Furthermore, geophysical analysis of the Main Ethiopian Rift supports the

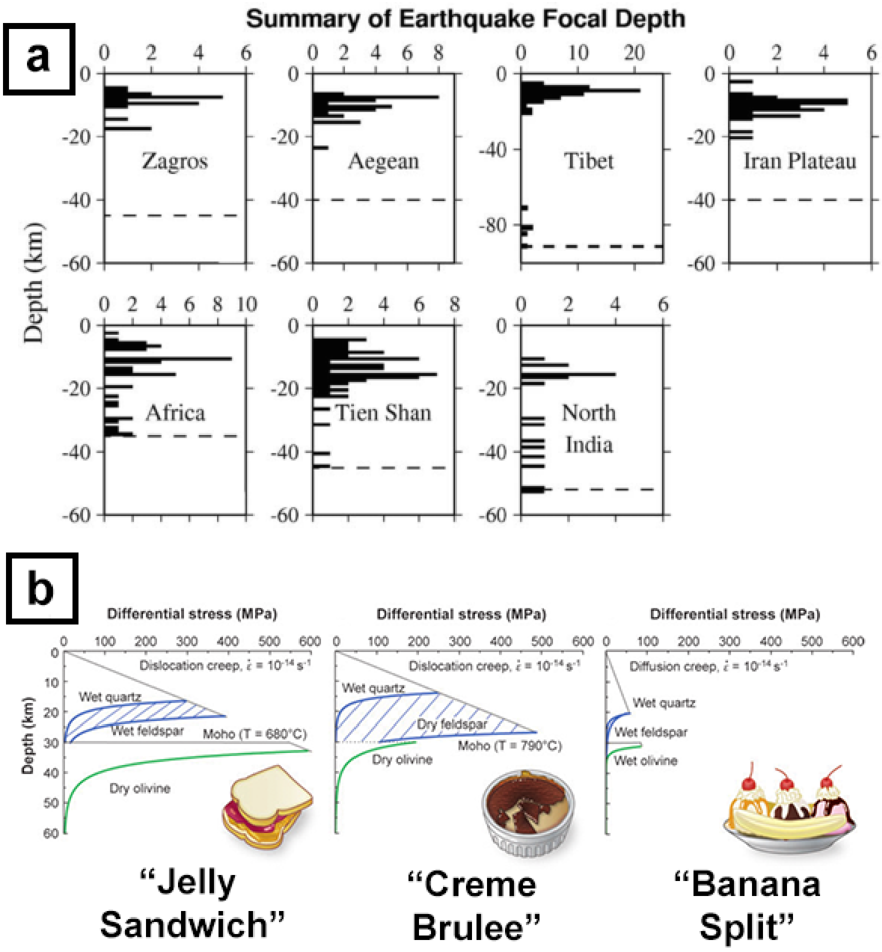

Fig. 1.5 a) Depths of earthquakes from waveform modelling in various continental regions where lower crustal earthquakes occur. The dashed lines show the depth of the Moho estimated using receiver functions. Taken from Mckenzie et al. (2005). b) Schematic view of alternative first-order models of strength through continental lithosphere. Taken from Bürgmann and Dresen (2008).

concept that the pre-rift lithospheric structure controlled the initial rift evolution (Corti, 2009). However, at a more local scale, faults along the Malawi Rift System have been observed to have an inconsistent angular relationship to pre-existing structures, where in sections the border faults follow the pre-rift fabric and in other sections the faults cross-cut the fabric (Laó-Dávila et al., 2015). Over the scale of an individual fault, the influence of pre-existing structures is even less clear (e.g., Phillips et al., 2016; Whipp et al., 2014). In the Suez rift, foliation-oblique faults reflecting the stress at fault initiation, are hard-linked by foliation-parallel faults (McClay and Khalil, 1998).

As well as field-based observations, laboratory-based experiments have been used to look at the influence of pre-existing structures on fault development. For example, sandbox models are a widely used tool to investigate normal fault geometries, evolution and propagation (e.g., Aanyu and Koehn, 2011; Athmer et al., 2010; Morley, 1999a; Ventisette et al., 2006). However, to mimic the natural systems, the sand itself should contain pre-existing fabrics (Morley, 1999a). Sand is used as an analogue for the brittle upper crust because it has the correct frictional characteristics; however, it lacks tensile strength due to a lack of cohesion between component grains. Silicone putty is also used to represent the ductile lower crustal layer (Bellahsen and Daniel, 2005). Many have found that activation within the brittle, upper crust is more likely to occur when the angle between the strike of the pre-existing structure and the extension orientation is large (i.e. $> 70°$, fig. 1.6; Bellahsen and Daniel, 2005). Analogue models also show that planar mechanical anisotropy (foliations in rocks) control fracture nucleation and evolution orientation (e.g., Gomez-Rivas and Griera, 2012), agreeing with rock deformation experiments that show foliated rocks are frictionally weaker than non-foliated samples (e.g., Collettini et al., 2009).

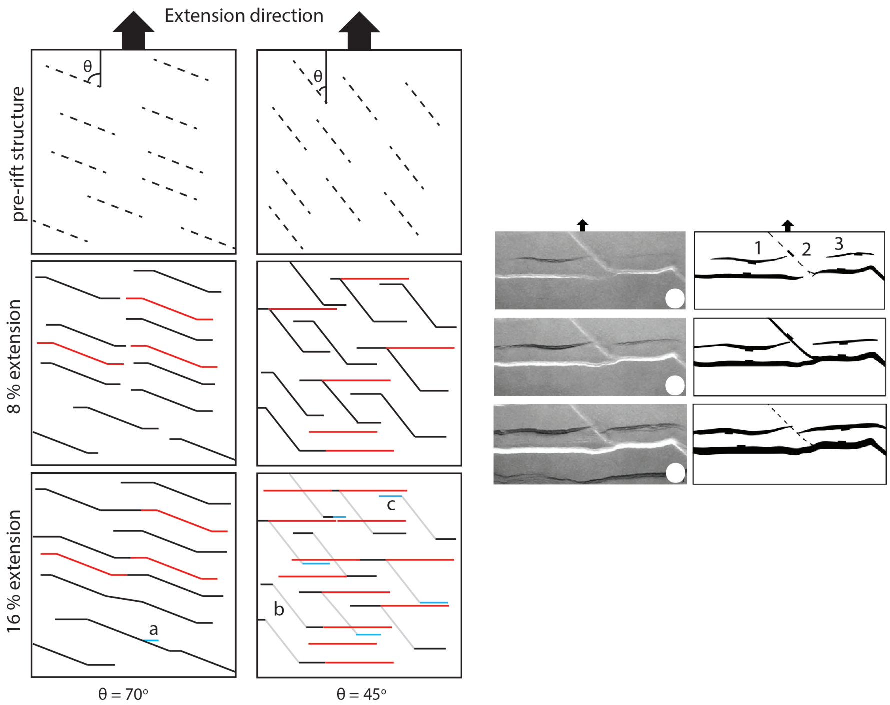

Fig. 1.6 Sandbox experiments by Bellahsen and Daniel (2005) showing the influence of pre-rift structure angle. Pre-existing structures here created by placing pieces of cardboard in the sand layer, down to the top of the lower silicone layer, at various strikes and dips. The introduction and removal of the cardboard creates zones of dilation as a result of grain re-arrangements. When θ is larger (left) fault activation is more favourable than when θ is smaller. Red lines indicate new surface ruptures, blue indicate unfavourable segments and grey represent inactive segments. With a large θ, fault development occurs along the pre-rift structures and perpendicular to the extension direction, segments that are less favourable may exist (a). As extension increases with a smaller θ angle, pre-rift structures become less favourable and eventually become inactive. This is shown on the right hand side where development of segment 2 ceases, allowing segments 1 and 3 to join as stress fields are overcome. Modified after Bellahsen and Daniel (2005).

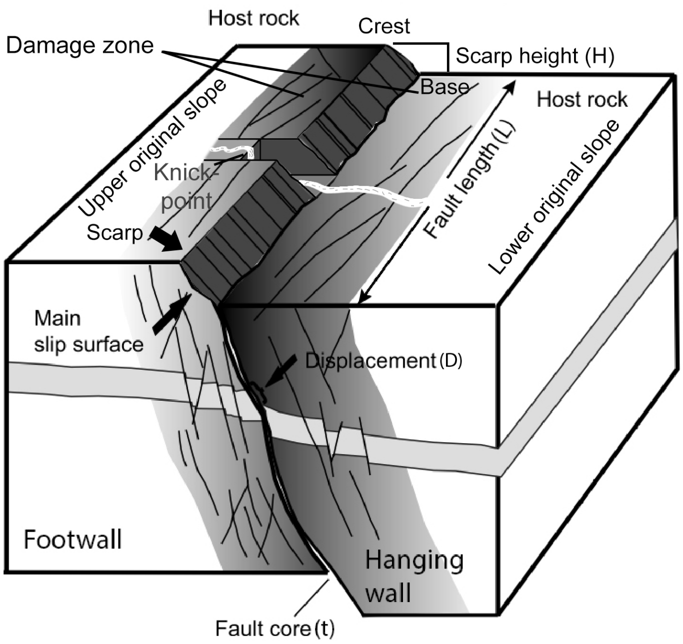

Fig. 1.7 Diagram of main fault attributes including displacement D, fault length L and scarp height H for a normal fault. A fluvial knickpoint has retreated from the scarp location. Modified after Kolyukhin and Torabi (2012).

1.1.5 Fault displacement and scarps

Following an earthquake rupture on a normal fault, footwall uplift is an isostatically driven viscoelastic response (e.g., Anders and Schlische, 1994), and although the role of isostasy is debated (e.g., Gibson et al., 1989), footwall uplift is proportional to displacement. Here, displacement D is the term used to describe the finite (total) relative movement of two fault blocks on a fault plane measured parallel to the slip vector, whereas slip u is used to describe the incremental movement per event (e.g., Walsh and Watterson, 1988; Xu et al., 2006). If the displacement is measured at the surface, we use the symbol D_s. The average ratio between maximum displacement D_{max} and fault length L for a normal fault is $\sim 10^{-2}$ (Kim and Sanderson, 2005), whereas the ratio between slip u and length is $\sim 5{\times}10^{-4}$ (Scholz, 2002). The component of vertical displacement on a fault, measured in a cross section parallel to the dip direction, is called 'throw' and the horizontal component, 'heave'. For normal faults operating under pure Andersonian conditions (i.e. dip of 60°), the majority of the displacement is represented by the throw, but for low-angle normal faults the heave may be considerably larger than the throw. Ruptures that propagate to and break the Earth's surface produce topographical offsets called fault scarps (fig. 1.7). Along rivers, the surface displacement produces vertical offsets in the longitudinal profile called knickpoints (Arrowsmith et al., 1996; Commins et al., 2005; He and Ma, 2015; Wei et al., 2015).

The term 'upper original surface' and 'lower original surfaces' describe the Earth's surfaces that have been offset by the fault (fig. 1.7). The base and the crest of the fault scarp refer to, respectively, the lower and upper edges of the scarp. The difference in elevation between the original surfaces is the scarp height H, which may represent the fault throw (Morley, 2002). However, subsurface displacements may be several times greater than what is represented at the surface (Villamor and Berryman, 2001), and the scarp height may be affected by erosional processes.

A newly formed fault scarp typically comprises a steep 'free face', a 'debris slope', the talus accumulation below the free face, and a 'wash slope', part of the scarp controlled by fluvial erosion or deposition (Wallace, 1977). The surface of a new fault scarp is steep, typically in a range from 50° to vertical (Bucknam and Anderson, 1979), and therefore exceeds the angle of repose of the material the scarp breaks through at the surface (Nash, 1984). As the fault scarp slope exceeds the angle of repose, erosional processes begin to alter its morphology. Loose debris fall from the scarp under the influence of gravity, and precipitation and surface waters wash material from the surface (Wallace, 1977). The initial dominant erosional process is gravitational displacement of scarp material, but over time, this is replaced by erosion from water. The shape of the scarp as a function of time is similar to the shape of a conductive temperature-distance profile evolving with time (Hanks et al., 1984), i.e., is diffusional, and results in a gradual smoothing of the scarp.

The geomorphology of a fault scarp can be used to infer a faults rupture history. A fault scarp formed due to a single earthquake rupture is termed a 'piedmont scarp' or 'single rupture scarp' (fig. 1.8a; Stewart and Hancock, 1990). If subsequent earthquakes along the same fault plane break the surface, the scarp height increases and a new steep free face can be observed. Scarps formed by multiple earthquakes along the same fault plane are coined 'composite scarps' (fig. 1.8b; e.g., Mayer, 1982). An example of a composite fault scarp is observed on the Kamishiro fault, Japan, where the 2014 Nagano earthquake produced 0.3 m of vertical surface displacement on a pre-existing scarp of height 0.7 m (e.g., Lin et al., 2017). Over time, degradation of a composite fault scarp removes the free face and creates a morphology indistinguishable from a piedmont scarp that has undergone degradation.

During earthquakes, however, faults may splay near the surface (e.g., Anders and Schlische, 1994; Kristensen et al., 2008; Nash, 1984; Slemmons, 1957). These splays cause fault planes separated by several metres even during surface ruptures of less than 10 km (e.g., Lin et al., 2017). In subsequent events, slip may occur on a different fault plane to the previous event, producing a series of fault scarps that are horizontally offset from one another, sometimes called multiple scarps, but here coined 'multi-scarps' (fig. 1.8c; e.g., Mayer, 1982). Fault healing processes

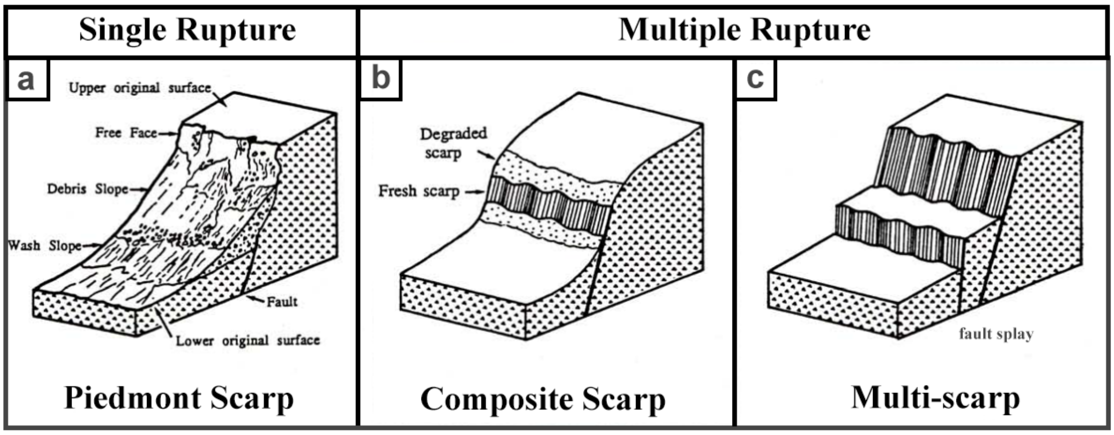

Fig. 1.8 Types of normal fault scarps. a) A piedmont scarp, or single rupture scarp, resulting from a single increment of displacement at the surface. A fresh fault comprises a steep free face, and debris and wash slope surfaces, separating the upper and lower original surfaces. b) A composite scarp, formed by multiple ruptures on a single fault plane. c) A multiple scarp, developed from a incremental ruptures on near surface fault splays. Scarp surfaces are separated by terraces. Modified after Stewart and Hancock (1990).

may also lead to slip on a different fault plane (e.g., Noda et al., 2013; Perrin et al., 2016a; Shaw and Scholz, 2001).

In addition to the morphology of the scarp surface, the surrounding geomorphology may also indicate rupture history of a fault. For normal faults comprising large throws, triangular facets may form at the end of ridges. Over multiple earthquake cycles, multiple steps of triangular facets can develop (Hamblin, 1976). Alluvial fans may also be used to provide relative dating between earthquake events (e.g., Amit et al., 1996; Mueller and Rockwell, 1995). Dating of scarp sediments may also allow for different events to be identified (e.g., Lin et al., 2017). In addition, the deposition of these sediments can cause successive sedimentary layers to build up; by excavating a trench at the base of the scarp, this succession can be recorded, and the fault surfaces associated with each event may be evident (e.g., Lin et al., 2017). Studying the fault rocks, using microstructural and mineralogical techniques, may also highlight the evolution of cataclastic deformation bands, slip surfaces and fractures associated with multiple events (e.g., Shipton et al., 2017).

In addition to providing a relative timing of earthquake events, fault scarp studies also reveal information regarding the spatial and temporal distribution of faults and faulting. For individual faults and fault systems, studying the complex geometry and morphology of a fault and fault scarp can lead to the understanding of fault evolution processes, including the identification of fault structural segmentation (e.g., Giba et al., 2012; Manighetti et al., 2015; Watterson, 1986), provide clues to the structural development of a fault (e.g., Ren et al., 2016; Sieh, 1978; Wallace, 1968; Zielke et al., 2012), indicate segment interaction

(Hilley et al., 2001; Willemse et al., 1996), the potential for hard-linkage between fault segments (e.g., Crider and Pollard, 1998), and can be used to infer fault displacement and the presence of a linking structures (e.g., Nicol et al., 2010; Soliva and Benedicto, 2004). These process are explored below in relation to normal faults in continental rift environments.

1.1.6 Fault evolution

Segmentation of faults appears to be an inherent characteristic of active normal faults (e.g., Crider and Pollard, 1998; Peacock and Sanderson, 1991; Schwartz and Coppersmith, 1984; Wesnousky, 1986). As a result, we define two assumptions about faults and their evolution: (i) faults are seldom isolated structures, they often exist in close proximity to other faults in fault zones or fault systems; and (ii) fault segments interact and establish linkages.

The term 'segment' when used to describe fault segmentation has many different definitions (DePolo et al., 1991). Earthquake segmentation involves the identification and characterization of discontinuities along faults that may potentially be barriers to rupture propagation (e.g., DuRoss et al., 2015; Ganas et al., 2006; Palyvos et al., 2005). Here, structural segmentations are defined by fault bends, step overs, separations, or gaps in the fault zone, also known as geometrical segments (e.g., Crone and Haller, 1991). Structural discontinuities comprise fault splays, fault intersections, and terminations at other structures. Thus, as fault zone ends can be considered as structural discontinuities, individual faults may be classified as structural segments. Earthquake segmentation may not be confined to structural segments (Wheeler, 1987), as ruptures may jump across geometrical gaps of several kilometres (Wesnousky, 1986). For normal faults, ruptures such as the 62 km long rupture of the 1954 M_W 7 Fairview Peak earthquake, Nevada have been observed to jump gaps as large as 10 km (Biasi and Wesnousky, 2016). In areas with limited data, it is difficult to quantify the earthquake segmentation length, as propagation through potential barriers may not have yet been observed due to the repeat time of ruptures being longer than the length of the instrumental earthquake catalogue. Throughout this thesis, the term 'fault segment' is used as a shorthand version for a structural segment along a fault.

Studying fault segmentation is crucial in estimating seismic hazard, as if a rupture terminates at structural segment boundaries, the rupture length, M_0, and M_W will be profoundly different to if a rupture propagates the entire fault length (Anders and Schlische, 1994; Gupta and Scholz, 2000; Kase, 2010; Segall and Pollard, 1980; Willemse et al., 1996, see Section 1.1.3; e.g.,). Furthermore, as structural segmentation can also occur with depth, significant seismic hazard can remain even after a devastating earthquake. For example, the 2008 M_W 6.3 Qaidam earthquake in northwestern China ruptured the lower half of the seismogenic layer, then in 2009 a second M_W 6.3 earthquake ruptured the upper section (Elliott et al., 2011). This depth segmentation may exist on the fault that hosted the 2003 M_W 6.6 Bam earthquake in Iran, as satellite radar and aftershock measurements show that the event only ruptured the upper half of the 15 to 20 km deep seismogenic region (Jackson et al., 2006).

If structural segmentation is indeed an inherent characteristic of active normal faults, then it is important to consider how fault segments coalesce to form the larger fault structure. In other words, to understand how the fault segments grow, interact and link. To infer the structural history of a fault, a fault's maximum total displacement D_{max} relative to its length, and variations in total displacement D along a fault's length, can be used (e.g., Kolyukhin and Torabi, 2012; Ren et al., 2016; Sieh, 1978; Wallace, 1968; Zielke et al., 2012).

1.1.7 Fault growth and interaction

The maximum total displacement on a fault relative to its length, termed a fault's displacement-length (D - L) ratio, has been found to be fairly constant within a particular setting (fig. 1.9; Dawers and Anders, 1995; Gupta and Scholz, 2000; Walsh et al., 2002). It is assumed that the relationship between maximum total displacement and length follows the equation $D_{max} = \gamma L^{\mathrm{n}}$, where the value of γ is an expression of the fault displacement at unit length, which is related to the properties of the rock such as shear strength and elasticity (Cowie, 1998; Gillespie et al., 1992; Kim and Sanderson, 2005; Schultz et al., 2008). The value of n is also important; a value of 1 denotes that the relationship is linear, implying that the fault grows under constant driving stresses and behaves similarly at a variety of scales (Schultz et al., 2008). Conversely, a value other than 1 would imply the fault system is scale-dependent (Kim and Sanderson, 2005). The average ratio between maximum displacement and fault length for a normal fault is $\sim 10^{-2}$ (Kim and Sanderson, 2005).

The differences in the D - L ratio between regions (fig. 1.9) implies that not all faults or fault zones behave in a consistent manner. Observations from field and seismic data, as well as analogue and numerical models, have led to two theories of how faults grow: (1) through agonistic increases in displacement and length (termed the 'isolated fault model', fig. 1.10a; Cartwright et al., 1995; Dawers and Anders, 1995; Dawers et al., 1993; Walsh and Watterson, 1988; Watterson, 1986); or (2) a rapid establishment of a fault's near-final length early in its slip history, followed by a longer period of displacement accumulation (the 'constant-length fault model', fig. 1.10b; Giba et al., 2012; Jackson and Rotevatn, 2013; Morley, 2002; Schultz et al., 2008; Walsh et al., 2003, 2002). The isolated fault model has been the

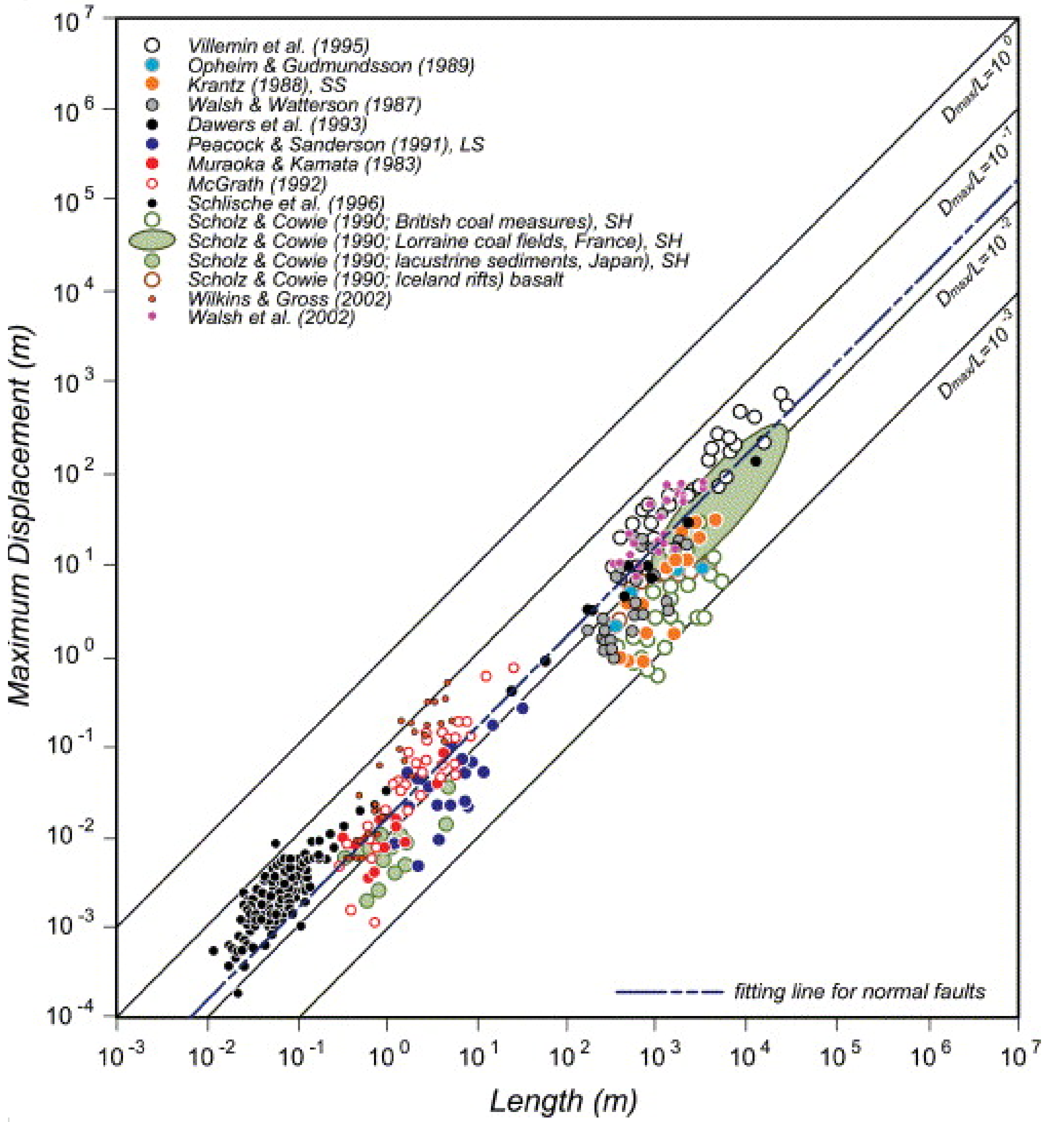

Fig. 1.9 Global maximum total displacement D_{max} for a fault compared to its length, i.e. the displacement-length (D - L) plot. Blue dotted line shows the best fitting line for normal faults (D_{max} = 0.02 L). Taken from Kim and Sanderson (2005).

mainstay theory of fault growth in recent decades, and the support of this growth mechanism was largely founded on geometrical criteria alone; however, for a number of reasons this may not be appropriate (Jackson et al., 2017). Firstly, as shown in fig. 1.10, it is difficult to discriminate between a fault formed by linkage of several low displacement segments (i.e. following the isolated fault model) and one that grew as a single structure and established its near-final length early in its slip history (i.e. following the constant-length fault model). This is because both would have low displacement values compared to their length. In addition, the mechanical properties of the stratigraphy the fault forms in may prohibit displacement accumulation due to decoupling and distributed deformation in bounding ductile layers (e.g., Benedicto et al., 2003; Soliva and Benedicto, 2005). Furthermore, these opposing mechanisms for growth may be specific to single faults, as some regions exhibit evidence for both, such as the Suez rift (e.g., Fossen and Rotevatn, 2016; Gawthorpe et al., 2003; Jackson et al., 2005, 2002). A fault's D - L ratio alone therefore may not provide enough information to infer its structural evolution.

Whereas the D - L ratio is suggested to remain fairly constant for a particular region, the displacement along an individual fault may be highly variable and can provide fundamental information regarding a fault's rupture history, such as structural and earthquake segmentation, fault development and linkage (e.g., Anders and Schlische, 1994; Cartwright et al., 1995; Jackson et al., 2017; Walsh et al., 2002; Whipp et al., 2014). In some studies, subsurface displacement D is used (e.g., Anders and Schlische, 1994; Cartwright et al., 1995; Jackson et al., 2017; Walsh et al., 2002), whereas in others the surface displacement D_s is used instead (e.g., Biasi and Weldon, 2006; Dawers et al., 1993; Peltzer and Rosen, 1995; Whipp et al., 2014). In addition, these profiles are sometimes constructed by measuring throw (e.g., Rotevatn and Bastesen, 2014), or the term slip is used to represent displacement (e.g., Manighetti et al., 2001). Here, we collectively refer to these types of plots as displacement-length profiles, but acknowledge that displacement can be measured in a number of ways.

The overall shape of a fault's displacement-length profile can display a range of geometries including an approximately symmetrical bell-shape with displacement maxima at the centre, triangular asymmetrical shape with relatively steep gradients towards one tip, or flat-topped profiles with high gradients at both tips (fig. 1.11; e.g., Manighetti et al., 2001; Nicol et al., 2010; Peacock and Sanderson, 1991; Walsh and Watterson, 1987, 1990). It has been suggested that bell-shaped appearance of the displacement-length profile forms as a result of the model of faulting proposed by Cowie and Scholz (1992b), which involves a process zone at the fault tips, and depict a mature, linked fault (e.g., Anders and Schlische, 1994; Schlische et al., 1996; Willemse, 1997). Triangular asymmetric profiles, however, are more common and are the result of segmented earthquake ruptures (e.g., Manighetti et al., 2015, 2001, 2009; Nicol et al., 2005; Soliva and Benedicto, 2004), where surface slip tapers in the direction of long-term fault propagation (e.g., Manighetti et al., 2015, 2001).

The displacement-length profile of a fault rarely conforms to such idealised shapes as described above. One reason may be that local variations in displacement are the result of variations in slip during an earthquake rupture (e.g., Rockwell et al., 2002). For example, the 2001 Kokoxili earthquake shows intense variability in its represented surface displacement, perhaps a result of variations in the fault's geometry (e.g., Klinger et al., 2005). Other reasons may be due to measurement

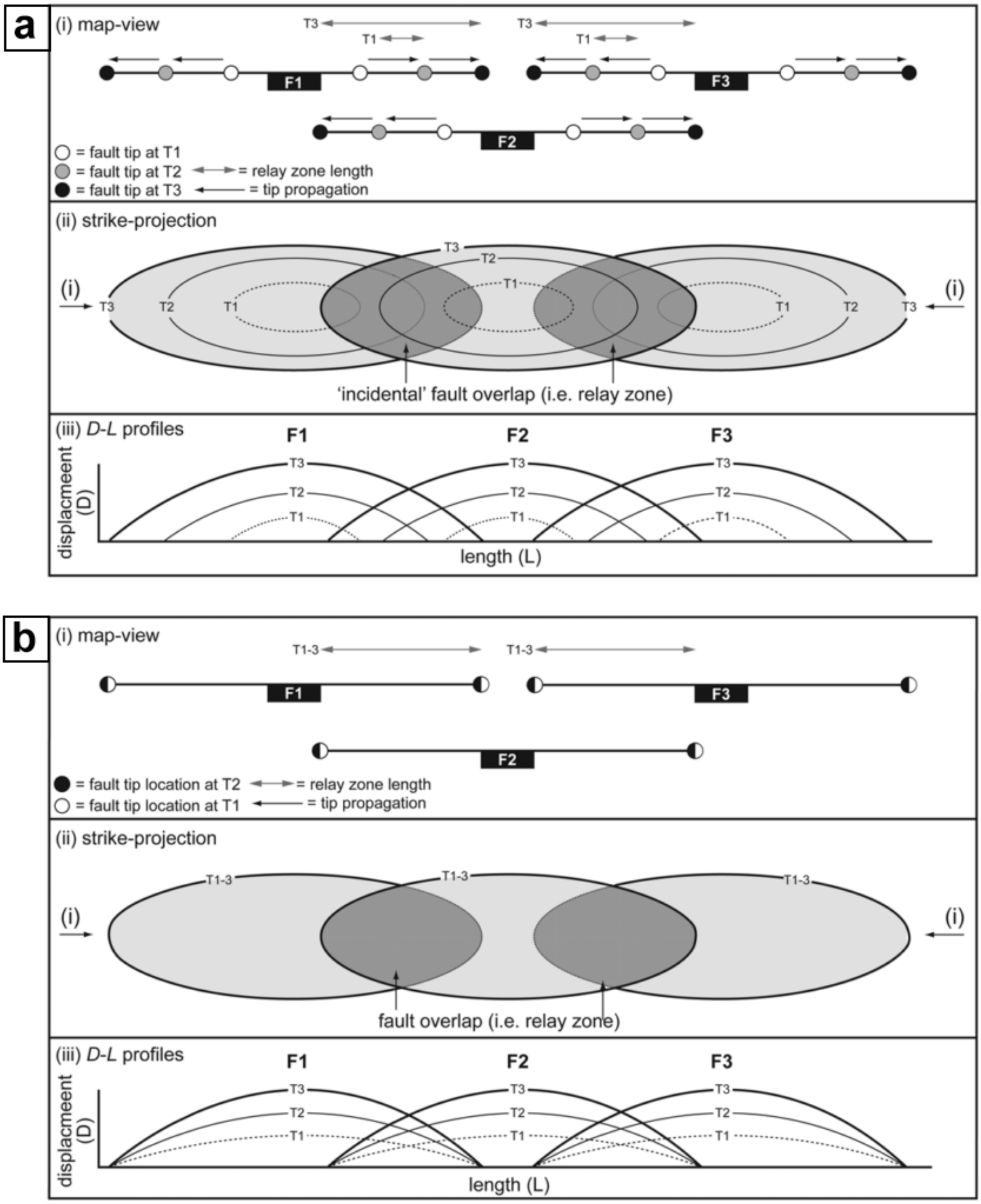

Fig. 1.10 Conceptual models for the development and growth of normal faults. a) The isolated fault model; and b) the constant-length fault model. The (i) map-view, (ii) strike-projection and (iii) subsurface displacement D - L profiles are shown to illustrate the key geometrical and evolutionary aspects of each model. Black arrows in (ii) show the fault level of the map shown in (i). F1-3, faults 1-3; T1-3, time-steps 1-3. Because the final fault length developed by both examples is similar, it may be difficult to conclude what model best described its evolution if observing from the end time-step. Taken from Jackson et al. (2017).

uncertainties and local site effects, or different responses to the seismically induced strains (Zielke et al., 2015). Variations in surface displacements may also result from the incremental evolution of a fault over multiple earthquake cycles (i.e. growth, interaction and linkage), and be used to infer structural segmentation.

For a segmented fault, structural segments are marked by peaks in surface displacement separated by narrow, pronounced displacement troughs (Manighetti et al., 2009). The area between structural segments is termed the inter-segment zone. The largest segments, whose lengths are approximately the same order of magnitude as the entire fault length, are termed 'major segments' (e.g., Crone and Haller, 1991; Gawthorpe and Hurst, 1993; Manighetti et al., 2007, 2009). Major segments then typically comprise a number of smaller 'secondary segments' (e.g., Cartwright et al., 1995). The number of segments may indicate the age of the fault, whereby the number of segments slightly decreases with fault structural maturity (Manighetti et al., 2015).

Fault segment interaction and linkage appears to be an essential feature on all fault systems and occurs on timescales of individual earthquakes to millions of years (Nicol et al., 2010). Understanding how the process of fault interaction and linkage occurs is important as a rupture of one fault segment can profoundly influence other fault segments and the rupture sequence, perturbing or promoting segment failure (Crider and Pollard, 1998; Gupta and Scholz, 2000).

There are two main types of fault linkage: hard linkage, where fault segments are physically linked to another fracture or fault (fig. 1.11e-f); and soft linkage, where faults only interact through their stress fields (fig. 1.11c-d; Gupta and Scholz, 2000). Rupture jumps across geometrical discontinuities are examples of soft linked fault interactions. Many have proposed that hard linkage occurs when faults grow in length until they overlap, this develops a relay ramp, which then becomes faulted and the initially independent faults eventually link to form a larger fault (fig. 1.11; e.g., Cartwright et al., 1996; Gupta et al., 1999; Peacock, 2002). Evidence from rift systems such as the Suez rift, however, indicate that hard linkage may occur during the underlapping phase (Jackson et al., 2002). Whether faults interact and link has been suggested to be dependent on the stress fields of each fault (Segall and Pollard, 1980, 1983). Faults respond to reductions in shear stress around other nearby faults by accumulating an anomalous displacement (Gupta and Scholz, 2000). On interacting faults the maximum displacement becomes shifted toward the interacting fault tip (Gupta and Scholz, 2000; Willemse et al., 1996). The ratios between separation and overlap may give an estimation of fault interaction and linkage potential (Childs et al., 1995).

Fault segment interactions have been proposed to occur through a number of mechanisms, including dynamic coseismic stresses (e.g., Duan and Oglesby, 2005; Harris and Day, 1999) and driving forces associated with interseismic strain accumulation (e.g., Dolan et al., 2007; Peltzer et al., 2001; Wedmore et al., 2017b). Static coseismic stress changes have also been shown to influence fault interactions (e.g., Duan and Oglesby, 2005; Harris, 1998; Harris and Day, 1999; King and Cocco, 2001; Stein, 1999). Much of the previous attempts to understand fault interaction and linkage has focused on strike-slip settings (e.g., Chemenda et al., 2016; Segall and Pollard, 1980; Stein, 1999), but as normal faults show evidence for structural segmentation, studies for normal fault evolution are required.

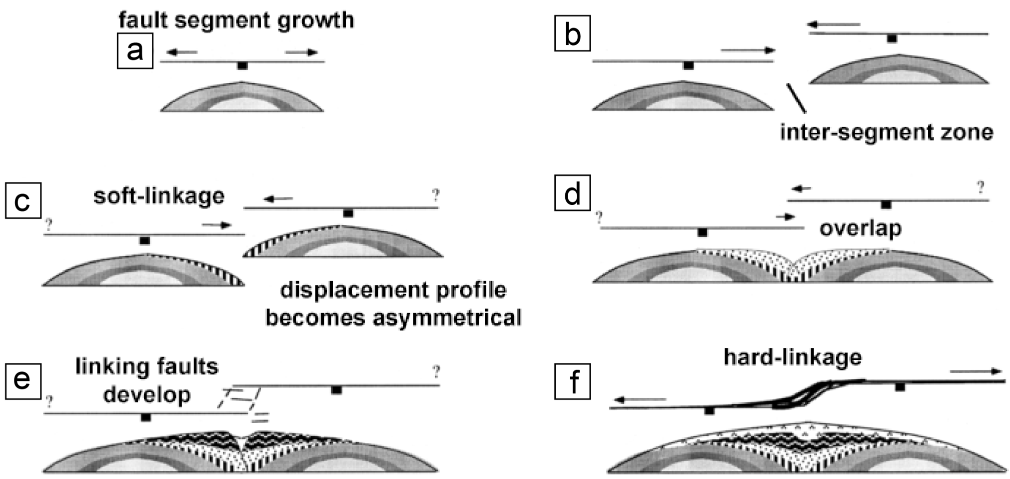

Fig. 1.11 The conceptual model of fault growth and hard linkage. a) Pre-interaction: fault segment growth in the direction shown. b) Initiation of interaction: during underlapping phase, an increase in shear stress may accelerate fault growth toward one another until a stress drop region is reached. c and d) Continued interaction: as faults reach the stress region, displacement occurs at tips of faults. Faults may overlap as shown in panel d. e) Formation of linking faults: once the critical stress drop is reached, minor linkage structures form and displacement occurs in the inter-segment zone. f) hard-linkage generation: linkage is complete and the displacement profile is similar to that of single fault segment (i.e. bell-shaped). Modified after Gupta and Scholz (2000).

1.2 Advances in remote sensing

Remote sensing techniques mean that distant faults over a wide area can be studied at relatively low cost. There are many advantages to using remote sensing, including pre-visit data collection and analysis, the ability to view an area at a much larger scale and at a variety of angles not possible on the ground, and to view the change in landscapes over time.

Over the past few decades satellite data has been used to extensively map active faults and geological structures (e.g., Johnson et al., 2014; Paton, 2006; Tronin, 2006), study fault kinematics and dynamics (e.g., Currenti et al., 2012; Ganas et al., 2005; Kinabo et al., 2008; Zhou et al., 2015), derive soil, geological and seismic maps (e.g., Reif et al., 2011; Shafique et al., 2011; Theilen-Willige, 2010), undertake geomorphological analyses (e.g., Arrowsmith and Zielke, 2009; Mildon et al., 2016; Peters and van Balen, 2007; Siart et al., 2009), as well as the analysis of lineaments from multi-spectral imagery (e.g., Duarah and Phukan, 2011; Geiß and Taubenböck, 2013; Kervyn et al., 2006; Masoud and Koike, 2011). Furthermore, remote sensing has also been used to quantify the strain partitioning between faulting and magmatism during discrete rifting episodes (e.g., Calais et al., 2008; Fielding et al., 2004), and quantify surface displacement and slip direction from an earthquake event (e.g., Biggs et al., 2010; De Lépinay et al., 2011; Shen et al., 2009). In addition, recent studies have used remote sensing tools such as InSAR to infer the interseismic strain accumulation across entire faults and fault zones, such as the central North Anatolian Fault (e.g., Hussain et al., 2016); this novel approach to calculating strain rate may become an invaluable tool for slow strain regions such as the Malawi Rift System that lack the geodetic coverage to resolve strain rate over the scale of individual faults.

As such, advances in remote sensing have increased the understanding of fault evolution at the surface, even in the most remote areas (e.g., Roux-mallouf et al., 2016; Talebian et al., 2016; Zhou et al., 2015). As mentioned previously (Section 1.1), brittle deformation may localise within slow strain rifts (Nestola et al., 2015). If the region also has a large seismogenic thickness, localization may occur on the wide, long faults the rift hosts (Jackson, 2001; Jackson and White, 1989; Scholz, 1998). Because slow strain rate regions typically have longer recurrence intervals between events (fig. 1.2) then it is possible that the maximum recorded earthquake magnitude does not reflect the maximum potential earthquake magnitude (e.g., Hodge et al., 2015; Li et al., 2017; Torizin et al., 2009). Therefore, it is important to study the geomorphology of faults and fault systems, which can help inform the record of prehistorical events (e.g., Torizin et al., 2009; Walker et al., 2015; Zhang et al., 1986).

Measuring surface displacements across a fault scarp has traditionally been performed by local field surveys, using levelling, or more recently, differential Global Positioning System (GPS) devices (e.g., Andrews and Hanks, 1985; Avouac, 1993; Bucknam and Anderson, 1979; Cartwright et al., 1995; Cowie and Scholz, 1992a; Delvaux et al., 2012; Gillespie et al., 1992). Whilst traditional geomorphological surveys of fault scarps using handheld devices are highly accurate, they are time-consuming, especially when a large number of measurements is required. In addition, coverage of measurements is governed by accessibility to the fault scarp. A limited number of displacement measurements along a fault scarp, however, limits the understanding of fault behaviour (e.g., Zielke et al., 2012, 2015). In addition, as changes in displacement along a fault scarp over a small scale may be missed due to accessibility, second-order or 'secondary' fault segments may not be identifiable from a low resolution displacement length profile (e.g., Cartwright et al., 1995; Manighetti et al., 2015; Trudgill and Cartwright, 1994).

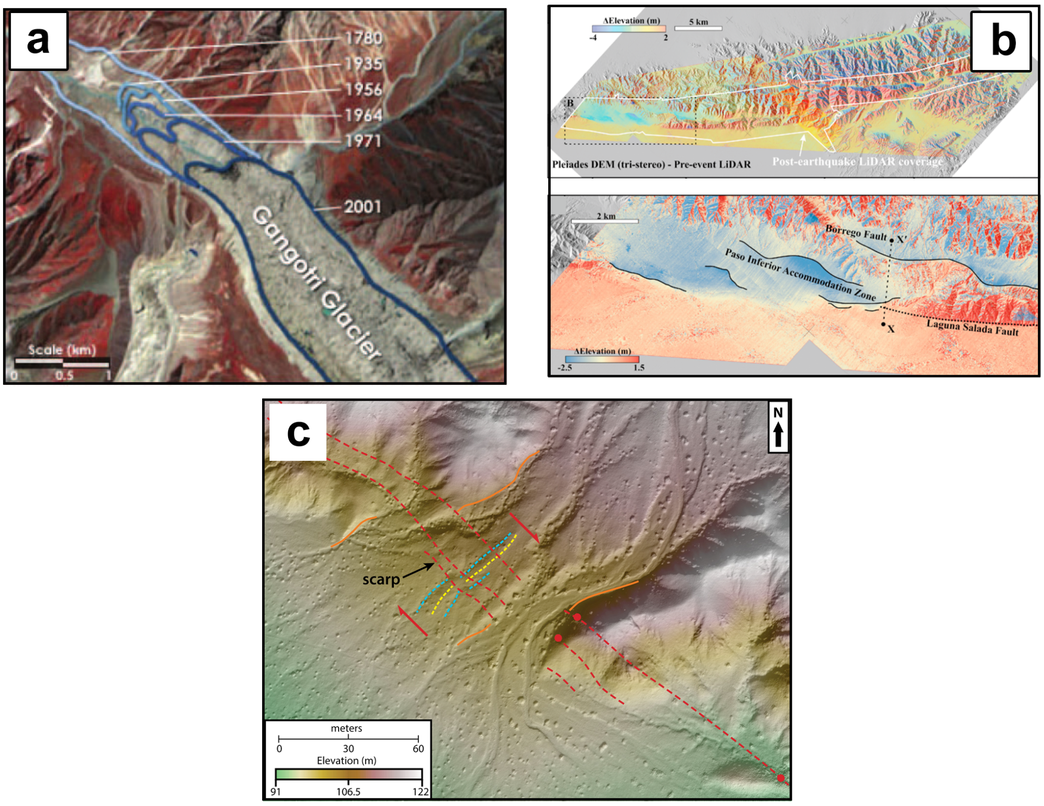

Fig. 1.12 A 10-year advance in remote sensing and satellite imagery. a) A 90 m ASTER DEM used by Toutin (2008) to measure glacial retreat. b) High resolution Pleiades tristereo used by Zhou et al. (2015) to compare satellite DEM performance against LiDAR DEM performance. In this study, sub-metre offsets were able to be measured for the El Mayor-Cucapah epicentral area. c) Sub-metre structure from motion (SfM) DEM along the San Andreas fault, taken from Johnson et al. (2014).

In recent decades, to address issues of accessibility and coverage, the use of satellite images in fault surface displacement studies has become increasingly prominent (e.g., Acocella et al., 2002; Gallant and Hutchinson, 1997; Manighetti et al., 2001). However, because photographs are inherently two-dimensional, the analysis of single optical images only allows for the identification and measurement of horizontal displacements. As a result, vertical displacements - which are a significant component of normal and reverse faults - cannot be measured. Using a two-pass stereoscopic correlation, panchromatic optical images can be processed to provide elevation data, which could be used to develop a digital elevation model (DEM); for example, the 10 m imagery obtained from the early SPOT 1 satellite could be used to generate a local DEM with a resolution of around 20 m (Allison et al., 1991). The creation of a DEM from satellite images meant that faults and fault scarps could be identified and vertical offsets measured remotely (e.g., Ganas et al., 1997). This approach meant that the large scale geomorphology of known fault systems could be analysed, but coverage was limited.

The launch of the Advanced Spaceborne Thermal Emission and Reflection Radiometer (ASTER) and Shuttle Radar Topography Mission (SRTM) programmes resulted in a near worldwide 90 m, and later 30 m, DEM. The ASTER and SRTM DEMs have become an important tool for the study of individual fault scarps (fig. 1.12a; e.g., Boulton and Whittaker, 2009; Hayes et al., 2010; Laó-Dávila et al., 2015; Manighetti et al., 2009; Toutin, 2008), but also allow for fault studies to be performed over the scale of an entire rift (e.g., Manighetti et al., 2015). Furthermore, SRTM data has been used to study the influence of inherited lithospheric heterogeneity for rifts such as the Malawi rift (Laó-Dávila et al., 2015), Rukwa basin (Delvaux et al., 2012), and the Albertine and Rhino grabens (Katumwehe et al., 2015). However, the resolution of SRTM and ASTER DEMs may not be sufficiently high to accurately identify and measure small displacements. This is especially problematic for fresh ruptures, since coseismic vertical displacements are typically less than the vertical resolution of ASTER or SRTM (e.g., Deng and Liao, 1996; Middleton et al., 2016; Walker et al., 2015; Yuan et al., 1991; Zhang et al., 1986).

The desire to produce a DEM with a higher resolution than the capabilities of ASTER and SRTM, lead to many geomorphologists using Light Detection and Ranging (LiDAR) (e.g., Arrowsmith and Zielke, 2009; Bubeck et al., 2015; Hilley et al., 2010). High resolution LiDAR DEMs have been used to assess the temporal development of a fault zone through the morphological relative dating of fault scarps (e.g., Hilley et al., 2010), and to infer relationships between faults and geomorphic processes, which have contributed to improved assessments of fault slip rates for rift environments such as the central Apennines (e.g., Bubeck et al., 2015). The cost and logistical demands of LiDAR, however, restrict its utilisation in many areas (Johnson et al., 2014). As a result, for remote regions, alternatives to LiDAR are required to understand fault evolution at the surface.

Through recent advances in technology and computing power, photogrammetric techniques applied to SPOT 1 imagery can be applied to very high resolution optical images from satellites including IKONOS, Pleiades 1A/1B, Quickbird, GeoEye-1, Worldview-1/2 and Worldview 3/4; each have a panchromatic resolution < 1 m. This technique, and its advanced counterpart, structure-from-motion (SfM) (e.g., Johnson et al., 2014; Joyce et al., 2009), can be used to create a high resolution DEM (< 1 m) from two or more optical images taken at oblique angles of the same location, or multiple overlapping geo-referenced images. The application of this technique has lead to numerous studies of fault scarps in which highly accurate and precise vertical displacements could be measured (fig. 1.12b; e.g., Roux-mallouf et al., 2016; Talebian et al., 2016; Zhou et al., 2015), with accuracies comparable to LiDAR, but at a fraction of the cost (Middleton et al., 2016; Zhou et al., 2015). Using high resolution DEMs to study faults and fault scarps provides new insights into the rupture history of slow slip faults such as the Huaxian fault (Zhou et al., 2014), and may help uncover seismic structures and geomorphic rupture markers obscured and removed by urban growth, as shown in central Tehran (Talebian et al., 2016).

Developing DEMs from high resolution satellite imagery can be expensive, and as this expense is proportional to the area covered, and storage and processing of vast datasets may be challenging, often large scale studies still use lower resolution DEMs (Delvaux et al., 2012; Katumwehe et al., 2015; Manighetti et al., 2015). In addition, many remote sensing studies for individual faults are coupled with field visits to validate their findings (e.g., Hamiel et al., 2012; Klinger et al., 2005; Rodgers and Little, 2006). The issue of cost and field visit requirements has meant that structure-from-motion techniques using Unmanned Aerial Vehicles (UAVs) have been utilised in generating small scale, high-resolution DEMs to map faults and undertake geomorphological analyses (e.g., Bemis et al., 2014; Gao et al., 2017; Johnson et al., 2014; Westoby et al., 2012). Furthermore, the use of UAVs and structure-from-motion can assist in generating very high resolution DEMs immediately following an earthquake rupture (Gao et al., 2017), or even during the aftershock sequence (Wedmore et al., 2017a), which may not be possible given the repeat times of satellites.

Here, we aim to combine field studies with a range of remote sensing tools to better understand fault evolution in early-stage rifts. A discussion of which remote sensing tools to use for each of our research aims is included within the thesis chapters.

1.3 Geological setting

1.3.1 East African Rift System

Above we have described fault and rift evolution processes in a number of rift settings. Each provides a unique case study for a distinct phase, or type, of rifting. Due to its size - the only currently active rift system present on a continent-wide scale (Yang and Chen, 2010) - and variation in magmatism, strain rate and seismogenic thickness, the 4,000 km long East African Rift System (EARS) displays a number of phases of rift maturity. For example, whereas the northern end of the EARS (i.e. Main Ethiopian Rift) is an example of an early rift system moving into a more mature phase, but not yet as mature as the Red Sea, the southern end of the EARS is still very immature in its evolution, akin to rifts such as the Baikal rift (Avallone et al., 2004; McKenzie, 1972; Roberts and Jackson, 1991). Ethiopia is a unique part of the rift, as from south to north, several stages of active rift development are exposed, ranging from continental rifting in the south to incipient oceanic spreading in Afar to the north. From the triple junction in Afar, moving southwards through Ethiopia, the EARS breaks into two separate branches, the western branch and the eastern branch. The eastern branch continues through the Ethiopian rift into the Gregory rift in Kenya and through to the Davie ridge (Mougenot et al., 1986), and is considered to represent a failed mature continental rift system (Morley et al., 1999). The western branch, regarded as a good model of a young continental rift (Morley et al., 1999), extends from northern Uganda through a seismically active region in Malawi (Ebinger, 2005) south to Mozambique (Fonseca, 2014) and/or west to Botswana (Modisi et al., 2000), hosting some of Africa's major lakes (Albert, Edward, Tanganyika and Malawi). The fact that the entire EARS is considered to be a narrow rift (Corti, 2009), despite passing through regions characterised by different lithospheric strength profiles (i.e., weak lithosphere in the MER and strong lithospheres in the eastern and western branches), likely indicates that inherited structure may be the primary control on the mode of extension in these continental rifts (Keranen et al., 2009). In the north, the western branch is characterised by a predominantly north-south orientation that follows early structural trends (Corti et al., 2007; Katumwehe et al., 2015). In the south, the major features of the rift are the border faults of Lake Malawi, after which the rift then passes south through the Shire trough into southern Mozambique and/or west into Botswana. The progressive maturity of the EARS along its length means it provides the ideal natural laboratory to study fault and rift evolution over a temporal (earthquake and rift cycle) and spatial (from individual sample to entire rift) scale, and to explore why some rifts succeed in forming new oceans, such as the Mid-Atlantic, whilst others fail, such as the Can-Hang failed rift in southeastern China (Goode et al., 1991).

The EARS is located on the eastern side of Africa and separates the Somalian and Nubian plates (Chorowicz and Mukoni, 1980), with the possible existence of two smaller plates: Victoria and Rovuma (Deprez et al., 2013; Stamps et al., 2008, fig. 1.13). Tomography studies and geodynamic modelling suggests that a major mantle upwelling may be the cause of rift initiation along the EARS (Grand et al., 1997; Hansen and Nyblade, 2013; Nyblade and Langston, 2002). The earliest basaltic volcanism in the EARS occurred in southwestern Ethiopia and north Kenya between 45 and 39 Ma (Ebinger et al., 1993, 2013; Morley et al., 1992). The onset of rifting at *ca.* 30 Ma coincided with very high magma production rates in the southern Red Sea (Wolfenden et al., 2005).

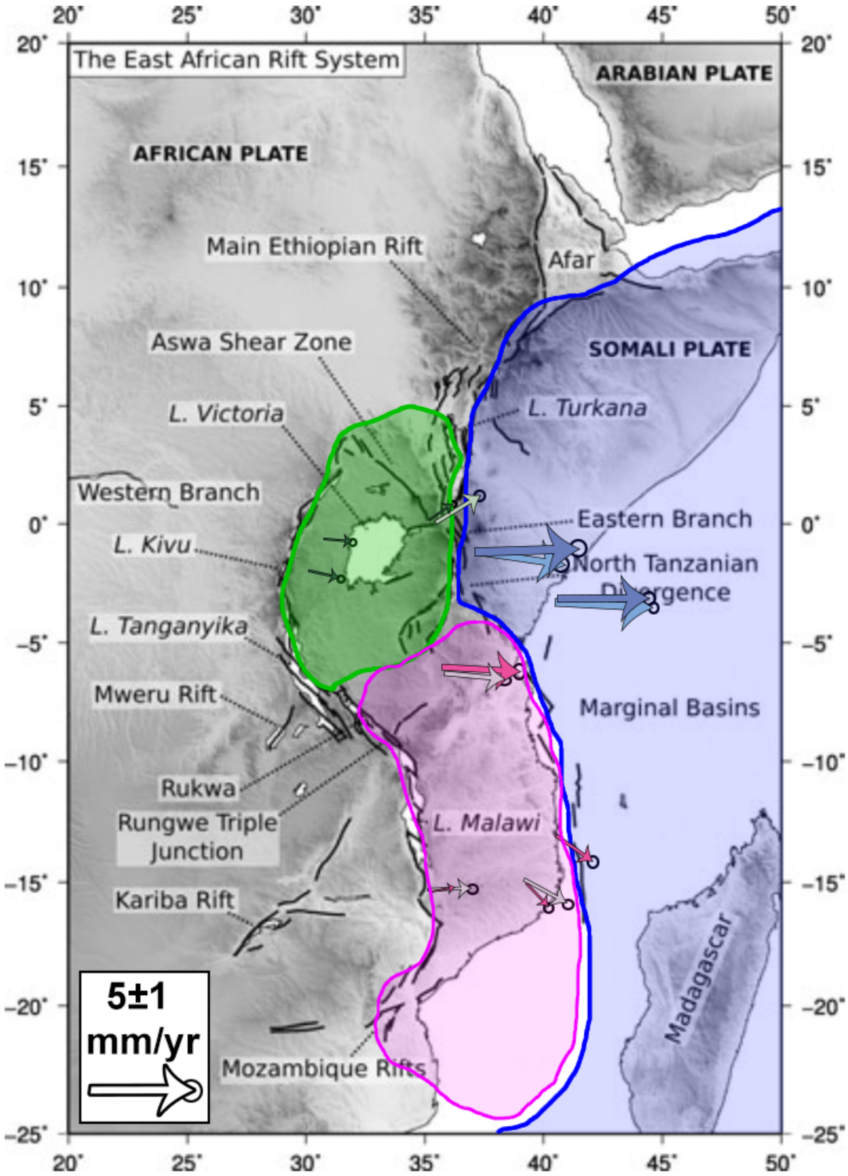

Fig. 1.13 The East African Rift System, edited from Craig et al. (2011) to include plate motion arrows as described by Deprez et al. (2013) for the Somalian (blue), Victoria (green), and Rovuma (pink) plates with respect to the Nubian plate to the west. The light colour arrow shows the observed velocity w.r.t. Nubia. The dark colour arrows shows the theoretical movement of the site w.r.t. Nubia deduced from the Euler poles determined by the inversion of the geodetic velocity field for each plate.

Country	Place	Year	Magnitude (M_W) [1]	Depth (km) [1]	Description
Ethiopia	Shoa	1906	6.	15†	Only slight damage due to sparsely populated region [2]
Tanzania	Kasanga/Rukwa	1910	7.3	15†	Unknown deaths but significant damage [2,3]
Zambia	North Eastern Region	1919	6.7	15†	Unknown deaths and damage
Ethiopia	Bako	1919	6.5	15†	Unknown deaths and damage
Tanzania-Zambia	Lake Tanganyika	1919	7.2	15†	Unknown deaths and damage
Kenya	Sebukia	1928	7.0	15†	No casualities due to sparsely populated region [2,4]
Uganda	Lake Edward	1952	6.5	15†	Unknown deaths and damage
DRC	Lake Tanganyika	1960	6.5	13.7	24 deaths, unknown damage [5]
Tanzania	Mbulu-Babati	1964	6.5	33.8	1 death, 19 injured, extensive property damage [6]
DRC-Uganda	Tooro	1966	6.6	29.3	160 deaths, 1300 injured, 700 buildings destroyed [1]
Djibouti	Galafi	1989	6.5	11.6	2 deaths, 2 injuries, damage to infrastructure [7]
Sudan	Juba	1990	7.2	14.9	31 deaths, some building damage [7,8]
Sudan	Juba	1990	7.1	16	No recorded deaths but some damage
Sudan	Juba	1990	6.6	12.6	No recorded deaths but some damage
Tanzania	Lake Tanganyika	2000	6.5	34	No deaths, 6 injured, 7 houses destroyed, 150 damaged [7]
DRC-Tanzania	Lake Tanganyika	2005	6.8	22	6 deaths, 300 houses destroyed [7]
Mozambique	Machaze	2006	7	11	4 deaths, 26 injured, 294 houses destroyed [7]
Botswana	Central District	2017	6.5	29	36 injured (indirectly)

Fig. 1.14 EARS $M_W > 6.5$ earthquake events since 1900. † depth estimated by [1] USGS. [2] Ismail-Zadeh et al. (2014), [3] Ambraseys (1991b), [4] Ambraseys (1991a), [5] Rothe (1969), [6] U.S. Department of the Interior, Geological Survey and U.S. Department of Commerce and Administration (1986), [7] National Earthquake Information Centre (2018), [8] Centre for Research on the Epidemiology of Disasters (CRED) and the U.S. Office of Foreign Disaster Assistance (OFDA) (2001)

The EARS has a complex boundary structure (Hartnady, 2002), but its structural evolution is similar to other narrow rifts, such as the Gulf of Corinth rift (see Section 1.1). Along the 2,000 km long western branch, individual rift basins are half graben bounded by a faulted rift escarpment on one side and a flexural warp on the other (Foster et al., 1997). Each basin is $\sim$ 100 km long and $\sim$ 50 km wide (Ebinger et al., 1997). This rift architecture may be explained by the self-organisation of fault networks apparent in other rifts (Cowie, 1998; Cowie et al., 2000, 2005), and the role of inherited topography (Crossley, 1984; Løseth et al., 2009). Like the Gulf of Corinth and northern North Sea, the pre-rift topography appears to play an important role in recording the evolution and the structural inheritance of fault and rift structures in the EARS (Crossley, 1984; Løseth et al., 2009). For example, the Malawi rift cuts across a dominantly west to east drainage system such that catchments are asymmetric and larger on the west side (Crossley, 1984). In addition, rivers in both Malawi and the Corinth rifts appear to be controlled by the pre-rift topography (Crossley, 1984).

The evolution of the western branch suggests modest lithospheric thinning, but that border faults penetrate the entire lower crust, consistent with deep seismicity (Ebinger, 1989; Lindenfeld and Rümpker, 2011). The EARS is and has experienced several M_W 7 or greater earthquakes since 1900 (Ebinger et al., 2013). During the 20th century up to 80% of the seismic moment release over the Somalian and Nubian plates was achieved by just two earthquakes, the M_W 7.3 1910 Rukwa event in southwestern Tanzania (Ambraseys and Adams, 1991) and the M_W 7.2 1990 Juba earthquake in South Sudan (Hartnady, 2002). A comprehensive list of EARS $M_W > 6.5$ earthquakes since 1900 can be found in Table 1.14. As such, much of the strain appears to localise along co-linear border faults; however, earthquakes such as the 2009 Karonga sequence in northern Malawi show activity within a border fault hanging wall rather than on a linear border fault (Biggs et al., 2010).

1.3.2 Malawi Rift System

The Malawi Rift System (MRS) extends 900 km from the Rungwe province in the north to the Urema graben in the south (Ebinger et al., 1987; Specht and Rosendahl, 1989, fig. 1.15). At the northern end of the rift system is the Mbeya box, which is a triple junction between the Somalian, Victoria and Rovuma plates (Ebinger et al., 1989). Rift development commenced with the formation of half-graben units bounded by fairly north-south striking normal faults and propagated in a zipper-like manner from the north (Ring et al., 1992). Rifting has been suggested to have initiated *ca.* 8 Ma (Ebinger et al., 1989), but coring of lake sediments suggests that initiation may be as young as early to middle Pliocene (Lyons et al., 2011). Kinematic models of plate motion suggest maximum average extension rates across the Malawi rift of $\sim$ 3 mm per year, decreasing southwards to less than 2 mm per year (Jackson and Blenkinsop, 1997; Jestin et al., 1994; Saria et al., 2014; Stamps et al., 2008). This extension rate is fairly slow in comparison to other rifting zones. For example, the Corinth rift is extending at a rate of around 15 mm per year (Gawthorpe et al., 2017). As a result, earthquake recurrence intervals are expected to be long for the MRS (Hodge et al., 2015). Also, due to the variation in the influence of inherited lithospheric heterogeneity and kinematics in the evolution of the MRS, the rift may be segmented into three, distinct sections (Laó-Dávila et al., 2015).

As shown in fig. 1.15, border fault systems exist with a predominantly north-south trend at the edges of Lake Malawi (Ebinger et al., 1987). The fault systems show remarkably similar patterns to those north around Lake Tanganyika (Rosendahl, 1987). Maximum displacement is observed in the central part of the border fault systems and they are typically separated from any adjacent segment by approximately 50 - 90 km. However, the Usisya fault system in the north comprises three $\sim$ 100 km long normal faults separated by $\sim$ 10 km (Contreras et al., 2000). On average, the fault systems alternate sides of Lake Malawi at around 100 km intervals (Ebinger et al., 1987; Rosendahl et al., 1986). The number of border faults has estimated to be between seven and ten (Ebinger et al., 1987; Flannery and Rosendahl, 1990; Specht and Rosendahl, 1989), with the majority bounding the lake edge. A 100 km long, continuous scarp at the southern end of the lake marks the surface expression of the Bilila-Mtakataka fault, whose last earthquake event has been proposed to be a complete rupture of the fault, equating to a M_W 8 earthquake (Jackson and Blenkinsop, 1997).

InSAR measurements, field observations and elastic modelling for the 2009-2010 Karonga earthquake sequence reveal widespread coseismic and localised post-seismic deformation (Hamiel et al., 2012). That is, following this event there was a very low seismic moment release and the effect of poroelastic relaxation on the post-seismic deformation was negligibly small, including no evidence for dyke intrusion. The MRS is therefore considered to be immature, with extension occurring primarily by seismic slip on border faults rather than during dyke intrusion episodes (Ebinger, 2005). As an immature rift environment, the MRS provides an ideal setting to study the fundamental controls on the early stages of rift basin development (Lezzar et al., 2002). Work by Versfelt and Rosendahl (1989) looked at the pre-rift structure of the entire MRS and found that for the central section, the basement foliations trend near perpendicular to the border faults, whilst for the northern section the border faults parallel the foliation (fig. 1.15).

Earthquake centroid depths for the MRS indicate that the seismogenic thickness is around 30 - 40 km, significantly larger than the global average for continents (Mckenzie et al., 2005; Scholz, 2002), and larger than average in the northern

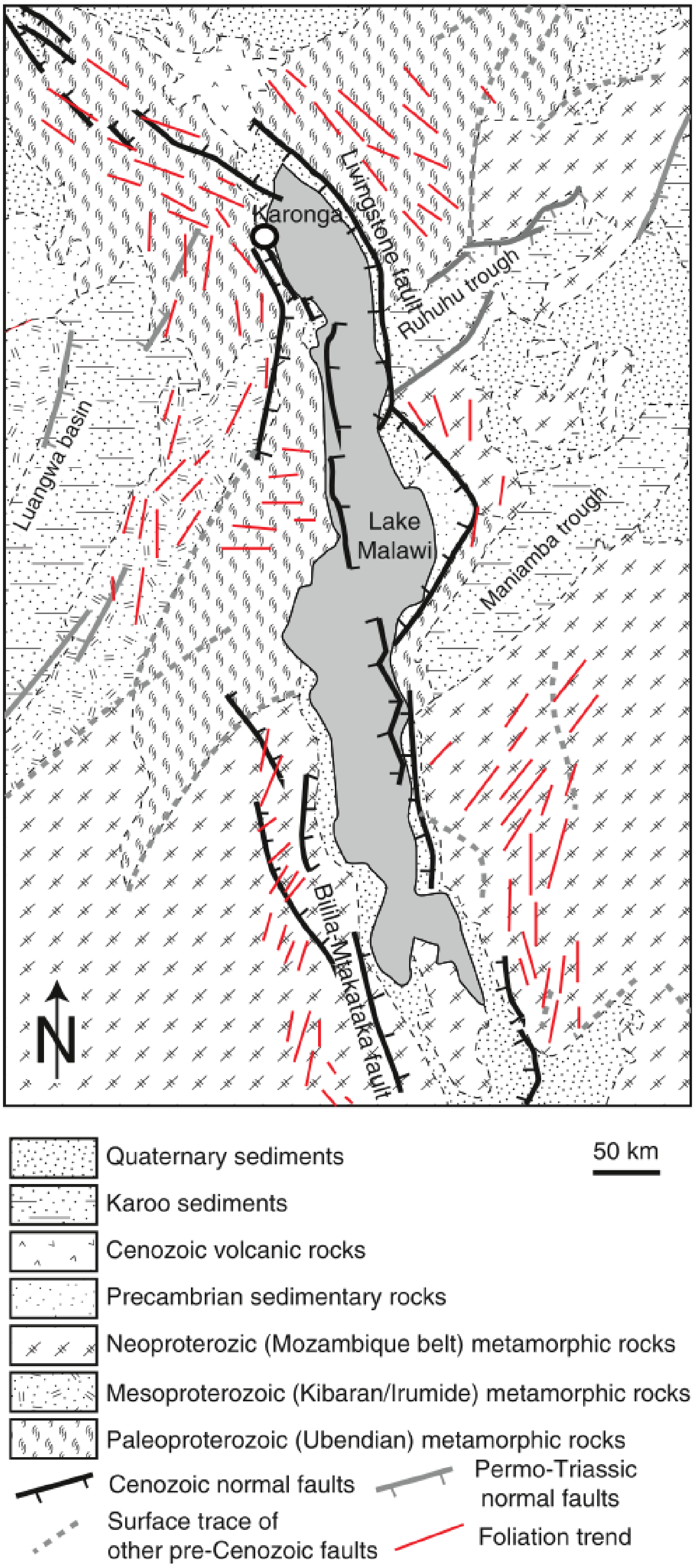

Fig. 1.15 The tectonic map of the Rukwa-Malawi rift zone by Fagereng (2013) showing basement geology and border fault systems. Red lines show underlying fabric trends.

section of the EARS. The large seismogenic thickness of the southern EARS is often attributed to the old (Archean-Proterozoic), cold, anhydrous material; this contrasts regions like the Gulf of Corinth which have undergone much younger orogenies and have a smaller seismogenic thickness (Jackson and Blenkinsop, 1993). Another reason may be the possible contribution of fluids, which would lower the brittle strength; however, fluids would lower the ductile strength too (Watts and Burov, 2003). Another explanation could be the presence of mafic material in the lower crust combined with higher heat production in the upper crust (Nyblade and Langston, 1995). Albaric et al. (2009) infer significant earthquake activity at 20 to 40 km to be a result of a dominant mafic lithology at these depths. Due to a lack of petrological and geochemical evidence, for example from xenoliths, the composition of the lower crust has yet to be confirmed in southern Malawi.

The relatively long fault lengths and thick seismogenic zone suggest that earthquakes of M_W 7 or greater are possible on the MRS (e.g., Ebinger et al., 1987; Hodge et al., 2015; Jackson and Blenkinsop, 1997). Despite the risk of such a potentially catastrophic event, no earthquakes of such magnitudes have been recorded on the Malawi rift (Table 1.14); however, a M_W 7.4 event occurred 200 km to the northwest on the Rukwa fault system in 1910 (Ambraseys and Adams, 1991). The earthquake triggered landslides and produced seiches (standing waves) in Lake Malawi and neighbouring Lake Tanganyika. Subsequent aftershocks with a maximum magnitude of M_s 6 were also recorded during the event. Two earthquakes of $M_W \geq 6$, however, have occurred on the MRS in recent years: the 1989 M_W 6.3 Salima earthquake (Jackson and Blenkinsop, 1993) and the 2009 Karonga earthquake sequence (Biggs et al., 2010). The Salima earthquake caused nine fatalities, and left tens of thousands homeless. The epicentre of this earthquake was close to the Malawi capital of Lilongwe, which has an estimated population greater than 1 million. The Karonga sequence had no accounted fatalities, but over 300 people were reported injured, with thousands left homeless.

The earliest historically recorded earthquake event in the MRS according to the International Seismological Centre (ISC) event catalogue is the 1956 M_W 6 earthquake that occurred at the northern end of Lake Malawi. Some older events, *ca.* 1919, have occurred close to the Malawian border, however. Due to the geometry and coverage of the seismic network in and around Malawi, the instrumental catalogue for the MRS is suggested to be complete only since 1965 for events with $M_W \geq 4.5$ (Hodge et al., 2015). For smaller magnitude events, the catalogue therefore remains incomplete. As a result the MRS has a very short complete instrumental catalogue ($\sim$ 50 years for $M_W \geq 4.5$) and historical catalogue ($\sim$ 100 years) compared to other rift environments, for example historical catalogues of $\sim$ 1,000 years and $\sim$ 2,000 years, and complete instrumental catalogues of $\sim$ 500 (≥ 6.0)

years and $\sim$ 300 ($\geq$ 6.0) years are suggested for the central Apennines (D'Addezio et al., 1995; Stucchi et al., 2011) and Corinth rift (Console et al., 2014), respectively. Furthermore, using the Gutenberg-Richter relationship, $\log_{10} N(\geq m) = a - bm$, where N is the annual number of earthquakes with magnitudes equal to or greater than m, with the MRS instrumental earthquake catalogue predicts a longer recurrence interval between large (M_W 7.8 or greater) earthquakes, $\sim$ 1,000 years, than predicted by geodetic and geomorphological studies of the major active border faults (Hodge et al., 2015).

In recent decades, the potential risk associated with large magnitude earthquakes along the EARS has been increased because of urbanisation and population growth. According to the African Development Bank (AfDB), the Organisation for Economic Co-operation and Development and the UN's Development Programme, the percentage of African population living in urban areas has increased from 14% in 1950 to around 40% at current estimates. This increase in urban development is broadly reflected in estimated damage caused by earthquake events in Table 1.14. Whereas many of the pre 1950's earthquakes indicate low levels of damage and casualties, typically due to sparse populations, the damage caused by recent earthquakes is much greater. For example, the 1990 South Sudan earthquake swarm caused the displacement of 100,000's of people. Such displacements require significant aid efforts and may leave those displaced vulnerable to secondary disasters (malnutrition, landslides). Whilst the World Bank states Malawi is urbanising slower than its neighbouring countries, it is still undergoing a rural to urban migration. Consequently, a $M_W > 7$ event on the MRS near populous and growing cities such as Lilongwe or Blantyre could have disastrous consequences (Goda et al., 2016).

A better understanding of how large, normal faults develop and deform in slow strain rate rift regions will allow for a better understanding of fault evolution processes and quantification of the seismic hazard (e.g., England and Jackson, 2011), which in turn can help inform building codes, policies and natural disaster preparedness.

1.4 Main research questions

Q1. What does a fault's surface geometry and morphology tell us about its development and deformation style?

In order to understand normal fault and rift evolution, and as the majority of fault traces are irregular, I must first explore how normal fault segments grow, interact and link to form major, geometrically segmented, faults. I shall observe a broad range of hard-linked normal faults at the kilometre scale from a variety of rift regions, then apply a Coulomb stress model to infer how each may have formed their link geometry. I will then investigate how a fault's surface geometry may reflect its growth history by observing the geometry of a natural example over a variety of scales, from the scale of an entire fault down to the scale of individual outcrops. By choosing a natural example within a slow strain rate, early-stage rift I will also consider the controls on the geometry of a major border fault within a young rift environment. After addressing this question I then ask:

Q2. In what ways can we improve the methodology for quantifying the fault processes?

I explore whether the current advancements in remote sensing and numerical models can be used to explore and quantify fault processes for a number of faults not previously studied in detail. I then develop new methodologies to calculate scarp parameters and morphologies in order to understand the growth and rupture history of large, normal faults, and consider what future requirements are needed to further improve these methods. I then put my research into the broad context of rift systems by asking:

Q3. What does our work tell us about the seismic hazard posed by faults in early-stage, slow strain rate rifts?

Are current seismic hazard estimates and methodologies appropriate for slowly deforming regions, where the earthquake catalogue is likely incomplete? I explore to what extent detailed geomorphological studies can be used to infer the seismic hazard for early-stage, slow strain rate rifts, and what the current gaps in our understanding of the regional fault evolution are. By using the Malawi Rift System as a case-study example, I then suggest what future work is required to increase our knowledge of seismic activity in the region.

1.5 Thesis outline

The work presented in this thesis follows a narrative aimed at addressing the main research questions. While each chapter provides an interdisciplinary approach to address one or more of these questions, each chapter is also self-contained and can be read in isolation. As a result, there is a small amount of overlap in the introductory material and methods sections of each chapter, to benefit the reader. To aid the reader, here I will refer back to the relevant introductory sections for key concepts.

Normal faults (1.1.1), especially those whose length is greater than or equal to the seismogenic thickness (1.1.2) they reside in, are considered to comprise smaller fault segments that have hard-linked over multiple earthquake cycles (1.1.6). Understanding the process of segment linkage is important as the formation of a larger fault increases the fault area that slip can occur on, increasing the maximum earthquake magnitude, and thus the seismic hazard (1.1.3). However, to date, observations of fault segment linkage have been confined to snap-shots in time provided by natural examples, laboratory experiments that may not scale appropriately, or geologically simplified computer simulations. In Chapter 2 I aim to understand the mechanism and evolution of fault linkage in normal faults by comparing a catalogue of natural observations to the favourable link geometry predicted by a numerical model. To do this I undertake a comprehensive search of normal fault link geometries in nature and apply a numerical model that calculates the stress change within the intersegment zone between two fault segments following an earthquake, or earthquakes, on one or both segments. This work will help me understand the processes forming large, normal border faults in young rift regions.

Following this I investigate the controls on large-scale rift and fault geometry in Chapter 3 using the natural laboratory provided by faults in southern Malawi. Previous studies suggest that the dominant control to rift geometry is the regional stress field (1.1.1), whereas others have postulated that structural heterogeneities such as pre-rift fabric influence fault geometry (1.1.4). As fault and rift geometry are inherently intertwined, I explore the angular relationship between fault geometry, pre-rift fabric and stress fields using the Bilila-Mtakataka fault (BMF) in southern Malawi as a case study. By undertaking a multi-scale approach, using both field and satellite observations, as well as developing a geometrical model, I can hypothesise the primary controls on the geometry of a major border fault in a young rift system.

In order to understand whether the structural evolution of the BMF is typical of that expected by a normal fault in a rift system, i.e. structurally segmented and linked (1.1.6), Chapter 3 uses a conventional manual-approach to calculate the surface throw, i.e. the scarp height (1.1.5). This approach, however, relies heavily on the user's interpretation of the data and therefore includes human-bias and may be unrepeatable. Attempts have been made to automate this calculation, although none have successfully replaced the manual-approach used by large swathes of the geomorphological community. In Chapter 4 I develop a semi-automated algorithm to calculate scarp height using a range of satellite digital elevation models (DEMs) with differing resolutions (1.2). I then use this new methodology to calculate the surface displacements along four southern Malawi faults, including three previously unreported scarps. By increasing measurement coverage, when compared to a manual-approach, a more detailed analysis of fault structural segmentation can be performed, and small-scale structures identified. I finish this chapter by examining what the new results mean for the seismic hazard of southern Malawi, and what the current gaps in our knowledge are.

New insights gained from the previous chapters suggest that the fault scarps in slow strain rate rift settings previously assumed to have formed by a single event may be formed from multiple rupture events (e.g., Ewiak et al., 2015; Gao et al., 2017; Zielke et al., 2015). In Chapter 5 I perform a detailed geomorphological analysis of a normal fault scarp using a very high-resolution DEM. In addition, I develop a forward model to calculate the amount of erosion that has occurred on the fault scarp, and use this to estimate the relative timing of rupture events. From this detailed study I can infer the number and temporal relationship between earthquakes along the fault, and use these to infer the slip magnitude and recurrence interval between earthquake events. Such findings will provide a detailed look at how large normal faults in early-stage rifts accommodate displacement.

I conclude in Chapter 6, where I combine the findings from each study to address my research questions. I also explain the relevance of the findings to a range of regions, as well as locally for the Malawi Rift System. I finish by discussing what future research is required to further understand the development, deformation and seismic hazard of large, normal faults in early-stage, slow strain rate rifts.

Chapter 2

The role of coseismic Coulomb stress changes in shaping the hard-link between normal fault segments.

ABSTRACT

The mechanism and evolution of fault linkage is important in the growth and development of large faults. Here we investigate the role of coseismic stress changes in shaping the hard-links between parallel normal fault segments (or faults), by comparing numerical models of the Coulomb stress change from simulated earthquakes on two en echelon fault segments to natural observations of hard-linked fault geometry. We consider three simplified linking fault geometries: 1) fault bend; 2) breached relay ramp; and 3) strike-slip transform fault. We consider scenarios where either one or both segments rupture and vary the distance between segment tips. Fault bends and breached relay ramps are favoured where segments underlap, or when the strike-perpendicular distance between overlapping segments is less than 20% of their total length, matching all 14 documented examples. Transform fault linkage geometries are preferred when overlapping segments are laterally offset at larger distances. Few transform faults exist in continental extensional settings, and our model suggests that propagating faults or fault segments may first link through fault bends or breached ramps before reaching sufficient overlap for a transform fault to develop. Our results suggest that Coulomb stresses arising from multi-segment ruptures or repeated earthquakes are consistent with natural observations of the geometry of hard-links between parallel normal fault segments.

This chapter is based upon the published paper: Hodge, M., Fagereng, Å., & Biggs, J. (2017). The role of coseismic Coulomb stress changes in shaping the hard link between normal fault segments. *Journal of Geophysical Research: Solid Earth, 123*. https://doi.org/10.1002/2017JB014927.

Author contributions and declarations: Hodge, M. is the main author of this work, undertook the data collection and analysis, and adapted the USGS Coulomb software. Fagereng, Å. and Biggs, J. provided supervision for the work and research manuscript. Anonymous reviewers provided constructive comments on the manuscript.

2.1 Introduction

Large continental faults - those whose lengths are much greater than the seismogenic thickness they reside within - typically comprise a number of smaller fault segments (e.g., Peacock and Sanderson, 1991; Schwartz and Coppersmith, 1984; Wesnousky, 1986), defined here as a portion of a master fault or fault zone. The number of 'major segments' in a fault, defined as those with length of the same order of magnitude as the fault they belong to (Manighetti et al., 2007, 2009), is typically between two and five (Manighetti et al., 2015, 2009), which are subdivided further into smaller 'secondary' (or second-order) segments (e.g., Cartwright et al., 1995; Laó-Dávila et al., 2015; Manighetti et al., 2015). The number of segments appears not to be controlled by fault length, displacement or slip rate (Manighetti et al., 2015, 2009). Because earthquake magnitude is proportional to rupture area (Wells and Coppersmith, 1994, see Section 1.1.3), larger earthquakes can occur along interacting fault segments that rupture together, than in single segment ruptures (e.g., Aki, 1979; King and Nabelek, 1985; Shen et al., 2009). For segmented faults, interaction between segments influences the maximum coseismic slip magnitude, where slip is underestimated by a single segment length and overestimated from the total fault length (e.g., Gupta and Scholz, 2000; Kase, 2010; Segall and Pollard, 1980; Willemse et al., 1996). In addition to altering the maximum rupture length and slip magnitude, interactions between fault segments increase the uncertainty in forecasting earthquakes (Segall and Pollard, 1980), as fault segments may rupture individually (e.g., 2004 Parkfield earthquake; Murray and Segall, 2002), consecutively (e.g., 1915 Pleasant Valley earthquake, DePolo et al., 1991, 2009 L'Aquila earthquake, Luccio et al., 2010), or continuously in a single event (e.g., 1868 Arica earthquake, Peru; Bilek and Ruff, 2002). Rupture type along a fault may also show temporal variability (e.g., Bilek and Ruff, 2002). Accounting for this uncertainty in maximum or expected earthquake magnitude on a fault is critical for seismic hazard assessments (e.g., Hodge et al., 2015; Kijko and Graham, 1998; Youngs and Coppersmith, 1985).

Fault segmentation appears to be an inherent characteristic of normal faults (e.g., Peacock and Sanderson, 1991; Schwartz and Coppersmith, 1984; Wesnousky, 1986), but how these segments form and coalesce into the hard-linked, segmented large structures observed at continental rifts has long been debated. One interpretation of how segmented faults form is that initially independent isolated faults undergo interaction and linkage, referred to as the 'isolated fault model' (e.g., Cartwright et al., 1995; Dawers and Anders, 1995; Morley et al., 1990; Trudgill and Cartwright, 1994; Wilcox et al., 1973; Withjack and Jamison, 1986). An alternative theory is that fault segments are already kinematically connected following the inception of a master fault, referred to as the 'constant-length fault model' (Walsh et al., 2003, 2002). This hypothesis implies that faults rapidly establish their length, which is followed by a longer phase of slip accumulation without significant fault tip propagation (e.g., Morewood and Roberts, 1999; Nicol et al., 2005). Despite these models implying very different predictions regarding the timescales fault lengthening and displacement accumulation occur at, it is challenging to discriminate between them using geometric criteria alone (Jackson et al., 2017). Furthermore, both isolated and constant-length scenarios for fault growth may fit observations within the same region (Fossen and Rotevatn, 2016, see Section 1.1.7). Where displacement is transferred between faults or fault segments, but no physical linkage exists, the interacting structures are said to be soft-linked (e.g., Childs et al., 1995; Kristensen et al., 2008). Hard-linkage is the term used when a physical connection is developed between faults or fault segments. Fault segments may splay from a continuous master fault at depth (Giba et al., 2012), and be geometrically unconnected at the surface for long-periods of time before a hard-linked connection is established (Walsh et al., 2003).

Previous studies of fault interaction and linkage have typically focused on strike-slip settings (e.g., Chemenda et al., 2016; Segall and Pollard, 1980; Stein, 1999), but normal fault systems also show patterns of fault segmentation (Giba et al., 2012; Willemse, 1997; Zhang et al., 1991). Interactions between fault segments can take place through a variety of mechanisms including dynamic coseismic stresses (e.g., Duan and Oglesby, 2005; Harris and Day, 1999) and driving forces associated with interseismic strain accumulation (e.g., Dolan et al., 2007; Peltzer et al., 2001; Wedmore et al., 2017b). Static coseismic stress changes, associated with fault slip or afterslip, have also been shown to influence interactions between fault segments, and deformation in the area between fault segment tips: the 'inter-segment zone' (e.g., Duan and Oglesby, 2005; Harris, 1998; Harris and Day, 1999; King and Cocco, 2001; Stein, 1999). In this study, we test the hypothesis that stress changes following one or more earthquakes drive fault linkage by promoting failure on well-oriented secondary faults within the inter-segment zone, here called linking faults. We investigate the role of coseismic stress changes in determining the geometry of hard links, by calculating the permanent stress change on linking faults of fixed orientations. These Coulomb stress changes are derived from the total coseismic slip in an earthquake, or earthquakes, on one or both of the fault segments.

2.1.1 Hard-link development and geometry

Direct evidence of linkage evolution between fault segments comes from observations of fault geometry using numerical and analogue models (e.g., Aanyu and Koehn, 2011; McBeck et al., 2016; Willemse, 1997), and geodetic and seismic studies (e.g., Galli et al., 2011; Long and Imber, 2012; Rotevatn and Bastesen, 2014; Taylor et al., 2004). One of the primary influences on initial fault geometry is the regional stress field orientation; in extensional settings, the regional stress supports development of rift-axis parallel, or en echelon, normal faults (e.g., Morley, 1999a; Ring, 1994, see Section 1.1 for more information). Tectonic loading then causes elastic stresses that may lead to failure of these faults (e.g., Cowie and Shipton, 1998; Freed, 2005; Harris and Simpson, 1996). Frictionally weak structures, and/or those with low cohesive strength have, however, been shown to localise deformation and alter the local stress field (e.g., Bellahsen and Daniel, 2005; Collettini et al., 2009; Ebinger et al., 1987; Morley, 2010, Section 1.1.4). As segments grow close to one another, stress changes can promote soft-links between fault segments (e.g., Childs et al., 1995; Kristensen et al., 2008; Walsh and Watterson, 1991). A hard-link may then be formed by iterative growth, through fault tip propagation, and intersection between segments (e.g., McBeck et al., 2016), or the failure of well-oriented linking faults within the inter-segment zone (e.g., Trudgill and Cartwright, 1994). Some suggest that soft-links predominantly develop when segments overlap, which then is followed by a phase of hard-linkage (e.g., Acocella et al., 2000). While linking faults may be reactivated pre-existing faults or fractures (e.g., Bellahsen and Daniel, 2005; Collettini et al., 2009; Fagereng, 2013; Whipp et al., 2014), the stresses at fault segment tips, accumulated over multiple earthquake cycles, can also be sufficient to produce secondary faults and/or fault splays that eventually form the linkage fault zone (e.g., Bouchon and Streiff, 1997; Crider, 2015; Perrin et al., 2016b; Scholz et al., 2010).

The influence of Coulomb stress change on the mechanical interaction between parallel normal faults has been explored before (e.g., Crider and Pollard, 1998), but our study provides an additional step by exploring various linking fault and inter-segment zone geometries between fault segments. We consider three end-member geometrical linking fault configurations: 1) fault bends; 2) breached ramps; and 3) transform faults. Each end-member geometry is outlined below, with reference to natural examples in Table 2.1 and fig. 2.1. Although some of the faults in Table 2.1 comprise more than two segments, we restrict our observations to the hard-link between the two segments with the longest scarp traces. Separation is defined as the strike-perpendicular distance between the tips of the two segments, and overlap as the along-strike distance (where underlap is negative overlap). We define θ as the angle between a line connecting the segment tips and the strike of the segments (where $\theta > 90°$ for overlaps) and α as the acute angle between the strike of a linking fault and that of the fault segments (fig. 2.2).

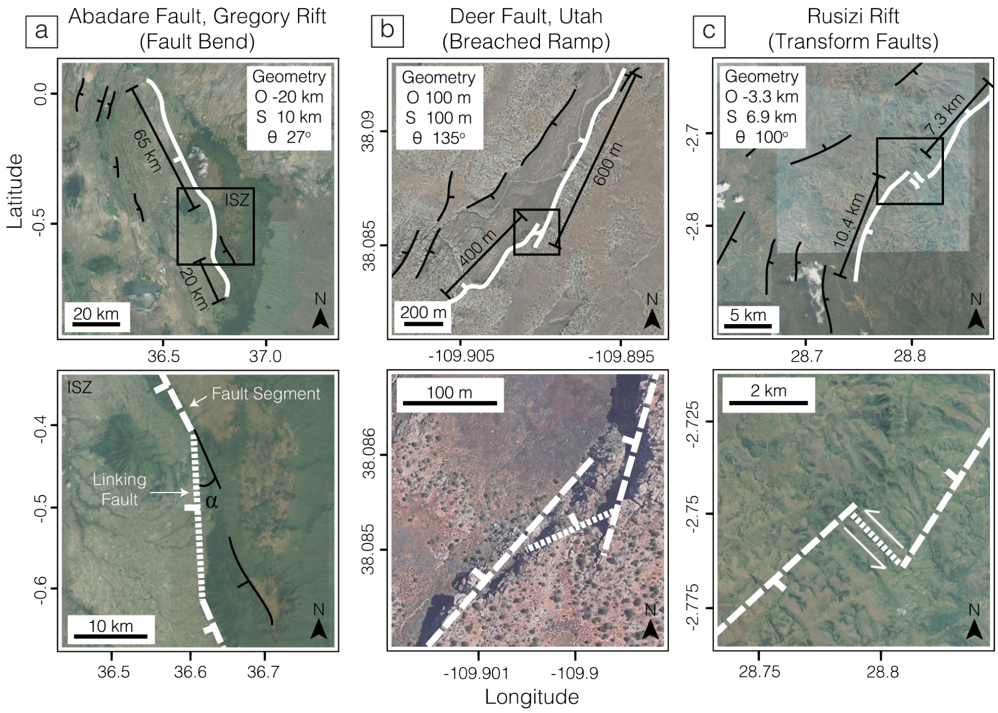

Fig. 2.1 Examples of hard-links between normal fault segments: a) A fault bend (α ~27°) on the Abadare Fault, Gregory Rift, East Africa (Gawthorpe and Hurst, 1993); b) A breached relay ramp (α ~34°) on Deer Fault, Utah, USA (Commins et al., 2005); c) A transform zone (α ~87°) across faults in the Rusizi Rift, East Africa (Acocella et al., 1999). Zoomed in map-view images of the inter-segment zone (ISZ) and end-member linking fault geometries are shown on the bottom panel. Images taken from Google Earth.

Fault bends

For faults growing in a homogenous, isotropic medium, under a uniformly loaded condition, fault strike should theoretically be constant. Most faults, however, are not perfectly straight, but curve or have abrupt changes in strike, due to interactions with other structures, pre-existing planes of weakness and/or strength anisotropies (e.g., Acocella et al., 2000; Faccenna et al., 1995; Fossen and Rotevatn, 2016; Morley et al., 2004). Fault segments may then establish a hard-link when secondary faults intersect their tips (e.g., McBeck et al., 2016); where this occurs, the angles θ and α are equivalent. We refer to this type of link as a 'fault bend'. Examples of fault bends include the 110 km Abadare border fault in the Gregory Rift, East Africa, whose 65 km and 20 km fault segments are linked by a ~ 10 km secondary fault oriented at an angle α of 27° from the average fault segment strike (fig. 2.1a), and the 25 km Fayette fault in the Wasatch fault zone, Salt Lake City, whose two ~ 10 km segments are linked by a 4 km secondary fault at an angle α

of 39° from the segments (Gawthorpe and Hurst, 1993). In the range of examples in Table 2.1, the angle α (and therefore θ) is between 24° and 45°, with an mean of ∼30° (n = 6, Table 2.1). As the examples were identified from low-resolution maps, the lower limit to α may be significantly less; as it is not always possible to identify and quantify small changes in strike.

Breached ramps

When fault segments grow towards one another, an elevation gradient called a relay ramp develops between the segments (Larsen, 1988). Segments separated by relay ramps are initially soft-linked (e.g., Childs et al., 1995; Kristensen et al., 2008). Hard-linkage occurs when secondary faults begin to nucleate and breach the relay ramp and eventually a through-going fault connects the two fault segments. Relay ramp hard-linkages are distinguishable from fault bends as their segment tips extend along-strike beyond the point of hard-linked connection (e.g., Trudgill and Cartwright, 1994, fig. 2.1). Examples include a ∼ 20 km section of the Parihaka Fault, New Zealand (Giba et al., 2012) formed of two ∼ 10 km segments, and the Deer Fault, USA (Commins et al., 2005), a small, segmented, 1 km long fault, both oriented at an angle α ∼34° from the strike of the fault segments (fig. 2.1b). All examples have a $\theta > 90°$, and the angle α is between 24° and 74°, with an mean of ∼45° (n = 8, Table 2.1).

Transform faults

The term transform fault has been used to describe strike-slip linking structures at various scales (Morley et al., 1990; Peacock and Sanderson, 1994; Trudgill and Cartwright, 1994). Here, transform faults are defined as sub-vertical structures, with a significant component of strike-slip displacement. While transform faults are common at mid-ocean ridge settings, examples of continental transforms linking normal faults are rare. Within the Rio Grande Rift, USA, 30 km to 40 km long fault segments are linked through transform faults oriented α ∼75° from the fault segments (Faulds and Varga, 1998; Gawthorpe and Hurst, 1993). In the Rusizi Rift, East Africa, a transform fault zone links normal fault segments at an angle α of ∼87°, where θ is 100° (fig. 2.1c). The angle α is found to be between 60° and 90°, with an mean of ∼75° (n = 6, Table 2.1).

Table 2.1 Examples of geometrical linkage configurations between fault segments for continental normal faults

Fault Name/ Fault Zone	Location	Segment 1 (km)	Segment 2 (km)	Overlap (km)	Separation (km)	α (°)	θ (°)	Ref
1) Fault Bends								
(1)Abadare Fault	Gregory Rift, East Africa	65.0	20.0	-20.0	10.0	27	27	1
(2)Gulf of Evvia Fault Zone	The Gulf of Evvia, Atalanti	7.7	5.5	-0.7	0.7	45	45	1
(3)Fayette Fault	Wasatch Fault Zone, Salt Lake City	12.7	8.8	-3.1	2.5	39	39	1
(4)Nguruman Fault	Gregory Rift, East Africa	20.0	15.5	-8.5	4.0	25	25	1
(5)Atalanti Fault	Atalanti Fault Zone, Central Greece	11.2	6.2	-3.7	1.6	24	24	2
(6)Skinos Fault	Gulf of Corinth, Central Greece	6.3	5.3	-1.8	0.8	24	24	3
2) Breached Ramps								
(7)Parihaka Fault	Taranaki Basin, New Zealand	10.2	8.4	2.1	1.4	34	146	4
(8)Marcusdal Relay Ramp	East Greenland	18.5	15.8	3.0	4.1	54	126	5
(9)Holger Danske Relay Ramp	East Greenland	18.5	9.5	1.7	3.0	61	120	5
(10)Deer Fault	Utah	0.6	0.4	0.1	0.1	34	135	6
(11)Summer Lake Basin	Oregon	5.0	2.2	1.1	0.5	24	156	7
(12)Murchison-Statfjord North Fault	Northern North Sea	25.0	10.0	1.4	1.9	55	126	8
(13)Hilina Fault System	Big Island, Hawaii	16.9	16.8	7.4	4.8	33	147	9
(14)Pearce and Tobin Faults	Pleasant Valley, Nevada	28.0	9.2	1.4	5.0	74	112	1
3) Transform Faults								
(15)Gulf of Evvia Fault Zone	The Gulf of Evvia, Atalanti	18.2	11.3	-1.8	3.6	63	63	1
(16)Bare Mountain Fault Zone	Crater flat area, Southwestern Nevada	6.9	3.8	-0.9	1.6	61	61	10
(17)Rusizi Rift System	East Africa	10.4	7.3	0.5	2.7	87	100	11
(18)Rio Grande Rift System	Colorado, New Mexico	44.8	30.2	-11.6	39.0	73	73	12
(19)North Craven and Middle Craven Faults	Bowland Basin, Northern England	19.8	10.0	1.3	25.0	87	93	13
(20)Central Betics Fault Zone	Betics, Southern Spain	4.0	2.6	-0.2	1.2	79	81	14

1: Gawthorpe and Hurst (1993), 2: Ganas et al. (2006), 3: Duffy et al. (2014), 4: Giba et al. (2012), 5: Larsen (1988), 6: Commins et al. (2005), 7: Crider (2001), 8: Young et al. (2001), 9: Peacock and Parfitt (2002), 10: Faulds and Varga (1998), 11: Acocella et al. (1999), 12: Aldrich et al. (1986), 13: Gawthorpe (1987), 14: Martinez-Martinez et al. (2006)

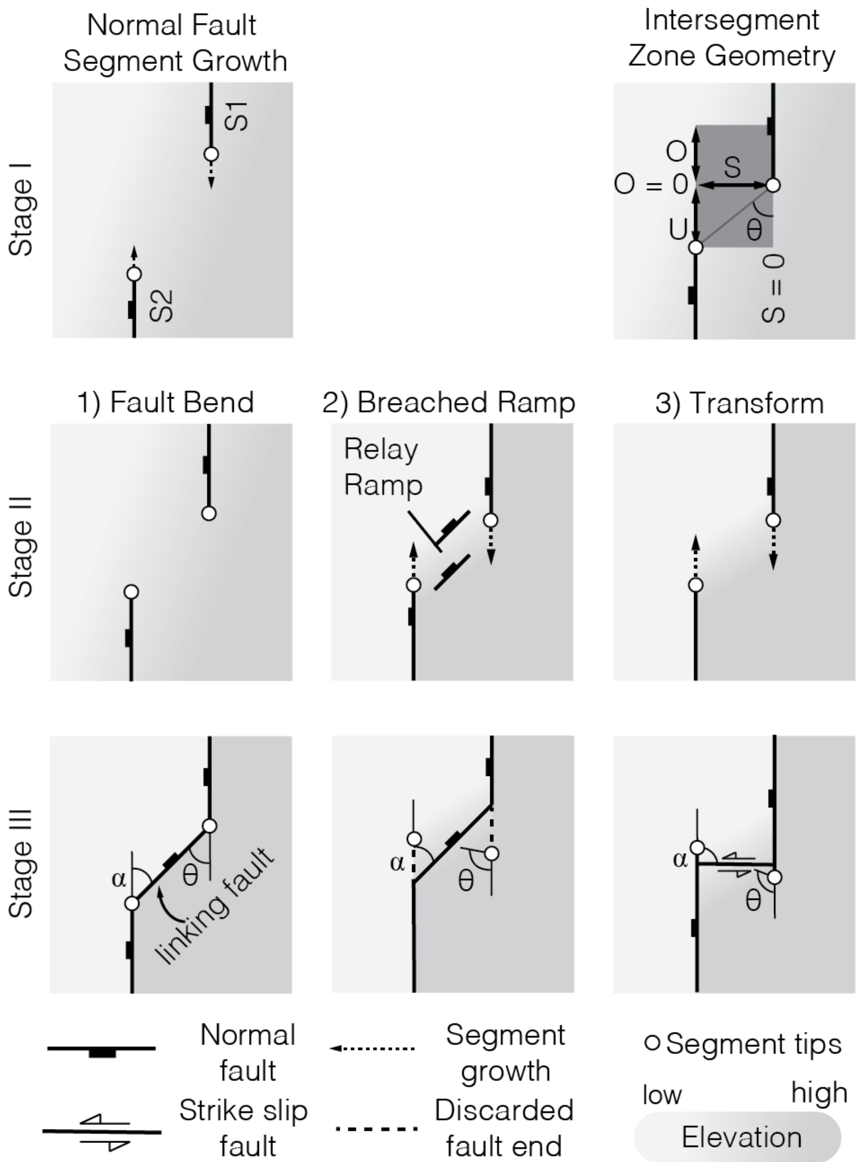

Fig. 2.2 Development of end-member linking fault configurations between parallel normal fault segments: 1) fault bend; 2) breached ramp; and 3) transform fault. Stage I shows incremental growth of one, or both, fault segments. 1) For fault bends, segment geometry begins to be influenced by the adjacent fault segment (Stage II); the linking fault then develops with strike at angle α (equal to θ) to the strike of the segments (Stage III). 2) For breached ramps, displacement becomes localised in the relay ramp, then secondary faults nucleate striking at angle α to the strike of the segments (Stage II); one of the secondary faults breach across the ramp, generating the hard-linked connection (Stage III). 3) For transforms, segment growth continues without a change in strike (Stage II), geometry becomes favourable for linkage with a strike-slip transform fault striking at angle α to the strike of the segments (Stage III).

2.2 Methods

2.2.1 Coulomb stress change

Coulomb stress change ($\Delta\sigma_c$) is the change in static stress state caused by slip on a source fault, resolved onto a receiver fault. It is defined by the following equation:

$$\Delta\sigma_c = \Delta\tau_s - \mu'\Delta\sigma_n \quad (2.1)$$

where $\Delta\tau_s$ is the shear stress change (positive in the inferred slip direction), $\Delta\sigma_n$ is the normal stress change (negative when the fault is unclamped) and μ the static friction coefficient. The effect of pore pressure p can be related to confining stress by Skemptons coefficient β, which typically has a value between 0 and 1. Pore pressure, p, is included through the effective friction coefficient, $\mu' = \mu(1-\beta)$, where $\beta = p/\sigma_n$. Thus, an increase in pore pressure will increase the Coulomb stress and bring a fault closer to failure.

Within static Coulomb stress change models, processes such as dynamic clamping or unclamping are not included (e.g., Freed, 2005; Toda et al., 2011), even though dynamic stresses produce larger, transient stress change magnitudes (Gomberg et al., 1998; Stein, 1999). Static Coulomb stress change models have, however, been shown to successfully model the distribution of aftershocks and provide a tool for forecasting earthquake sequences (e.g., Gomberg, 1996; Harris and Simpson, 1992; Hill et al., 1995; Lin and Stein, 2004; Stein et al., 1997; Wedmore et al., 2017b; Ziv and Rubin, 2000). Coulomb stress change may either increase or decrease the time to the next failure on a fault (King et al., 1994); positive values are said to promote failure (clock advance) and negative values retard failure, where a positive $\Delta\sigma_c$ is associated with earthquake triggering at distances of a few fault lengths (e.g., Harris, 1998; King and Cocco, 2001; Nicol et al., 2010; Stein, 1999). Increasing the Coulomb stress on a fault is not in itself enough to generate failure as it is also important whether the fault is already close to failure. Previous studies suggest a $\Delta\sigma_c$ of 0.1 MPa is sufficient to generate aftershocks on a range of nearby faults (e.g., King et al., 1994; Lin and Stein, 2004); but the precise value is sensitive to a range of factors (e.g., Gomberg, 2001; King et al., 1994).

We used Coulomb 3.4 (Toda et al., 2011), a homogenous elastic half-space model based on Okada (1992), to investigate the coseismic Coulomb stress changes around a normal source fault, on evenly spaced receiver faults. Source fault earthquake parameters were kept constant and related to an earthquake of $\sim M_W$ 6.5 (M_o 5.5 x 10^{22} Nm) on an Andersonian normal fault with strike = 0°, dip = 60°W, rupture length l = 20 km, rupture width w =17 km, fault top depth = 0 km, fault bottom depth = 15 km, and uniform slip u = 1 m. Although slip to rupture length ratios can vary considerably (e.g., Wells and Coppersmith, 1994), we use a slip to rupture length ratio of 5×10^{-5} (Walsh et al., 2002), a value in the middle of global extrema (Scholz, 2002). Receiver fault strike, dip and slip vector rake (vector which shear stress is resolved along) are fixed for each model but varied systematically to explore end-member linking fault geometries. We do not apply any background stresses; in essence, we study the static stress change of an earthquake, or earthquakes, on a particular receiver fault geometry. The concept of tectonic loading is discussed later. A grid size of 1 x 1 km was chosen for receiver fault calculations as this was found to be optimal for resolution and processing times.

The effect of Poisson's ratio, v, on $\Delta\sigma_c$ is negligible, and therefore we set v to the default 0.25 as used in previous Coulomb stress change studies (e.g., Crider and Pollard, 1998; Willemse, 1997; Zhao et al., 2004). For Young's modulus E we use an upper to mid crustal value of 60 GPa (Bilham et al., 1995; Zhao et al., 2004), and set the effective friction coefficient μ' to 0.4, a value suitable for large continental faults (Harris, 1998). In our sensitivity tests we run our model using a range of μ' values, including larger values that are more appropriate to the development of new secondary faults (e.g., Byerlee, 1978), and smaller values associated with weak zones where reactivation of pre-existing structures may occur (e.g., Collettini et al., 2009).

2.2.2 Model setup

In order to compare coseismic Coulomb stress changes for a number of linking fault configurations and distances between parallel normal fault segments, we simplify the geometry of the source fault(s), inter-segment zone and receiver faults. Source faults mimic the active fault segments and are modelled as planar, with constant strike, as illustrated in fig. 2.3. As inter-segment zones are densely faulted and fractured (e.g., Anders and Wiltschko, 1994; Faulkner et al., 2011), we assume there will be a fracture surface available in any geometry and consider only a single receiver fault in the centre of the zone, which denotes the linking fault (fig. 2.3c). We consider two scenarios: the 'single segment rupture scenario', in which an earthquake rupturing only one fault segment changes the Coulomb stress on a linking fault; and the 'two segment rupture scenario', where two earthquakes, or a single earthquake propagating across the geometrical discontinuity, rupture(s) both fault segments. We vary the along-strike distance between fault segments from 10 km underlap to 4 km overlap in 2 km increments, and the fault separation from 2 km to 10 km in 2 km increments (fig. 2.3). Table 2.2 shows the geometries for the three end-member linking fault configurations: 1) fault bend; 2) breached ramp; and 3) transform faults.

Table 2.2 End-member receiver fault geometries where the source fault strikes 0° and dips 60°W

	Geometry	Slip	Strike	Dip	Slip Vector Rake
i)	Fault Bend	Normal	θ	60°W	-90°
ii)	Breached Ramp	Normal	45°	60°NW	-90°
iii)	Transform	Strike-Slip	90°	90°	0°
iv)	Along-strike	Normal	0°	60°W	-90°

$\theta = \tan^{-1}(S/U)$ for underlapping faults,
or $\theta = \tan^{-1}(S/O)$ for overlapping faults.

We also consider whether at certain inter-segment zone geometries continued growth of fault segments without a change in strike is preferred to our linkage configurations ('Along-strike', Table 2.2). This scenario is analysed by calculating $\Delta\sigma_c$ on a receiver fault located along-strike from the fault segment, hereafter called the 'along-strike secondary fault'. If the $\Delta\sigma_c$ magnitude of this along-strike secondary fault is larger than all linking fault configurations, we determine this growth scenario to be preferred. The receiver fault is located at half the along-strike distance between the fault segments (marked G, fig. 2.3c), except where it falls within one grid space of the fault segment, in which case an along-strike distance of 2 km from the segment tip is used instead.

2.3 Results

2.3.1 Numerical models

Fig. 2.4a shows the coseismic Coulomb stress changes between en echelon fault segments, for our three end-member linking fault geometries, using the single segment rupture scenario. For results for the entire range of inter-segment zone geometries, please refer to Appendix B. For fault bends and breached ramps, $\Delta\sigma_c$ is positive for all underlapping inter-segment zone geometries and negative for all overlapping geometries. In both cases, the magnitude decreases with increasing separation. In contrast, for transform faults, $\Delta\sigma_c$ is positive for large values of separation and negative for small values when segments are underlapping, and $\Delta\sigma_c$ is positive for all overlapping geometries. The preferred link geometry, that with the largest $\Delta\sigma_c$ magnitude, is presented in fig. 2.4b for all values of overlap/underlap and separation. Fault bends are preferred in underlapping geometries when the amount of separation is equal to, or less, than the underlap ($\theta \leq 45°$). Breached ramps are preferred only in underlapping geometries when

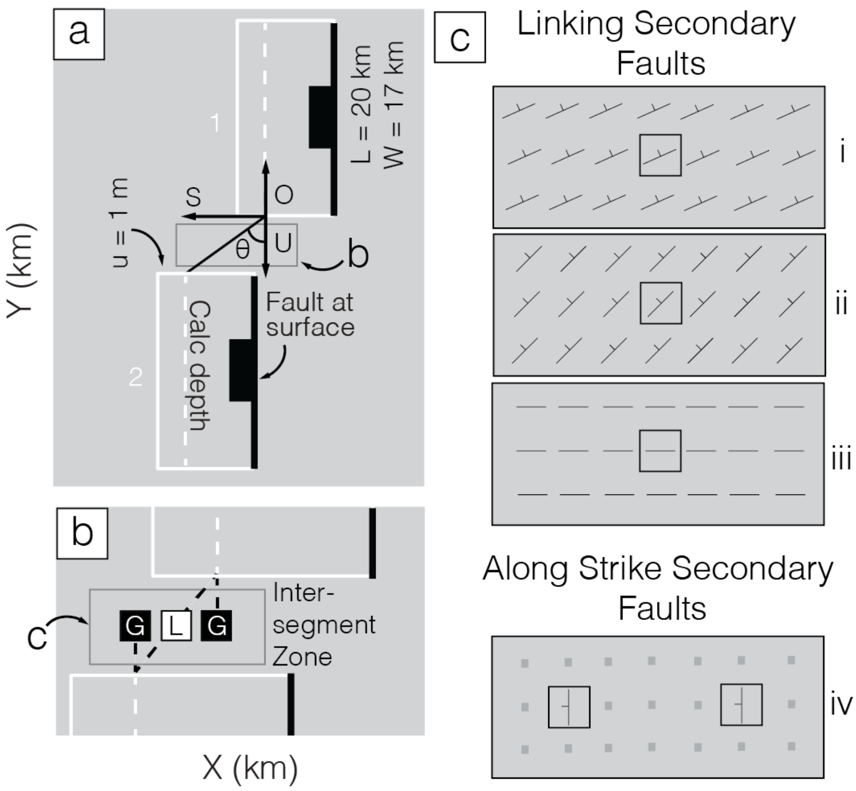

Fig. 2.3 a) Model setup showing the fault segments at the surface (black line), fault plane surface projection (white box), and calculation depth (dotted white line). Distance between fault segments comprises separation (S), the strike-perpendicular distance between the tips of segments, and overlap (O), the along-strike distance (where underlap, U, is negative overlap). The distance is measured at the calculation depth and projected to the surface. The angle between a line joining the segment tips and the strike of the segments, θ, is used in calculating strike for the fault bend configuration. Slip u is set to 1 m for the active fault(s). b) The receiver fault location where $\Delta\sigma_c$ is recorded. Linking fault $\Delta\sigma_c$ is taken from 'L', along-strike secondary fault $\Delta\sigma_c$ is taken from point 'G'. c) Map-view of linking fault configurations for: i) fault bends; ii) breached ramps; iii) transform faults; and iv) along-strike secondary faults. The boxes mark where $\Delta\sigma_c$ is taken from.

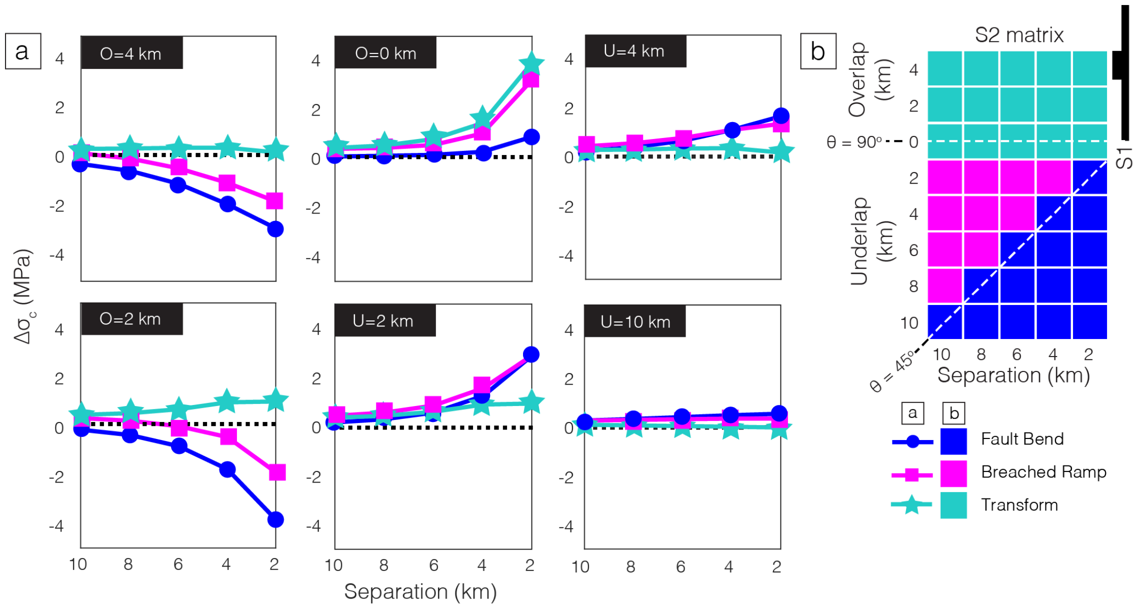

Fig. 2.4 a) Results for linking fault $\Delta\sigma_c$ for the single segment rupture scenario for selected inter-segment zone geometries (see Appendix B for all geometries). b) Preferred link geometry, that with the largest $\Delta\sigma_c$ magnitude, for the single segment rupture scenario.

separation is greater than underlap ($\theta > 45°$). Transform faults are preferred when the segments overlap.

In general the two segment rupture scenario produces larger magnitude $\Delta\sigma_c$ compared to the single segment rupture scenario (fig. 2.5a). For fault bends and breached ramps, the exceptions are where O $\geq$ 0 km, in which case $\Delta\sigma_c$ is slightly larger for the single segment rupture scenario for large values of separation (fig. 2.4a). This is because fault bends and ramps are unfavourable geometries for linking overlapping faults, so that $\Delta\sigma_c$ is negative for a single rupture, and becomes more negative in the two rupture scenario. The only difference in preferred link geometry occurs at separations of 8 km to 10 km when underlap is 2 km, where transform faults are preferred to breached ramps using the two segment rupture scenario (fig. 2.5b).

We now compare the $\Delta\sigma_c$ of the preferred linking fault geometry to the $\Delta\sigma_c$ of the along-strike secondary fault for each inter-segment zone geometry (fig. 2.6). For the single segment rupture scenario, along-strike secondary faults have a larger Coulomb stress magnitude for most cases, except for separations of 2 km, where linkage of en echelon fault segments through transform faults are preferred when O = 0 km, and faults bends or breached ramps at an underlap of 2 km (fig. 2.6a). For the two segment rupture scenario, along-strike secondary faults are not as dominant but are always favoured if separation is greater than 8 km (fig. 2.6b). Where fault bends were the favoured link geometry without considering along-strike secondary faults, they are still preferred over along-strike secondary

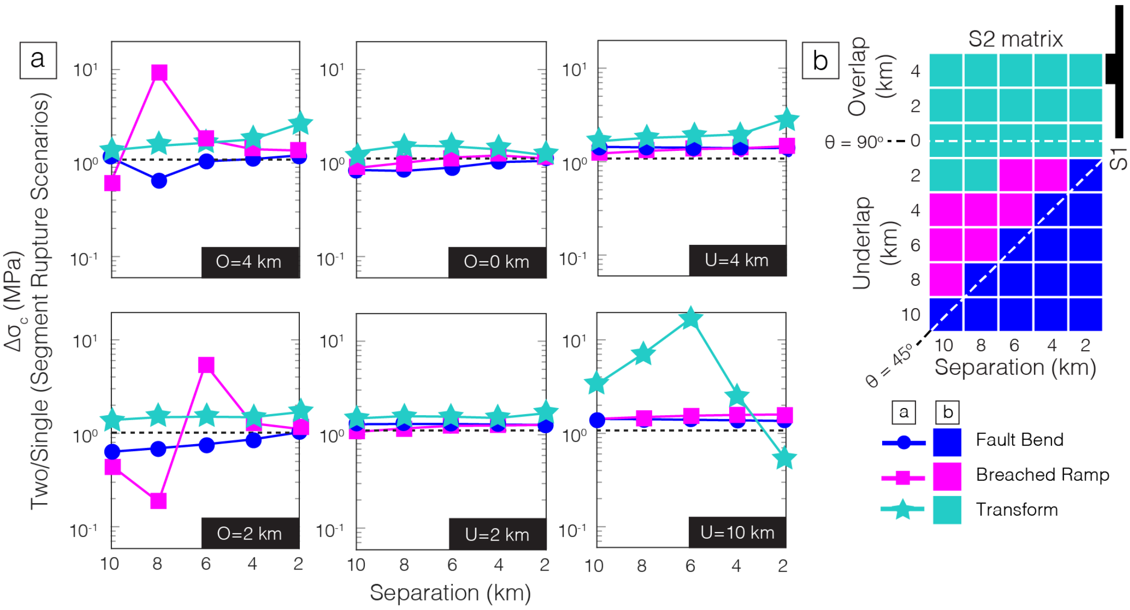

Fig. 2.5 a) The $\Delta\sigma_c$ difference between single and two segment rupture scenarios. A positive difference denotes that the two segment rupture $\Delta\sigma_c$ magnitude was larger. b) Preferred link geometry for two segment rupture scenario. For $\Delta\sigma_c$ results from the two segment rupture scenario, see Appendix B.

faults, i.e. they have a larger Coulomb stress magnitude. Transform faults are still preferred for O $\geq$ 0 km providing the separation is less than 8 km. Where breached ramps were the favoured linking geometry, along-strike secondary faults are now favoured in all cases except for those of low underlap and separation 4 km or less.

2.3.2 Sensitivity tests

The numerical modelling uses simplified end-member fault geometries and slip distributions, thus we test the sensitivity of our results to the model assumptions, including: 1) slip distribution on, and between, fault segments; 2) linking fault geometry; 3) linking fault location; and 4) calculation depth. For more information, including figures, on these sensitivity tests, see Appendix C. Applying a different magnitude of slip on each fault segment, or applying a tapered rather than uniform slip distribution along the segments (e.g., Cowie and Scholz, 1992a; Perrin et al., 2016b; Schultz et al., 2008; Wesnousky, 2008), does not change the preferred link geometry in the majority of cases. More complex slip distributions may, however, influence link geometry through modification of the stress distribution within the inter-segment zone (e.g., Noda et al., 2013). Further details of the limited number of exceptions are given in Appendix C. Similarly, we find that the same link geometry is preferred regardless of the calculation depth, since although the absolute values of $\Delta\sigma_c$ change, the relative values do not. In addition, we changed the effective friction coefficient from 0.4 to 0.2 and 0.6 to reflect hard-

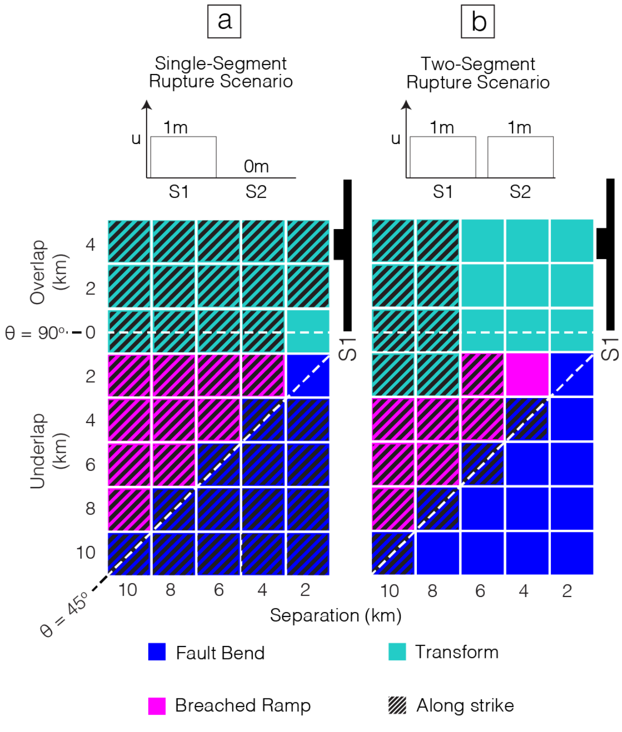

Fig. 2.6 Along-strike secondary fault $\Delta\sigma_c$ compared to linking fault $\Delta\sigma_c$ for a) single and b) two segment rupture scenarios. Diagonal black lines denote the magnitude of the along-strike secondary fault $\Delta\sigma_c$ magnitude was greatest.

links establishing in strong or weak zones, respectively. This change increased, or decreased, $\Delta\sigma_c$ by less than 1 MPa, respectively, but had no effect on the preferred link geometry.

We fix the linking fault geometry to simplified end-member configurations, so we test whether an alternative orientation would experience larger Coulomb stress change, using three representative examples, one for each end-member link style (fig. 2.7a-c). For geometries where end-member fault bend and breached ramp configurations were preferred, a greater $\Delta\sigma_c$ magnitude occurs on linking faults striking with a slightly lower angle to the fault segment strike, with a steeper dip and small left-lateral component of slip (fig. 2.7a,b). For a geometry where our end-member transform fault configuration (fig. 2.7c) was preferred, a greater $\Delta\sigma_c$ magnitude occurs on linking faults with shallower dip and significant normal component. This is consistent with studies on faults in the Gulf of Suez, which show that secondary faults with an oblique sense of slip and a larger normal component form hard-links between normal fault segments (McClay and Khalil, 1998).

Furthermore, by fixing the location of the linking fault within the inter-segment zone, we neglect the possibility that linking faults form off-centre. In particular, there is evidence that through-going secondary faults preferentially breach the base of relay ramps, rather than at the crest (e.g., Commins et al., 2005; Crider,

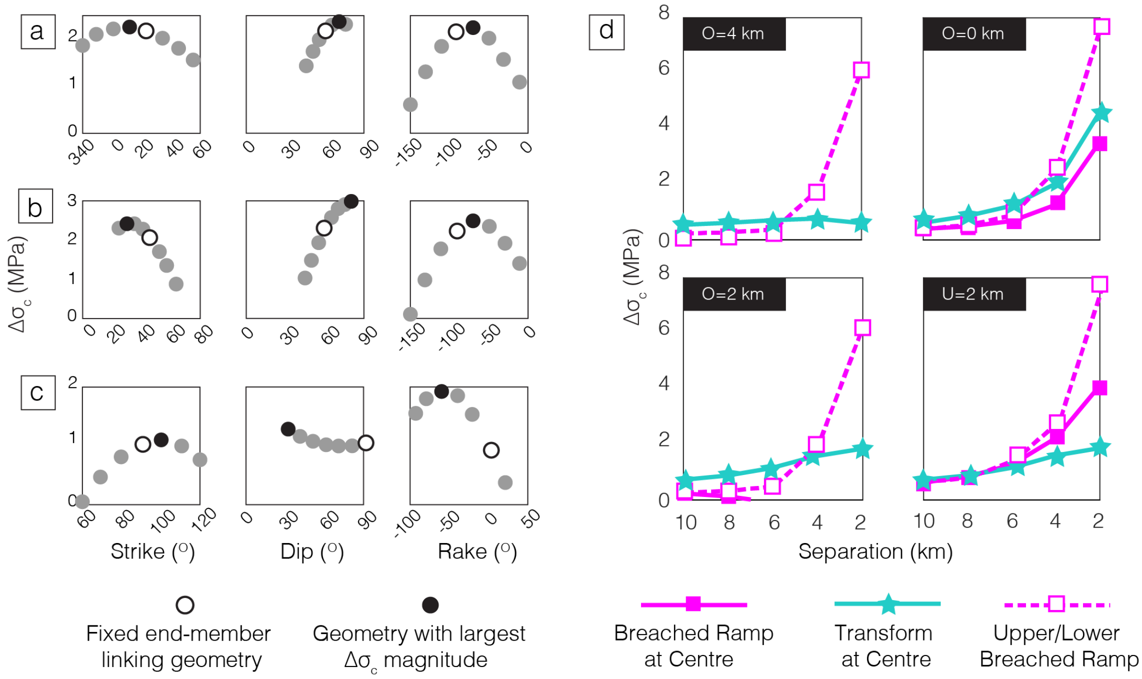

Fig. 2.7 a to c) $\Delta\sigma_c$ based on varying receiver fault strike, dip and slip vector rake. Three geometries were considered, each with a different preferred end-member link geometry: a) fault bend: 4 km underlap and 2 km separation; b) breached ramp: 2 km underlap and 4 km separation; c) transform fault: 2 km overlap and 6 km separation. White circles indicate the $\Delta\sigma_c$ of the preferred fixed end-member linking fault at that inter-segment zone geometry, whereas black circles indicate the linking fault geometry with the largest $\Delta\sigma_c$ magnitude. d) $\Delta\sigma_c$ calculated for relay ramps breached at an optimal location, compared to the $\Delta\sigma_c$ on transform faults and for ramps breached at their centre.

2001; Crider and Pollard, 1998; Fossen and Rotevatn, 2016; Peacock, 2002; Soliva and Benedicto, 2004). Sensitivity tests for a range of locations within a relay ramp show that the largest $\Delta\sigma_c$ occurs closer to the fault segment tip at the upper or lower end of the relay ramp. Importantly, the $\Delta\sigma_c$ at the upper and lower end of relay ramps does in some cases exceed that of other, otherwise preferred linkage geometries (fig. 2.7d). In the further discussion, we use the breached relay ramp linking fault at the inter-segment zone location with greatest $\Delta\sigma_c$ in fig. 2.7d.

2.3.3 Comparison to observations

To test the hypothesis that the stress field in the inter-segment zone is dominated by coseismic Coulomb stress changes and hence shapes the geometry of the hard-link between fault segments, we compare our model results to observations of normal fault surface trace geometry (Table 2.1). In fig. 2.8a we plot the observations alongside the two segment rupture scenario results. We extend our model to include inter-segment zone geometries up to 10 km overlap; observations outside the model space are shown by an arrow. As fault and segment lengths varied over an order of magnitude among observations, we normalised overlap and separation to compare with model results. For model results, segment separation and overlap were normalised to the total length of the segments used in this study (40 km). For observations, we normalised to the total length of the two hard-linked segments (Table 2.1). The natural observations of hard-links between fault segments are recorded at the surface, whereas our model results are taken from a calculation depth of 10 km. However, we found that link type does not vary with calculation depth (see Appendix C for more information). Furthermore, as our observations come from similar tectonic settings, we assumed all other fault parameters are the within the same magnitude as used in this study. The slip to length ratio may show variation between observations (e.g., Scholz, 2002), but this would only change the absolute $\Delta\sigma_c$ magnitude, not the relative magnitude between linking configurations that is pertinent here.

All fourteen fault bend and breached ramp observations match model results (fig. 2.8a). No fault bend or breached ramp observations fell within regions predicted by the model to favour along-strike secondary faults, suggesting there is a maximum inter-segment zone geometry hard-links do not occur beyond - relative to the segment length that is. Half of observations of transform faults, three out of six, fell within model predictions for breached ramp linking faults: The Rusizi Rift (17), North Craven and Middle Craven (19) and Central Betics Fault Zone (20) transform faults. The Gulf of Evvia (15) and Bare Mountain Fault Zone (16) transform faults are within one model grid space. However, our model predicts a preference of along-strike secondary faults for the majority of transform

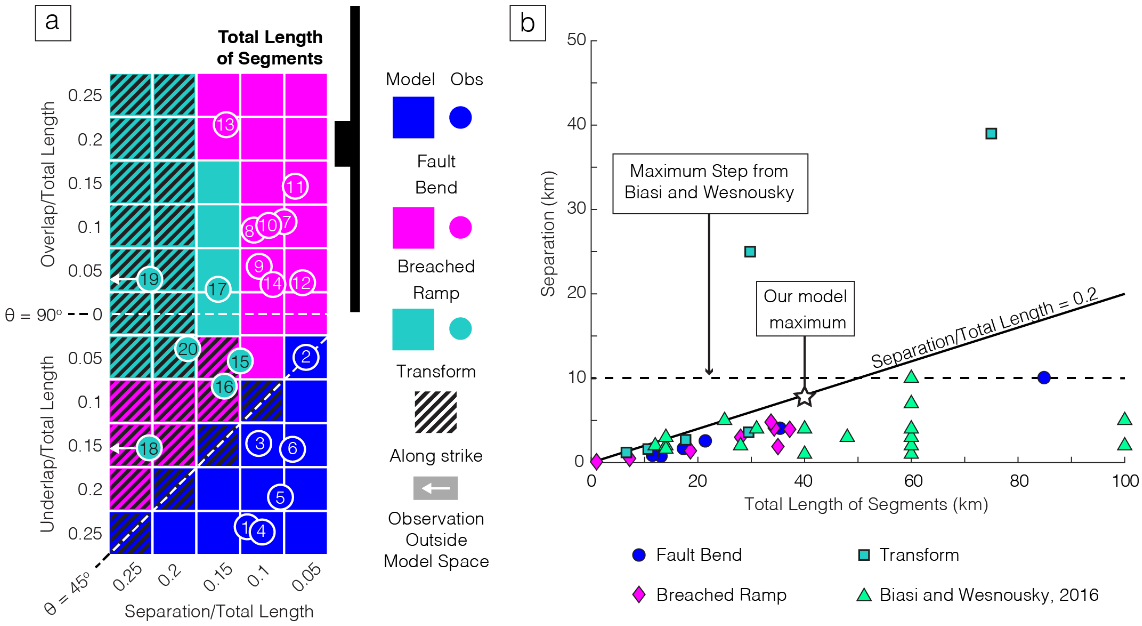

Fig. 2.8 a) Natural observations of hard-links between normal fault segments from Table 1 (numbered) plotted against model predictions of preferred end-member link geometry. Model results are normalised to the length of both segments (40 km), for the two segment rupture scenario, uniform slip distribution run (for tapered slip see Appendix C). Breached ramp results from fig. 2.7 are included here too. Natural observation examples have been normalised to the total length of both segments (for maximum segment and minimum segment length, see Appendix B). Black diagonal lines indicate that along-strike secondary faults are preferred to linking faults between parallel fault segments. Observations that fall outside the model area are shown with an arrow. b) Separation against the length of both segments for natural observations used in this study, and surface rupture examples from Biasi and Wesnousky (2016). Maximum separation is ∼20% of the total length of the segments.

observations (five out of six), even those that fall within breached ramp regimes in underlapping geometries.

Observations of normal faults and surface ruptures show linkage and rupture propagation between segments separated up to 10 km (Table 2.1; Biasi and Wesnousky, 2016). In our model, for two 20 km fault segments, coseismic Coulomb stress change magnitude was larger on along-strike secondary faults than linking faults for fault segments separated by distances of 8 km or greater (fig. 2.8a). Using data from Biasi and Wesnousky (2016), and results from this study, a correlation between maximum separation and total length of segments is found (fig. 2.8b). Here, empirically, it appears that the maximum step distance does not exceed 20% the total length of the interacting segments. Only two transform faults from our twenty natural observations of hard-linkage had a larger separation. Small intermediate fault segments within the inter-segment zone may also hinder hard-linkage at the largest separations, by perturbing rupture propagation across the inter-segment zone (e.g., Lozos et al., 2012, 2015). Assuming constant stress drop, the empirical scaling between maximum separation and total fault segment length arises from that stress intensity at the fracture tip increases with fault length (Rudnicki, 1980; Segall and Pollard, 1980). This relationship from linear elastic fracture mechanics implies that fault linkage is promoted in the zone between en echelon cracks, in a zone where shape depends on slip sense, and which size increases with fault length (Cowie and Scholz, 1992b; Segall and Pollard, 1980).

2.4 Discussion

2.4.1 Hard-link development and geometry

The comparison between natural observations and our model results (fig. 2.8a) is consistent with the concept that the type of hard-link is influenced by the inter-segment zone geometry. Contrary to previous studies that suggest that hard-links establish in overlapping regimes (e.g., Acocella et al., 2000), our results suggest that linkage may also develop in underlapping geometries through breached relay ramps, but predominantly as fault bends. Coulomb stress change calculations may also estimate whether continued along-strike growth of segments, through links with along-strike secondary faults, is preferred to hard-linkage between parallel fault segments; however, we are unable to compare our results to real-world examples because along-strike growth or linkage does not produce a change in strike, so cannot be easily identified in the geomorphology.

Continental transform faults are rarely observed linking normal fault segments in nature, and those that we could find evidence for occurred over a wide range of fault geometries (Table 2.1). There are a number of explanations for why our models do not match observations for transform faults. A possibility is that coseismic Coulomb stress changes could promote the establishment of hard-links before fault segments reach the geometrically preferred criteria for transform faults, i.e. through fault bends or breached relay ramps at underlapping geometries, or segments may continue to grow along-strike if separation is large (fig. 2.6). Even when fault segments reach the preferred geometry for transform faults, Coulomb stress change magnitude is larger on high-angle linking faults that have a dip-slip component (fig. 2.7); therefore, transform faults that were previously thought to be strike-slip, may in fact involve a significant dip-slip motion (e.g., McClay and Khalil, 1998).

Our results indicate that when only one fault segment ruptures, continued along-strike growth of segments is preferred (fig. 2.4). Discrete earthquakes on two parallel segments, or a single earthquake whose rupture propagates across the inter-segment zone, favours the promotion of a hard-link between offset segments (fig. 2.5). Earthquakes that rupture multiple faults or fault segments such as Landers 1992 M_W 7.3 (Sieh et al., 1993), Wenchuan 2008 M_W 7.9 (Shen et al., 2009), Haiti 2010 M_W 7.0 (De Lépinay et al., 2011; Hayes et al., 2010) and Kaikoura 2016 M_W 7.8 (Hamling et al., 2017), or earthquake sequences such as Friuli 1976 sequence (Cipar, 1980), the Umbria-Marche 1997 sequence (Amato et al., 1998), Karonga 2009 sequence (Biggs et al., 2010) and the Amatrice-Norcia 2016 sequence (Cheloni et al., 2017), therefore promote the development of hard-links. Furthermore, Coulomb stress changes in regions with dense fault networks can cause periods of increased seismic activity (e.g., Wedmore et al., 2017b), increasing the frequency of interactions between faults segments, and thus, the potential for hard-linkages to establish. The geometry of the inter-segment zone at the time of a multi-segment rupture, or earthquake sequence, then influences the geometry of the hard-link. For example, segments with small amounts of separation may link through fault bends if a multi-segment rupture or earthquake sequence occurs during the underlapping phase, whereas consecutive single segment ruptures may promote continued along-strike growth to overlapping inter-segment zone geometries, where breached ramps are then preferred (fig. 2.4). However, this ultimately depends on the time between coseismic events on the segments and surrounding ruptures that may cause stress shadows within the inter-segment zone (e.g., Stein, 1999).

If segment growth and linkage is considered to occur via the isolated fault model (e.g., Cartwright et al., 1995; Dawers and Anders, 1995; Morley et al., 1990; Trudgill and Cartwright, 1994), rupture propagation across inter-segment zones and/or earthquake interaction between fault segments is required (e.g., Gomberg et al., 2001; Harris and Day, 1993, 1999; Kilb et al., 2000). The constant-length fault model assumes kinematic connectivity, and thus soft-links at depth exists already, promoting the two segment rupture scenario through a continuous rupture (Walsh et al., 2003, 2002). Whether a rupture propagates through the inter-segment zone in either model depends on the zone's mechanical properties, which are related to certain fault properties such as slip maturity (e.g., Ikari et al., 2011; Savage and Brodsky, 2011).

Similar to previous models that sought to understand growth processes occurring at fault tips following an earthquake, an assumption made here is that coseismic stress perturbations exceed the stresses from tectonic loading (e.g., Cowie and Shipton, 1998). Ignoring tectonic loading allows us to examine the influence of coseismic Coloumb stress change on linking fault geometry without the complicating effect of faults nucleating due to background stresses (Fialko, 2006). However, tectonic loading may cause slip on secondary faults that are poorly oriented for segment linkage but well-oriented for reshear in the tectonically induced stress field (Freed, 2005; Harris and Simpson, 1996). Formation of new faults controlled by tectonic loading is also likely if the segment separation is large and off-fault deformation accommodates slip transfer between segments (Duan and Oglesby, 2005). Tectonic loading may therefore promote along-strike growth of segments that are well-oriented in the current stress field, and favour hard-links between overlapping segments whose tips propagate into a stress shadow (e.g., Ganas et al., 2006; Harris, 1998; Lin and Stein, 2004).

Dynamic coseismic, interseismic or multi-cycle effects likely further influence fault linkage (e.g., Harris, 1998; Kase, 2010) and may also cause failure of faults with geometries that are deemed retarded by Coulomb stress models (e.g., Gomberg et al., 2001; Kilb et al., 2000). Multi-cycle effects include increasing fault zone structural maturity, which reduces the strength of the inter-segment zone between fault segments (e.g., Otsuki and Dilov, 2005; Wesnousky, 1988) and can cause interaction and rupture propagation to occur over larger fault lengths, including several segments (e.g., Manighetti et al., 2007), and changes to the frictional strength of fault surfaces due to the grinding away of asperities (Sagy et al., 2007). Furthermore, multiple earthquake cycles will also increase the stress concentration at fault tips (e.g., Cowie and Scholz, 1992a; Pollard and Segall, 1987) and thus within the inter-segment zone.

Linking faults may establish through incremental earthquake rupture and associated damage around the fault tip (Herbert et al., 2015; McBeck et al., 2016). Fault segments where $\theta < 30°$ may propagate toward one another, whereas at higher angles new oblique-slip secondary faults may develop to form a relay ramp hard-link (Hatem et al., 2015). Our model results show that fault bends form up to a θ of 45°, however, the majority of our natural observations for fault bends had a $\theta < 30°$. Analogue models have shown that pre-existing structures may provide a pathway for fault bends to establish when θ is between 30° and 45° (e.g., Morley et al., 2004).

2.4.2 The influence of pre-existing structures

The geometry and development of normal faults is primarily influenced by the regional and local stress fields (e.g., Morley, 1999b; Ring, 1994). However, in this study we have shown how coseismic Coulomb stress changes influence the geometry of a hard-link between en echelon faults by altering the local stress field (fig. 2.8; e.g., Crider and Pollard, 1998; Harris and Simpson, 1992; King et al., 1994). Pre-existing structures that have a lower cohesive or frictional strength than the surrounding intact rock have been shown to localise deformation and alter the local stress field (e.g., Bellahsen and Daniel, 2005; Collettini et al., 2009; Ebinger et al., 1987), and therefore may also influence the establishment and geometry of the hard-link (e.g., Bellahsen et al., 2013; Corti et al., 2007; Lezzar et al., 2002; Morley et al., 2004; Reeve et al., 2015; Rosendahl, 1987) by reducing the required $\Delta\sigma_c$ for failure. Here, we provide conceptual examples of pre-existing weak planes striking at various angles to normal faults, with an extension vector E-W (fig. 2.9).

When weak pre-existing structures strike parallel to the faults (fig. 2.9a), fault linkage is likely perturbed until faults overlap and cannot propagate further at their tips due to stress shadows (e.g., Ganas et al., 2006; Harris, 1998; Lin and Stein, 2004), at which point a hard-link can only establish by cross-cutting the pre-existing fabric. Rift-parallel pre-existing crustal weaknesses around Lake Albert, East Africa have helped formed overlapping, en echelon normal faults arrays (Aanyu and Koehn, 2011) and may therefore help faults develop the inter-segment geometry required for breached ramps or continental transform faults (e.g., Bellahsen et al., 2013; Rosendahl, 1987). If the strike of pre-existing structures are well-oriented for fault linkage (i.e. at angle θ to the fault segments), but oblique to the extension direction (fig. 2.9b, right-stepping), fault bends or breached ramps may be promoted during underlapping and overlapping geometries, respectively, if the pre-existing structure is sufficiently weak compared to along-strike structures. Several examples of hard-linkages along border faults in Lake Tanganyika have been shown to exploit well-oriented, pre-existing planes of weakness (e.g., Corti et al., 2007; Lezzar et al., 2002). Lastly, hard-links are promoted if pre-existing structures are favoured by the regional stress orientation and have a strike close to θ, however, this requires a stress rotation from a regional stress orientation that formerly favoured the geometry of the en echelon faults ('left-stepping', fig. 2.9c). Conversely, weak pre-existing structures may inhibit fault linkage by providing surfaces for failure that are poorly-oriented for fault linkage.

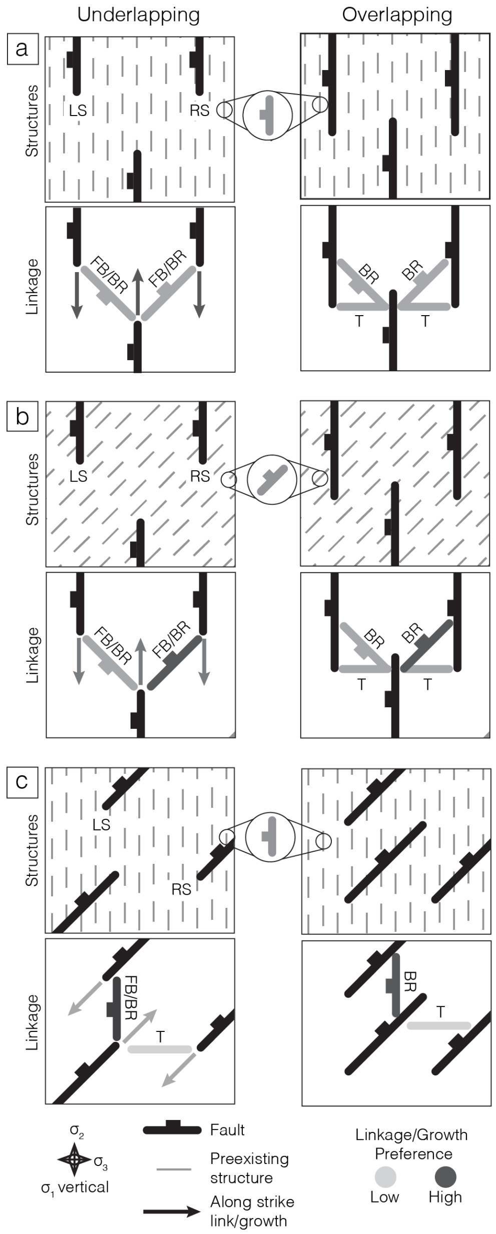

Fig. 2.9 A diagram showing the influence of pre-existing structures on hard-links between normal fault segments. The preference of linking faults (FB = fault bend, BR = breached ramp and T = transform) are compared against along-strike growth (arrows). Fault segments (LS, left-stepping, RS, right-stepping) are indicated by thick black lines and pre-existing structures by smaller, grey lines. Both fault segments and pre-existing structures dip at 60°, and the extension direction is E-W. a) Segment and pre-existing structures striking perpendicular to σ_3. b) Segment strike perpendicular and pre-existing structures strike oblique to σ_3. c) Both segments and pre-existing structures strike oblique to σ_3. Geometry of the linking fault between en echelon faults, or along-strike secondary faults, is shown for underlapping and overlapping geometries.

2.5 Conclusion

In this paper we have discussed the role of coseismic Coulomb stress change on shaping the hard-link between two en echelon normal fault segments (or faults). Coulomb stress changes can promote failure on a well-oriented secondary fault, a linking fault, incrementally forming a hard-link between segments. Linking faults may nucleate within the inter-segment damage zone, or reactivate pre-existing structures. Our calculations indicate that the two segments must both rupture for the greatest stress change to occur on a linking fault within the inter-segment zone, rather than on a segment-parallel secondary fault aligned along strike from the segment tip. This may occur either through the aggregate effect of discrete events on both segments (i.e. an earthquake sequence), or as a single earthquake whose rupture propagates across the geometrical discontinuity (i.e. a multi-segment rupture). When only one segment ruptures, the Coulomb stress change is largest for the along-strike secondary fault, and thus continued segment growth is preferred at all geometries except very close to the segment tips.

Our results match well with natural examples of hard-links between normal fault segments, and show that the linking fault geometry that experiences the greatest coseismic Coulomb stress change is related to the geometry of the inter-segment zone. Here, we suggest that underlapping parallel normal segments preferentially link through fault bends or breached ramps when separation is $\leq$ 20% of the total length of both segments, and $\theta \leq 45°$ or $\theta > 45°$, respectively. Fault segments that grow to overlapping geometries preferentially link through either transform faults when separation is $\gtrsim$ 15% of the total length, or breached ramps at smaller separations. Maximum separation for segment hard-linkage was found to be $\sim$ 20% the total segment lengths, agreeing with previous studies of normal fault surface rupture traces. At larger separations the coseismic Coulomb stress change is largest for along-strike secondary faults.

Whilst natural examples of hard-links between normal fault segments through fault bends and breached ramps are plentiful, the same is not true for continental transform faults. An explanation from this study is that normal fault segments may link through fault bends or breached ramps in underlapping regimes before they reach the geometries required for transform faults.

Chapter 3

Controls on early-rift geometry: new perspectives from the Bilila-Mtakataka fault, Malawi

ABSTRACT

We use the $\sim$ 110 km long Bilila-Mtakataka fault in the amagmatic southern East African Rift, Malawi, to investigate the controls on early-rift geometry at the scale of a major border fault. Morphological variations along the 14±8 m high scarp define six 10 to 40 km long segments, which are either foliation parallel, or oblique to both foliation and the current regional extension direction. As the scarp is neither consistently parallel to foliation, nor well oriented for the current regional extension direction, we suggest the segmented surface expression is related to the local reactivation of well oriented weak shallow fabrics above a broadly continuous structure at depth. Using a geometrical model, the geometry of the best-fitting subsurface structure is consistent with the local strain field from recent seismicity. In conclusion, within this early-rift, pre-existing weaknesses only locally control border fault geometry at subsurface.

This chapter is based upon the published paper: Hodge, M., Fagereng, Å., Biggs, J. & Mdala, H. Controls on early-rift geometry: new perspectives from the Bilila-Mtakataka fault, Malawi. *Journal of Geophysical Research Letters, 45 (9)*. https://doi.org/10.1029/2018GL077343.

Author contributions and declarations: Hodge, M. is the main author of this work, undertook the data analysis and fieldwork, and wrote a proposal for the purchase of the TanDEM-X DEM. Fagereng, Å. and Biggs, J. provided supervision for the work and research manuscript. Mdala, H. of the Geological Survey Department, Malawi helped with fieldwork and provided comments on the manuscript. Delvaux, D., Fossen, H., McCaffrey, K., Keir, D., and two anonymous reviewers provided constructive comments on versions of the manuscript at *Geology* and *Geophysical Research Letters*.

3.1 Introduction

Rift structure is controlled by the geometry of border faults. In intact, isotropic rocks, normal border faults would strike perpendicular to the least principal stress and dip 60° (e.g., Anderson, 1905; Byerlee, 1978, see Section 1.1.1 for more information). Frictionally weak and/or low cohesive strength caused by pre-existing structures can, however, localise strain and provide surfaces for fault reactivation (e.g., Bellahsen et al., 2013; Walker et al., 2015; Worthington and Walsh, 2016), including structures that are not ideally oriented in the current stress field (e.g., Ebinger et al., 1987). Therefore, pre-existing structures formed in both current and previous deformation phases can have a fundamental influence on rift geometry (e.g., Phillips et al., 2016; Whipp et al., 2014). For young rifts where the initial structure is currently being established, such as parts of the East African Rift System (Macgregor, 2015), pre-rift structures such as basement foliations, or structures originating from older rift events, have been suggested as primary controls on the current rift geometry and evolution (Corti, 2009; Delvaux et al., 2012; Morley, 2010). However, alternative hypotheses suggest that early rifting is controlled by the stress field at the time of fault nucleation (Fazlikhani et al., 2017; McClay and Khalil, 1998), anisotropy in the lithospheric mantle (Tommasi and Vauchez, 2001) or thermal weakening (Claringbould et al., 2017).

As well as rift-scale observations, the influence of pre-existing structures has been demonstrated in laboratory rock deformation (e.g., Collettini et al., 2009) and analogue experiments (e.g., Aanyu and Koehn, 2011; Athmer et al., 2010; Bellahsen and Daniel, 2005; Morley, 1999a; Ventisette et al., 2006); yet, at the scale of an individual fault their influence is less clear (e.g., Phillips et al., 2016; Whipp et al., 2014). An expectation is that a major fault is either parallel to reactivated weak surfaces, or in an orientation consistent with fault nucleation in the current stress field. In the Suez Rift, a combination of these options is illustrated by foliation-oblique faults reflecting the stress at fault initiation, hard-linked by foliation-parallel faults (McClay and Khalil, 1998). A more detailed review of pre-existing structures can be found in Section 1.1.4.

Here we address the relative importance of the controls on rift and fault geometry, by using high-resolution satellite and field measurements to describe the geometry of the Bilila-Mtakataka fault (BMF) and foliations in the crystalline footwall rocks (fig. 3.1a). The BMF is a normal border fault at the southern end of the amagmatic Malawi Rift System (MRS), whose surface trace has been suggested to comprise a continuous ~ 10 m high scarp for ~ 100 km (Jackson and Blenkinsop, 1997). Rift initiation in the southern MRS may be as recent as early to middle Pliocene (Lyons et al., 2011), so the BMF provides a rare natural laboratory for the relationship between basement foliation and fault geometry in the early stages of rifting (see Section 1.3 for a more comprehensive overview of the EARS and MRS). We discuss whether BMF geometry is consistent with basement reactivation, stresses inferred from regional extension, and/or a different local stress field at the time of initiation. With the availability of this dataset, we also aim to provide new insights into the morphology of one of the Earth's longest, continental normal fault scarps.

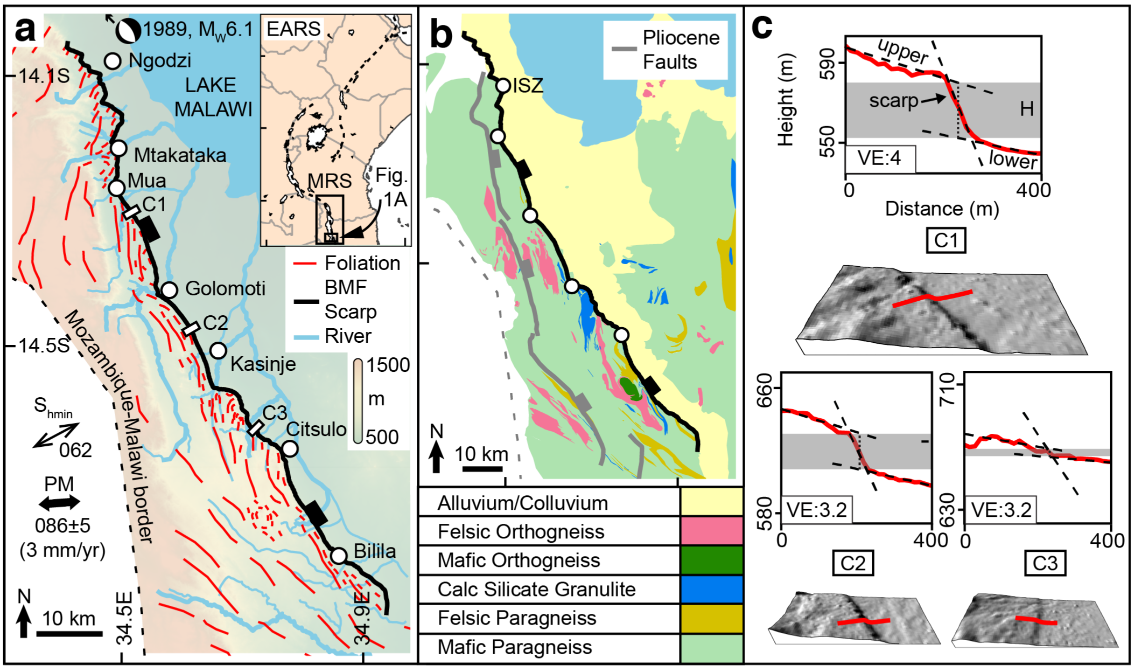

Fig. 3.1 a) Geographical context of the Bilila-Mtakataka fault (BMF) scarp. S_{hmin} = current inferred minimum horizontal stress from Delvaux and Barth (2010), PM = current regional extension direction from Saria et al. (2014), EARS = East African Rift System, MRS = Malawi Rift System. b) Geological map modified after Walshaw (1965) and Dawson and Kirkpatrick (1968). White filled circles denote inferred intersegment zones (ISZ, fig. 3.2). c) Elevation profiles and hillshade digital elevation models (DEMs), numbers refer to locations in panel A. Definitions of upper and lower surfaces, and the method for deriving scarp height, *H*, follow Avouac (1993). Vertical exaggeration (VE) is displayed on the profiles.

3.2 Data collection and methodology

We analyse a 12 m resolution TanDEM-X digital elevation model (DEM) using QGIS to calculate scarp height and width from elevation profiles along the BMF scarp at 1 km intervals (fig. 3.1c). The BMF scarp was mapped in QGIS at 1:100 scale from 14.04°S, 34.34°E to 14.93°S, 34.94°E; 128 profiles were extracted, each with a length of 400 m. As the slip direction is considered to be pure normal (Chorowicz and Sorlien, 1992; Jackson and Blenkinsop, 1997), elevation profiles were oriented perpendicular to the local scarp trend. Previous regional fault studies in Malawi have used a 30 m SRTM DEM to map faults (e.g., Laó-Dávila et al., 2015); however, TanDEM-X is higher-resolution and has higher absolute and relative vertical accuracies (e.g., Gruber et al., 2012). Here, for a subsample of 50 control points, the median elevation difference between the TanDEM-X DEM and an SRTM DEM was found to be less than 5 m.

Scarp height is defined as the elevation difference between regression lines fitted to the footwall and hanging wall surfaces, extrapolated to a line through the point of maximum slope on the fault scarp (fig. 3.1c; Avouac, 1993). To generate the regression lines, the bottom and top of the scarp were picked manually. Measurements were repeated three times in random order to calculate uncertainty. Interpretation of each profile can be found in Appendix D. The root mean square error (RMSE) for the regression lines was on average $\sim$ 1.5 m and the standard deviation of errors between measurements was $\sim$ 0.4 m (red circles, fig. 3.2b). Please refer to Appendix E for tabular results of scarp height and RMSE errors for all profiles, for each run. Measurement repeatability (here defined as horizontal error between all scarp-picks of less than 10 m) was achieved for 102 of the 128 profiles (blue circles, fig. 3.2b), with fewer repeatable measurements at the ends of the fault where the scarp is smaller and therefore more difficult to recognise in the DEM (fig. 3.2b). To reduce measurement errors or other local site effects (e.g. erosion, Zielke et al., 2015), a 5 km moving average and standard deviation are applied to the repeatable measurements (blue line and envelope, fig. 3.2b).

In the field, the scarp is expressed as a soil-mantled hillslope. Bedrock exposures are scattered, and there are no known exposures where displacement can be directly measured across the fault. No fault plane slip direction indicators unequivocally formed by rift-related faulting were found. Dip and dip azimuth of the scarp slope were measured at seventeen locations (fig. 3.2e), but note that given the weathered, soil-dominated nature of the scarp, the dip is representative of the angle of repose and may be less than the dip of the fault plane. Thus, whereas the uncertainty in the absolute dip measurements is $\sim 5°$, this dip may differ significantly from fault plane dip. Basement foliation orientation was also measured in the footwall amphibolite to granulite facies gneisses at each location and augmented by interpolation of composition and fabric orientations from geological maps (fig. 3.1b; Dawson and Kirkpatrick, 1968; Walshaw, 1965). The mineralogy of the gneisses is dominated by biotite, feldspar and quartz in variable modal proportions, with smaller but variable modes of hornblende and garnet. The gneissic foliation is continuous, cohesive, and typically planar, but locally anastomosing, and defined by both mineral segregation banding and preferred mineral orientations.

3.3 Results

3.3.1 Scarp morphology and segmentation

Analysis of the TanDEM-X DEM shows that the trend of the BMF scarp is locally variable, with an average of $\sim 150°$ (fig. 3.2a). This average trend is at an angle of 64° to the current regional plate motion vector estimate of $086°\pm5°$ (fig. 3.2d; Saria et al., 2014). On the other hand, this average scarp trend is 88° to a local, minimum horizontal stress (Sh_{min}) inferred from 13 earthquake focal mechanisms in the Malawi rift (fig. 3.2d; Delvaux and Barth, 2010). The footwall basement foliation has a bimodal strike distribution with peaks at 160° and 205°, but varies considerably along the BMF (fig. 3.2a).

The average scarp height is 14 m (σ = 8 m) but varies by an average of 6 m per km; the largest measured scarp height is $\sim$ 34 m (fig. 3.2b). Only minor changes in scarp morphology occur at major rivers. The scarp height displays two bell-shaped, near-symmetrical profiles; one in the north (0$\sim$80 km) and one in the south (95$\sim$128 km). Between 80 and 95 km, scarp height is almost zero and the scarp trend varies considerably, forming two bends around surface exposures of calc-silicate granulite (figs. 3.1b and 3.2c). Based on major gaps in fault scarp continuity or distinct along-strike changes in scarp morphology and/or scarp trend (e.g., Crone and Haller, 1991), the BMF can be divided into six segments (fig. 3.2, Table 3.1). These segments are now described from north to south.

3.3.2 Structural analysis of BMF segments

In the northernmost segment, Ngodzi, the fault scarp orientation alternates in a zig-zag pattern between a predominant trend of 110°, which crosscuts gneissic foliations, and a foliation-parallel trend of 210°, where the scarp is steepest. For the northernmost few kilometres, a scarp is not obvious on the DEM profiles, but then a scarp of 13 ± 8 m can be traced (fig. 3.2b).

Along the Mtakataka segment an 18 ± 5 m high scarp is sub-parallel to the eastward-dipping foliation (dip $48°\pm22°$, fig. 3.2e), except at the river Nadzipulu where the scarp (locally 25 m high) crosscuts the foliation to trend $\sim 120°$ for two kilometres. As in the Ngodzi segment, the scarp dips more gently ($\sim 30°$) where the scarp and foliation are sub-parallel, than where the scarp crosscuts the foliation ($\sim 40°$, fig. 3.2e).

The Mua segment is convex in shape, consistently oblique to the foliation, and its trend rotates south-westward from 150° to 200° at 2° per km (fig. 3.2a). Scarp height is 20 ± 6 m and decreases slightly at both ends of the segment (fig. 3.2b). Toward the northern end, at the Naminkokwe river, a 13 m high knickpoint has

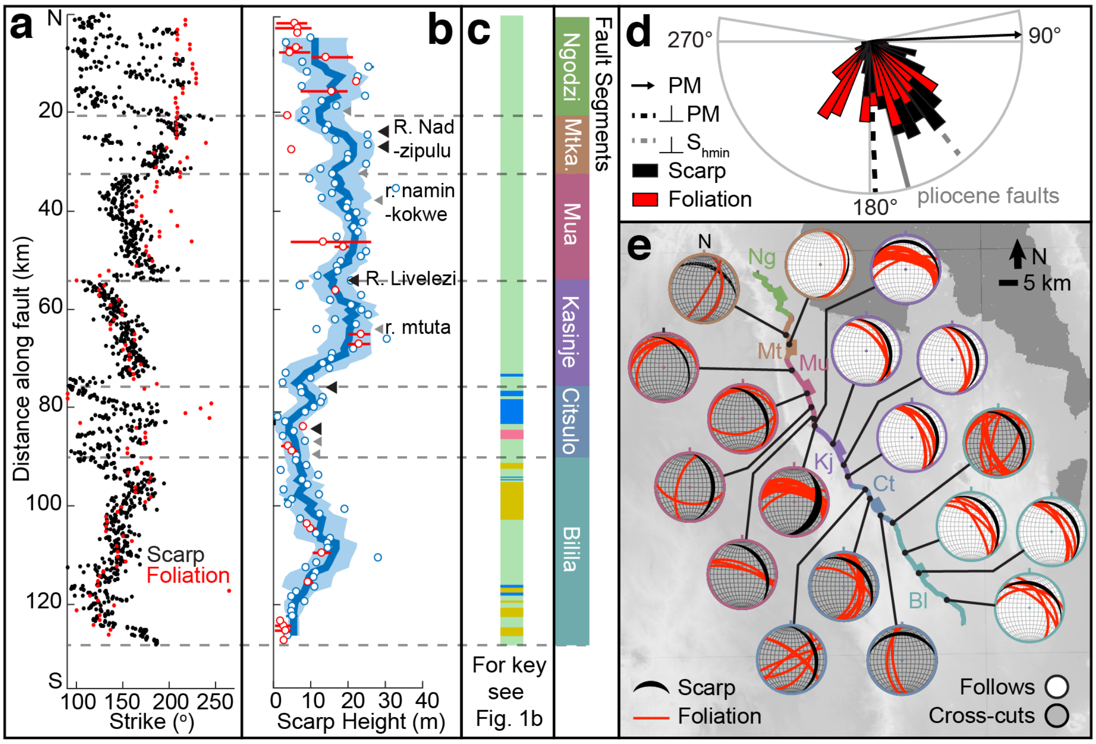

Fig. 3.2 Panels a to c are plots of distance along the Bilila-Mtakataka fault scarp against: a) scarp trend and foliation strike from DEM and geological maps; b) scarp height measured from DEM. Repeatable measurements are blue circles, and non-repeatable are red circles (error bars included). A 5 km moving average (solid blue line) and standard deviation (blue shaded area) are also given. Black and grey triangles mark major and minor rivers respectively; and c) footwall lithology, see fig. 3.1b for key (Mtka = Mtakataka). d) Angular relationship between scarp trend (black), foliation strike (red), current regional extension direction (PM, black arrow; from Saria et al., 2014), and planes perpendicular to current regional extension direction (⊥PM, black dotted line) and to local minimum horizontal stress (⊥Sh_{min}, grey dotted line; from Delvaux and Barth, 2010). e) Map of BMF segments (coloured: Ng = Ngodzi; Mt = Mtakataka; Mu = Mua; Kj = Kasinje; Ct = Citsulo; and Bl = Bilila), including lower hemisphere, equal angle, stereoplots showing field measurements of scarp and basement rock foliation, indicating where the scarp follows (white) or cross-cuts (grey) local foliation.

eroded back 70 m; and a number of steeply dipping extensional fractures - likely associated with recent fault-related deformation - strike parallel to the scarp and cross-cut the gently dipping foliation (fig. 3.3a-c). The Mua segment intersects the Kasinje segment at the river Livelezi, where the scarp abruptly rotates from trending 185° to a trend of 115° (fig. 3.2a). This change coincides with an increase in scarp dip to 45° (fig. 3.2e).

In contrast to the Mua segment, the entire Kasinje segment is parallel to foliation that dips eastward at 53°±9° (fig. 3.2a,e). The scarp is concave in map view, and scarp trend and foliation strike both increase southward by around 2° per km. The scarp is clearly defined with an average height of 16±8 m, reaching a maximum of 24 m near the segment centre. A 16 m high knickpoint in the Mtuta river is set back 40 m from the scarp front, and shows that the fault is parallel to the local foliation and lacks a fractured footwall damage zone (fig. 3.3d-f). Scarp height decreases to less than 10 m several kilometres from the intersection with the Citsulo segment.

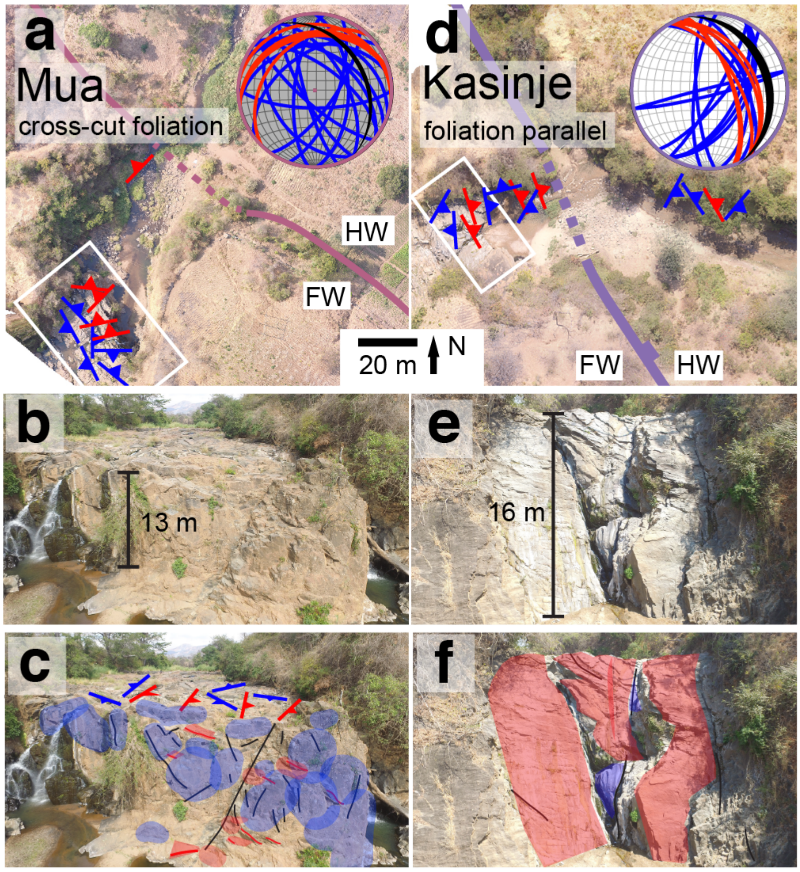

Fig. 3.3 Photographs of a) Mua and d) Kasinje knickpoints showing foliation (red) and fracture (blue) orientations from above (panels b and e) and on the waterfall (panels c and f). For panels c and f, where the waterfall is parallel to a foliation or fracture surface, the surface is coloured appropriately (i.e. red or blue). Foliation dips much more gently at Mua than Kasinje. The scarp trend and waterfall surface at the Mua knickpoint (setback 70 m from the scarp) cross-cut the high-grade metamorphic foliation, whereas both are parallel to foliation at the Kasinje knickpoint that is setback 40 m from the fault scarp.

The Citsulo segment has an irregular scarp trend that alternates between $\sim 120°$ and $\sim 185°$. The scarp trace forms two large, approximately right angle bends (fig. 3.1a). In the field, the scarp can be traced around both bends; however, it is difficult to identify the fault scarp from the hills behind it between these features. Although two < 10 m high north-south trending scarps can be identified in the DEM, they are offset by several kilometres (fig. 3.2b). This is the only discontinuity of the scarp trace along the entire surface length of the BMF, and we define this as the 'Citsulo discontinuity'. The footwall lithology is more variable here than

Table 3.1 Description of the six structural segments along the Bilila-Mtakataka fault including foliation measurements.

Distance on fault (km)	Segment Name	Length (km)	Scarp Height (m)	Lithology	Foliation Strike	Foliation Dip
0 - 21	Ngodzi	21	13±8	Mafic Paragneiss	N/A	N/A
21 - 34	Mtakataka	13	18±5	Mafic Paragneiss	156±70°	48±22°
34 - 55	Mua	21	20±6	Mafic Paragneiss	116±76°	40±24°
55 - 77	Kasinje	22	16±8	Mafic Paragneiss Calc Silicate Granulite	157±10°	53±9°
77 - 90	Citsulo	13	7±4	*Intercalated:* Mafic Paragneiss Calc Silicate Granulite Felsic Orthogneiss	158±86°	62±13°
90 - 128	Bilila	38	9±6	Mafic Paragneiss Calc Silicate Granulite Felsic Orthogneiss	164±99°	53±19°

elsewhere along the fault, and comprises intercalated bands of felsic orthogneisses, mafic paragneisses and calc-silicate granulite (fig. 3.2c), with a steeply dipping (62°±13°), variably folded and locally discontinuous foliation.

The southernmost segment, Bilila, has a concave scarp parallel to strike of foliations that dip eastward at 53°±19°. A scarp of height 9±6 m can be seen along along the entire segment before the scarp becomes indistinguishable on the DEM after 120 km. Lithology along the Bilila segment varies between a volumetrically dominant mafic paragneiss unit, and bands of calc-silicate granulite and felsic paragneisses.

3.4 Discussion

3.4.1 Variations in scarp trend

The total length of the surface fault trace where a scarp was identified in the DEM is ∼ 110 km. The along-strike profile of scarp height displays two bell-shaped profiles, and comprises several peaks and troughs indicative of fault segmentation (fig. 3.2b; e.g., Crider and Pollard, 1998; Crone and Haller, 1991; Walker et al., 2015). Segmented, but bell-shaped scarp height profiles generally result from hard-links between initially independent segments (e.g., Anders and Schlische, 1994; Dawers and Anders, 1995; Trudgill and Cartwright, 1994), and/or interactions with other structures or strength anisotropies (e.g., Fossen and Rotevatn, 2016). An increase in scarp dip at intersegment zones along the fault (e.g., between the Mua and Kasinje segments) may also be due to hard-links established by progressive growth of secondary faults, such as breached relay ramps or transfer faults (e.g., Gawthorpe and Hurst, 1993; Peacock, 2002; Trudgill and Cartwright, 1994).

Scarp height on the Citsulo segment is too low to fit a bell-shaped height curve to the entire fault scarp. This low height, and the observation that the scarp is discontinuous near Citsulo, may indicate that the BMF comprises two separate faults. In this interpretation, there is no hard link between a 65 km long northern fault comprising the four segments north of Citsulo, and a 30 km long southern fault represented by the Bilila segment.

Similar to other faults whose surface trace is discontinuous, the BMF may be continuous at depth (e.g., Nicol et al., 2005; Worthington and Walsh, 2016). Note, however, that the low scarp height in the Citsulo segment may be related to local change in surface lithology. Whereas the majority of the fault displaces foliated, biotite-bearing gneisses, the scarp at Citsulo bends around poorly foliated, diopside-tremolite calc-silicate granulite, which is both frictionally strong (He et al., 2013) and lacks any pre-existing weak planes.

The BMF scarp parallels the strike of local foliation along 60% of its length (fig. 3.2a). Where the scarp locally bends to crosscut the foliation, e.g., Ngodzi and Mtakataka, such bends form high angle links between en echelon foliation-parallel scarps. These bends create a zig-zag pattern similar to other faults that locally reactivate weak planes (e.g., Bellahsen and Daniel, 2005; McClay and Khalil, 1998), except that the cross-foliation segments do not have a consistent strike (fig. 3.2a). The only major segment that crosscuts foliation along its full length is Mua, where foliation dips more gently than elsewhere along the scarp. This corroborates existing hypotheses that gently dipping structures are difficult to frictionally reactive in rifts (e.g., Collettini and Sibson, 2001; Phillips et al., 2016). On the Ngodzi and Mtakataka segments, the scarp is steeper where it cross-cuts the foliation, and a more gentle scarp is also present on the foliation-parallel Kasinje segment, compared to the Mua segment. Whilst to the first-order, the BMF scarp systematically appears steeper where it crosscuts foliation, a combination of factors including erosion rate, scarp age, footwall damage zone parameters, and original scarp shape influence the current scarp slope (Arrowsmith et al., 1998; Avouac, 1993), and the interpretation of this tentative relation between scarp slope and foliation orientation is highly uncertain.

3.4.2 Relations between fault scarp geometry, local and regional stresses, and pre-existing structures

The average trend of the BMF scarp is comparable to the strike of the nearest instrumentally recorded earthquake, the 1989 Salima M_W 6.1 event (strike 154°±25°, dip 32°±5°, rake -92°±25°), whose epicenter was $\sim$ 40 km from the northern tip of the BMF scarp (Jackson and Blenkinsop, 1993). Whereas a normal fault striking perpendicular to the current plate motion would strike 176°±5° (Saria et al., 2014), the BMF average scarp trend fits well with the current local stress field estimated from focal mechanisms (Sh_{min} = 062°; Delvaux and Barth, 2010). This estimate, however, relies on only 13 earthquakes throughout the Malawi rift, and could reflect local strain as accommodated on reactivated faults rather than local stress (Twiss and Unruh, 1998). However, reorientation of the local stress field along zones of weak fabric in rifts has been suggested to occur in close proximity to major border faults along the East African Rift System (Corti et al., 2013; Morley, 2010).

The BMF scarp is neither consistently parallel to foliation, nor in an orientation expected from current plate motion. We therefore propose that the fault segments are linked within the brittle zone to a deeper structure that controls the average surface trace (fig. 3.5a). Variations in scarp height are greatest in the north (fig. 3.2b), where very pronounced zig-zags in scarp trend are observed (fig. 3.2a). We therefore infer that these peaks and troughs in scarp height, which have previously been interpreted as indicators of deeper segmented ruptures (e.g., Cartwright et al., 1996), may in fact result from local variations in fault geometry (e.g., Mildon et al., 2016; Zielke et al., 2015), here caused by heterogeneous reactivation of weak shallow fabrics above a broadly continuous structure. In fact, the local variability in BMF scarp geometry and morphology is similar to other scarps suggested to have formed due to reactivation of a deep structure (e.g., the Egiin Davaa scarp, Mongolia; Walker et al., 2015). Furthermore, the angular relationship between scarp trend and foliation strike at the surface on the BMF are also consistent with field observations by Pennacchioni and Mancktelow (2007), who describe reactivation of deeper structures in the ductile field, but that shallower brittle fractures largely crosscut cohesive, metamorphic structures and foliations, except where well oriented. We also note that the foliation-oblique scarp segments, big or small, do not have a consistent trend (fig. 3.2a), as opposed to what one would expect if a consistent stress field, at the scale of the fault, controlled their orientation. Our findings are similar to those by Kolawole et al. (2018) for northern Malawi, who through field observations and aeromagnetic data suggest the 2009 Karonga earthquake sequence (Biggs et al., 2010) occurred on a deep structure that reactivated basement fabric. They found that the basement fabric was associated with the Precambrian Mughese Shear Zone, and the strike of the deep structure is oblique to the regional stress field. As inferred here, the deep structure likely caused a rotation of the local stress field, as suggested elsewhere along the East African Rift System (e.g., Corti et al., 2013; Morley, 2010).

The current scarp height along the BMF may also be evidence of reactivation of a pre-existing weakness at depth (fig. 3.2b). As no fault plane slip direction indicators were found, we assume the faults are purely normal (Chorowicz and Sorlien, 1992; Jackson and Blenkinsop, 1997). Under this assumption the scarp height may be used to represent the surface displacement (Morley, 2002), except where the scarp trend varies considerably from the average trend (Mackenzie and Elliott, 2017). Relative to the fault length, the average vertical surface displacement ($\sim$ 14 m) is greater than would be expected by a single earthquake event ($\sim$ 6 m; Scholz, 2002), but the maximum surface displacement ($\sim$ 28 m) is significantly less than expected for the total displacement ($\sim$ 1,000 m; Kim and Sanderson, 2005). Although surface displacements may be several times less than those at depth (e.g., Villamor and Berryman, 2001), the BMF is still under-displaced compared to its length. This may suggest that the length of the BMF established rapidly in its slip history, before undergoing a current phase of displacement accumulation, i.e. following the constant-length model of fault growth (e.g., Walsh et al., 2002). This fault growth model has been suggested to occur in reactivated faults systems where fault lengths are inherited from underlying structures (Walsh et al., 2002). As such, this morphological analysis of the BMF is consistent with our structural interpretation that the fault is controlled by a pre-existing weak zone at depth oriented oblique to the regional stress direction.

3.4.3 A hypothesis test for a deep structure controlling the average surface fault trace

To test our deep structure hypothesis, we construct a simple geometrical model to fit an irregular surface between the observed BMF scarp trend and an inferred planar deep structure (fig. 3.4). Whereas we recognise that this deeper structure may itself be geometrically complex, segmented or controlled by subsurface fabrics, we assume a planar form for simplicity of this hypothesis test.

We start by defining the location and orientation of the deep fault plane, using its inferred surface projection $(x_f, y_f, 0)$ (red line, fig. 3.4a,b). The surface projection is pinned to either the northern or southern end of the BMF scarp trace, or the centre. We assume that the fault exists as a single planar structure below a depth Z_l, which we call the linking depth, while above this, the fault is discontinuous and/or non-planar. To calculate the location of the fault at the linking depth, we project each point on the surface projection downwards to the corresponding point at the linking depth (x_l, y_l, z_l) using a constant dip, δ (orange line, fig. 3.4a,b), so that:

$$[x_l, y_l, z_l] = \left[x_f - \frac{Z_l \cos\phi}{\tan\delta}, y_f - \frac{Z_l \sin\phi}{\tan\delta}, Z_l\right] \tag{3.1}$$

where ϕ is the strike of the fault (fig. 3.4c).

We produce a fault surface above the linking depth by connecting these co-ordinates (x_l, y_l, z_l) and the co-ordinates of the observed fault scarp (x_s, y_s, 0) (grey polygons, fig. 3.4). The dip of this surface (δ_s) at z = 0 km and the local scarp trend are then used to calculate the resulting scarp height, H, for a given value of slip (u), $H = \sin\delta_s\,(u\sin\alpha)$. Where, α is the angle between the scarp trend and the strike of the deep structure. As no strike-slip offsets were found in the field or on the DEM, we assume that the slip direction on the deep structure is purely normal (Chorowicz and Sorlien, 1992; Jackson and Blenkinsop, 1997). Slip is distributed with a bell-shape with u as the maximum slip at the centre. For some geometries, particularly those with shallow linking depths, the fault will be overturned close to the surface. Since this is unrealistic, we calculate the minimum linking depth (Z_{lmin}) which can be used to construct a fault surface geometry which is not overturned for each case. This is defined as $Z_{lmin} = D_{max} \tan\delta$ (fig. 3.4c), where D_{max} is the maximum horizontal distance between the surface projection of the deep fault (x_f, y_f) and the scarp (x_s, y_s) measured perpendicular to the chosen strike.

We test a range of locations and orientations for the deep fault, and compare the predictions of scarp height to our observations from the BMF scarp (fig. 3.5b). Initially, we pin the surface projection at the centre of the fault scarp trace (red line, fig. 3.4a), with strike of 150°, a bell-shaped slip distribution and an Andersonian dip of 40°. These initial conditions yield a minimum linking depth of $\sim$ 6.8 km (fig. 3.4c) and a surface displacement that generally matches the BMF scarp height with 29 m normal slip (RMSE 6.4 m, fig. 3.5b). The best match (RMSE 5.8 m) to the observed scarp height profile for a continuous deep structure is for a linking depth of 8 km, a shallow dipping (22°) deep fault striking 141°. The slip required to match the BMF scarp is on the order of 50 m, which suggests that the scarp may have built up over multiple earthquakes (Scholz, 2002). Greater linking depths (>10 km) lead to smoother surface displacement profiles and poorer RMSE fits to the observed scarp height, but require less slip.

The specified strike, dip and position of the deep fault have a significant influence on the resulting geometry (fig. 3.4d). Fixing the strike of the deep structure to be perpendicular to current plate motion (174°), and dip to be between 40° and 60° requires a linking depth greater than 25 km (RMSE $\sim$ 8 m; figs. 3.4c and 3.5b). This linking depth is approximately equal to, or greater than, the inferred fault locking depth in south Malawi ($\sim$ 30 km; Jackson and Blenkinsop,

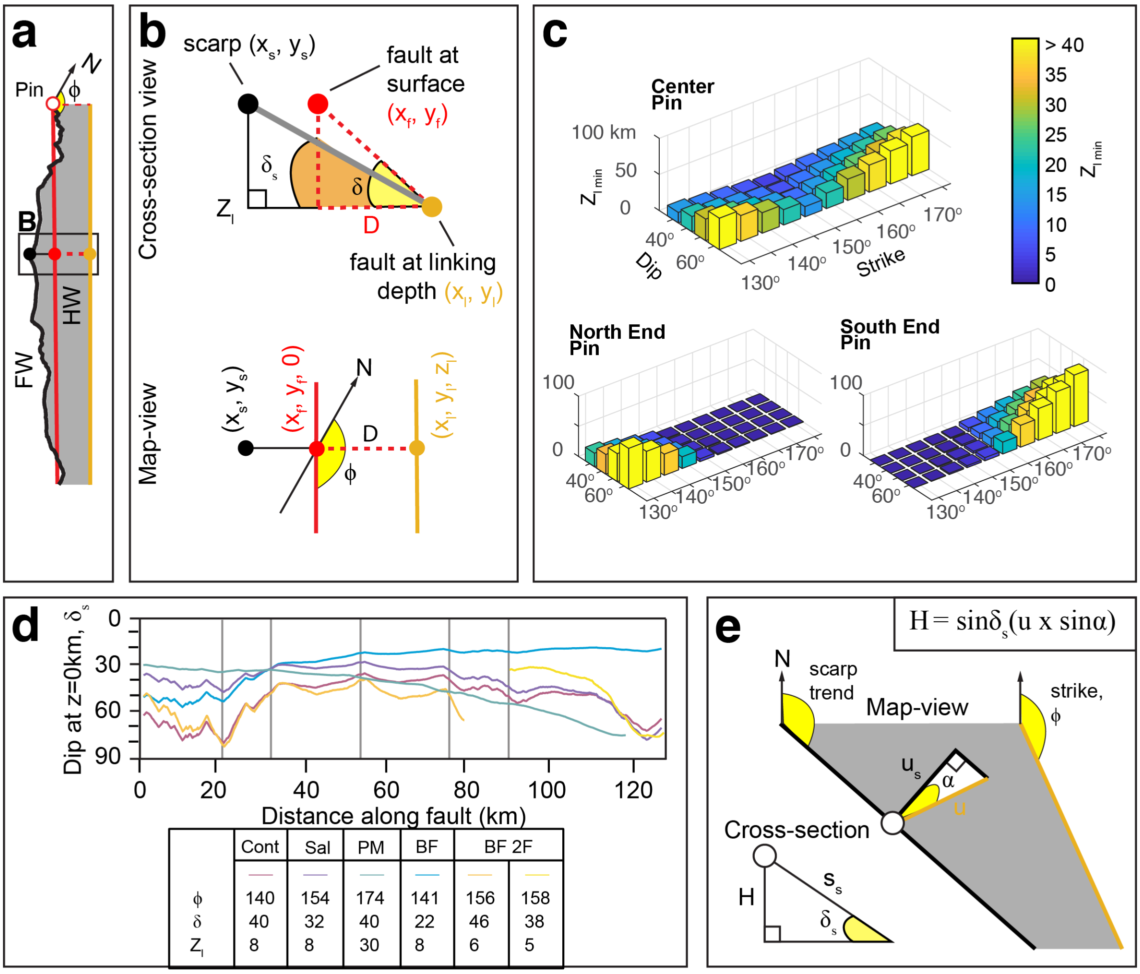

Fig. 3.4 Diagrams showing the method and additional results for testing whether a deep, planar fault can be well fitted to the Bilila-Mtakataka surface trace. a) Map view depiction of how the surface trace of an inferred, planar, deep fault (red line) of strike ϕ (pinned at either the northern or southern end, or the centre) is projected to its specified linking depth, Z_l (orange line). The black line shows the observed fault surface trace. b) Geometrical definitions for calculating the position of the inferred deep fault at the imposed linking depth. The location, dip (δ) and strike (ϕ) of the planar deep fault are imposed, to calculate the strike-normal horizontal distance D between the inferred surface trace of the deep fault (coordinates $[x_f, y_f, 0]$) and the trace of this deep fault at the linking depth (coordinates $[x_l, y_l, Z_l]$). c) Minimum linking depths (Z_{lmin}) for various deep fault orientations for each pin location. d) Calculated fault dip at the surface (δ_s) along the fault, from north to south, for specified parameters of Z_l, ϕ, and δ for scenarios presented in fig. 3.5b. Vertical lines are proposed segment boundaries. e) Calculation of scarp height using δ_s and the angle between the scarp trend and ϕ. Slip u is bell-shaped with the maximum in the centre.

1993) and implies that if the fault formed in the current stress regime, it would exist as a series of discontinuous segments. Inferring a deep structure that strikes sub-parallel to the average BMF scarp trend (150°), or is parallel to the strike of the 1989 Salima earthquake, however, produces a better match (RMSE 6 - 7 m) to the observed scarp height with a shallower linking depth (fig. 3.5b). The best fitting continuous deep structure strikes 141°, dips 22°, and requires a linking depth of 8 km and a slip of 49 m (RMSE $\sim$ 6 m; fig. 3.5b).

A single, continuous structure with $Z_l \leq 10$ km requires slip > 30 m, significantly more than anticipated in a single rupture (Scholz, 2002), but could represent cumulative slip from several events. Any single continuous structure we tested over-estimates the height of the Citsulo segment, whereas two deep faults (a 65 km long northern fault striking 156° and a 30 km long southern fault striking 158°), separated by the Citsulo discontinuity, better fit surface observations (RMSE $\sim$ 4 m) and require a smaller amount of slip (fig. 3.5b). The peaks and troughs in scarp height from all simulations broadly match the observations at the surface, suggesting that the surface displacement is influenced by the near-surface fault geometry (e.g., Mildon et al., 2016; Zielke et al., 2015).

More complex models might fit surface observations better; however, our calculations confirm that the BMF surface expression is not compatible with a deep structure whose strike is perpendicular to the current E-W regional extension direction (Saria et al., 2014), but is compatible with upward propagation of a buried NW-SE striking weak zone (e.g., Worthington and Walsh, 2016).

3.5 Conclusions

Analysis of a high-resolution DEM and field observations suggest that the scarp of the $\sim$ 110 km long Bilila-Mtakataka fault, Malawi, comprises six 10 - 40 km long segments. The scarp averages 14 m in height, but in places exceeds 25 m. This suggests that either multiple earthquake events have ruptured the segments, or a continuous rupture with an extraordinarily large amount of slip ($>$ 30 m) has occurred. Although the scarp trace parallels the foliation for more than half of the fault length, large sections do not. We propose that the BMF scarp is a surface expression of a weak zone (or zones) at depth, that is not well oriented relative to regional extension, but whose strike is sub-parallel to both the average scarp trend and the strike of the largest magnitude earthquake in southern Malawi (the 1989 Salima event). A simple geometrical model does not reject this hypothesis, and indicates that BMF scarp height is likely influenced by the near-surface fault geometry, where locally well oriented metamorphic foliations are reactivated in preference over growth of new faults. Our findings are in agreement with others for north Malawi and elsewhere along the East African Rift System, and suggest deep, weak structures cause a reorientation of the local stress field. These conclusions highlight the importance of considering three-dimensional relationships over a range of length scales when interpreting fault scarps mapped at the surface.

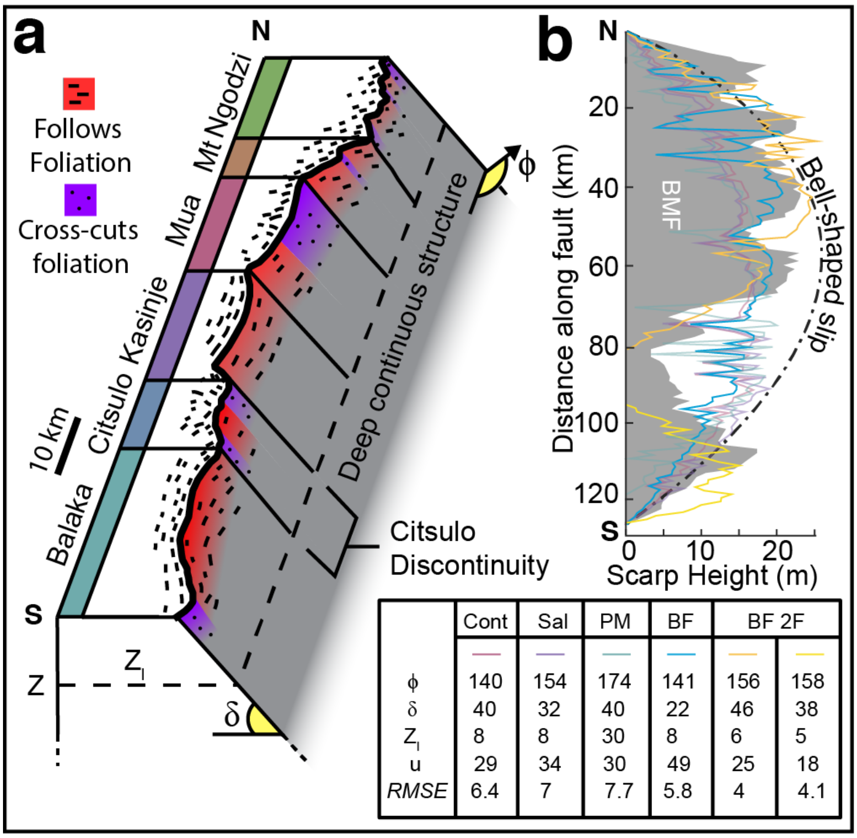

	Cont	Sal	PM	BF	BF 2F	
ϕ	140	154	174	141	156	158
δ	40	32	40	22	46	38
Z_l	8	8	30	8	6	5
u	29	34	30	49	25	18
RMSE	6.4	7	7.7	5.8	4	4.1

Fig. 3.5 a) Schematic of the Bilila-Mtakataka fault, showing where it follows (red) or cross-cuts (purple) the high-grade metamorphic foliation, and an inferred link to a deep structure of strike ϕ and dip δ, at a linking depth Z_l. b) Calculated scarp height, H, for the current BMF scarp if it is linked to a deep structure with maximum slip at the centre, for various deep structure Z_l, ϕ, δ, maximum slip u and length L (Cont = continuous structure that strikes parallel to the average scarp trend; Sal = continuous structure with ϕ and δ from 1989 Salima earthquake; PM = continuous structure with a ϕ perpendicular to the current regional extension direction (taken from, Saria et al., 2014); BF = best-fitting continuous structure; and BF 2F = best-fitting scenario with two separate faults at depth). The observed BMF scarp height is also plotted for comparison (see table for RMSE).

Chapter 4

A semi-automated algorithm for quantifying scarp morphology - application to normal faults in southern Malawi

ABSTRACT

The along-strike variation in scarp morphology along a fault is a useful tool in identifying segmentation and inferring the structural development; however, to date, the calculation of scarp parameters (height, width, slope) has largely been performed manually, meaning human bias exists in both in the methodology and interpretation. Furthermore, the manual approach is time-consuming, meaning measurement resolution is poor and small-scale morphological variations are not considered. Here, we develop a semi-automated algorithm to quantify scarp morphological parameters. We compare our findings against a traditional, manual analysis and assess the performance of the algorithm using a range of elevation model resolutions. We then apply our new algorithm to a TanDEM-X DEM (12 m) for four southern Malawi fault scarps, located at the southern end of the East African Rift System, including three previously unreported scarps: Thyolo, Muona and Malombe. All but Muona comprise first-order structural segmentation at their surface, and by using a high resolution Pleiades DEM (5 m) for the Bilila-Mtakataka fault scarp, we are able to quantify secondary structural segmentation. Our scarp height calculations from all four fault scarps suggests that if each scarp was formed by a single, complete rupture, the slip-length ratio for each fault exceeds the proposed global upper limit. The distribution of vertical displacement at the surface implies the structural segments of the Bilila-Mtakataka and Thyolo faults have hard-linked through several earthquake cycles, and that the Malombe segments have soft-linked. Our findings shed new light on the seismic hazard in southern Malawi, as well as providing a new semi-automated methodology for calculating scarp morphological parameters, which can be used on other fault scarps to infer structural development.

This chapter is based upon the paper in review: Hodge, M., Biggs, J., Fagereng, Å., Elliott, A., Mdala, H. & Mphepo, F. A Semi-Automated Algorithm to Quantify Scarp Morphology (SPARTA): Application to Normal Faults in Southern Malawi. *Solid Earth Discussions*. https://doi.org/10.5194/se-2018-38.

Author contributions and declarations: Hodge, M. is the main author of this work, undertook the data analysis, developed the Pleiades digitial elevation mod-

els (DEM), coded the algorithm and wrote a proposal for the purchase of the TanDEM-X DEM. Fagereng, Å. and Biggs, J. provided supervision for the work. Elliott, A. of Oxford University helped process the Pleiades data and provided feedback on the chapter. Mdala, H. and Mphepo, F. of the Geological Survey Department, Malawi helped assist fieldwork in Malawi over the past few years. Hodge, M. and Biggs, J. each received a grant from the Centre for Observation and Modelling of Earthquakes, Volcanoes and Tectonics (COMET) for the purchase of the Pleiades satellite data.

4.1 Introduction

Earthquake ruptures that break the Earth's surface result in the offset of landforms such as river channels, alluvial fans and other geomorphic features (e.g., Hetzel et al., 2002; Zhang and Thurber, 2003), and create fault scarps that are themselves indicative of the style and magnitude of the earthquake event (Wallace, 1977). By measuring the offsets of landforms and fault scarps, the earthquake-induced surface displacement along the fault can be determined, which can provide information about the rupture and slip history on the fault (e.g., Ren et al., 2016; Sieh, 1978; Wallace, 1968; Zielke et al., 2012), and be used to identify structural segmentation (e.g., Giba et al., 2012; Manighetti et al., 2015; Watterson, 1986) and the presence of linking structures (e.g., Nicol et al., 2010; Soliva and Benedicto, 2004). An example of this can be found in Chapter 3, where our geomorphological analysis of the Bilila-Mtakataka fault scarp indicated the presence of first-order structural segmentation. For faults whose component segments remain unconnected at the surface, the distribution of displacement along a fault can also provide clues to the future structural development (e.g., Cowie and Scholz, 1992a; Dawers and Anders, 1995; Dawers et al., 1993; Peacock, 2002; Walsh and Watterson, 1988) by indicating soft-linkages between segments (Hilley et al., 2001; Willemse et al., 1996). Over time, these segments may hard-link, a concept explored in detail in Chapter 2. Thus, using a combination of the displacement distribution along a fault and the inter-segment zone geometry, we can understand what linkage might exist at depth (e.g., Crider and Pollard, 1998).

In the past, calculating the displacement across a fault scarp was performed by local field surveys or using Global Positioning System (GPS) devices (e.g., Andrews and Hanks, 1985; Avouac, 1993; Bucknam and Anderson, 1979; Cartwright et al., 1995; Cowie and Scholz, 1992a; Delvaux et al., 2012; Gillespie et al., 1992). However, as described in Section 1.2, recent advances in remote sensing has meant that highly accurate and precise vertical displacements could be measured using satellite images and digital elevation models (DEM) (e.g., Bemis et al., 2014; Johri et al., 2014; Roux-mallouf et al., 2016; Talebian et al., 2016; Westoby et al., 2012; Zhou et al., 2015). Depending on resolution, DEMs are categorised as low ($\geq$ 30 m), intermediate ($\sim$ 10 m) or high resolution ($\leq$ 5 m). There is a trade-off between DEM resolution and cost as launching satellites and acquiring (tasking) images is expensive. High resolution DEMs generated by the newest satellites are expensive, somewhat due to minimum coverage areas (typically $\sim$ 100 km^2). Furthermore, generating a DEM using high resolution satellite images may require pre-processing steps including pan-sharpening, and stereo-alignment. As a satellite programme becomes discontinued, satellite images and DEMs are often released for scientific use at no cost (e.g., the SPOT Historical archive, SRTM). These products require limited, to no, post-processing.

With the current drive toward acquisition of high resolution DEMs for paleoseismological studies (e.g., Roux-mallouf et al., 2016; Talebian et al., 2016; Zhou et al., 2015), two scientific questions arise: (1) what DEM resolution is required to successfully locate, calculate and accurately analyse the significant changes in displacement along a fault scarp; and (2) does our interpretation of the distribution of displacement scale with DEM resolution (i.e. how much more are we able to infer using an expensive, high resolution DEM compared to a free, lower resolution alternative)?

Despite the advances in satellite and computing technology, and thus the resolution of DEMs, calculating the vertical displacement along a scarp is largely a manual process that has remained consistent over several decades (e.g., Avouac, 1993; Bucknam and Anderson, 1979; Ganas et al., 2005; Walker et al., 2015; Wallace, 1977; Wu and Bruhn, 1994). Scarp height is typically used as a proxy for minimum vertical displacement (e.g., Morewood and Roberts, 2001), and is calculated by first identifying the fault scarp from an elevation profile by manually picking the crest (top) and base (bottom) of the fault scarp. As shown in Appendix D, picking the fault scarp location manually can be unrepeatable for intermediate or low resolution DEMs, with more than half the measurements showing a variation in picked scarp location for three, independent analyses on the same profiles. Manually processing data can also be subject to human bias; one person's definition of the crest and base of a fault scarp may be different to another person's (Middleton et al., 2016). These inconsistencies ultimately lead to errors within the scarp height calculations and are a contributing factor for the scatter observed in global maximum displacement-length profiles (Gillespie et al., 1992) and along-strike displacement profiles (Zielke et al., 2015).

In this chapter, we develop an algorithm that calculates the parameters (height, width and slope) of a fault scarp from a scarp elevation profile. Using the scarp height as a proxy for vertical displacement (e.g., Morewood and Roberts, 2001), a displacement profile can be created by calculating scarp height at intervals along a fault scarp. This displacement profile can then be used to infer fault structural segmentation and the existence of secondary linking faults (e.g., Cartwright et al., 1995; Childs et al., 1996; Crone and Haller, 1991; Dawers and Anders, 1995; Giba et al., 2012). Automating the morphological calculations will allow a greater number of measurements to be taken along a fault scarp than feasible with ground based methods, improving the understanding of fault behaviour and segmentation (e.g., Cartwright et al., 1995; Manighetti et al., 2015; Trudgill and Cartwright, 1994; Zielke et al., 2012, 2015). Our goal is to develop an algorithm that is open-source and able to run on a personal computer. We test the performance of the algorithm using a number of synthetic and real fault scarps, for a variety of DEM resolutions.

Attempts to create an algorithm for relative dating of fault scarps, by performing best fit calculations to a scarp-like template, have already been attempted (e.g., Gallant and Hutchinson, 1997; Hilley et al., 2010; Stewart et al., 2017); however, these methods may falsely identify geomorphic features that are not fault scarps, and require a very high resolution DEM, usually obtained using LiDAR. These autonomous algorithms therefore still require post-processing, manual quality checks. In addition, Shaw and Lin (1993) developed an algorithm to identify fault scarps by measuring topographic curvature within a moving window, however, their method only distinguishes between different relative scarp heights, rather than provide a quantitative measurement of scarp height.

4.2 Normal faults in southern Malawi

In Chapter 3 we conclude that the Bilila-Mtakataka fault scarp breaks the surface along almost its entire length, a distance of ~ 110 km (fig. 4.1b). The morphology and geometry of the scarp, however, varies along strike and is typical of a large, structurally segmented normal fault (e.g., Peacock and Sanderson, 1991; Schwartz and Coppersmith, 1984; Wesnousky, 1986). Based on the criteria from Crone and Haller (1991) we concluded that the fault comprises six, 'major' (or first-order) segments, varying in length from 13 km to 38 km, and that the distribution of scarp height represents two symmetrical bell-shaped profiles separated by the Citsulo gap. Due to the relatively coarse resolution of our analysis (profiles taken at 1 km intervals), however, we were unable to identify or characterise 'secondary' (or 'second-order') segments within the major segments, i.e. subordinate segments that have a length of the same order of magnitude as the major segment they exist within (Manighetti et al., 2015). Although secondary segments are unlikely to contain gaps of sufficient distance (typically inferred to be ≥ 6 km) to perturb rupture propagation (e.g., Biasi and Wesnousky, 2016; Gupta and Scholz, 2000), their existence may provide evidence for the earliest structural development of the fault (e.g., Manighetti et al., 2007). Furthermore, understanding structural segmentation is crucial in estimating earthquake magnitude, as faults segments may rupture individually, consecutively or continuously (e.g., Anderson et al., 2017; Hodge et al., 2015).

Chapter 3 also concludes that there may be a gap in the Bilila-Mtakataka fault scarp across the Citsulo segment. This discontinuity extends for a maximum length of ~ 10 km. A break in continuity of this length may be sufficient to perturb rupture propagation (Biasi and Wesnousky, 2016) and prevent hard-linkage along a normal fault (see Chapter 2, fig. 2.8). A reduced maximum rupture length would reduce the maximum expected earthquake magnitude (Wells and Coppersmith, 1994) and also the earthquake repeat time (Hodge et al., 2015). Therefore, in order to conclude whether the fault scarp is discontinuous across the Citsulo segment, and the existence of secondary segments and associated linking faults, a higher resolution DEM and a greater number of scarp profiles is required.

Although the Bilila-Mtakataka fault provides an ideal case study of a large, continental normal fault, in order to understand whether it is unique or representative of early-stage rift faulting, we extend our research to other fault scarps within the southern, amagmatic Malawi Rift System (MRS). We investigate three additional faults in the southern MRS identified during fieldwork, which have previously unreported scarps, the Malombe, Thyolo and Muona faults. The Malombe fault is a north-south striking, east-dipping normal fault located $\sim$ 40 km east of the Bilila-Mtakataka fault, on the edge of Lake Malombe; the fault scarp contains at least two major gaps in its surface expression (fig. 4.1c). Lithology varies considerably along the fault length, alternating between felsic and mafic paragneisses with fingers of calc-silicate granulite that intersect the scarp (Manyozo et al., 1972). The Thyolo and Muona faults, south of the Bilila-Mtakataka fault, are two overlapping northwest-southeast striking, southwest-dipping parallel normal fault scarps separated by an offset of $\sim$ 5 km (fig. 4.1d). The lithology of the scarp footwall is very homogeneous at the regional scale, mapped as mafic paragneiss along its entire length (Habgood et al., 1973). To infer the distribution of scarp height, structural segmentation and linkage structures along the Malombe, Thyolo and Muona fault scarps, we develop an algorithm to calculate profiles of the height and width of the scarp. We then compare our findings for these newly studied faults with the Bilila-Mtakataka fault, and assess their morphology and structural development. We also calculate the slip-length ratio for each fault and compare against typical values for normal faults (Scholz, 2002).

4.3 Data and methods

4.3.1 Datasets

As high resolution DEMs have been considered a prerequisite for automated scarp algorithms (e.g., Gallant and Hutchinson, 1997; Hilley et al., 2010), we purchase imagery and create a DEM using Pleiades 1A imagery. The Pleiades 1A satellite was launched on 17th December, 2011 and the Pleiades 1B satellite on the 2nd December 2012. Both operate in the same phased orbit, offset at 180°, offering a daily revisit capability. The sun-synchronous, polar orbit has a mean altitude of 694 km and an inclination of 98.2°. The commercially available resolution of the panchromatic imagery is around 0.7 m and 2.8 m in multispectral imagery. Three 10

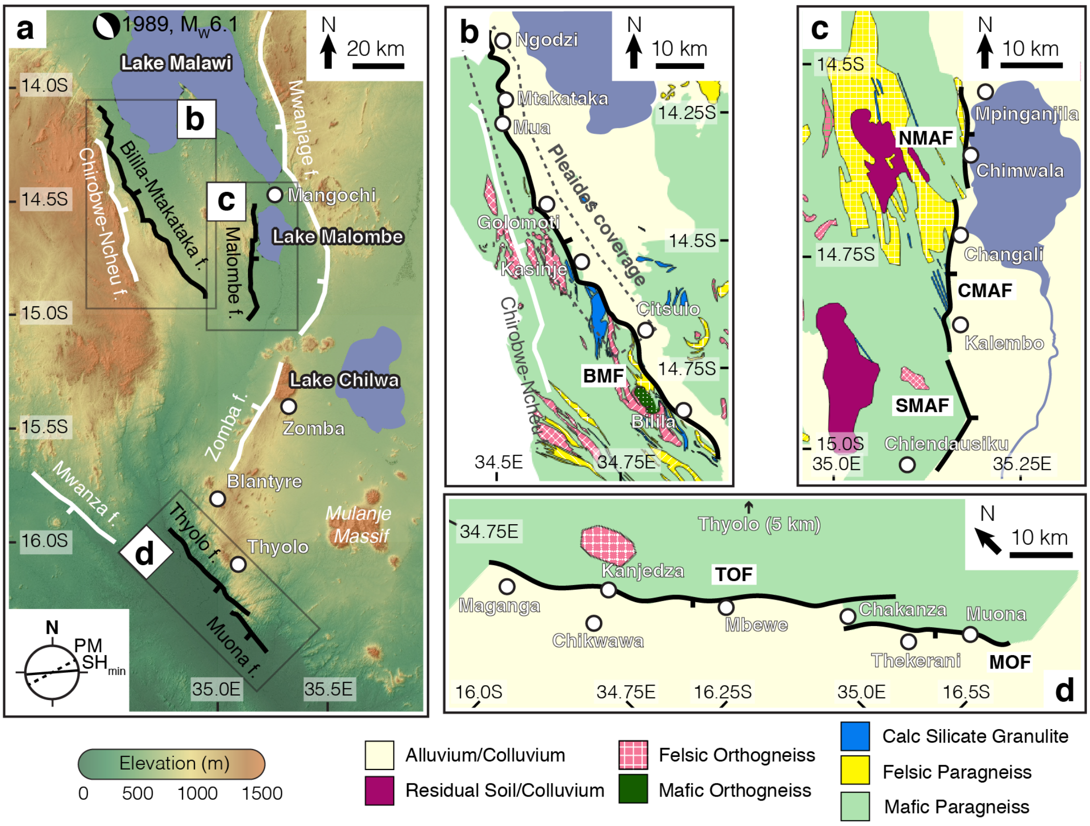

Fig. 4.1 a) Map of faults in southern Malawi; those used in this study are coloured black. Tick marks show the dip direction. Lower left corner shows the plate motion (PM; 86° ± 5°) from Saria et al. (2014) and local minimum horizontal stress (SH_{min}; 62°) from Delvaux and Barth (2010). Panels b to d are geological maps of: b) The Bilila-Mtakataka fault (BMF) showing the coverage of the Pleiades satellite imagery (taken from Dawson and Kirkpatrick, 1968; Walshaw, 1965); c) The Malombe faults (MAF): northern Malombe fault (NMAF); central Malombe fault (CMAF); and southern Malombe fault (SMAF) (taken from Manyozo et al., 1972); and d) The Thyolo fault (TOF) and Muona fault (MOF) (taken from Habgood et al., 1973).

km wide scenes of Pleiades stereo-pairs, covering $\sim$ 90 km of the Bilila-Mtakataka fault scarp (fig. 4.1), were purchased. They were captured on 1^{st} June 2016 with a sun azimuth of $\sim$ 35° and sun elevation of $\sim$ 46°. Cloud cover is $<$ 10%. A panchromatic band and four multispectral bands were recorded; the multispectral band was converted to 8-bit colour. A 0.7 m pan-sharpened multispectral image was created using the higher resolution panchromatic image. The panchromatic stereo-pair was used to create the high resolution DEM.

A $\sim$ 50 cm point cloud was constructed using the Photogrammetric toolbox in ERDAS Imagine 2015®. For each scene, $\sim$ 20 tie points between stereo-pair images were identified to refine the alignment between images at each tie point, producing a root-mean-square error of less than 0.2 pixels ($<$ 0.1 m). Due to the large storage size of the Pleiades data, a DEM was produced at a resolution of 5 m for $\sim$ 900 km^2 of the Bilila-Mtakataka fault scarp (Pleiades 5 m) and complimented by a $\sim$ 50 cm DEM for a number of target locations (Pleiades 50 cm). The Pleiades DEMs were constructed using the open-source software CloudCompare®; void space was filled using an minimum value interpolation. Two areas where cloud cover fell on the fault scarp at the southern end of the DEM were clipped, removing a total length of $\sim$ 2.5 km along the fault scarp.

As the Pleiades 5 m DEM only covers a portion of the Bilila-Mtakataka fault scarp, a 30 m SRTM and 12 m TanDEM-X DEM were obtained for Bilila-Mtakataka, Malombe, Thyolo and Muona fault scarps, covering 13°S to 17°S and 34°E to 36°E. The TanDEM-X DEM comprises eight tiles, purchased through the German Aerospace Centre (DLR), whereas the SRTM DEM was obtained through the USGS EarthExplorer programme at no cost. The coordinate system used for all DEMs is the Universal Transverse Mercator (UTM) projection (zone 36S; EPSG 32736) in World Geodetic System (WGS84).

The relative vertical accuracy for the TanDEM-X DEM is $\sim$ 2 m ($\sim$ 4 m for slopes greater than 20%), and for the SRTM DEM, $\leq$ 10 m. We found that the absolute vertical difference between the TanDEM-X DEM and the SRTM DEM was on average $\sim$ 20 m (n = 20); however, the standard deviation σ was small ($<$ 3 m) suggesting the difference is small throughout the entire sampled area and therefore will not significantly affect our calculations. This is consistent with other findings that suggest that TanDEM-X accuracy is comparable to other DEMs for non-extreme terrains (e.g., Destro et al., 2003). The absolute vertical difference between the Pleiades 5 m DEM and the TanDEM-X DEM was found to be on average $\sim$ 5 m, with a σ of $\sim$ 2 m (n = 20).

4.3.2 Scarp algorithm

Algorithm thresholds

For a given profile perpendicular to the local scarp trend, the first step in calculating the scarp's morphological parameters (height, width and slope) is to identify the crest and base of the scarp. Fig. 4.2a-c shows three profiles from the Bilila-Mtakataka fault scarp taken using the Pleiades 50 cm DEM. The black line is the elevation data extracted from the DEM, the red line the change in elevation per unit distance $\partial z/\partial X$ (i.e. slope, θ), and the blue circles are the derivative of slope $\partial^2 z/\partial X^2$ (ϕ). Each of the three profiles is characteristic of a different challenge associated with picking the fault scarp manually. The quality of the profile is determined by the signal-to-noise ratio, whereby a profile with a clear scarp and little background noise has a high signal-to-noise ratio. Profile A has a high signal-to-noise ratio, and a large, wide scarp; however, the gradient of the scarp is not constant, leading to large slope derivative values (fig. 4.2a). Profile B has a low signal-to-noise ratio, caused by vegetation or other topographical features; this noise creates local variability in slope θ, yet the gradient on the scarp itself is fairly constant (fig. 4.2b). Profile C has a low signal-to-noise ratio, the scarp width is small and the magnitude of the change in slope at the fault scarp is not large; it is therefore difficult to accurately identify the scarp from the footwall topography (fig. 4.2c). Furthermore, Profile C's morphology makes picking a fault scarp even more challenging when using a lower resolution DEM.

For each profile in fig. 4.2, grey triangles denote a manual pick of the crest and base of the fault scarp. We consider the basic assumption that the base of the fault scarp represents the approximate position of the fault. A linear regression (least squares method) is then applied to the upper original and lower original surfaces. The best-fitting lines for the upper and lower original surfaces (grey dotted lines) are then extrapolated to the point of maximum slope (θ_{max}) on the identified fault scarp. The scarp height H is then taken as the elevation difference between the regression lines at this point, the gradient of the best-fit line through the fault scarp is the scarp slope α, and the horizontal distance between fault scarp crest and base is the scarp width W.

Our algorithm picks the crest and base of the fault scarp based on the first and last values of the scarp profile that satisfy *a priori* threshold values of slope (θ_T) and the derivative of slope (ϕ_T). For the algorithm to calculate accurate values for scarp height, width and slope, the thresholds need to be appropriate for the scarp's morphology, i.e. for gently dipping fault scarps the slope threshold should also be of a gentle angle. Two examples for slope threshold are shown for the profiles in fig. 4.2, one where the slope threshold is set to 20° (pink triangles)

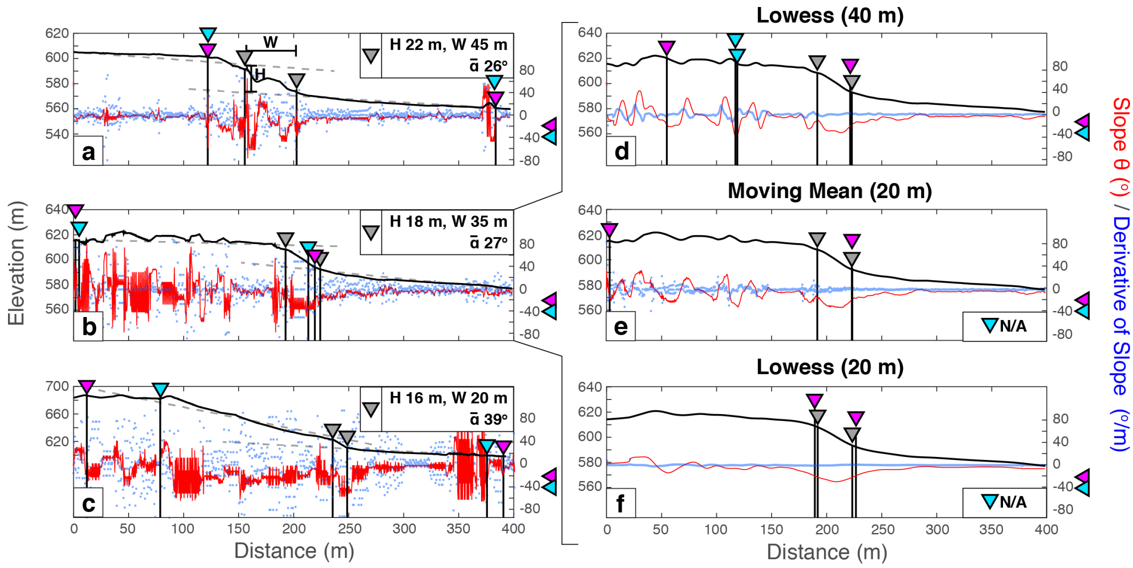

Fig. 4.2 Panels a to c) Three profiles across the Bilila-Mtakataka fault scarp using the Pleiades 50 cm DEM. Each is characteristic of the different challenges associated with picking the fault scarp manually and using an algorithm. Profile A has a high signal-to-noise ratio but contains noise on the fault scarp. Profile B and C have a lower signal-to-noise ratio, and Profile C has a scarp that is difficult to accurately identify as the magnitude of the change in slope at the fault scarp is not large. Using Profile B, three different digital filters and/or bin widths were applied: d) Lowess (bin width 20 m); e) Moving Mean (bin width 20 m); and f) Lowess (bin width 40 m). The black line is the elevation profile, the red line is the slope (θ) profile and blue circles denote the derivative of slope (ϕ). Grey triangles show the location of the crest and base of the fault scarp based on a manual pick. Pink and blue triangles denote the algorithms pick of the crest and base based on a slope threshold of 20° (pink) and 40° (blue), respectively.

and one where it is 40° (blue triangles). For all profiles, neither threshold value performs well at automatically identifying a fault scarp equivalent to the one that was determined manually. The reason for the poor algorithm performance is the low signal-to-noise ratio, whereby noise within the original surfaces may lead to the misidentification of the fault scarp by the algorithm. For example, in fig. 4.2a and 4.2c, the algorithm fails to accurately identify the base of the fault scarp due to noise in the lower original surface. For all examples, the crest of the fault scarp is misidentified by the algorithm due to noise within the upper original surface. Furthermore, as the values of ϕ have a high amplitude than θ, the algorithm is more sensitive to the slope derivative threshold than the slope threshold. To enhance the signal-to-noise ratio of the elevation profiles, we apply and test a range of digital filters.

Filtering

Here, we test the suitability of our four digital filters (Moving Mean, Moving Media, Savitzky-Golay and Lowess) in improving the signal-to-noise ratio of the scarp profiles and improving the accuracy with which morphological parameters such as height and width can be extracted by automated processing. Each filter uses a moving window over a specified bin width, which must be an odd integer. The moving window is incrementally shifted along the profile for each datapoint.

The Moving Mean and Moving Median filters calculate the mean and median values from the moving window. Here, we use the rolling mean algorithm from the *pandas* Python module and the moving median algorithm from the *SciPy* Python module. Both filters are commonly used signal-processing algorithms because they are the easiest and fastest digital filters to understand and use. In image processing, the Median filter is usually the preferred digital filter because it better represents the average. This is because an individual unrepresentative value in the window will not affect the median value as significantly as it affects the mean. However, the Median filter also preserves sharp edges and therefore may lead to step-like features, which could cause steep slope artefacts in our profiles. The Savitzky-Golay filter is based on local least-squares polynomial approximation (Savitzky and Golay, 1964); it is less aggressive than simple moving filters and is therefore better at preserving data features such as peak height and width. The Lowess filter uses a non-parametric regression method and requires larger sample sizes than the other filters (Cleveland, 1981). The Lowess filter can be performed iteratively, but since it requires much more computational power than the other filter methods, we apply a single pass over the data.

Fig. 4.2d-f shows the results of applying a digital filter to Profile B (fig. 4.2b). This profile was chosen because of the extensive noise within the upper original surface. Such noise is typical for fault scarp profiles, as topographic features from previous deformation events, valleys and dense vegetation are common. The elevation data was filtered using the following parameters: d) Lowess (bin width 20 m); e) Moving Mean (bin width 20 m); and f) Lowess (bin width 40 m). Filter parameters for Profiles D and E were chosen as a comparison between two different filter methods using the same bin width, whilst parameters for Profiles D and F were chosen for a comparison between different bin widths for the same filter method.

The Lowess filter smoothes the elevation, and subsequently the profiles of slope θ and slope derivative ϕ, more than the Moving Mean filter. As expected, a larger bin width smoothes the data more than a smaller bin width. By smoothing the data, the relative amplitude of ϕ becomes smaller than that of θ, meaning that the algorithm becomes less sensitive to the slope derivative threshold than the slope threshold. For the same bin width (20 m), the algorithm using the Lowess filter estimates the scarp location more accurately than the Moving Mean for this profile, as the latter fails to significantly reduce the noise within the upper original surface; however, for both filters, the algorithm still falsely identifies the crest of the fault scarp using a slope threshold of 20° or 40°. The algorithm, using a slope threshold of 20°, performs reasonably well once the profile has been filtered using the Lowess filter and a bin width of 40 m (fig. 4.2f), for this example.

4.3.3 Assessing algorithm performance

We assess the performance of our algorithm by testing it on various scarp profiles. Performance is assessed by defining a misfit value for scarp height (H_m), width (W_m) and slope (α_m) as the difference between ground-truthed (H_g, W_g, α_g) and algorithm calculated (H_c, W_c, α_c) scarp parameters - based on the selected *a priori* parameters b, θ_T, ϕ_T and filter method - for each profile. Misfit values can be positive or negative. This approach relies on the assumption that the ground-truthed value is correct, and is the value that we want the algorithm to calculate. One approach, as shown above, is to use a manual analysis to calculate the ground-truthed values. For example, for Profile F, the crest and base were both identified by the algorithm within 5 m of the manual pick, leading to a height misfit of less than 1 m, a width misfit of less than 6 m, and a slope misfit smaller than 1° (fig. 4.2f). Another way to test algorithm performance is to generate a synthetic fault scarp profile where the ground-truthed values are the known synthetic scarp parameters.

Although the ultimate goal is to design an algorithm to calculate scarp parameters for real fault scarps, the creation of a synthetic catalogue will allow us to robustly test the algorithm, and the relationship between filter and threshold parameters, using a large number of scarp profiles. This would not be feasible using the manual process. Therefore, the algorithm is run iteratively on a number (n) of synthetic profiles, using a range of *a priori* filter and threshold values. Average height ($\bar{H}_m$), width ($\bar{W}_m$) and slope ($\bar{\alpha}_m$) misfit values are then calculated using the mean of individual misfit values from the profiles (equations 4.1 to 4.3). The total number of profiles where a fault scarp is identified by the algorithm is given as the count C. The total misfit value, ε, is then calculated using equation 4.4; all algorithm runs where number of fault scarps identified is fewer than 50% are removed. Although the calculating the correct scarp height is the most important element of our algorithm, an equal weight is applied to all scarp parameters because all contribute to how well the scarp is identified. The smallest ε value is then used to denote the best performing set of filter and threshold parameters.

$$\bar{H}_m = \frac{1}{n}\sum_{i=1}^{n} H_{c(i)} - H_{g(i)} \tag{4.1}$$

$$\bar{W}_m = \frac{1}{n}\sum_{i=1}^{n} W_{c(i)} - W_{g(i)} \tag{4.2}$$

$$\bar{\alpha}_m = \frac{1}{n}\sum_{i=1}^{n} \alpha_{c(i)} - \alpha_{g(i)} \tag{4.3}$$

$$\varepsilon = \frac{|\bar{H}_m| + |\bar{W}_m| + |\bar{\alpha}_m|}{C/n}, \text{ for } C \geq 0.5n \tag{4.4}$$

4.4 Synthetic tests

4.4.1 Synthetic catalogue

In order to test the possible combinations of filtering, bin sizes etc using a Monte Carlo approach, we construct two synthetic catalogues, noise-free and noisy, each comprising 1,000 fault scarp profiles.

The parameters used in the construction of both catalogues are: the location of the scarp crest along the profile (x_s); the slope of the upper original surface (β_u); and the slope of the lower original surface (β_l, Table 4.1, fig. 4.3a). Profile length x and resolution r are constants set to 400 m and 1 m, respectively. Parameters β_u and β_l could be omitted if the synthetic catalogue is used to mimic an environment where fault scarps offset flat surfaces (e.g., Borah Peak fault scarp, Idaho; Ward and Barrientos, 1986), and included for regions where fault scarps offset sloped surfaces (e.g., Mangola fault scarp, Central Apennines; Tucker et al., 2011). A down-dip, normal sense of displacement parallel to the scarp is then imposed and Z and X are defined as the vertical (throw) and horizontal (heave) components of this displacement. The synthetic fault scarp width W_g therefore equals the horizontal displacement X and scarp slope α_g equals $\tan(Z/X)$. The height of the synthetic fault scarp H_g is then calculated using equation 4.5. The larger the values of β_u and β_l, the larger the difference between measured throw and actual throw, H_g and Z (fig. 4.3b).

$$H_g = Z - \frac{X}{2}(\tan\beta_u + \tan\beta_l) \tag{4.5}$$

The noisy catalogue includes noise in the form of vegetation, hills and ditches, as well as scarp degradation by diffusion (Table 4.1; fig. 4.3c). A random number of these noisy features are then placed at a random location along the profile. The shape of these noisy features is a negative parabola between a and b, created using equation 4.6, where a is the first root at the random location and b is the second root at a horizontal distance from the first root equating to the feature width, with a height $\frac{-kb^2}{4}$.

$$y = -k(x-a)(x-a-b) \tag{4.6}$$

Diffusion is applied in a Monte Carlo approach by using equation 4.7 for a diffusion constant κ and time t, resulting in erosion of material from the upper portion of the scarp and deposition at the base (fig. 4.3c). Diffusion can be included for environments where hillslopes are mantled with a continuous soil cover (i.e. transport-limited) and excluded for those with extensive areas of bare bedrock (i.e. weathering-limited) (e.g., Boncio et al., 2016; Bubeck et al., 2015; Tucker et al., 2011). Early studies of scarp degradation suggested that the value of κ should typically be between 0.5 and 1.5 m^2/kyr (e.g., Andrews and Hanks, 1985; Arrowsmith et al., 1996; Hanks et al., 1984); however, more recent studies from Mongolia (Carretier et al., 2002), the Gulf of Corinth (Kokkalas and Koukouvelas, 2005) and the upper Rhine valley (Nivière and Marquis, 2000) have suggested κ values in the range of 3 to 10 m^2/kyr. Locally on scarps in the Gulf of Corinth, κ has been measured to be as low as 0.2 m^2/kyr (Kokkalas and Koukouvelas, 2005), however, errors in calculations can be as large as 0.5 m^2/kyr. Here, we set algorithm limits to 0.5 and 10 m^2/kyr.

$$\frac{dh}{dt} = \kappa \cdot \frac{d^2h}{dx^2} \tag{4.7}$$

4.4.2 Individual profiles

We test the performance of the algorithm by comparing ground-truthed synthetic scarp values to scarp parameter values calculated by the algorithm. The synthetic catalogue input values are shown in Table 4.1. All filters from Section 4.3.2 were tested, using a bin width between 9 and 99 m, increasing in increments of 10 m. We vary slope threshold, θ_T, between 1° and 41°, in increments of 10°, and fix the slope derivative threshold, ϕ_T, to 5°/m.

Fig. 4.4a shows five examples with various morphologies from the noise-free synthetic catalogue: P1) randomly selected; P2) small scarp height; P3) steep, large scarp; P4) gently dipping, parallel original surfaces; and P5) non-parallel original surfaces. The algorithm was tested using all combinations of filter methods, bin widths and slope thresholds. For each profile, misfit values were calculated (fig. 4.4a). For scarp width and slope misfit for synthetic catalogues, see Appendix F. For all examples, the algorithm was able to identify a fault scarp and report

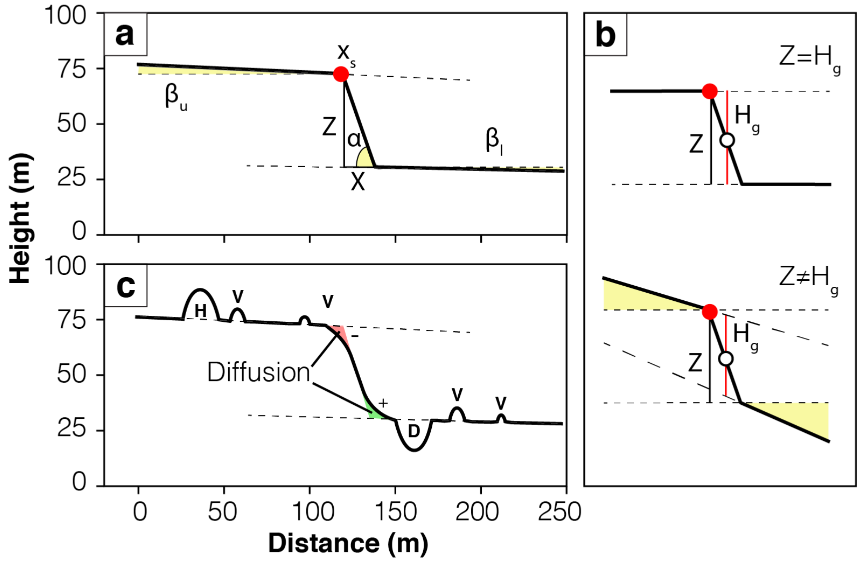

Fig. 4.3 An example of a synthetic catalogue fault scarp. a) Visual description of the parameters in Table 4.1 used in the noise-free synthetic catalogue. b) The difference between vertical displacement Z and synthetic profile scarp height H_g, resulting from sloping original surfaces. c) The additional noisy synthetic catalogue parameters (H = hill; V = vegetation; and D = ditch) and diffusion (red - erosion, green - deposition).

Table 4.1 Parameters used in creating the synthetic catalogues.

Algorithm Parameters			This Study	
Parameter	Symbol	Unit	Minimum value	Maximum value
		All Catalogue Parameters		
Profile length	x	metres (m)	400	-
Scarp location	x_s	metres (m)	100	300
Vertical offset	Z	metres (m)	2	50
Horizontal offset	X	metres (m)	2	100
Upper slope	β_u	degrees (°)	5	0
Lower slope	β_l	degrees (°)	5	0
		Additional Noisy Catalogue Parameters		
Diffusion constant	κ	m^2/kyr	0.5	10
Chronological age	t	kyr	0	50
Vegetation number	v_n	dimensionless	0	20
Vegetation height	v_H	metres (m)	1	3
Vegetation width	v_W	metres (m)	1	3
Hill number	h_n	dimensionless	0	3
Hill height	h_H	metres (m)	3	10
Hill width	h_W	metres (m)	8	15
Ditch number	d_n	dimensionless	0	3
Ditch depth	d_H	metres (m)	3	10
Ditch width	d_W	metres (m)	8	15

scarp height with a misfit of less than 2.5 m (5% - 60% of the scarp height for some combination of parameters); however, for Profile 2, the algorithm was unable to identify a fault scarp when the bin width was greater than 30 m. In this case, the filter was too aggressive and over-smoothed the scarp, such that no clear break in slope was detectable. Detectability of the scarp slope is a function of resolution, scarps may not be identified if the bin width is three times the scarp width and height, and the misfit values are greater for bin widths twice the scarp width and/or height.

To illustrate the process, we chose three examples from the noisy synthetic catalogue based on their signal-to-noise ratio and diffusion parameters (fig. 4.4b). Profile 6 includes lots of vegetation but no hills or ditches (moderate signal-to-noise ratio), nor any scarp diffusion. Profile 7 includes hills, ditches and scarp diffusion, but no vegetation (high signal-to-noise ratio). Profile 8 includes vegetation, hills and ditches and therefore has the largest amount of noise (low signal-to-noise ratio), and also includes scarp diffusion. For all three profiles, using no filter or the Moving Median filter gave the largest misfit values (fig. 4.4b). For scarp width and slope misfit, see Appendix F. The Moving Mean filter provided a small scarp height misfit (< 2.5 m) for Profiles 6 and 7, but produced a larger misfit ($H_m > 7.5$ m) for Profile 8. The Savitzky-Golay and Lowess filters performed equally well on all profiles, with the former able to identify fault scarps with a slightly larger bin width and steeper slope threshold than the latter.

4.4.3 Exploration of parameter space using synthetic catalogue

For each of the 1,000 profiles in the synthetic catalogues, we test 250 unique combinations of algorithm parameters (filter method, bin width, and slope threshold) and assess their ability to accurately determine the synthetic input parameters. Where the algorithm is not able to identify a fault scarp, a result is not recorded.

Fig. 4.5a shows the average misfit values for the noise-free synthetic profiles where the algorithm identified a fault scarp (equations 4.1 to 4.3). The best performing bin width and slope threshold depended on the filter method used, but in general a smaller bin width and steeper slope threshold provided smaller misfit values. When not applying a filter, or using the Median filter, the algorithm performed poorly; but using these filters meant the fault scarp was identified in more profiles. For the Moving Mean, Savitzky-Golay and Lowess filters, a gentle slope threshold ($\theta_T < 11°$) gave large misfit values, but using a steep threshold ($\theta_T \geq 31°$) meant fault scarps were identified in less than 50% of the profiles.

The poor algorithm performance when not using a filter, or using the Moving Median filter, is apparent for the average misfit values using the noisy catalogue (fig. 4.5b). On average, the scarp width misfit values are larger than the scarp

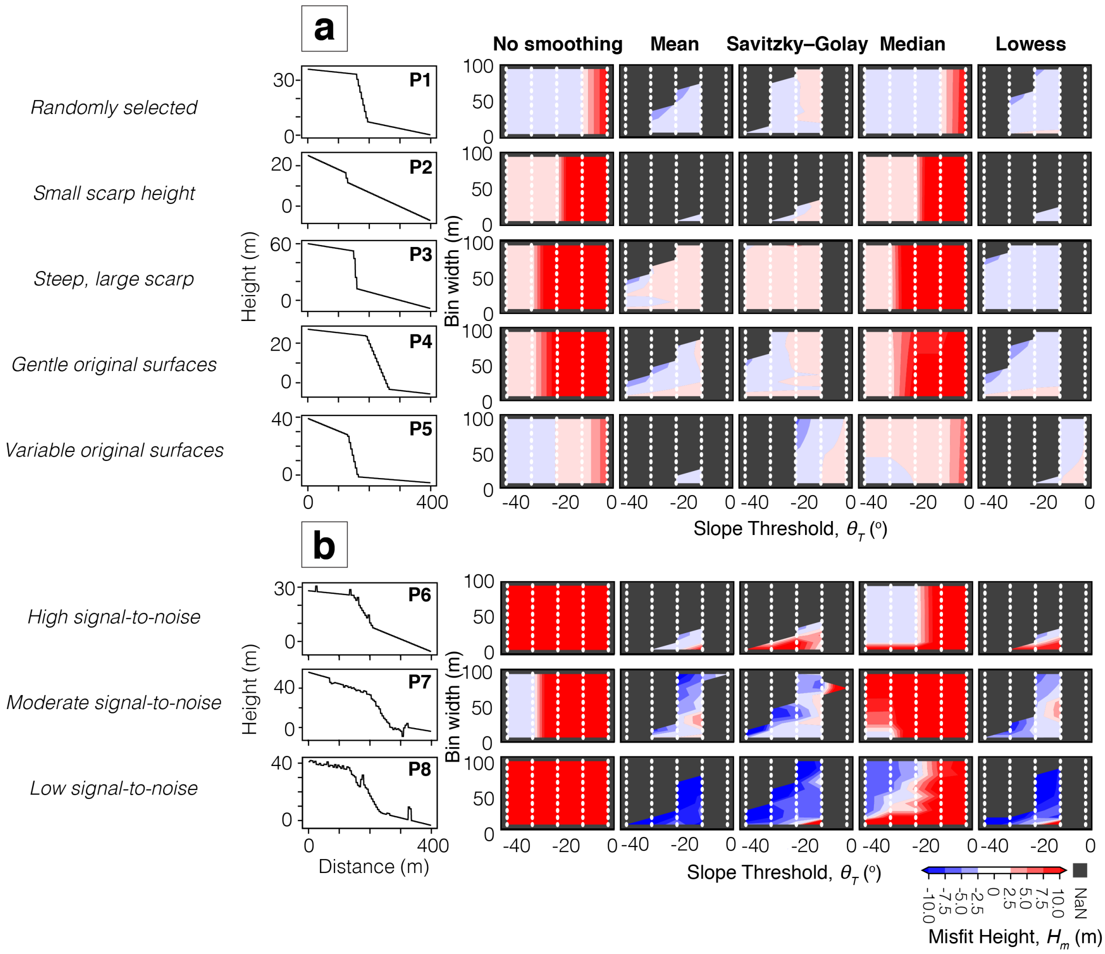

Fig. 4.4 Scarp height misfit H_m for a) five noise-free synthetic catalogue examples, and b) three noisy synthetic catalogue examples. See Appendix F for scarp width W_m and slope misfit α_m results for the noise-free and noisy catalogues.

height misfit values. Whereas scarp height is estimated by linear extrapolation of the original surfaces and is therefore less influenced by noise and exact position of the fault scarp, scarp width is highly sensitive to the exact location of the fault scarp crest and base picked by the algorithm.

For both synthetic catalogs, the best performing filters were the Savitzky-Golay and Lowess filters, the slope threshold with the smallest total misfit (equation 4.4) was 21°, and a bin width 50 m or smaller was found to perform better than a larger bin width. Thus these are the optimal filters which we choose to employ in our natural measurements, but we shall undertake another misfit analysis to identify the best performing bin width and slope threshold.

4.5 Case study example: The Bilila-Mtakataka fault

For the SRTM, TanDEM-X and Pleiades DEMs, hillshade and slope maps were produced in QGIS 2.18 and used to identify the breaks in slope associated with the Bilila-Mtakataka fault, i.e. the scarp. Fig. 4.6 shows the hillshade image produced by each DEM for an area of the Bilila-Mtakataka fault scarp. The scarp trace was manually picked from each hillshade image and is shown by a red line. Large-scale changes in scarp trend can be identified using the SRTM DEM (box A, fig. 4.6), however, small-scale changes may not be identifiable (boxes B and C, fig. 4.6).

We use the station lines toolbox in QGIS to draw profile lines perpendicular to the manually picked fault scarp trace. The total length of the profile x was set to 400 m. To obtain accurate calculations of the scarp's morphological parameters (especially width and slope), profiles need to be taken perpendicular to the scarp trend. Therefore, where the scarp trend varies considerably, such as at the ends of fault segments and at linking structures, failing to account for the small changes in scarp trend may lead to inaccurate morphological measurements. To prevent the station lines being drawn oblique to the true fault scarp, resulting from small-scale changes in scarp geometry, the distance between nodes (points picked on the fault scarp that when joined represent the scarp trace) should be significantly less than the distance between profiles. Here, we select scarp-perpendicular profiles at intervals of 100 m along the fault scarp trace, and therefore use a nodal distance of $\sim$ 20 m. Therefore, as the resolution of the TanDEM-X DEM is smaller than the nodal distance, we use this to pick the surface trace of the Bilila-Mtakataka fault scarp.

A total of 913 scarp profiles were extracted from the SRTM, TanDEM-X and Pleiades 5 m DEMs, for $\sim$ 90 km of the Bilila-Mtakataka fault scarp that was covered by the Pleiades DEM, starting $\sim$ 7.4 km from the northern fault end (fig. 4.1b). Due to clouds over the fault scarp on the Pleiades optical images, 26 profiles between 94 and 97 km from the northern fault end, were removed.

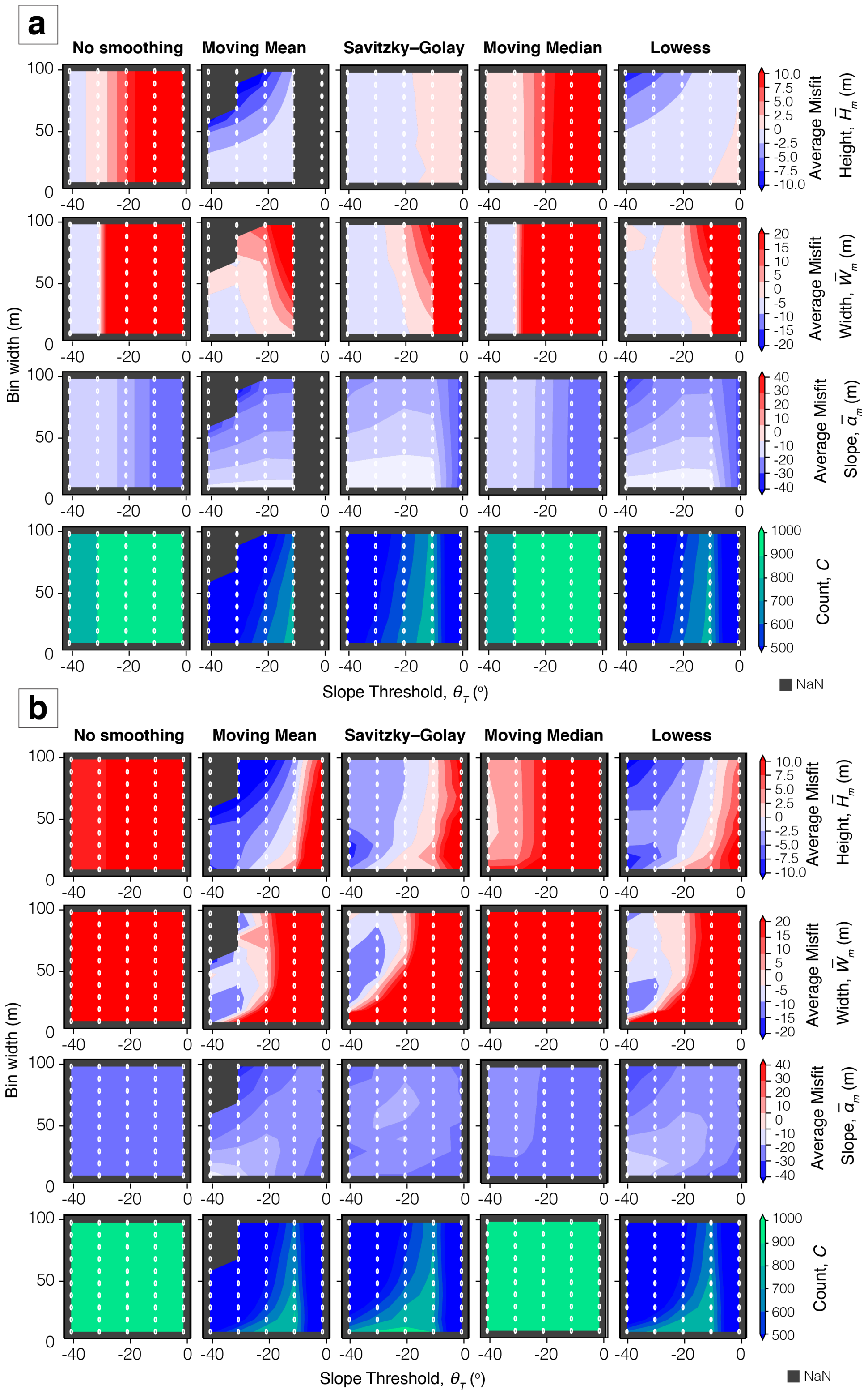

Fig. 4.5 The average misfit and count for 1,000 a) noise-free and b) noisy synthetic catalogue fault scarps. Grey values denote no fault scarp was identified for all profiles. For resolutions of 5, 10 and 30 m, see Appendix H.

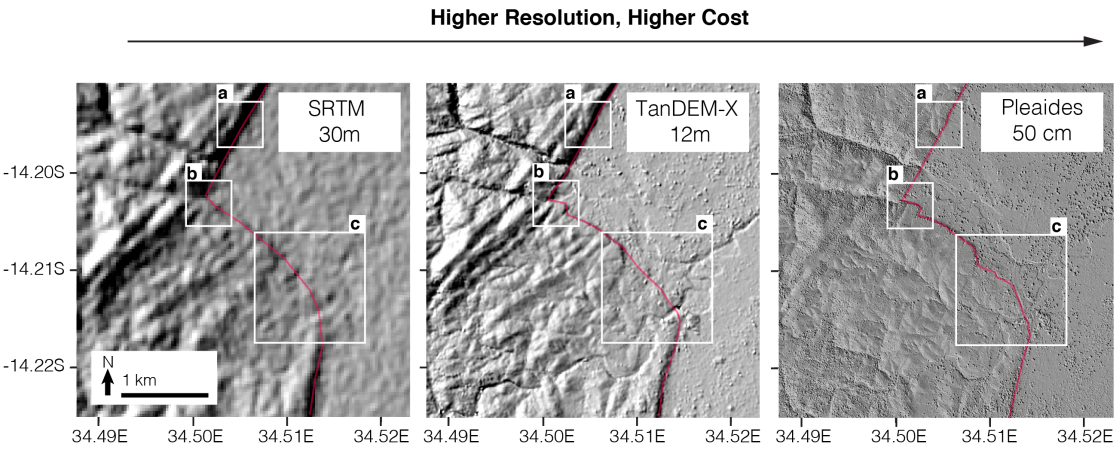

Fig. 4.6 Bilila-Mtakataka fault scarp hillshade DEM examples using SRTM 30 m, TanDEM-X 12 m and Pleiades 50 cm DEMs. The red line represents the fault scarp trace picked using each DEM. Box A represents the typical trend of the Bilila-Mtakataka fault scarp, boxes B and C show changes in variation in scarp trend.

Elevation values were taken along each profile at a spacing equal to the resolution of the DEM (e.g., 5 m for the Pleiades DEM).

4.5.1 Algorithm results (Pleiades 5 m DEM)

To test the algorithm using a range of resolution datasets we first use the Pleiades profiles along the Bilila-Mtakataka fault. A manual analysis is conducted for twenty profiles, taken at increments of ~ 5 km along the Bilila-Mtakataka fault scarp (fig. 4.7). A misfit analysis is performed by comparing scarp parameters estimated manually and from the automated analysis.

Based on the algorithm performance in the synthetic tests, we only use the Savitzky-Golay and Lowess filters. The maximum bin width is reduced to 49 m, and slope threshold limits are 11° and 26°, with increments of 5°. We find that the algorithm using the Lowess filter, on average, had smaller misfit values and identified a greater number of fault scarps than using the Savitzky-Golay filter (fig. 4.8). As with the synthetic tests, larger bin widths and steeper slope thresholds generated smaller misfit values, especially for scarp width; however, they also identified fewer fault scarps. The algorithm using the Savitzky-Golay filter gave a large width misfit (> 20 m), except when using the largest bin widths and steepest slope thresholds in the study. Based on the total misfit value, the best results were achieved by the Lowess filter when bin width is 39 m, and a slope and slope derivative thresholds were 21° and 5°/m, respectively. The average misfit values using this algorithm setup were $\bar{H}_m$ = 1.4 m, $\bar{W}_m$ = -6.6 m and $\bar{\alpha}_m$ = -12.6°. These

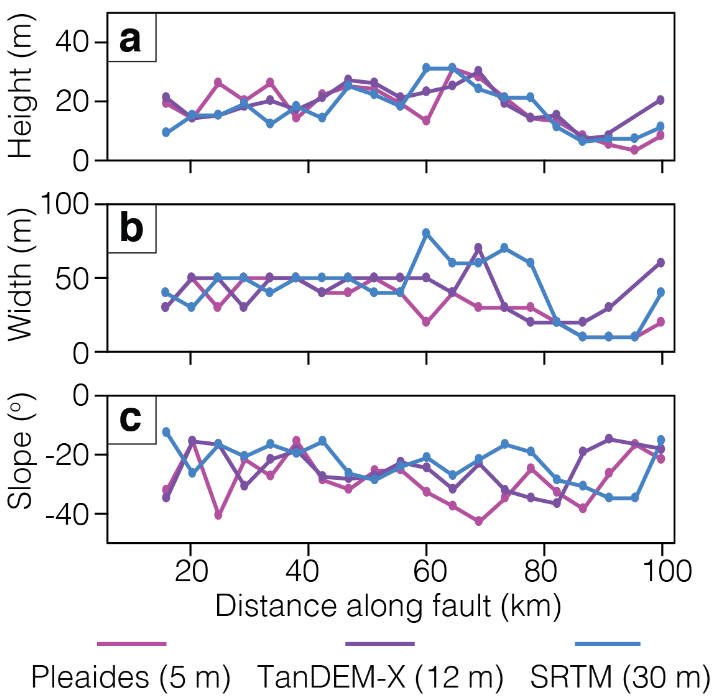

Fig. 4.7 Manual Bilila-Mtakataka fault profile for a) height H, b) width W and c) slope α taken at $\sim$ 5 km intervals using the Pleiades 5 m, TanDEM-X 12 m and SRTM 30 m DEMs. For tabular results see Appendix H.

values are specific to this example, and would vary according to DEM resolution, scarp characteristics and location.

Using the best performing parameters the algorithm was able to identify a fault scarp for 79% of the 913 profiles. A histogram of the scarp height, width and slope, as well as the mean and standard deviation (σ), are shown in fig. 4.9a (black). The average Bilila-Mtakataka fault scarp height, width and slope were 19 m ($\pm$ 17 m), 73 m ($\pm$ 71 m) and 20° ($\pm$ 12°), respectively. However, as the standard deviation was of the same order of magnitude as the values themselves, this suggests there was a wide spread of results due to natural variability. Furthermore, the extremes exceeded the minimum and maximum values obtained in the manual analysis.

Outlier identification

To improve the accuracy of the results obtained using the algorithm, we conduct a number of quality checks. First, algorithm results with negative scarp heights and positive slopes are removed. Next, because misfit values for scarp width were larger than for scarp height and slope, and scarp width is the primary influence on height and slope calculations, algorithm results where scarp width was twice as large as the maximum found in the manual analysis are also discarded. This value is arbitrary, however, we choose a value above the manual maximum (fig. 4.7b) as we do not want to discard wide fault scarps that are real and did not appear

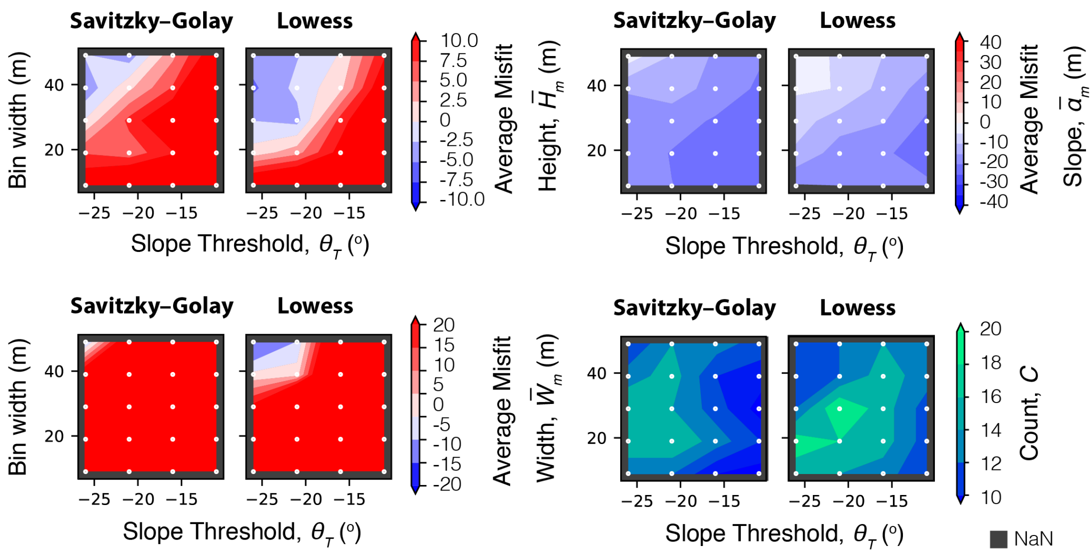

Fig. 4.8 Average misfit values between algorithm and manual scarp parameters for twenty Bilila-Mtakataka fault profiles using the Pleiades 5 m DEM.

in the manual analysis by random chance. Here, this removes all results where the scarp width was greater than $\sim$ 100 m. Then, as the algorithm results are approximately normally distributed (black, fig. 4.9a), outliers are removed by applying a threshold, set to 2σ ($\sim$ 95% confidence interval) of the remaining data. For the Bilila-Mtakataka fault, these quality checks removed 223 (31%) results and significantly reduced the standard deviation of the remaining data (pink, fig. 4.9a). The estimates of average scarp height decreased by 3 m, width dramatically by 47 m, and slope increased in steepness by 3°.

Improving width estimate

The results from this natural study corroborate those found in the performance test for the algorithm, and suggest that the algorithm calculates scarp height with less error and scarp width (fig. 4.2). Scarp width can also be calculated as a function of the scarp height and slope, using the equation $W = H/\tan\alpha$. We compare scarp widths and find that they correlate well (R^2 = 0.75) for widths of 100 m, or less (fig. 4.9b), but scarp widths obtained directly from the algorithm may be an overestimation by up to $\sim$ 15 m for widths under 100 m. This may explain why scarp width misfit values were larger than height or width misfit values (fig. 4.8). Since no fault scarp on the Bilila-Mtakataka fault was measured to be wider than 100 m, as reported in Chapter 3, nor in the manual analysis in this chapter, results wider than this may be a result of poor algorithm performance, likely due to a low signal-to-noise ratio. However, as it is difficult to consistently apply an exact angle threshold when manually picking, we don't necessarily expect automated

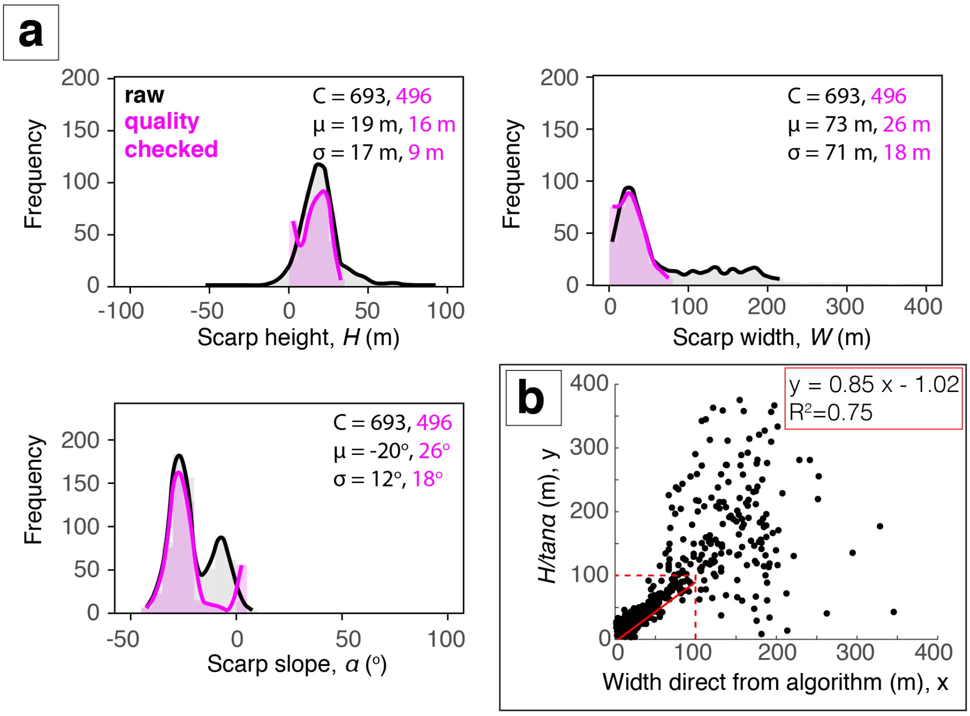

Fig. 4.9 a) Histogram of the estimated scarp parameters for the Bilila-Mtakataka fault for all (raw) algorithm estimates (black) and post-quality checked (pink) results. b) A comparison between the scarp width obtained directly from the algorithm against the scarp width calculated using the algorithm's scarp height and slope values ($W_c = H_c / \tan \alpha_c$). A linear regression is applied where width is less than 100 m.

and manual results to be exactly the same. As a result, some differences been manual and automated approaches may be due to the misidentification of scarp crest and base in the manual approach. From hereafter, we calculate scarp width as a function of height and slope. We find that this approach is appropriate here as we are simplifying the scarp to be planar, but would not be appropriate if adapting this algorithm to calculate other morphological parameters such as scarp/diffusion age.

Resolution analysis

Manual analyses were performed for the twenty chosen profiles along the Bilila-Mtakataka fault scarp using the TanDEM-X and SRTM DEMs, and compared to the Pleiades DEM manual results (fig. 4.7). Scarp height esimates between manual analyses differed by a maximum of 18 m, width by up to 60 m and slope by up to 24°, but the average differences were much less: $\sim$ 4 m, $\sim$ 13 m and $\sim$ 8°, respectively. The calculated scarp height and slope were the smallest and most gentle using the SRTM DEM, and tallest and steepest using the Pleiades DEM, likely due to the differing DEM resolutions.

The algorithm was then run for the 913 fault scarps using the TanDEM-X and SRTM DEMs, using the best performing algorithm setup found for the Pleiades analysis. For plots from this resolution analysis, see Appendix H. Although the misfit values were comparable regardless of DEM resolution, the lower the resolution, the fewer the fault scarps that were identified: 69% for TanDEM-X and 64% for SRTM, compared with 79% for Pleiades. The standard deviation of results was smaller for both TanDEM-X and SRTM results than the Pleiades DEM, leading to fewer outliers being removed after the quality check tests were performed. Misfit values were smaller using the higher resolution DEMs. In agreement with the manual analysis, the algorithm scarp parameters were smaller, wider and more gentle on average using the SRTM DEM, but the algorithm was still able to identify scarps with heights less than 5 m.

The average scarp height, width and slope obtained through the algorithm using each DEM were similar. The difference in scarp height between resolutions was smallest between Pleiades and TanDEM-X ($2\sigma < 10$ m) and largest between TanDEM-X and SRTM ($2\sigma \sim 12$ m). The greatest difference in algorithm performance between resolutions was found for scarp width (40 m $> 2\sigma >$ 20 m), whereas the difference between scarp slope using each resolution typically was less than 15°. The difference in scarp height between resolutions did not show any clear along-strike pattern, and was on average less than 5 m. Using a moving mean, the along-strike changes in scarp parameters between DEMs are similar and match the manual analyses well. For a scarp whose height is comparable to that of the Bilila-Mtakataka's, we find that DEM using a low resolution DEM does not profoundly affect the results, however, for smaller scarps and for accurate slope calculations, a high resolution DEM is more appropriate.

4.6 Application to Malombe, Thyolo and Muona faults

We have shown that an automated approach performs well in comparison to a manual analysis for the Bilila-Mtakataka fault scarp. We now apply the algorithm to three further normal fault scarps, the Malombe, Thyolo and Muona fault scarps in southern Malawi (fig. 4.1). The Thyolo fault (TOF) and Muona fault (MOF) are two distinct, overlapping fault scarps. As such, they may be part of the same fault system; however, a physical connection between them is not obvious in the TanDEM-X DEM. The Malombe fault (MAF) is split into three scarps: the northern (NMAF), central (CMAF), and southern (SMAF) scarps. As the algorithm performed comparatively well using TanDEM-X DEM and the Pleaides DEM for the Bilila-Mtakataka fault, we can reliably use TanDEM-X where Pleiades is not available. Therefore for each fault, scarp parameters were calculated using the algorithm from 400 m long scarp-perpendicular profiles taken using the TanDEM-

X DEM. Nodal distance for the manually picked scarp traces is again set to ~ 20 m and scarp-perpendicular profiles are taken at intervals of 100 m. For each, we select a subsample of twenty-five scarp profiles for a misfit analysis against a manual method (equations 4.1 to 4.4), and limit our filter methods to Savitzky-Golay and Lowess.

4.6.1 Scarp morphology of Malombe, Thyolo and Muona faults (TanDEM-X 12 m DEM)

The Thyolo fault scarp is ~ 70 km long and trends predominantly northwest-southeast (fig. 4.1c). Results from the manual analysis indicate that the average height of the TOF scarp is ~ 18 m, and its average slope is 18°. For results, see Appendix G. The scarp of the parallel Muona fault steps to the right of the Thyolo fault and is shorter, measuring ~ 28 km long. The faults overlap for a distance of ~ 10 km and are separated by ~ 5 km (fig. 4.1c). The manual analysis suggests that the MOF scarp is less high (10 m on average) and more gentle (14° on average) than the TOF fault scarp. The scarp width for both faults was ~ 65 m on average, equivalent to ~ 5 pixels. The scarp height for both faults increases by up to ~ 9 m per kilometre toward the overlap zone. Scarp measurements for the TOF within the overlap zone may contain significant errors due to the complex topography within the footwall of the Muona scarp affecting the linear regression of original surfaces. The best performing filter for the TOF was the Lowess filter, whereas the Savitzky-Golay filter performed better for the Muona scarp (Table 4.2). Both faults required similar slope thresholds, but the TOF required a larger bin width (41 m compared to 29 m). The algorithm misfit values for the subsampled profiles are shown in Table 4.2. The algorithm performed less well for the MOF, with an average height misfit of ~ 12 m, compared to ~ 6 m for the Thyolo fault.

The lengths of the Malombe fault scarps are between 16 km and 23 km, with the central scarp being the longest. Again, for results, see Appendix G. All trend approximately north-south with small local changes in scarp trend (fig. 4.1d). No hard-linking structures between individual fault scarps were identifiable. Results from the manual analysis show that the scarps of NMAF and CMAF are morphologically similar, with an average height ~ 7 m and slope $\sim 9°$. The scarp of the SMAF is smaller ~ 4 m and more gentle $\sim 5°$. The widths for all varied on average between 60 m and 80 m. Due to their similar average slopes, the best performing parameters for NMF and CMAF were similar, with the Savitzky-Golay filter preferred (Table 4.2). The algorithm using the Lowess filter performed best for SMAF, which also performed well using smaller slope threshold and bin width than the fault scarps to the north.

Table 4.2 The best performing algorithm parameters for the Thyolo, Muona and Malombe faults based on a misfit analysis using the TanDEM-X DEM. Lowess (LW) or Savitzky-Golay (SG).

Fault Name	Filter	θ	b	$\bar{H}_m$ (m)	$\bar{W}_m$ (m)	$\bar{\alpha}_m$ (°)	Count, C (%)
TOF	LW	19	41	6.2	-1.5	-0.6	60%
MOF	SG	23	29	11.9	-2.3	-6.0	52%
NMAF	SG	15	21	1.1	-4.1	-0.8	52%
CMAF	SG	15	29	8.4	2.3	-6.7	52%
SMAF	LW	7	9	5.8	-13.3	1.8	56%

The percentage of fault scarps identified for Thyolo and Malombe profiles was between 50% and 60% (Table 4.2), yet there were a wide spread of results. To improve the algorithm outcome, first negative scarp heights and positive scarp slopes were removed. Then, as scarp height values for both Thyolo and Malombe were normally distributed, the remaining results were quality checked using a 2σ (95% confidence interval) threshold. Following the quality control, the percentage of scarp profiles that morphological parameters were measured for was $\sim$ 30% for all scarps except the southern Malombe fault (13%). This is likely because the small and gentle SMAF scarp may be beyond the detectable limit of profiles using the TanDEM-X DEM.

4.7 Indicators of structural segmentation

4.7.1 Bilila-Mtakataka

In agreement with the findings in Chapter 3, the distribution of scarp height - a proxy for the vertical displacement (Hetzel et al., 2004; Jackson et al., 1996; Keller et al., 1998; King et al., 1988) - defines six major (first-order) structural segments along the Bilila-Mtakataka fault (fig. 4.10). Scarp slope is less variable than found in Chapter 3, especially within the Citsulo segment (fig. 4.10c). This is likely due to the lower spatial resolution of measurements used in Chapter 3, where poor quality measurements - unrepeatable and inaccurate due to the reasons give in Section 4.3.2 - greatly influenced the along-strike profile. The ability to measure scarp parameters at a high spatial resolution is a major benefit of an automated algorithm. Using the traditional, manual approach, increasing the number of fault scarp profiles would dramatically increase the time required.

In addition, by increasing the spatial resolution of measurements, along-strike changes in displacement may be identified at a smaller scale. As regular, frequent

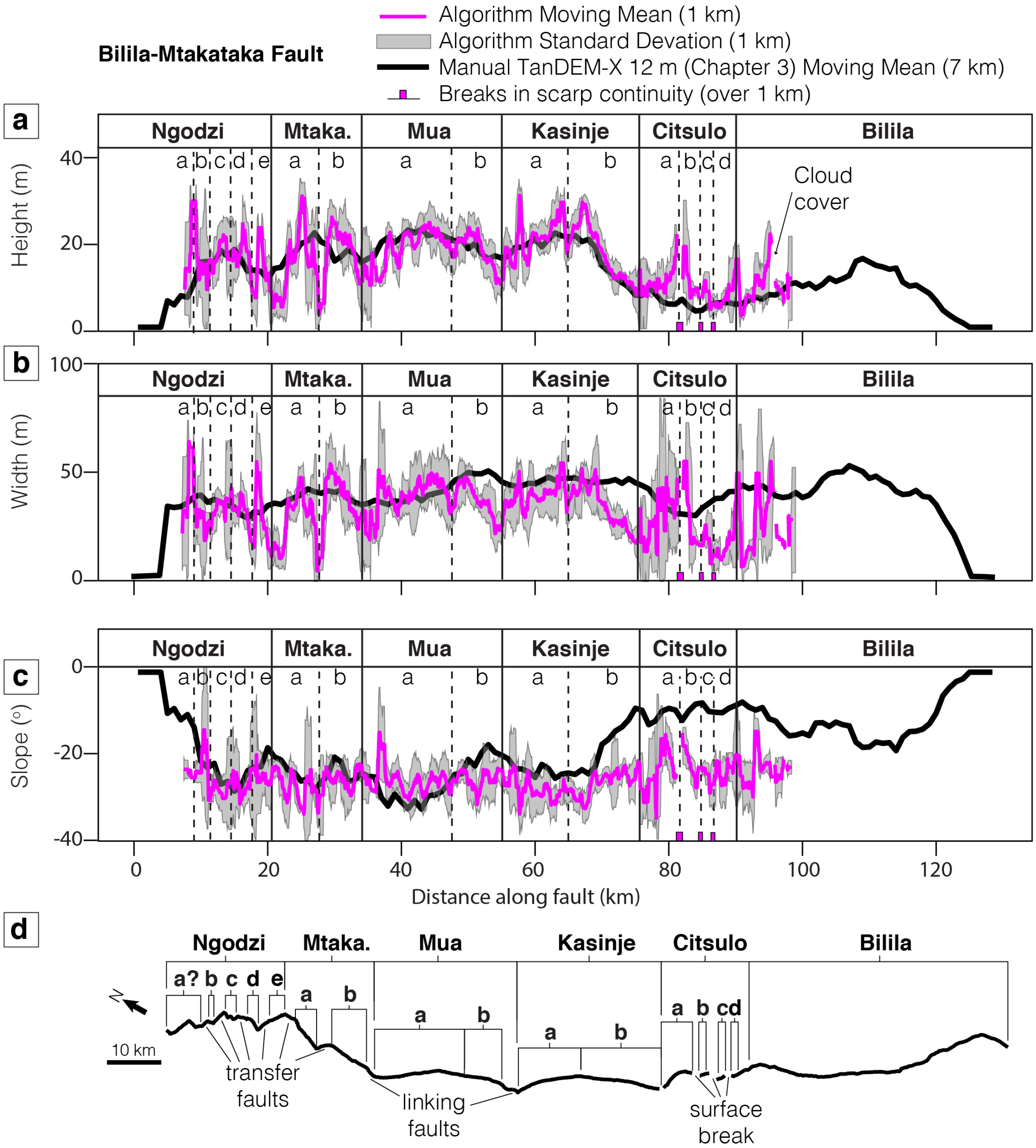

Fig. 4.10 Panels a to c) Height, width and slope profiles for the Bilila-Mtakataka fault scarp using the Pleiades DEM, indicating the major segments proposed in Chapter 3 (Ngodzi, Mtakataka etc.) and newly identified secondary segments (a, b etc.) from this study. d) A map-view showing fault structural segmentation, breaks in scarp and the location of inferred linkage structures.

spacing cannot account for scarp height differences caused by local geomorphology (i.e. erosion, deposition, non-fault related landforms), many of the measurements and signals may not be entirely tectonic (Zielke et al., 2015). A moving mean is therefore used to minimise such local influences. In fig. 4.10 the moving mean window size is set to 1 km for the Pleiades algorithm results. The general trend of the algorithm results still follows the manually derived trend taken using a larger window size, but variations in height occur along-strike at an even smaller scale than previously considered, as detailed below.

Changes in scarp height with a magnitude larger than the typical algorithm error (≥ 5 m) are considered to be real along-fault changes in scarp morphology. As the algorithm assumes only a single scarp surface, multi-scarps (also known as multiple scarps) or composite scarps associated with individual ruptures (Crone and Haller, 1991; Ganas et al., 2005; Nash, 1984; Wallace, 1977; Zhang et al., 1991), will be treated as a single scarp. In other words, the calculated scarp height is the cumulative vertical displacement at the surface. The results indicate that (second-order) secondary structural segments exist along the Bilila-Mtakataka fault, as typically expected for a large, structurally segmented fault (e.g., Dawers and Anders, 1995; Manighetti et al., 2015; Peacock and Sanderson, 1991, 1994; Trudgill and Cartwright, 1994; Walsh and Watterson, 1990, 1991). Faults forming hard-links between major segments, and those linking secondary segments, are also observed and we discuss specific examples below.

For the Ngodzi segment, at least five small (2 to 5 km long) secondary segments, joined by high-angled linkage structures, are identifiable by the local highs and lows in scarp height (fig. 4.11a). The separation-to-length ratio between each secondary segment is around ~ 1, an ideal geometry for a transfer fault to establish (Chapter 2, fig. 2.8; e.g., Bellahsen et al., 2013). The scarp appears to splay at the intersection between the southern most Ngodzi secondary segment and the Mtakataka segment, potentially comprising a single, or series of, small transfer faults (fig. 4.11a). A small rural settlement exists on top of the elevated surface caused by the footwalls of the two major segments; this has lead to a significant amount of erosion to the scarp face making it difficult to identify a hard-link between the major segments (fig. 4.11b).

The intersection between two parallel, slightly offset secondary segments on the Mtakataka segment is distinguishable by a low in scarp height. The sharp change in scarp trend at this intersection suggests the existence of a high-angled transfer fault. The Mtakataka and Mua segments are then linked by a ~ 2 km long linking fault angled on average $\sim 35°$ from the scarp trend. The geometry between segments is most favourable for a fault bend (Chapter 2, fig. 2.8; e.g., Jackson and Rotevatn, 2013). Furthermore, there is no evidence of a breached relay ramp.

The height of the fault scarp along the Mua segment is indicative of a single, major structural segment (i.e. bell-shaped height/displacement-length profile with slip maximum at the centre); however, a small decrease in height at $\sim$ 47 km may be evidence of a inter-segment zone between secondary structural segments (fig. 4.11c). If so, the subtle change in scarp morphology suggests that the secondary segments initiated as separate faults but have since hard-linked and matured, as the displacement deficit is minor. At the southern tip of the Mua segment, there is a decrease in height ($\sim$ 10 m) and change in geometry several kilometres from the northern tip of the Golomoti segment, which is marked by the river Livelezi (fig. 4.11c). The river itself marks the only break in scarp continuity between the Mua and Kasinje segments. The $> 45°$ change in scarp trend and slight overlap between segments, suggest that the offset may have been bridged with a relay ramp that has since breached, forming a hard-link and subsequently been exploited by the Livelezi River. Similar to the Mua segment, the displacement distribution along the Kasinje segment is characteristic of a single, major segment, but a local decrease in scarp height (< 5 m) at $\sim$ 63 km suggests that two secondary segments may have once existed as isolated structures (fig. 4.11c). These segments have since hard-linked, matured and the cumulative displacement has reduced much of the deficit within the inter-segment zone.

In Chapter 3 we suggested that the Citsulo segment had a $\sim$ 10 km long zone of scarp discontinuity. Here, we find evidence of several small breaks along the fault scarp within the Citsulo segment (fig. 4.11d). Breaks are up to 2 km in length suggesting that the Citsulo segment comprises several small ($\sim$ 2 km), en echelon secondary segments.

Thyolo and Muona

Fig. 4.12 shows the along-strike profile for the Thyolo and Muona faults. Scarp slope for both Thyolo and Muona faults is fairly uniform, averaging around $\sim$ 22° with a small standard deviation $< 5°$ (fig. 4.12c). Scarp height and width, however, show more variation along-strike (fig. 4.12a,b). We interpret three major segments along the TOF from the numerous peaks and troughs in scarp height, called TOFS1, TOFS2 and TOFS3, whose lengths are between 15 km and 30 km. In contrast, the height of the shorter MOF is fairly consistent before it tapers off toward the southeastern fault end. We therefore interpret the Muona fault to consist of a single major segment. Below we describe each major segment and any associated secondary segments and linkage structures. The faults do not appear hard-linked, likely due to the large separation-to-length ratio ($\gtrsim 0.1$), which may favour continued along-strike growth or a transfer-style link (Chapter 2, fig. 2.8;

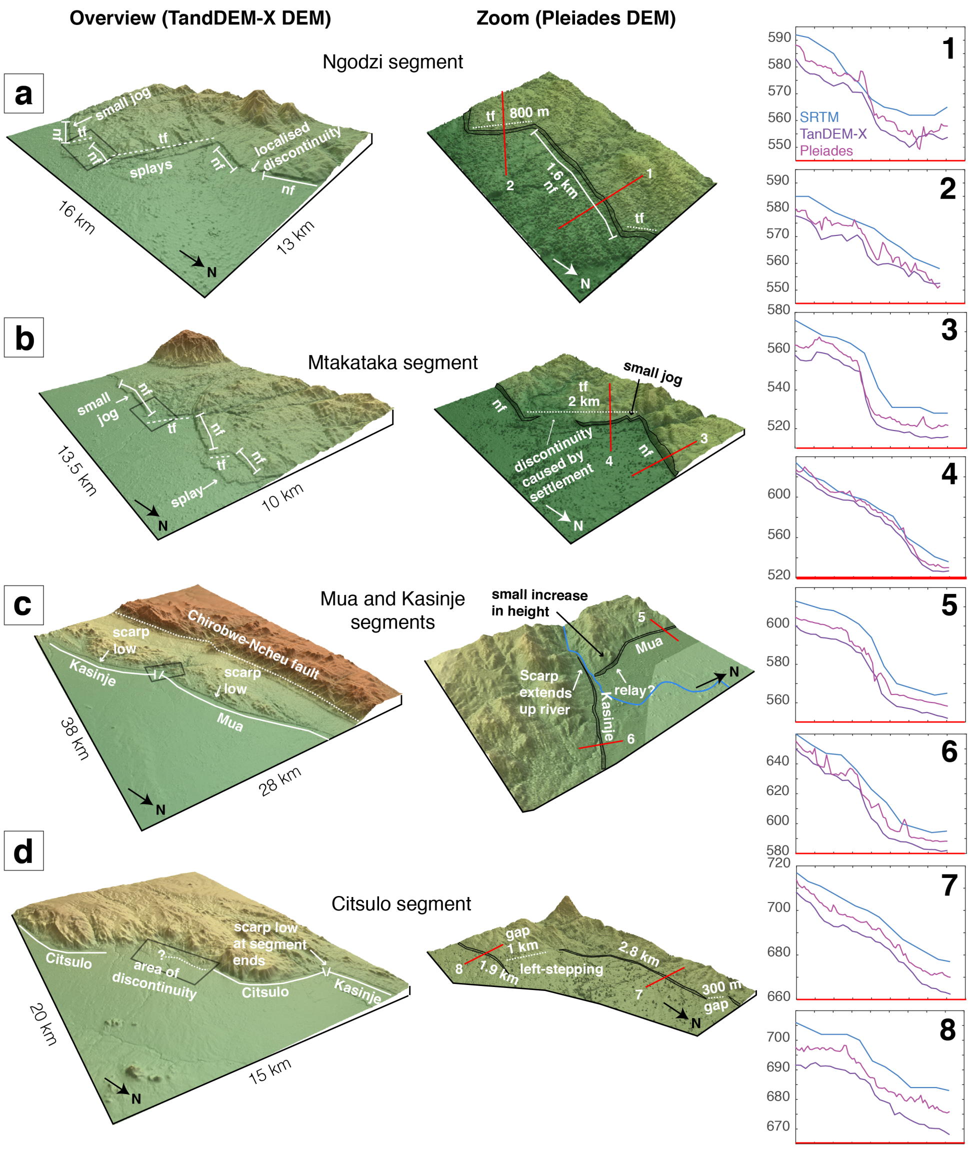

Fig. 4.11 Oblique perspective images taken from the TanDEM-X and Pleiades DEMs for the Bilila-Mtakataka fault. a) Ngodzi segment normal (nf) and transfer faults (tf) trend in a zig-zag pattern. b) Mtakataka segment normal and transfer faults. c) Mua and Kasinje segments intersecting at the river Livelezi. A small increase in scarp height on the Mua segment may relate to a relay ramp linkage. d) The Citsulo segment and area of discontinuity. Small, north-striking, left-stepping faults are offset by up to 1 km. Example profiles for SRTM, TanDEM-X and Pleiades DEMs are also shown.

e.g., Bellahsen et al., 2013). Below we describe each major segment of the faults and any associated secondary segments and linkage structures.

For both TOFS1 and TOFS2, the distribution of scarp height is bell-shaped with slightly asymmetry of the TOFS2 profile toward the inter-segment zone. For TOFS1, scarp height is larger and increases from ~ 10 m at the segment ends to ~ 30 m at the centre; an increase in width is also observed at the centre, resulting from the consistent scarp slope. The maximum height of the TOFS2 scarp is ~ 20 m. For both, the peaks in scarp height coincide with the apex of the convex geometry of the fault scarp (fig. 4.12d). The scarp height and width of TOFS3 increases gradually toward the southeast, where the segment extends into the footwall of the MOF. The scarp height of TOFS3 within the overlapping zone between the Thyolo and Muona faults exceeds the MOF scarp height by, on average, ~ 5 m. The standard deviation of measurements here is larger than elsewhere along both fault scarps, indicating intense local variability in scarp parameters.

The low count of scarps recognised by the algorithm along the Thyolo fault meant that we cannot conclusively interpret the existence of secondary segments. There are several > 1 km long breaks in where the algorithm could not recognise a scarp along TOFS1 and TOFS2; however, the distribution of scarp heights does not conclusively imply second-order segmentation. For TOFS3, several major breaks in scarp continuity coincide with sharp changes in scarp trend. Based on these changes in trend, we interpret three secondary segments, called TOFS3a, TOFS3b and TOFS3c, and associated linkage structures (fig. 4.14a). Each of these secondary segments has a length ~ 10 km and TOFS3c coincides with the length of the overlapping zone between Thyolo faults. There is no conclusive evidence of structural segmentation along the Muona fault. Two major ~ 4 km breaks in scarp continuity toward the segment end suggest a shorter fault scarp (~ 20 km) than our manual analysis suggested. Large gaps between profiles, typical of a manual analysis, may therefore fail to account for small-scale changes in morphology and over/under-estimate fault lengths.

Malombe

In agreement with the manual analysis, the slope of the NMAF and CMAF fault scarps are remarkably similar, averaging $\sim 18°$ (fig. 4.13). Based on the remarkably uniform scarp height, averaging ~ 8 m, the NMAF appears to comprise a single major segment. A small break in scarp continuity and ~ 10 m decrease in scarp height along the CMAF at ~ 24 km suggest an inter-segment zone between two major segments, called CMAFS1 and CMAFS2 (fig. 4.14b). The scarp height of CMAFS1 is the largest of all Malombe faults, averaging ~ 8 m. The distribution of scarp height along the CMAFS1 is roughly bell-shaped with an asymmetry

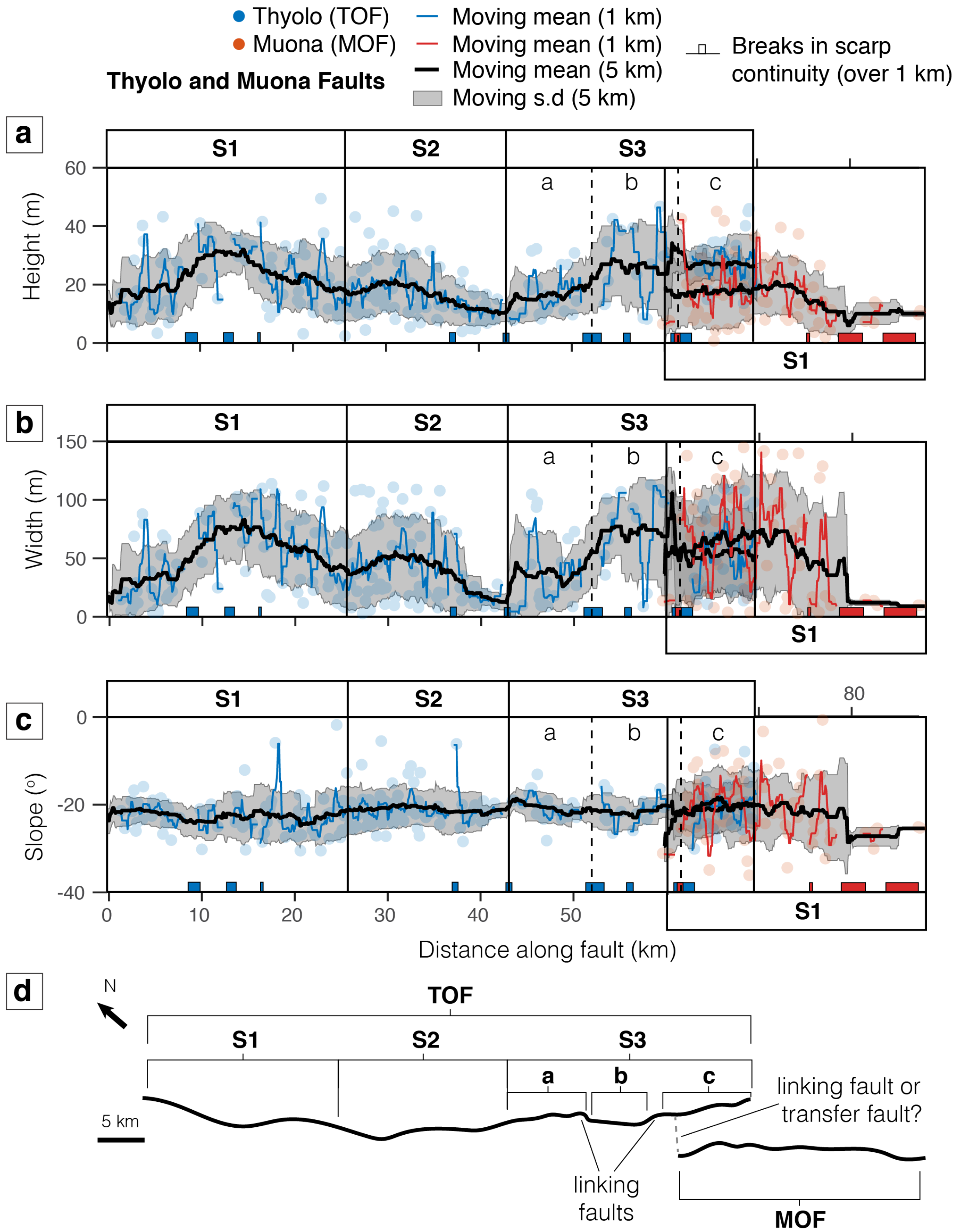

Fig. 4.12 Panels a to c) Height, width and slope profiles for the Thyolo and Muona fault scarps using the TanDEM-X DEM. d) A map-view showing fault structural segmentation, breaks in scarp and the location of inferred linkage structures.

leaning toward the NMAF. The height of the short CMAFS2 segment decreases by around 1 m per kilometre from north to south. A major ~ 6 km break in the SMAF scarp continuity implies either two major segments, SMAFS1 and SMAFS2, or a continuous deeper fault that has not broken the surface continuously. The scarp height for the SMAF is relatively constant, averaging ~ 5 m, and does not display a bell-shaped profile. No secondary segments were inferred from the distribution of scarp height along any Malombe fault scarp. The longest segment, CMAFS1 (18 km), does comprise several breaks in scarp continuity and changes in morphology typical of second-order segmentation, however, a higher spatial resolution of measurements would need to confirm this.

4.8 Discussion

4.8.1 Algorithm performance

In this study we developed an algorithm for calculating the height, width and slope of a fault scarp from scarp elevation profiles. A series of sensitivity analyses were performed using a synthetic catalogue prior to using the algorithm on real fault scarps. The benefits of creating a synthetic catalogue are two-fold: (1) a vast number of scarp profiles can be built to improve the performance of the algorithm through an in-depth misfit analysis; and (2) by creating a synthetic catalogue that mimics the typical fault scarp morphology of interest, and performing a sensitivity test for resolution, the benefits of high resolution satellite data can be assessed prior to purchasing costly data (see Appendix F for synthetic catalogue test results). The synthetic catalogue should mimic the typical fault scarp morphology of interest. This can be achieved by selecting *a prior* catalogue parameters based on initial findings using a free, low resolution data DEM (e.g., SRTM). The general morphology of the fault scarp and climatic conditions heavily influence the chosen catalogue parameters. For example, for regions where transport-limited fault scarps and vegetation are typical, the catalogue parameters can include diffusion and noise. In contrast, for regions typical of diffusion-limited fault scarps and limited vegetation, no diffusion and less noise can be used.

We found that the major influence on algorithm performance was the signal-to-noise ratio within the elevation profiles. Profiles containing a low signal-to-noise ratio will likely require the inclusion of a filter within the algorithm. In contrast, the algorithm may perform well without a filter for profiles with a high signal-to-noise ratio. In general, the algorithm was able to calculate scarp height and slope with a smaller misfit, compared to a manual analysis, than scarp width. The performance was improved by calculating scarp width based on the estimated scarp height and slope, rather than directly (fig. 4.9b). However, this approach assume scarp

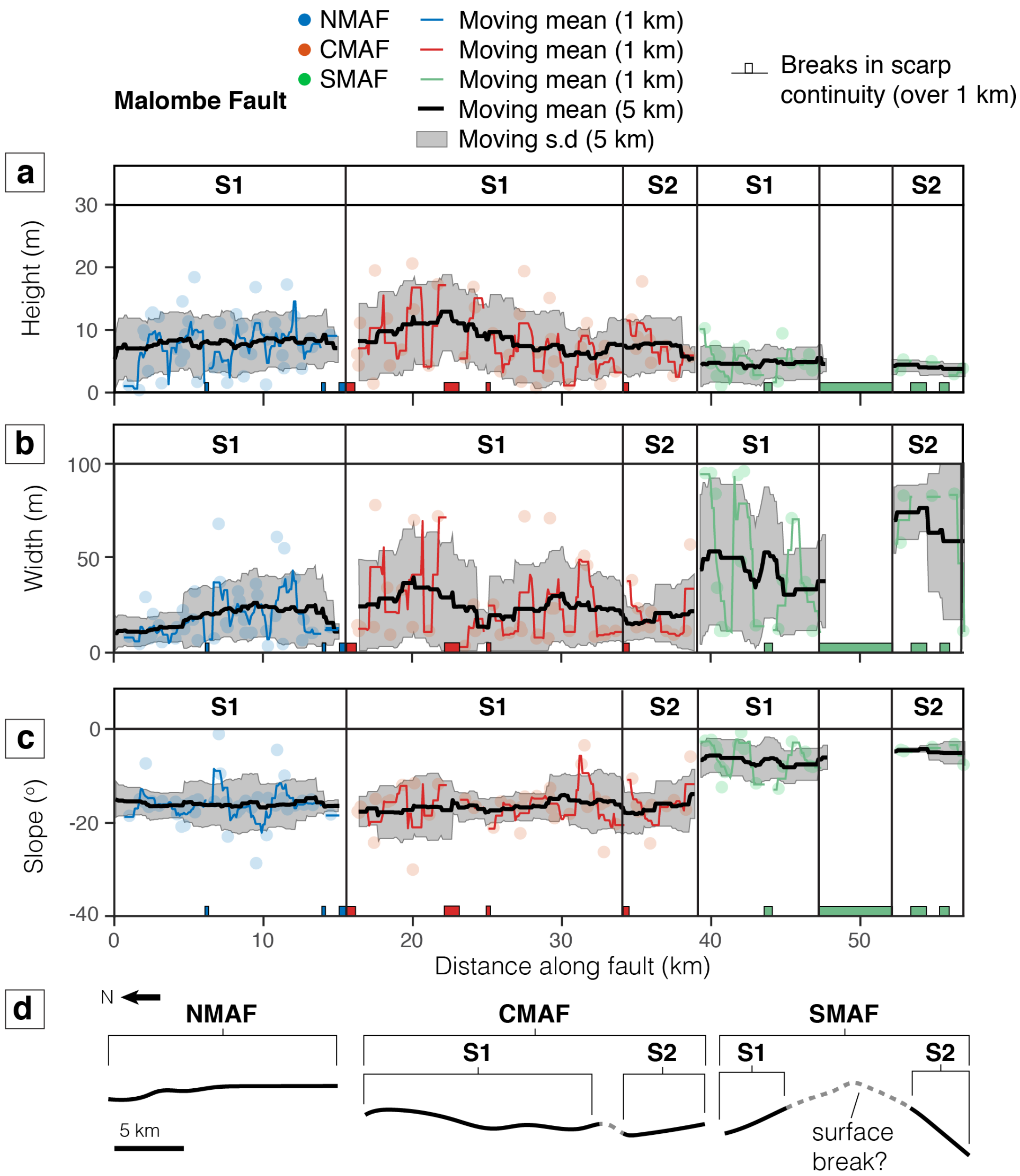

Fig. 4.13 Panels a to c) Height, width and slope profiles for the Malombe fault scarps using the TanDEM-X DEM. d) A map-view showing fault structural segmentation, breaks in scarp and the location of inferred linkage structures.

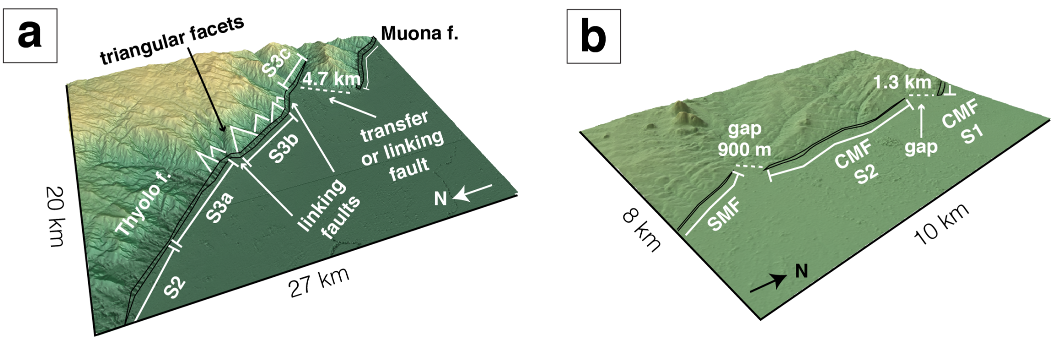

Fig. 4.14 Oblique perspective images taken from the TanDEM-X DEM for sections of the a) Thyolo and Muona faults and b) Malombe fault scarps. a) The secondary segments along TOFS3 of the Thyolo fault, showing the triangular facets synonymous with an mature scarp, and the structure that connects the Thyolo and Muona faults. b) The soft-linkage between the central fault segments (CMAFS1 and CMAFS2) and between the central and southern faults, each are offset by around 1 km.

planarity and therefore precludes use of the results for scarp degradation analysis or interpretation of single-rupture versus composite scarps.

In our case studies, the percentage of fault scarps where the algorithm was able to identify the scarp varied between $\sim 50\%$ and $\sim 80\%$. Lower returns coincided with fault scarps identified manually to contain large breaks in scarp continuity. Although the algorithm selects the best performing parameters from the misfit analysis, individual profiles may still fit poorly. Quality checks were applied to remove outliers and improve the results, but this decreased the number of identified scarps for each case study to between $\sim 15\%$ and $\sim 55\%$ of profiles.

The performance of the algorithm was not significantly affected by DEM resolution, but a number of differences were apparent between datasets (see Appendix H for more information). The lower the DEM resolution, the smaller the number of identifiable fault scarps, but the smaller the standard deviation of parameters. We found that a 30 m resolution DEM identified on average 20% fewer fault scarps than a high resolution 5 m DEM. Scarp width and slope calculated by the algorithm were on average wider and more gentle using a low resolution DEM. In general though, we found that for these southern Malawi faults, the use of expensive, high resolution DEMs in quantifying large-scale changes in scarp height over the scale of an entire fault, did not bring any additional benefits over using a medium- or low-resolution DEM. An exception is where scarp height is smaller than the elevation changes produced by background noise such as vegetation. This is an important finding if using this algorithm to study fresh ruptures, which are apparent as steep faces of fault scarps (Wallace, 1977), or scarps whose vertical displacement is less than 10 m, for which we recommend using a very high (≤ 1 m) resolution DEM and a large slope θ threshold.

Although our algorithm performed well against a number of manual analyses, the algorithm has some limitations including the reliance on manually picking the fault scarp trace. As low resolution DEMs smooth small-scale changes in scarp trend, this is most pertinent when using a high resolution DEM and a high spatial frequency of sample points (fig. 4.6). In addition, we have here used scarp-perpendicular scarp profiles, which may not be appropriate for oblique slip faults or sections of the scarp that trend at a high-angle to the slip vector (Mackenzie and Elliott, 2017). Slip vectors could not be measured for the southern Malawi faults (Chapter 3). Using the regional extension direction, the total surface slip may not be truly represented by the scarp height for the northern BMF segments, nor the Thyolo and Muona faults. If the slip vector of a fault is known, this can be accounted for in the algorithm.

We found that the distance between nodes (vertices of the scarp trace) should not exceed an order of magnitude above the horizontal resolution of the DEM. However, as long as the large-scale fault trend is correctly chosen, a wide profile length x (here set to around four times the largest scarp width) should cover a sufficient amount of the upper and lower original surfaces for the algorithm to calculate the scarp height correctly. In addition, as the algorithm uses a fixed slope threshold, if there is a lot of noise within the data, or there is a significant amount of heterogeneity in the scarp's morphology along-strike, small, or gently dipping, fault scarps may not be identified by the algorithm. This can be alleviated by either: (1) identifying morphologically different parts of a fault scarp and running the algorithm on these profiles separately, as we have done for Malombe; or (2) following the first algorithm run, running the algorithm again on poorly resolved regions, including a manual analysis to identify the best algorithm parameters to use. We suggest that the algorithm may face additional limitations in a more complex or varying terrain than considered here.

4.8.2 Normal faults in southern Malawi

As fault scarps are indicative of past earthquake events (Wallace, 1977), we use our geomorphological findings to better understand the rupture history for each fault. Assuming that a scarp is formed from a single earthquake event, the average scarp height can be used as a proxy for average coseismic slip (e.g., Morewood and Roberts, 2001) to calculate the slip-length ratio (Scholz, 2002). The typical global slip-length ratio range for a single earthquake is 10^{-5} to 10^{-4} (Scholz, 2002). Note, however, that fault slip at the surface may be several times less than the slip at depth (e.g., Villamor and Berryman, 2001). We simplify the length value

Table 4.3 Slip-length ratios for southern Malawi faults: Bilila-Mtakataka (BMF), Thyolo (TOF), Muona (MOF) and Malombe (MAF)

Fault Name	Fault Length L (km)	First-order Segment Lengths (km)	Average Scarp Height $\bar{H}$ (m)	Average slip-length ratio ($\times 10^{-5}$)	Slip-length ratio range ($\times 10^{-5}$)
BMF	110	13 - 38	17±7	16	9 - 22
TOF	65	18 - 27	20±11	31	13 - 49
MOF	28	28	10±5	36	17 - 58
MAF	55	5 - 18	7±5	13	4 - 23

to be the straight-line distance between the tips of the surface trace, which is less than the length of the irregular surface trace. Here, we found that the $\sim$ 65 km long Thyolo and $\sim$ 110 km long Bilila-Mtakataka faults have scarp heights that average $\sim$ 20±11 m and $\sim$ 17±7 m, respectively. The average scarp height of the Bilila-Mtakataka fault found here is larger than found in Chapter 3, but this is because only $\sim$ 90 km of the fault was analysed and the non-analysed sections of the Bilila-Mtakataka fault, predominantly the $\sim$ 35 km long Bilila segment, have a smaller scarp height. Due to the close agreement between algorithm and manual calculations, we hereafter use the average scarp height from Chapter 3 (11±7 m). The average scarp height of the $\sim$ 28 km long Muona fault and the $\sim$ 55 km long Malombe fault was found to be $\sim$ 10±5 m and $\sim$ 7±5 m, respectively. If each scarp is representative of a single earthquake event, then the average slip-length ratios for each fault (1×10^{-4} to 4×10^{-4}), which are greater than or equal to 10^{-4}, fall on or above the upper limit of the typical global range (Table 4.3; Scholz, 2002). To account for errors in fault length measurements we apply an uncertainty of 2 km.

Whilst large slip-length ratio values are rare (Middleton et al., 2016), they have been calculated for the 1897 $\sim$ M_W 8.1 Assam earthquake (2.2×10^{-4}; Bilham and England, 2001), the 2001 $\sim$ M_W 7.6 Bhuj earthquake (3×10^{-4}; Copley et al., 2011) and the M_W 7.6 1999 Chi-Chi earthquake (1×10^{-4}; Lee et al., 2003); however, none of these earthquakes occurred on normal faults and all exist within regions of higher strain rate than the EARS. In comparison, the only well-documented event we could find with a recorded slip-length ratio within the EARS was for the $\sim$ Ms 6.8 1928 Kenya earthquake (Ambraseys and Adams, 1991), whose 1 m scarp could be traced for $\sim$ 38 km at the surface (Ambraseys, 1991a), resulting in a ratio of $\sim$ 2.8×10^{-5}.

Abnormally large slip-length ratios may be a result of overestimating surface slip, as shown by Middleton et al. (2016) for the $\sim$ M_W 7.3 1739 Yinchuan earthquake in China, whose original slip-length estimate was 1.3×10^{-4}. They recalculated this value to be 3.8×10^{-5} based on a slightly shorter surface rupture length (87 km compared to 88 km) and a smaller average slip value (3.3 m compared to $\sim$ 12 m). Thus, the new slip-length ratio is within the global range (Scholz, 2002). Here, even when accounting for measurement errors within the satellite data and algorithm calculations, we find that each of our southern Malawi fault scarps have slip-length ratios larger than the global mean (Table 4.3; Scholz, 2002).

Number of events

The slip-length ratio calculation uses the assumption that the current scarp was formed by a single earthquake event. Therefore, the large values for our southern Malawi faults either are a result of local effects, such as large seismogenic thickness (Jackson and Blenkinsop, 1993), or suggest that each scarp has been produced by multiple earthquake events. Whether the current scarps were each formed by single, large slip rupture, or multiple, smaller slip ruptures is an important question for assessing the seismic hazard in the region. As the surface length is well constrained, and are in fact smaller than the longest faults in the EARS (e.g., Morley, 1999b; Vittori et al., 1997), the validity of the slip-length ratios are governed by the scarp height for each fault (Table 4.3).

Well-documented, historically-recorded continental normal fault scarps formed by single earthquake events typically have a height less than 10 m (Walker et al., 2015; Zhang et al., 1986). A short, incomplete earthquake catalogue (Midzi et al., 1999), and slow extension rates along the Malawi Rift (Saria et al., 2014; Stamps et al., 2008) leading to long recurrence intervals (Hodge et al., 2015) mean that there is a lack of recorded earthquake events in the Malawi Rift with visible surface offsets. Historical earthquakes that have occurred in the Malawi Rift, either did not rupture the surface, such as the 1989 $\sim$ M_W 6.1 Salima earthquake (Jackson and Blenkinsop, 1993), or small (< 1 m) amounts of surface displacement, such as the 2009 M_s 6.2 Karonga sequence (Biggs et al., 2010; Macheyeki et al., 2015). The latter resulted in an average scarp height of $\sim$ 10 cm and surface rupture length of 9 km. There are a number of reported events however within the EARS, but outside the Malawi Rift, that have been suggested to have produced significant (> 10 m) vertical displacement. For example, within the Rukwa Rift, just north of the Malawi Rift, there is evidence of a Late Pleistocene earthquake producing $\sim$ 10 m of uplift in the Songwe valley, Rukwa (Hilbert-Wolf and Roberts, 2015). Constraining this displacement to a single event however is challenging due to its age. This event occurred within the same region reported to have hosted one of the largest recorded earthquakes on the EARS, the 1910 $\sim$ M 7.4 Rukwa earthquake

(Ambraseys, 1991b). The most likely fault to have hosted this event is the Kanda fault, which has a reported maximum scarp height of 50 m (Vittori et al., 1997). The Kanda scarp is reported to comprise a fresh face synonymous with a recent rupture (Vittori et al., 1997); but due to the a lack of absolute age estimates on the Kanda fault scarp, and because the region has experienced frequent earthquakes since the Late Pleistocene (Hilbert-Wolf and Roberts, 2015), its unclear whether this scarp was formed by a single event. More modest scarp heights such as the 1.5 m scarp along the $\sim$ 50 km Katavi fault have been recorded in the Rukwa Rift (Kervyn et al., 2006). The Katavi fault however is considered to be a possible aftershock site resulting from the 1910 event (Kervyn et al., 2006) and does not reflect a main earthquake event.

Using the global mean slip-length ratio of 5×10^{-5} (Scholz, 2002), and assuming slip on each fault is pure normal, the number of events required to generate the current scarp heights along the Bilila-Mtakataka, Thyolo, Muona and Malombe faults is between 2 and 5, with the Thyolo fault requiring the greatest number of events. This does not account for vertical erosion between events and therefore may be an underestimate.

Displacement profile and segmentation

Fault scarps developed through multiple events have been observed in many regions (Crone and Haller, 1991; Ganas et al., 2005; Nash, 1984; Wallace, 1977; Zhang et al., 1991). Multiple earthquake events have also been suggested as a method for fault development, where large faults form iteratively through fault growth and linkage of smaller, fault segments (e.g., Anders and Schlische, 1994; Cowie and Scholz, 1992a; Peacock and Sanderson, 1991).

The along-strike pattern of scarp height for the Bilila-Mtakataka (at least up to the Citsulo segment) and Malombe fault scarps show a symmetrical bell-shaped profile, with the maximum scarp height near the centre of the fault (e.g Manighetti et al., 2001; Nicol et al., 2010; Peacock and Sanderson, 1991; Walsh and Watterson, 1987, 1990), whereas the Thyolo fault displays a distinctive asymmetric, triangular appearance (e.g., Manighetti et al., 2015, 2001, 2009; Nicol et al., 2005; Soliva and Benedicto, 2004). Height along the Thyolo fault scarp decreases southeastward before increasing toward the overlap zone with the Muona fault. Geological maps indicate that there may be a physical connection between the Thyolo and Muona faults (Habgood et al., 1973). The triangular distribution and tapering of scarp height along the Thyolo fault scarp may denote that the direction of long-term fault propagation is southeastward onto the Muona fault (e.g., Manighetti et al., 2015, 2001).

By observing the along-strike variation in scarp height for each fault, we found evidence for structural segmentation on each fault. We found that the $\sim$ 110 km long Bilila-Mtakataka fault comprises six major segments, the $\sim$ 70 km long Thyolo fault three, and the $\sim$ 25 km long central Malombe fault two. The Muona fault did not show signs of along-strike segmentation and is considered a single major segment. Segments along the Thyolo fault and Bilila-Mtakataka fault, with the exception of fault splays within the Citsulo segment, have hard-linked. These hard-links imply fault maturity (Trudgill and Cartwright, 1994; Young et al., 2001). In contrast, gaps between the three Malombe faults indicate soft-linkage (Walsh and Watterson, 1991). Our results are consistent with findings from other parts of the EARS, which suggest that the major faults are segmented at least to the first-order (Ambraseys and Adams, 1991; Manighetti et al., 2015). For example, the $\sim$ 180 km long Kanda fault comprises at least three major, hard-linked segments (Ambraseys and Adams, 1991).

In addition, the increase in spatial resolution in this study, a benefit of an automated approach, meant that secondary segments and linking structures could also been identified for the Bilila-Mtakataka and Thyolo faults. Each major segment along the Bilila-Mtakataka fault scarp comprised between two and five secondary segments, whereas (three) secondary segments were only identified on the southern-most major segment of the Thyolo fault. Thus, the number of secondary segments, where identified, is consistent with the number found on normal faults in Afar, further north in the EARS (Manighetti et al., 2015). We also found that the length of the major segments correlated with the length of the fault (Table 4.3). If we consider that these faults grow by linkage of smaller structures (e.g., Anders and Schlische, 1994; Cowie and Scholz, 1992a; Peacock and Sanderson, 1991), the existence of fault segments along each fault is evidence of multiple earthquake cycles.

The accumulation of displacement at the segment tips and/or hard-links suggests that each fault has hosted ruptures that have propagated across adjacent segments (e.g., Cartwright et al., 1995; Peacock and Sanderson, 1991). Multi-segment ruptures have been attributed to some of the largest earthquakes on the continents; for example, the $\sim$ M_W 8 1889 Chilik earthquake (Abdrakhmatov et al., 2016). For normal faults, rupture propagation may continue across gaps as large as 10 km (e.g., Biasi and Wesnousky, 2016). The Malombe fault is the only fault studied here with persistent gaps along its surface trace; however, these gaps are less than 10 km, and may be controlled by the changes in lithology. Some of the gaps coincide with calc-silicate granulite outcrops, which were also observed to cause discontinuities along the BMF (Chapter 3). Discontinuous scarps are also a common occurrence of many earthquakes; for example, the $\sim$ Ms 6.9 1928 Laikipia-Marmanet earthquake resulted in a discontinuous surface rupture (Ambraseys and Adams, 1991). No gaps in scarp continuity greater than 5 km were found on either of the Thyolo or Muona faults, and even the Citsulo segment on the Bilila-Mtakataka fault comprises small en echelon scarps separated by distances of less than 5 km.

Earthquake magnitude

The Bilila-Mtakataka fault has the longest scarp in this study, with a total surface trace measuring $\sim$ 110 km in length. The second longest scarp trace is this study was the Thyolo fault, which measured $\sim$ 70 km in length. The length of the Muona fault was $\sim$ 25 km. The length of each Malombe fault scarp is between 15 and 25 km, with a total cumulative length of $\sim$ 50 km. Whereas the more mature northern part of the East African Rift System (EARS) comprises faults whose maximum length is $\sim$ 65 km and median length is 10 km (Manighetti et al., 2015), the Bilila-Mtakataka and Thyolo faults are more comparable to the large fault scarps observed on the western and eastern branches of the EARS, such as the 140 km long Lokichar fault in the Kenya Rift (Morley, 1999b) and the 180 km long Kanda fault in the Rukwa Rift (Vittori et al., 1997). In addition, the thick ($\sim$ 40 km) seismogenic layer in southern Malawi (Jackson and Blenkinsop, 1993) implies that the down-dip fault width is also large (Wallace, 1989).

Of primary concern is the seismic hazard posed by these faults, as empirical relationships (e.g., Hanks and Kanamori, 1979; Wells and Coppersmith, 1994) suggest that the larger the fault, the larger the maximum earthquake magnitude. It has been suggested that the most recent earthquake on the Bilila-Mtakataka fault ruptured its entire length, with an average slip of 10 m, an event that would equate to a $\sim \mathrm{M}_W$ 8 earthquake (Jackson and Blenkinsop, 1997). Using the equation $M_W = \frac{2}{3} \cdot \log(G\alpha L^2 W) - 6.05$ (Aki, 1966; Hanks and Kanamori, 1979), where G is the modulus of rigidity (here taken as 30$\pm$5 GPa, e.g., Biggs et al., 2009; Crider and Pollard, 1998), α is the slip-length ratio (see Table 4.3), L is the fault length (Table 4.3), W is the fault width, and the fault dip is δ = 60° - the moment magnitude M_W for each fault can be found. We assume here that the rupture occurs through the full thickness of the seismogenic zone, and as such is calculated using $W = Z_{ST}/\delta$, where the seismogenic thickness Z_{ST} is 40$\pm$15 km (e.g., Jackson and Blenkinsop, 1993). By accounting for uncertainties within the parameters a M_W range is given. A complete rupture of the Bilila-Mtakataka, Thyolo, Muona and Malombe faults would equate to a M_W range of 7.9 - 8.4, 7.7 - 8.3, 7.2 - 7.9 and 7.2 - 8.0, respectively. Assuming the average subsurface displacement is 1.6 times greater than the average surface displacement (Villamor and Berryman, 2001), the maximum M_W increases to 8.5, 8.4, 8.0 and 8.1 in the respective order above.

Whilst large magnitude strike-slip and reverse-slip subduction zone earthquakes have been known to produce surface ruptures with lengths comparable to these southern Malawi scarps (e.g., M_W 8.1 1855 Wairarapa earthquake; Rodgers and Little, 2006, and M_W 8.1 2001 Central Kunlun earthquake; Lin, 2002), observations of continental normal or reverse earthquakes producing such surface rupture lengths are rare. Examples include the $\sim$ M 8 1556 Huaxian (Yuan et al., 1991) and $\sim$ M 8 1739 Yinchuan events (Deng and Liao, 1996; Zhang et al., 1986), both in central China, and the $\sim$ M_W 7.7 Egiin Davaa earthquake in central Mongolia (Walker et al., 2015). The only EARS event that may have resulted in a surface rupture with length of similar magnitude to our fault scarps is the 1910 $\sim$ M 7.4 earthquake in the Rukwa region of Tanzania (Ambraseys, 1991b), which had a magnitude similar to our estimates above for Muona and Malombe, but smaller than for the BMF and Thyolo.

Not all large magnitude earthquakes produce a surface rupture, and not all earthquakes rupture the entire fault length. Many of the largest recorded earthquakes along the EARS, including the 1990 $\sim$ Ms 7.2 southern Sudan earthquake (Ambraseys and Adams, 1991) and the $\sim$ M_W 6.8 2005 Lake Tanganyika earthquake (Manyele and Mwambela, 2014), lack a corresponding scarp. Even the subsurface rupture lengths of these events have been modelled to be just $\sim$ 26 km and $\sim$ 16 km, respectively (Moussa, 2008), significantly smaller than the total lengths of each of fault scarps in this study. In addition, one of the few recorded surface ruptures for a large magnitude event along the EARS, the $\sim$ Ms 6.9 1928 earthquake on the Laikipia-Marmanet fault in Kenya - the largest instrumentally recorded earthquake in the Kenya rift - resulted in just a $\sim$ 38 km long surface rupture (Ambraseys, 1991a).

As all faults but the Muona fault comprise several structural segments, ruptures that terminate at the geometrical ends of each structural segment (i.e. a single-segment rupture), or ruptures that occur across multiple segments but not the whole fault (i.e. multi-segment rupture), may occur on each fault. The geomorphology on each also shows evidence for segmented ruptures. The triangular slip distribution on the Thyolo fault may be evidence of segmented ruptures (Manighetti et al., 2005, 2001), the discontinuity at the Citsulo segment on the Bilila-Mtakataka fault may be evidence that the fault is actually two discrete structures, and the soft-linked Malombe fault segments may also rupture individually. Using the moment magnitude equations and the average scarp height for each structural segment, single-segment ruptures (with lengths between 20 and 40 km) on each of fault would generate an earthquake with a M_W between 6.8 $\sim$ 8.1 if the earthquake ruptures the entire down dip width, or 6.7 $\sim$ 8.0 if the rupture width is constrained to be less than the rupture length (i.e. 20 km). Therefore, single-segment ruptures on each fault can still generate earthquakes with magnitudes comparable to the largest events recorded within the EARS, and larger than any historically-recorded earthquake in Malawi. However, as single-segment ruptures with a slip value equal to the average scarp heights measured here imply an even larger slip-length ratio (up to 10^{-3}), and are therefore unlikely, the question that still needs addressing is whether the scarp of each fault comprises a single rupture, or multiple ruptures.

4.9 Conclusion

In this study, we have developed a semi-automated algorithm for quantifying along-strike variations in scarp morphology. We show that the algorithm performs comparatively well against traditional, manual analyses, but allows for a greater spatial resolution of measurements, improving the understanding of the morphological parameters along a fault scarp. We have shown that DEM resolution does not greatly influence the algorithm's performance when used to infer first-order fault structural segmentation and associated linkage structures. However, a high resolution DEM may be required to conclusively infer second-order structural segmentation, especially along faults with small scarp heights. For the southern Malawi faults, the distribution of scarp height along-strike, found using our algorithm, indicates that all three of the four faults, Bilila-Mtakataka, Thyolo, and Malombe, comprise first-order segmentation at their surface. The Muona fault is a single, major segment. Using a Pleiades DEM, second-order segmentation is clearly apparent along the Bilila-Mtakataka fault. Assuming the average scarp height reflects the average slip at the surface, if each scarp was formed by a single earthquake event, the slip-length ratio for each fault exceeds the global upper limit proposed by Scholz (2002). The distribution of scarp height close to, and within, the inter-segment zones for each fault suggests that the Bilila-Mtakataka and Thyolo fault segments have hard-linked, incrementally through several earthquake cycles, and the Malombe faults are soft-linked. Our results suggest that each fault has likely formed through multiple events; however, to constrain the co-seismic slip and rupture length of each event, a detailed study is required for each fault scarp.

Chapter 5

Identifying multiple earthquake rupture indicators on scarps and river profiles using a high-resolution DEM

Abstract

Global scaling laws suggest that the ratio of maximum finite fault displacement over fault length exceeds the slip-length ratio in single earthquake. Therefore, faults appear to accumulate displacement over multiple seismic cycles and their surface expressions may display evidence for multiple earthquakes. Incremental increases in surface displacement resulting from multiple earthquake events have been observed on scarp and river profiles, for example, in Basin and Range Province. For faults in low strain rate settings, which have not hosted an instrumentally recorded earthquake event but do have an obvious and large surface expression, we may therefore be able to infer multiple rupture events from the geomorphology. Previous chapters have shown that the surface expression of the $\sim$ 110 km Bilila-Mtakataka fault comprises a scarp whose height exceeds what would be expected from a single, complete rupture. The largest scarps occur on the two central structural segments of the BMF, the Mua and Kasinje segments, where the average scarp height is 20 m on average. Here, we undertake a geomorphological analysis of the fault scarps for the Mua and Kasinje segments using a high resolution DEM, in order to quantify the number of earthquakes that have ruptured the surface on each segment. We also perform a knickpoint analysis for several rivers and streams that pass over the fault scarp, in order provide an independent estimate of the number of surface ruptures. Both analyses suggest that a minimum of two surface-rupturing earthquakes have occurred on each segment. The cumulative and individual displacement of each rupture is then quantified using the scarp and river profiles in order to estimate the magnitude of paleoearthquakes on the BMF. By performing an inverse solution to a forward model of scarp degradation, we also estimate the diffusion age κt and infer the relative timing of each rupture. Displacement calculations and diffusion age estimates suggest that the two latest surface ruptures along the BMF resulted in an equal amount of vertical surface displacement along the Mua and Kasinje segments ($\sim$ 10 m), and that these ruptures were continuous across both segments, or near-concurrent in time. The results of this study suggest that the slip per earthquake across the entire BMF is likely lower than previously thought, here estimated to be 7$\pm$4 m per event, but also that Kasinje and Mua segments appear to rupture together simultaneously or in temporally proximate earthquakes. We

estimate that a continuous rupture of the BMF would equate to a M_W range of 7.5 - 8.1, greater than the largest recorded earthquake events along the entire EARS.

Author contributions and declarations: Hodge, M. is the main author of this work, undertook the data analysis and developed the numerical model. Fagereng, Å. and Biggs, J. provided supervision for the work. Hodge, M. and Biggs, J. each received a grant from the Centre for Observation and Modelling of Earthquakes, Volcanoes and Tectonics (COMET) for the purchase of the Pleiades satellite data. Elliott, A. of Oxford University helped process the Pleiades data and create the digital elevation model (DEM), and provided comments on the chapter. Hobley, D. of Cardiff University gave guidance on the knickpoint analysis.

5.1 Introduction

Historical and instrumental catalogues alone provide a short and incomplete record of past earthquakes (e.g., Hodge et al., 2015; McCalpin, 2009), and devastating earthquakes may occur on faults that have no historical earthquake activity (e.g., 2003 M_W = 6.6 Bam earthquake in Iran; Fu et al., 2004). By investigating fault-generated landforms such as fault scarps, the earthquake and rupture history along a fault, and the probability and hazard of future earthquakes can be assessed (e.g., Andrews and Hanks, 1985; Bucknam and Anderson, 1979; Duffy et al., 2014; Hanks et al., 1984; Nash, 1980; Wallace, 1977; Zhang et al., 1991; Zielke et al., 2015). Paleoseismological trenching can provide information about timing and magnitude of prehistoric earthquakes (e.g., Michetti and Brunamonte, 1996; Palyvos et al., 2005; Schwartz and Coppersmith, 1984), but trenching requires particular geomorphic conditions and is limited by site accessibility. Geomorphological analyses of fault scarps have long been used to estimate the displacement and age along a fault scarp caused by a single earthquake rupture (e.g., Avouac, 1993; Bucknam and Anderson, 1979), but subtle changes in morphology, such as slope breaks, may also indicate multiple ruptures (Wallace, 1984a, 1980). By using high resolution DEMs in order to study fault scarps, geomorphological analyses have been shown to corroborate paleoseismological findings (Ewiak et al., 2015). Rivers and streams crossing fault scarps may preserve indicators of past earthquakes in the form of vertical steps - called knickpoints - in an otherwise convex and smooth longitudinal profile (e.g., Burbank and Anderson, 2011; Holbrook and Schumm, 1999; Ouchi, 1985; Wei et al., 2015). Examples of where knickpoints have been successfully used for paleoseismological analysis include the Huoshan Piedmont Fault, eastern China (Wei et al., 2015) and the Atacama Fault System, northern Chile (Ewiak et al., 2015).

We have previously shown how surface morphology, particularly the along-strike displacement profile, can be used to infer the structural development and segmentation of a fault (Chapter 3, fig. 3.2; e.g., Crone and Haller, 1991; Manighetti et al., 2005; Perrin et al., 2016a). We have also discussed how over multiple earthquake cycles, a fault segment may grow and form hard-linkages with other segments, and that the type of link is related to the geometry between the structurally-defined segments (Chapter 2; e.g., Anders and Schlische, 1994; Cowie and Scholz, 1992a; Peacock and Sanderson, 1991; Whipp et al., 2016). In Chapter 4, we analysed the large-scale changes in scarp morphology along four faults in southern Malawi: Bilila-Mtakataka, Thyolo, Muona, and Malombe, and discussed whether each scarp may have formed through a single, complete rupture of the faults. We concluded that each scarp displays geomorphological indicators of fault segment growth and the establishment of hard-linkages; processes that are indicative of multiple earthquake cycles (Anders and Schlische, 1994; Cowie and Scholz, 1992a). The scarp height-length ratio on each of the four southern Malawi faults is also larger than expected for a single earthquake event (Scholz, 2002).

In this study, we investigate whether indicators of multiple ruptures exist along two major structural segments of the Bilila-Mtakataka fault (BMF), the Mua and Kasinje segments, using a very high resolution (< 1 m) point cloud and DEM (fig. 5.1a). The Mua and Kasinje segments were chosen as they contain the largest scarp heights along the BMF (fig. 4.10), and thus are the most likely BMF segments to preserve evidence of multiple ruptures. By detecting changes or breaks in slope on individual scarp profiles, we estimate the number of ruptures that may have occurred on each segment. In addition, we use the fault scarp morphology to quantify the total and individual displacements of each earthquake rupture.

We then apply an inversion solution to a forward model of scarp degradation to estimate the diffusion age κt of the scarp profiles, i.e. the amount of erosion that has occurred at the scarp's crest since the scarps formation. Diffusion age, having dimension [length]^2, is the product of diffusivity κ and chronological age t (Andrews and Hanks, 1985). By making assumptions about the typical diffusion constant κ of the region, we can then convert diffusion age to chronological age and infer the timing of each rupture. This will help us understand whether the BMF ruptures as a series of individual segmented ruptures, or can host multi-segment or complete fault ruptures. Finally, we consider knickpoints on rivers and streams crossing the scarp as markers of uplift (scarp formation) from past earthquakes, and compare the number and height of the identified knickpoints to findings from our scarp analysis.

This study aims to better understand the rupture history and seismic hazard of the BMF, but we also aim to develop a process that can be used to identify surface ruptures from multiple earthquakes on other large, prehistoric normal fault scarps. Candidates for this are faults whose scarp height exceeds what would be anticipated by a single earthquake event (Scholz, 2002), such as the Kanda fault, Lake Rukwa (Macheyeki et al., 2007; Vittori et al., 1997), the Nahef East fault, northern Israel (Mitchell et al., 2001), the Wasatch fault zone faults, Utah (DuRoss et al., 2015; Swan et al., 1980) and the Dixie Valley-Pleasant Valley faults (Zhang et al., 1991). Results could also be compared to subsurface studies of displacement accumulation, such as throw-depth and displacement-depth plots (e.g., Baudon and Cartwright, 2008; Jackson and Rotevatn, 2013; Ward et al., 2016) in order to understand the relationship between surface and subsurface displacement on active, deforming faults.

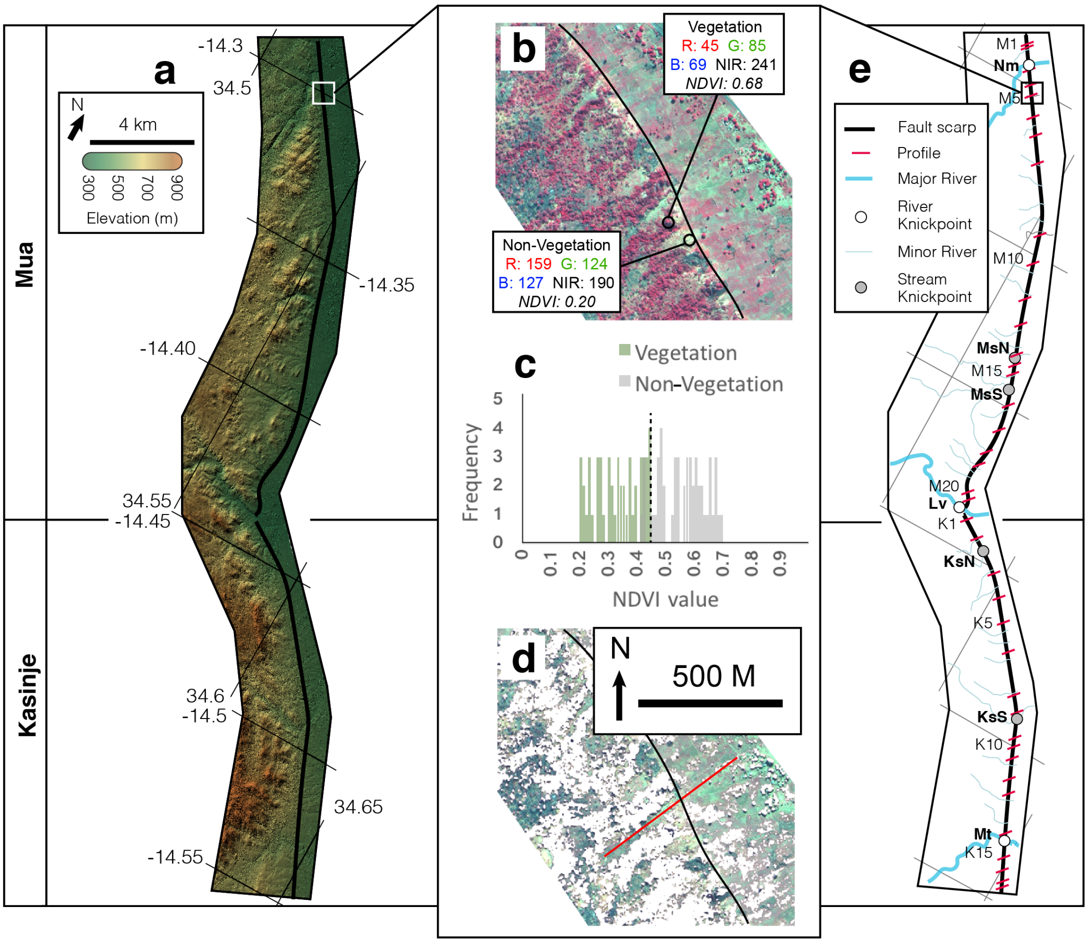

Fig. 5.1 a) A DEM and hillshade image of the Mua and Kasinje segments, showing the fault scarp (black). White box is zoomed in area for panels b to d. b) False colour (NIR, R, G) image showing the R, G, B, NIR and NDVI values for a vegetated and non vegetated sample point. c) Histogram of NDVI values for vegetated and non vegetated areas (50 samples for each). The best threshold value to identify vegetation was found to be 0.45. d) Vegetation masked image showing the location of a suitable scarp profiles (high density of points). e) Location of scarp profiles, oriented perpendicular to the average trend (150°) of the BMF from Chapter 3 (Mua: M1 to M21, Kasinje: K1 to K18), and knickpoints (from north to south: Nm = Naminkokwe River, MsN = Mua north stream, MsS = Mua south stream, Lv = Livelezi River, KsN = Kasinje south stream, KsS = Kasinje north stream, and Mt = Mtuta River).

5.2 Geomorphic indicators of multiple ruptures

Studying landforms generated by surface ruptures during earthquakes, such as fault scarps, can provide discrete information about earthquake events, such as magnitude and recurrence intervals, but also be informative of fault evolution over time (e.g., Avouac, 1993; Hanks et al., 1984; Nash, 1980, 1984; Wallace, 1977). The morphology of a fault scarp is dependent on many factors, including the type of earthquake, amount of slip, and the material properties of the surface it displaces. Typically, a single rupture fault scarp will comprise a free face whose gradient is greater than the angle of repose of the hillslope sediments (fig. 5.2a; e.g., Lin et al., 2017; Nash, 1984; Wallace, 1977). These distinctive free faces, however, erode away within a few hundred years (e.g., Bucknam and Anderson, 1979; Nash, 1984; Wallace, 1980), forming smoother, degraded scarp profiles (fig. 5.2b).

When more than a single surface rupture has occurred along a fault, the scarps may comprise either a single scarp face with differing slopes within it, or an array/stack of multiple discrete scarps set back from one another (Crone and Haller, 1991; Ganas et al., 2005; Nash, 1984; Wallace, 1977; Zhang et al., 1991). Composite scarps comprise a single band of oversteepened terrain where vertical offsets have accumulated onto the same slope over multiple earthquake cycles (fig. 5.2c; e.g., Ganas et al., 2005; Zhang et al., 1991), whereas the vertical offsets of multi-scarps are horizontally offset by terraces (fig. 5.2d; e.g., Crone and Haller, 1991; Nash, 1984; Wallace, 1977). Composite fault scarps develop when near surface slip is confined to the same fault plane, but multi-scarps form when slip is confined to a different near-surface fault splay during each earthquake event (e.g., Anders and Schlische, 1994; Kristensen et al., 2008; Nash, 1984; Slemmons, 1957). Composite scarp surfaces within multi-scarps can develop if a splay is reactivated. Both multi-scarps and composite scarps can exist along the same fault or within the same fault zone, as shown in the Serghaya Fault Zone, Syria (Gomberg et al., 2001), the northern Upper Rhine Graben, Germany (Peters and van Balen, 2007) and northern Baja California, Mexico (e.g., Mueller and Rockwell, 1995).

Multiple surface ruptures on composite scarps may be identified by changes in scarp slope, marked by slope breaks on the scarp's elevation profile (fig. 5.2c; e.g., Lin et al., 2017; Nash, 1984; Wallace, 1977); however, as the scarp degrades, these multiple rupture markers will disappear over time (e.g., Bucknam and Anderson, 1979; Nash, 1984; Wallace, 1980). The terraces between individual scarps on a multi-scarp (fig. 5.2d; e.g., Mayer, 1982) provide a more lasting record of earthquake activity, but multi-scarps too are considered to degrade to a morphology similar to a degraded single rupture fault scarp over sufficient timescales (e.g., Andrews and Hanks, 1985; Nash, 1984).

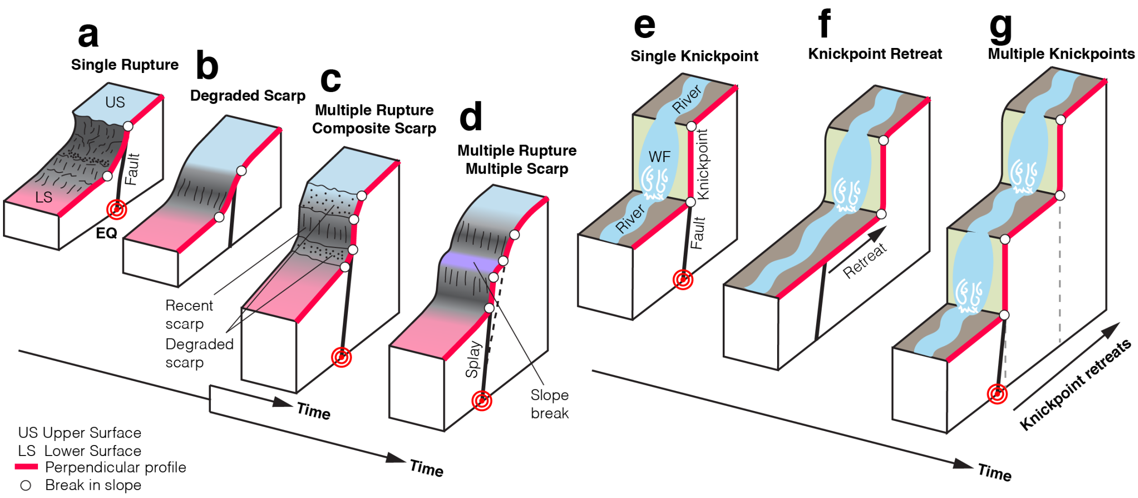

Fig. 5.2 Various geomorphic indicators of multiple ruptures. a) A single rupture scarp, where the upper original surface (US) and lower original surface (LS) are separated by a scarp formed of a steep free face, and wash and debris faces. The elevation profile (red line) shows two prominent changes in slope marked by breaks in slope (white circles). b) A degraded scarp. Erosion and deposition of material smoothes the scarp surface. Following another surface rupture, either: c) A composite scarp forms, where the most recent rupture is indicated by a steeper slope on the scarp surface; or d) A multi-scarp forms where individual scarps/events are separated by a break in slope. Multiple rupture indicators are also observed along a river's longitudinal profile. e) A knickpoint forms during a rupture. f) Between rupture events the knickpoint retreats upstream. g) Another knickpoint forms following a subsequent rupture. The knickpoints are separated by reaches of the river which are at their equilibrium gradient.

The offset produced by surface ruptures also generates a change in fluvial systems. Studying the topographical variations within rivers has been an effective tool in understanding the evolution of tectonically active landscapes (e.g., Finlayson et al., 2002; Montgomery and Brandon, 2002). In fluvial geomorphology, the change in the appearance of a river's longitudinal profile can be a response to tectonic activity (e.g., Burbank and Anderson, 2011; Holbrook and Schumm, 1999; Ouchi, 1985; Wei et al., 2015). Typically, the longitudinal profile is smooth and concave in appearance; however, surface ruptures can produce knickpoints (fig. 5.2e; e.g., Commins et al., 2005; He and Ma, 2015; Sun et al., 2016; Wallace, 1977; Yang et al., 1985). Over time, knickpoints retreat upstream from their original position during the process of channel regrading (fig. 5.2f). As knickpoints migrate upstream they reduce in height, and may eventually disappear (Holland and Pickup, 1976). Subsequent surface ruptures can cause additional knickpoints to develop, separated by reaches of the river which are at their equilibrium gradient (fig. 5.2g).

If the retreat rate is known, the age of formation can be calculated by measuring the retreat distance, and the knickpoint height may be used (assuming rupture area is known) to estimate the magnitude of each earthquake event (e.g., Castillo, 2017; He and Ma, 2015; Rosenbloom and Anderson, 1994; Sun et al., 2016; Wei et al., 2015). However, numerical models and field observations have shown that many complex processes including sediment flux, channel morphology, channel slope and drainage area contribute to the rate of knickpoint retreat (Attal et al., 2011, 2008; Cowie et al., 2006; Gasparini et al., 2006; Whittaker et al., 2007a,b).

In the past, analysis of knickpoints was a field-based exercise (e.g., Rosenbloom and Anderson, 1994; Yang et al., 1985); however, by using high resolution DEMs and mathematical models, knickpoints can be identified using slope-area relationships and stream gradient calculations (e.g., Bishop et al., 2005; Hayakawa and Oguchi, 2006, 2009; Howard and Kerby, 1983). As shown by the two representative DEMs in fig. 5.3, the geomorphology of the Bilila-Mtakataka fault scarp may show evidence of multiple surface ruptures. In addition, a knickpoint is observed in each DEM, set back slightly from the scarp. We therefore aim to use the high resolution DEM of the Bilila-Mtakataka fault scarp to identify indicators of multiple surface ruptures from scarp and river profiles.

5.3 Scarp analysis

5.3.1 Data acquisition and processing

To analyse whether the Bilila-Mtakataka fault scarp shows evidence of multiple earthquake events, we use the Pleiades sub-metre point cloud generated in Chapter

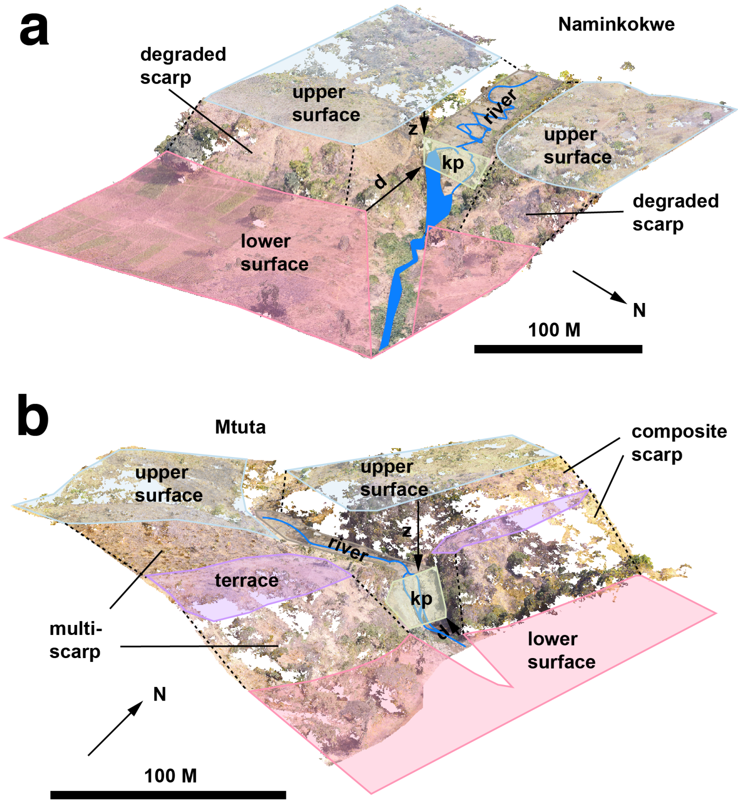

Fig. 5.3 Oblique high resolution DEMs of the Bilila-Mtakataka fault scarp and knickpoints (kp): a) Naminkokwe River (Mua segment), b) Mtuta River (Kasinje segment)

4. Because of the size of the point cloud (in excess of 30 Gb), to save computational resources we restrict our study area to the two major segments at the centre of the BMF: the Mua and Kasinje segments (fig. 5.1a). In Chapters 3 and 4, these segments were found to contain the largest scarps (> 20 m high) along the entire fault. Both the average height of these segments and the average scarp height (used as a proxy for vertical displacement; e.g., Morewood and Roberts, 2001) along the entire fault (~ 14 m) exceed the magnitude of slip typical of a single event for a fault the size of the BMF (< 10 m; Scholz, 2002). Therefore, the Mua and Kasinje segments may be the most likely segments along the BMF to show evidence of multiple ruptures at the surface.

Our analysis requires scarp profiles with a high signal-to-noise ratio; however, the BMF scarp is soil-mantled and the area surrounding it is densely vegetated (figs. 5.3 and 5.1b). In Chapter 4 we showed how vegetation causes significant, local fluctuations in elevation data. This noise propagates into slope calculations and affects scarp parameter calculations. To analyse the sub-metre point cloud used in this study, we must first improve the signal-to-noise ratio. To mask vegetation, a normalised difference vegetation index (NDVI) is calculated from the red (R) and near-infrared (NIR) bands (e.g., Elvidge and Lyon, 1985; Grigillo et al., 2012; Rawat and Joshi, 2012; Yu et al., 2011):

$$NDVI = \frac{NIR - R}{NIR + R} \tag{5.1}$$

Previous studies have reported that a NDVI value greater than 0.2 coincides with vegetation coverage (Grigillo et al., 2012). Here, for 50 sample points, the median NDVI value for vegetated and non vegetated areas was found to be 0.57 and 0.33, respectively (fig. 5.1c). Non vegetated areas were also found to have a larger composite RGB value than vegetated areas. The best performing NDVI threshold to reflect the transition to vegetation was 0.45, where just 4% of sample points were incorrectly identified (n=100, fig. 5.1c). We remove points whose NDVI value is greater than 0.45 from the point cloud. In addition, we manually remove additional large-scale noise features such as buildings that cannot be captured using the NDVI method.

Twenty-one scarp profiles along the Mua segment and eighteen from the Kasinje segment were identified as having a sufficient point cloud density ($> 90\%$ coverage and no gaps > 10 m) to be analysed (fig. 5.1d,e). To account for geometrical variations along the segments influencing our vertical displacement calculations (e.g., Mackenzie and Elliott, 2017), profiles were oriented to perpendicular to the average trend of the BMF found in Chapter 3 (150°). For each profile, points were taken at intervals of a half-metre. The minimum scarp profile length is 300 m.

5.3.2 Identifying individual events

To detect slope breaks in the scarp profiles we need to calculate the gradient from the elevation profiles. Despite improving the signal-to-noise ratio by removing the majority of the vegetation from the point cloud using both an NDVI threshold and manually cleaning the profiles, local noise still resulted in variations in the gradient with an amplitude comparable to that expected by a scarp or knickpoint (fig. D.27). To further improve the signal-to-noise ratio we apply a digital filter to the elevation profiles. As we do not want to artificially reduce the scarp slope or smooth over smooth breaks, we choose a smaller bin width than Chapter 4, here set to 15 m. Smaller window sizes failed to successfully eliminate background noise close to scarps. Furthermore, we use a more robust version of the Loess filter (Cleveland, 1981), using the *rloess* function in MATLAB, whose quadratic regression is a more computationally expensive version of Loess, but is better at removing outliers whilst not over-smoothing the slope. For an example profile, M6 on the Mua segment, applying the filter does not drastically influence the elevation or slope profiles, but does make the scarp easier to identify from the slope profile.

By identifying the slope characteristics typical of single or multiple surface ruptures on fault scarps (fig. 5.2), we categorise each profile as either: (i) a single rupture scarp, (ii) a degraded scarp, (iii) a composite scarp, or (iv) a multi-scarp. Scarp surfaces are marked by steep gradients and troughs in the calculated slope profile. Slope breaks are marked by gentle gradients separating multiple troughs. For composite scarps, the number of ruptures is quantified by the number of slope changes (i.e. pairs of major slope break points), and for multi-scarps, the number of slope breaks. We note that degraded scarps may be fault scarps that have experienced multiple ruptures, but have undergone significant degradation such that individual rupture markers have been lost (e.g., Bucknam and Anderson, 1979; Nash, 1984; Wallace, 1980). As a result, for all scarp types the number of ruptures is a minimum estimate.

5.3.3 Calculating scarp heights

The total scarp height H for each profile was calculated as described in Chapter 3 and represents the cumulative surface displacement along the fault (fig. 5.4). First, the crest and base of the entire scarp (regardless of whether it contains multiple rupture indicators) were picked manually, then a regression line was fitted to the upper and lower original slopes. The scarp height is then calculated as the difference between the two regression lines at a location corresponding to the maximum slope on the scarp surface.

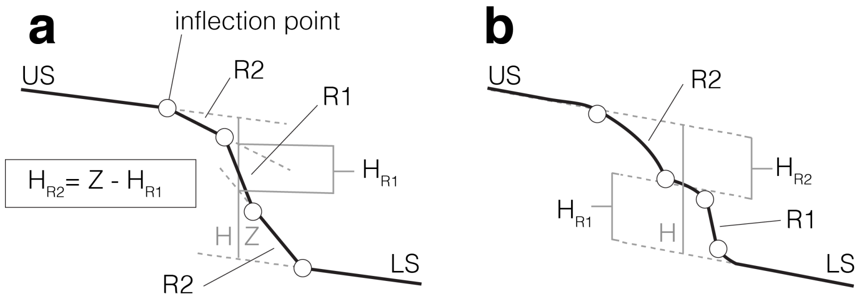

Fig. 5.4 Calculating individual scarp height for multiple events on a: a) composite scarp and b) multi-scarp profile. a) The scarp height of the most recent rupture event R1 (H_{R1}) is calculated by fitting a regression line to the R2 rupture surfaces and calculating the elevation difference at the location corresponding to the maximum slope on the R1 scarp surface. The scarp height of a subsequent rupture event (i.e. H_{R2}) is then found by calculating the elevation difference (Z) using the regression line approach and the next older rupture surface, or original surfaces if calculating the oldest rupture, and subtracting the cumulative scarp heights of earlier ruptures (i.e. H_{R1}). b) Regression lines are fitted to the upper (US) and lower (LS) original surfaces, and the terraced surface (slope break) between scarps. The scarp height for each rupture event is then calculated as the elevation difference between regression lines at the slope maxima.

For multi-scarp profiles, the crest and base of each individual scarp surface (identified by breaks in slope) were manually picked and the scarp height of each calculated using the regression line method (fig. 5.4b). As scarps smooth over time due to degradation (e.g., Bucknam and Anderson, 1979; Nash, 1984; Wallace, 1980), and as the lithology along both segments is uniform at fault-scale (Chapter 3) implying limited spatial variability in diffusivity, we order the scarp surfaces in terms of slope steepness: from steepest to gentlest. We then infer the steepest surface to be a less degraded, younger scarp surface and hence represent the most recent rupture event (R1), the next steepest surface to represent the next most recent (penultimate) rupture event (R2), and so forth. The horizontal distance between scarp surfaces (i.e. between one scarp surfaces base and another's crest) was also measured for multi-scarps.

For composite scarps, the scarp height of R1 (H_{R1}) - identified as the steepest scarp surface at the centre of the scarp - was calculated by fitting a regression line to the R2 surfaces and calculating the elevation difference at the location corresponding to the maximum slope on the R1 scarp surface (fig. 5.4a). The scarp height of subsequent rupture events are then found by calculating the elevation difference (Z) using the regression line approach and the next older rupture surface, or original surfaces if calculating the oldest rupture, and subtracting the cumulative scarp heights of earlier ruptures, i.e. $H_{Rn} = Z - \sum_{i=1}^{n-1} H_{Ri}$.

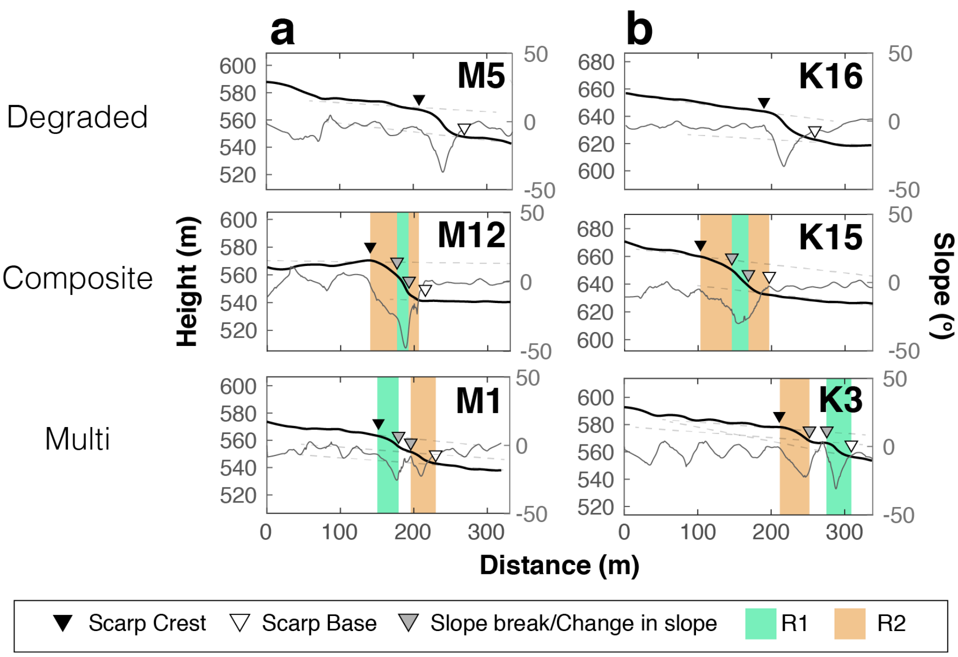

Fig. 5.5 Three scarp profile examples from the a) Mua and b) Kasinje segment: a degraded scarp with no indicators of multiple ruptures, a composite scarp with multiple events, and a multi-scarp with multiple rupture events. Filled black triangles denote the crest of the entire fault scarp. Filled white triangles denote the scarp base. Filled grey triangles denote breaks or changes in slope between individual scarp surfaces formed by multiple ruptures. The steepest surfaces corresponding to R1 are coloured green, and the gentler surfaces corresponding to R2 are coloured orange.

5.3.4 Estimated number of events

Fig. 5.5 shows examples of degraded, composite and multi- scarps from the Mua and Kasinje segments. As no free faces were identified on any profile, no profile was categorised as a single rupture scarp. Profiles M5 and K16 are examples of degraded fault scarps, displaying a smooth elevation profile and symmetrical slope profile. M12 and K15 however show an increase in slope toward the scarp centre (highlighted green), typical of a recent rupture on a pre-existing scarp; these profiles are examples of composite scarps. Breaks in slope typical of multi-scarps can be found on M1 and K3, where the steepest scarp surface is shown in green.

Out of the 39 profiles, 19 were categorised as degraded scarps (9 on Mua, 10 on Kasinje), 14 as composite scarps (9 on Mua, 5 on Kasinje), and 6 as multi-scarps (3 on both Mua and Kasinje). For multi-scarps, the steepest scarp surface (R1) was nearest the lower original surface for all but one profile (M1). For the 20 profiles where multiple events could be identified (i.e. composite scarps or multi-scarps), all but one showed evidence for two rupture events (R1 and R2, fig. 5.13). Multi-scarp profile K12 has an additional break in slope representative of an older, third rupture event (R3).

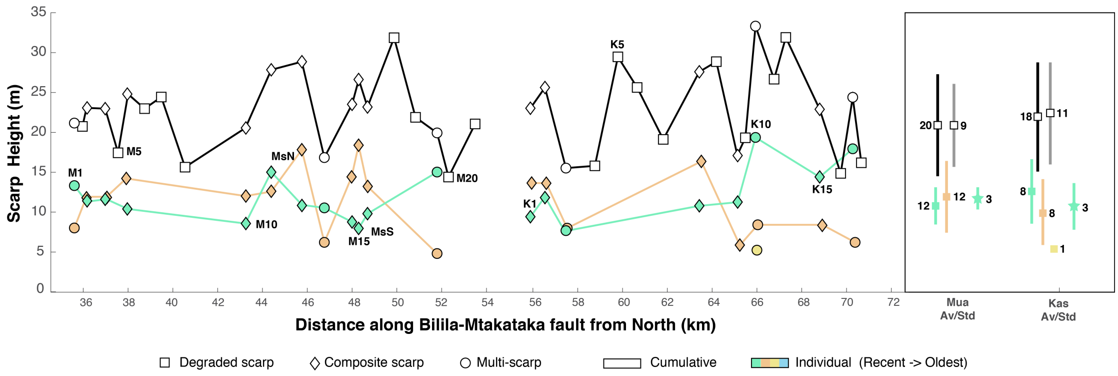

Fig. 5.6 The total scarp height for scarp profiles (white filled), against individual scarp heights for the last rupture event (R1; green), penultimate rupture event (R2; orange), and third rupture event (R3; yellow), for scarp analyses. The box at the end of the profile shows the average (squares) and standard deviation (error bars) values for the scarp height of the following: total (black), degraded (grey), R1 (green), R2 (orange), and R3 (yellow).

5.3.5 Total and individual scarp heights

The average total scarp height for all profiles was 22±5 m; the average total scarp height for Mua profiles was slightly smaller (21 m) than Kasinje (22 m), but had a smaller standard deviation (6 m compared to 7 m, fig. 5.6). On average, the total scarp height is larger at the centre of the segments than the edges, consistent with observations in Chapters 3 and 4. For several kilometres toward the intersegment zone (Livelezi River), the total scarp height for both segments decreases by up to 15 m; however, the local scarp height near the river increases by up to 10 m on both segments.

For the degraded scarps, the average scarp heights were 21±5 m and 22±5 m, respectively for Mua and Kasinje. The total scarp heights for composite scarps and multi-scarps was ∼ 23 m for both segments and therefore comparable to the average height of the degraded scarps. For the 6 multi-scarp profiles, the scarp height from each rupture (R1, R2 and R3) and the horizontal distance between each scarp is shown in Table 5.2. For composite scarps and multi-scarps, the scarp height of R1 was on average 11±2 m for the Mua segment, and 13±4 m for the Kasinje segment (green symbols, fig. 5.6). For the Mua segment, the R1 scarp height was fairly constant, whereas it was more variable on the Kasinje segment and increased southward. The scarp related to R2 (orange symbols, fig. 5.6) had a height of 12±4 m and 10±4 m for Mua and Kasinje, respectively. The scarp height of R2 is greatest at the centre of the segments. A third event (R3) on profile K12 was identified, comprising a scarp 5 m high.

5.4 Modelling multiple rupture events and estimating scarp age

The development and degradation of normal fault scarps has long been studied and used to estimate scarp age and erosion rates (e.g., Andrews and Hanks, 1985; Arrowsmith et al., 1998; Culling, 1963; Hanks et al., 1984; Nash, 1980). The process is simplified in two-dimensions by using a numerical model to calculate changes in elevation Z along a scarp profile (where x is the horizontal distance) over time t. Assuming the scarp erosion is transport-limited (where more debris is available for removal than processes are capable of removing), the vertical component of scarp degradation is governed by the conservation of mass, and can be applied using the equation (Smith and Bretherton, 1972):

$$\frac{dZ}{dt} = \kappa \frac{d^2 Z}{dx^2} \tag{5.2}$$

where κ is the diffusion constant (m^2/kyr).

As the mechanical properties of bedrock are not considered by this equation, it is only valid for soil-mantled fault scarps such as the Bilila-Mtakataka fault scarp. Scarp degradation models simplify the mass failure of the scarp, so that steep, free faces rapidly degrade to smoother slopes (Arrowsmith et al., 1998). In nature, free faces of transport-limited fault scarps have been observed to smooth to the angle of repose over timescales shorter (e.g., 10's to 100's of years) than the interseismic period between earthquake events (e.g., Arrowsmith and Rhodes, 1994; Wallace, 1980). This is particularly true for the BMF, where the slow extension rate (Saria et al., 2014) and large elastic thickness (Jackson and Blenkinsop, 1993) may lead to long recurrence intervals between earthquake events (e.g., Hodge et al., 2015; Midzi et al., 1999). Furthermore, we found no evidence of free faces from our studies of the BMF scarp in the field (see Chapter 3), nor from the high resolution DEM scarp profiles in this study.

Here, we develop and run a series of numerical models to understand and quantify scarp degradation processes during multiple ruptures. First, we setup and test the conditions of the numerical model by simulating the formation and degradation of a synthetic fault scarp in response to a single or multiple ruptures; by doing so we consider what processes may form composite scarps or multi-scarps, and over what timescales degraded scarps may develop. Then, we create our forward model, and use an inversion solution to estimate diffusion age κt (i.e. the amount of erosion that has occurred) at the crest of the BMF scarps. Note, whilst the term diffusion age may allude to an 'age', it is in fact an area, and is the product of diffusivity κ times chronological age t (Andrews and Hanks, 1985). The term is widely used in the literature, and therefore we shall continue to use it here for consistency.

5.4.1 Multiple rupture morphology

We construct synthetic fault scarps using MATLAB. The *a priori* parameters used in creation of our synthetic fault scarp catalogue are: the location of the scarp crest along the profile, x_s in units m; the dip of the fault, δ in units °; the slip of the earthquake event, u in units m; and the slip rate of the fault, r in units mm/yr (fig. 5.7).

An initial synthetic scarp is generated at distance x_s along the profile assuming a down-dip, normal sense of displacement on a fault with dip δ, following an earthquake of slip u (fig. 5.7a). We assume an even slip distribution on the fault, including its surface displacement. Here, the scarp's morphology is simplified so that the slope of the scarp and dip of the fault are equal following the rupture. By dividing the slip by the fault slip rate r, the time between ruptures T_R can be found (also known as the recurrence interval, or return period). Between ruptures, the scarp is degraded according to equation 5.2, where κ is the diffusion constant, whose value is typically between 0.5 and 10 m^2/kyr (e.g., Andrews and Hanks, 1985; Arrowsmith et al., 1996, 1998; Carretier et al., 2002; Hanks et al., 1984; Kokkalas and Koukouvelas, 2005; Nivière and Marquis, 2000, see Chapter 4 for more details). No estimates for κ have previously been suggested for Malawi, but considering the sub-tropical climate we suggest a κ between those proposed for semi-arid climates (0.5 to 5 m^2/kyr; e.g., Andrews and Hanks, 1985; Arrowsmith et al., 1996; Carretier et al., 2002; Hanks et al., 1984; Kokkalas and Koukouvelas, 2005; Nivière and Marquis, 2000) and tropical climates (10 m^2/kyr; e.g., Zielke and Strecker, 2009) to be reasonable. The largest κ estimates we could find are 16 m^2/kyr, from the Raymond fault in southern California (Hanks et al., 1984); however, this is likely due to the less competent material the Raymond fault passes through, and the lack of vegetation causing overland flow and increased erosion. Due to the high vegetation coverage along the BMF, and consistent with its climate, we therefore suggest a κ range between 5 and 10 m^2/kyr for southern Malawi. Scarp degradation processes transport material from the crest of the fault scarp and deposit it at the base of the scarp, smoothing the scarp and reducing the average slope below the fault dip angle δ (fig. 5.7b).

The model simulation is run over a fixed period of time T, for a certain number of events. For multiple ruptures, model parameters (u, r, δ, x_s etc) may be fixed for the entire simulation period (referred to as the fixed parameter scenario) or varied per event (the variable parameter scenario).

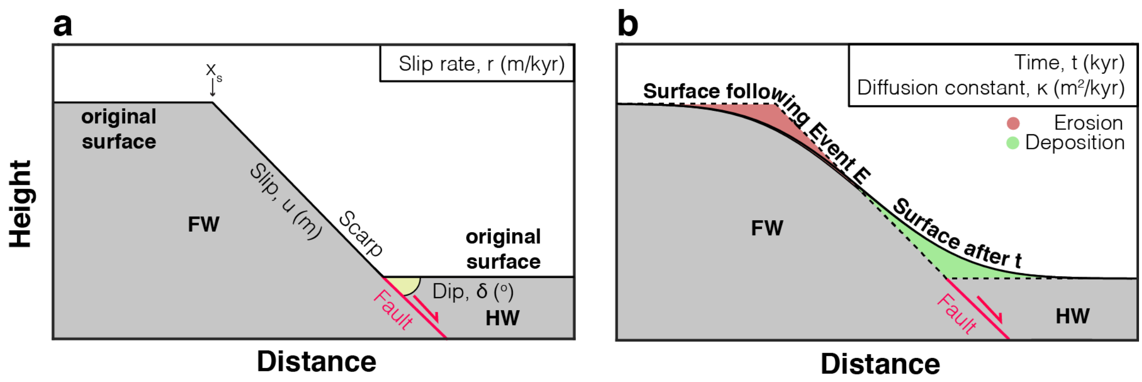

Fig. 5.7 a) Parameters used to generate a catalogue of synthetic fault scarps. FW = Footwall. HW = Hanging-wall. b) Parameters used for the degradation of a fault scarp profile.

The formation of composite scarps and multi-scarps

Here, we present the plots for scenarios that form the unusual and rare multi-scarps, for plots of scenarios forming composite scarps, see Appendix I. As expected to occur according to equation 5.2, a larger diffusion constant κ causes more erosion and decreases the slope of the scarp. For the fixed parameter scenario, a fault scarp caused by a single rupture and a composite fault scarp generated by three smaller ruptures (on the same fault plane) both degraded to identical profiles after a certain diffusion age (fig. 5.8a,b). For a 60° dipping normal fault the transition from composite scarps to degraded scarp (i.e. when clear slope break points were removed) occurred at $\kappa t \sim 36$ m^2. For a 40° fault the transition occurred at $\kappa t \sim 20$ m^2.

The only variable parameter scenario simulations that generated multi-scarps were decreases in fault dip and changes to the active fault location, i.e the formation of splays (fig. 5.8c-f). Decreasing fault dip by less than $\sim 10°$ per rupture, however, did not create a multi-scarp. Moving the active fault plane toward the lower original surface created an asymmetric slope profile with a smoother tail toward the scarp top (fig. 5.8d), whereas the opposite was observed when the active fault was moved toward the upper original surface (fig. 5.8e). By alternating the active fault plane between two parallel surfaces, two composite scarps separated by a break in slope (i.e. a hybrid composite-multi-scarp) may develop (fig. 5.8f). The length between the base of one scarp and the crest of another was slightly smaller than the distance between faults due to the degradation of two scarp surfaces the terrace separates.

5.4.2 Estimating diffusion age of natural scarps

Previous studies have used the slip and slip rate along a fault to estimate the date of the scarp-forming earthquake or earthquakes, then used a scarp degradation

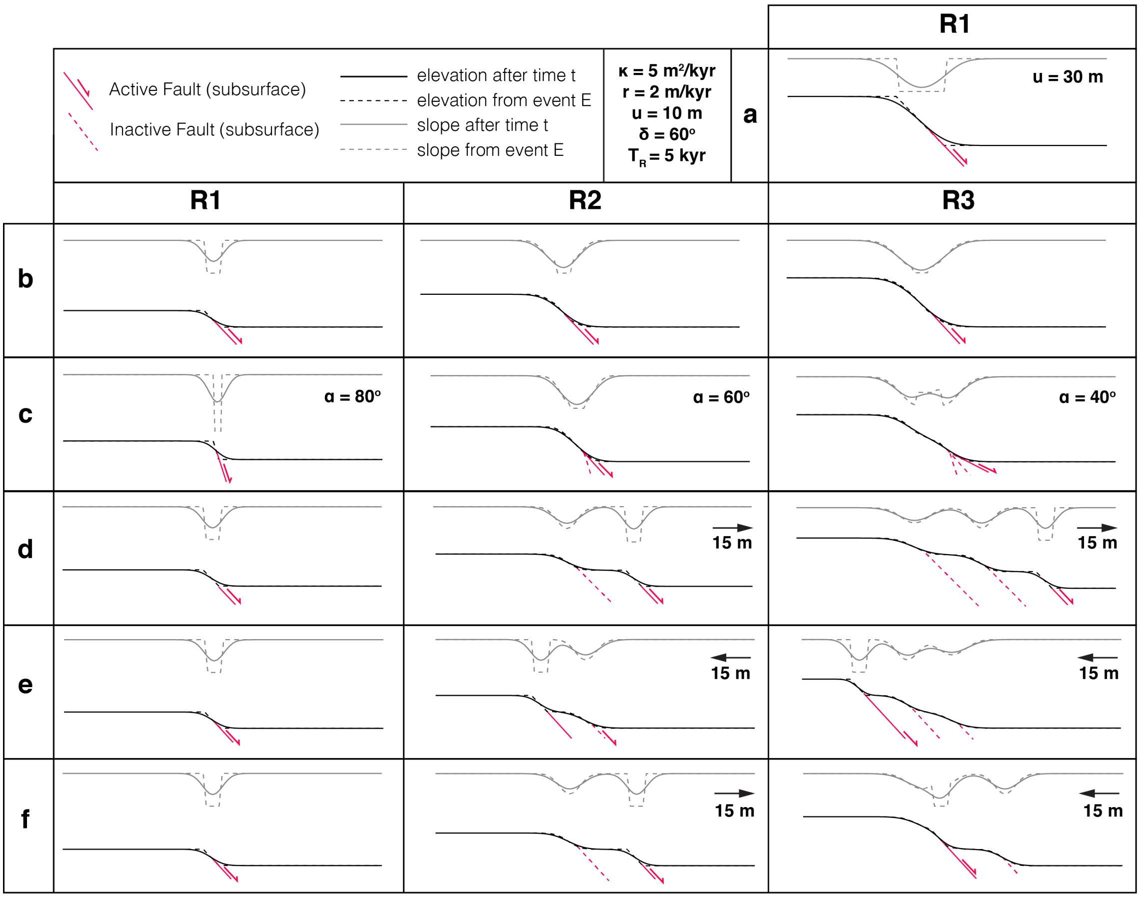

Fig. 5.8 The synthetic fault scarp formation and degradation. a) A single rupture scarp. b) A composite scarp formed by three equally-sized ruptures (R1, R2 and R3). Panels c-f) Multi-scarps formed by: c) decreases in fault dip δ per rupture; d) movement of the active fault plane (solid red line) into the hanging-wall; e) movement of the active fault plane into the footwall; and f) alternating the active fault between two fault planes. The solid lines denote the elevation (black) and slope (grey) profiles immediately following the rupture. The dashed lines denote the profiles at the end of the recurrence interval T_R.

model to calculate the diffusion constant κ (e.g., Arrowsmith et al., 1998; Avouac, 1993; Carretier et al., 2002). For the Bilila-Mtakataka fault, although Section 5.3.4 alludes to multiple surface ruptures forming the Mua and Kasinje scarps, the slip rate is not known. Thus, we cannot estimate the diffusion constant κ. Instead we develop a scarp degradation model, and apply an inverse solution against an inferred initial scarp profile to estimate the diffusion age κt (i.e. the amount of erosion that has occurred on the scarp). By making some assumptions about κ, we may then be able to convert κt to find the relative differences in age between scarp profiles. As the negative change in elevation at the upper portion of the scarp should correspond to an equal positive change elevation at the bottom of the scarp, for computational efficiencies, only the erosion at the upper scarp is calculated.

The 33 composite or degraded scarp profiles along the Mua and Kasinje segments were used to setup the initial synthetic scarp geometry for the forward model. Real scarp profiles are termed 'observed scarp profiles'. Multi-scarps were excluded from the model due to a poor signal-to-noise ratio. Scarp profiles were cropped to contain the largest portion of the upper original surface that had no significant variability in elevation (to reduce RMSE error) and half the scarp surface (fig. 5.9). Here, we make an assumption about the initial scarp shape being non-vertical, hence, we are calculating the 'inferred age' according to Andrews and Hanks (1985). First, the intersection is found between a regression line fitted to the upper surface and one fitted to the scarp surface. The two regression lines are then joined to form the initial 'synthetic scarp profile', which represents the original scarp surface before degradation.

Using equation 5.2 the synthetic scarp is degraded by κ over a period of time of T at intervals of t. At each interval, the diffusion age κt (m^2) is calculated by multiplying t (kyr) by κ (m^2/kyr). An inversion solution is then applied: the synthetic scarp profile (x^{syn}) is compared against the observed scarp profile (x^{obs}) at each interval using a root-mean-square error (RMSE) approach:

$$RMSE = \sqrt{\frac{1}{N}\sum_{n=1}^{N}\left|x_n^{obs} - x_n^{syn}\right|^2} \tag{5.3}$$

The RMSE is then used as a goodness of fit indicator, where $RMSE_{min}$ corresponds to the best-fitting value of κt. Confidence intervals are defined by considering profiles within a 5 cm range of $RMSE_{min}$ (Arrowsmith et al., 1998; Avouac, 1993). The choice of 5 cm as an acceptable RMSE is consistent with the observation that the minimum RMSE in this study and in that of Avouac (1993) and Arrowsmith et al. (1998) was 10 cm, so one half of that is used as a measure of significance and considered to represent a typical misfit. For consistency between this study and previous studies (Arrowsmith et al., 1998; Avouac, 1993), we retain the 5 cm criterion.

As the model is compared to observations from the upper scarp for composite and degraded scarps, we are estimating the diffusion age of a single scarp surface. More precisely, as the oldest scarp surface is located at the upper section of the scarp for composite scarps, we are estimating the κt since the oldest rupture event. This is therefore inferred to be the diffusion age since scarp formation. We later convert this to chronological age using some assumptions of the diffusion constant κ. Assuming a constant κ for the entire scarp history may be invalid for regions where intense climatic variations occur over long timescales; however, drill cores from Lake Malawi suggest that the climatic conditions of Malawi have been relatively stable for the past 70,000 years (Scholz et al., 2011). However, as variations in climate are likely to occur over a few thousands of years within Malawi (Barker et al., 2007), some variation in κ since scarp formation is expected.

Estimated κt from the scarp degradation model

For all 33 scarp profiles, the average diffusion age is $\sim$ 48 m^2; the standard deviation is $\sim$ 25 m^2 and the range is $\sim$ 1 to 98 m^2, indicating a large spread of results. Results from the scarp degradation model for each scarp profile can be found in Appendix I. Minimum misfit (RMSE$_{min}$) between forward model and observations varies from less than 0.1 m (e.g., profiles M3, M17, K5 and K13) to $\sim$ 1 m (profile M9), with an average of $\sim$ 0.2 m. Profile M2 is an example of a reasonably well fitting profile (RMSE$_{min}$ 0.3 m) for a small diffusion age (11$\pm$8 m^2; fig. 5.9a). In comparison, profile K2 was estimated to have a similarly low diffusion age (16$\pm$5 m^2), but the model fit was worse (RMSE$_{min}$ 0.4 m, fig. 5.9b). The poor fit for profile K2 is due to the variable scarp slope near the scarp crest, a feature typical of composite scarps. In comparison profile M2 is a degraded scarp and therefore has a smoother slope profile. Profile M8 is an example of a scarp that has a large estimated diffusion age (98$\pm$17 m^2), where the fit between the model and observations were good but uncertainty was large (RMSE$_{min}$ 0.1 m, fig. 5.9c).

The Mua and Kasinje segments have the same average κt value within error (fig. 5.10a). The estimated κt value for the Mua segment is 52$\pm$24 m^2 (n=18) and for the Kasinje segment is 42$\pm$26 m^2 (n=15). For both segments, degraded and composite scarps have a similar average diffusion age ($\sim$ 50 m^2), but degraded scarps have a larger standard deviation. This may imply that there is no major difference in diffusion (or age) between the two types of scarps. Profiles M8 and K6 have the largest estimated diffusion age (95$\pm$20 m^2) and M2 and K4, the smallest (11$\pm$0 m^2, fig. 5.10a). The inverse solution of the model estimated a κt of just $\sim$ 1 m^2 for profile M9, but the RMSE$_{min}$ was $\sim$ 1 m, indicating a very poor fit. This is

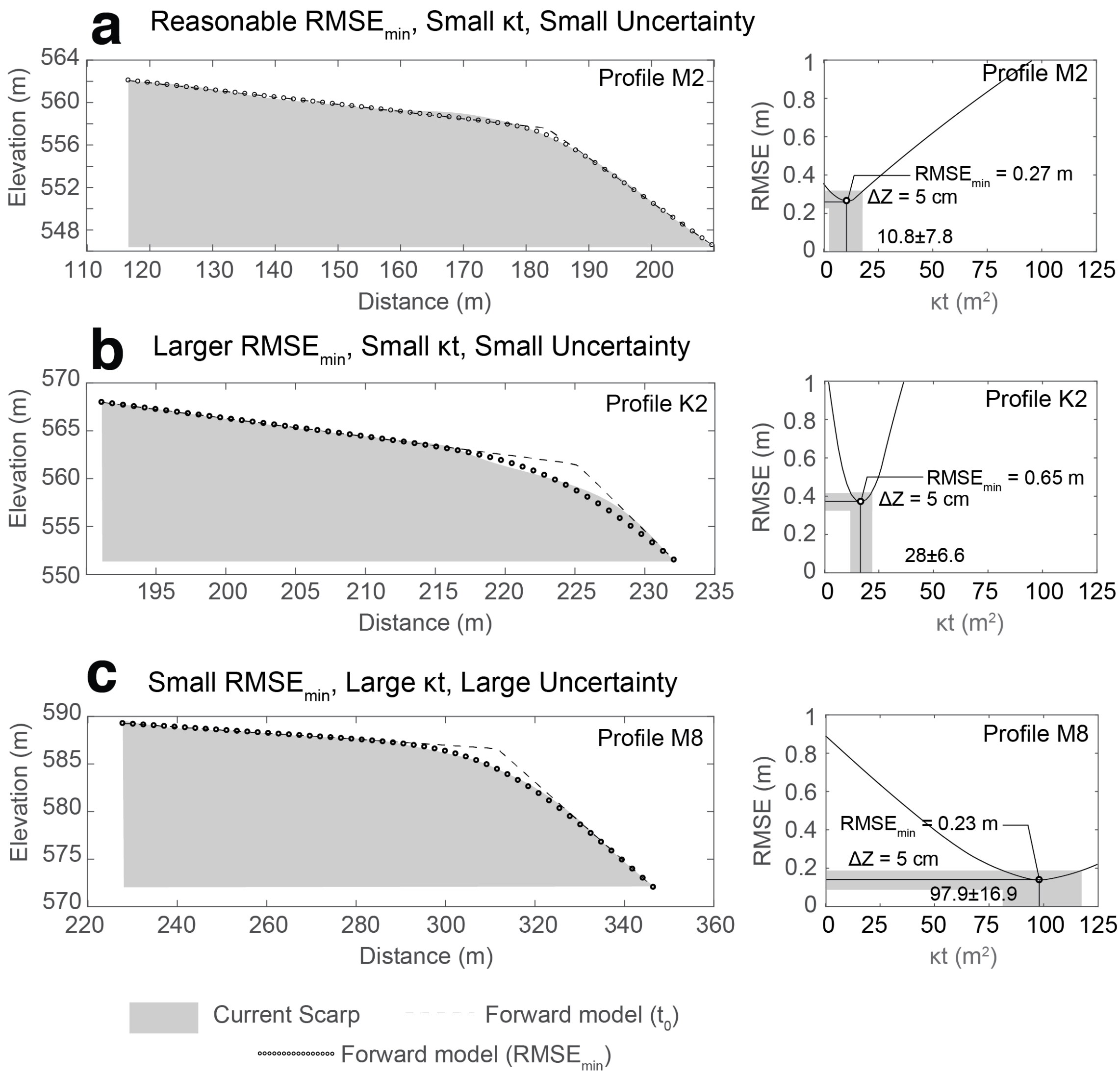

Fig. 5.9 Diffusion age κt results from the forward model for three examples: a) Profile M2 where a reasonable RMSE$_{min}$ (0.27) was found for a κt of 11±8 m^2, b) profile K2 where a large RMSE$_{min}$ (0.65) was found for a κt of 28±7 m^2, and c) profile M8 whose RMSE$_{min}$ of 0.23 shows a good model fit to a κt of 98±17 m^2.

likely due to the steep surface near the scarp crest, which the model could not fit a reasonable degraded surface to. Typically, κt values are lower at the segment ends than the centre, but variations do occur (fig. 5.10a).

In general, a better model fit was found for scarps with a larger diffusion age (fig. 5.10b). Of the 18 profiles whose κt is estimated to be less than 50 m^2, six have a RMSE$_{min}$ of 0.3 m or greater (M4, M9, M10, M11, K1 and K2), whereas only one profile has an equivalent RMSE$_{min}$ where κt is > 50 m^2 (M6). Smaller scarps typically have a smaller κt than larger scarps (fig. 5.10c). The smallest scarp (K16, ~ 15 m high) has a κt of ~ 24±7 m^2, whereas the largest scarp (M17, ~ 31 m high) has a κt of ~ 65±8 m^2. Profile M20 is the anomalous result to this relationship, where a ~ 14 m high scarp has a κt of 80±17 m^2. This scarp is located within 5 km of the intersegment zone. Typically, Mua segment scarps close to the intersegment

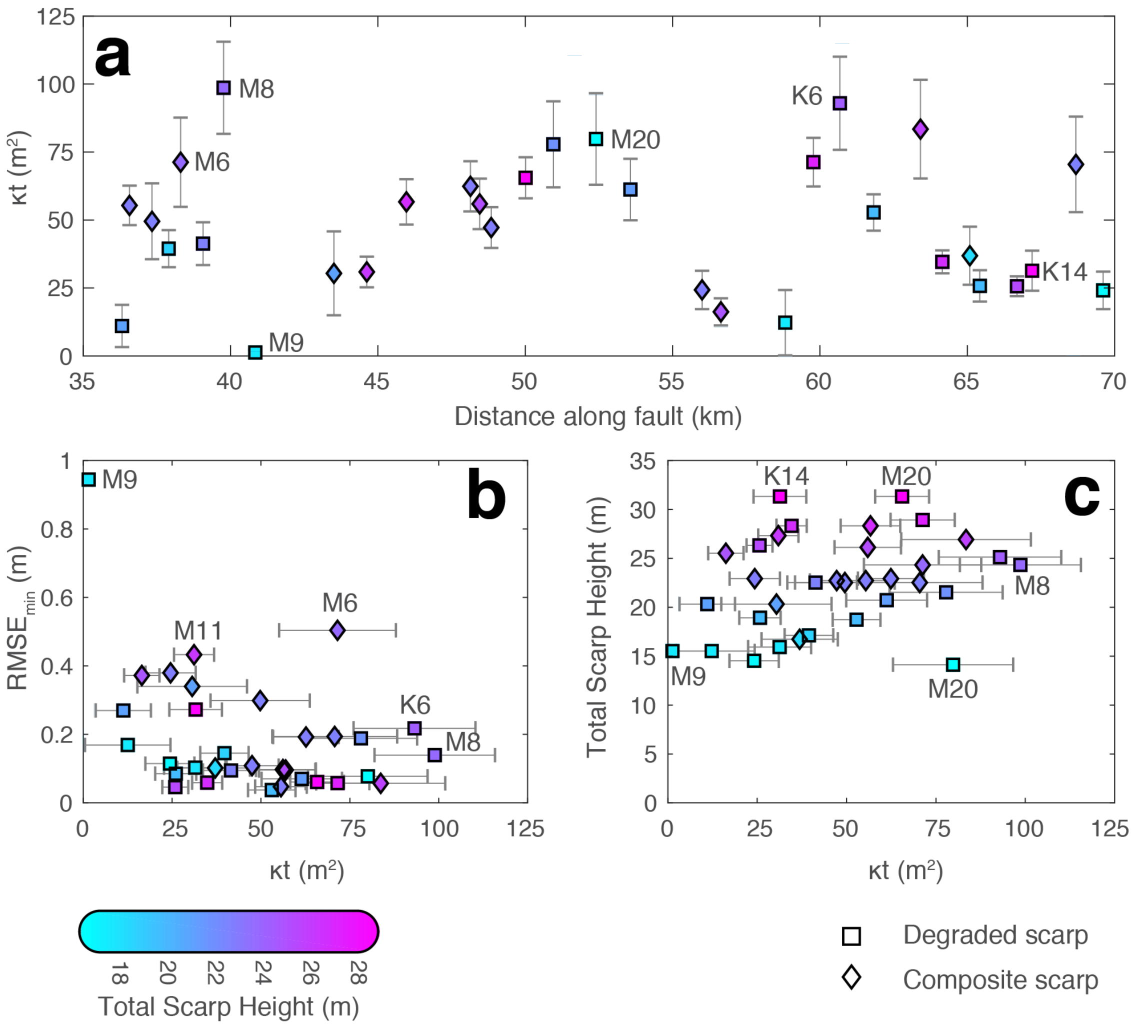

Fig. 5.10 The results from the forward model for: a) the estimated κt plotted against the distance along the fault; b) RMSE$_{min}$ versus κt, and c) total scarp height versus κt.

zone have larger estimated κt values than those at comparable distances on the Kasinje segment (fig. 5.10a).

5.5 Knickpoint analysis

5.5.1 Identification of rivers and streams

Using the vegetation-masked DEM previously described in Section 5.3 we performed a detailed knickpoint analysis of rivers along the Mua and Kasinje segments (fig. 5.1). Fieldwork on the Bilila-Mtakataka fault scarp identified three major rivers; the Naminkokwe, Livelezi and Mtuta rivers. The geological map of Dawson and Kirkpatrick (1968) shows the Naminkokwe River as the only major river that crosses the fault scarp in our study area. The Naminkokwe River is located at the northern end of the Mua segment ($\sim$ 37 km from the northern end of the fault). It is $\sim$ 10 m wide on average, including where it crossed the fault scarp, but has a prominent 20 to 30 m wide section between 50 and 200 m from the scarp. However, we found that the Livelezi River, which is located at the intersection between the Mua and Kasinje segments (near the town of Golomoti), is reasonably well-defined where it crosses onto the valley floor, comprising a width of around 20 m. Upstream the river is locally up to 100 m wide, but averages $\sim$ 30 m. The larger channel width of the Livelezi River compared to the Naminkokwe River suggests it has a larger flow discharge (Leopold and Maddock, 1953). A small river at the southern end of the Kasinje segment, called the Mtuta River, has a maximum width of $\sim$ 10 m, but had significantly less discharge passing through it than the other rivers during our fieldwork. All are marked on fig. 5.1c as white circles. From the DEM, two additional river channels on each segment were also observed to cross the fault scarp (grey circles, fig. 5.1c). These river channels are small ($<$ 5 m wide) and are not named on the geological maps.

5.5.2 Calculation of drainage area

Knickpoints are transient, and as the size of a drainage area is considered to be an important factor in the speed at which a knickpoint retreats through a river system (e.g., Berlin and Anderson, 2007; Bishop et al., 2005; Crosby and Whipple, 2006; Hayakawa and Oguchi, 2006; Seidl et al., 1994), we calculated the drainage area of each river (Table 5.1). To do this a hydrological analysis was performed on a 30 m SRTM DEM in QGIS (fig. 5.11a) to compute drainage direction (fig. 5.11b) and discharge capacity (fig. 5.11c). A 30 m DEM was used to save on computational resources. A polygon was then drawn around the tributaries that drained into each river or stream at the point they incised the scarp. As we are not certain of the hydrological processes acting over the Pliocene faults to the west, and whether discharge flows over these landforms and into the rivers or streams in this study, our polygons do not extend into the footwall of these faults. The area of the polygons then are used to reflect the estimated drainage area (fig. 5.11c). The results show that the Livelezi River has a drainage area in excess of 200 km^2, significantly larger than the other rivers and streams in this study (Table 5.1). Because the four DEM derived river channels have small ($<$ 20 km^2) drainage areas and assumed discharge rates based on their narrow widths (Leopold and Maddock, 1953), we refer to them as streams and name each Mua/Kasinje north/south depending on their relative position along the segment, i.e. north or south.

Table 5.1 The location, drainage area and number of knickpoints found for each river or stream in this study.

River/Stream Name	Lat. at scarp (decimal °)	Long. at scarp (decimal °)	Drainage Area (DA, km^2)	Number of Knickpoints
Naminkokwe River	-14.294	34.520	43	3
Mua north stream	-14.340	34.552	5	2
Mua south stream	-14.363	34.559	13	2
Livelezi River	-14.438	34.576	220	1
Kasinje north stream	-14.446	34.590	5	1
Kasinje south stream	-14.490	34.628	18	2
Mtuta River	-14.530	34.646	32	3

5.5.3 Extracting longitudinal profiles

For each river or stream, the streambed channel was traced from the Pleiades point cloud using the polyline tool in CloudCompare® (fig. J.1a to g). The nearest point from the Pleiades point cloud to the polyline was selected within a parallel distance of 2 m, at an interval of a half-metre. The extracted point cloud was manually cleaned to remove noise. Because of smaller channel widths, the streams had more noise due to overhanging vegetation from the channel sides. This resulted in significant gaps in the extracted profiles for some streams. The points were then plotted along the length of the detailed channel, to form a two-dimensional profile where the horizontal axis is the distance from the fault scarp. As a smoothed longitudinal profile also better represents the true channel bottom (Wei et al., 2015), we apply a digital filter to improve the signal-to-noise ratio. As we want to preserve the vertical to sub-vertical gradients of the knickpoints to identify them in the river profiles, we use the Savitzky-Golay filter, which is based on local least-squares polynomial approximation (Savitzky and Golay, 1964) and helps preserve data features such as peak height and width. Due to the large elevation artefacts of the noise on the channels, we set the window size to be 20 m.

5.5.4 Identifying individual events

We use the gradient of a river's longitudinal profile to identify knickpoints. The gradient, G_d (m/m), is calculated for each sample point using a rolling window of length d (m):

$$G_d = \frac{e_2 - e_1}{d} \tag{5.4}$$

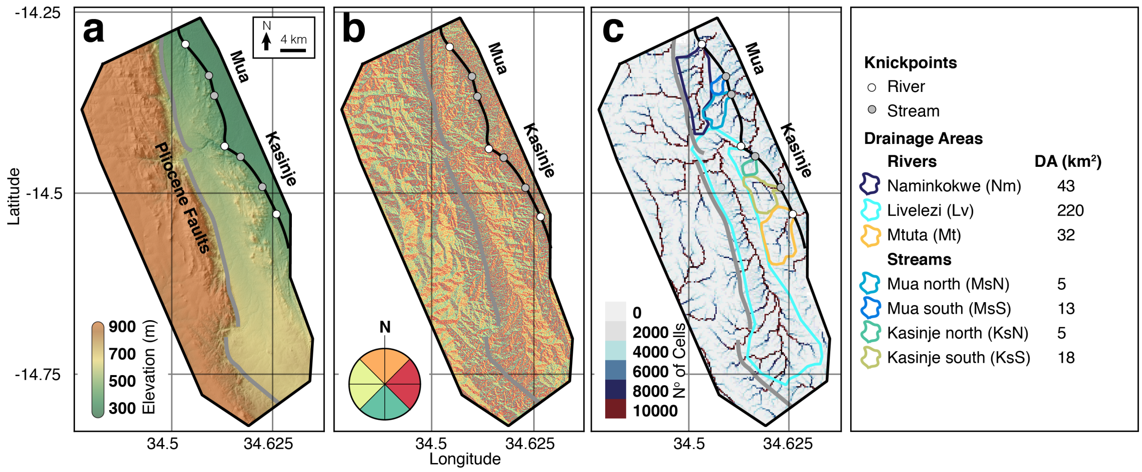

Fig. 5.11 a) 30 m SRTM DEM and hillshade for the Mua and Kasinje segments, showing the location of where the major rivers cross the scarp (identified in the field). b) The drainage direction image, where cell colour relates to the direction on the inserted compass. c) The number of cells that drain through each cell, i.e. the discharge capacity, with the inferred drainage basins represented by polygons. Drainage area (DA) is also given in km^2.

where e_1 and e_2 are elevations (m) at $d/2$ either side of the measurement point respectively (see Appendix J for the methodology figure).

The value of G_d changes as a function of d in response to the local riverbed morphology (Wei et al., 2015). Local features are best reflected in G_d when d is less than 20 m, whereas larger values (20 to 90 m) are best used to identify larger scale gradients. Here, we test a d of 10 and 70 m. Attempts have been made to automate knickpoint identification using G_d (Hayakawa and Oguchi, 2006); however, choosing an appropriate threshold value to objectively define knickpoints is challenging for small drainage areas (Wei et al., 2015). Here, we choose a minimum G_d value of 0.2 to represent a knickpoint, and manually analyse smaller peaks in the G_d plot.

Not all knickpoints are caused by faulting, they may also be generated by changes in local lithology or inflow from tributaries. To combat these challenges we follow a number of conditions proposed by Wei et al. (2015) in our knickpoint identification. First, knickpoints are only considered if they are located upstream of the fault scarp, as knickpoints generated by normal faulting should only exist within the footwall. We then inspect the profile near where the knickpoint is identified, and if elevation fluctuates considerably either side of the knickpoint, we consider such knickpoints as singular points generated by noise.

The spatial relationship between knickpoint location, lithology, tributary junctions and changes in river/stream direction are also considered, as each of these factors may produce knickpoints in bedrock rivers (Wohl, 1993). Using geological and topographical maps, knickpoints are removed from this study if they are positioned at lithologic contacts, at the confluence of tributaries and/or bends in the river profile. Note, regional geological maps may not account for local lithological variation, a possible source of error within the profiles.

5.5.5 Calculating knickpoint height

Calculation of knickpoint heights from river profiles follows the same method as for scarp height from the scarp profiles. The top and bottom of the knickpoint, identified by the onset and end of the trough in the calculated profile gradient, were picked manually and a regression line fitted through the upper and lower surface. The knickpoint height is then calculated as the elevation difference between these regression lines at the centre of the knickpoint.

Because knickpoints may become destroyed over time, and a number of factors influence this, such as drainage area, channel morphology and sediment flux (e.g., Attal et al., 2008; Gasparini et al., 2006; Whittaker et al., 2007a,b), we do not categorise them as R1, R2 etc. Instead we refer to the findings from each river separately and number them chronologically based on their distance from the scarp. For example, the knickpoint closest to the scarp is referred to as K_p1 (note, K_p is different to 'K', which refers to the Kasinje scarp profile), the second closest K_p2, and so forth. The distance between the knickpoint and the scarp is measured as the distance upstream from the scarp.

5.5.6 Number and height of knickpoints

Longitudinal river and stream profiles are shown in fig. 5.12. The point cloud density of stream profiles (fig. 5.12b,c,e,f) was worse than that for river profiles (fig. 5.12a,d,g). Knickpoints are best identified in the G_d profile using a d of 10 m (blue), although large knickpoints could be identified using a d of 70 m (red). Knickpoints identified by our $G_d > 0.2$ threshold (black dotted line, fig. 5.12), or following a manual analysis of the profiles, are shown with grey triangles. Identified knickpoints where elevation locally fluctuates considerably upstream and downstream of the knickpoint are considered to be manifestations of noise and are therefore removed (orange triangles). All knickpoints inferred to be related to faulting are shown by green triangles.

Each river or stream has at least one inferred knickpoint, K_p1. This knickpoint is well-defined, and is located within 100 m of the fault scarp on all profiles except for the Livelezi River (fig. 5.12d), where it is set back $\sim$ 900 m from the scarp. For the river profiles, a second knickpoint K_p2 was identified on Naminkokwe and Mtuta, but not on Livelezi. For the stream profiles, a second knickpoint could be identified on both Mua streams and the northern Kasinje stream. However, due to the poor quality of the stream profiles, where large gaps and fluctuations are present in the

Table 5.2 The six multi-scarp profiles for the Mua and Kasinje segments showing the last rupture event (R1), penultimate rupture event (R2) and third, older rupture (R3) scarp heights and distances between events (i.e. horizontal length between base of one scarp surface and the crest of another).

Profile	R1 Height (m)	R1 to R2 Distance (m)	R2 Height (m)	R2 to R3 Distance (m)	R3 Height (m)
M1	8	16	13		
M13	10	27	6		
M19	15	52	5		
K3	8	18	8		
K12	19	11	8	10	5
K17	18	31	6		

elevation data, subsequent knickpoints formed by surface ruptures could not be conclusively separated from those produced by noise. Where identified, K_p2 is setback between 130 and 190 m from the scarp (fig. 5.12). A third knickpoint K_p3 was identified on both the Naminkokwe and Mtuta rivers and is setback 160 to 250 m from the scarp.

The average height of K_p1 (green stars, fig. 5.13b) was 12±3 m on the Mua segment and 13±3 m on the Kasinje segment. This corroborates the findings from the fault scarp analysis; a more detailed comparison between scarp and river profiles will be done in Section 5.6.2. Additional knickpoints (K_p2 and K_p3) were typically lower, measuring around 5 m on average; however, K_p2 on the southern Kasinje stream measured 19 m in height, larger than the height of K_p1 measured along the stream (10 m). We will discuss this anomalous result later in the chapter.

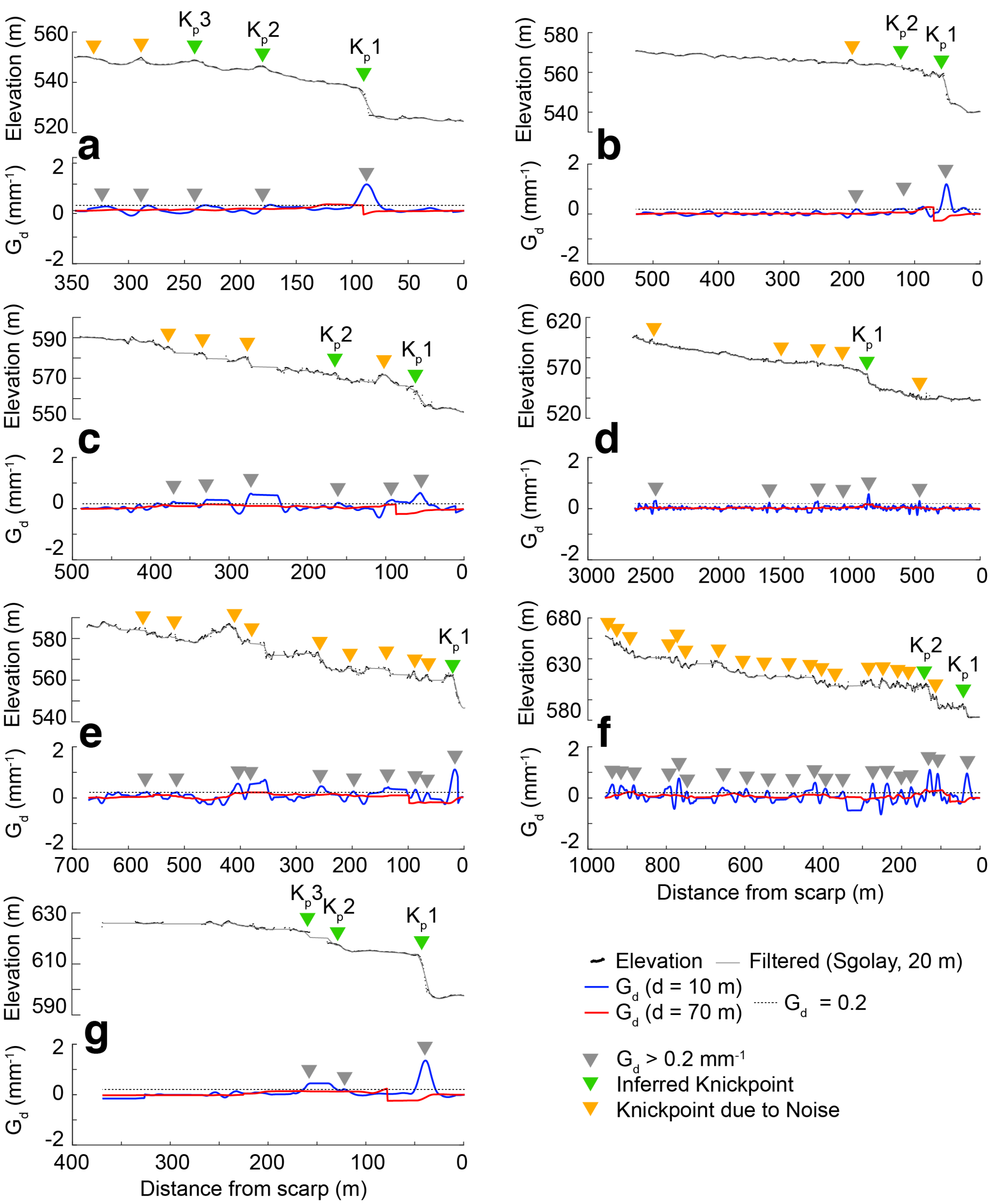

Fig. 5.12 River and stream profiles for: a) Naminkokwe River; b) Mua north stream; c) Mua south stream; d) Livelezi River; e) Kasinje north stream; f) Kasinje south stream; and g) Mtuta River. Profile elevation (black circles) was filtered using the Savitzky-Golay digital filter and window size of 20 m. For the G_d plot a d of 10 (blue) and 70 m (red) were used to identify knickpoints. The dotted black line indicates a G_d of 0.2. Knickpoints identified in the gradient G_d profile are shown as grey triangles. These were then quality checked and considered tectonic knickpoints (green triangles) or artefacts of noise (orange triangles). Knickpoints are numbered K_p1, K_p2 etc based on their distance from the scarp.

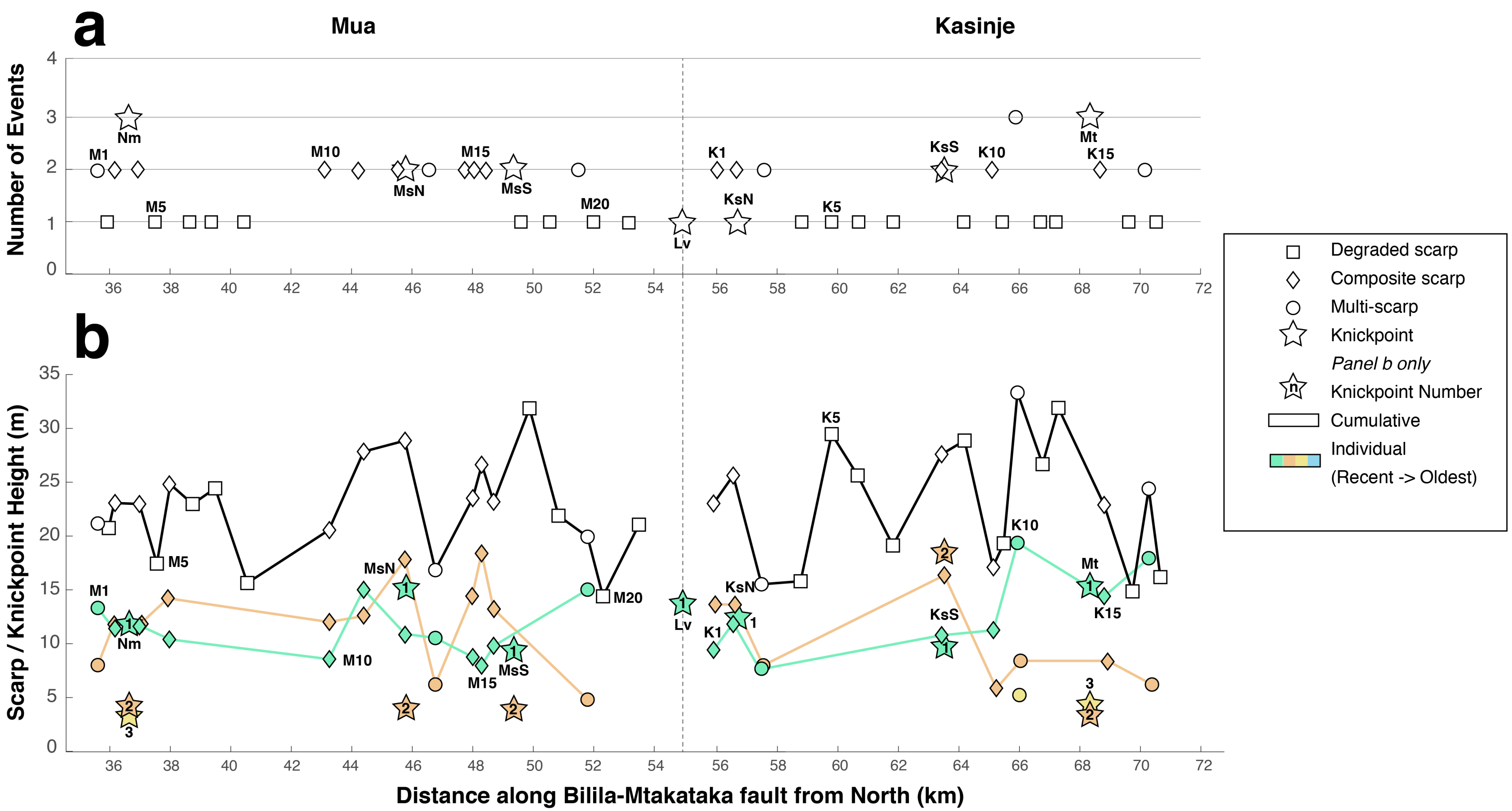

Fig. 5.13 a) The number of rupture events inferred from the scarp profiles (square = degraded scarps, diamond = composite scarps, circle = multi-scarps) and knickpoints (stars) for the Mua and Kasinje segments. b) The profile from fig. 5.6 including knickpoint analyses. Knickpoint results are shown as stars corresponding to the inferred rupture event.

5.6 Discussion

5.6.1 Multiple ruptures on the Bilila-Mtakataka fault

Changes in scarp slope, or breaks in slope, have been suggested to characterise surface ruptures from multiple earthquakes on a number of faults or faults zones, including the Serghaya Fault Zone, Syria (Gomberg et al., 2001), the northern Upper Rhine Graben, Germany (Peters and van Balen, 2007) and northern Baja California, Mexico (e.g., Mueller and Rockwell, 1995). Historical earthquake records and morphological studies for the Pearce scarp in Nevada have shown that the scarp was re-ruptured by the 1915 Pleasant Valley earthquake (Wallace, 1984a). Understanding whether multiple earthquake ruptures have occurred on a fault scarp is important as surface displacements may be used in quantifying paleomagnitude estimates for faults (e.g., Swan et al., 1980; Walker et al., 2015; Wei et al., 2015), and overestimating slip per earthquake will influence recurrence interval calculations, and thus the inferred seismic hazard (e.g. Middleton et al., 2016).

Over half the scarp profiles analysed in this study showed clear slope changes typical of multiple surface ruptures (i.e. were identified as composite scarps or multi-scarps), and 15% of profiles had clear slope breaks representative of multi-scarps (e.g., Crone and Haller, 1991; Nash, 1984; Wallace, 1977). Whilst it is possible that the slope criterion used in this study to define multiple ruptures may be representative of local erosion or concurrent slip on near-surface splays during the same earthquake event (McCalpin, 2009), several symptomatic indicators of multiple ruptures are observed along the Mua and Kasinje segments of the Bilila-Mtakataka fault. For example, profiles identified as scarps formed by multiple earthquake ruptures spanned the entire length of the Mua and Kasinje segments. All but one of the composite scarp or multi-scarp profiles showed consistent evidence for two rupture events (R1 and R2). Profile K12 showed evidence for a potential third rupture event (R3), which may well have not been preserved elsewhere. Thus, while the influence of small-scale erosional processes should not be conclusively ruled out for each profile, such processes would be expected to occur locally, and not over a scale as large as that observed in this study ($\sim$ 40 km).

Due to the existence of degraded, composite and multi- scarps along the Mua and Kasinje segments, a question arises as to why they have formed differently. Here, using a simple numerical simulation we could create multi-scarps by either moving the active fault plane toward the footwall or hanging-wall surfaces, or decreasing the fault dip by 10° or more, between ruptures (fig. I.2). These findings are consistent with earlier studies that have suggested multi-scarps develop when slip is confined to a unique near-surface fault splay during each earthquake event (e.g., Anders and Schlische, 1994; Kristensen et al., 2008; Nash, 1984; Slemmons, 1957), and whilst large changes in fault dip may not be realistic, some variations must occur for horizontally-offset splays to originate from the same deep, master fault (Walsh and Watterson, 1991). The influence of near-surface fault splays appears to only have a local influence on scarp morphology along the BMF, however, with the majority of multi-scarps recorded at the ends of the two segments, including near the intersegment zone. Fault splays at segment tips have been observed in natural examples (Giba et al., 2012; Manighetti et al., 2001; Wu and Bruhn, 1994), and experiments and theoretical models (Perrin et al., 2016a,b; Segall and Pollard, 1983; Willemse and Pollard, 1998). Furthermore, within the Malawi Rift System, faulting of anisotropic rocks may lead to activation of different surfaces during different rupture events, making the near-surface fault migrate between different slip surfaces (e.g., Lee et al., 2002, Chapter 3).

Our numerical simulation confirms that composite scarps develop when slip is confined onto the same slope over multiple earthquake cycles (e.g., Ganas et al., 2005; Zhang et al., 1991), but over time the individual rupture indicators such as changes in slope erode and a degraded scarp develops. In a simple test we found the transition from composite to degraded scarps needs a diffusion age κt larger than 20 m^2 for faults whose dip is 40° or greater. The chronological time t that degraded scarps form over depends on the diffusion constant κ. In Section 5.4.1, we suggested a κ range between 5 and 10 m^2/kyr to be reasonable for southern Malawi. For this κ range, we estimate a minimum t of 2,000 years to create degraded scarps from composite scarps. Of course, this also depends on many factors that may have localised influences such as lithology, geological discontinuities (for example, joints), and moisture content.

5.6.2 Quantifying the number of ruptures

Due to the long recurrence intervals between events in southern Malawi (Hodge et al., 2015; Midzi et al., 1999), owing to slow extension rates (e.g., Saria et al., 2014) and the large earthquakes allowed by above-average elastic thickness (Jackson and Blenkinsop, 1993), it is likely that the fault undergoes a significant degradation between earthquake events. Although almost all the composite scarps and multi-scarps on the Mua and Kasinje segments suggest two rupture events, a third event was identified on the K12 scarp profile. This event marker may have survived due to the lower diffusion age estimated on this section of the Kasinje segment (fig. 5.10c).

As a separate test for the number of rupture events, we undertook a rigorous knickpoint analysis for three rivers and four streams that crossed the Bilila-Mtakataka fault scarp along the Mua and Kasinje segments. The number of

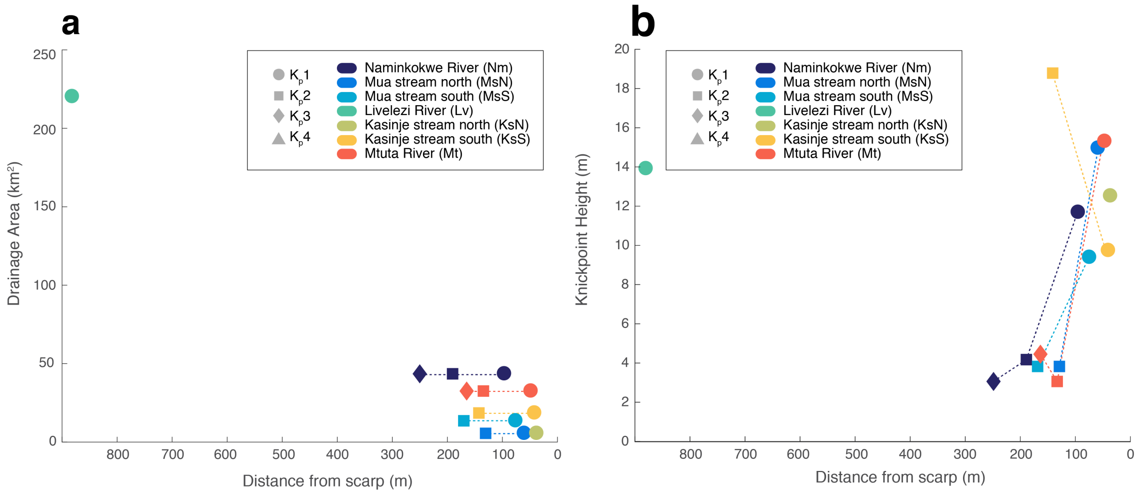

Fig. 5.14 a) Knickpoint distance from scarp versus drainage area. b) Knickpoint distance from scarp versus scarp height. Filled symbols are knickpoints deemed to tectonic knickpoints, whereas outlined symbols have been considered to be noise artefacts and have been removed from the analysis. See text in Section 5.6.2 for detail.

knickpoints on river or stream profiles typically agreed with the number of ruptures identified on the scarp profiles, suggesting more than one rupture event has occurred. The knickpoint closest to the scarp (K_p1) was well-defined, and all but the Livelezi River's K_p1 were within 100 m of the scarp (fig. 5.14). The larger distance of K_p1 from the scarp for Livelezi ($\sim$ 900 m) may suggest that the retreat rate of the Livelezi River is faster than the others, consistent with its larger discharge rate (assumed by its larger width) and drainage area (fig. 5.14a; e.g., Berlin and Anderson, 2007; Bishop et al., 2005; Crosby and Whipple, 2006; Hayakawa and Oguchi, 2006; Seidl et al., 1994). The river with the second largest drainage area/discharge is the Naminkokwe River (Dawson and Kirkpatrick, 1968), whose K_p1 is setback the second furthest from the scarp ($\sim$ 95 m). We consider that the clustering of K_p1, in terms of distance from the scarp and when accounting for differences in discharge, suggests they were formed by the same event: the last rupture event (R1).

For the identification of surface displacements related to older ruptures, the rivers provided better quality longitudinal profiles than the streams, owing to their larger widths, which minimised the influence of vegetation within the valleys they had incised. Whilst the Livelezi River only showed evidence for one knickpoint, both the Naminkokwe and Mtuta rivers showed evidence for three knickpoints. The lack of additional knickpoints on the Livelezi River may be due to the larger catchment area and discharge rate causing knickpoints to migrate upstream at a faster rate, beyond the limits of our profile (Attal et al., 2011, 2008; Wallace, 1977; Whittaker et al., 2008, 2007a,b). We attribute the similar distances of K_p2 from the scarp on all profiles (fig. 5.14) to be due to a concurrent, or near concurrent, older rupture: the penultimate event (R2). A third event was found on both Naminkokwe and Mtuta rivers. As K_p3 on the Naminkokwe and Mtuta rivers are setback a similar distance, and the knickpoint of the Mtuta River is situated a few kilometres south of where a third rupture event was found on scarp profile K12, we suggest that this third knickpoint may be representative of a potential third, older rupture (R3).

5.6.3 Surface displacement along the Mua and Kasinje segments

Total scarp heights along the Mua and Kasinje segments broadly match the results from Chapters 3 and 4, and show that while there is an intense local variability in the scarp height, the average total scarp height is over 20 m on both segments, and is largest at the segment centres. Whereas our previous Chapters (3 and 4) have focused solely on the total scarp height, here using the high resolution DEM we were able to estimate the incremental vertical surface displacements from each individual rupture event. The average scarp height of the most recent rupture event (R1) was $\sim$ 12 m on both segments. The penultimate rupture event (R2) identified from the composite and multi-scarps had a similar scarp height ($\sim$ 11 m). Like the total scarp height profile, the R1 and R2 scarp height profiles show variability along the segments. A third potential event recorded on K12 had a scarp height of 5 m.

The height of individual knickpoints that have formed during consecutive ruptures may be a proxy for potential seismic displacement (Wei et al., 2015). We compare the cumulative knickpoint height measured from each river profile to the total scarp height measured from the closest scarp profile and find that the river profiles on average express 80% of the total scarp height. When comparing R1 knickpoint and scarp heights, the knickpoints record over 100% of the scarp height; as scarp height is locally variable, the closest scarp used here may not represent a larger scarp local to the knickpoint. The good correlation between knickpoint and scarp heights suggests that the well-defined first knickpoints (K1) are therefore likely true reflections of the latest vertical surface displacement from the most recent rupture on the two segments. The height of R2 from the river profiles is between 20% and 50% of the nearest R2 scarp height, when not including the abnormally large K2 height on the southern Kasinje stream. However, the nearest scarp profiles were all composite scarps, which may comprise additional ruptures that have been masked. When compared the R2 knickpoint height to the closest R2 scarp height from multi-scarps, the knickpoints express between 55% and 80% of the vertical offset. The R3 knickpoint on the Mtuta River has a height that expresses 90% of the nearest R3 scarp height from a multi-scarp.

The abnormally large knickpoint height of second knickpoint ($\sim$ 19 m) on the southern Kasinje stream, when compared to other K_p2 heights (< 5 m) may be explained by a localised displacement high during an older event, or the inability to distinguish multiple older ruptures. The nearest scarp profile was taken only a few hundred metres from the stream and shows evidence for an older rupture producing a $\sim$ 16 m high scarp (fig. 5.13). Because these profiles are from the centre of the Kasinje segment, this may imply that a larger displacement occurred here (conforming to a bell-shaped profile); however, the large κt values from this region (fig. 5.10) may also suggest that older rupture markers may have been destroyed, and that the scarp and knickpoint R2 may be formed from multiple, older events. In addition, the small discharge and catchment area for the southern Kasinje stream means that if a subsequent ruptures did occur here, and did so within a short enough period of time, a break in the longitudinal profile between knickpoints may not have developed.

These findings suggest that the vertical offsets from earthquakes can be estimated from both scarp and river profiles. Event markers for two ruptures were found along the entire Mua and Kasinje segments. However, there are gaps in where R2 was recorded, due to significant gaps between where profiles were taken (resulting from noise on the scarp). On average, both R1 and R2 events produced vertical surface displacements of $\sim$ 10 m along the Mua and Kasinje segments. Our findings are in agreement with other studies that show variability in surface displacement along a fault (e.g., Klinger et al., 2005; Mildon et al., 2016).

If the entire BMF scarp formed by two ruptures of equal slip, then the average scarp height for each rupture for the entire fault would be half that found in the previous chapters ($\sim$ 14 m). This would equate to an average scarp height of 7 m ($\pm$4 m) per rupture for the entire fault, with greater values in the Mua and Kasinje segments ($\sim$ 10 m) and smaller values at the fault ends, which would fit well with global scaling laws for a $\sim$ 110 km long normal fault using a slip-length ratio range of 10^{-4} to 10^{-5} (equating to 1 to 10 m of slip; e.g., Scholz, 2002).

5.6.4 Estimating the timing of ruptures

As no historical rupture has been observed on the Bilila-Mtakataka fault, the last rupture event (R1) must precede the oldest event in the earthquake catalogue, i.e. older than 100 years (Hodge et al., 2015; Midzi et al., 1999). As scarps degrade rapidly over these timescales (e.g., Arrowsmith and Rhodes, 1994; Wallace, 1980), this explains why no free faces were observed along the Mua and Kasinje segments using our high resolution DEM, nor for field observations (see Chapter 3). A simple numerical model is consistent with these findings, suggesting that even for regions with a small diffusion constant κ, a free face degrades and disappears within approximately a hundred years (fig. I.3).

Almost half the scarp profiles for the Mua and Kasinje segments were identified as degraded scarps. The observed degraded scarps may be composite scarps that have eroded individual event indicators, or single rupture scarps. We also found that the total scarp height of the composite scarps and multi-scarps was equivalent to the height of the degraded scarps, suggesting that the degraded scarps may have also formed through multiple events, but their slope break points have since eroded. For our simple model, we found that a κt larger than 20 m^2 was required to remove individual event markers on composite scarps, equating to a minimum t of 2,000 years for a κ range reasonable for southern Malawi (5 to 10 m^2/kyr). The presence of degraded scarps may therefore imply that the formation of the BMF scarp must be older than 2,000 years.

In our forward model for the BMF scarps, we found that the diffusion age was typically between 10 and 100 m^2, apart from one outlier (M9, κt 1 m^2) whose $RMSE_{min}$ was ~ 1 m and therefore deemed to be a poor-fit. This variability in κt either suggests that κ is variable along the segments (i.e. fixed t), or the onset of scarp formation along the segments was not uniform in time (i.e. fixed κ). The diffusion age is converted to κ or age t by dividing κt by the opposing parameter. To fit κ of 5 - 10 m^2/kyr, t must be approximately 10,000 - 20,000 years. The variations in κ along a single fault, required for a consistent scarp formation age on the BMF, have been observed elsewhere (e.g., Kokkalas and Koukouvelas, 2005).

Instead of a fixed t, variable κ scenario, using a fixed κ of 10 m^2/kyr would give a range of t estimates equal to around 8,000 years. Decreasing κ to our lower value of 5 m^2/kyr doubles this range. Such a difference in t estimates implies sections of the Mua and Kasinje segments are 16,000 years older than others, and therefore may have experienced several more earthquakes. It would also imply that for the earlier earthquakes the surface expression remained discontinuous. Although discontinuous surface ruptures have been observed on other normal faults (e.g., Nicol et al., 2005; Worthington and Walsh, 2016), it seems unlikely the slip distribution would remain consistently heterogeneous over several earthquake cycles, unless slip distribution is controlled by the fault geometry (e.g., Klinger et al., 2005; Mildon et al., 2016). However, neither segment displays intense local variability in scarp trend (Chapter 3).

As we find that some degraded scarps have higher diffusion age estimates than composite scarps, we suggest that variations in diffusion age is more likely related to localised erosional processes (i.e. variations in κ; e.g., Kokkalas and Koukouvelas, 2005) rather than such a significant variation in the timing of scarp formation. Furthermore, we did not find a significant correlation between diffusion age and scarp height (fig. 5.10c), nor is the distribution of multiple rupture indicators and their associated scarp heights representative of several small discontinuous ruptures.

We found that the diffusion age for the Mua and Kasinje segments is the same within error, implying the scarps likely formed at the same time. Yet, the scarp height of R2 from both segments decreases at both the segment ends and the intersegment zone at the Livelezi River, and may imply two separate ruptures. However, two segmented ruptures $\sim$ 20 km in length with 10 m of surface displacement would again imply an unusually large slip-length ratio for this region (5×10^{-4}). We therefore suggest that the R2 event ruptured both segments concurrent, or near concurrent in time, as supported by the near same diffusion age. The slight variation in κt between the segments may also be a result of the wider damage zone on the Mua segment generated by a cross-cutting relationship between the scarp trend and the gneissic foliation (Chapter 3), leading to more erosion. The fairly constant scarp height of R1 implies that the most recent event also ruptured both segments at the same time. The R1 scarp height does not decrease at the segment ends either, implying that the rupture likely propagated onto the more northern (Mtakataka) and southern (Bilila) segments of the BMF. Our findings suggest therefore that the BMF segments, over the last two earthquake cycles, have not ruptured individually. This finding profoundly influences the seismic hazard of the area, as the rupture length is not constrained by the structural segment lengths.

5.6.5 Magnitude estimates

In Chapter 4 we concluded that for the 110 km long Bilila-Mtakataka fault to produce the current scarp in a single, complete rupture, the magnitude of the earthquake would be around M_W 7.9 - 8.4, comparable to the estimate by Jackson and Blenkinsop (1997) but greater than any recorded event on the East African Rift System (Hodge et al., 2015; Midzi et al., 1999). This was based on the assumption that average scarp height ($\sim$ 14 m) represented the average surface displacement $\bar{D}_s$ per event; however, in this study we have concluded that the BMF scarp likely formed through multiple ruptures, where slip per event is less than the average scarp height of the BMF.

By using the average scarp height found in this study - extrapolated for the entire BMF - to represent the average surface displacement $\bar{D}_s$ (7$\pm$4 m), the estimated magnitude range for a complete rupture is M_W 7 to 7.4 according to a displacement-magnitude scaling law by Wells and Coppersmith (1994) (Table 5.3, eq. 2). The magnitude estimates using average surface displacement $\bar{D}_s$ are therefore comparable to those estimated using the surface rupture length L scaling laws (Table 5.3, eq. 3 to 5, Stirling et al., 2002; Wells and Coppersmith, 1994), which range between M_W 7.4 and 7.6 for a complete BMF rupture. However, both the average surface displacement and surface rupture length equations may underestimate the magnitude of an earthquake in the MRS due to its unusually large elastic thickness ($\sim$ 30 km, Jackson and Blenkinsop, 1993), which means the fault rupture width W is likely greater than for other continental settings. The fault rupture width is calculated as $W = T_s/\delta$, where T_s is the seismogenic thickness and δ is the fault dip.

Using an average surface displacement $\bar{D}_s$ of 7$\pm$4 m and a fault length L of 110$\pm$2 km, the slip-length ratio α is 6.4$\pm$4$\times$10^{-5}. Applying this fault length and slip-length ratio to the magnitude scaling laws by Hanks and Kanamori (1979) and Wells and Coppersmith (1994) (Table 5.3, eq. 1), including a modulus of rigidity G of 30$\pm$5 GPa (Stein and Liu, 2009), T_s of 30$\pm$5 km (Jackson and Blenkinsop, 1993) and δ of 60°$\pm$5° (Byerlee, 1978), the estimated M_W range for a complete rupture of the BMF is 7.5 to 8.1. This large range is due to all the uncertainties in the parameters; the average M_W is 7.9. As the average subsurface displacement $\bar{D}_d$ may be 1.6 times the average surface displacement $\bar{D}_s$ (Villamor and Berryman, 2001), this M_W range may be slightly larger, at 7.7 to 8.3.

Using the new findings from this study we suggest that the estimated earthquake magnitude from a complete rupture of the BMF is slightly greater than the largest naturally recorded earthquake events on the EARS, the M_W 7.3 1910 Rukwa event (Ambraseys and Adams, 1991) and the M_W 7.0 1990 Juba earthquake (Hartnady, 2002), and larger than the M_W 7 2006 Machaze earthquake (Fenton and Bommer, 2006). The BMF is situated $\sim$ 600 km south of the Rukwa fault, and $\sim$ 710 km north of the Machaze fault, and poses a substantial seismic hazard risk to Malawi and the surrounding regions. However, the average M_W of 7.9 is slightly lower than previously estimated (Jackson and Blenkinsop, 1997) and is another example of where better constraining rupture slip has lead to lower magnitude estimates (e.g., the 1739 Yinchuan earthquake, China; Middleton et al., 2016).

These calculations assume a characteristic earthquake model for the BMF, and whilst the geomorphological analysis in this study found no evidence for single segment ruptures along the Mua and Kasinje segments, multi-segment ruptures may occur across both segments but not the entire fault. For example, the Citsulo segment may be a barrier to rupture propagation as described in Chapter 3. Such ruptures would have a lower earthquake magnitude, due to the shorter rupture length, but also have a shorter recurrence interval. Complete and segmented ruptures along the BMF pose different seismic hazards for the region (Hodge et al., 2015). A detailed geomorphological analysis on the remaining BMF segments (Ngodzi, Mtakataka, Citsulo and Bilila) is required.

Table 5.3 Earthquake magnitude (including lower and upper) estimates using L = 110 km ($\pm$2 km), $\bar{D}_s$ = 7 m ($\pm$4 m), α = 6.5$\times$10^{-5} ($\pm$4$\times$10^{-5}), G = 30 GPa ($\pm$5 GPa, Stein and Liu (2009)), and $W = T_s/\delta$ (where seismogenic thickness T_s = 40 km $\pm$15 km Jackson and Blenkinsop (1993), and dip δ = 60°$\pm$5°). [1] Wells and Coppersmith (1994). [2] Hanks and Kanamori (1979). [3] Stirling et al. (2002)

Eq N°	Description	Equation	Average M_W	M_W Range
(1)	Normal fault slip [1,2]	$M_W = \frac{2}{3} \cdot \log(G\alpha L^2 W)$-6.05	7.9	7.5 - 8.1
(2)	Normal fault slip [1]	$M_W = 6.61 + 0.71 \cdot \log(\bar{D}_s)$	7.2	7.0 - 7.4
(3)	All slip type [1]	$M_W = 5.08 + 1.16 \cdot \log(L)$	7.5	7.4 - 7.5
(4)	Normal fault slip [1]	$M_W = 4.86 + 1.32 \cdot \log(L)$	7.6	7.5 - 7.6
(5)	Instrumental data [3]	$M_W = 5.45 + 0.95 \cdot \log(L)$	7.4	7.4 - 7.4
(6)	Preinstrumental data [3]	$M_W = 5.89 + 0.79 \cdot \log(L)$	7.5	7.5 - 7.6

5.7 Conclusion

In Chapters 3 and 4 we concluded that the surface expression of the $\sim$ 110 km Bilila-Mtakataka fault comprises a scarp whose height averages $\sim$ 14 m. Using global slip-length scaling laws, however, the estimated slip per event for a fault the length of the BMF is less than 10 m. In addition, the two central structural segments - the Mua and Kasinje segments - have scarps more than 20 m high in places. Previous work has suggested that scarps of similar heights form through multiple ruptures on the same fault plane (a composite scarp) or unique near-surface fault planes (a multi-scarp). Here, by undertaking a geomorphological analysis of the fault scarps along the Mua and Kasinje segments, using a high resolution DEM, we suggest there is evidence for at least two ruptures. A separate knickpoint analysis on three rivers and four streams that cross the fault scarp agree with these findings. By calculating the individual vertical displacement of each rupture from the scarp and knickpoints, we estimate the average vertical surface displacement along the two segments to be $\sim$ 10 m per rupture. Results from a scarp degradation model used to estimate diffusion age κt on each scarp profile, by finding a best fit to the current profile, imply that the most recent rupture was continuous across both structural segments, and that the penultimate rupture was concurrent, or near-concurrent, in time across both segments. Extrapolating these findings for the entire BMF, we suggest that the surface slip per event is less than 10 m, as expected by global slip-length scaling laws, and that a complete rupture would equate to a M_W range of 7.5 to 8.1. The average M_W of 7.9 is therefore smaller than previously suggested for the fault, but greater than the largest earthquakes recorded along the entire EARS. Extending this work onto the remaining BMF segments will help conclude whether the past two ruptures were multi-segment or complete ruptures.

CHAPTER 6

GENERAL DISCUSSION

In this thesis I have been motivated to understand how large, normal faults develop and deform in early-stage rifts. In a multidisciplinary approach, I have combined field and satellite observations with numerical models. I have utilised advances in remote sensing techniques to develop high resolution digital elevation models (DEMs) from satellite and UAV imagery. Here, I will discuss overall conclusions, broader implications, and future directions of research.

6.1 Summary of research

At the beginning of this thesis I posed three main research questions that I aimed to address. These were:

Q1. What does the geometry and morphology of a fault at the surface tell us about a fault's development and deformation style?

Q2. In what ways can we improve the methodology for quantifying the fault processes?

Q3. What does our work tell us about the seismic hazard posed by faults in early-stage, slow strain rate rifts?

Here, I revisit these questions and suggest how my research has addressed them. I refer back to relevant introductory material and sections, as well as material from my main research chapters. I then end with a brief section on potential future work related to my research, before a conclusion section.

Q1. What does the geometry and morphology of a fault at the surface tell us about a fault's development and deformation style?

In a pure Andersonian stress field and in intact rock (1.1.1), the primary influence on fault geometry is assumed to be the regional stress field orientation (Anderson, 1905). For rift environments, acting under plane strain conditions and rock friction, the regional stress would support the development of rift-axis parallel normal faults (Morley, 1999a; Ring, 1994). Many rifts, such as the Recôncavo-Tucano rift (Destro et al., 2003) and the Gulf of Aden rift (Withjack and Jamison, 1986), however, have been shown to not conform to this geometry and are oriented oblique to the idealised orientation (Philippon et al., 2015). Furthermore, as shown in Chapter 2, most faults are curved or have abrupt changes in their strikes when viewed in map-view (Table 2.2, fig. 2.1). In addition, large continental faults - defined as those whose lengths are much greater than the seismogenic thickness they reside within - typically comprise a number of smaller fault segments (e.g., Peacock and Sanderson, 1991; Schwartz and Coppersmith, 1984; Wesnousky, 1986). We first ask, what can the geometry and morphology of faults and their segments tell us about a fault's development and deformation style?

The non-planarity of faults along their strike has long been interpreted to be a result of interactions with other faults, structures, pre-existing planes of weakness and/or strength anisotropies (e.g., Bellahsen and Daniel, 2005; Collettini et al., 2009; Ebinger et al., 1987; Morley, 2010). For example, the relay ramp structures that are common on normal faults have been inferred to form through incremental fault segment growth, overlap, interaction and eventual linkage through the nucleation of linking faults oriented oblique to the strike of the fault segments (fig. 2.2; e.g., Acocella et al., 2000; Childs et al., 1995; Kristensen et al., 2008; Larsen, 1988). Section 1.1.7 explains this process in further detail. The literature review in Chapter 2, however, shows that a number of segmented normal faults have changes in strike between distinct fault segments, but lack the corresponding relay ramp structure(s). These types of links between segments are termed 'fault bends' in Chapter 2. An example is found on the 110 km long Abadare Fault in the Gregory Rift, whose 65 km and 20 km fault segments are linked by a $\sim$ 10 km fault oriented at an angle of 27° from the average fault segment strike (fig. 2.1a; Gawthorpe and Hurst, 1993). None of the four southern Malawi normal faults studied in Chapter 4 (Bilila-Mtakataka, Thyolo, Muona and Malombe) showed signs of relay ramp structures, but were all structurally segmented, and most hard-linked (figs. 4.10, 4.12 and 4.13). This suggests that hard-linkage between fault segments also occurs in the underlapping phase (fig. 2.2).

The style of hard-linkage between faults

In Chapter 2 we developed a numerical model to calculate the coseismic Coulomb stress change in the (inter-segment) zone between two active parallel fault segments. We then analysed whether this stress change could be used to infer the preference for, and style of, linkage between faults. We then compared our model results to natural observations of hard-linked normal faults from a variety of rift regions (e.g., the Gulf of Evvia rift, Gulf of Corinth rift, Taranaki Basin, Rio Grande rift, East African Rift System) for three end-member linkage styles: (a) fault bends; (b) breached (relay) ramps; and (c) transform faults. The first two have been briefly introduced above, but for a more detailed distinction between each type of linkage, please see Section 2.1.1. In general, we found that model results agreed with the observations and suggest that whether faults preferentially grow along-strike or form linkages between segments is influenced by: (i) whether one or both segments rupture; and (ii) the geometry of the inter-segment zone (fig. 2.8).

A scenario where both segments rupture simultaneously, or near simultaneously, would typically promote fault linkage, whereas single segment ruptures favoured along-strike growth (i.e. the Coulomb stress change is greater on growth faults along-strike of the segments, than linking faults within the inter-segment zone). Earthquakes that rupture multiple faults or fault segments such as Landers 1992 M_W 7.3 (Sieh et al., 1993), Wenchuan 2008 M_W 7.9 (Shen et al., 2009), Haiti 2010 M_W 7.0 (De Lépinay et al., 2011; Hayes et al., 2010) and Kaikoura 2016 M_W 7.8 (Hamling et al., 2017), or earthquake sequences such as Friuli 1976 sequence (Cipar, 1980), the Umbria-Marche 1997 sequence (Amato et al., 1998), Karonga 2009 sequence (Biggs et al., 2010) and the Amatrice-Norcia 2016 sequence (Cheloni et al., 2017), may therefore promote the development of hard-links between segments.

The geometry of the inter-segment zone was deemed pertinent to the style of linkage, supported by the close agreement between observations and model results. For underlapping fault segments to favour linkage over continued individual along-strike growth, the angle between a line connecting the segment tips and the segment strike must not exceed 45°. At greater angles, underlapping fault segments preferentially grow along-strike into overlapping regimes. When fault segments overlap with small amounts of scarp-perpendicular separation (here found to be $\leq$ 10% of the segment length), relay ramp linkages are favourable. These results agree with the rare observational studies, such as those from the East Tanka fault zone in the Suez rift (e.g., Jackson et al., 2002), and numerical models of fault growth through fracture initiation, propagation, interaction, and linkage (e.g., McBeck et al., 2016), which suggest that stress interactions at segment tips may promote hard-linkage between underlapping fault segments. The linking process either requires the nucleation of well-oriented linking faults within the inter-segment zone or pre-existing fault planes that can act as linking faults. The latter may be facilitated by segment tip fault splays generated over several earthquake cycles (e.g., Anders and Schlische, 1994; Kristensen et al., 2008; Nash, 1984; Slemmons, 1957).

Numerous natural examples (e.g., Giba et al., 2012; Manighetti et al., 2001; Wu and Bruhn, 1994), experiments and theoretical models (e.g., Perrin et al., 2016a,b; Segall and Pollard, 1983; Willemse and Pollard, 1998), suggest that faults splay at their segment tips. In our detailed geomorphological study of the Bilila-Mtakataka fault (BMF), a $\sim$ 110 km long normal fault in southern Malawi (Jackson and Blenkinsop, 1997), in Chapter 5, we found the presence of multi-scarps (see Section 1.1.5 for a description of the different types of normal fault scarps) most commonly occurred at the ends of inferred structural segments (fig. 5.13). The existence of multi-scarps has previously been attributed to near surface coseismic slip on fault splays (e.g., Anders and Schlische, 1994; Kristensen et al., 2008; Nash, 1984; Slemmons, 1957). Fault splays on normal faults typically occur at a similar range of mean angles to parent fault (10° to 20°; Perrin et al., 2016b). The presence of multi-scarps at the ends of the BMF structural segments may therefore indicate why faults such as the BMF are able to hard-link in the underlapping phase, through the failure of well-oriented segment tip fault splays. These findings may suggest that hard-linkages in slow strain rate rifts establish early in a fault's structural evolution, i.e. following the constant-length fault model (fig. 1.10b; e.g., Giba et al., 2012; Jackson and Rotevatn, 2013; Morley, 2002; Schultz et al., 2008; Walsh et al., 2003, 2002), and where hard-linkages are not apparent at the surface (such as found on the Malombe fault in southern Malawi in Chapter 4) they may be hard-linked at depth for numerous earthquake cycles before the linkage propagates to the surface (e.g., Henstra et al., 2015; Nicol et al., 2005; Worthington and Walsh, 2016). Such hard-linkages at depth are considered to have occurred on the BMF prior to the formation of the current scarp, as discussed in Chapter 3.

In addition to how hard-linkages may form in underlapping phases through fault bends, Chapter 2 also explores how transform fault linkage in continental rift environments may form. This is an important question because unlike mature rift environments, where transform fault linkage is commonly observed (e.g., the Gulf of Aden rift and Dead Sea rift; Girdler, 1990; Laughton et al., 1970), transform fault linkages in incipient continental rifts are rare. The Coulomb stress model results in Chapter 2 imply that transform fault geometries would be favourable as a normal fault segment linkage style only when segments overlap and the scarp-perpendicular separation between them is large, here found to be $\sim$ 15% of the segment length (fig. 2.8). However, for these inter-segment zone geometries, continued along-strike segment growth was preferred to segment linkage. For simplicity, our models assume planar faults (fig. 2.3), but fault tip growth orientation may be influenced by the neighbouring segment, where the ends of segments incrementally grow toward one another (e.g., McBeck et al., 2016). This scenario would reduce the separation distance at the fault ends and linkages may preferentially occur in underlapping regimes as fault bends, and overlapping regimes as breached ramps. We suggest that transform fault style linkages may preferentially occur at the later stages of rifting, where magmatic processes may localise strain on high-angled pre-existing structures (fig. 2.9; e.g., North Iceland; Tibaldi et al., 2016), which could be why on the continents they are rarely observed. Furthermore, sensitivity tests in Appendix C show that high-angled linking faults with oblique slip, comprising a large component of normal slip, would be favourable to pure strike-slip transform linking fault geometries (fig. 2.7). Continental transform faults that were previously thought to be strike-slip, may therefore involve a significant dip-slip motion (e.g., McClay and Khalil, 1998). Although a number of other processes likely influence segment interaction and linkage, such as dynamic coseismic stresses (e.g., Duan and Oglesby, 2005; Harris and Day, 1999) and driving forces associated with interseismic strain accumulation (e.g., Dolan et al., 2007; Peltzer et al., 2001; Wedmore et al., 2017b), the findings from Chapter 2 show that static coseismic Coulomb stress changes and the geometry between fault segments also influences fault interaction and linkage potential (e.g., Duan and Oglesby, 2005; Harris, 1998; Harris and Day, 1999; King and Cocco, 2001; Stein, 1999).

The processes influencing fault orientation

Our work in Chapter 2 shows that changes in fault geometry may be used to infer a fault's development (i.e. linkage) and deformation style (i.e. multi-segment ruptures required to facilitate linkage), but what are the major controls on the orientation of faults and their segments? Over a variety of scales, from the scale of an entire fault to the scale of individual outcrops, Chapter 3 explores the fundamental controls to rift and fault geometry in an early-stage rift environment. This is achieved using structural and geometrical measurements from field and satellite observations for the BMF. The BMF provides an ideal case study of an active normal fault in a slow strain rate rift not only because it exists within the amagmatic southern end of the EARS (Hamiel et al., 2012; Lezzar et al., 2002), but because it also has a well-defined fault scarp that can be traced for over 100 km (Jackson and Blenkinsop, 1997). The average trend of the $\sim$ 110 km long BMF scarp (150°) is oblique to the extension direction inferred from plate motion estimates (e.g., 086°±5°; Saria et al., 2014) and therefore suggests that its surface expression is not purely governed by the regional stress field as expected in a pure Andersonian environment (Anderson, 1905). Over half the scarp trends parallel to the strike of the local high-grade, gneissic foliation, but there are large sections where the scarp cross-cuts this foliation (fig. 3.2a). In addition, the scarp trend varies considerably where the footwall lithology changes from the dominant mafic or felsic gneiss lithology to calc-silicate granulite, forming two large bends near the town of Citsulo, causing several kilometres of offset between the northern and southern sections (fig. 3.1).

In order to test the hypothesis that the fault scarp geometry is controlled by something other than the regional stress field, a geometrical model was developed to join the surface expression of the BMF to a deep, planar fault structure (fig. 3.4). Slip was then projected toward the surface and compared to the current scarp height along the BMF. The best-fitting (smallest RMSE) strike of a deeper planar fault was found to be sub-parallel to the surface trend (fig. 3.5); therefore, oblique to that expected if governed by a regional stress field in a pure Andersonian environment. Whilst a deep structure, like the surface expression, is likely not planar, this simplification of the deep fault's average strike shows that the regional stress field itself is unlikely to be responsible for the current fault orientation. The simplified geometry of this deep fault also corroborates the orientation proposed by the inferred local stress field (Sh_{min} = 062°; Delvaux and Barth, 2010) and the strike of the nearest, largest earthquake, the 1989 M_W 6.3 Salima earthquake (∼154°; Jackson and Blenkinsop, 1993), which occurred ∼ 30 km north of the BMF. In addition, our findings are similar to those suggested by Kolawole et al. (2018) for northern Malawi, who through field observations and interpretation of aeromagnetic data suggest the 2009 Karonga earthquake sequence (Biggs et al., 2010) occurred on a deep structure that reactivated basement fabric. Our findings show the importance of scale when considering controls to fault and rift geometries, as at the regional scale pre-existing structures may appear to influence fault geometry, but locally, neither pre-existing structures, nor the regional stress field, were the primary control on fault geometry in this case study. Furthermore, the relationship between pre-existing structures and fault structure may be different for sections of the same rift and for different depths (e.g., Laó-Dávila et al., 2015). Rift scale studies (e.g., Chorowicz, 2005; Corti, 2009; Ebinger et al., 1987; Katumwehe et al., 2015; Ring, 1994) may therefore oversimplify the influence of pre-existing structures. These findings are important when considering the controls to fault and rift geometry in more mature rift environments, where magmatic processes may also influence local stress fields, or for multi-phase rifts where previous rift phases may precondition the lithosphere for strain localisation to occur on older structures.

The growth model of faults

A morphological analysis of the BMF scarp was also undertaken in Chapter 3 and showed that the fault comprises six structural segments (fig. 3.2). For the definition of a structural segment, please refer to Section 1.1.6. The geomorphology of three additional southern Malawi faults (Malombe, Thyolo and Muona) were then analysed in Chapter 4 and each were found to show first-order segmentation (figs. 4.12 and 4.13). As all studied faults are considered structurally segmented, we now discuss whether the structural evolution of early-rift faults can be inferred from our case study faults, i.e. can the relative morphological differences between each fault be used to infer how segments coalesce to form the current geometry and morphology?

There are two main theories regarding fault growth, the 'isolated fault model' and the 'constant-length fault model' (1.1.7), but it is often difficult to discriminate between the two based purely on geometrical criteria alone (fig. 1.10; Jackson et al., 2017). A fault formed through the linkage of several low displacement segments and one that grew as a single structure and established its near-final length early in its slip history, will both appear to have a lower displacement than predicted according to global maximum displacement-length ratios (e.g., Dawers and Anders, 1995; Gupta and Scholz, 2000; Walsh et al., 2002). For each of the studied southern Malawi faults (Table 4.3), the surface displacement is smaller than expected by global maximum displacement-length ratios (i.e. $< 10^{-2}$; Kim and Sanderson, 2005), but larger than expected by single rupture slip-length ratios (i.e. $> 10^{-4}$; Scholz, 2002), suggesting that the faults are relatively immature but have accumulated displacement over multiple earthquake cycles (1.1). Yet, whereas the BMF appears to be under-displaced (~ 14 m average scarp height) relative to its length, the similarly long, mature Pliocene-aged faults to the west of it have accumulated several hundred metres of vertical surface displacement (Dawson and Kirkpatrick, 1968; Walshaw, 1965). This may be evidence therefore that normal faults in slow strain rate, early-stage rifts either: (i) follow the constant-length fault model, whereby they establish their near-final length early on in their slip history, and then accumulate displacement over multiple earthquake cycles; (ii) they follow the isolated fault model but displacement in slow strain regions is smaller than fast strain regions (Nicol et al., 2005); or (iii) they do not conform to either end-member over their entire slip history, but rather start as isolated faults, then experience a rapid stage of linkage, followed by displacement accumulation until the fault dies and displacement migrates into the hanging-wall.

If the faults were assumed to grow by the isolated fault model but with significantly smaller amounts of displacement per event than global scaling laws predict (Scholz, 2002), then we would expect to see a large number of rupture indicators in the geomorphology (1.1.5). In Chapter 5, a sub-metre Pleiades DEM was used to study multiple rupture indicators on the two central segments (Mua and Kasinje) of the BMF. The Mua and Kasinje segments were chosen as the results from Chapters 3 and 4 indicate that each has an average scarp height larger than 20 m (figs. 3.2 and 4.10). The results from Chapter 5 showed evidence for at least two potential ruptures on each segment; each rupture was measured to comprise an average vertical surface displacement of $\sim$ 10 m (fig. 5.13). The most recent rupture was evident on the majority of the scarp profiles, and a separate knickpoint analysis of river profiles agrees with the relative timing and surface slip magnitude of this rupture. A penultimate rupture of similar magnitude found in the scarp profiles was also apparent in the knickpoint analysis (fig. 5.12). A scarp degradation model was used to infer the relative timing of scarp formation, and we concluded that for both events the Mua and Kasinje segments ruptured concurrently, and the rupture likely propagated across the neighbouring segments and perhaps the entire BMF (fig. 5.10). If the BMF displacement follows a typical bell-shaped profile (e.g., Giba et al., 2012; Walsh and Watterson, 1990; Willemse and Pollard, 1998), with displacement maxima at the centre (i.e. on the Mua and Kasinje segments), this implies an average surface displacement per complete rupture of the BMF of less $\sim$ 7 m, consistent with slip-length scaling laws (Scholz, 2002).

Older rupture markers may have been destroyed by erosion due to the long repeat time of earthquakes in the region due to the slow extension rates ($<$ 2 mm per year; Saria et al., 2014) and large seismogenic thickness (30 to 40 km; Jackson and Blenkinsop, 1993); however, the combined scarp height of both ruptures equalled the total scarp height and the data therefore do not require that additional surface ruptures occurred along the Mua and Kasinje segments, or if so they were moderate in magnitude (there was some local evidence for a third rupture) and did not propagate across the entire segments (fig. 5.13). Because the Mua and Kasinje scarps likely only express two surface ruptures, and both suggest a complete rupture across both segments, it may suggest that the BMF's length established early in its slip history, i.e. following the constant-length fault model (e.g., Giba et al., 2012; Jackson and Rotevatn, 2013; Morley, 2002; Schultz et al., 2008; Walsh et al., 2003, 2002). Subsurface analysis is required to confirm this, as the fault may also have evolved as separate segments that hard-linked over multiple earthquake cycles, i.e. the isolated fault model, without producing a surface expression.

Above we show that normal faults in slow strain rate, early-rift systems appear to deform as they do in faster strain rate environments such as the Gulf of Corinth rift, which explains why the structural evolution of the rifts is so similar (e.g., Bell et al., 2017, 2009; Cowie et al., 2005; Ebinger et al., 1999; Gawthorpe et al., 2003, 2017; Gupta et al., 1999; Nixon et al., 2016), i.e.: (i) initiation and growth of the distributed conjugate fault network; (ii) segment growth and linkage; (iii) early development of dip domains; (iv) changes in fault activity, new faults developing and some dying, associated with: (v) progressive evolution of rift asymmetry with development of a border fault system; and (vi) rapid linkage and localization of deformation onto the border fault system. However, the lack of relay ramp structures along the southern Malawi faults may suggest linkage processes are different, and perhaps the type of fault growth is influenced by the strain rate, whereby in slow strain rifts the constant-length fault model better fits observations due to intense strain localization (e.g., Brun, 1999; Nestola et al., 2015). It is also likely that the proposed continuous weak structures at depth, as suggested for the BMF in Chapter 3, help localise strain and promote this type of fault growth (Childs et al., 2017). As such, we have shown that the regional stress may not be the primary influence to border faults developing in slow strain, early stage rifts.

Q2. In what ways can we improve the methodology for quantifying the surface displacement?

Over the past few decades we have seen a substantial increase in remote sensing capabilities, including satellite numbers and sensor performance, which has lead to the reduced repeat times for image acquisition and increased the resolution of imagery. In 1986 SPOT 1 acquired the first 10 m resolution panchromatic images, in 1995 the 5 m limit was surpassed by IRS-1C; the metre mark was broken in 1999 by IKONOS, and the half-metre mark by WorldView 1 in 2007 (Belward and Skøien, 2015). Multispectral imaging has always had lower resolutions, starting with the ~ 80 m resolution capabilities of with Landsat 1 in 1972, and sub-metre resolutions only possible since GeoEye-1 in 2013 (Belward and Skøien, 2015). Today, over a dozen satellites are in orbit with the capabilities of sub-metre panchromatic imagery and metre multispectral imagery. In tandem, technological advances in computing power, especially in personal computers, has meant that techniques such as photogrammetry and structure from motion (SfM) can be utilised by geomorphologists to study landforms in more detail than ever before (e.g., Johnson et al., 2014; Joyce et al., 2009).

In the quest to understand how normal faults in early-stage rifts develop and what their deformation style is (Q1), our research has utilised key advances in remote sensing and has undertaken a number of multi-disciplinary studies over a variety of scales. In Chapter 3, we performed a geomorphological analysis of the BMF scarp using a 12 m resolution TanDEM-X DEM. Prior to this work the BMF was considered to have fairly uniform scarp height (e.g., Jackson and Blenkinsop, 1997), however, by studying the variations in surface displacement along the fault we were able to infer first-order structural segmentation (fig. 3.2).

Due to accessibility issues and the length of the fault ($\sim$ 110 km), this analysis would have taken considerably longer using traditional ground-survey techniques (e.g., Andrews and Hanks, 1985; Avouac, 1993; Bucknam and Anderson, 1979; Cartwright et al., 1995; Cowie and Scholz, 1992a; Delvaux et al., 2012; Gillespie et al., 1992), and regular spacing of measurements may not have been possible. Despite the benefits of the satellite data, the manual-approach used to calculate the scarp height (e.g., Crone and Haller, 1991) meant that the spatial resolution of measurements was restricted to 1 km, despite having a DEM with a horizontal resolution of 12 m. The manual-approach in calculating coseismic surface offsets has been used for decades (e.g., Avouac, 1993; Bucknam and Anderson, 1979; Ganas et al., 2005; Walker et al., 2015; Wallace, 1977; Wu and Bruhn, 1994), however, it is restrictive in a number of ways. Firstly, manually processing data means the calculations and interpretations are subject to human bias (Middleton et al., 2016). Secondly, measurement inconsistencies may lead to errors within the calculations, and may be a contributing factor for the scatter observed in global maximum displacement-length profiles (Gillespie et al., 1992) and along-strike displacement profiles (Zielke et al., 2015). To combat this, in Chapter 3 we randomised the profile order of BMF scarp profiles and calculated the scarp height on three separate runs. Despite this, of the 128 profiles, the location of the scarp for 20% of the profiles could not be consistently identified within an acceptable horizontal error across all three runs.

Automating processes to minimise human bias

To minimise human bias, and create a consistent methodology to calculate scarp morphological parameters (height, width and slope), in Chapter 4 we developed a semi-automated algorithm. In addition to reducing the human bias and measurement inconsistencies (Middleton et al., 2016; Zielke et al., 2015), automating the morphological calculations would allow for a greater number of measurements to be taken along the fault scarps than feasible with ground based methods. This is important as an increase in spatial resolution will increase the understanding of fault behaviour and segmentation (e.g., Cartwright et al., 1995; Manighetti et al., 2015; Trudgill and Cartwright, 1994; Zielke et al., 2012), and will reduce the influence of local uncertainties on the displacement-length profile (Zielke et al., 2015). Previous attempts to create an algorithm to calculate relative dating of fault scarps have already been attempted (Gallant and Hutchinson, 1997; Hilley et al., 2010; Stewart et al., 2017), however, these methods may falsely identify other geomorphic features as fault scarps, and many require a very high resolution LiDAR DEM. As the cost and logistical demands of LiDAR restrict its utilisation in many areas (Johnson et al., 2014), our aim was to develop an algorithm that worked with lower resolution satellite-derived DEMs.

The results gained for the BMF using the algorithm and the 12 m TanDEM-X DEM were similar to those gained through the manual approach in Chapter 3, but measurement frequency was ten times larger (fig. 4.10). The only limit to the measurement frequency is the spatial resolution of the DEM. Because of the increase in measurement frequency along the BMF (profiles taken at 100 m intervals), second-order structural segments and associated linking structures were also identified (see Section 1.1.7). The number of primary and secondary segments within the immature southern end of the EARS therefore appears to be similar to the quantity found in the more mature northern end of the EARS (e.g., Manighetti et al., 2015). Our findings also show that the structural evolution of the BMF is similar to other rift faults, i.e. variations in scarp height and trend indicate growth and linkage between fault segments (Section 1.1.7), but the timing of linkage appears to occur relatively short in the fault's structural history (see Q1 discussion above)

The algorithm may be used to both infer maximum surface displacement and length of faults in order to calculate slip-length ratios (e.g., Scholz, 2002), estimate moment magnitudes for seismic hazard (Hanks and Kanamori, 1979; Wells and Coppersmith, 1994), or infer the structural history along a fault (e.g., Kolyukhin and Torabi, 2012; Ren et al., 2016; Sieh, 1978; Wallace, 1968; Zielke et al., 2012). The latter could be undertaken for an entire early-stage rift such as the MRS in order to compare with such studies undertaken on more mature rifts such as the Ethiopian rift (Manighetti et al., 2015). By coding the algorithm in the Python coding language, the ultimate aim was to make it open access and adaptable to the users needs. The code is available online at:

https://github.com/mshodge/FaultScarpAlgorithm

One of the major limitations of the algorithm currently is that it cannot discriminate between multiple rupture events, which would also require a very high resolution DEM. In Chapter 5 we developed a sub-metre DEM using Pleiades stereo-imagery and the structure from motion technique (e.g., Roux-mallouf et al., 2016; Talebian et al., 2016; Zhou et al., 2015). By undertaking a manual geomorphological analysis for scarp and river profiles, multiple rupture indicators were identified along the two central segments of the BMF: the Mua and Kasinje segments. In time, the algorithm from Chapter 4 could be coded to identify individual scarp surfaces and thus, quantify the displacement of multiple ruptures. However, this would require a significantly higher resolution DEM than used in Chapter 4, and require the algorithm to discriminate between single rupture, degraded, composite and multi- scarps. This could be achieved through a machine-learning approach, but would increase the computational resource requirement.

The desire for high-resolution data

One of the research questions we asked in Chapter 5 was: does our interpretation of the distribution of displacement scale with DEM resolution (i.e. how much more are we able to infer using an expensive, high resolution DEM compared to a free, lower resolution alternative)? In Chapter 4 we tested our algorithm using a higher resolution (Pleiades 5 m) and lower resolution (SRTM 30 m) DEM, and whilst its performance was not largely affected, the higher resolution DEM was: (i) able to more accurately calculate the scarp slope (when compared to field measurements), and (ii) identify a larger number of scarps. For example, for the 913 profiles, the algorithm would only identify a fault scarp in 64% of the SRTM DEM profiles, whereas for the Pleiades DEM profiles this increased to 79%. Note, however, that quality checks reduced the number of profiles extracted from the Pleiades DEM greater than the SRTM DEM, due to lower signal-to-noise ratio of the raw Pleiades data (see Appendix H for a more detailed discussion of the algorithms performance with various resolutions of data). Ultimately, the choice of DEM resolution relates to the users needs; for a detailed study of scarp morphology, a high resolution, more expensive DEM is required (as shown in Chapter 5), but if the aim is to measure large scale features, a lower resolution, cheaper DEM will suffice, and will reduce the required computational power.

Whilst high resolution DEMs are useful in analysing subtle changes in morphology (see Chapter 5), they contain lots of noise, particularly from vegetation. Whenever we used a high resolution DEM to study the fault scarps we applied a digital filter to increase the signal-to-noise ratio. Therefore, higher resolution DEMs do not necessarily imply better DEMs. In fact, low resolution DEMs are more efficient for fitting a linear regression to upper and lower surfaces to calculate total scarp height (cumulative surface displacement). An optimal DEM would therefore comprise a resolution pyramid structure, whereby the fault scarp is mapped using high resolution DEM and the resolution decreases with increasing distance from the scarp (i.e. the feature of interest). However, as many satellite imagery providers set minimum acquisition widths, which are many times the width of a typical fault scarp (in this work the minimum acquisition width we were quoted was 10 km, compared to the sub-hundred metre wide fault scarps), many users feel obliged to use the excessive areas of high resolution imagery they have purchased. Idealistically, the ability to obtain more local high resolution DEMs of features of interest, which can then be stitched to lower resolution DEMs for regional context, would solve this issue.

Unmanned Aerial Vehicles (UAV) have been used to generate sub-metre DEMs for a number of years (e.g., Bemis et al., 2014; Johri et al., 2014; Westoby et al., 2012) and may be the perfect tool to bridge the gap between regional low resolution DEMs and the need for high resolution, local DEMs. However, spatial coverage is currently limited (< 1 km^2 for rotary UAVs, ~ 10 km^2 for fixed wing UAVs). Furthermore, the requirement to be present at the site means that they are a pseudo-remote sensing tool, whereas satellite images can be acquired remotely. During my fieldwork in Malawi, I used a Phantom 3 Advanced quadcopter UAV to photograph parts of the BMF scarp and generate very high resolution DEMs (10 cm resolution). As the relative and absolute accuracy of a UAV DEM is around 1-3 times the pixel size (Barry and Coakley, 2013), the relative error of using UAV DEMs to study fault scarps the size of the BMF is small. To improve the absolute accuracy though, differential GPS devices can be used to constrain ground control points (GCPs) (e.g., Bemis et al., 2014; Johri et al., 2014; Westoby et al., 2012). However, dGPS equipment is often not very portable and therefore for remote regions it can be impractical. For this reason, we were unable to take a differential GPS with us on fieldwork in Malawi. The future may be pairing lightweight UAVs with unmanned ground vehicles (UGVs) that have more accurate GPS modules, providing a relative position between devices and improving relative and absolute accuracies (e.g., Jung and Ariyur, 2017). Although the UAV data we gained on fieldwork was useful in revisiting field locations through our research (in particular, Chapters 3 and 5), the lack of coverage meant that studies at the scale of entire faults could not be performed; hence, for the majority of our research we preferred to use satellite-derived data instead.

Q3. What does our work tell us about the seismic hazard posed by faults in early-stage, slow strain rate rifts?

Seismic hazard assessments typically use historical earthquakes as a tool to inform future earthquake magnitude and frequency (e.g., Midzi et al., 1999; Zhang et al., 1999). However, assessing seismic hazard in continental interiors is challenging because these regions may be characterised by low strain rates, and long recurrence intervals between earthquakes can lead to infrequent, unforeseen and destructive earthquakes (England and Jackson, 2011), such as the 2009 M_W 7.7 Bhuj earthquake (Bendick et al., 2001), the 1928 M 6.8 Chirpan earthquake (Vanneste et al., 2006), the 1904 M_s 6.8 Struma earthquake (Meyer et al., 2007), the 2010 M_W 7.0 Haiti earthquake (Bilham, 2010), and 1811 M 7.5 New Madrid earthquake (Tuttle et al., 2002). Because of the long recurrence interval between large magnitude events, the historical catalogue for seismicity may not document an entire earthquake cycle. In addition, erosion of surface expressions may lead to the removal of paleoseismological markers, such as observed in central Tehran (Talebian et al., 2016).

Even in some of the most seismically active slow strain rate regions of the world, such as the Central Apennines, where a long history of earthquakes has been observed ($\sim$ 1,000 years; D'Addezio et al., 1995; Stucchi et al., 2011), seismic hazard assessments may fail to capture all possible scenarios and need continuous reappraisals (Murru et al., 2016). For example, prior to the 2009 M_W 6.3 L'Aquila earthquake the Paganica fault was neglected relative to other nearby faults, partly because of its subdued geomorphological expression (D'Agostino et al., 2001), even though the fault had been suggested as the source of larger earthquakes in 1461 and 1762 (Boncio et al., 2004). In contrast, nearby faults such as the L'Aquila and Campo Imperatore faults had not produced any historical earthquakes, but have paleoseismological evidence for prehistoric ruptures (Galli et al., 2002; Giraudi and Frezzotti, 1995). A study of the Coulomb stress change resulting from the L'Aquila earthquake found that the seismic strain deficit in the region may have only partially been alleviated by the 2009 L'Aquila earthquake sequence and therefore still represented a seismic hazard in the region (Walters et al., 2009). In 2016, the region experienced another deadly earthquake sequence of M_W 5.9 - 6.5 (Cheloni et al., 2017).

Similarly to the Central Apennines, the long earthquake catalogues in Central Asia also may not account for large, devastating earthquakes, such as the Wenchaun 2008 M_s 8.0 earthquake. Prior to this earthquake, the seismic hazard assessment for Central Asia was underestimated using the historical earthquake record alone (Zhang et al., 1999). The consequences of underestimating the seismic hazard can be devastating, especially when underestimating the maximum potential earthquake magnitude, which may be used for building design codes. For example, the number of casualties resulting from the Wenchaun earthquake was close to 100,000. The Wenchaun earthquake came as a surprise because for the Longmen Shan region, where geodetic measurements show a horizontal shortening of less than 3 mm per year (Zhao et al., 2004), no historical record of a M 7 or greater earthquake had been recorded in the last 500 years (Liu-Zeng et al., 2009; Qi et al., 2011). In addition, the southern Longmen Shan fault zone did not rupture in 2008, but did in 2013 with the M_W 6.6 Lushan earthquake, resulting in several hundred fatalities. These events lead to a reevaluation of the seismic hazard posed by active faults in the Longmen Shan region, which suggested that a M_W 7.3 - 7.7 event may occur every 1,000 to 1,400 years (Li et al., 2017). Another Central Asian region where seismic hazard may have been previously underestimated was northern Tien Shan, where the $\sim$ 120 km long Lepsy fault is suggested to have ruptured around $\sim$ 400 BP in an estimated M_W 7.5 - 8.2 earthquake (Campbell et al., 2015). Accounting for fault geometries is therefore important in northern

Tien Shan (Torizin et al., 2009), and new seismic hazard assessments for Central Asia now account for the increase hazard posed by active faults (e.g., Ullah et al., 2015).

For regions with short instrumental and historical earthquake catalogues, such as the Malawi Rift System (MRS), calculating the seismic hazard is even more challenging. Because the instrumental earthquake catalogue for the MRS is only complete above M_W 4.5 since *ca.* 1965, and the slow strain rate (Saria et al., 2014) and thick seismogenic layer (Jackson and Blenkinsop, 1993) produce long, wide faults, potentially capable of producing large magnitude events (see Sections1.1.3 and 1.1.2), producing a seismic hazard assessment using only the earthquake catalogue alone (e.g., Midzi et al., 1999) may drastically under-estimate the true hazard (Hodge et al., 2015). Similar to Central Asia, attempts to improve the seismic hazard by accounting for the increased seismic hazard and risk posed by the active border faults has been performed for the Malawi rift (Goda et al., 2016; Hodge et al., 2015), but these studies used low resolution fault maps (e.g., Ebinger et al., 1987; Specht and Rosendahl, 1989). As such, only seven border faults were considered in the last seismic hazard assessment. In southern Malawi alone, our work highlights no fewer than eight normal faults (opposed to just two previously). The geomorphological study performed on four of these faults in Chapter 4 concluded that each has a scarp height larger than expected by a single rupture event, and the detailed analysis on the BMF in Chapter 5 concluded that the scarp may have formed through multiple ruptures. Due to the influence of displacement per event on seismic hazard assessments, a detailed fault mapping and geomorphological exercise for the remainder of the MRS is required.

Current seismic hazard assessments based on active fault mapping often use simplified rupture scenarios too. Typically, the total fault length L is used to estimate moment magnitude using scaling laws (Hanks and Kanamori, 1979; Wells and Coppersmith, 1994), and the recurrence interval is based on the complete failure of the fault. However, earthquake ruptures are complex and may not completely rupture the entire fault (e.g., 2004 Parkfield earthquake, Murray and Segall, 2002), or may also jump across structural segments producing earthquakes larger than anticipated (Biasi and Wesnousky, 2016; Wesnousky, 1986). For example, seismological, field and geodetic observations of the 2016 Amatrice earthquake sequence show that ruptures occurred across two normal faults that had previously been identified as separate structures (Walters et al., 2016). This type of rupture behaviour has been observed in previous earthquakes in Italy. For example, the 1980 M_W 6.9 Irpinia earthquake in southern Italy comprised multiple M_W 6.2-6.5 earthquakes on four separate segments (Amato and Selvaggi, 1993), and largest known events in central Italy, the 1703 M_W 6.7-7 Norcia and L'Aquila earthquakes and the 1915 M_W 6.7 Avezzano earthquake are also thought to be multi-segment ruptures (Cello et al., 1998). A complete rupture of the Amatrice earthquake segments would equate to a $M_W > 7$ event, and whilst such large earthquakes are absent in the long and detailed historical and palaeoseismological record of the region, more detailed studies are required to understand the increased seismic hazard posed by multi-fault ruptures (Walters et al., 2016). In addition, the failure of one segment may promote or retard the failure of another through a variety of mechanisms, including dynamic coseismic stresses (e.g., Duan and Oglesby, 2005; Harris and Day, 1999), driving forces associated with interseismic strain accumulation (e.g., Dolan et al., 2007; Peltzer et al., 2001; Wedmore et al., 2017b) and static stress changes (e.g., Duan and Oglesby, 2005; Harris, 1998; Harris and Day, 1999; King and Cocco, 2001; Stein, 1999). Thus, the rate of seismicity is therefore not constant, and the probability of earthquakes on one fault is not independent of the rate on another (Stein, 1999); therefore, seismic hazard assessments need to reproduce such observations.

A new deterministic view of the seismic hazard in Malawi

In Chapter 2, we show that the interaction between fault segments may lead to incremental hard-linkage of segments over multiple earthquake cycles, which in regions where pre-existing structures are well-oriented such as shown along the BMF in southern MRS (Chapter 3), may result in the formation of large border faults early in their structural evolution. Current seismic hazard estimates using geological observations use the surface geometry to infer simplified rupture scenarios. For the MRS, the current seismic hazard assessment (Hodge et al., 2015) assumes two such scenarios: (i) a complete rupture of a fault, or (ii) a rupture of an individual segment. The segmented rupture scenario used an arbitrary number of segments (three) of equal length, however, in our research here, we have shown that up to six structural segments may exist along each of the southern Malawi faults (Chapters 3 and 4), and the number of segments may be related to the maturity of the fault (Manighetti et al., 2015). Alas, despite the existence of multiple structural segments, this does not imply that each structural segment may rupture individually (i.e. structural segmentation equating to earthquake segmentation), in fact, in Chapter 5 we concluded that the surface displacement of historical ruptures along the Mua and Kasinje segments of the BMF did not taper at segment ends (fig. 5.13), implying that multi-ruptures (or a complete fault rupture) historically occurred on the fault rather than single-segment rupture events. Accounting for multi-rupture scenarios (e.g., Erdik et al., 2004; Gülerce and Ocak, 2013), based on palaeoseismological studies of prehistoric earthquake ruptures on active faults is important in understanding the seismic hazard within all environments, but especially for slow strain rate regions where the earthquake catalogue does not reflect the variety of potential rupture styles. Even in well-studied, fast strain rate regions, not all rupture styles may have been accounted for, as shown by the 2016 M_W 7.8 Kaikoura earthquake (Hamling et al., 2017).

Specifically for the southern MRS, deterministic magnitude estimates for the four faults in Chapter 4 alluded to potential $M_W > 7$ ruptures for each fault. Given that the largest historically recorded earthquake in Malawi was the 1989 $\sim M_W$ 6.1 Salima earthquake (Jackson and Blenkinsop, 1993), events of $M_W > 7$ are considered catastrophic for Malawi, a country consistently ranked in the lowest 10th percentile of world development indicators, and experiencing rural-urban migration. Our detailed geomorphological analysis of the BMF in Chapter 5 suggested that the magnitude of a complete BMF rupture may be slightly less than predicted in Chapter 4 and by Jackson and Blenkinsop (1997), but the M_W range of 7.2 to 8.2 also shows a large amount of uncertainty. To better understand how normal faults develop and deform, and their seismic hazard, I suggest lines of future research in the final section of this thesis.

6.2 Future work

The methodologies developed in this thesis could be applied to a number of other regions to better understand fault and rift evolution, and seismic hazard.

Chapter 3 highlights the importance of performing a multi-scale, three dimensional approach when inferring the influence of pre-existing structures and stresses on fault evolution. The findings from this work on the Bilila-Mtakataka Fault could be complemented by subsurface data, which would help constrain the orientation of the deep structure. The multi-scale, multi-disciplinary approach to understanding the role of pre-existing structures, lithology and stresses on controlling fault geometry could be extended to other southern Malawi faults, such as Malombe, which shows variations in lithology along its length (as described in Chapter 4). This method could also be applied on other faults where the influence of the regional stress field influence has been previously debated, such as the major faults of the Rukwa rift in southern Tanzania (e.g., Delvaux, 2001; Delvaux et al., 2012; Ring, 1994; Vittori et al., 1997), Recôncavo-Tucano rift in northeast Brazil (e.g., Destro et al., 2003) and the Gulf of Aden rift (e.g., Withjack and Jamison, 1986).

The new semi-automated methodology for calculating total scarp height presented in Chapter 4 could be used on a range of normal faults in various rift regions in order to consider whether global displacement-length scaling ratios (e.g., Dawers and Anders, 1995; Kim and Sanderson, 2005) are consistent for all regions, or whether unique scaling laws apply to different types of rifts (i.e. narrow v wide, magma-poor v magma-rich). In addition, the efficiency of the algorithm compared to a manual-approach in generating displacement-length profiles, means it could be used to understand structural segmentation and slip propagation on faults over the scale of entire rifts (e.g., Manighetti et al., 2001). The algorithm could also be adapted to measure displacements on subsurface data to generate throw-depth and displacement-depth plots (e.g., Baudon and Cartwright, 2008; Jackson and Rotevatn, 2013; Ward et al., 2016).

The methodology for identifying and quantifying multiple surface ruptures in Chapter 5 could be used to better understand the rupture style and earthquake magnitude per event on other large, prehistoric normal fault scarps, where the current scarp height is larger than expected - compared to its length - from a single earthquake event (Scholz, 2002). Possible candidates include: the Kanda fault in the Rukwa rift (Macheyeki et al., 2007; Vittori et al., 1997), the Nahef East fault in northern Israel (Mitchell et al., 2001), the Wasatch fault zone faults in Utah (DuRoss et al., 2015; Swan et al., 1980), the Dixie Valley-Pleasant Valley faults in Nevada (Zhang et al., 1991), and the Sparta fault, southern Greece (Armijo et al., 1991). Furthermore, this methodology could be used to improve the seismic hazard in regions other than the Malawi Rift System, where the earthquake catalogue likely doesn't reflect the true hazard. For example, the presence of large normal faults within the Baikal rift may generate larger earthquakes than found in the instrumental catalogue (Calais et al., 2008; Chipizubov et al., 2007), such as the 1862 M $\sim$ 7.5 Tsagan earthquake (Lunina et al., 2012).

6.3 Conclusions

In this thesis, I have added to the vast body of research that suggests an inherent characteristic of large, normal faults is that they are structurally segmented. The potential for fault segments to link may be a function of the rupture style of, and distance between, segments. Pre-existing structures may play an important role in shaping this hard-linkage, and may also help faults develop in orientations oblique to the regional stress field. They may also play an important role in the structural development of a fault, providing a pathway for faults to rapidly increase in length. For southern Malawi, this work forms an important step in constraining prehistorical earthquake information required in producing a new seismic hazard assessment, as traditional methodologies are hampered by the short, incomplete earthquake catalogue.

Bibliography

Aanyu, K. and Koehn, D. (2011). Influence of pre-existing fabrics on fault kinematics and rift geometry of interacting segments: Analogue models based on the Albertine Rift (Uganda), Western Branch-East African Rift System. *Journal of African Earth Sciences*, 59:168–184.

Abdrakhmatov, K. E., Walker, R. T., Campbell, G. E., Carr, A. S., Elliott, A., Hillemann, C., Hollingsworth, J., Landgraf, A., Mackenzie, D., Mukambayev, A., Rizza, M., and Sloan, R. A. (2016). Multisegment rupture in the 11 July 1889 Chilik earthquake (Mw 8.0–8.3), Kazakh Tien Shan, interpreted from remote sensing, field survey, and paleoseismic trenching. *Journal of Geophysical Research: Solid Earth*, 121(6):4615–4640.

Acocella, V., Gudmundsson, A., and Funiciello, R. (2000). Interaction and linkage of extension fractures and normal faults: Examples from the rift zone of Iceland. *Journal of Structural Geology*, 22(9):1233–1246.

Acocella, V., Korme, T., and Salvini, F. (2002). Formation of normal faults along the axial zone of the Ethiopian Rift. *Journal of Structural Geology*, 25(4):503–513.

Acocella, V., Salvini, F., Funiciello, R., and Faccenna, C. (1999). The role of transfer structures on volcanic activity at Campi Flegrei (Southern Italy). *Journal of Volcanology and Geothermal Research*, 91:123–139.

Afonso, J. C. and Ranalli, G. (2004). Crustal and mantle strengths in continental lithosphere: is the jelly sandwich model obsolete? *Tectonophysics*, 394(3-4):221–232.

Aki, K. (1966). Generation and Propagation of G Waves from the Niigata Earthquake of June 16, 1964.

Aki, K. (1967). Scaling law of seismic spectrum. *Journal of Geophysical Research*, 72(4):1217.

Aki, K. (1979). Characterization of barriers on an earthquake fault. *Journal of Geophysical Research*, 84(B11):6140–6148.

Albaric, J., Déverchère, J., Petit, C., Perrot, J., and Le Gall, B. (2009). Crustal rheology and depth distribution of earthquakes: Insights from the central and southern East African Rift System. *Tectonophysics*, 468:28–41.

Aldrich, M. J., Chapin, C. E., and Laughlin, A. W. (1986). Stress History and Tectonic Development of the Rio Grande Rift, New Mexico. *Journal of Geodynamics*, 91(4):6199–6211.

Allemand, P. and Brun, J.-P. (1991). Width of continental rifts and rheological layering of the lithosphere. *Tectonophysics*, 188(1-2):63–69.

Allison, D., Zemerly, M. J. A., and Muller, J. P. (1991). Automatic seed point generation for stereo matching and multi-image registration. In *Geoscience and Remote Sensing Symposium, 1991. IGARSS'91. Remote Sensing: Global Monitoring for Earth Management., International*, volume 4, pages 2417–2421. IEEE.

Amato, A., Azzara, R., Chiarabba, C., Cimini, G., Cocco, M., Di Bona, M., Margheriti, L., Mazza, S., Mele, F., Selvaggi, G., Basili, A., and Boschi, E. (1998). The 1997 Umbria-Marche, Italy, earthquake sequence: a first look at the main shocks and aftershocks. *Geophysical Research Letters*, 25(15):2861–2864.

Amato, A. and Selvaggi, G. (1993). Aftershock location and P-velocity structure in the epicentral region of the 1980 Irpinia earthquake. *Annals of Geophysics*, 36(1).

Ambraseys, N. and Adams, R. (1991). Reappraisal of major African earthquakes, south of 20 N, 1900–1930. *Natural Hazards*, 4:389–419.

Ambraseys, N. N. (1991a). Earthquake hazard in the Kenya Rift: the Subukia earthquake 1928. *Geophys. J. Int.*, 105:253–269.

Ambraseys, N. N. (1991b). The Rukwa earthquake of 13 December 1910 in East Africa. *Terra Nova*, 3(2):202–211.

Amit, R., Harrison, J. B. J., Enzel, Y., and Porat, N. (1996). Soils as a tool for estimating ages of quaternary fault scarps in a hyperarid environment - The southern Arava valley, the dead sea rift, Israel. *Catena*, 28:21–45.

Anders, M. H. and Schlische, R. W. (1994). Overlapping Faults, Intrabasin Highs, and the Growth of Normal Faults. *The Journal of Geology*, 102(2):165–179.

Anders, M. H. and Wiltschko, D. V. (1994). Microfracturing, paleostress and the growth of faults. *Journal of Structural Geology*, 16(6):795–815.

Anderson, E. M. (1905). The dynamics of faulting. *Transactions of the Edinburgh Geological Society*, 8(3):387–402.

Anderson, J. G., Biasi, G. P., and Wesnousky, S. G. (2017). Fault-Scaling Relationships Depend on the Average Fault-Slip Rate. *Bulletin of the Seismological Society of America*, 107(6):2561–2577.

Andrews, D. J. and Hanks, T. C. (1985). Scarp Degraded by Linear Diffusion: Inverse Solution for Age. *Journal of Geophysical Research*, 90(B12):10193–10208.

Armijo, R., Lyon-Caen, H., and Papanastassiou, D. (1991). A possible normal-fault rupture for the 464BC Sparta earthquake.

Arrowsmith, J. R., Pollard, D. D., and Rhodes, D. D. (1996). Hillslope development in areas of active tectonics. *Journal of Geophysical Research*, 101(B3):6255–6275.

Arrowsmith, J. R., Rhodes, D. D., and Pollard, D. D. (1998). Morphologic dating of scarps formed by repeated slip events along the San Andreas Fault, Carrizo Plain, California. *Journal of Geophysical Research Solid Earth*, 103(B5):10141–10160.

Arrowsmith, J. R. and Zielke, O. (2009). Tectonic geomorphology of the San Andreas Fault zone from high resolution topography: An example from the Cholame segment. *Geomorphology*, 113:70–81.

Arrowsmith, R. J. and Rhodes, D. D. (1994). Original Forms and Initial Modifications of the Galway Lake Road Scarp Formed along the Emerson Fault during the 28 June 1992 Landers , California , Earthquake. *Bull. Seism. Soc. Am.*, 84(3):511–527.

Athmer, W., Groenenberg, R. M., Luthi, S. M., Donselaar, M. E., Sokoutis, D., and Willingshofer, E. (2010). Relay ramps as pathways for turbidity currents: A study combining analogue sandbox experiments and numerical flow simulations. *Sedimentology*, 57(3):806–823.

Attal, M., Cowie, P. A., Whittaker, A. C., Hobley, D., Tucker, G. E., and Roberts, G. P. (2011). Testing fluvial erosion models using the transient response of bedrock rivers to tectonic forcing in the Apennines, Italy. *Journal of Geophysical Research: Earth Surface*, 116(2):1–17.

Attal, M., Tucker, G. E., Whittaker, A. C., Cowie, P. A., and Roberts, G. P. (2008). Modelling fluvial incision and transient landscape evolution: Influence of dynamic Channel adjustment. *Journal of Geophysical Research: Earth Surface*, 113(3):1–16.

Avallone, A., Briole, P., Agatza-Balodimou, A. M., Billiris, H., Charade, O., Mitsakaki, C., Nercessian, A., Papazissi, K., Paradissis, D., and Veis, G. (2004). Analysis of eleven years of deformation measured by GPS in the Corinth Rift Laboratory area. *Comptes Rendus - Geoscience*, 336(4-5):301–311.

Avouac, J.-p. (1993). Analysis of Scarp Profiles: Evaluation of Errors in Morphologic Dating. *Journal of Geophysical Research*, 98(B4):6745–6754.

Ayalew, D., Ebinger, C., Bourdon, E., Wolfenden, E., Yirgu, G., and Grassineau, N. (2006). Temporal compositional variation of syn-rift rhyolites along the western margin of the southern Red Sea and northern Main Ethiopian Rift. *Geological Society, London, Special Publications*, 259(1):121–130.

Barker, P. A., Leng, M. J., Gasse, F., and Huang, Y. (2007). Century-to-millennial scale climatic variability in Lake Malawi revealed by isotope records. *Earth and Planetary Science Letters*, 261(1-2):93–103.

Barry, P. and Coakley, R. (2013). Accuracy of UAV photogrammetry compared with network RTK GPS. *International Archives of the Photogrammetry, Remote Sensing and Spatial Information Sciences*, 2:27–31.

Bassi, G. (1991). Factors controlling the style of continental rifting: insights from numerical modelling. *Earth and Planetary Science Letters*, 105(4):430–452.

Baudon, C. and Cartwright, J. (2008). The kinematics of reactivation of normal faults using high resolution throw mapping. *Journal of Structural Geology*, 30(8):1072–1084.

Beckers, A., Hubert-Ferrari, A., Beck, C., Bodeux, S., Tripsanas, E., Sakellariou, D., and De Batist, M. (2015). Active faulting at the western tip of the Gulf of Corinth, Greece, from high-resolution seismic data. *Marine Geology*, 360:55–69.

Bell, R. E., Duclaux, G., Nixon, C. W., Gawthorpe, R. L., and McNeill, L. C. (2017). High-angle, not low-angle, normal faults dominate early rift extension in the Corinth Rift, central Greece. *Geology*, 46(2):115–118.

Bell, R. E., McNeill, L. C., Bull, J. M., and Henstock, T. J. (2008). Evolution of the offshore western Gulf of Corinth. *Geological Society of America Bulletin*, 120(1-2):156–178.

Bell, R. E., McNeill, L. C., Bull, J. M., Henstock, T. J., Collier, R. E., and Leeder, M. R. (2009). Fault architecture, basin structure and evolution of the Gulf of Corinth rift, central Greece. *Basin Research*, 21(6):824–855.

Bellahsen, N. and Daniel, J. M. (2005). Fault reactivation control on normal fault growth: an experimental study. *Journal of Structural Geology*, 27(4):769–780.

Bellahsen, N., Leroy, S., Autin, J., Razin, P., D'Acremont, E., Sloan, H., Pik, R., Ahmed, A., and Khanbari, K. (2013). Pre-existing oblique transfer zones and transfer/transform relationships in continental margins: New insights from the southeastern Gulf of Aden, Socotra Island, Yemen. *Tectonophysics*, 607:32–50.

Belward, A. S. and Skøien, J. O. (2015). Who launched what, when and why; trends in global land-cover observation capacity from civilian earth observation satellites. *ISPRS Journal of Photogrammetry and Remote Sensing*, 103:115–128.

Bemis, S. P., Micklethwaite, S., Turner, D., James, M. R., Akciz, S., T. Thiele, S., and Bangash, H. A. (2014). Ground-based and UAV-Based photogrammetry: A multi-scale, high-resolution mapping tool for structural geology and paleoseismology. *Journal of Structural Geology*, 69:163–178.

Bendick, R., Bilham, R., Fielding, E., Gaur, V. K., Hough, S. E., Kier, G., Kulkarni, M. N., Martin, S., Mueller, K., and Mukul, M. (2001). The 26 January 2001 "Republic Day" earthquake, India. *Seismological Research Letters*, 72(3):328–335.

Benedicto, A., Schultz, R. A., and Soliva, R. (2003). Layer thickness and the shape of faults. *Geophysical Research Letters*, 30(20):1–4.

Berlin, M. M. and Anderson, R. S. (2007). Modeling of knickpoint retreat on the Roan Plateau, western Colorado. *Journal of Geophysical Research: Earth Surface*, 112(3):1–16.

Biasi, G. P. and Weldon, R. J. (2006). Estimating surface rupture length and magnitude of paleoearthquakes from point measurements of rupture displacement. *Bulletin of the Seismological Society of America*, 96(5):1612–1623.

Biasi, G. P. and Wesnousky, S. G. (2016). Steps and Gaps in Ground Ruptures: Empirical Bounds on Rupture Propagation. *Bulletin of the Seismological Society of America*, 106(3):1110–1124.

Biggs, J., Amelung, F., Gourmelen, N., Dixon, T. H., and Kim, S.-W. (2009). InSAR observations of 2007 Tanzania rifting episode reveal mixed fault and dyke extension in an immature continental rift. *Geophysical Journal International*, 179(1):549–558.

Biggs, J., Nissen, E., Craig, T., Jackson, J., and Robinson, D. P. (2010). Breaking up the hanging wall of a rift-border fault: The 2009 Karonga earthquakes, Malawi. *Geophysical Research Letters*, 37(11):1–5.

Bilek, S. L. and Ruff, L. J. (2002). Analysis of the 23 June 2001 M w = 8.4 Peru underthrusting earthquake and its aftershocks. *Geophysical Research Letters*, 29(20):1–4.

Bilham, R. (2010). Lessons from the Haiti earthquake. *Nature*, 463(7283):878.

Bilham, R., Bodin, P., and Jackson, M. (1995). Entertaining a great earthquake in western Nepal: Historic inactivity and geodetic tests for the present state of strain. *Journal of Nepal Geological Society*, 11(1):73–78.

Bilham, R. and England, P. (2001). Plateau 'pop-up' in the great 1897 Assam earthquake. *Letters to Nature*, 410(6830):806–809.

Bishop, P., Hoey, T. B., Jansen, J. D., and Lexartza Artza, I. (2005). Knickpoint recession rate and catchment area: The case of uplifted rivers in Eastern Scotland. *Earth Surface Processes and Landforms*, 30(6):767–778.

Boncio, P., Dichiarante, A. M., Auciello, E., Saroli, M., and Stoppa, F. (2016). Normal faulting along the western side of the Matese Mountains: Implications for active tectonics in the Central Apennines (Italy). *Journal of Structural Geology*, 82:16–36.

Boncio, P., Lavecchia, G., and Pace, B. (2004). Defining a model of 3D seismogenic sources for Seismic Hazard Assessment applications: the case of central Apennines (Italy). *Journal of Seismology*, 8(3):407–425.

Bouchon, M. and Streiff, D. (1997). Propagation of a Shear Crack on a Nonplanar Fault: A Method of Calculation. *Bulletin of the Seismological Society of America*, 87(1):61–66.

Boulton, S. J. and Whittaker, A. C. (2009). Quantifying the slip rates, spatial distribution and evolution of active normal faults from geomorphic analysis: Field examples from an oblique-extensional graben, southern Turkey. *Geomorphology*, 104(3-4):299–316.

Brace, W. F. and Kohlstedt, D. L. (1980). Limits on lithospheric stress imposed by laboratory experiments. *Journal of Geophysical Research: Solid Earth*, 85(B11):6248–6252.

Brown, D., Carbonell, R., Kukkonen, I., Ayala, C., and Golovanova, I. (2003). Composition of the Uralide crust from seismic velocity (Vp, Vs), heat flow, gravity, and magnetic data. *Earth and Planetary Science Letters*, 210(1-2):333–349.

Brun, J. P. (1999). Narrow rifts versus wide rifts: inferences for the mechanics of rifting from laboratory experiments. *Philosophical Transactions of the Royal Society A: Mathematical, Physical and Engineering Sciences*, 357:695–712.

Brune, S., Heine, C., Clift, P. D., and Pérez-Gussinyé, M. (2017). Rifted margin architecture and crustal rheology: Reviewing Iberia-Newfoundland, Central South Atlantic, and South China Sea. *Marine and Petroleum Geology*, 79:257–281.

Bubeck, A., Wilkinson, M., Roberts, G. P., Cowie, P. A., McCaffrey, K. J., Phillips, R., and Sammonds, P. (2015). The tectonic geomorphology of bedrock scarps on active normal faults in the Italian Apennines mapped using combined ground penetrating radar and terrestrial laser scanning. *Geomorphology*, 237:38–51.

Buck, W. R. (1991). Modes of continental lithospheric extension. *Journal of Geophysical Research: Solid Earth*, 96(B12):20161–20178.

Buck, W. R. (2006). The role of magma in the development of the Afro-Arabian Rift System. *Geological Society, London, Special Publications*, 259(1):43–54.

Buck, W. R., Lavier, L. L., and Poliakov, A. N. B. (1999). How to make a rift wide. *PHILOSOPHICAL TRANSACTIONS-ROYAL SOCIETY OF LONDON SERIES A MATHEMATICAL PHYSICAL AND ENGINEERING SCIENCES*, pages 671–689.

Bucknam, R. C. and Anderson, R. E. (1979). Estimation of fault-scarp ages from a scarp-height-slope-angle relationship. *Geology*, 7:11–14.

Burbank, D. W. and Anderson, R. S. (2011). *Tectonic geomorphology*. John Wiley & Sons.

Bürgmann, R. and Dresen, G. (2008). Rheology of the Lower Crust and Upper Mantle: Evidence from Rock Mechanics, Geodesy, and Field Observations. *Annual Review of Earth and Planetary Sciences*, 36(1):531–567.

Byerlee, J. (1978). Friction of rocks. *Pure and applied Geophysics*, 116(4):615–626.

Calais, E., D'Oreye, N., Albaric, J., Deschamps, A., Delvaux, D., Déverchère, J., Ebinger, C., Ferdinand, R. W., Kervyn, F., Macheyeki, A. S., Oyen, A., Perrot, J., Saria, E., Smets, B., Stamps, D. S., and Wauthier, C. (2008). Strain accommodation by slow slip and dyking in a youthful continental rift, East Africa. *Nature*, 456(7223):783–788.

Calais, E., Lesne, O., Deverchere, J., San'kov, V., Lukhnev, A., Mironshnitchenko, A., Buddo, V., Levi, K., Zalutzky, V., and Bashkuev, Y. (1998). Crustal deformation in the Baikal rift from GPS measurements. *Geophysical Research Letters*, 25(21):4003–4006.

Campbell, G. E., Walker, R. T., Abdrakhmatov, K., Jackson, J., Elliott, J. R., MacKenzie, D., Middleton, T., and Schwenninger, J. L. (2015). Great earthquakes in low strain rate continental interiors: An example from SE Kazakhstan. *Journal of Geophysical Research B: Solid Earth*, 120(8):5507–5534.

Carretier, S., Ritz, J. F., Jackson, J., and Bayasgalan, A. (2002). Morphological dating of cumulative reverse fault scarps: Examples from the Gurvan Bogd fault system, Mongolia. *Geophysical Journal International*, 148(2):256–277.

Cartwright, J. a., Mansfield, C., and Trudgill, B. (1996). The growth of normal faults by segment linkage. *Geological Society, London, Special Publications*, 99(1):163–177.

Cartwright, J. A., Trudgill, B. D., and Mansfield, C. S. (1995). Fault growth by segment linkage: an explanation for scatter in maximum displacement and trace length data from the Canyonlands Grabens of SE Utah. *Journal of Structural Geology*, 17(9):1319–1326.

Castillo, M. (2017). Landscape evolution of the graben of Puerto Vallarta (west-central Mexico) using the analysis of landforms and stream long profiles. *Journal of South American Earth Sciences*, 73:10–21.

Célérier, B. (2008). Seeking Aderson's faulting in seismicity: A centennial celebration. *Reviews of Geophysics*, 46(4):1–34.

Cello, G., Mazzoli, S., and Tondi, E. (1998). The crustal fault structure responsible for the 1703 earthquake sequence of central Italy. *Journal of Geodynamics*, 26(2-4):443–460.

Centre for Research on the Epidemiology of Disasters (CRED) and the U.S. Office of Foreign Disaster Assistance (OFDA) (2001). *EM-DAT: The OFDA/CRED International Disaster Database, Universite Catholique de Louvain, Brussels, Belgium*.

Cheloni, D., De Novellis, V., Albano, M., Antonioli, A., Anzidei, M., Atzori, S., Avallone, A., Bignami, C., Bonano, M., Calcaterra, S., Castaldo, R., Casu, F., Cecere, G., De Luca, C., Devoti, R., Di Bucci, D., Esposito, A., Galvani, A., Gambino, P., Giuliani, R., Lanari, R., Manunta, M., Manzo, M., Mattone, M., Montuori, A., Pepe, A., Pepe, S., Pezzo, G., Pietrantonio, G., Polcari, M., Riguzzi, F., Salvi, S., Sepe, V., Serpelloni, E., Solaro, G., Stramondo, S., Tizzani, P., Tolomei, C., Trasatti, E., Valerio, E., Zinno, I., and Doglioni, C. (2017). Geodetic model of the 2016 Central Italy earthquake sequence inferred from InSAR and GPS data. *Geophysical Research Letters*, 44(13):6778–6787.

Chemenda, A. I., Cavalié, O., Vergnolle, M., Bouissou, S., and Delouis, B. (2016). Numerical model of formation of a 3-D strike-slip fault system. *Comptes Rendus Geoscience*, 348(1):61–69.

Childs, C., Holdsworth, R. E., Jackson, C. A.-L., Manzocchi, T., Walsh, J. J., and Yielding, G. (2017). Introduction to the geometry and growth of normal faults. *Geological Society, London, Special Publications*, page SP439.23.

Childs, C., Manzocchi, T., Walsh, J. J., Bonson, C. G., Nicol, A., and Schöpfer, M. P. (2009). A geometric model of fault zone and fault rock thickness variations. *Journal of Structural Geology*, 31(2):117–127.

Childs, C., Nicol, A., Walsh, J. J., and Watterson, J. (1996). Growth of vertically segmented normal faults. *Journal of Structural Geology*, 18(12):1389–1397.

Childs, C., Watterson, J., and Walsh, J. J. (1995). Fault overlap zones within developing normal fault systems. *Journal - Geological Society (London)*, 152(3):535–549.

Chipizubov, A. V., Arzhannikov, S. G., Semenov, R. M., and Smekalin, O. P. (2007). Prehistoric earthquakes and fault scarps in the Barguzin fault zone (Baikal Rift system). *Russian Geology and Geophysics*, 48(7):581–592.

Chorowicz, J. (2005). The East African rift system. *Journal of African Earth Sciences*, 43(1-3):379–410.

Chorowicz, J. and Mukoni, M. N. B. (1980). Comptes Rendus de l'Academie du Science a Paris. *Ser D*, 220:1245–1247.

Chorowicz, J. and Sorlien, C. (1992). Oblique extensional tectonics in the Malawi Rift, Africa. *Geological Society of America Bulletin*, 104(8):1015–1023.

Christensen, N. I. and Mooney, W. D. (1995). Seismic velocity structure and composition of the continental crust: A global view. *Journal of Geophysical Research: Solid Earth*, 100(B6):9761–9788.

Cipar, J. (1980). Teleseismic observations of the 1976 Friuli, Italy earthquake sequence. *Bulletin of the Seismological Society of America*, 70(4):963–983.

Claringbould, J. S., Bell, R. E., Jackson, C. A.-L., Gawthorpe, R. L., and Odinsen, T. (2017). Pre-existing normal faults have limited control on the rift geometry of the northern North Sea. *Earth and Planetary Science Letters*, 475:190–206.

Cleveland, W. S. (1981). LOWESS: A program for smoothing scatterplots by robust locally weighted regression. *The American Statistician*, 35(1):54.

Collettini, C., Niemeijer, A., Viti, C., and Marone, C. (2009). Fault zone fabric and fault weakness. *Nature*, 462(7275):907–10.

Collettini, C. and Sibson, R. H. (2001). Normal faults, normal friction? *Geology*, 29(10):927–930.

Commins, D., Gupta, S., and Cartwright, J. A. (2005). Deformed streams reveal growth and linkage of a normal fault array in the Deformed streams reveal growth and linkage of a normal fault array in the Canyonlands graben , Utah. *Geology*, 33(8):645–648.

Console, R., Carluccio, R., Papadimitriou, E., and Karakostas, V. (2014). Synthetic earthquake catalogs simulating seismic activity in the Corinth Gulf, Greece, fault system. *Journal of Geophysical Research: Solid Earth*, 121:6235–6249.

Contreras, J., Anders, M. H., and Scholz, C. H. (2000). Growth of a normal fault system: observations from the Lake Malawi basin of the east African rift. *Journal of Structural Geology*, 22(2):159–168.

Copley, A., Avouac, J. P., Hollingsworth, J., and Leprince, S. (2011). The 2001 Mw 7.6 Bhuj earthquake, low fault friction, and the crustal support of plate driving forces in India. *Journal of Geophysical Research: Solid Earth*, 116(8):1–11.

Corti, G. (2009). Continental rift evolution: From rift initiation to incipient break-up in the Main Ethiopian Rift, East Africa. *Earth-Science Reviews*, 96(1-2):1–53.

Corti, G., Philippon, M., Sani, F., Keir, D., and Kidane, T. (2013). Re-orientation of the extension direction and pure extensional faulting at oblique rift margins: Comparison between the Main Ethiopian Rift and laboratory experiments. *Terra Nova*, 25(5):396–404.

Corti, G., van Wijk, J., Cloetingh, S., and Morley, C. K. (2007). Tectonic inheritance and continental rift architecture: Numerical and analogue models of the East African Rift system. *Tectonics*, 26(6):1–13.

Cowie, P. (1998). A healing–reloading feedback control on the growth rate of seismogenic faults. *Journal of Structural Geology*, 20(8):1075–1087.

Cowie, P. A., Attal, M., Tucker, G. E., Whittaker, A. C., Naylor, M., Ganas, A., and Roberts, G. P. (2006). Investigating the surface process response to fault interaction and linkage using a numerical modelling approach. *Basin Research*, 18(3):231–266.

Cowie, P. A., Gupta, S., and Dawers, N. H. (2000). Implications of fault array evolution for synrift depocentre development: Insights from a numerical fault growth model. *Basin Research*, 12:241–261.

Cowie, P. a. and Scholz, C. H. (1992a). Growth of faults by accumulation of seismic slip. *Journal of Geophysical Research*, 97(B7):11085.

Cowie, P. A. and Scholz, C. H. (1992b). Physical Explanation for the Displacement Length Relationship of Faults Using a Post-Yield Fracture-Mechanics Model. *Journal of Structural Geology*, 14(10):1133–1148.

Cowie, P. A. and Shipton, Z. K. (1998). Fault tip displacement gradients and process zone dimensions. *Journal of Structural Geology*, 20(8):983–997.

Cowie, P. A., Underhill, J. R., Behn, M. D., Lin, J., and Gill, C. E. (2005). Spatio-temporal evolution of strain accumulation derived from multi-scale observations of Late Jurassic rifting in the northern North Sea: A critical test of models for lithospheric extension. *Earth and Planetary Science Letters*, 234:401–419.

Craig, T. J., Jackson, J. a., Priestley, K., and McKenzie, D. (2011). Earthquake distribution patterns in Africa: their relationship to variations in lithospheric and geological structure, and their rheological implications. *Geophysical Journal International*, 185(1):403–434.

Crider, J. G. (2001). Oblique slip and the geometry of normal-fault linkage: Mechanics and a case study from the Basin and Range in Oregon. *Journal of Structural Geology*, 23(12):1997–2009.

Crider, J. G. (2015). The initiation of brittle faults in crystalline rock. *Journal of Structural Geology*, 77:159–174.

Crider, J. G. and Pollard, D. D. (1998). Fault linkage : Three-dimensional mechanical interaction faults. *Journal of Geophysical Research*, 103(B10):24,373–24,391.

Crone, A. J. and Haller, K. M. (1991). Segmentation and the coseismic behavior of Basin and Range normal faults: examples from east-central Idaho and southwestern Montana, U.S.A. *Journal of Structural Geology*, 13(2):151–164.

Crosby, B. T. and Whipple, K. X. (2006). Knickpoint initiation and distribution within fluvial networks: 236 waterfalls in the Waipaoa River, North Island, New Zealand. *Geomorphology*, 82(1-2):16–38.

Crossley, R. (1984). Controls of sedimentation in the Malawi rift valley, Central Africa. *Sedimentary Geology*, 40(1-3):33–50.

Culling, W. E. H. (1963). Soil creep and the development of hillside slopes. *The Journal of Geology*, 71(2):127–161.

Currenti, G., Solaro, G., Napoli, R., Pepe, A., Bonaccorso, A., Del Negro, C., and Sansosti, E. (2012). Modeling of ALOS and COSMO-SkyMed satellite data at Mt Etna: Implications on relation between seismic activation of the Pernicana fault system and volcanic unrest. *Remote sensing of environment*, 125:64–72.

D'Addezio, G., Cinti, F. R., and Pantosti, D. (1995). A large unknown historical earthquake in the Abruzzi region (Central Italy): combination of geological and historical data. *Annali Di Geofisica*, 38:491–501.

D'Agostino, N., Jackson, J. A., Dramis, F., and Funiciello, R. (2001). Interactions between mantle upwelling, drainage evolution and active normal faulting: an example from the central Apennines (Italy). *Geophysical Journal International*, 147(2):475–497.

Daly, E., Keir, D., Ebinger, C. J., Stuart, G. W., Bastow, I. D., and Ayele, A. (2008). Crustal tomographic imaging of a transitional continental rift: the Ethiopian rift. *Geophysical Journal International*, 172(3):1033–1048.

Davis, G. and Reynolds, S. (1996). *Structural Geology of Rocks and Regions*. John Wiley, New York, 2nd edition.

Dawers, H. and Anders, M. H. (1995). Displacement-length scaling and fault linkage. *Journal of Structural Geology*, 17(5):607–614.

Dawers, N. H., Anders, M. H., and Scholz, C. H. (1993). Growth of normal faults: Displacement-length scaling. *Geology*, 21(12):1107–1110.

Dawson, A. and Kirkpatrick, I. (1968). The geology of the Cape Maclear peninsula and Lower Bwanje valley. *Bulletin of the Geological Survey, Malawi*, 28(71).

De Lépinay, B. M., Deschamps, A., Klingelhoefer, F., Mazabraud, Y., Delouis, B., Clouard, V., Hello, Y., Crozon, J., Marcaillou, B., Graindorge, D., Vallée, M., Perrot, J., Bouin, M. P., Saurel, J. M., Charvis, P., and St-Louis, M. (2011). The 2010 Haiti earthquake: A complex fault pattern constrained by seismologic and tectonic observations. *Geophysical Research Letters*, 38(22):1–7.

Delvaux, D. (2001). Tectonic and palaeostress evolution of the Tanganyika-Rukwa-Malawi rift segment, East African Rift System. *Mémoires du Muséum national d'histoire naturelle*, 186:545–567.

Delvaux, D. and Barth, A. (2010). African stress pattern from formal inversion of focal mechanism data. *Tectonophysics*, 482:105–128.

Delvaux, D., Kervyn, F., Macheyeki, A., and Temu, E. (2012). Geodynamic significance of the TRM segment in the East African Rift (W-Tanzania): Active tectonics and paleostress in the Ufipa plateau and Rukwa basin. *Journal of Structural Geology*, 37:161–180.

Deng, Q. and Liao, Y. (1996). Paleoseismology along the range-front fault of Helan Mountains, north central China. *Journal of Geophysical Research: Solid Earth*, 101(B3):5873–5893.

DePolo, C. M., Clark, D. G., Slemmons, D., and Ramelli, A. R. (1991). Historical surface faulting in the Basin and Range province, western North America: implications for fault segmentation. *Journal of Structural Geology*, 13(2):123–136.

Deprez, a., Doubre, C., Masson, F., and Ulrich, P. (2013). Seismic and aseismic deformation along the East African Rift System from a reanalysis of the GPS velocity field of Africa. *Geophysical Journal International*, 193(3):1353–1369.

Destro, N., Alkmim, F. F., Magnavita, L. P., and Szatmari, P. (2003). The Jeremoabo transpressional transfer fault, Recôncavo- Tucano Rift, NE Brazil. *Journal of Structural Geology*, 25(8):1263–1279.

Déverchere, J., Petit, C., Gileva, N., Radziminovitch, N., Melnikova, V., and San'Kov, V. (2001). Depth distribution of earthquakes in the Baikal rift system and its implications for the rheology of the lithosphere. *Geophysical Journal International*, 146(3):714–730.

Dixon, T. H., Miller, M., Farina, F., Wang, H., and Johnson, D. (2000). Present-day motion of the Sierra Nevada block and some tectonic implications for the Basin and Range province, North American Cordillera. *Tectonics*, 19(1):1–24.

Dolan, J. F., Bowman, D. D., and Sammis, C. G. (2007). Long-range and long-term fault interactions in Southern California. *Geology*, 35(9):855–858.

Doré, T. and Lundin, E. (2015). Hyperextended continental margins — Knowns and unknowns. *Geology*, 43(1):95–96.

Doser, D. (1991). Faulting within the western Baikal rift as characterized by earthquake studies. *Tectonophysics*, 196:87–107.

Duan, B. and Oglesby, D. D. (2005). Multicycle dynamics of nonplanar strike-slip faults. *Journal of Geophysical Research*, 110:1–16.

Duarah, B. P. and Phukan, S. (2011). Understanding the tectonic behaviour of the Shillong Plateau, India using remote sensing data. *Journal of the Geological Society of India*, 77(2):105–112.

Duffy, O. B., Brocklehurst, S. H., Gawthorpe, R. L., Leeder, M. R., and Finch, E. (2014). Controls on landscape and drainage evolution in regions of distributed normal faulting: Perachora Peninsula, Corinth Rift, Central Greece. *Basin Research*, 27:1–22.

DuRoss, C. B., Personius, S. F., Crone, A. J., Olig, S. S., Hylland, M. D., Lund, W. R., and Schwartz, D. P. (2015). Fault segmentation: New concepts from the Wasatch Fault Zone, Utah, USA. *Journal of Geophysical Research:Solid Earth*, 121:1131–1157.

Ebinger, C. (1989). Tectonic development of the western branch of the East African rift system. *Geological Society of America Bulletin*, 101:885–903.

Ebinger, C. (2005). Continental break-up: the East African perspective. *Astronomy & Geophysics*, 46:16–21.

Ebinger, C., Deino, A., Tesha, A., Becker, R., and Ring, U. (1993). Tectonic controls on rift basin morphology: evolution of the Northern Malawi (Nyasa) Rift. *Research: Solid Earth*, 98(B10):17,821–17,836.

Ebinger, C., Djomani, Y. P., Mbede, E., Foster, A., and Dawson, J. B. (1997). Rifting archaean lithosphere: the eyasi-manyara-natron rifts, east africa. *Journal of the Geological Society*, 154(6):947–960.

Ebinger, C., Drake, R., Deino, A., and Tesha, A. (1989). Chronology of Volcanism and Rift Basin Propagation: Rungwe Volcanic Province, East Africa. *Journal of Geophysical Research*, 94:15,785–15,803.

Ebinger, C., Rosendahl, B., and Reynolds, D. (1987). Tectonic model of the Malawi rift, Africa. *Tectonophysics*, 141:215–235.

Ebinger, C., Wijk, J. V., and Keir, D. (2013). The time scales of continental rifting: Implications for global processes. *Geological Society of America Special Papers*, 2500(11):1–26.

Ebinger, C. J., Jackson, J. A., Foster, A. N., and Hayward, N. J. (1999). Extensional basin geometry and the elastic lithosphere. *Philosophical Transactions of the Royal Society A: Mathematical, Physical and Engineering Sciences*, 357(1753):741–765.

Elliott, J. R., Parsons, B., Jackson, A., Shan, X., Sloan, A., and Walker, T. (2011). Depth segmentation of the seismogenic continental crust: The 2008 and 2009 Qaidam earthquakes. *Geophysical Research Letters*, 38:1–6.

Elvidge, C. and Lyon, R. (1985). Estimate of the vegetation contribution to the 1.65/2.22 μm ratio in airborne thematic-mapper imagery of the Virginia Range, Nevada. *International Journal of Remote Sensing*, 6:75–88.

England, P. (1983). Constraints on extension of continental lithosphere. *Journal of Geophysical Research: Solid Earth*, 88(B2):1145–1152.

England, P. and Jackson, J. (2011). Uncharted seismic risk. *Nature Geoscience*, 4(6):348–349.

Erdik, M., Demircioglu, M., Sesetyan, K., Durukal, E., and Siyahi, B. (2004). Earthquake hazard in Marmara region, Turkey. *Soil Dynamics and Earthquake Engineering*, 24(8):605–631.

Ewiak, O., Victor, P., and Oncken, O. (2015). Investigating multiple fault rupture at the Salar del Carmen segment of the Atacama Fault System (northern Chile): Fault scarp morphology and knickpoint analysis. *Tectonics*, 34(2):187–212.

Faccenna, C., Nalpas, T., Brun, J.-P., Davy, P., and Bosi, V. (1995). The influence of pre-existing thrust faults on normal fault geometry in nature and in experiments. *Journal of Structural Geology*, 17(8):1139–1149.

Fagereng, Å. (2013). Fault segmentation, deep rift earthquakes and crustal rheology: Insights from the 2009 Karonga sequence and seismicity in the Rukwa-Malawi rift zone. *Tectonophysics*, 601(December 2009):216–225.

Faulds, J. E. and Varga, R. J. (1998). The role of accommodation zones and transfer zones in the regional segmentation of extended terranes. *Geological Society of America Special Papers*, 323:1–45.

Faulkner, D. R., Mitchell, T. M., Jensen, E., and Cembrano, J. (2011). Scaling of fault damage zones with displacement and the implications for fault growth processes. *Journal of Geophysical Research*, 116:1–11.

Fazlikhani, H., Fossen, H., Gawthorpe, R. L., Faleide, J. I., and Bell, R. E. (2017). Basement structure and its influence on the structural configuration of the northern North Sea rift. *Tectonics*, 36(6):1151–1177.

Fenton, C. H. and Bommer, J. J. (2006). The Mw7 Machaze, Mozambique, earthquake of 23 February 2006. *Seismological Research Letters*, 77(4):426–439.

Fialko, Y. (2006). Interseismic strain accumulation and the earthquake potential on the southern San Andreas fault system. *Nature*, 441(7096):968–971.

Fielding, E. J., Wright, T. J., Muller, J., Parsons, B. E., and Walker, R. (2004). Aseismic deformation of a fold-and-thrust belt imaged by synthetic aperture radar interferometry near Shahdad, southeast Iran. *Geology*, 32(7):577–580.

Finlayson, D. P., Montgomery, D. R., and Hallet, B. (2002). Spatial coincidence of rapid inferred erosion with young metamorphic massifs in the Himalayas. *Geology*, 30(3):219–222.

Flannery, J. and Rosendahl, B. (1990). The seismic stratigraphy of Lake Malawi, Africa: implications for interpreting geological processes in lacustrine rifts. *Journal of African Earth Sciences*, 10(3):519–548.

Fonseca, J. (2014). MOZART: A Seismological Investigation of the East African Rift in Central Mozambique. *Seismological Research Letters*, 85(1):108–116.

Forsyth, D. (1975). On the relative importance of the driving forces of plate motion. *Geophysical Journal International*, 43(1):163–200.

Fossen, H. (2016). *Structural geology*. Cambridge University Press.

Fossen, H. and Rotevatn, A. (2016). Fault linkage and relay structures in extensional settings-A review. *Earth-Science Reviews*, 154:14–28.

Foster, A., Ebinger, C., Mbede, E., and Rex, D. (1997). Tectonic development of the northern Taiizaiiian sector of the East African Rift System. *Journal of the Geological Society*, 154(4):689–700.

Freed, A. M. (2005). Earthquake Triggering By Static, Dynamic, and Postseismic Stress Transfer. *Annual Review of Earth and Planetary Sciences*, 33(1):335–367.

Fu, B., Ninomiya, Y., Lei, X., Toda, S., and Awata, Y. (2004). Mapping active fault associated with the 2003 Mw 6.6 Bam (SE Iran) earthquake with ASTER 3D images. *Remote Sensing of Environment*, 92:153–157.

Gallant, J. C. and Hutchinson, M. F. (1997). Scale dependence in terrain analysis. *Mathematics and Computers in Simulation*, 43(3-6):313–321.

Galli, P., Galadini, F., Moro, M., and Giraudi, C. (2002). New paleoseismological data from the Gran Sasso d'Italia area (central Apennines). *Geophysical Research Letters*, 29(7).

Galli, P. A., Giaccio, B., Messina, P., Peronace, E., and Zuppi, G. M. (2011). Palaeoseismology of the L'Aquila faults (central Italy, 2009, Mw 6.3 earthquake): Implications for active fault linkage. *Geophysical Journal International*, 187(3):1119–1134.

Ganas, A., Pavlides, S., and Karastathis, V. (2005). DEM-based morphometry of range-front escarpments in Attica , central Greece , and its relation to fault slip rates. *Geomorphology*, 65(September 2004):301–319.

Ganas, A., Sokos, E., Agalos, A., Leontakianakos, G., and Pavlides, S. (2006). Coulomb stress triggering of earthquakes along the Atalanti Fault, central Greece: Two April 1894 M6+ events and stress change patterns. *Tectonophysics*, 420(3):357–369.

Ganas, A., White, K., and Wadge, G. (1997). SPOT DEM analysis for fault segment mapping in the Lokris region, central Greece. *EARSEL advances in remote sensing*, 5:46–53.

Gao, M., Xu, X., Klinger, Y., Van Der Woerd, J., and Tapponnier, P. (2017). High-resolution mapping based on an Unmanned Aerial Vehicle (UAV) to capture paleoseismic offsets along the Altyn-Tagh fault, China. *Scientific Reports*, 7(1):1–11.

Gao, S., Luo, T.-C., Zhang, B.-R., Zhang, H.-F., Han, Y.-w., Zhao, Z.-D., and Hu, Y.-K. (1998). Chemical composition of the continental crust as revealed by studies in East China. *Geochimica et Cosmochimica Acta*, 62(11):1959–1975.

Gasparini, N. M., Bras, R. L., and Whipple, K. X. (2006). Numerical modeling of non-steady river profile evolution using a sediment-flux-dependent incision model. *Geological Society of America Special Paper*, 398(08):127–141.

Gawthorpe, R. L. (1987). Tectono-sedimentary evolution of the Bowland Basin , N England , during the Dinantian. *Journal of the Geological Society*, 144:59–71.

Gawthorpe, R. L. and Hurst, J. M. (1993). Transfer zones in extensional basins: their structural style and influence on drainage development and stratigraphy. *Journal of the Geological Society*, 150:1137–1152.

Gawthorpe, R. L., Jackson, C. A. L., Young, M. J., Sharp, I. R., Moustafa, A. R., and Leppard, C. W. (2003). Normal fault growth, displacement localisation and the evolution of normal fault populations: The Hammam Faraun fault block, Suez rift, Egypt. *Journal of Structural Geology*, 25(6):883–895.

Gawthorpe, R. L., Leeder, M. R., Kranis, H., Skourtsos, E., Andrews, J. E., Henstra, G. A., Mack, G. H., Muravchik, M., Turner, J. A., and Stamatakis, M. (2017). Tectono-sedimentary evolution of the Plio-Pleistocene Corinth rift, Greece. *Basin Research*, pages 1–32.

Geiß, C. and Taubenböck, H. (2013). Remote sensing contributing to assess earthquake risk: From a literature review towards a roadmap. *Natural Hazards*, 68:7–48.

Ghosh, A., Holt, W. E., Wen, L., Haines, A. J., and Flesch, L. M. (2008). Joint modeling of lithosphere and mantle dynamics elucidating lithosphere-mantle coupling. *Geophysical Research Letters*, 35(16):1–5.

Giba, M., Walsh, J., and Nicol, A. (2012). Segmentation and growth of an obliquely reactivated normal fault. *Journal of Structural Geology*, 39:253–267.

Gibson, J., Walsh, J., and Watterson, J. (1989). Modelling of bed contours and cross-sections adjacent to planar normal faults. *Journal of Structural Geology*, 11:317–328.

Gillard, M., Sauter, D., Tugend, J., Tomasi, S., Epin, M.-E., and Manatschal, G. (2017). Birth of an oceanic spreading center at a magma-poor rift system. *Scientific reports*, 7(1):15072.

Gillespie, P., Walsh, J., and Watterson, J. (1992). Limitations of dimension and displacement data from single faults and the consequences for data analysis and interpretation. *Journal of Structural Geology*, 14(10):1157–1172.

Giraudi, C. and Frezzotti, M. (1995). Palaeoseismicity in the Gran Sasso Massif (Abruzzo, central Italy). *Quaternary International*, 25:81–93.

Girdler, R. (1990). The Dead Sea transform fault system. *Tectonophysics*, 180(1):1–13.

Girdler, R. W. and Styles, P. (1974). Two stage Red Sea floor spreading. *Nature*, 247(5435):7–11.

Goda, K., Gibson, E. D., Smith, H. R., Biggs, J., and Hodge, M. (2016). Seismic Risk Assessment of Urban and Rural Settlements around Lake Malawi. *Frontiers in Built Environment*, 2(30):1–17.

Gomberg, J. (1996). Stress/strain changes and triggered seismicity following the Mw 7.3 Landers, California, earthquake. *Journal of geophysical research*, 101:733–749.

Gomberg, J. (2001). The failure of earthquake failure models. *Journal of Geophysical Research*, 106:16,253–16,263.

Gomberg, J., Beeler, N. M., Blanpied, M. L., and Bodin, P. (1998). Earthquake triggering by transient and static deformations. *Journal of Geophysical Research*, 103:24,411–24,426.

Gomberg, J., Reasenberg, P. a., Bodin, P., and Harris, R. a. (2001). Earthquake triggering by seismic waves following the Landers and Hector Mine earthquakes. *Nature*, 411(6836):462–466.

Gomez-Rivas, E. and Griera, A. (2012). Shear fractures in anisotropic ductile materials: An experimental approach. *Journal of Structural Geology*, 34:61–76.

Goode, P. C., Gilder, S., and Fang, X. (1991). A preliminary description of the Can-Hang failed rift , southeastern China. *Tectonophysics*, 197:245–255.

Grand, S. P., van der Hilst, R. D., and Widiyantoro, S. (1997). High resolution global tomography: a snapshot of convection in the Earth. *Geological Society of America Today*, 7(4).

Grigillo, D., Fras, M. K., and Petrovič, D. (2012). Automated building extraction from IKONOS images in suburban areas. *International Journal of Remote Sensing*, 33(16):5149–5170.

Gruber, A., Wessel, B., Huber, M., and Roth, A. (2012). Operational TanDEM-X DEM calibration and first validation results. *ISPRS Journal of Photogrammetry and Remote Sensing*, 73:39–49.

Gudmundsson, A. (2004). Effects of Young's modulus on fault displacement. *Comptes Rendus Geoscience*, 336(1):85–92.

Gülerce, Z. and Ocak, S. (2013). Probabilistic seismic hazard assessment of Eastern Marmara Region. *Bulletin of Earthquake Engineering*, 11(5):1259–1277.

Gupta, A. and Scholz, C. H. (2000). A model of normal fault interaction based on observations and theory. *Journal of Structural Geology*, 22(7):865–879.

Gupta, S., Underbill, J. R., Sharp, I. R., and Gawthorpe, R. L. (1999). Role of fault interactions in controlling synrift sediment dispersal patterns: Miocene, Abu Alaqa Group, Suez Rift, Sinai, Egypt. *Basin Research*, 11(2):167–189.

Habgood, F., Holt, D. N., and Walshaw, R. D. (1973). The Geology of the Thyolo area. Bulletin No. 22. *Bulletin of the Geological Survey, Malawi*, 22.

Hamblin, W. K. (1976). Patterns of displacement along the Wasatch fault. *Geology*, 4(10):619–622.

Hamiel, Y., Baer, G., Kalindekafe, L., Dombola, K., and Chindandali, P. (2012). Seismic and aseismic slip evolution and deformation associated with the 2009-2010 northern Malawi earthquake swarm, East African Rift. *Geophysical Journal International*, 191:898–908.

Hamling, I. J., Hreinsdóttir, S., Clark, K., Elliott, J., Liang, C., Fielding, E., Litchfield, N., Villamor, P., Wallace, L., Wright, T. J., D'Anastasio, E., Bannister, S., Burbidge, D., Denys, P., Gentle, P., Howarth, J., Mueller, C., Palmer, N., Pearson, C., Power, W., Barnes, P., Barrell, D. J. A., Van Dissen, R., Langridge, R., Little, T., Nicol, A., Pettinga, J., Rowland, J., and Stirling, M. (2017). Complex multifault rupture during the 2016 M w 7.8 Kaikoura earthquake, New Zealand. *Science*, 356(154):1–10.

Handy, M. R. and Brun, J. P. (2004). Seismicity, structure and strength of the continental lithosphere. *Earth and Planetary Science Letters*, 223(3-4):427–441.

Hanks, T. and Kanamori, H. (1979). A moment magnitude scale. *Journal of Geophysical Research*, 84(B5):2348–2350.

Hanks, T. C., Bucknam, R. C., Lajoie, K. R., and Wallace, R. E. (1984). Modification of Wave-Cut and Faulting-Controlled Landforms. *Journal of Geophysical Research*, 89(10):5771–5790.

Hansen, S. E. and Nyblade, A. A. (2013). The deep seismic structure of the Ethiopia/Afar hotspot and the African superplume. *Geophysical Journal International*, 194(1):118–124.

Harris, R. a. (1998). Introduction to Special Section: Stress Triggers, Stress Shadows, and Implications for Seismic Hazard. *Journal of Geophysical Research*, 103:24,347–24,358.

Harris, R. A. and Day, S. M. (1993). Dynamics of Fault Interaction : Parallel Strike-Slip Faults. *Journal of Geophysical Research*, 98(B3):4461–4472.

Harris, R. A. and Day, S. M. (1999). Dynamic 3D simulations of earthquakes on en echelon faults. *Journal of Geophysical Research*, 26(14):2089–2092.

Harris, R. A. and Simpson, R. W. (1992). Changes in static stress on southern California faults after the 1992 Landers earthquake. *Nature*, 360(6401):251–254.

Harris, R. a. and Simpson, R. W. (1996). In the shadow of 1857-the effect of the Great Ft. Tejon Earthquake on subsequent earthquakes in southern California. *Geophysical Research Letters*, 23(3):229–232.

Hartnady, C. (2002). Earthquake hazard in Africa: perspectives on the Nubia-Somalia boundary: news and view. *South African journal of science*, 98:425–428.

Hatem, A. E., Cooke, M. L., and Madden, E. H. (2015). Evolving efficiency of restraining bends within wet kaolin analog experiments. *Journal of Geophysical Research: Solid Earth*, 120:1975–1992.

Hayakawa, Y. S. and Oguchi, T. (2006). DEM-based identification of fluvial knickzones and its application to Japanese mountain rivers. *Geomorphology*, 78:90–106.

Hayakawa, Y. S. and Oguchi, T. (2009). GIS analysis of fluvial knickzone distribution in Japanese mountain watersheds. *Geomorphology*, 111:27–37.

Hayes, G. P., Briggs, R. W., Sladen, A., Fielding, E. J., Prentice, C., Hudnut, K., Mann, P., Taylor, F. W., Crone, a. J., Gold, R., Ito, T., and Simons, M. (2010). Complex rupture during the 12 January 2010 Haiti earthquake. *Nature Geoscience*, 3(11):800–805.

Hayward, N. J. and Ebinger, C. J. (1996). Variations in the along-axis segmentation of the Afar Rift system. *Tectonics*, 15(2):244–257.

He, C., Luo, L., Hao, Q. M., and Zhou, Y. (2013). Velocity-weakening behavior of plagioclase and pyroxene gouges and stabilizing effect of small amounts of quartz under hydrothermal conditions. *Journal of Geophysical Research: Solid Earth*, 118(7):3408–3430.

He, Z. and Ma, B. (2015). Holocene paleoearthquakes of the Daqingshan fault detected from knickpoint identification and alluvial soil profile. *Journal of Asian Earth Sciences*, 98:261–271.

Henstra, G. a., Rotevatn, A., Gawthorpe, R. L., and Ravnås, R. (2015). Evolution of a major segmented normal fault during multiphase rifting: The origin of plan-view zigzag geometry. *Journal of Structural Geology*, 74:45–63.

Herbert, J. W., Cooke, M. L., Souloumiac, P., Madden, E. H., Mary, B. C. L., and Maillot, B. (2015). The work of fault growth in laboratory sandbox experiments. *Earth and Planetary Science Letters*, 432:95–102.

Herd, D. G. and McMasters, C. R. (1982). Surface faulting in the Sonora, Mexico, earthquake of 1887. In *Geological Society of America, Abstracts with Programs*, volume 14, page 172.

Hetzel, R., Niedermann, S., Tao, M., Kubik, P. W., Ivy-Ochs, S., Gao, B., and Strecker, M. R. (2002). Low slip rates and long-term preservation of geomorphic features in Central Asia. *Nature*, 417(6887):428–432.

Hetzel, R., Tao, M., Niedermann, S., Strecker, M. R., Ivy-Ochs, S., Kubik, P. W., and Gao, B. (2004). Implications of the fault scaling law for the growth of topography: Mountain ranges in the broken foreland of north-east Tibet. *Terra Nova*, 16(3):157–162.

Hilbert-Wolf, H. L. and Roberts, E. M. (2015). Giant seismites and megablock uplift in the East African rift: Evidence for late pleistocene large magnitude earthquakes. *PLoS ONE*, 10(6):1–18.

Hill, P., Johnston, M. J. S., and Langbein, J. O. (1995). Response of Long Valley caldera to the Mw - 7.3 Landers, California, Earthquake. *Journal of Geophysical Research*, 100:12,985–13,005.

Hilley, G. E., Arrowsmith, J. R., and Amoroso, L. (2001). Interaction between normal faults and fractures and fault scarp morphology. *Geophysical Research Letters*, 28(19):3777–3780.

Hilley, G. E., Delong, S., Prentice, C., Blisniuk, K., and Arrowsmith, J. R. (2010). Morphologic dating of fault scarps using airborne laser swath mapping (ALSM) data. *Geophysical Research Letters*, 37(4):0–5.

Hodge, M., Biggs, J., Goda, K., and Aspinall, W. (2015). Assessing infrequent large earthquakes using geomorphology and geodesy: the Malawi Rift. *Natural Hazards*, 76(3):1781–1806.

Holbrook, J. and Schumm, S. A. (1999). Geomorphic and sedimentary response of rivers to tectonic deformation: A brief review and critique of a tool for recognizing subtle epeirogenic deformation in modern and ancient settings. *Tectonophysics*, 305(1-3):287–306.

Holland, W. N. and Pickup, G. (1976). Flume study of knickpoint development in stratified sediment. *Bulletin of the Geological Society of America*, 87(1):76–82.

Howard, A. D. and Kerby, G. (1983). Channel changes in badlands. *Geological Society of America Bulletin*, 94(6):739–752.

Hussain, E., Hooper, A., Wright, T. J., Walters, R. J., and Bekaert, D. P. (2016). Interseismic strain accumulation across the central North Anatolian Fault from iteratively unwrapped InSAR measurements. *Journal of Geophysical Research: Solid Earth*, 121(12):9000–9019.

Ikari, M. J., Marone, C., and Saffer, D. M. (2011). On the relation between fault strength and frictional stability. *Geology*, 39(1):83–86.

Ismail-Zadeh, A., Fucugauchi, J. U., Kijko, A., Takeuchi, K., and Zaliapin, I. (2014). *Extreme natural hazards, disaster risks and societal implications*, volume 1. Cambridge University Press.

Jackson, C. A., Gawthorpe, R. L., Carr, I. D., and Sharp, I. R. (2005). Normal faulting as a control on the stratigraphic development of shallow marine syn-rift sequences: The Nukhul and Lower Rudeis Formations, Hammam Faraun fault block, Suez Rift, Egypt. *Sedimentology*, 52(2):313–338.

Jackson, C. A. and Rotevatn, A. (2013). 3D seismic analysis of the structure and evolution of a salt-influenced normal fault zone: A test of competing fault growth models. *Journal of Structural Geology*, 54:215–234.

Jackson, C. A.-L., Bell, R. E., Rotevatn, A., and Tvedt, A. B. M. (2017). Techniques to determine the kinematics of synsedimentary normal faults and implications for fault growth models. *Geological Society, London, Special Publications*, 439.

Jackson, C. A.-L., Gawthorpe, R. L., and Sharp, I. R. (2002). Growth and linkage of the East Tanka fault zone, Suez rift: structural style and syn-rift stratigraphic response. *Journal of the Geological Society*, 159(2):175–187.

Jackson, J. (2001). Living with earthquakes: Know your faults. *Journal of Earthquake Engineering*, 5(S1):5–123.

Jackson, J. (2002). Strength of the continental lithosphere: time to abandon the jelly sandwich? *GSA today*, 12(9):4–9.

Jackson, J., Austrheim, H., McKenzie, D., and Priestley, K. (2004). Metastability, mechanical strength, and the support of mountain belts. *Geology*, 32(7):625.

Jackson, J. and Blenkinsop, T. (1993). The Malawi earthquake of March 10, 1989: Deep faulting within the East Africa Rift System. *Tectonics*, 12(5):1131–1139.

Jackson, J. and Blenkinsop, T. (1997). The Bilila-Mtakataka fault in Malawi: An active, 100-km long, normal fault segment in thick seismogenic crust. *Tectonics*, 16(1):137–150.

Jackson, J., Bouchon, M., Fielding, E., Funning, G., Ghorashi, M., Hatzfeld, D., Nazari, H., Parsons, B., Priestley, K., and Talebian, M. (2006). Seismotectonic, rupture process, and earthquake-hazard aspects of the 2003 December 26 Bam, Iran, earthquake. *Geophysical Journal International*, 166(3):1270–1292.

Jackson, J., Norris, R., and Youngson, J. (1996). The structural evolution of active fault and fold systems in central Otago, New Zealand: evidence revealed by drainage patterns. *Journal of Structural Geology*, 18(1994):217–234.

Jackson, J. and White, N. (1989). Normal faulting in the upper continental crust: observations from regions of active extension. *Journal of Structural Geology*, 11:15–36.

Jagoutz, O., Muntener, O., Manatschal, G., Rubatto, D., Péron-Pinvidic, G., Turrin, B. D., and Villa, I. M. (2007). The rift-to-drift transition in the North Atlantic: A stuttering start of the MORB machine? *Geology*, 35(12):1087–1090.

Jestin, F., Huchon, P., and Gaulier, J. M. (1994). The Somalia plate and the East African Rift System: present-day kinematics. *Geophysical Journal International*, 116(3):637–654.

Johnson, K., Nissen, E., Saripalli, S., Arrowsmith, J. R., McGarey, P., Scharer, K., Williams, P., and Blisniuk, K. (2014). Rapid mapping of ultrafine fault zone topography with structure from motion. *Geosphere*, 10(5):969–986.

Johri, M., Dunham, E., Zoback, M., and Fang, Z. (2014). Predicting fault damage zones by modeling dynamic rupture propagation and comparison with field observations. *Journal of Geophysical Research: Solid Earth*, 119:1251–1272.

Joyce, K. E., Belliss, S. E., Samsonov, S. V., McNeill, S. J., and Glassey, P. J. (2009). A review of the status of satellite remote sensing and image processing techniques for mapping natural hazards and disasters. *Progress in Physical Geography*, 33(2):183–207.

Jung, S. and Ariyur, K. B. (2017). Compensating UAV GPS data accuracy through use of relative positioning and GPS data of UGV. *Journal of Mechanical Science and Technology*, 31(9):4471–4480.

Kanamori, H. and Anderson, D. L. (1975). Theoretical basis of some empirical relations in seismology. *Bulletin of the Seismological Society of America*, 65(5):1073–1095.

Kase, Y. (2010). Slip-length scaling law for strike-slip multiple segment earthquakes based on dynamic rupture simulations. *Bulletin of the Seismological Society of America*, 100(2):473–481.

Katumwehe, A., Abdelsalam, M., and Atekwana, E. (2015). The Role of Pre-existing Precambrian Structures in Rift Evolution: The Albertine and Rhino Grabens, Uganda. *Tectonophysics*, 646:117–129.

Keir, D., Bastow, I. D., Pagli, C., and Chambers, E. L. (2013). The development of extension and magmatism in the Red Sea rift of Afar. *Tectonophysics*, 607:98–114.

Keller, E. A., Zepeda, R. L., Rockwell, T. K., Ku, T. L., and Dinklage, W. S. (1998). Active tectonics at Wheeler ridge, southern San Joaquin valley, California. *GSA Bulletin*, 110(3):298–310.

Kendall, J.-M. and Lithgow-Bertelloni, C. (2016). Why is Africa rifting? *Geological Society, London, Special Publications*, 420(1):11–30.

Keranen, K., Klemperer, S. L., Gloaguen, R., and Group, E. W. (2004). Three-dimensional seismic imaging of a protoridge axis in the Main Ethiopian rift. *Geology*, 32(11):949–952.

Keranen, K. M., Klemperer, S. L., Julia, J., Lawrence, J. F., and Nyblade, A. A. (2009). Low lower crustal velocity across Ethiopia: Is the Main Ethiopian Rift a narrow rift in a hot craton? *Geochemistry, Geophysics, Geosystems*, 10(5).

Kervyn, F., Ayub, S., Kajara, R., Kanza, E., and Temu, B. (2006). Evidence of recent faulting in the Rukwa rift (West Tanzania) based on radar interferometric DEMs. *Journal of African Earth Sciences*, 44(2):151–168.

Kijko, a. and Graham, G. (1998). Parametric-historic Procedure for Probabilistic Seismic Hazard Analysis Part I: Estimation of Maximum Regional Magnitude m max. *Pure and Applied Geophysics*, 152:413–442.

Kilb, D., Gomberg, J., and Bodin, P. (2000). Triggering of earthquake aftershocks by dynamic stresses. *Nature*, 408(6812):570–574.

Kim, Y.-S. and Sanderson, D. J. (2005). The relationship between displacement and length of faults: a review. *Earth-Science Reviews*, 68(3-4):317–334.

Kinabo, B. D., Hogan, J. P., Atekwana, E. a., Abdelsalam, M. G., and Modisi, M. P. (2008). Fault growth and propagation during incipient continental rifting: Insight from a combined aeromagnetic and Shuttle Radar Topography Mission digital elevation model investigation of the Okavango Rift Zone, northwest Botswana. *Tectonics*, 27:1–16.

King, G. and Nabelek, J. (1985). Role of fault bends in the initiation and termination of earthquake rupture. *Science*, 228(4702):984–987.

King, G., Stein, S., and Lin, J. (1994). Static stress changes and the triggering of earthquakes. *Bulletin of the Seismological Society of America*, 84(3):935–953.

King, G. C. P. and Cocco, M. (2001). Fault interaction by elastic stress changes: New clues from earthquake sequences. *Advances in Geophysics*, 44:1–38.

King, G. C. P., Stein, R. S., and Rundle, J. B. (1988). The Growth of Geological Structures by Repeated Earthquakes 1. Conceptual Framework. *Journal of Geophysical Research:*, 93(B11):13,319–13,331.

Klinger, Y., Xu, X., Tapponnier, P., Van der Woerd, J., Lasserre, C., and King, G. (2005). High-resolution satellite imagery mapping for the surface rupture and slip distribution of the Mw 7.8, 14 November 2001 Kokoxili earthquake, Kunlun fault, northern Tibet, China. *Bulletin of the Seismological Society of America*, 95(5):1970–1987.

Kokkalas, S. and Koukouvelas, I. K. (2005). Fault-scarp degradation modeling in central Greece: The Kaparelli and Eliki faults (Gulf of Corinth) as a case study. *Journal of Geodynamics*, 40(2-3):200–215.

Kolawole, F., Atekwana, E. A., Laó-Dávila, D. A., Abdelsalam, M. G., Chindandali, P. R., Salima, J., and Kalindekafe, L. (2018). Active deformation of Malawi Rift's North Basin hinge zone modulated by reactivation of pre-existing Precambrian shear zone fabric. *Tectonics*, pages 1–22.

Kolyukhin, D. and Torabi, A. (2012). Statistical analysis of the relationships between faults attributes. *Journal of Geophysical Research*, 117:1–14.

Kreemer, C., Klein, E., Shen, Z.-K., Wang, M., Estey, L., Wier, S., and Boler, F. (2014). A geodetic platemotion and Global Strain Rate Model. *Geochemistry, Geophysics, Geosystems*, page 130.

Kristensen, M. B., Childs, C. J., and Korstgard, J. A. (2008). The 3D geometry of small-scale relay zones between normal faults in soft sediments. *Journal of Structural Geology*, 30(2):257–272.

Laó-Dávila, D. A., Al-Salmi, H. S., Abdelsalam, M. G., and Atekwana, E. A. (2015). Hierarchical segmentation of the Malawi Rift: The influence of inherited lithospheric heterogeneity and kinematics in the evolution of continental rifts. *Tectonics*, 34:2399–2417.

Larsen, P. H. (1988). Relay structures in a Lower Permian basement- involved extension system, East Greenland. *Journal of Structural Geology*, 10(1):3–8.

Laughton, A. S., Whitmash, R. B., and Jones, M. T. (1970). A discussion on the structure and evolution of the Red Sea and the nature of the Red Sea, Gulf of Aden and Ethiopia rift junction-The evolution of the Gulf of Aden. *Phil. Trans. R. Soc. Lond. A*, 267(1181):227–266.

Le Pichon, X. and Angelier, J. (1981). The Aegean Sea. *Phil. Trans. R. Soc. Lond. A*, 300(1454):357–372.

Lee, J.-c., Chu, H.-t., Angelier, J., Chan, Y.-c., Hu, J.-c., Lu, C.-y., and Rau, R.-j. (2002). Geometry and structure of northern surface ruptures of the 1999 Mw 7.6 Chi-Chi Taiwan earthquake : influence from inherited fold belt structures. *Journal of Structural Geology*, 24:173–192.

Lee, Y. H., Hsieh, M. L., Lu, S. D., Shih, T. S., Wu, W. Y., Sugiyama, Y., Azuma, T., and Kariya, Y. (2003). Slip vectors of the surface rupture of the 1999 Chi-Chi earthquake, western Taiwan. *Journal of Structural Geology*, 25(11):1917–1931.

Leonard, M. (2010). Earthquake Fault Scaling: Self-Consistent Relating of Rupture Length, Width, Average Displacement, and Moment Release. *Bulletin of the Seismological Society of America*, 100(5A):1971–1988.

Leopold, L. B. and Maddock, T. (1953). *The hydraulic geometry of stream channels and some physiographic implications*, volume 252. US Government Printing Office.

Lezzar, K. E., Tiercelin, J.-j., Turdu, C. L., Cohen, A. S., Reynolds, D. J., Gall, B. L., and Scholz, C. A. (2002). Control of normal fault interaction on the distribution of major Neogene sedimentary depocenters, Lake Tanganyika, East Africa rift. *The American Association of Petroleum Geologists*, 86(6):1027–1059.

Li, Z., Liu-Zeng, J., Almeida, R., Hubbard, J., Sun, C., and Yi, G. (2017). Re-evaluating seismic hazard along the southern Longmen Shan, China: Insights from the 1970 Dayi and 2013 Lushan earthquakes. *Tectonophysics*, 717(135):519–530.

Lin, A. (2002). Co-Seismic Strike-Slip and Rupture Length Produced by the 2001 Ms 8.1 Central Kunlun Earthquake. *Science*, 296(5575):2015–2017.

Lin, A., Sano, M., Wang, M., Yan, B., Bian, D., Fueta, R., and Hosoya, T. (2017). Paleoseismic study of the Kamishiro Fault on the northern segment of the Itoigawa–Shizuoka Tectonic Line, Japan. *Journal of Seismology*, 21(4):683–703.

Lin, J. and Stein, R. S. (2004). Stress triggering in thrust and subduction earthquakes and stress interaction between the southern San Andreas and nearby thrust and strike-slip faults. *Journal of Geophysical Research*, 109(B2):1–19.

Lindenfeld, M. and Rümpker, G. (2011). Detection of mantle earthquakes beneath the East African Rift. *Geophysical Journal International*, 186(1):1–5.

Lithgow-Bertelloni, C. and Silver, P. G. (1998). Dynamic topography, plate driving forces and the African superswell. *Nature*, 395(6699):269–272.

Liu-Zeng, J., Zhang, Z., Wen, L., Tapponnier, P., Sun, J., Xing, X., Hu, G., Xu, Q., Zeng, L., Ding, L., Ji, C., Hudnut, K. W., and van der Woerd, J. (2009). Co-seismic ruptures of the 12 May 2008, Ms8.0 Wenchuan earthquake, Sichuan: East-west crustal shortening on oblique, parallel thrusts along the eastern edge of Tibet. *Earth and Planetary Science Letters*, 286:355–370.

Long, J. J. and Imber, J. (2012). Strain compatibility and fault linkage in relay zones on normal faults. *Journal of Structural Geology*, 36:16–26.

Løseth, T. M., Ryseth, A. E., and Young, M. (2009). Sedimentology and sequence stratigraphy of the middle Jurassic Tarbert Formation, Oseberg South area (northern North Sea). *Basin Research*, 21(5):597–619.

Lozos, J. C., Oglesby, D. D., Brune, J. N., and Olsen, K. B. (2012). Small intermediate fault segments can either aid or hinder rupture propagation at stepovers. *Geophysical Research Letters*, 39(17):5–8.

Lozos, J. C., Oglesby, D. D., Brune, J. N., and Olsen, K. B. (2015). Rupture propagation and ground motion of strike-slip stepovers with intermediate fault segments. *Bulletin of the Seismological Society of America*, 105(1):387–399.

Luccio, F. D., Ventura, G., Giovambattista, R. D., Piscini, A., and Cinti, F. R. (2010). Normal faults and thrusts reactivated by deep fluids : The 6 April 2009 Mw 6.3 L 'Aquila earthquake , central Italy. *Journal of Geophysical Research*, 115(3):1–15.

Lunina, O. V., Andreev, A. V., and Gladkov, A. S. (2012). The Tsagan earthquake of 1862 on Lake Baikal revisited: A study of secondary coseismic soft-sediment deformation. *Russian Geology and Geophysics*, 53(6):594–610.

Lyons, R. P., Scholz, C. A., Buoniconti, M. R., and Martin, M. R. (2011). Late Quaternary stratigraphic analysis of the Lake Malawi Rift, East Africa: An integration of drill-core and seismic-reflection data. *Palaeogeography, Palaeoclimatology, Palaeoecology*, 303(1-4):20–37.

Macgregor, D. (2015). History of the development of the East African Rift System: A series of interpreted maps through time. *Journal of African Earth Sciences*, 101:232–252.

Machette, M., Personius, S., and Nelson, A. (1991). The Wasatch fault zone, Utah-segmentation and history of Holocene earthquakes. *Journal of Structural Geology*, 13(2):137–149.

Macheyeki, A., Mdala, H., Chapola, L., Manhiça, V., Chisambi, J., Feitio, P., Ayele, A., Barongo, J., Ferdinand, R., Ogubazghi, G., Goitom, B., Hlatywayo, J., Kianji, G., Marobhe, I., Mulowezi, A., Mutamina, D., Mwano, J., Shumba, B., and Tumwikirize, I. (2015). Active fault mapping in Karonga-Malawi after the December 19, 2009 Ms 6.2 seismic event. *Journal of African Earth Sciences*, 102(December 2009):233–246.

Macheyeki, A. S., Delvaux, D., Kervyn, F., Petermans, T., and Verbeeck, K. (2007). Occurrence of large earthquakes along the major Kanda fault system (Tanganyika-Rukwa rift, SW highlands of Tanzania). *Geophysical Research Abstracts,*, 9:9–10.

Mackenzie, D. and Elliott, A. (2017). Untangling tectonic slip from the potentially misleading effects of landform geometry. *Geosphere*, 13(4):1310–1328.

Maggi, A., Jackson, J., Mckenzie, D., and Priestley, K. (2000). Earthquake focal depths, effective elastic thickness, and the strength of the continental lithosphere. *Geology*, 28(6):495–498.

Manighetti, I., Campillo, M., Bouley, S., and Cotton, F. (2007). Earthquake scaling, fault segmentation, and structural maturity. *Earth and Planetary Science Letters*, 253:429–438.

Manighetti, I., Campillo, M., Sammis, C., Mai, P. M., and King, G. (2005). Evidence for self-similar, triangular slip distributions on earthquakes: Implications for earthquake and fault mechanics. *Journal of Geophysical Research B: Solid Earth*, 110(5):1–25.

Manighetti, I., Caulet, C., De Barros, D., Perrin, C., Cappa, F., and Gaudemer, Y. (2015). Generic along-strike segmentation of Afar normal faults, East Africa: Implications on fault growth and stress heterogeneity on seismogenic fault planes. *Geochem. Geophys. Geosyst.*, 16:443–467.

Manighetti, I., King, G. C. P., and Gaudemer, Y. (2001). Slip accumulation and lateral propagation of active normal faults in Afar. *Journal of Geophysical Research*, 106(B7):13,667–13,696.

Manighetti, I., Zigone, D., Campillo, M., and Cotton, F. (2009). Self-similarity of the largest-scale segmentation of the faults: Implications for earthquake behavior. *Earth and Planetary Science Letters*, 288:370–381.

Manyele, A. and Mwambela, A. (2014). Simulated PGA Shaking Maps for the Magnitude 6.8 Lake Tanganyika earthquake of December 5 , 2005 and the observed damages across South Western Tanzania. *International Journal of Scientific and Research Publications*, 4(6):1–5.

Manyozo, D. M., M'ndala, A. T., and Phiri, F. R. (1972). The Geology of the Lake Malombe area, Bulletin No. 33. *Bulletin of the Geological Survey, Malawi*, 33.

Martinez-Martinez, J. M., Booth-Rea, G., Azanon, J. M., and Torcal, F. (2006). Active transfer fault zone linking a segmented extensional system (Betics, southern Spain): Insight into heterogeneous extension driven by edge delamination. *Tectonophysics*, 422(1-4):159–173.

Masoud, A. a. and Koike, K. (2011). Auto-detection and integration of tectonically significant lineaments from SRTM DEM and remotely-sensed geophysical data. *ISPRS Journal of Photogrammetry and Remote Sensing*, 66(6):818–832.

Mats, V. D. (1993). The structure and development of the Baikal rift depression. *Earth-Science Reviews*, 34(2):81–118.

Mayer, L. (1982). *Quantitative Tectonic Geomorphology with Applications to Neotectonics of Northwestern Arizona*. PhD thesis, The University of Arizona.

McBeck, J. A., Madden, E. H., and Cooke, M. L. (2016). Growth by Optimization of Work (GROW): A new modeling tool that predicts fault growth through work minimization. *Computers & Geosciences*, 88:142–151.

McCalpin, J. P. (2009). *Paleoseismology*, volume 95. Academic press.

McClay, K. and Khalil, S. (1998). Extensional hard linkages, eastern Gulf of Suez, Egypt. *Geology*, 26(6):563–566.

McKenzie, D. (1972). Active Tectonics of the Mediterranean Region. *Geophysical Journal International*, 30(2):109–185.

McKenzie, D. (1978). Some remarks on the development of sedimentary basins. *Earth and Planetary science letters*, 40(1):25–32.

Mckenzie, D., Jackson, J., and Priestley, K. (2005). Thermal structure of oceanic and continental lithosphere. *Earth and Planetary Science Letters*, 233(3-4):337–349.

Meyer, B., Sébrier, M., and Dimitrov, D. (2007). Rare destructive earthquakes in Europe: The 1904 Bulgaria event case. *Earth and Planetary Science Letters*, 253(3-4):485–496.

Micarelli, L., Moretti, I., and Daniel, J. M. (2003). Structural properties of rift-related normal faults: the case study of the Gulf of Corinth, Greece. *Journal of Geodynamics*, 36(1-2):275–303.

Michetti, M. and Brunamonte, F. (1996). Trench investigations of the 1915 Fucino earthquake fault scarps (Abruzzo, central Italy): Geological evidence of large historical events. *Journal of Geophysical Research*, 101:5921–5936.

Middleton, T. A., Walker, R. T., Parsons, B., Lei, Q., Zhou, Y., and Ren, Z. (2016). A major, intraplate, normal-faulting earthquake: The 1739 Yinchuan event in northern China. *Journal of Geophysical Research B: Solid Earth*, 121(1):293–320.

Midzi, V., Hlatywago, D. J., Chapola, L. S., Kebede, F., Atakan, K., Lombe, D. K., Turyomurugyendo, G., and Tugume, F. A. (1999). Seismic hazard assessment in Eastern and Southern Africa. *Annali Di Geofisica*, 42(6):1067–1083.

Mildon, Z. K., Roberts, G. P., Faure Walker, J. P., Wedmore, L. N., and McCaffrey, K. J. (2016). Active normal faulting during the 1997 seismic sequence in Colfiorito, Umbria: Did slip propagate to the surface? *Journal of Structural Geology*, 91:102–113.

Mitchell, S. G., Matmon, A., Bierman, R., Enzel, Y., Caffee, M., and Rizzo, D. (2001). Displacement history of a limestone normal fault scarp, northern Israel, from cosmogenic 36Cl. *Journal of Geophysical Research*, 106:4247–4264.

Modisi, M., Atekwana, E., Kampunzu, A., and Ngwisanyi, T. (2000). Rift kinematics during the incipient stages of continental extension: Evidence from the nascent Okavango rift basin, northwest Botswana. *Geology*, 28(10):939.

Montgomery, D. R. and Brandon, M. T. (2002). Topographic controls on erosion rates in tectonically active mountain ranges. *Earth and Planetary Science Letters*, 201(3-4):481–489.

Morewood, N. C. and Roberts, G. P. (1999). Lateral propagation of the surface trace of the South Alkyonides normal fault segment, central Greece: Its impact on models of fault growth and displacement-length relationships. *Journal of Structural Geology*, 21(6):635–652.

Morewood, N. C. and Roberts, G. P. (2001). Comparison of surface slip and focal mechanism slip data along normal faults: An example from the eastern Gulf of Corinth, Greece. *Journal of Structural Geology*, 23:473–487.

Morley, C. (1999a). How successful are analogue models in addressing the influence of pre-existing fabrics on rift structure? *Journal of Structural Geology*, 21:1267–1274.

Morley, C. K. (1999b). Marked along-strike variations in dip of normal faults-the Lokichar fault, N. Kenya rift: A possible cause for metamorphic core complexes. *Journal of Structural Geology*, 21:479–492.

Morley, C. K. (2002). A tectonic model for the Tertiary evolution of strike-slip faults and rift basins in SE Asia. *Tectonophysics*, 347(4):189–215.

Morley, C. K. (2010). Stress re-orientation along zones of weak fabrics in rifts: An explanation for pure extension in 'oblique' rift segments? *Earth and Planetary Science Letters*, 297:667–673.

Morley, C. K., Haranya, C., Phoosongsee, W., Pongwapee, S., Kornsawan, A., and Wonganan, N. (2004). Activation of rift oblique and rift parallel pre-existing fabrics during extension and their effect on deformation style: Examples from the rifts of Thailand. *Journal of Structural Geology*, 26:1803–1829.

Morley, C. K., Nelson, R. A., Patton, T. L., and Munn, S. G. (1990). Transfer zones in the East African Rift system and their relevance to hydrocarbon exploration in rifts. *AAPG Bulletin*, 74(8):1234–1253.

Morley, C. K., Ngenoh, D. K., and Ego, J. K. (1999). Introduction to the East African Rift System. *Geoscience of Rift Systems - Evolution of East Africa*, 44:1–18.

Morley, C. K., Wescott, W. A., Stone, D. M., Harper, R. M., Wigger, S. T., and Karanja, F. M. (1992). Tectonic evolution of the northern Kenyan Rift. *Journal of the Geological Society*, 149(3):333–348.

Mougenot, D., Recq, M., Virlogeux P, and Lepvrier, C. (1986). Seaward extension of the East African Rift. *Nature*, 321(5):599–603.

Moussa, H. H. M. (2008). Spectral P-wave magnitudes, magnitude spectra and other source parameters for the 1990 southern Sudan and the 2005 Lake Tanganyika earthquakes. *Journal of African Earth Sciences*, 52(3):89–96.

Mueller, K. J. and Rockwell, T. K. (1995). Late Quaternary activity of the Laguna Salada fault in northern Baja California, Mexico. *Geological Society of America Bulletin*, 107(1):8–18.

Murray, J. and Segall, P. (2002). Testing time-predictable earthquake recurrence by direct measurement of strain accumulation and release. *Nature*, 14:287–291.

Murru, M., Taroni, M., Akinci, A., and Falcone, G. (2016). What is the impact of the August 24, 2016 Amatrice earthquake on the seismic hazard assessment in central Italy? *Annals of Geophysics*, 59.

Musson, R. M. W. (1996). The seismicity of the British Isles.

Naliboff, J. and Buiter, S. J. H. (2015). Rift reactivation and migration during multiphase extension. *Earth and Planetary Science Letters*, 421:58–67.

Nash, D. B. (1980). Morphologic dating of degraded normal fault scarps. *The Journal of Geology*, 88(3):353–360.

Nash, D. B. (1984). Morphologic dating of fluvial terrace scarps and fault scarps near West Yellowstone, Montana. *Geological Society of America Bulletin*, 95(12):1413–1424.

National Earthquake Information Centre (2018). *Preliminary Determination of Epicenters (PDE), a weekly and monthly publication, National Earthquake Information Center, U.S. Geological Survey, Golden, Colorado, 1971 to present.*

Nestola, Y., Storti, F., and Cavozzi, C. (2015). Strain rate-dependent lithosphere rifting and necking architectures in analog experiments. *Journal of Geophysical Research: Solid Earth*, 120:584–594.

Nicol, A., Walsh, J., Berryman, K., and Nodder, S. (2005). Growth of a normal fault by the accumulation of slip over millions of years. *Journal of Structural Geology*, 27:327–342.

Nicol, a., Walsh, J., Villamor, P., Seebeck, H., and Berryman, K. (2010). Normal fault interactions, paleoearthquakes and growth in an active rift. *Journal of Structural Geology*, 32(8):1101–1113.

Nivière, B. and Marquis, G. (2000). Evolution of terrace risers along the upper Rhine graben inferred from morphologic dating methods: Evidence of climatic and tectonic forcing. *Geophysical Journal International*, 141(3):577–594.

Nixon, C. W., McNeill, L. C., Bull, J. M., Bell, R. E., Gawthorpe, R. L., Henstock, T. J., Christodoulou, D., Ford, M., Taylor, B., Sakellariou, D., Ferentinos, G., Papatheodorou, G., Leeder, M. R., Collier, R. E., Goodliffe, A. M., Sachpazi, M., and Kranis, H. (2016). Rapid spatiotemporal variations in rift structure during development of the Corinth Rift, central Greece. *Tectonics*, 35:1225–1248.

Noda, H., Lapusta, N., and Kanamori, H. (2013). Comparison of average stress drop measures for ruptures with heterogeneous stress change and implications for earthquake physics. *Geophysical Journal International*, 193(3):1691–1712.

Nyblade, A. A. and Langston, C. A. (1995). East African earthquakes below 20 km depth and their implications for crustal structure. *Geophysical Journal International*, 121(1):49–62.

Nyblade, A. A. and Langston, C. A. (2002). Broadband seismic experiments probe the East African rift. *EOS, Transactions American Geophysical Union*, 83(37):405–409.

Okada, Y. (1992). Internal deformation due to shear and tensile faults in half-space. *Bulletin of the Seismological Society of America*, 82(2):1018–1040.

Ori, G. G. (1989). Geologic history of the extensional basin of the Gulf of Corinth (Miocene-Pleistocene), Greece. *Geology*, 17(10):918–921.

Otsuki, K. and Dilov, T. (2005). Evolution of hierarchical self-similar geometry of experimental fault zones : Implications for seismic nucleation and earthquake size. *Journal of Geophysical Research*, 110:1–9.

Ouchi, S. (1985). Response of Alluvial Rivers to Slow Active Tectonic Movement. *Geological Society of America Bulletin*, 96:504–515.

Palyvos, N., Pantosti, D., De Martini, P. M., Lemeille, F., Sorel, D., and Pavlopoulos, K. (2005). The Aigion-Neos Erineos coastal normal fault system (western Corinth Gulf Rift, Greece): Geomorphological signature, recent earthquake history, and evolution. *Journal of Geophysical Research B: Solid Earth*, 110(9):1–15.

Patane, D., Chiarabba, C., Cocina, O., De Gori, P., Moretti, M., and Boschi, E. (2002). Tomographic images and 3D earthquake locations of the seismic swarm preceding the 2001 Mt. Etna eruption: evidence for a dyke intrusion. *Geophysical Research Letters*, 29(10).

Paton, D. a. (2006). Influence of crustal heterogeneity on normal fault dimensions and evolution: southern South Africa extensional system. *Journal of Structural Geology*, 28(5):868–886.

Peacock, D. (2002). Propagation, interaction and linkage in normal fault systems. *Earth-Science Reviews*, 58:121–142.

Peacock, D. and Sanderson, D. (1991). Displacements, segment linkage and relay ramps in normal fault zones. *Journal of Structural Geology*, 13(6):721–733.

Peacock, D. C. P. and Parfitt, E. A. (2002). Active relay ramps and normal fault propagation on Kilauea Volcano, Hawaii. *Journal of Structural Geology*, 24(4):729–742.

Peacock, D. C. P. and Sanderson, D. J. (1994). Geometry and development of relay ramps in normal fault systems. *AAPG bulletin*, 78(2):147–165.

Peltzer, G., Crampé, F., Hensley, S., and Rosen, P. (2001). Transient strain accumulation and fault interaction in the Eastern California shear zone. *Geology*, 29(11):975–978.

Peltzer, G. and Rosen, P. (1995). Surface Displacement of the 17 May 1993 Eureka Valley, California, Earthquake Observed by SAR Interferometry. *Science*, 268(5215):1333–1336.

Pennacchioni, G. and Mancktelow, N. S. (2007). Nucleation and initial growth of a shear zone network within compositionally and structurally heterogeneous granitoids under amphibolite facies conditions. *Journal of Structural Geology*, 29(11):1757–1780.

Péron-Pinvidic, G., Manatschal, G., Minshull, T. A., and Sawyer, D. S. (2007). Tectonosedimentary evolution of the deep Iberia-Newfoundland margins: Evidence for a complex breakup history. *Tectonics*, 26(2).

Perrin, C., Manighetti, I., Ampuero, J.-p., Cappa, F., and Gaudemer, Y. (2016a). Location of largest earthquake slip and fast rupture controlled by along-strike change in fault structural maturity due to fault growth. *Journal of Geophysical Research: Solid Earth*, 121:3666–3685.

Perrin, C., Manighetti, I., and Gaudemer, Y. (2016b). Off-fault tip splay networks : A genetic and generic property of faults indicative of their long-term propagation. *Comptes Rendus Geoscience*, 348:52–60.

Peters, G. and van Balen, R. T. (2007). Tectonic geomorphology of the northern Upper Rhine Graben, Germany. *Global and Planetary Change*, 58:310–334.

Petit, C. and Deverchere, J. (2006). Structure and evolution of the Baikal rift: a synthesis. *Geochemistry, Geophysics, Geosystems*, 7(11).

Petit, C. and Ebinger, C. (2000). Flexure and mechanical behavior of cratonic lithosphere: Gravity models of the East African and Baikal rifts. *Journal of Geophysical Research*, 105(B8).

Philippon, M., Willingshofer, E., Sokoutis, D., Corti, G., Sani, F., Bonini, M., Cloetingh, S., and Pira, V. G. L. (2015). Slip re-orientation in oblique rifts. *Geology*, 43(2):1–4.

Phillips, T. B., Jackson, C. A., Bell, R. E., Duffy, O. B., and Fossen, H. (2016). Reactivation of intrabasement structures during rifting: A case study from offshore southern Norway. *Journal of Structural Geology*, 91:54–73.

Picazo, S., Müntener, O., Manatschal, G., Bauville, A., Karner, G., and Johnson, C. (2016). Mapping the nature of mantle domains in Western and Central Europe based on clinopyroxene and spinel chemistry: Evidence for mantle modification during an extensional cycle. *Lithos*, 266:233–263.

Pollack, H. N. and Chapman, D. S. (1977). On the regional variation of heat flow, geotherms, and lithospheric thickness. *Tectonophysics*, 38(3-4):279–296.

Pollard, D. D. and Segall, P. (1987). Theoretical displacements and stresses near fractures in rock: with applications to faults, joints, veins, dikes, and solution surfaces. *Fracture mechanics of rock*, 277(349):277–349.

Poulimenos, G. (2000). Scaling properties of normal fault populations in the western Corinth Graben, Greece: implications for fault growth in large strain settings. *Journal of Structural Geology*, 22(3):307–322.

Qi, W., Xuejun, Q., Qigui, L., Freymueller, J., Shaomin, Y., Caijun, X., Yonglin, Y., Xinzhao, Y., Kai, T., and Gang, C. (2011). Rupture of deep faults in the 2008 Wenchuan earthquake and uplift of the Longmen Shan. *Nature Geoscience*, 4(9):634–640.

Rattey, R. P. and Hayward, A. B. (1993). Sequence stratigraphy of a failed rift system: the Middle Jurassic to Early Cretaceous basin evolution of the Central and Northern North Sea. *Petroleum Geology of Northwest Europe: Proceedings of the 4th Conference*, pages 215–249.

Rawat, J. S. and Joshi, R. C. (2012). Remote-sensing and GIS-based landslide-susceptibility zonation using the landslide index method in Igo River Basin, Eastern Himalaya, India. *International Journal of Remote Sensing*, 33(12):3751–3767.

Reeve, M. T., Bell, R. E., Duffy, O. B., Jackson, C. A., and Sansom, E. (2015). The growth of non-colinear normal fault systems; What can we learn from 3D seismic reflection data? *Journal of Structural Geology*, 70:141–155.

Reif, D., Grasemann, B., and Faber, R. H. (2011). Quantitative structural analysis using remote sensing data: Kurdistan, northeast Iraq. *AAPG bulletin*, 95(6):941–956.

Ren, Z., Zhang, Z., Chen, T., Yan, S., Yin, J., Zhang, P., Zheng, W., Zhang, H., and Li, C. (2016). Clustering of offsets on the Haiyuan fault and their relationship to paleoearthquakes. *GSA Bulletin*, 128:3–18.

Ring, U. (1994). The influence of preexisting structure on the evolution of the Cenozoic Malawi rift (East African rift system). *Tectonics*, 13(2):313–326.

Ring, U., Betzler, C., Delvaux, D., Geowissenschaften, I., Mainz, U., and Mainz, D. (1992). Normal vs . strike-slip faulting during rift development in East Africa : The Malawi rift. *Geology*.

Roberts, S. and Jackson, J. (1991). Active normal faulting in central Greece: an overview. *Geological Society, London, Special Publications*, 56(1):125–142.

Rockwell, T. K., Lindvall, S., Dawson, T., Langridge, R., Lettis, W., and Klinger, Y. (2002). Lateral offsets on surveyed cultural features resulting from the 1999 Izmit and Duzce earthquakes, Turkey. *Bulletin of the Seismological Society of America*, 92(1):79–94.

Rodgers, D. W. and Little, T. A. (2006). World's largest coseismic strike-slip offset: The 1855 rupture of the Wairarapa Fault, New Zealand, and implications for displacement/length scaling of continental earthquakes. *Journal of Geophysical Research: Solid Earth*, 111(12):1–19.

Rosenbloom, N. A. and Anderson, R. S. (1994). Hillslope and channel evolution in a marine terraced landscape , Santa Cruz , California Abstract . A flight of marine terraces along California coastline provides a unique posits m tall decaying sea become rounded of the Five bedrock sueam channels to th. *Journal of Geophysical Research*, 99(94):13–14.

Rosendahl, B. (1987). Architecture of Continental Rifts with special reference to East Africa. *Annual Review of Earth and Planetary Sciences*, 15:445–503.

Rosendahl, B. R., Reynolds, D. J., Lorber, P. M., Burgess, C. F., McGill, J., Scott, D., Lambiase, J. J., and Derksen, S. J. (1986). Structural expressions of rifting: lessons from Lake Tanganyika, Africa. *Geological Society, London, Special Publications*, 25(1):29–43.

Rotevatn, A. and Bastesen, E. (2014). Fault linkage and damage zone architecture in tight carbonate rocks in the Suez Rift (Egypt): implications for permeability structure along segmented normal faults. *Geological Society, London, Special Publications*, 374(1):79–95.

Rothe, J. P. (1969). The Seismicity of the Earth 1953–1965, United National Educational, Scientific, and Cultural Organization.

Roux-mallouf, R. L., Ferry, M., Ritz, J.-f., Berthet, T., Cattin, R., and Drukpa, D. (2016). First paleoseismic evidence for great surface-rupturing earthquakes in the Bhutan Himalayas. *Journal of Geophysical Research Solid Earth*, 121:7271–7283.

Rubin, A. M. and Pollard, D. D. (1988). Dike-induced faulting in rift zones of Iceland and Afar. *Geology*, 16(5):413–417.

Rudnicki, J. W. (1980). Fracture Mechanics Applied to the Earth's Crust. *Annual Review of Earth and Planetary Sciences*, 8:489–525.

Sagy, A., Brodsky, E. E., and Axen, G. J. (2007). Evolution of fault-surface roughness with slip. *Geology*, 35(3):283–286.

Saria, E., Calais, E., Stamps, D. S., Delvaux, D., and Hartnady, C. J. H. (2014). Journal of Geophysical Research : Solid Earth Present-day kinematics of the East African Rift. *Journal of Geophysical Research: Solid Earth*, 119:3584–3600.

Savage, H. M. and Brodsky, E. E. (2011). Collateral damage: Evolution with displacement of fracture distribution and secondary fault strands in fault damage zones. *Journal of Geophysical Research*, 116:1–14.

Savitzky, A. and Golay, M. J. (1964). Smoothing and Differentiation of Data by Simplified Least Squares Procedures. *Analytical Chemistry*, 36(8):1627–1639.

Schlische, R. W., Young, S. S., Ackermann, R. V., and Gupta, A. (1996). Geometry and scaling relations of a population of very small rift: related normal faults. *Geology*, 24(8):683–686.

Scholz, C. (2002). *The mechanics of earthquakes and faulting*. Cambridge university press.

Scholz, C. A., Cohen, A. S., Johnson, T. C., King, J., Talbot, M. R., and Brown, E. T. (2011). Scientific drilling in the Great Rift Valley: The 2005 Lake Malawi Scientific Drilling Project - An overview of the past 145,000years of climate variability in Southern Hemisphere East Africa. *Palaeogeography, Palaeoclimatology, Palaeoecology*, 303(1-4):3–19.

Scholz, C. H. (1982). Scaling laws for large earthquakes: Consequences for physical models. *Bulletin of the Seismological Society of America*, 72(1):1–14.

Scholz, C. H. (1998). Earthquakes and friction laws. *Nature*, 391:37–42.

Scholz, C. H., Ando, R., and Shaw, B. E. (2010). The mechanics of first order splay faulting: The strike-slip case. *Journal of Structural Geology*, 32(1):118–126.

Scholz, C. H., Aviles, C. A., and Wesnousky, S. G. (1986). Scaling differences between large interplate and intraplate earthquakes. *Bulletin of the Seismological Society of America*, 76(1):65–70.

Schultz, R. a., Soliva, R., Fossen, H., Okubo, C. H., and Reeves, D. M. (2008). Dependence of displacement-length scaling relations for fractures and deformation bands on the volumetric changes across them. *Journal of Structural Geology*, 30(11):1405–1411.

Schwartz, D. P. and Coppersmith, K. J. (1984). Fault behavior and characteristic earthquakes: Examples from the Wasatch and San Andreas Fault Zones. *Journal of Geophysical Research*, 89:5681–5698.

Segall, P. and Pollard, D. D. (1980). Mechanics of discontinuous faults. *Journal of Geophysical Research: Solid Earth (1978–2012)*, 85:4337–4350.

Segall, P. and Pollard, D. D. (1983). Nucleation and growth of strike slip faults in granite. *Journal of Geophysical Research: Solid Earth (1978–2012)*, 88:555–568.

Seidl, M. A., Dietrich, W. E., and Kirchner, J. W. (1994). Longitudinal Profile Development into Bedrock: An Analysis of Hawaiian Channels. *The Journal of Geology*, 102(4):457–474.

Shafique, M., van der Meijde, M., and Ullah, S. (2011). Regolith modeling and its relation to earthquake induced building damage: A remote sensing approach. *Journal of Asian earth sciences*, 42:65–75.

Shaw, B. E. and Scholz, C. H. (2001). Slip-length scaling in large earthquakes: Observations and theory and implications for earthquake physics. *Geophysical Research Letters*, 28(15):2995–2998.

Shaw, P. R. and Lin, J. (1993). Causes and consequences of variations in faulting style at the Mid-Atlantic Ridge. *Journal of Geophysical Research: Solid Earth*, 98:21,839–21,851.

Shen, Z.-K., Sun, J., Zhang, P., Wan, Y., Wang, M., Bürgmann, R., Zeng, Y., Gan, W., Liao, H., and Wang, Q. (2009). Slip maxima at fault junctions and rupturing of barriers during the 2008 Wenchuan earthquake. *Nature Geoscience*, 2(10):718–724.

Sherman, S. I. (1992). Faults and tectonic stresses of the Baikal rift zone. *Tectonophysics*, 208(19921):297–307.

Shillington, D. J., Scott, C. L., Minshull, T. A., Edwards, R. A., Brown, P. J., and White, N. (2009). Abrupt transition from magma-starved to magma-rich rifting in the eastern Black Sea. *Geology*, 37(1):7–10.

Shimazaki, K. (1986). Small and large earthquakes: the effects of the thickness of seismogenic layer and the free surface. *Earthquake source mechanics*, pages 209–216.

Shipton, Z. K., Meghraoui, M., and Monro, L. (2017). Seismic slip on the west flank of the upper rhine graben (france-germany): Evidence from tectonic morphology and cataclastic deformation bands. *Geological Society Special Publication*, 432(1):147–161.

Siart, C., Bubenzer, O., and Eitel, B. (2009). Combining digital elevation data (SRTM/ASTER), high resolution satellite imagery (Quickbird) and GIS for geomorphological mapping: A multi-component case study on Mediterranean karst in Central Crete. *Geomorphology*, 112(1-2):106–121.

Sieh, K., Jones, L., Hauksson, E., Hudnut, K., Eberhart-Phillips, D., Heaton, T., Hough, S., Hutton, K., Kanamori, H., Lilje, A., Lindvall, S., McGill, S. F., Mori, J., Rubin, C., Spotila, J. a., Stock, J., Thio, H. K., Treiman, J., Wernicke, B., and Zachariasen, J. (1993). Near-field investigations of the landers earthquake sequence, april to july 1992. *Science*, 260(5105):171–176.

Sieh, K. E. (1978). Slip along the San Andreas fault associated with the great 1857 earthquake. *Bulletin of the Seismological Society of America*, 68(5):1421–1448.

Slemmons, D. B. (1957). Geological effects of the Dixie Valley-Fairview Peak Nevada, Earthquakes of December 16, 1954. *Bulletin of the Seismological Society of America*, 47(1934):353–357.

Smith, T. R. and Bretherton, F. P. (1972). Stability and the Conservation of Mass in Drainage Basin Evolution. *Water Resources Research*, 8(6):1506–1529.

Soliva, R. and Benedicto, A. (2004). A linkage criterion for segmented normal faults. *Journal of Structural Geology*, 26(12):2251–2267.

Soliva, R. and Benedicto, A. (2005). Geometry, scaling relations and spacing of vertically restricted normal faults. *Journal of Structural Geology*, 27(2):317–325.

Sonder, L. J. and England, P. (1989). Effects of a temperature-dependent rheology on large-scale continental extension. *Journal of Geophysical Research*, 94(B6):7603–7619.

Specht, T. D. and Rosendahl, B. R. (1989). Architecture of the Lake Malawi Rift, East Africa. *Journal of African Earth Sciences*, 8:355–382.

Stamps, D. S., Calais, E., Saria, E., Hartnady, C., Nocquet, J.-M., Ebinger, C. J., and Fernandes, R. M. (2008). A kinematic model for the East African Rift. *Geophysical Research Letters*, 35(5):1–6.

Stamps, D. S., Iaffaldano, G., and Calais, E. (2015). Role of mantle flow in Nubia-Somalia plate divergence. *Geophysical Research Letters*, 42(2):290–296.

Stefatos, A., Papatheodorou, G., Ferentinos, G., Leeder, M., and Collier, R. (2002). Seismic reflection imaging of active offshore faults in the Gulf of Corinth: their seismotectonic significance. *Basin Research*, 14(4):487–502.

Stein, R. S. (1999). The role of stress transfer in earthquake occurrence. *Nature*, 402(6762):605–609.

Stein, R. S., Barka, A. A., and Dieterich, J. H. (1997). Earthquake Stress Triggering. *Geophysical Journal International*, 128:594–604.

Stein, S. and Liu, M. (2009). Long aftershock sequences within continents and implications for earthquake hazard assessment. *Nature*, 462(7269):87–89.

Stewart, I. S. and Hancock, P. L. (1990). What is a fault scarp. *Episodes*, 13(4):256–263.

Stewart, N., Gaudemer, Y., Manighetti, I., Serreau, L., Vincendeau, A., Dominguez, S., Mattéo, L., and Malavieille, J. (2017). "3D_Fault_Offsets", a Matlab code to automatically measure lateral and vertical fault offsets in topographic data; application to San Andreas, Owens Valley and Hope faults. *Journal of Geophysical Research: Solid Earth*, 123:1–21.

Stirling, M., Rhoades, D., and Berryman, K. (2002). Comparison of earthquake scaling relations derived from data of the instrumental and preinstrumental era. *Bulletin of the Seismological Society of America*, 92(2):812–830.

Stucchi, M., Meletti, C., Montaldo, V., Crowley, H., Calvi, G. M., and Boschi, E. (2011). Seismic hazard assessment (2003-2009) for the Italian building code. *Bulletin of the Seismological Society of America*, 101(4):1885–1911.

Sun, C., Wan, T., Xie, X., Shen, X., and Liang, K. (2016). Knickpoint series of gullies along the Luoyunshan Piedmont and its relation with fault activity since late Pleistocene. *Geomorphology*, 268:266–274.

Swan, F. H., Schwartz, D. P., and Cluff, L. S. (1980). Recurrence of Moderate to Large Magnitude Earthquakes Produced by Surface Faulting on the Wasatch Fault Zone, Utah. *Bulletin of the Seismological Society of America*, 70(5):1431–1462.

Talebian, M., Copley, A. C., Fattahi, M., Ghorashi, M., Jackson, J. A., Nazari, H., Sloan, R. A., and Walker, R. T. (2016). Active faulting within a megacity: The geometry and slip rate of the Pardisan thrust in central Tehran, Iran. *Geophysical Journal International*, 207(3):1688–1699.

Taylor, S. K., Bull, J. M., Lamarche, G., and Barnes, P. M. (2004). Normal fault growth and linkage in the Whakatane Graben, New Zealand, during the last 1.3 Myr. *Journal of Geophysical Research: Solid Earth*, 109:1–22.

Thatcher, W., Foulger, G. R., Julian, B. R., Svarc, J., Quilty, E., and Bawden, G. W. (1999). Present-Day Deformation Across the Basin and Range Province, Western United States. *Science*, 283(5408):1714–1718.

Theilen-Willige, B. (2010). Detection of local site conditions influencing earthquake shaking and secondary effects in Southwest-Haiti using remote sensing and GIS-methods. *Natural Hazards and Earth System Sciences*, 10(6):1183.

Tibaldi, A., Bonali, F. L., and Pasquaré Mariotto, F. A. (2016). Interaction between Transform Faults and Rift Systems: A Combined Field and Experimental Approach. *Frontiers in Earth Science*, 4(April):1–18.

Tirel, C., Brun, J. P., and Sokoutis, D. (2006). Extension of thickened and hot lithospheres: Inferences from laboratory modeling. *Tectonics*, 25(1):1–13.

Toda, S., Lin, J., and Stein, R. S. (2011). Using the 2011 Mw 9.0 off the Pacific coast of Tohoku Earthquake to test the Coulomb stress triggering hypothesis and to calculate faults brought closer to failure. *Earth, Planets and Space*, 63(7):725–730.

Tommasi, A. and Vauchez, A. (2001). Continental rifting parallel to ancient orogenic belts: an effect of the mechanical anisotropy of the lithospheric mantle. *Earth and Planetary Science Letters*, 185:199–210.

Torabi, A. and Berg, S. S. (2011). Scaling of fault attributes: A review. *Marine and Petroleum Geology*, 28(8):1444–1460.

Torizin, J., Jentzsch, G., Malischewsky, P., Kley, J., Abakanov, N., and Kurskeev, A. (2009). Rating of seismicity and reconstruction of the fault geometries in northern Tien Shan within the project "Seismic Hazard Assessment for Almaty". *Journal of Geodynamics*, 48(3-5):269–278.

Toutin, T. (2008). ASTER DEMs for geomatic and geoscientific applications: a review. *International Journal of Remote Sensing*, 29(7):1855–1875.

Tronin, a. a. (2006). Remote sensing and earthquakes: A review. *Physics and Chemistry of the Earth*, 31:138–142.

Trudgill, B. and Cartwright, J. (1994). Relay-ramp forms and normal-fault linkages, Canyonlands National Park, Utah. *Geological Society of America Bulletin*, 106(9):1143–1157.

Tucker, G. E., McCoy, S. W., Whittaker, A. C., Roberts, G. P., Lancaster, S. T., and Phillips, R. (2011). Geomorphic significance of postglacial bedrock scarps on normal-fault footwalls. *Journal of Geophysical Research: Earth Surface*, 116(1):1–14.

Tuttle, M. P., Schweig, E. S., Sims, J. D., Lafferty, R. H., Wolf, L. W., and Haynes, M. L. (2002). The earthquake potential of the New Madrid seismic zone. *Bulletin of the Seismological Society of America*, 92(6):2080–2089.

Twiss, R. J. and Unruh, J. R. (1998). Analysis of fault slip inversions: Do they constrain stress or strain rate? *Journal of Geophysical Research: Solid Earth*, 103:12,205–12,222.

Ullah, S., Bindi, D., Pilz, M., Danciu, L., Weatherill, G., Zuccolo, E., Ischuk, A., Mikhailova, N. N., Abdrakhmatov, K., and Parolai, S. (2015). Probabilistic seismic hazard assessment for Central Asia. *Annals of Geophysics*, 58(1).

U.S. Department of the Interior, Geological Survey and U.S. Department of Commerce, N. O. and Administration, A. (1986). *United States Earthquakes, Annual publication, published 1928-1986. vol.s for 1928-1965 issued by the U.S. Coast and Geodetic Survey; volumes for 1966-1969 issued by the National Earthquake Information Center; volume for 1970 issued by the National Geophy*.

van Der Zee, W., Wibberley, C., and Urai, J. (2008). The influence of layering and pre-existing joints on the development of internal structure in normal fault zones: the Lodève basin, France. *Geological Society, London, Special Publications*, 299:57–74.

Vanneste, K., Radulov, A., De Martini, P., Nikolov, G., Petermans, T., Verbeeck, K., Camelbeeck, T., Pantosti, D., Dimitrov, D., and Shanov, S. (2006). Paleoseismologic investigation of the fault rupture of the 14 April 1928 Chirpan earthquake (M 6.8), southern Bulgaria. *Journal of Geophysical Research: Solid Earth*, 111(B1).

Ventisette, C. D., Montanari, D., Sani, F., and Bonini, M. (2006). Basin inversion and fault reactivation in laboratory experiments. *Journal of Structural Geology*, 28:2067–2083.

Versfelt, J. and Rosendahl, B. (1989). Relationships between pre-rift structure and rift architecture in Lakes Tanganyika and Malawi, East Africa. *Nature*, 337(26):354–357.

Villamor, P. and Berryman, K. (2001). A late quaternary extension rate in the Taupo Volcanic Zone, New Zealand, derived from fault slip data. *New Zealand Journal of Geology and Geophysics*, 44(2):243–269.

Vittori, E., Delvaux, D., and Kervyn, F. (1997). Kanda fault: A major seismogenic element west of the Rukwa Rift (Tanzania, East Africa). *Journal of Geodynamics*, 24:139–153.

Walker, R. T., Wegmann, K. W., Bayasgalan, A., Carson, R. J., Elliott, J., Fox, M., Nissen, E., Sloan, R. A., Williams, J. M., and Wright, E. (2015). The Egiin Davaa prehistoric rupture, central Mongolia: a large magnitude normal faulting earthquake on a reactivated fault with little cumulative slip located in a slowly deforming intraplate setting. *Seismicity, Fault Rupture and Earthquake Hazards in Slowly Deforming Regions*, 432:187–212.

Wallace, R. (1977). Profiles and ages of young fault scarps, north-central Nevada. *Geological Society of America Bulletin*, 88:1267–1281.

Wallace, R. (1989). Fault plane segmentation in brittle crust and anisotropy in loading system, in Fault Segmentation and Controls of Rupture Initiation and Termination, edited by D.P. Schwartz and R.H. Sibson. *U.S. Geol. Survey*, pages 400–408.

Wallace, R. E. (1968). Notes on stream channels offset by the San Andreas fault, southern Coast Ranges, California. In *Conference on Geologic Problems of the San Andreas Fault System. Stanford University Publication in Geological Sciences*, volume 11, pages 6–21.

Wallace, R. E. (1984a). *Fault scarps formed during the earthquakes of October 2, 1915, in Pleasant Valley, Nevada, and some tectonic implications*. US Government Printing Office.

Wallace, R. E. (1984b). Patterns and timing of late Quaternary faulting in the Great Basin province and relation to some regional tectonic features. *Journal of Geophysical Research: Solid Earth*, 89(B7):5763–5769.

Wallace, R. W. (1980). Degradation of the Hebgen Lake fault scarps of 1959. *Geology*, 8(5):225–229.

Walsh, J. J., Bailey, W. R., Childs, C., Nicol, A., and Bonson, C. G. (2003). Formation of segmented normal faults: A 3-D perspective. *Journal of Structural Geology*, 25(8):1251–1262.

Walsh, J. J., Nicol, A., and Childs, C. (2002). An alternative model for the growth of faults. *Journal of Structural Geology*, 24(11):1669–1675.

Walsh, J. J. and Watterson, J. (1987). Distributions of cumulative displacement and seismic slip on a single normal fault surface. *Journal of Structural Geology*, 9(8):1039–1046.

Walsh, J. J. and Watterson, J. (1988). Analysis of the relationship between displacements and dimensions of faults. *Journal of Structural Geology*, 10(3):239–247.

Walsh, J. J. and Watterson, J. (1990). New methods of fault projection for coalmine planning. *Proceedings of the Yorkshire Geological Society*, 42(2):209–219.

Walsh, J. J. and Watterson, J. (1991). Geometric and kinematic coherence and scale effects in normal fault systems. *Geological Society, London, Special Publications*, 56(1):193–203.

Walshaw, R. D. (1965). The geology of the Ncheu-Balaka area. *Bulletin of the Geological Survey, Malawi*, 19(96).

Walters, R. J., Elliott, J. R., D'agostino, N., England, P. C., Hunstad, I., Jackson, J. A., Parsons, B., Phillips, R. J., and Roberts, G. (2009). The 2009 L'Aquila earthquake (central Italy): A source mechanism and implications for seismic hazard. *Geophysical Research Letters*, 36(17).

Walters, R. J., Gregory, L. C., Wedmore, L. N. J., Craig, T. J., Elliott, J. R., Wilkinson, M. W., McCaffrey, K. J. W., Michetti, A., Vittori, E., and Livio, F. (2016). Insight on fault segmentation, linkage and hazard from the 2016 Mw6. 2 Amatrice earthquake (central Italy). In *AGU Fall Meeting Abstracts*.

Ward, N. I., Alves, T. M., and Blenkinsop, T. G. (2016). Reservoir leakage along concentric faults in the Southern North Sea: Implications for the deployment of CCS and EOR techniques. *Tectonophysics*, 690(PartA):97–116.

Ward, S. N. and Barrientos, S. E. (1986). An Inversion for Slip Distribution and Fault Shape from Geodetic Observations of the 1983, Borah Peak, Idaho, Earthquake. *Journal of Geophysical Research*, 91:4909–4919.

Watterson, J. (1986). Fault dimensions, displacements and growth. *Pure and Applied Geophysics*, 124:365–373.

Watts, A. and Burov, E. (2003). Lithospheric strength and its relationship to the elastic and seismogenic layer thickness. *Earth and Planetary Science Letters*, 213:113–131.

Wedmore, L., Gregory, L., Roberts, G., Wilkinson, M., McCaffrey, K., Faure Walker, J., Ferrario, F., Frigerio, C., Goddall, H., and Iezzi, F. (2017a). Co-seismic and shallow post-seismic slip during the 2016 central Italy earthquake sequence revealed by differential terrestrial laser scanning and photogrammetry. In *EGU General Assembly Conference Abstracts*, volume 19, page 13492.

Wedmore, L. N. J., Faure Walker, J. P., Roberts, G. P., Sammonds, P. R., McCaffrey, K. J. W., and Cowie, P. A. (2017b). A 667-year record of co-seismic and interseismic Coulomb stress changes in central Italy reveals the role of fault interaction in controlling irregular earthquake recurrence intervals. *Journal of Geophysical Research Solid Earth*, 122:1–21.

Wei, Z., Bi, L., Xu, Y., and He, H. (2015). Evaluating knickpoint recession along an active fault for paleoseismological analysis: The Huoshan Piedmont, Eastern China. *Geomorphology*, 235:63–76.

Wells, D. and Coppersmith, K. (1994). New empirical relationships among magnitude, rupture length, rupture width, rupture area, and surface displacement. *Bulletin of the Seismological Society of America*, 84(4):974–1002.

Wesnousky, S. G. (1986). Earthquakes, Quaternary faults, and seismic hazard in California. *Journal of Geophysical Research*, 91:12,587–12,631.

Wesnousky, S. G. (1988). Seismological and structural evolution of strike-slip faults.

Wesnousky, S. G. (2008). Displacement and geometrical characteristics of earthquake surface ruptures: Issues and implications for seismic-hazard analysis and the process of earthquake rupture. *Bulletin of the Seismological Society of America*, 98(4):1609–1632.

Westoby, M. J., Brasington, J., Glasser, N. F., Hambrey, M. J., and Reynolds, J. M. (2012). 'Structure-from-Motion' photogrammetry: A low-cost, effective tool for geoscience applications. *Geomorphology*, 179:300–314.

Wheeler, R. L. (1987). Boundaries between segments of normal faults: criteria for recognition and interpretation. In *Proceedings of conference XXXIX; Directions in Paleoseismology, US Geol Surv Open File Rep*, pages 385–398. Citeseer.

Whipp, P. S., Jackson, C. a. L., Gawthorpe, R. L., Dreyer, T., and Quinn, D. (2014). Normal fault array evolution above a reactivated rift fabric; a subsurface example from the northern Horda Platform, Norwegian North Sea. *Basin Research*, 26(4):523–549.

Whipp, P. S., Jackson, C. A.-L., Schlische, R. W., Withjack, M. O., and Gawthorpe, R. L. (2016). Spatial distribution and evolution of fault-segment boundary types in rift systems: observations from experimental clay models. *Geological Society, London, Special Publications*, 439:1–29.

Whittaker, A. C., Attal, M., Cowie, P. A., Tucker, G. E., and Roberts, G. (2008). Decoding temporal and spatial patterns of fault uplift using transient river long profiles. *Geomorphology*, 100(3-4):506–526.

Whittaker, A. C., Cowie, P. A., Attal, M., Tucker, G. E., and Roberts, G. P. (2007a). Bedrock channel adjustment to tectonic forcing: Implications for predicting river incision rates. *Geology*, 35(2):103–106.

Whittaker, A. C., Cowie, P. A., Attal, M., Tucker, G. E., and Roberts, G. P. (2007b). Contrasting transient and steady-state rivers crossing active normal faults: New field observations from the central apennines, Italy. *Basin Research*, 19(4):529–556.

Wibberley, C., Yielding, G., and Di Toro, G. (2008). Recent advances in the understanding of fault zone internal structure: a review. *Geological Society, London, Special Publications*, 299:5–33.

Wilcox, R. E., Harding, T. P. t., and Seely, D. R. (1973). Basic wrench tectonics. *Aapg Bulletin*, 57(1):74–96.

Willemse, E. J. M. (1997). Segmented normal faults: Correspondence between three-dimensional mechanical models and field data. *Journal of Geophysical Research*, 102:675–692.

Willemse, E. J. M. and Pollard, D. D. (1998). On the orientation and patterns of wing cracks and solution surfaces at the tips of a sliding flaw or fault. *Journal of Geophysical Research: Solid Earth*, 103:2427–2438.

Willemse, E. J. M., Pollard, D. D., and Aydin, A. (1996). Three-dimensional analyses of slip distributions on normal fault arrays with consequences for fault scaling. *Journal of Structural Geology*, 18:295–309.

Withjack, M. O. and Jamison, W. R. (1986). Deformation produced by oblique rifting. *Tectonophysics*, 126:99–124.

Wohl, E. E. (1993). Bedrock channel incision along Piccaninny Creek, Australia. *The Journal of Geology*, 101(6):749–761.

Wolfenden, E., Ebinger, C., Yirgu, G., Renne, P. R., and Kelley, S. P. (2005). Evolution of a volcanic rifted margin: Southern Red Sea, Ethiopia. *Geological Society of America Bulletin*, 117(7):846.

Worthington, R. P. and Walsh, J. J. (2016). Timing , growth and structure of a reactivated basin-bounding fault. *Geological Society, London, Special Publications*, 439:511–531.

Wright, T. J., Ebinger, C., Biggs, J., Ayele, A., Yirgu, G., Keir, D., and Stork, A. (2006). Magma-maintained rift segmentation at continental rupture in the 2005 Afar dyking episode. *Nature*, 442(7100):291–294.

Wu, D. and Bruhn, R. L. (1994). Geometry and kinematics of active normal faults, South Oquirrh Mountains, Utah: implication for fault growth. *Journal of Structural Geology*, 16(8):1061–1075.

Xu, S.-S., Nieto-Samaniego, a. F., Alaniz-Álvarez, S. a., and Velasquillo-Martínez, L. G. (2006). Effect of sampling and linkage on fault length and length–displacement relationship. *International Journal of Earth Sciences*, 95(5):841–853.

Yang, H., Chemia, Z., Artemieva, I. M., and Thybo, H. (2018). Control on off-rift magmatism: A case study of the Baikal Rift Zone. *Earth and Planetary Science Letters*, 482:501–509.

Yang, J., Guo, Z., and Cao, J. (1985). Investigation on the Holocene activities of the Helan mountain piedmont fault by use of geomorphological method. *Seismology and Geology (in Chinese with English abstract)*, 7(4):23–31.

Yang, Z. and Chen, W. (2010). Earthquakes along the East African Rift System: A multiscale, system-wide perspective. *Journal of Geophysical Research: Solid Earth*, 115:1–31.

Young, M. J., Gawthorpe, R. L., and Hardy, S. (2001). Growth and linkage of a segmented normal fault zone; the Late Jurassic Murchison-Statfjord North Fault, Northern North Sea. *Journal of Structural Geology*, 23(12):1933–1952.

Youngs, R. R. and Coppersmith, K. J. (1985). Implications of fault slip rates and earthquake recurrence models to probabilistic seismic hazard estimates. *Bulletin of the Seismological society of America*, 75(4):939–964.

Yu, L., Porwal, A., Holden, E.-J., and Dentith, M. C. (2011). Suppression of vegetation in multispectral remote sensing images. *International Journal of Remote Sensing*, 32(22):7343–7357.

Yuan, T. H., Feng, X. J., and Deng, B. Z. (1991). The 1556 Huaxian Earthquake. *Earthquake Press, China [in Chinese]*.

Zhang, B., Liao, Y., Guo, S., Wallace, R. E., Bucknam, R. C., and Hanks, T. C. (1986). Fault scarps related to the 1739 earthquake and seismicity of the Yinchuan graben, Ningxia huizu zizhiqu, China. *Bulletin of the Seismological Society of America*, 76(5):1253–1287.

Zhang, H. and Thurber, C. H. (2003). Double-difference tomography: The method and its application to the Hayward fault, California. *Bulletin of the Seismological Society of America*, 93(5):1875–1889.

Zhang, P., Slemmons, D. B., and Mao, F. (1991). Geometric pattern, rupture termination and fault segmentation of the Dixie Valley-Pleasant Valley active normal fault system, Nevada, U.S.A. *Journal of Structural Geology*, 13(2):165–176.

Zhang, P., Yang, Z.-x., Gupta, H. K., Bhatia, S. C., and Shedlock, K. M. (1999). Global Seismic Hazard Assessment Program (GSHAP) in continental Asia. *Annali Di Geofisica*, 42(6):1167–1190.

Zhao, S., Müller, R. D., Takahashi, Y., and Kaneda, Y. (2004). 3-D finite-element modelling of deformation and stress associated with faulting: Effect of inhomogeneous crustal structures. *Geophysical Journal International*, 157:629–644.

Zhou, Y., Ma, J., Walker, R. T., Feng, X., Song, X., and Parsons, B. (2014). Are we missing earthquakes? A new insight into the M 8 1556 Huaxian earthquake. In *AGU Fall Meeting Abstracts*.

Zhou, Y., Parsons, B., Elliott, J. R., Barisin, I., and Walker, R. T. (2015). Assessing the ability of Pleiades stereo imagery to determine height changes in earthquakes: A case study for the El Mayor-Cucapah epicentral area. *Journal of Geophysical Research B: Solid Earth*, 120(12):8793–8808.

Ziegler, P. A. (1975). Geologic evolution of North Sea and its tectonic framework. *AAPG Bulletin*, 59(7):1073–1097.

Zielke, O., Arrowsmith, J. R., Ludwig, L. G., and Akciz, S. O. (2012). High-resolution topography-derived offsets along the 1857 Fort Tejon earthquake rupture trace, San Andreas fault. *Bulletin of the Seismological Society of America*, 102(3):1135–1154.

Zielke, O., Klinger, Y., and Arrowsmith, J. R. (2015). Fault slip and earthquake recurrence along strike-slip faults - Contributions of high-resolution geomorphic data. *Tectonophysics*, 638(1):43–62.

Zielke, O. and Strecker, M. R. (2009). Recurrence of large earthquakes in magmatic continental rifts: Insights from a paleoseismic study along the Laikipia-Marmanet fault, Subukia Valley, Kenya rift. *Bulletin of the Seismological Society of America*, 99(1):61–70.

Ziv, A. and Rubin, A. M. (2000). Static stress transfer and earthquake triggering: No lower threshold in sight? *Journal of Geophysical Research*, 105:13,631–13,642.

Zoback, M. L., Thompson, G. A., and Anderson, R. E. (1981). Cainozoic evolution of the state of stress and style of tectonism of the Basin and Range province of the western United States. *Phil. Trans. R. Soc. Lond. A*, 300(1454):407–434.

Zorin, Y. A., Kozhevnikov, V. M., Novoselova, M. R., and Turutanov, E. K. (1989). Thickness of the lithosphere beneath the Baikal rift zone and adjacent regions. *Tectonophysics*, 168(4):327–337.

Appendix A

Glossary

This Appendix provides a list of the symbols used in this thesis, and their descriptions and units. To help the reader, the majority of symbols are used consistently throughout the entire thesis and relate to symbols used in the wider literature, i.e. δ will always refer to fault dip (Table A.1). However, due to a lack of relevant symbols, and to avoid overusing subscripts, some symbols are unique to each Chapter (see Tables A.2 to appA:table5). For example, it is common in this thesis that the symbols α, β, θ and ϕ are used for a variety of meanings. The only brief interchange between a symbols meaning within a Chapter is for W in Chapter 4, where (as it does for all other chapters) it means fault width in Section 4.8.2, but is used for scarp width in the algorithm (thus, the majority of the text).

Table A.1 A table of the common symbols used through this thesis.

Symbol	Description	Units
$\Delta\sigma_c$	Coulomb stress change	MPa
κt	Diffusion age	m^2
κ	Diffusion constant	m^2/kyr
D	Displacement (total)	m
D_{max}	Displacement (maximum)	m
D_s	Displacement (surface)	m
T_e	Elastic thickness	km
A	Fault area	m^2
δ	Fault dip	$^\circ$
L	Fault length	m
l	Fault rupture length	m
w	Fault rupture width	m
u	Fault slip	m
W	Fault width	m
x_s	Location of scarp crest	m
G	Modulus of rigidity	GPa
M_0	Moment	
M_W	Moment magnitude	
σ_n	Normal stress	MPa
v	Poissons ratio	
σ_1	Principal stress (maximum)	
σ_2	Principal stress (intermediate)	
σ_3	Principal stress (minimum)	
T_R	Return period	kyr
T_s	Seismogenic thickness	km
H	Scarp height	m
O	Segment overlap	m
S	Segment separation	m
τ_s	Shear stress	MPa
r	Slip rate	m/kyr
μ	Static stress coefficient	
σ	Standard deviation	
t	Time	kyr
E	Young's modulus	GPa

Table A.2 A table of the unique symbols used in Chapter 2.

Symbol	Description	Units
α	Acute angle between the strike of a linking fault and the strike of a fault segment	$^\circ$
θ	Angle between a line connecting segment tips and the strike of a fault segment	$^\circ$
β	Skempton's coefficient	

Table A.3 A table of the unique symbols used in Chapter 3.

Symbol	Description	Units
Z	Depth	m
α	Angle between scarp trend and strike of deep structure	$^\circ$
ϕ	Fault strike	$^\circ$

Table A.4 A table of the unique symbols used in Chapter 4.

Symbol	Description	Units
$\bar{H_m}$	Average scarp height misfit	m
$\bar{\alpha_m}$	Average scarp slope misfit	$^\circ$
$\bar{W_m}$	Average scarp width misfit	m
C	Count	
ϕ	Derivative of slope	$^\circ$/m
ϕ_T	Derivative of slope threshold	$^\circ$/m
d_h	Ditch height	m
d_n	Ditch number	
d_w	Ditch width	m
h_h	Hill height	m
h_n	Hill number	
h_w	Hill width	m
X	Horizontal component of displacement (heave)	m
β_l	Lower original surface slope	$^\circ$
x	Profile length	m
r	Resolution	
H_g	Scarp height ground-truth	m
H_m	Scarp height misfit	m
α	Scarp slope	$^\circ$
α_g	Scarp slope ground-truth	$^\circ$
α_m	Scarp slope misfit	$^\circ$
W_g	Scarp width ground-truth	m
W_m	Scarp width misfit	m
θ	Slope	$^\circ$
θ_T	Slope threshold	$^\circ$
ε	Total misfit	
β_u	Upper original surface slope	$^\circ$
v_h	Vegetation height	m
v_n	Vegetation number	
v_w	Vegetation width	m
Z	Vertical component of displacement (throw)	m

Table A.5 A table of the unique symbols used in Chapter 5.

Symbol	Description	Units
G_d	Gradient over a moving window size	
d	Gradient G_d window size	m
x^{obs}	Observed results for point x	
α	Slip-length ratio	
x^{syn}	Synthetic results for point x	

Appendix B

Coulomb stress change model results for rupture scenario

In Chapter 2, the static Coulomb stress change model results were presented only for selected inter-segment zone geometries. This Appendix presents the static Coulomb stress change model results for all geometries (see figs. B.1 and B.2). In addition, fig. B.3 shows a plot for natural observations of hard-linked normal faults from Table 2.1 against Coulomb model results normalised for: (a) the maximum segment length; and (b) the minimum segment length. All results in this Appendix are for a uniform slip distribution, for other slip distributions, refer to Appendix C.

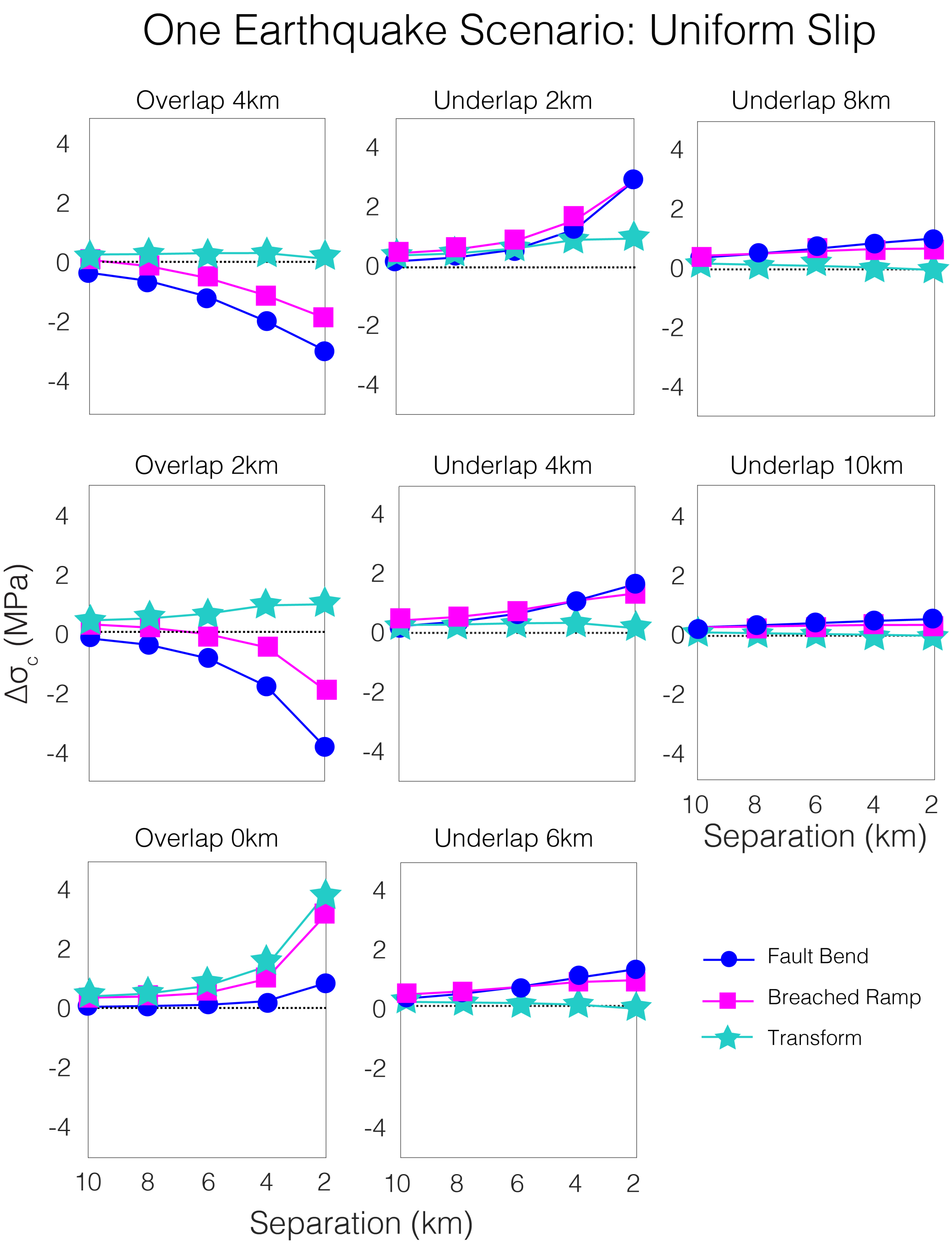

Fig. B.1 Link geometry $\Delta\sigma_c$ for the single segment rupture scenario and uniform slip distribution.

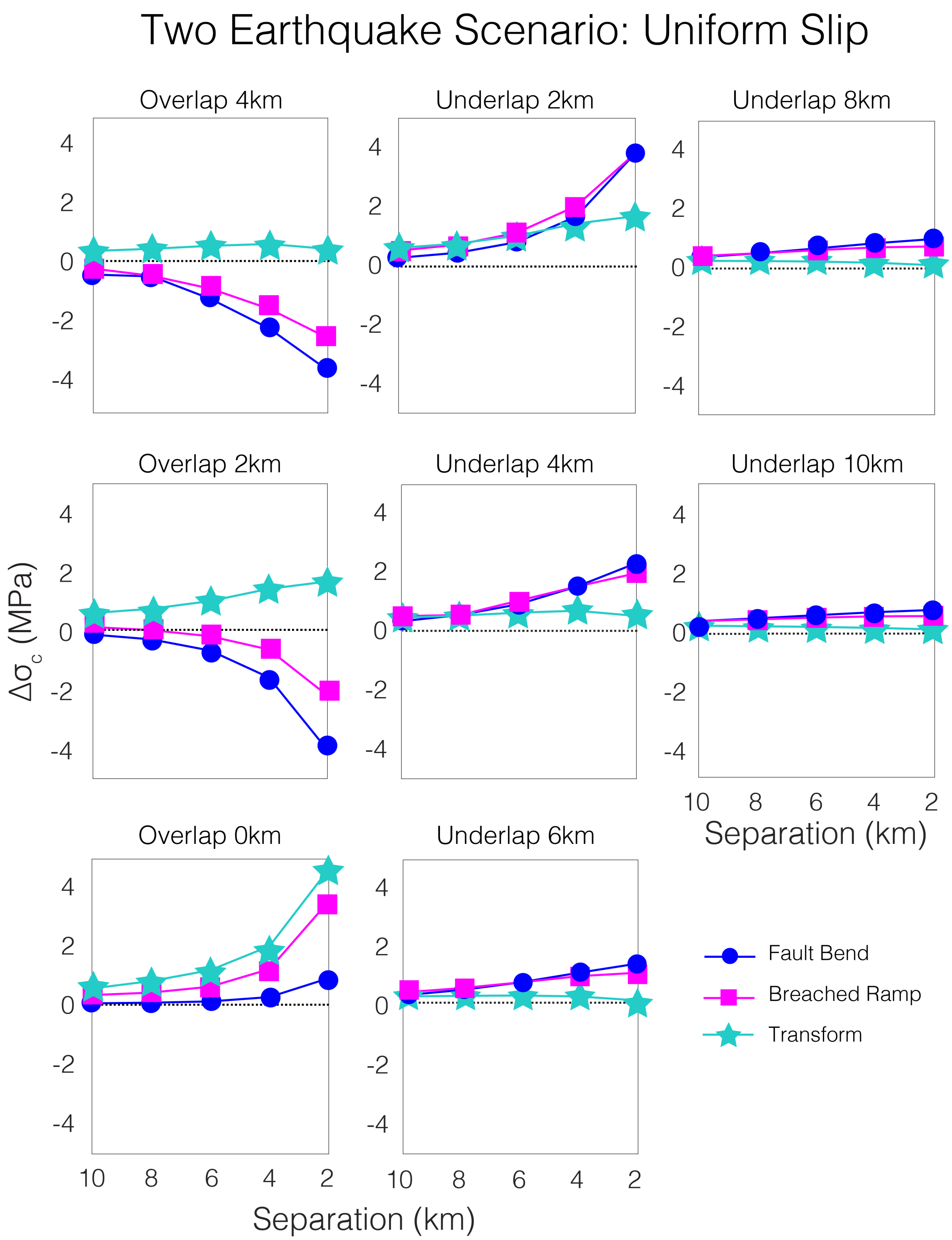

Fig. B.2 Link geometry $\Delta\sigma_c$ for the two segment rupture scenario and uniform slip distribution.

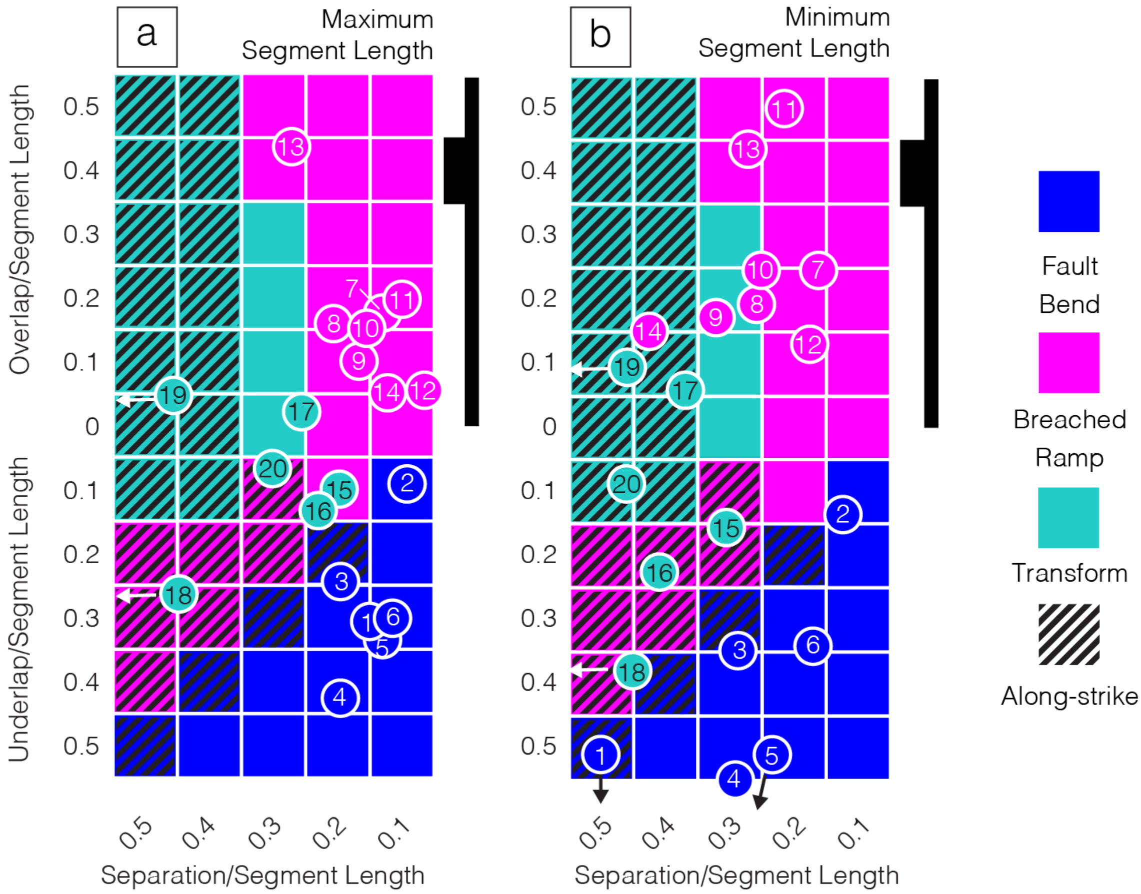

Fig. B.3 Natural observations of hard-links between normal faults from Table 1 (numbered) plotted against model predictions of preferred end-member link geometry. Model results are normalised to a single segment length (20 km), for the two segment rupture scenario, uniform slip distribution run (for tapered see Figure S10), and include the upper/lower breached ramp analysis (Figures S6,S7). Observed examples have been normalised to a) the maximum segment length and b) the minimum segment length. Black diagonal lines indicate that along-strike secondary faults are preferred to linking faults between en echelon faults. Observations that fall outside the model area are shown with an arrow.

Appendix C

Sensitivity test for Coulomb stress change model

This Appendix presents the static Coulomb stress change model results for a range of sensitivity tests described in Section 2.3.2 of Chapter 2: 1) slip distribution on, and between, fault segments; 2) linking fault location; 3) calculation depth; and 4) friction coefficient. Each is described below.

1. Figs. C.1 to C.2 show the Coulomb stress change for each linking fault style for all inter-segment zone geometries considered in the study using a tapered slip distribution, rather than a uniform slip distribution. Fig. C.3 is a comparison between model results for the two slip distributions. Comparisons between the model using the tapered slip distribution and natural observations are shown in fig. C.4, normalised to: a) total length of segments, b) maximum segment length and c) minimum segment length.

2. Fig. C.5 shows the Coulomb stress change for the entire inter-segment zone for four unique inter-segment zone geometries: a) 2 km overlap and 4 km separation; b) 2 km overlap and 6 km separation; c) 4 km overlap and 4 km separation; and d) 4 km overlap and 6 km separation. The linking fault geometry used here is the breached ramp geometry. Plots show that the greatest $\Delta\sigma_c$ does not occur at the centre of the intersegment zone (black circle), but toward the segment tips (red dashed circle). In Section 2.3.2 of Chapter 2, the largest $\Delta\sigma_c$ is taken within one parallel grid space of the zone centre (red solid circles). Fig. C.6 compares the results from the breached relay ramp location test (red circles, fig. C.5) to the results gained from the centre of the inter-segment zone (black circles, fig. C.5), and shows that the centre of the zone may not be the optimal location for a ramp to breach (i.e. the largest $\Delta\sigma_c$ is not found at the centre). The results are also compared against the transform fault linking geometry (blue stars), and show that the upper/lower breached ramp geometry may give a larger $\Delta\sigma_c$ than the transform fault geometry, especially a small segment separations.

3. As the model presented in Chapter 2 uses a fixed calculation depth, fig. C.7 shows the changes to $\Delta\sigma_c$ resulting from different calculation depths. Results show that the preferred linking fault style is not depth-dependent.

4. Finally, the model in the chapter uses a fixed friction coefficient μ of 0.4. We vary this in fig. C.8, which shows that the preferred linking style does not change with μ.

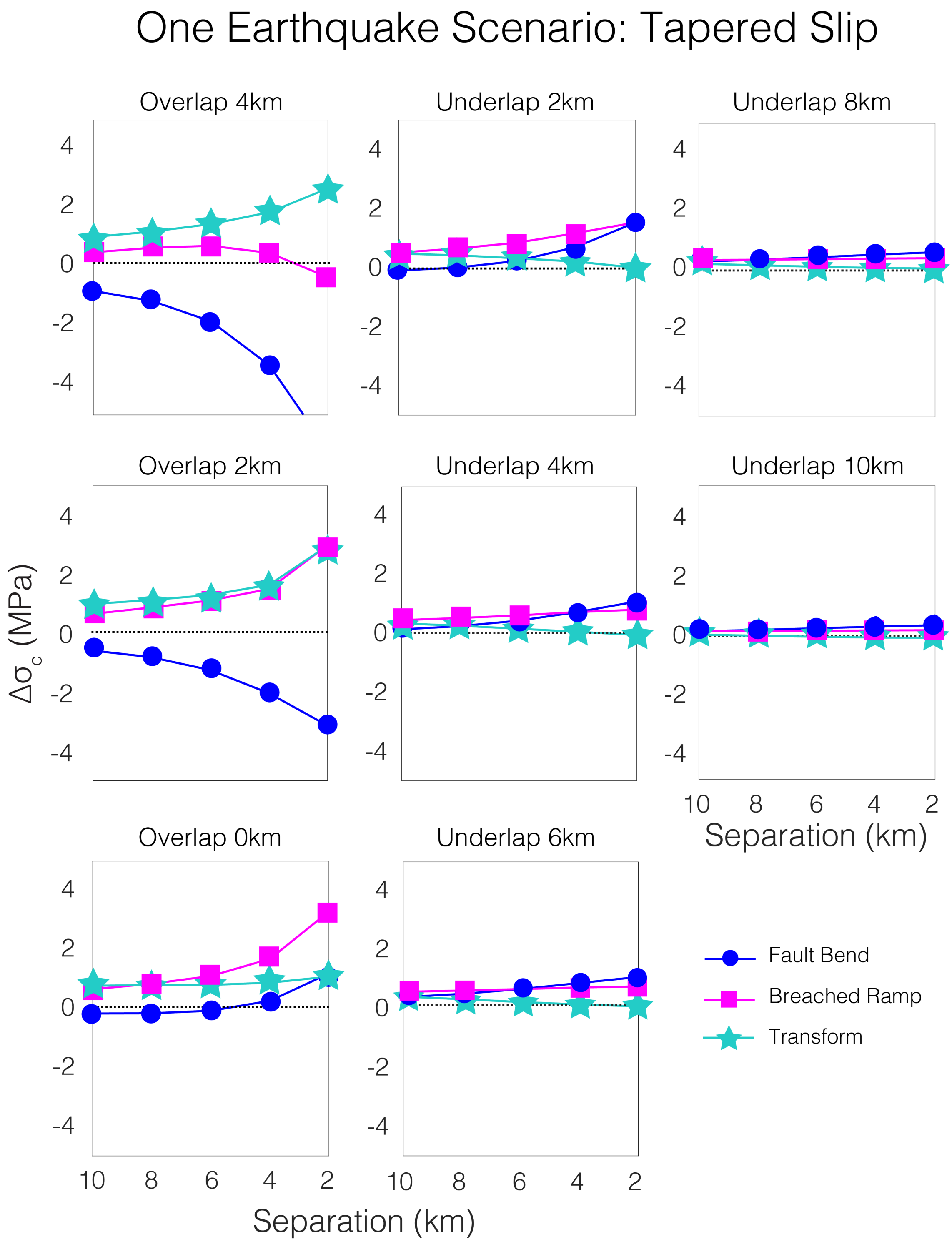

Fig. C.1 Link geometry $\Delta\sigma_c$ for the single segment rupture scenario and tapered slip distribution.

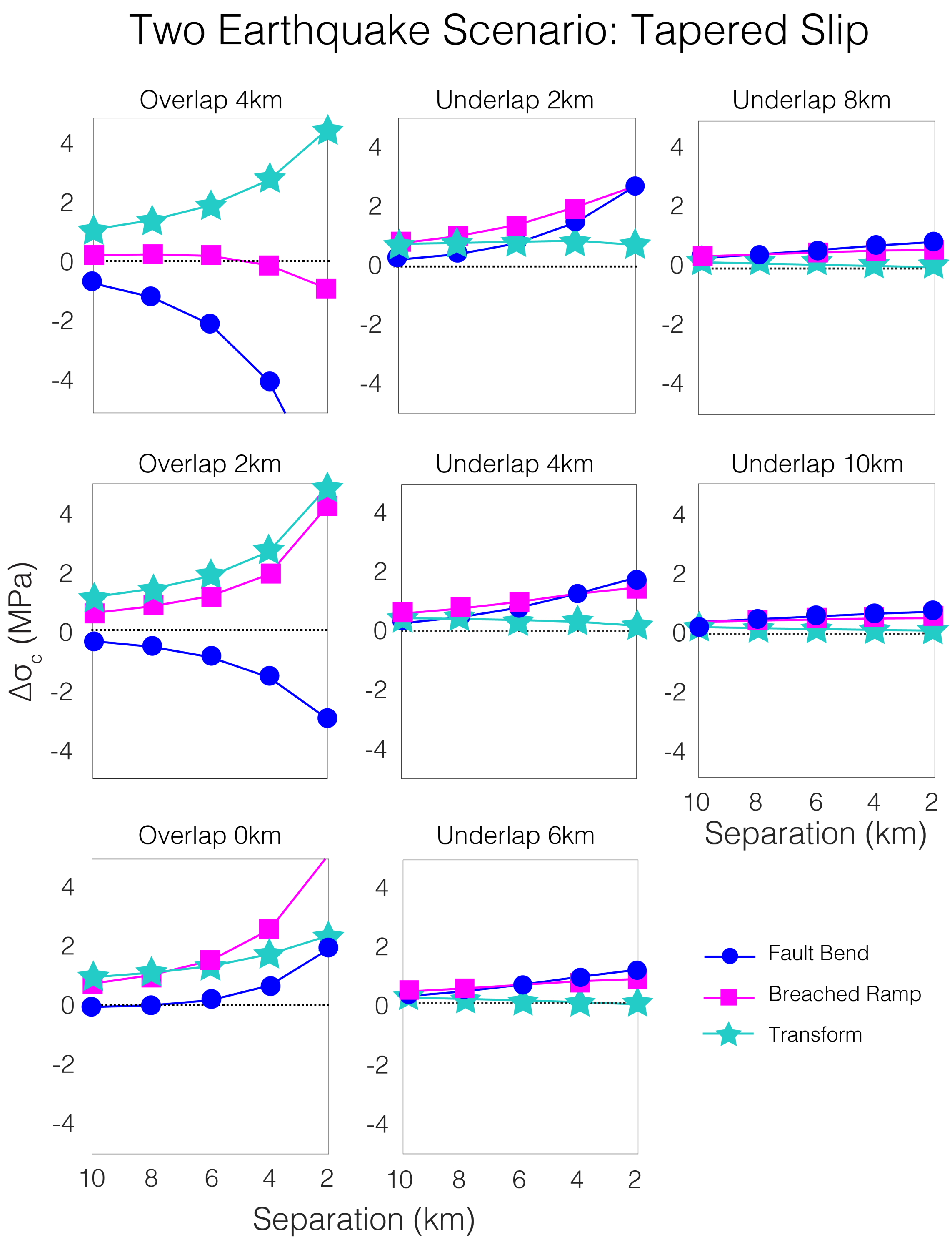

Fig. C.2 Link geometry $\Delta\sigma_c$ for the two segment rupture scenario and tapered slip distribution.

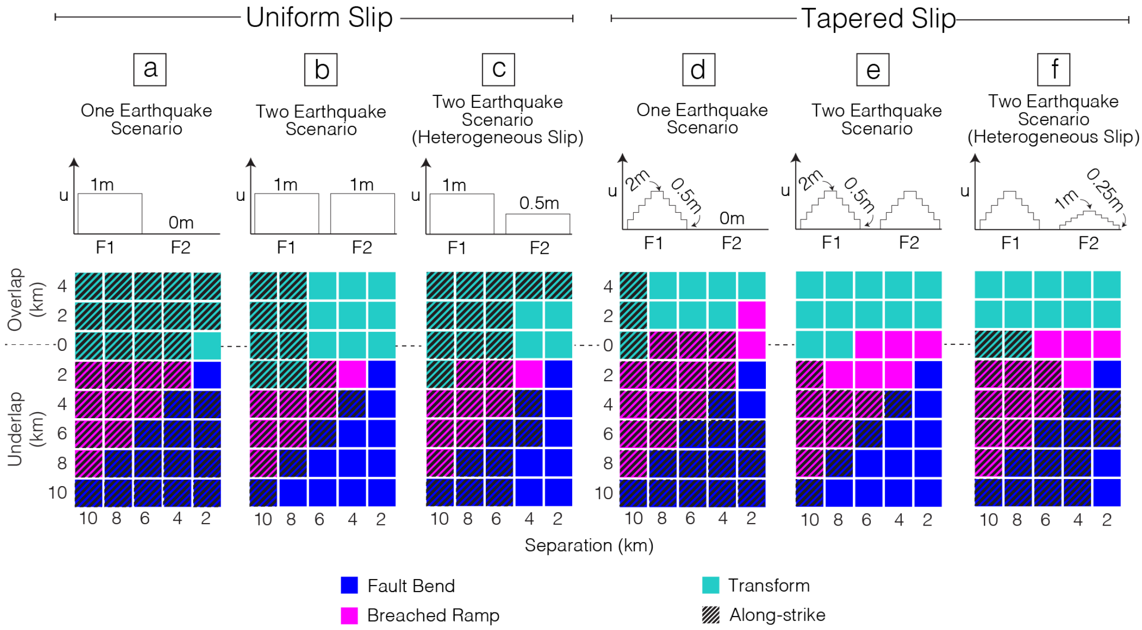

Fig. C.3 a) Along-strike secondary fault $\Delta\sigma_c$ compared to en echelon link geometry $\Delta\sigma_c$ for the single and two segment rupture scenarios. Diagonal black lines denote the along-strike secondary fault $\Delta\sigma_c$ magnitude was larger. b) Tapered slip distribution $\Delta\sigma_c$ including along-strike fault analysis.

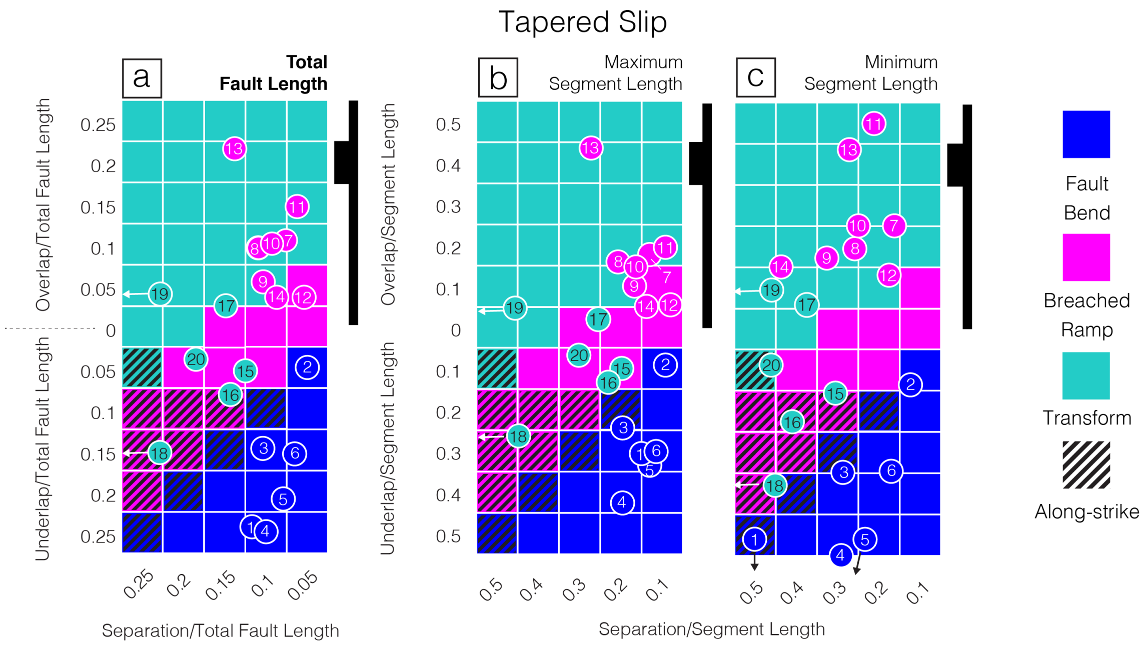

Fig. C.4 Observed examples using a) total length of segments, b) maximum segment length and c) minimum segment length, versus model results using the tapered slip distribution.

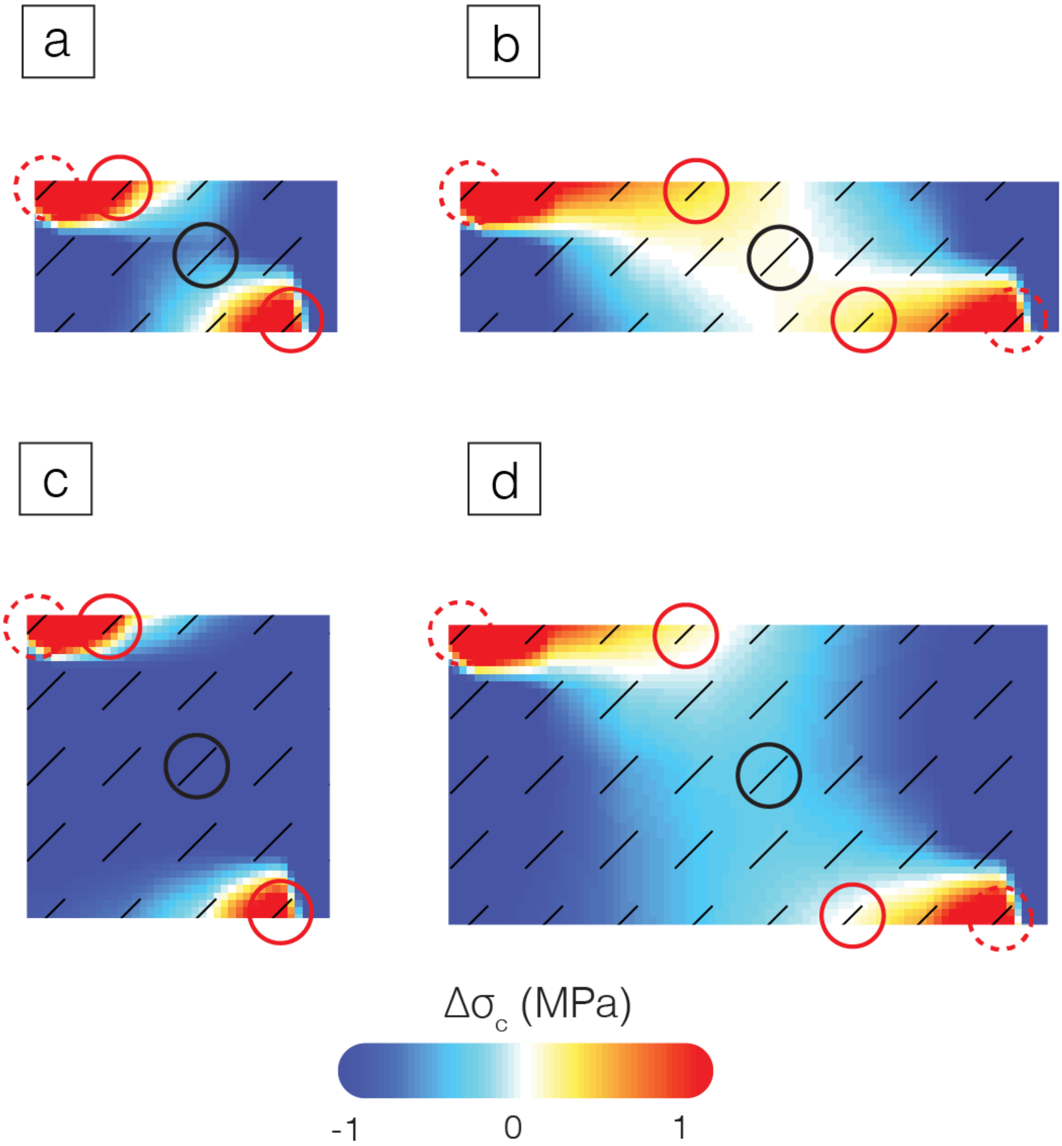

Fig. C.5 Examples of $\Delta\sigma_c$ for optimal breached ramp location analysis: a) 2 km overlap and 4 km separation; b) 2 km overlap and 6 km separation; c) 4 km overlap and 4 km separation; and d) 4 km overlap and 6 km separation. Results indicate that the centre of the relay ramp (black circles) do not experience the greatest $\Delta\sigma_c$ within the relay ramp. The largest $\Delta\sigma_c$ is found near the fault segment tips (red dashed circles). The largest $\Delta\sigma_c$ within 1 km strike-perpendicular distance from the centre of the relay ramp is found either at the top or the bottom of the relay ramp (red solid circles).

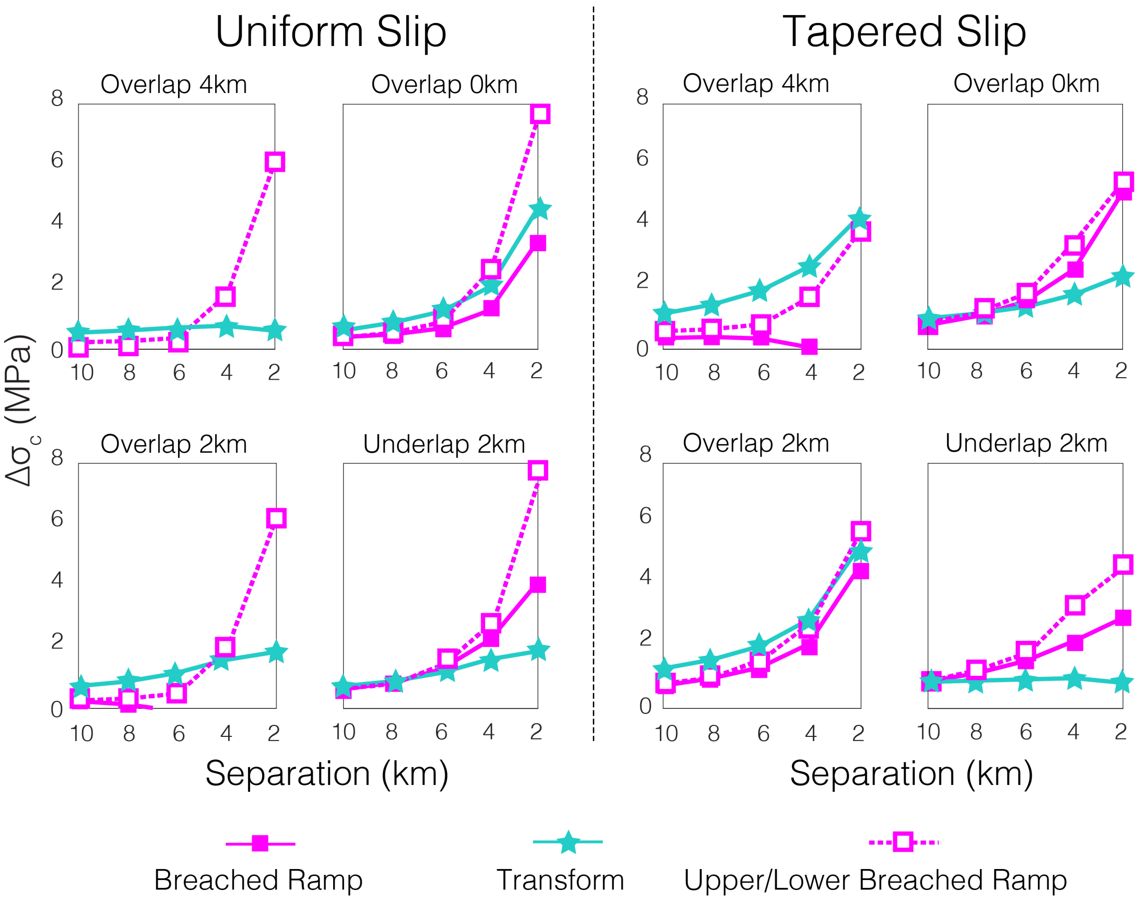

Fig. C.6 Link geometry $\Delta\sigma_c$ for upper/lower breached ramp.

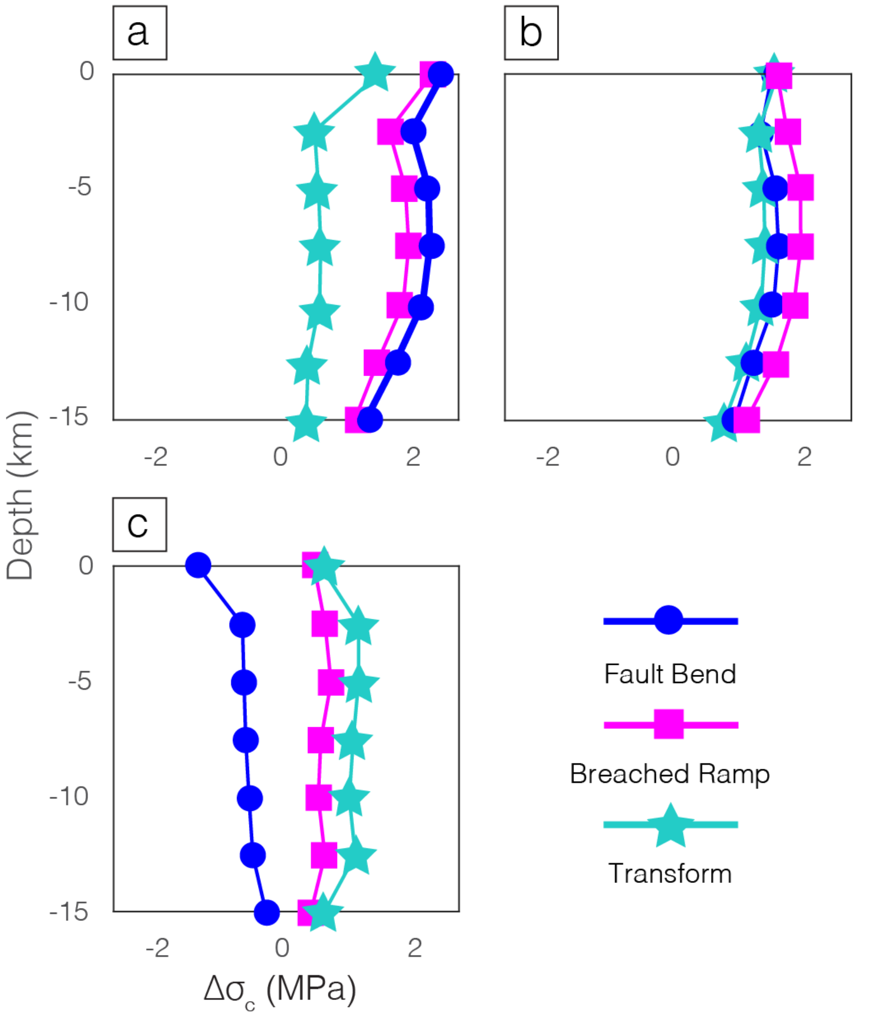

Fig. C.7 Coulomb stress change for depths between 0 km and 15 km at 2.5 km intervals. The same geometries as fig. 2.7 have been considered in order to analyse any changes in preferred link geometry: a) 4 km underlap and 2 km separation; b) 2 km underlap and 4 km separation; c) 2 km overlap and 6 km separation. The $\Delta\sigma_c$ magnitude increases toward the centre of the fault plane. The preferred link type does not change with depth, indicating that results from 10 km can be used to infer preferred surface linking fault geometry.

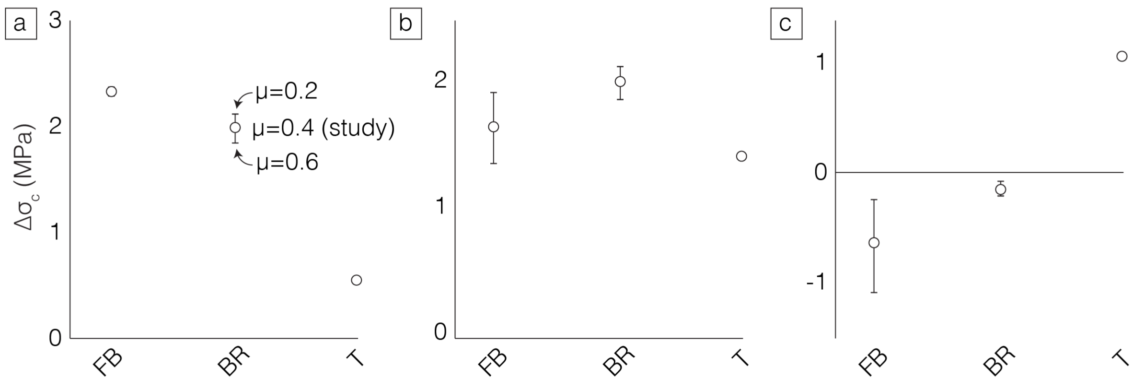

Fig. C.8 Coulomb stress change for friction coefficient μ 0.2-0.6 using examples from fig. 2.7.

Appendix D

Individual scarp profiles for the Bilila-Mtakataka fault

In this Appendix we present the individual scarp profiles used in Chapters 3 and 5 used to undertake a morphological analysis of the BMF fault scarp. Figs. D.1 to D.26 show the scarp profiles taken from a 12 m TanDEM-X DEM for a manual morphological analysis in Chapter 3. For each, the top and bottom of the scarp (red circles) was picked manually during three separate runs. Once the top and bottom of the scarp has been picked, a regression line is fitted to the upper and lower surfaces (dotted line). The profiles show the inaccuracies of manually-picking a scarp top and bottom, and how these can inaccuracies can propagate into scarp height and width calculations.

In Chapter 5 a sub-metre DEM was used to identify multiple rupture markers along a scarp profile. Figs. D.27 show the 39 profiles selected. As the signal-to-noise ratio was poor on each, each profile was filtered using the *rloess* function in MATLAB at a window size of 15 m. The smoothed profiles are shown in fig. D.28. Each has been categorized either as: (i) a degraded scarp (DEG), where only a single rupture surface could be identified; (ii) a composite scarp (CMP), where a change in slope denotes a younger rupture at the centre of the scarp; or (iii) a multi-scarp (MLT), where a clear break in slope separates individual scarps. The number of breaks or changes in slope denote the minimum number of ruptures.

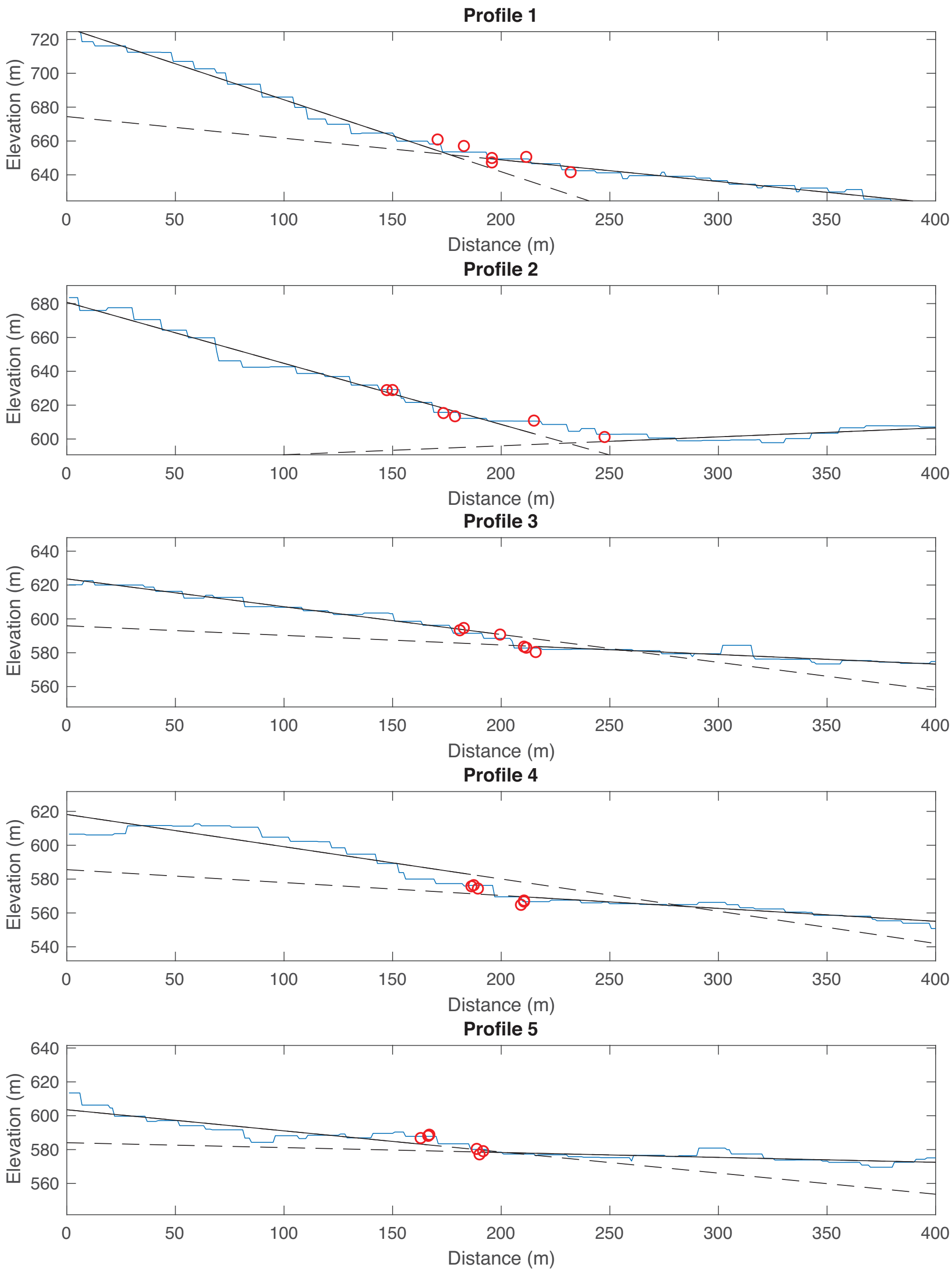

Fig. D.1 Profile 1 to Profile 5. Manual scarp picks (red circles) and regression lines fitted to the upper and lower surfaces.

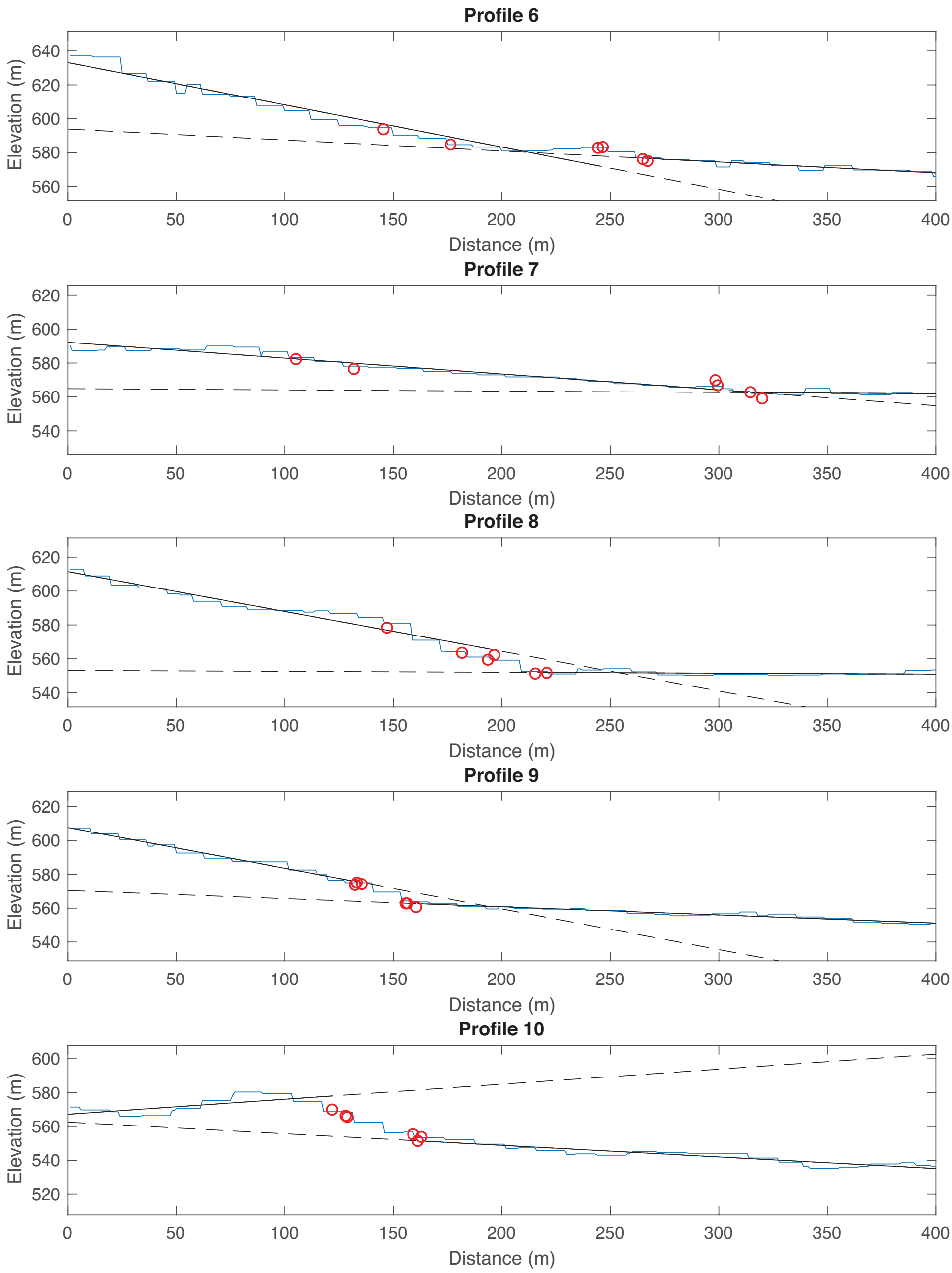

Fig. D.2 Profile 6 to Profile 10. Manual scarp picks (red circles) and regression lines fitted to the upper and lower surfaces.

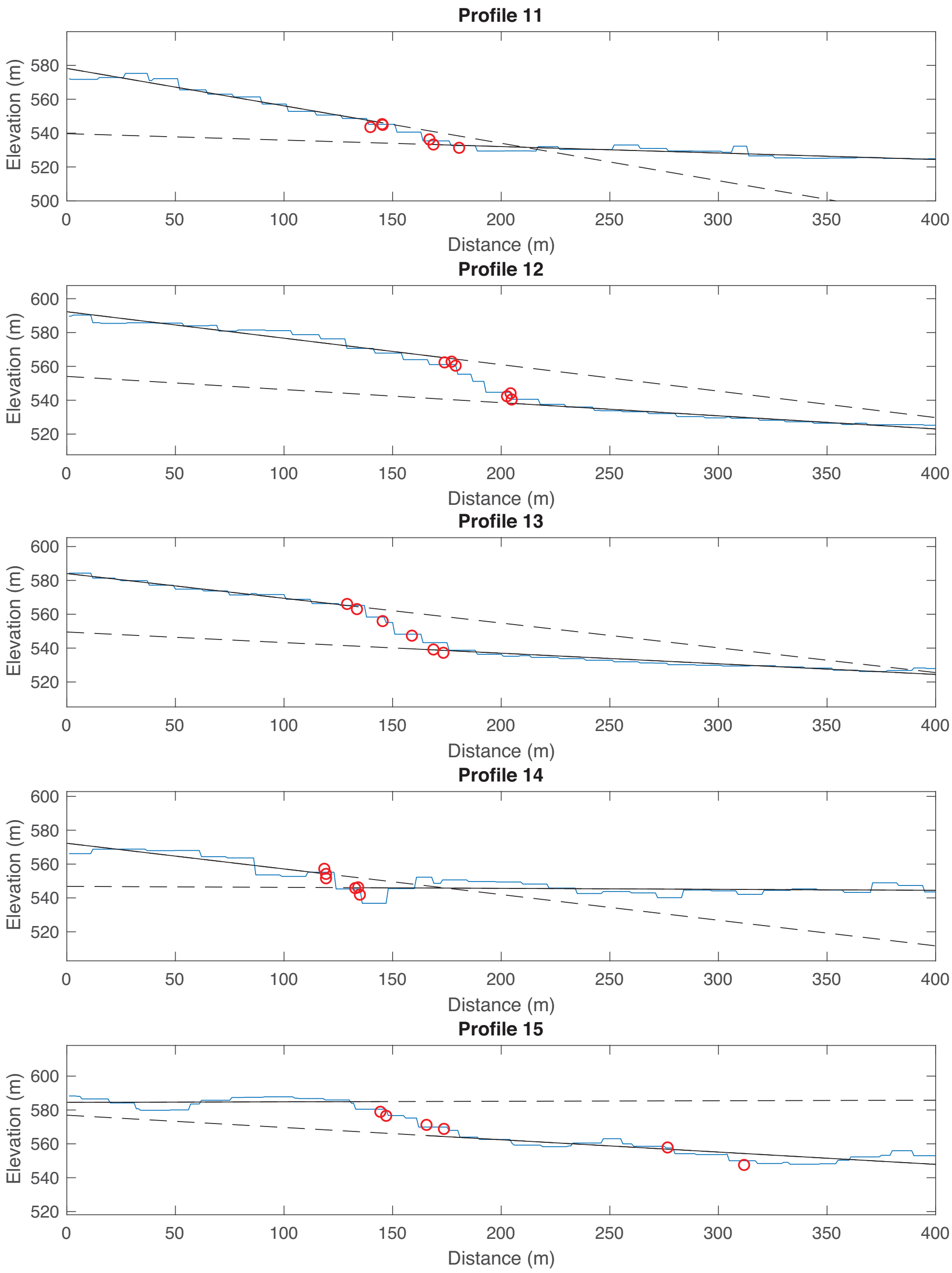

Fig. D.3 Profile 11 to Profile 15. Manual scarp picks (red circles) and regression lines fitted to the upper and lower surfaces.

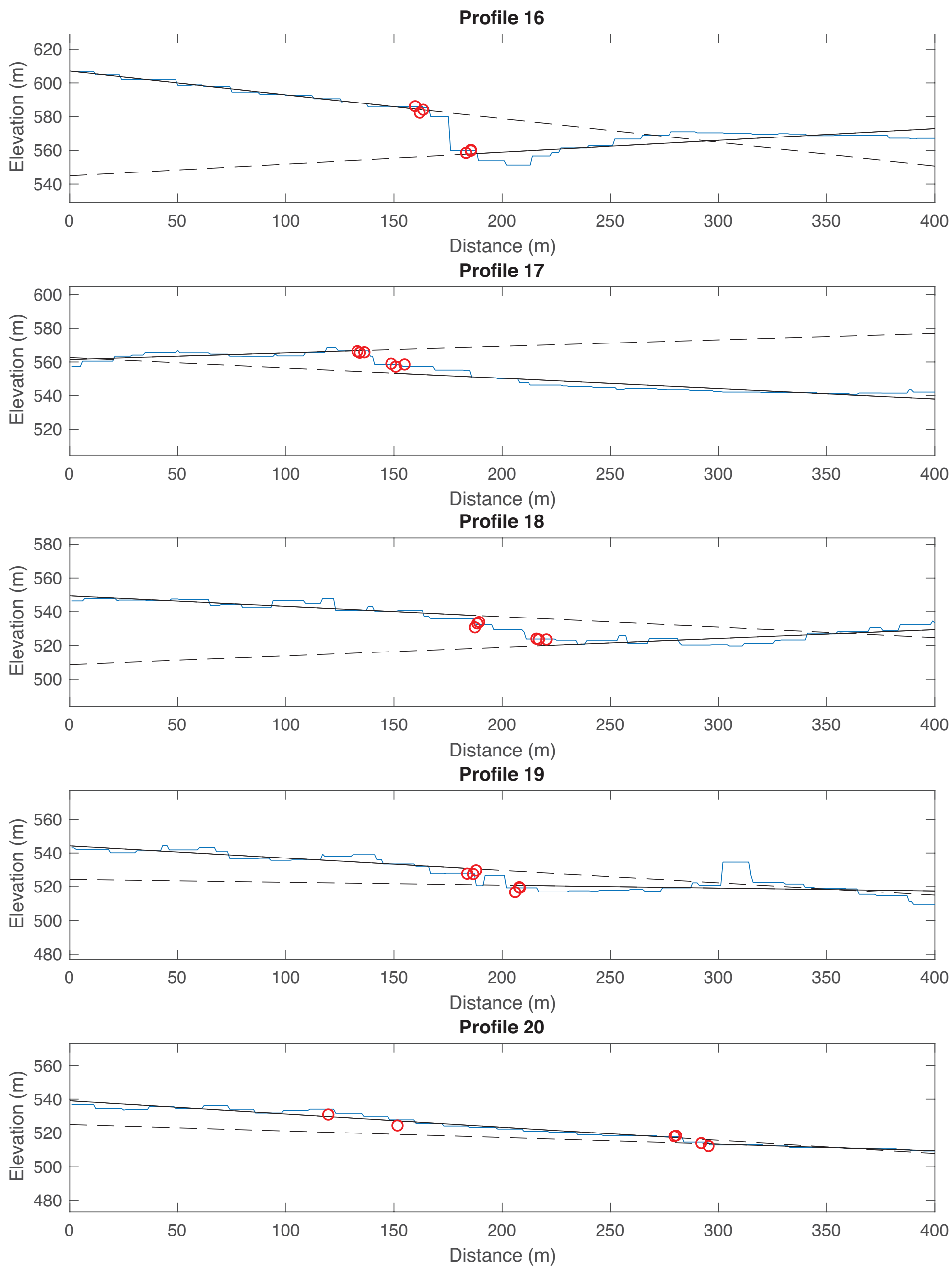

Fig. D.4 Profile 16 to Profile 20. Manual scarp picks (red circles) and regression lines fitted to the upper and lower surfaces.

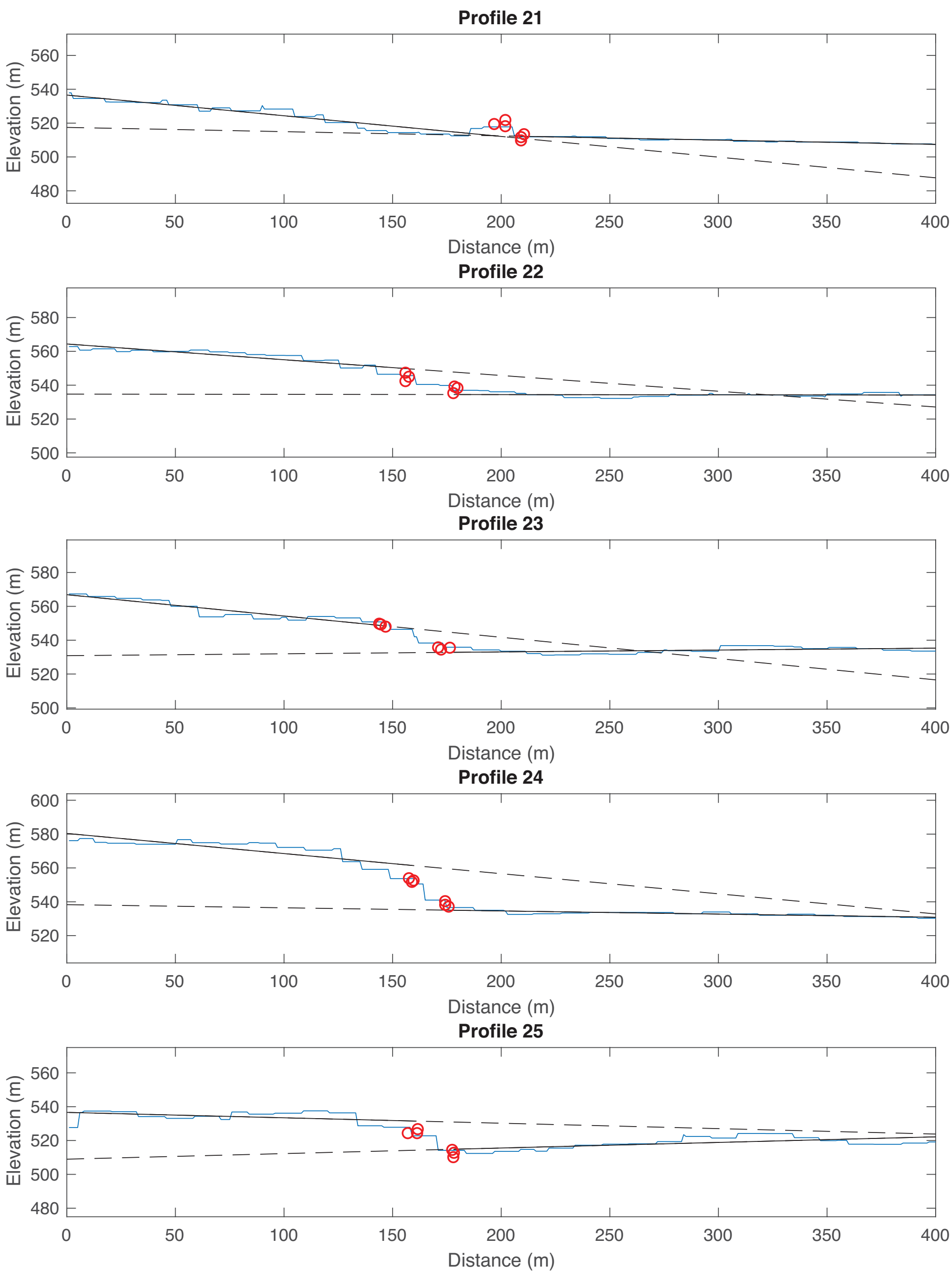

Fig. D.5 Profile 21 to Profile 25. Manual scarp picks (red circles) and regression lines fitted to the upper and lower surfaces.

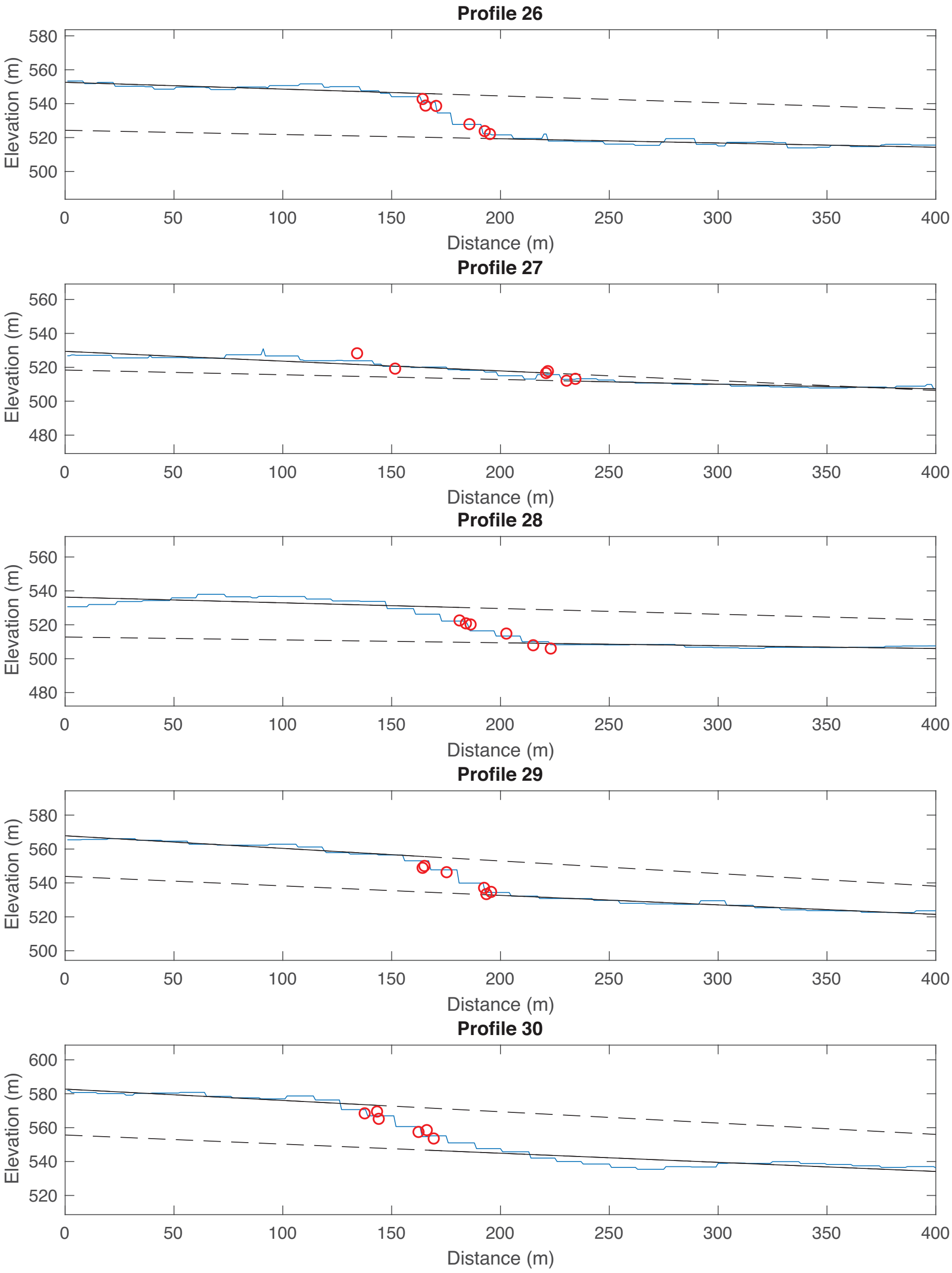

Fig. D.6 Profile 26 to Profile 30. Manual scarp picks (red circles) and regression lines fitted to the upper and lower surfaces.

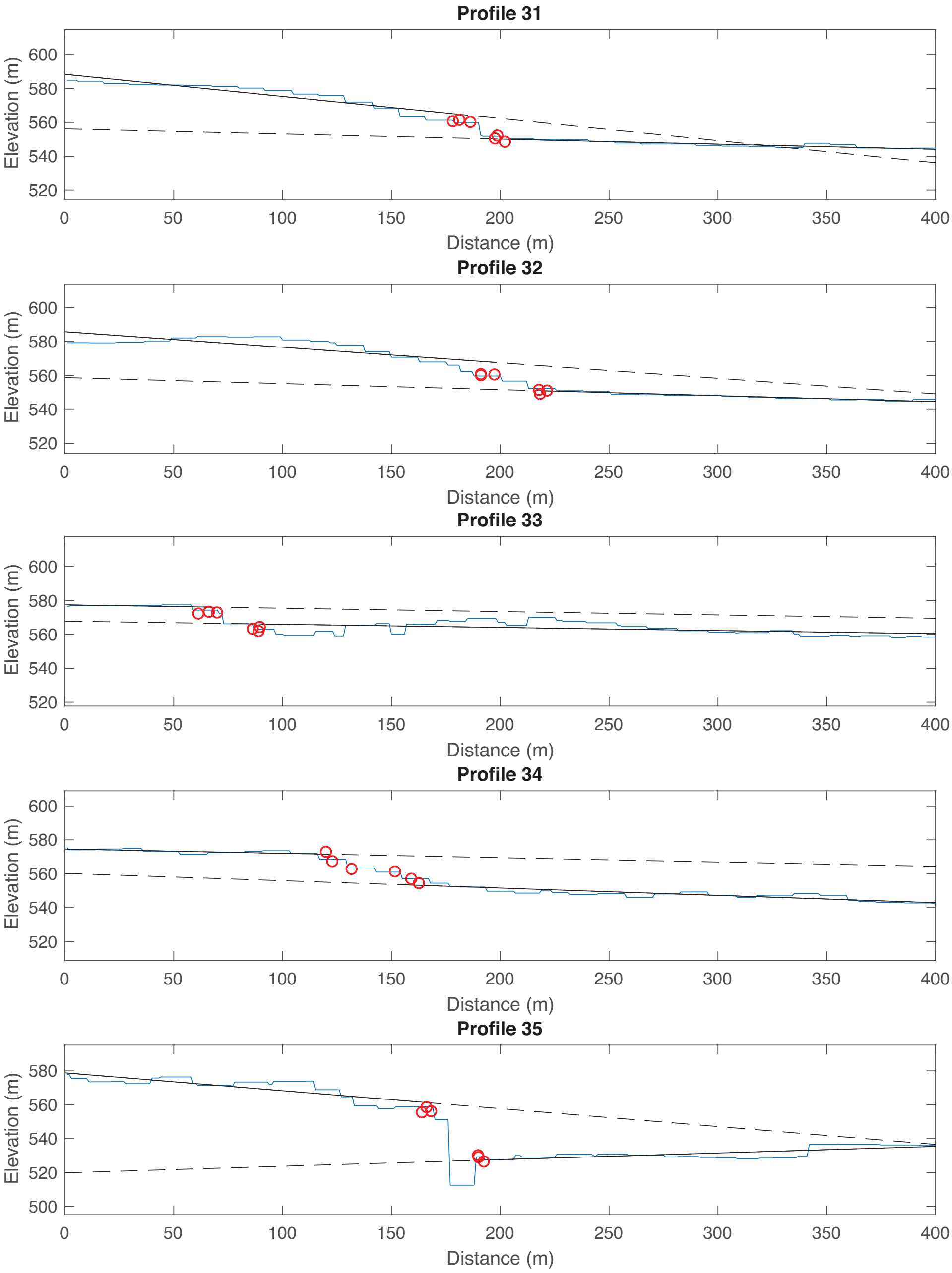

Fig. D.7 Profile 31 to Profile 35. Manual scarp picks (red circles) and regression lines fitted to the upper and lower surfaces.

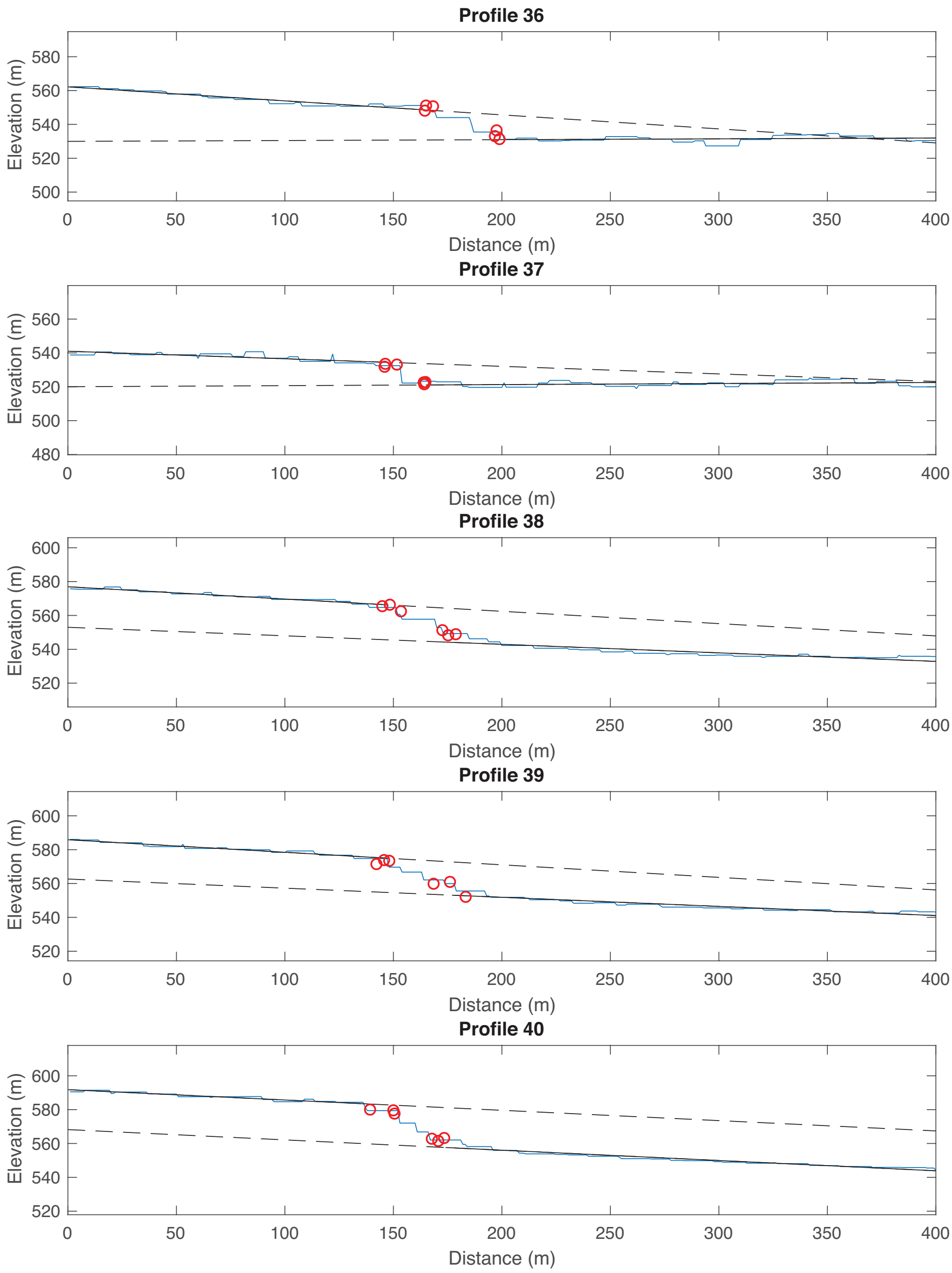

Fig. D.8 Profile 36 to Profile 40. Manual scarp picks (red circles) and regression lines fitted to the upper and lower surfaces.

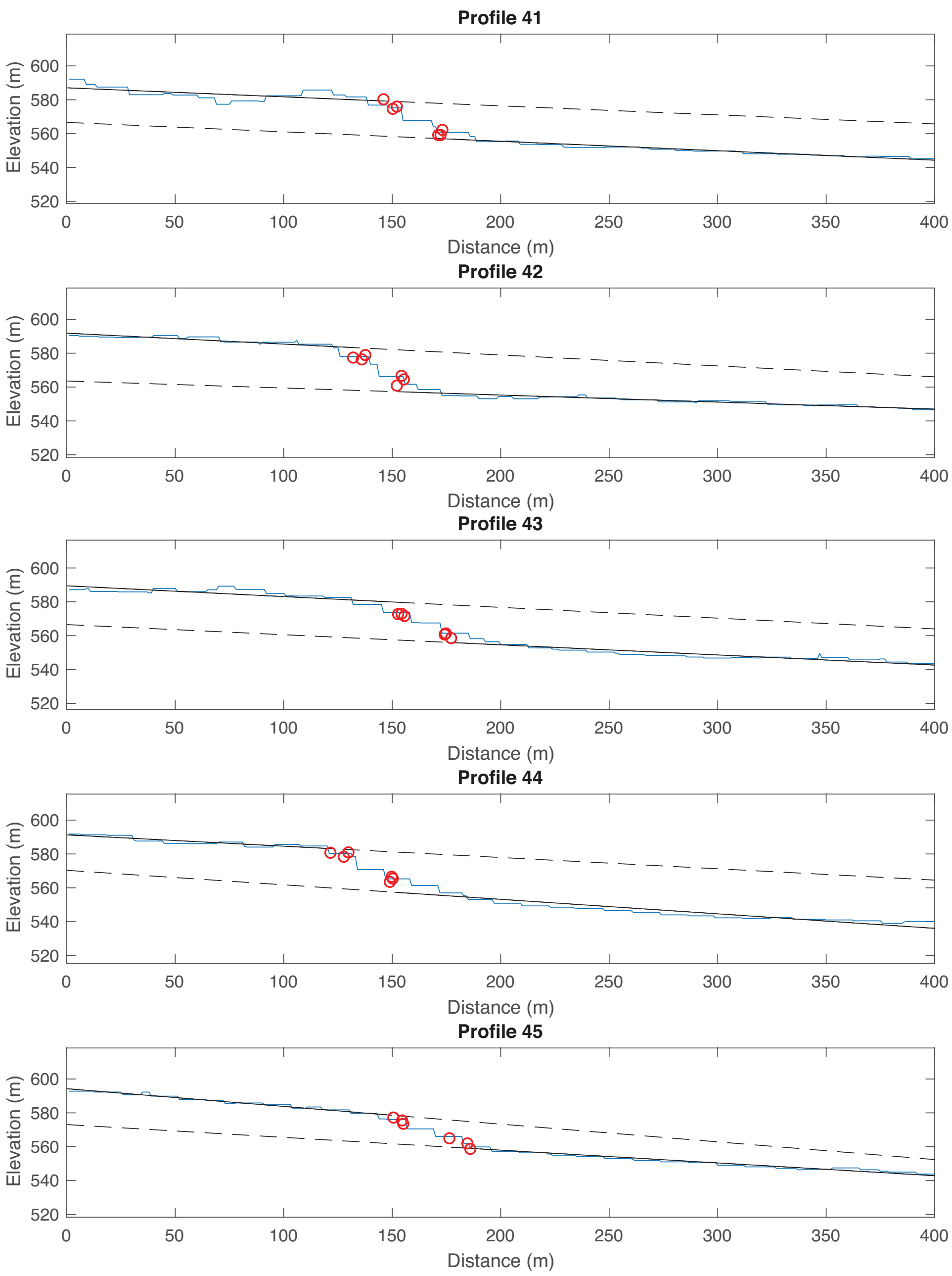

Fig. D.9 Profile 41 to Profile 45. Manual scarp picks (red circles) and regression lines fitted to the upper and lower surfaces.

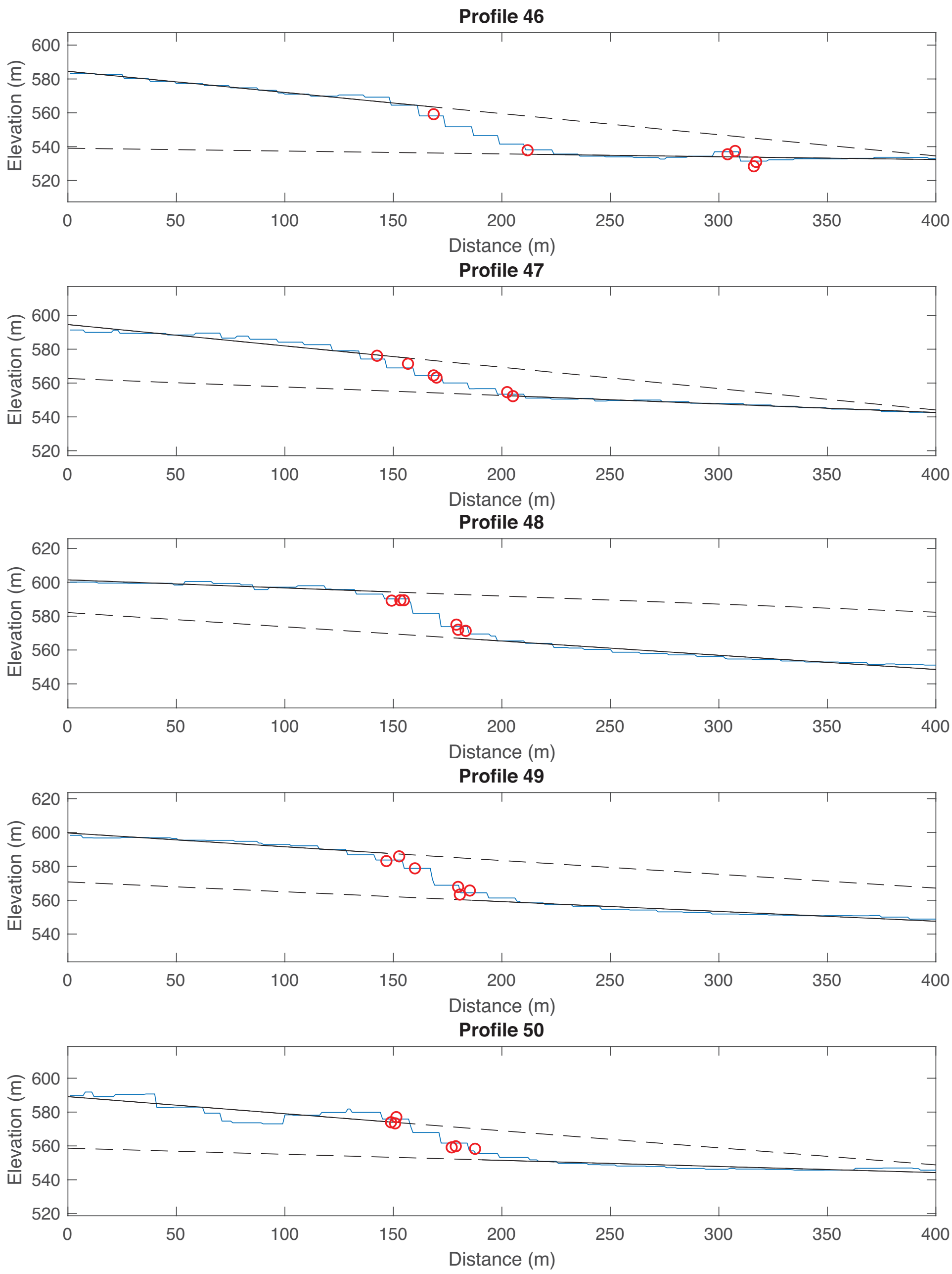

Fig. D.10 Profile 46 to Profile 50. Manual scarp picks (red circles) and regression lines fitted to the upper and lower surfaces.

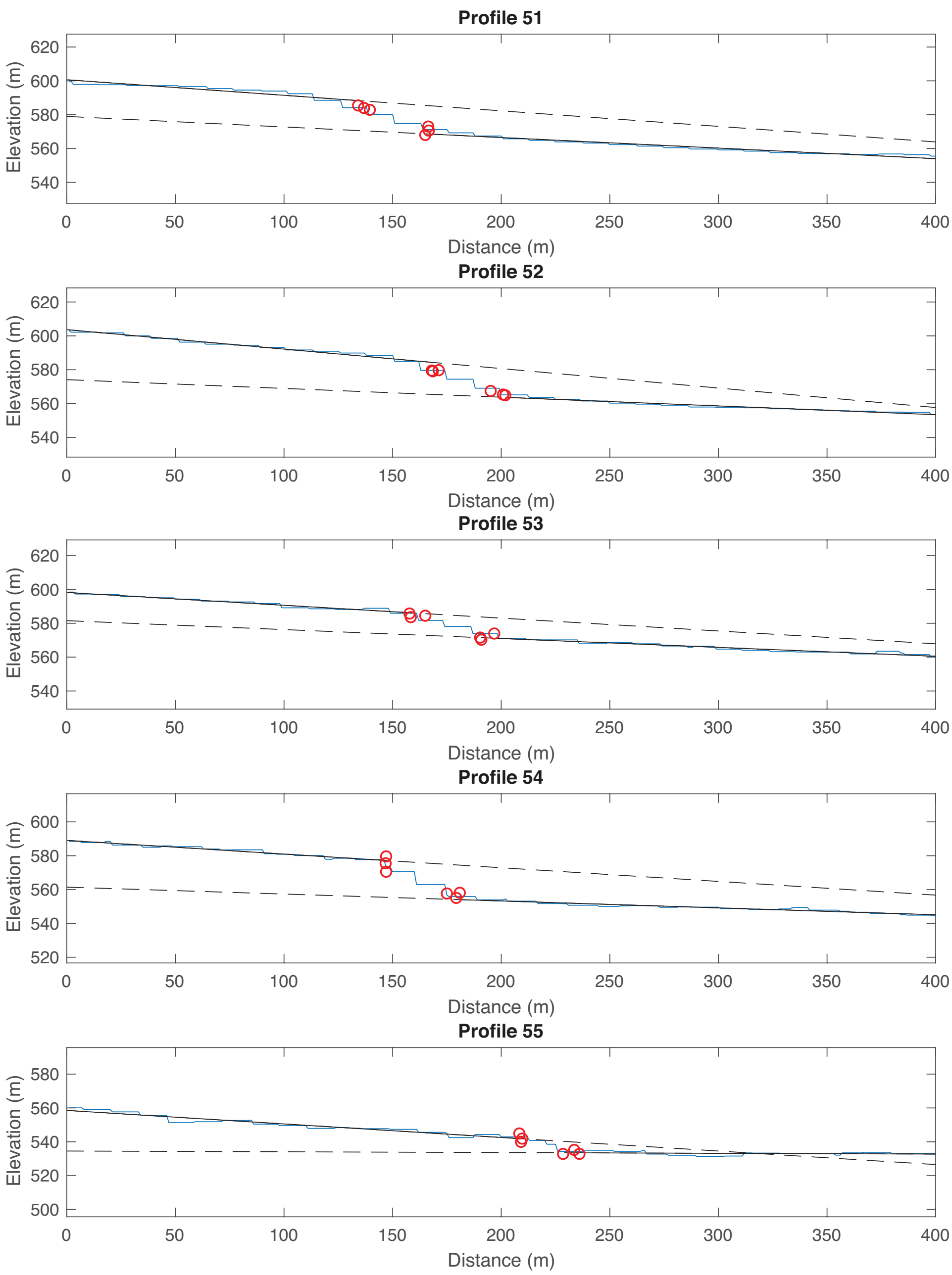

Fig. D.11 Profile 51 to Profile 55. Manual scarp picks (red circles) and regression lines fitted to the upper and lower surfaces.

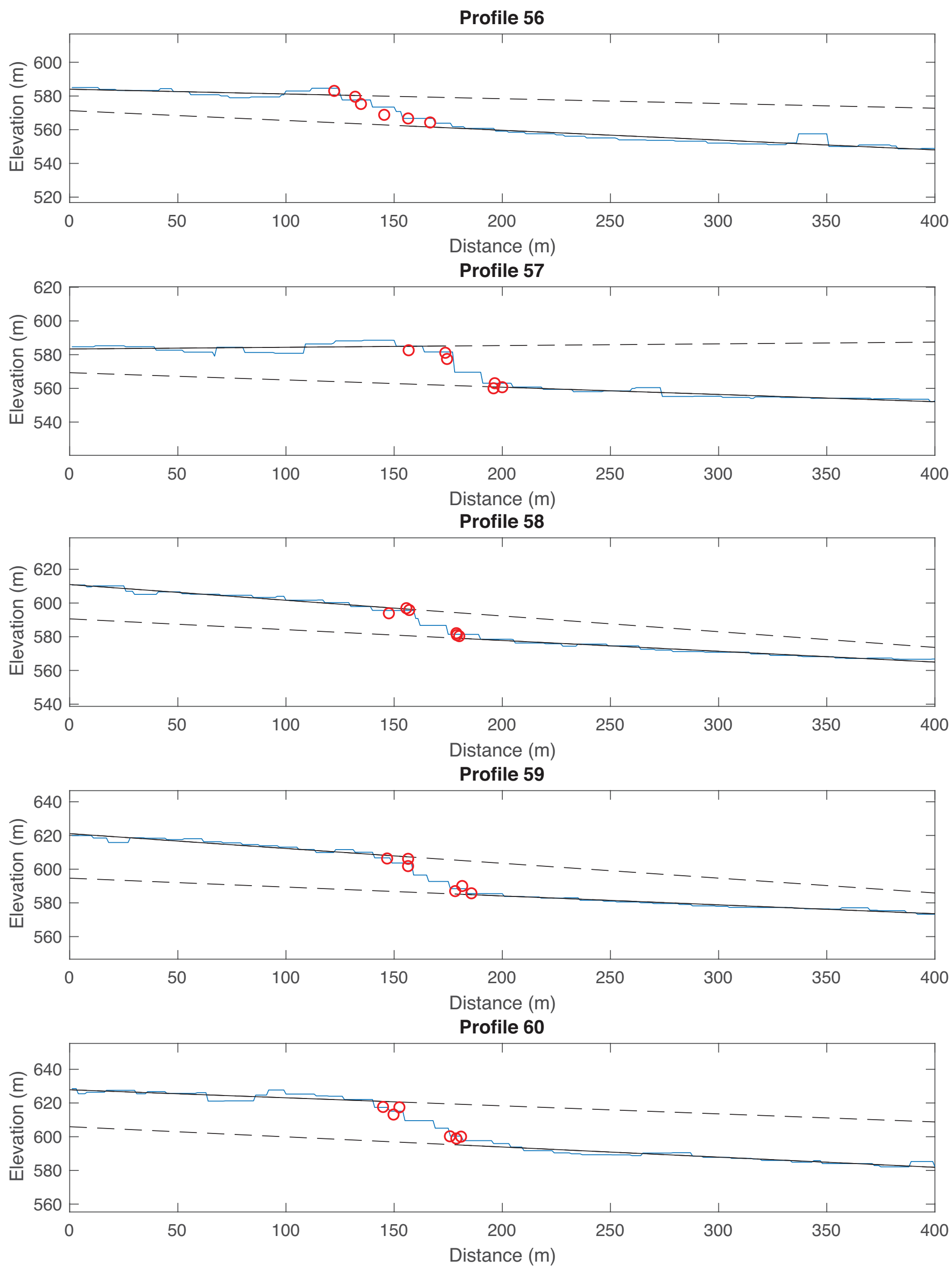

Fig. D.12 Profile 56 to Profile 60. Manual scarp picks (red circles) and regression lines fitted to the upper and lower surfaces.

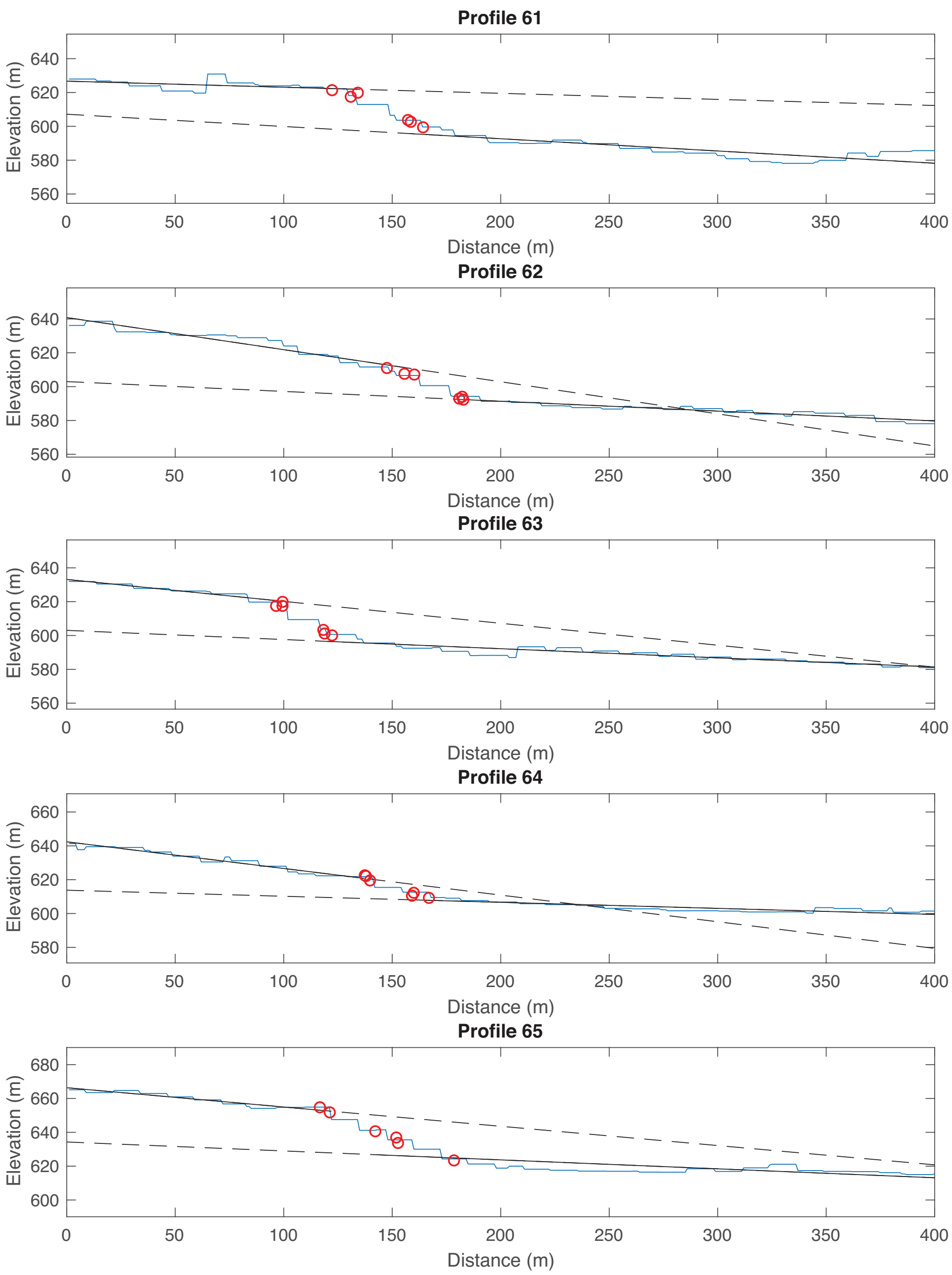

Fig. D.13 Profile 61 to Profile 65. Manual scarp picks (red circles) and regression lines fitted to the upper and lower surfaces.

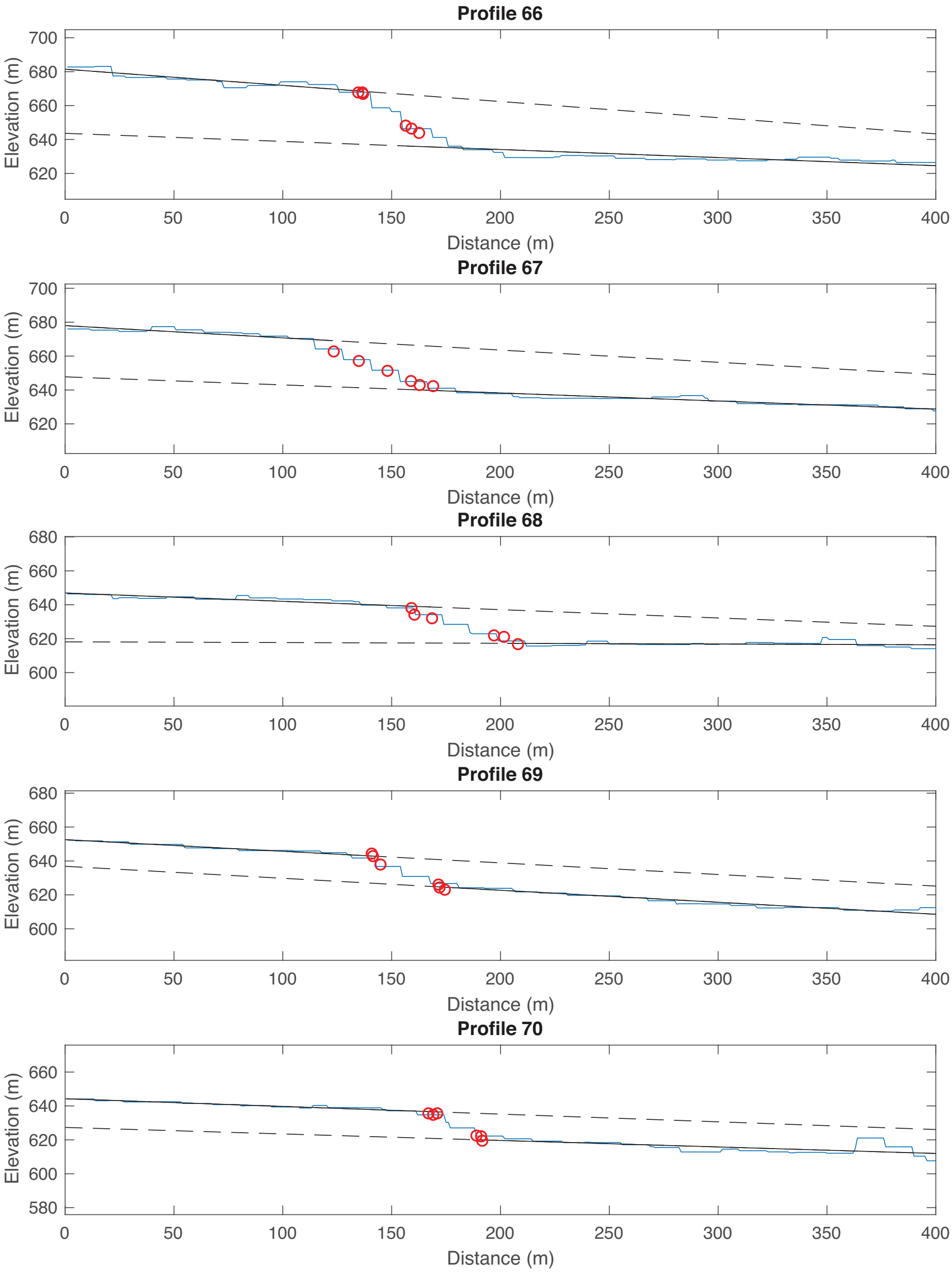

Fig. D.14 Profile 66 to Profile 70. Manual scarp picks (red circles) and regression lines fitted to the upper and lower surfaces.

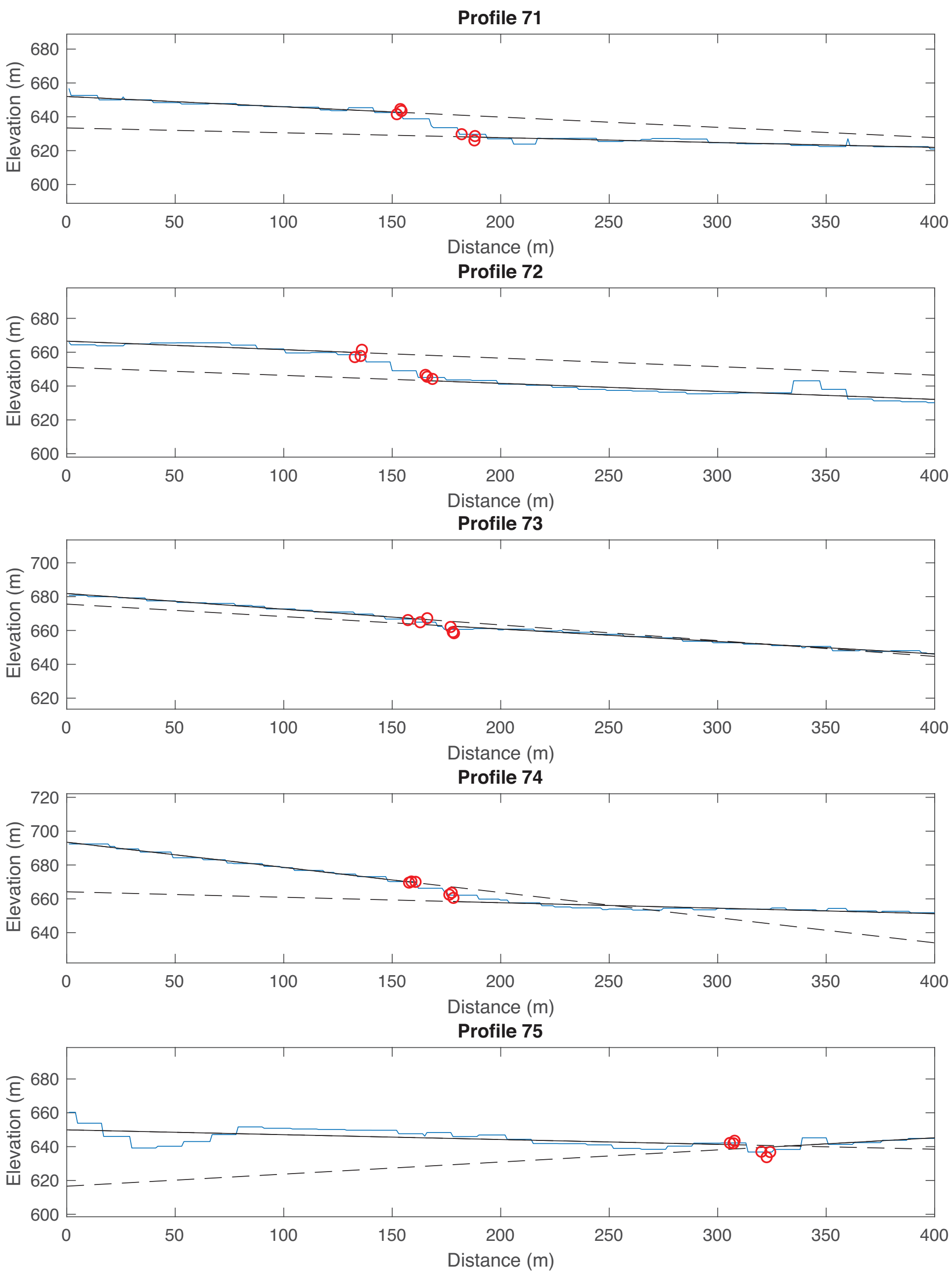

Fig. D.15 Profile 71 to Profile 75. Manual scarp picks (red circles) and regression lines fitted to the upper and lower surfaces.

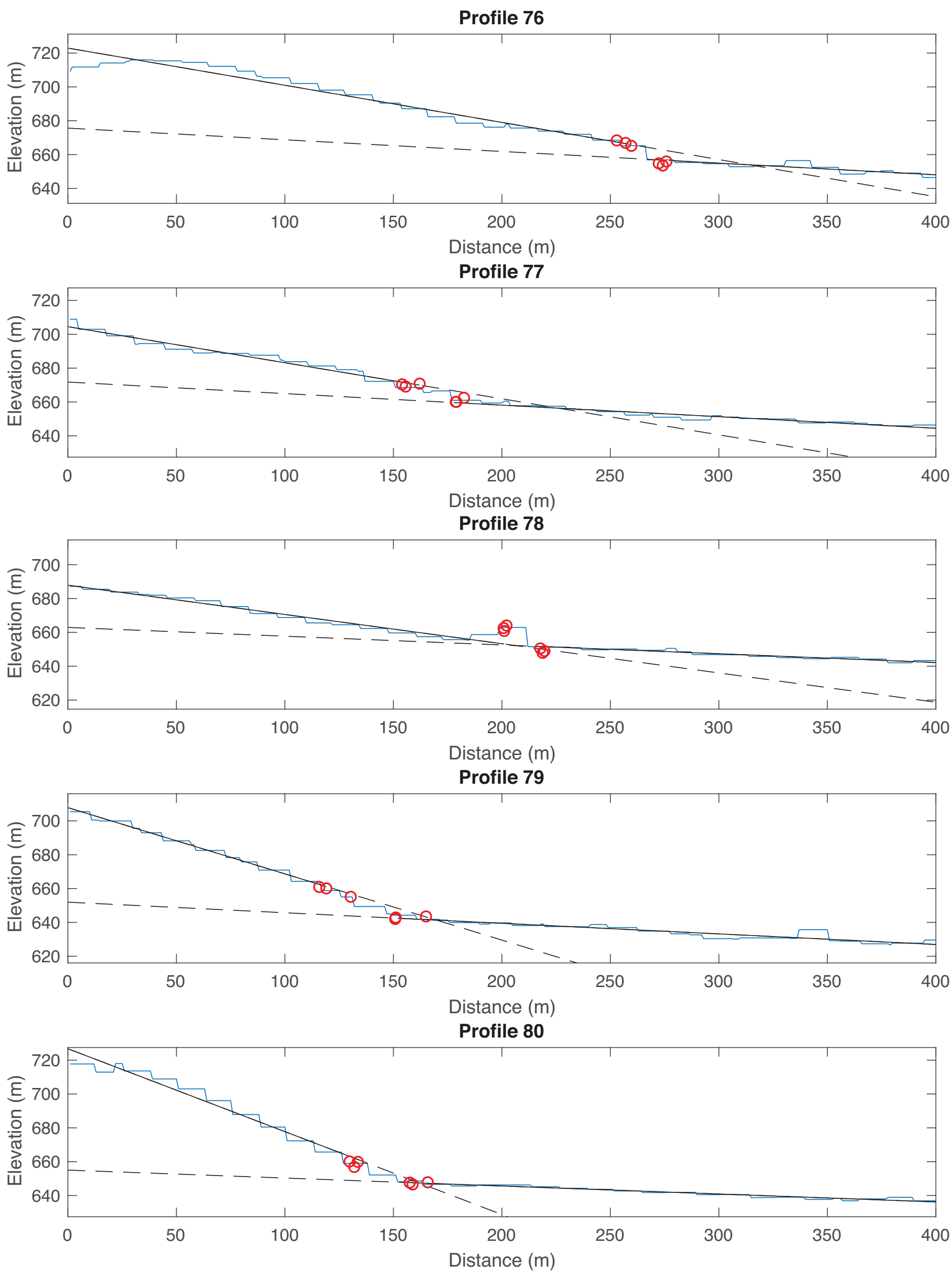

Fig. D.16 Profile 76 to Profile 80. Manual scarp picks (red circles) and regression lines fitted to the upper and lower surfaces.

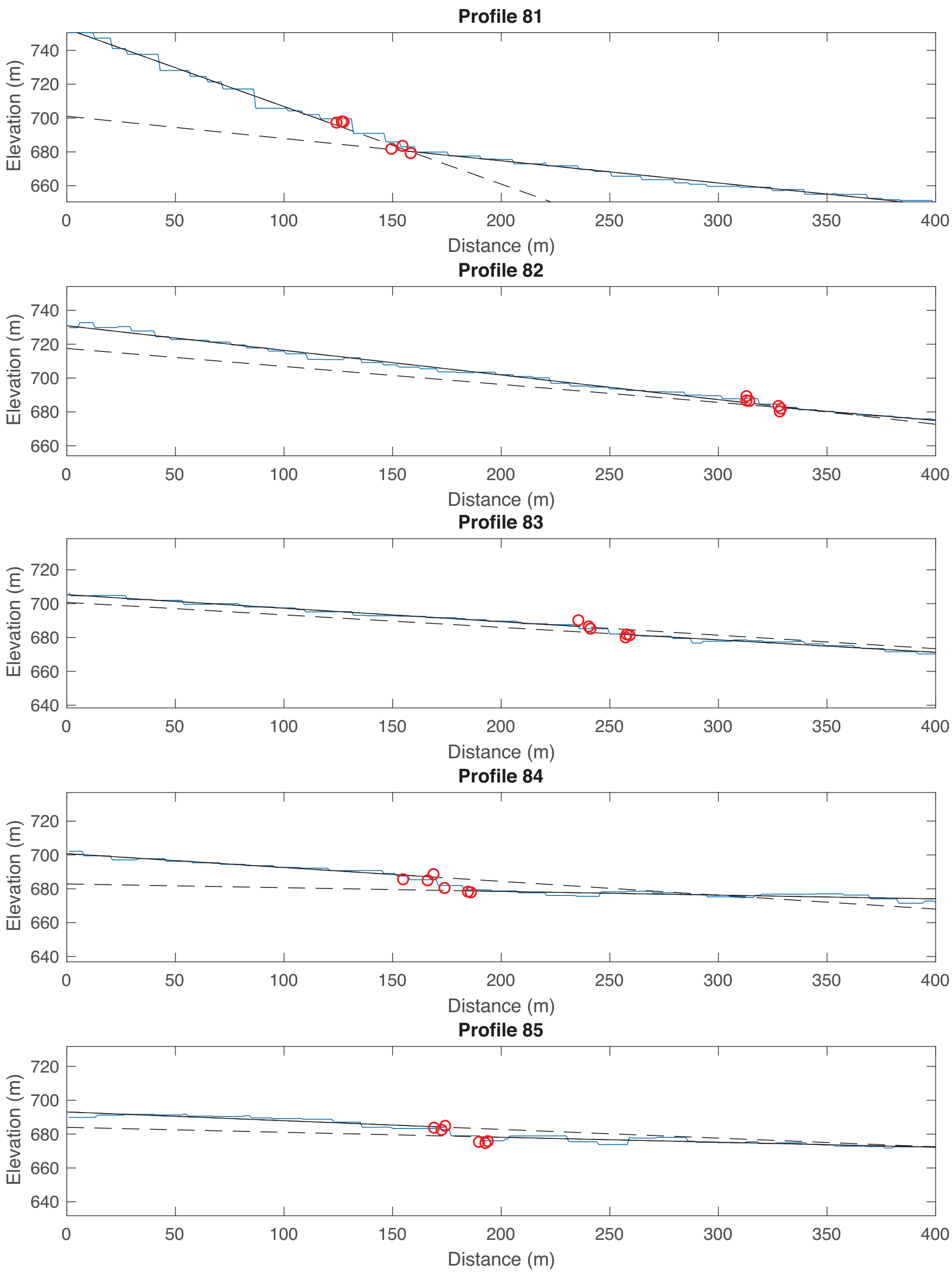

Fig. D.17 Profile 81 to Profile 85. Manual scarp picks (red circles) and regression lines fitted to the upper and lower surfaces.

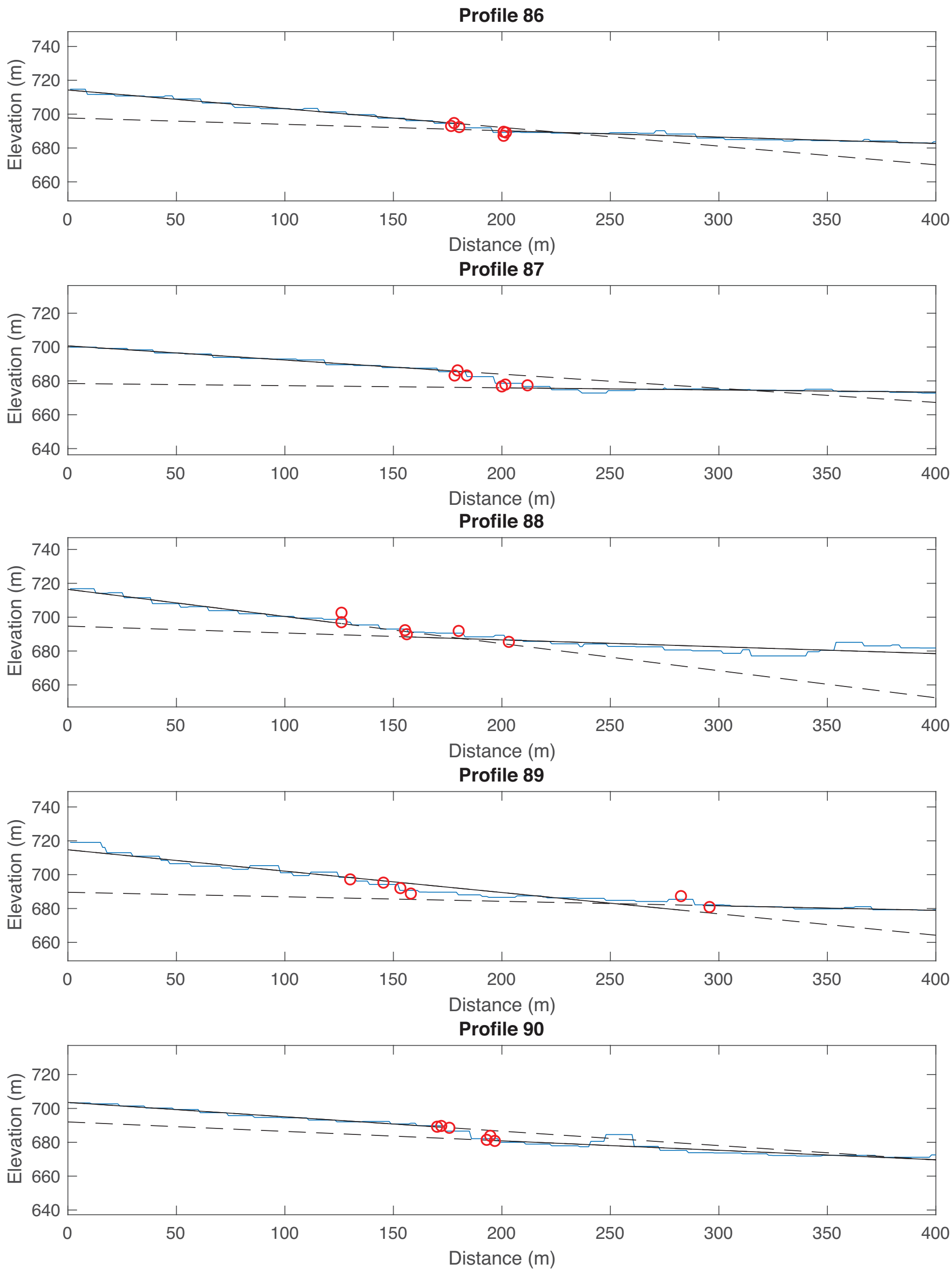

Fig. D.18 Profile 86 to Profile 90. Manual scarp picks (red circles) and regression lines fitted to the upper and lower surfaces.

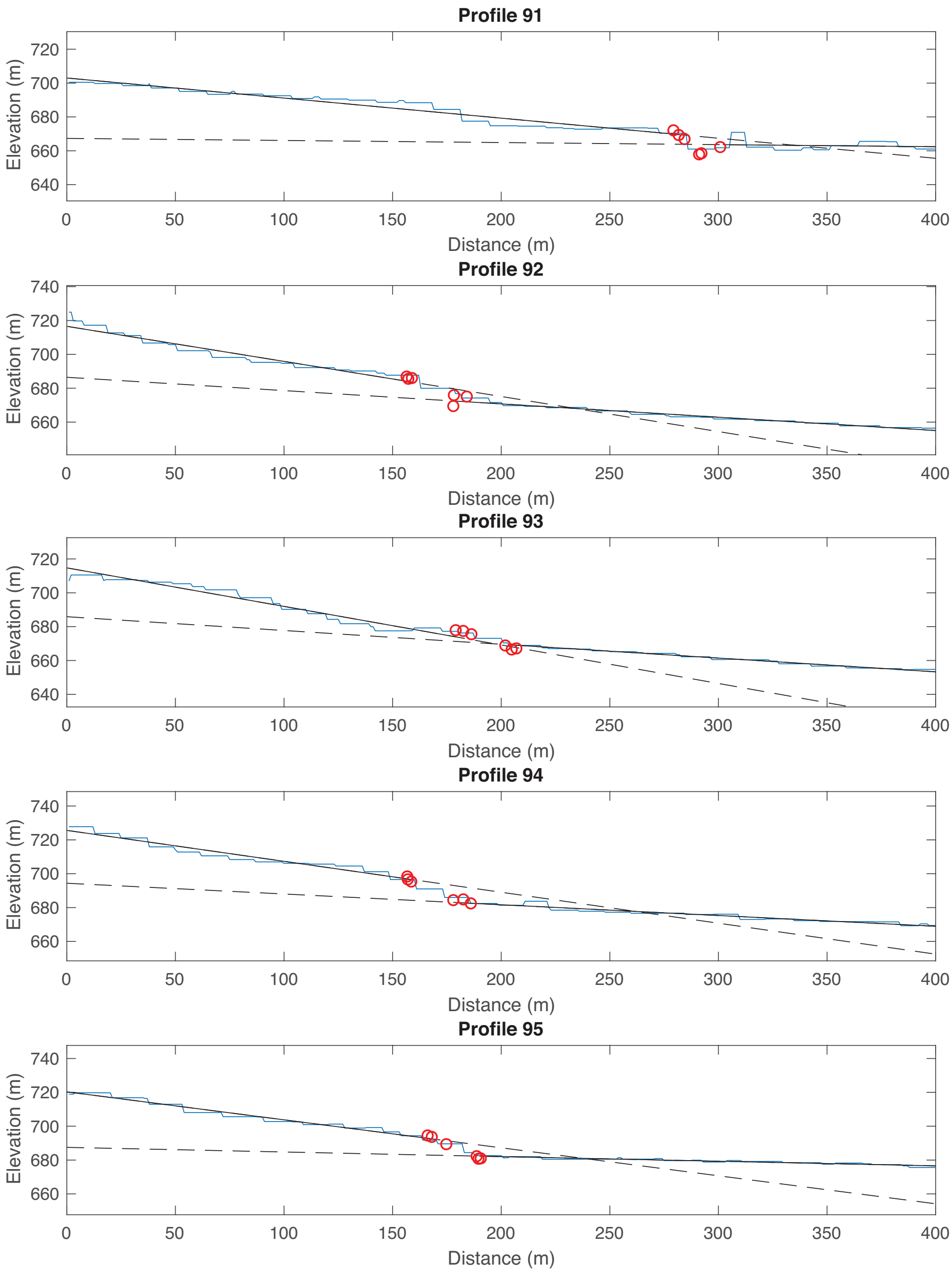

Fig. D.19 Profile 91 to Profile 95. Manual scarp picks (red circles) and regression lines fitted to the upper and lower surfaces.

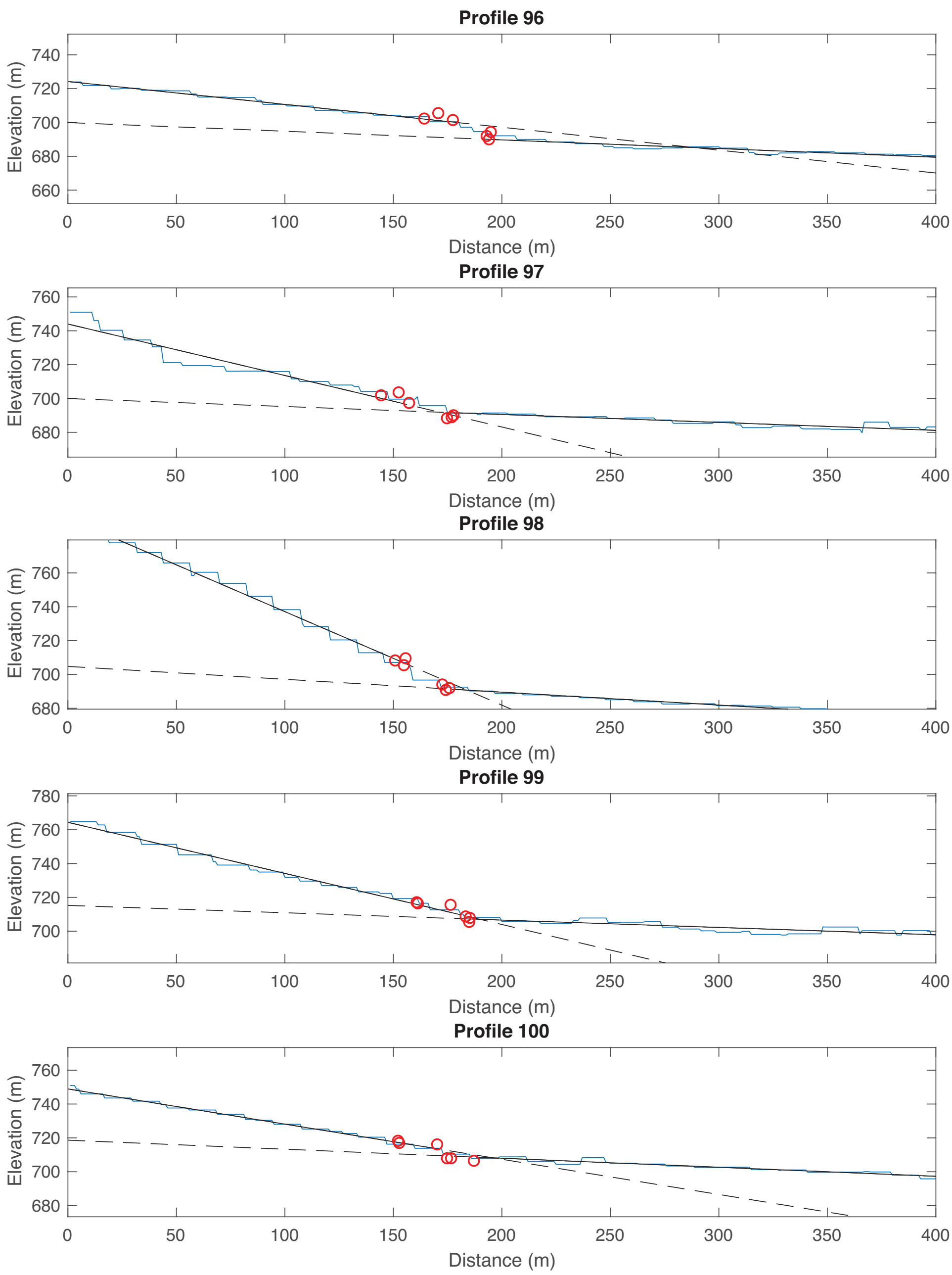

Fig. D.20 Profile 96 to Profile 100. Manual scarp picks (red circles) and regression lines fitted to the upper and lower surfaces.

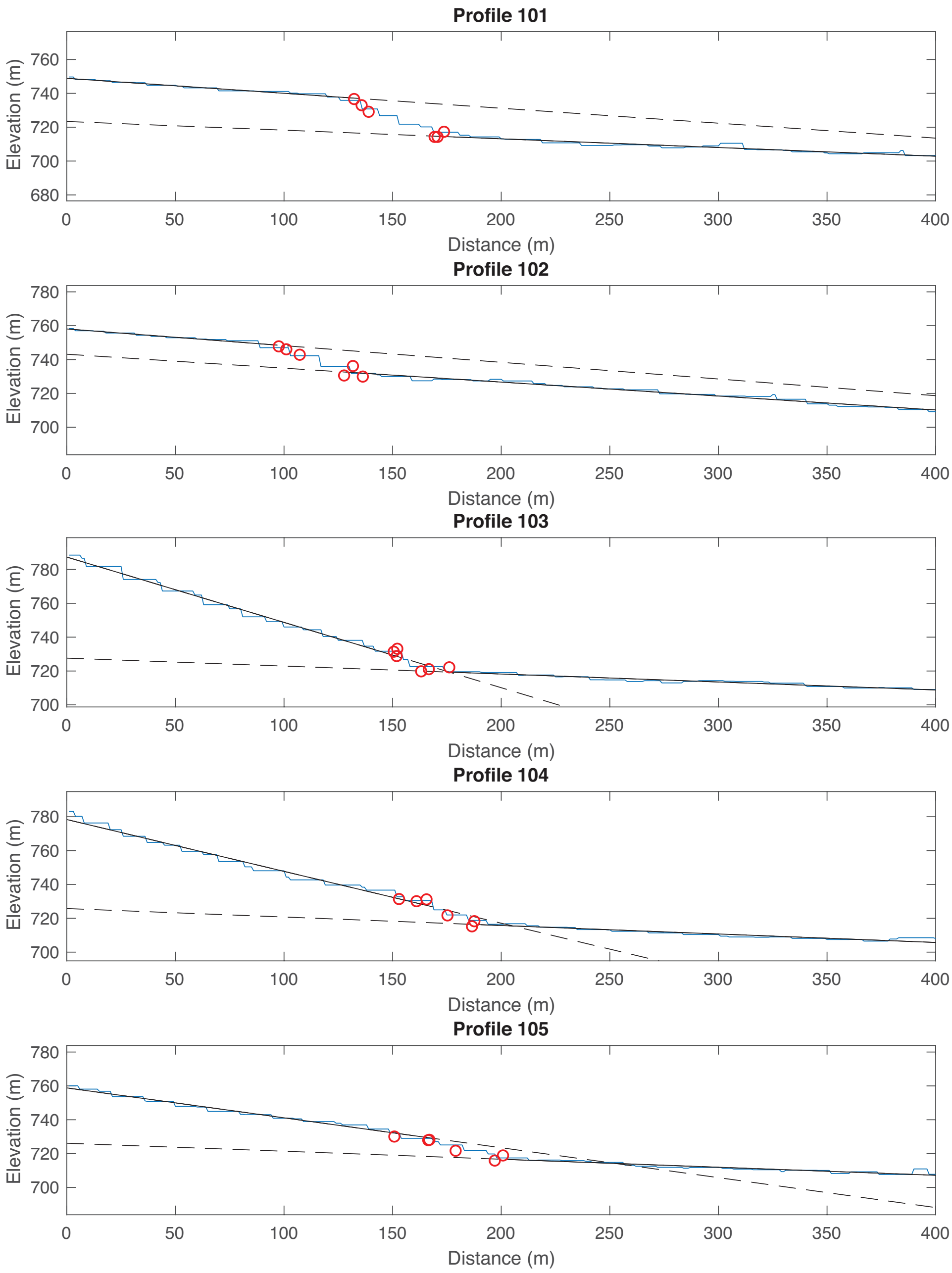

Fig. D.21 Profile 101 to Profile 105. Manual scarp picks (red circles) and regression lines fitted to the upper and lower surfaces.

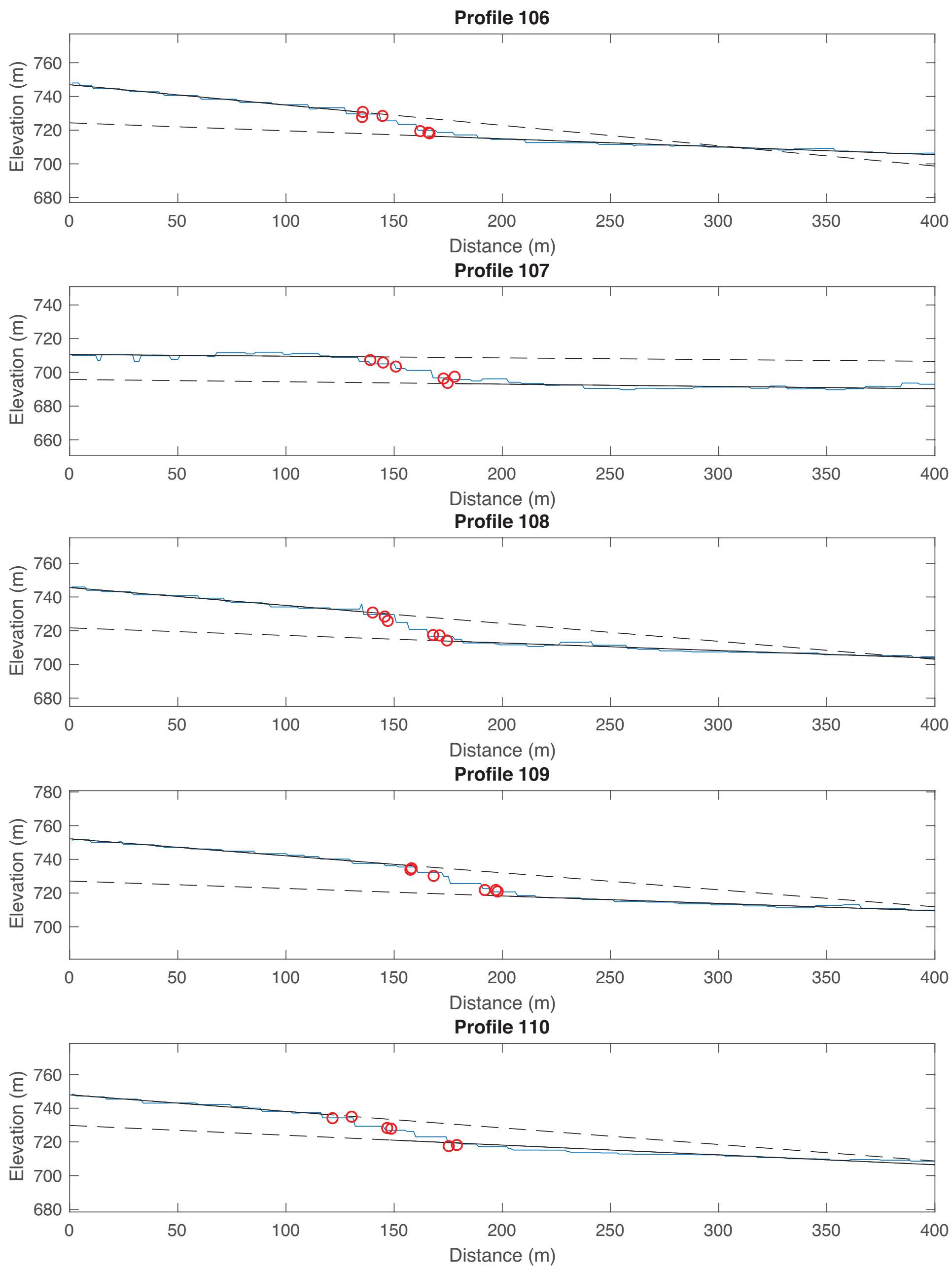

Fig. D.22 Profile 106 to Profile 110. Manual scarp picks (red circles) and regression lines fitted to the upper and lower surfaces.

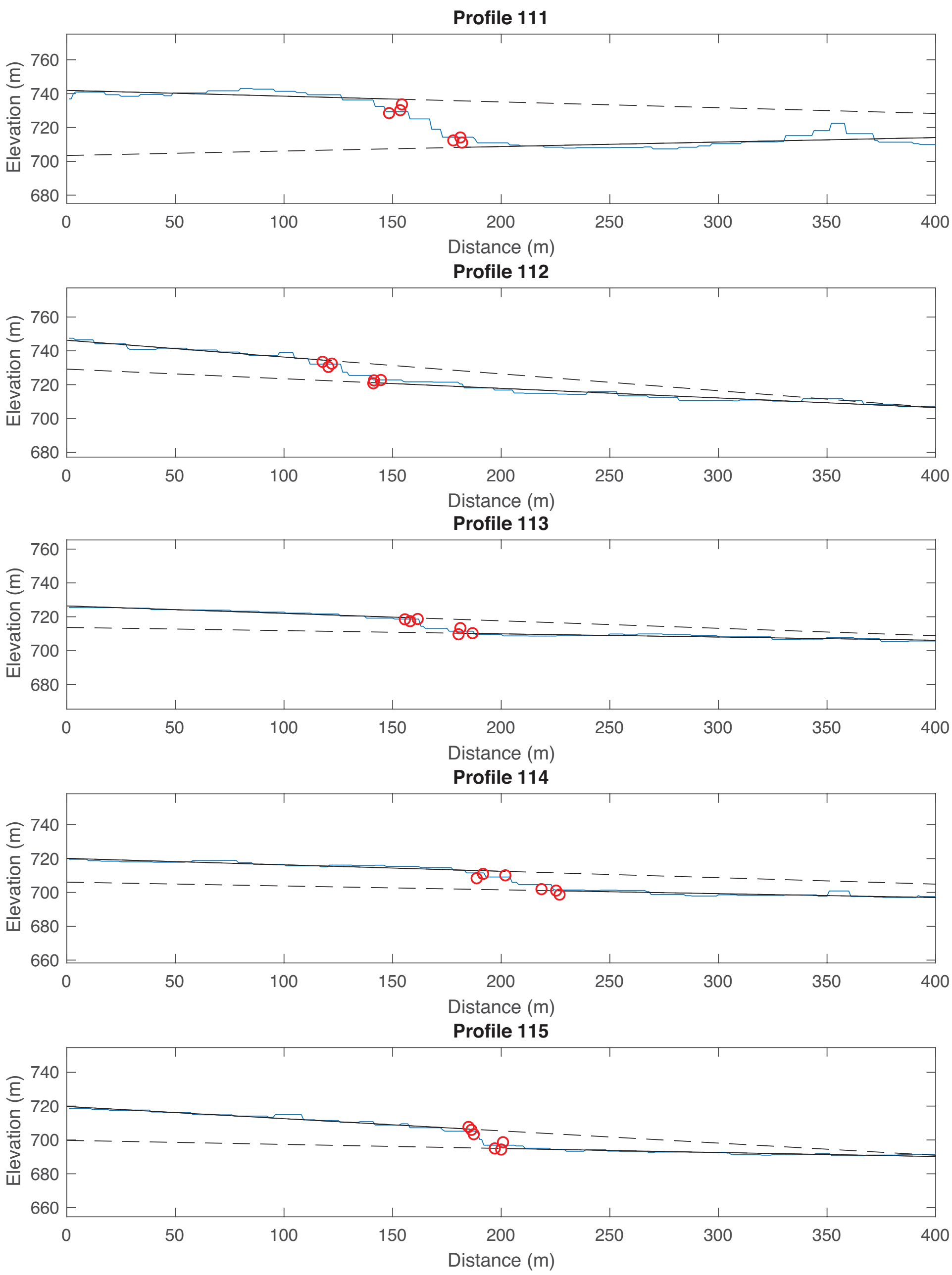

Fig. D.23 Profile 111 to Profile 115. Manual scarp picks (red circles) and regression lines fitted to the upper and lower surfaces.

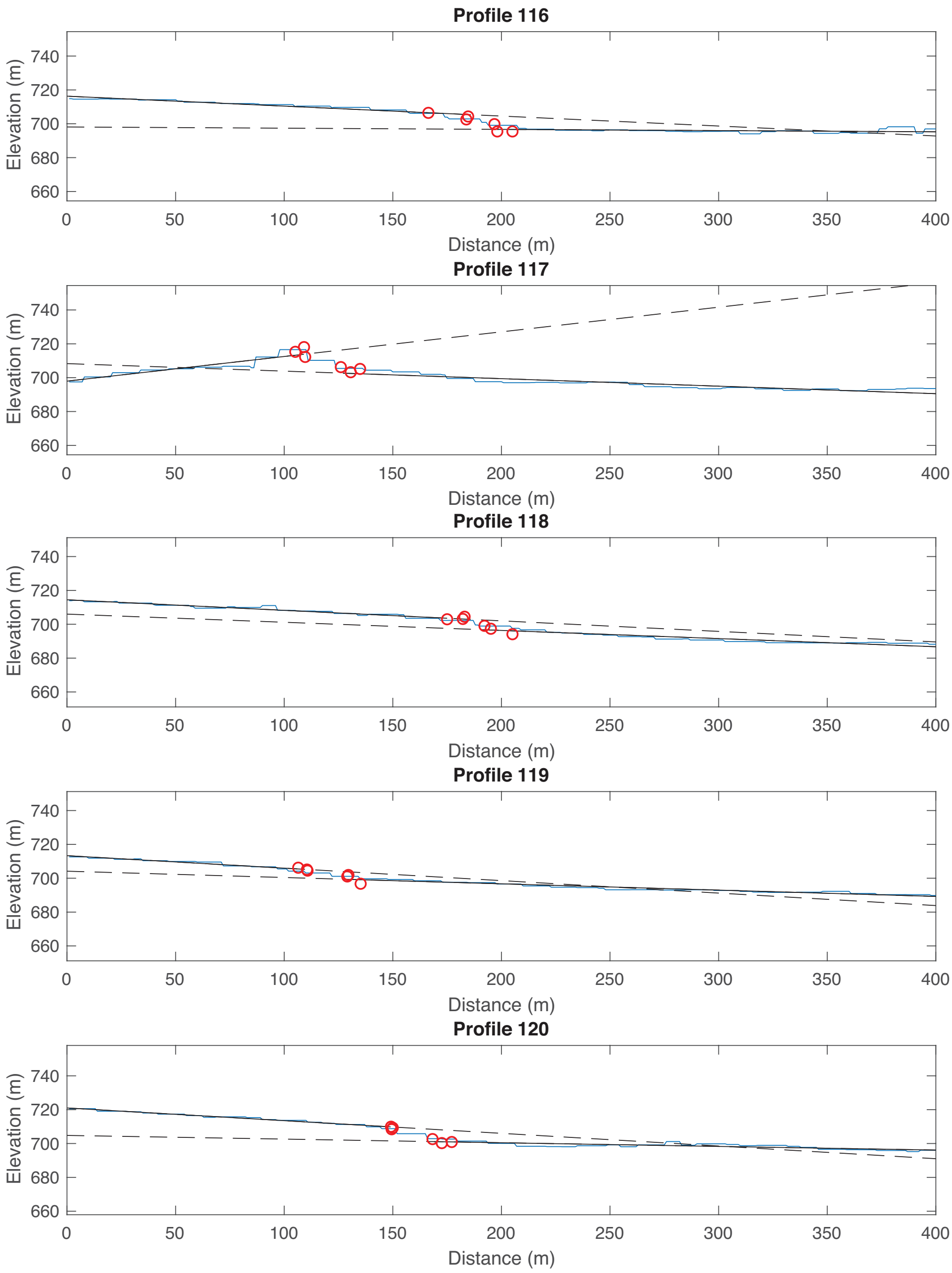

Fig. D.24 Profile 116 to Profile 120. Manual scarp picks (red circles) and regression lines fitted to the upper and lower surfaces.

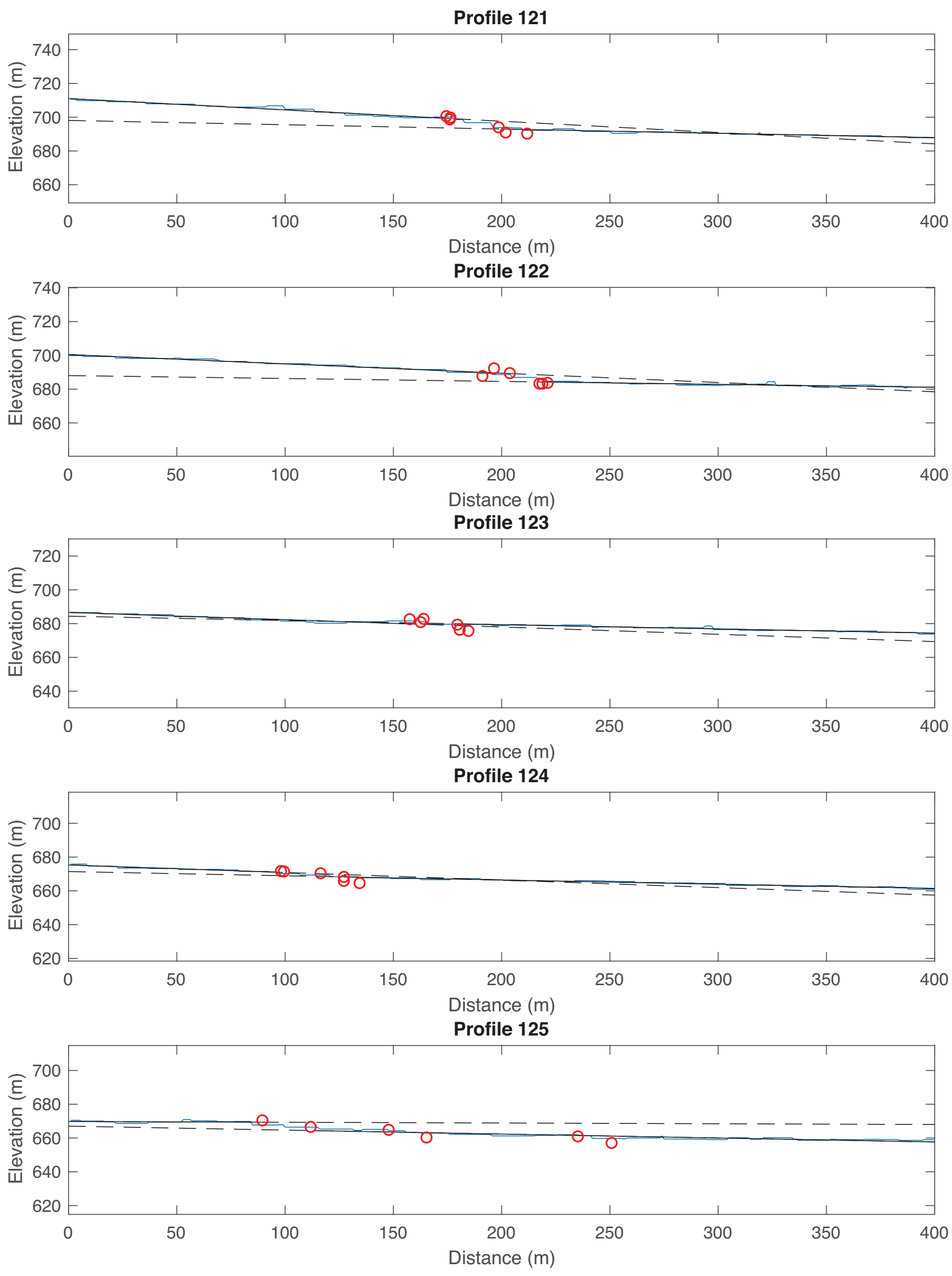

Fig. D.25 Profile 121 to Profile 125. Manual scarp picks (red circles) and regression lines fitted to the upper and lower surfaces.

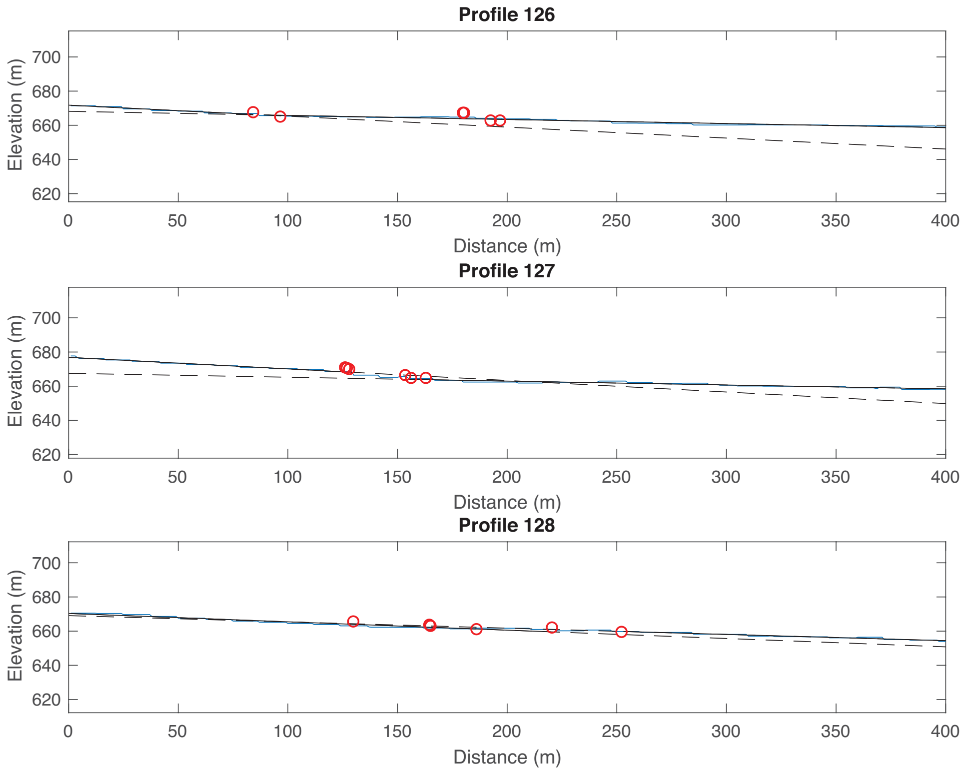

Fig. D.26 Profile 126 to Profile 128. Manual scarp picks (red circles) and regression lines fitted to the upper and lower surfaces.

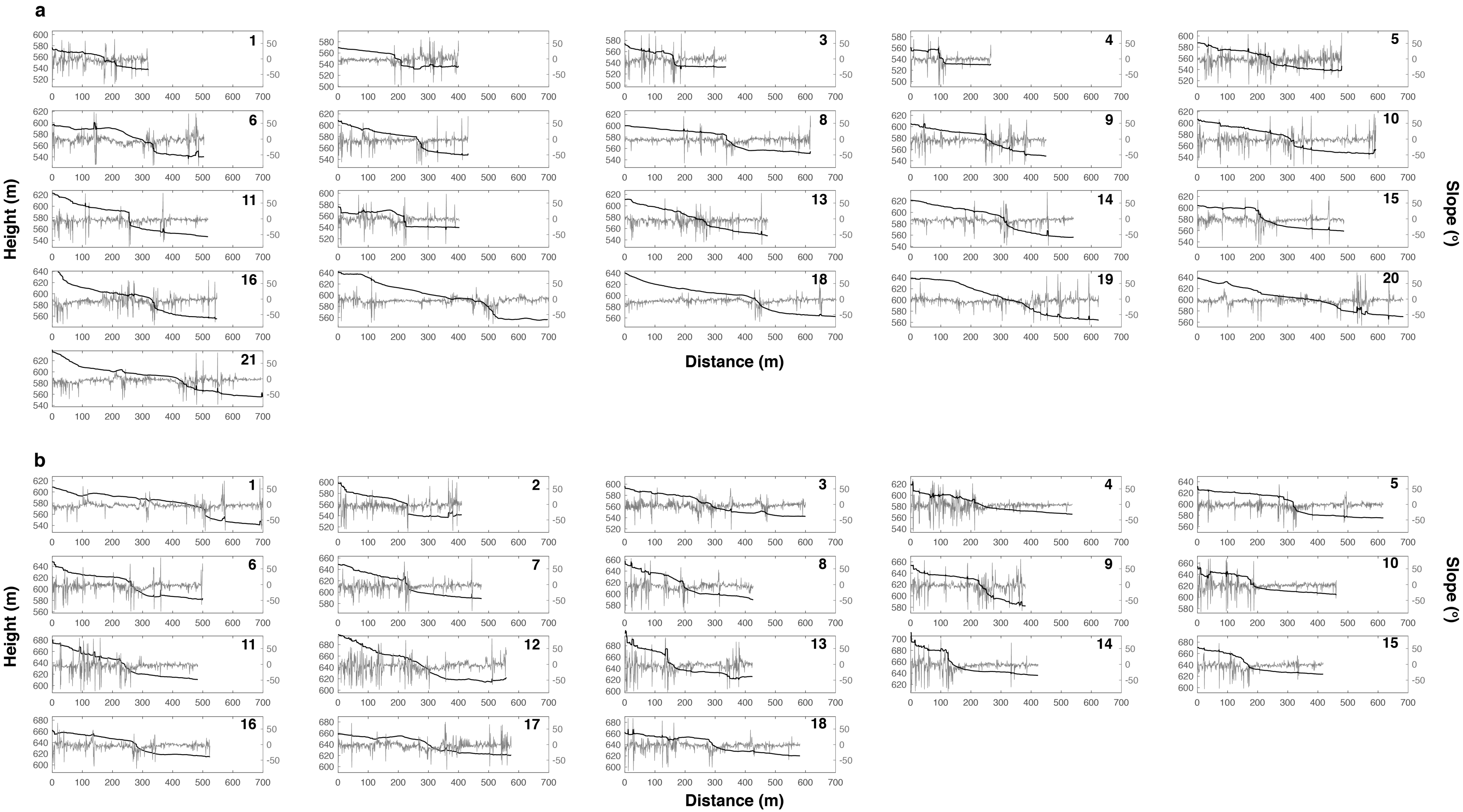

Fig. D.27 Mua and Kasinje scarp profiles for scarp analysis.

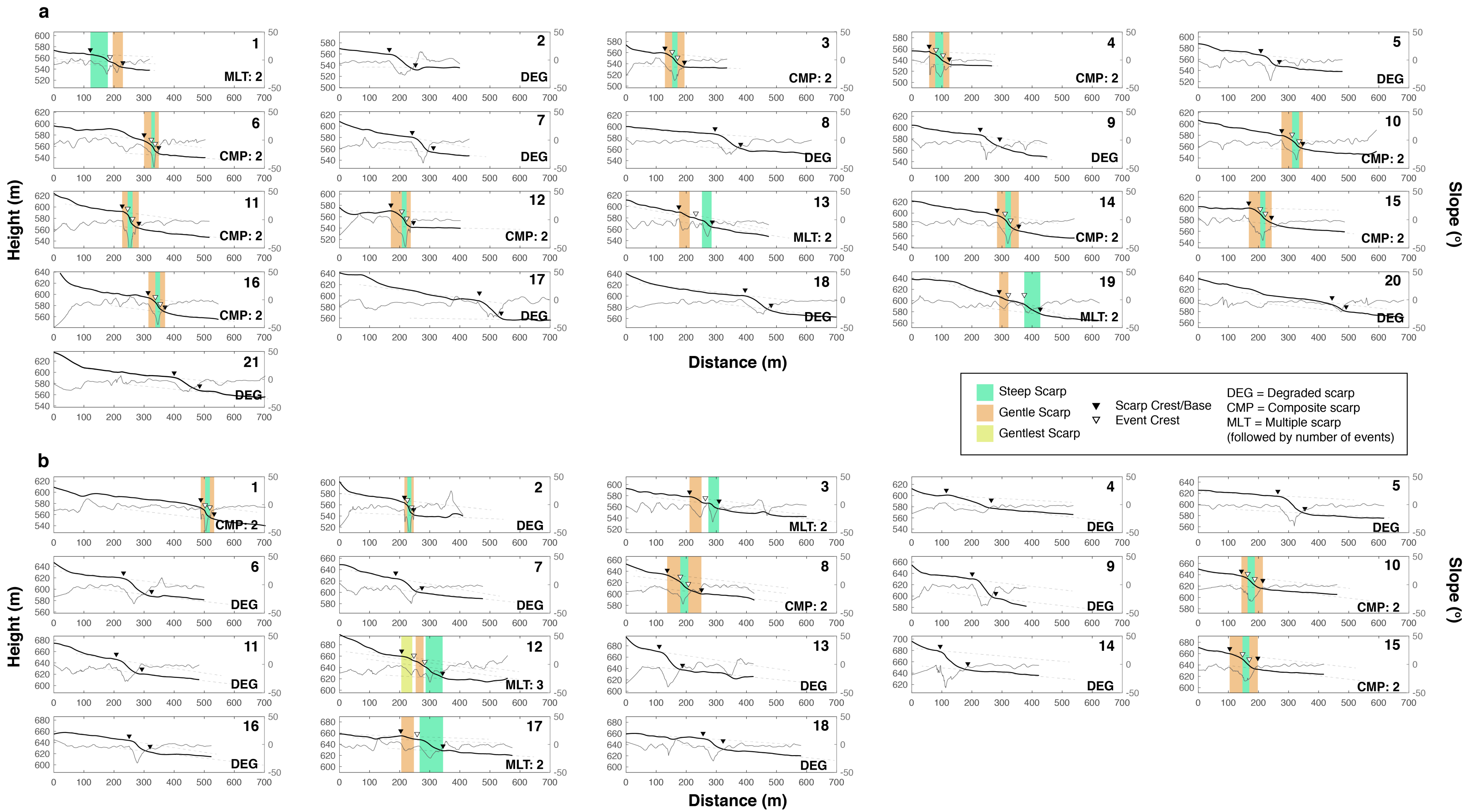

Fig. D.28 Mua and Kasinje scarp profiles for scarp analysis. Profiles have been smoothed with the Rloess filter and a window size of 15 m. Multiple scarp interpretation is displayed.

Appendix E

Scarp morphology results

In this Appendix, the results of the morphological analysis performed in Chapter 3 on the 128 BMF profiles are displayed. The scarp height was calculated for each profile during three separate runs. The RMSE of the upper (LS) and lower (LS) original surfaces, based on the manual selection of the top and bottom of the scarp, are also given. Scarps are determined to be 'repeatable' if the horizontal error between all scarp-picks was less than 10 m. Of the 128 profiles, 102 were deemed repeatable. The average and standard deviation of all three runs is given in the end columns.

Table E.1 Scarp RMSE and Height calculations

Profile No./ Dist. along fault (km)	Repeat-able?	Run 1			Run 2			Run 3			Average			Standard Deviation		
		H (m)	RMSE LS (m)	RMSE US (m)	H (m)	RMSE LS (m)	RMSE US (m)	H (m)	RMSE LS (m)	RMSE US (m)	H (m)	RMSE LS (m)	RMSE US (m)	H (m)	RMSE LS (m)	RMSE US (m)
1	No	7.10	1.57	3.09	9.03	1.62	3.72	0.55	1.57	3.08	5.56	1.59	3.29	4.45	0.03	0.37
2	No	0.20	2.58	3.64	10.25	4.23	3.75	8.78	4.37	3.73	6.41	3.73	3.71	5.43	0.99	0.06
3	No	5.62	1.91	1.67	6.60	1.90	1.55	6.87	1.89	1.52	6.36	1.90	1.58	0.66	0.01	0.08
4	Yes	10.21	1.59	6.07	9.93	1.59	6.07	9.81	1.59	6.07	9.98	1.59	6.07	0.20	0.00	0.00
5	Yes	3.18	2.04	4.03	3.50	2.04	4.05	2.90	2.05	4.01	3.20	2.04	4.03	0.30	0.00	0.02
6	No	7.10	1.22	4.19	7.74	1.23	4.08	3.17	1.51	2.35	6.00	1.32	3.54	2.48	0.16	1.03
7	No	1.44	1.11	2.02	9.85	1.27	1.50	1.28	1.14	2.02	4.19	1.17	1.85	4.91	0.09	0.30
8	No	10.55	1.22	3.55	21.71	2.52	2.33	10.18	1.21	3.56	14.15	1.65	3.15	6.55	0.75	0.71
9	Yes	7.77	1.00	1.52	7.73	1.01	1.53	7.75	1.01	1.53	7.75	1.01	1.53	0.02	0.00	0.01
10	Yes	27.45	1.88	3.79	25.30	1.88	4.15	25.24	1.88	4.15	26.00	1.88	4.03	1.25	0.00	0.21
11	Yes	8.72	1.63	2.48	9.10	1.63	2.50	9.14	1.60	2.48	8.99	1.62	2.48	0.23	0.02	0.02
12	Yes	23.09	1.20	2.69	23.11	1.35	2.67	22.93	1.20	2.70	23.05	1.25	2.69	0.10	0.09	0.02
13	No	21.99	1.93	0.89	23.16	1.39	0.88	22.71	1.12	1.38	22.62	1.48	1.05	0.59	0.41	0.29
14	Yes	7.53	3.40	3.28	7.55	3.41	3.27	7.59	3.39	3.27	7.56	3.40	3.27	0.03	0.01	0.01
15	No	19.78	3.34	2.94	7.25	1.55	5.30	20.20	3.23	2.97	15.74	2.71	3.74	7.36	1.00	1.35
16	Yes	25.22	3.99	0.88	25.12	3.99	0.86	24.95	3.97	0.84	25.10	3.98	0.86	0.14	0.01	0.02
17	Yes	12.90	2.48	1.71	13.35	2.38	1.72	12.99	2.46	1.70	13.08	2.44	1.71	0.24	0.05	0.01
18	Yes	16.93	2.72	2.09	16.89	2.71	2.12	17.45	2.68	2.06	17.09	2.71	2.09	0.31	0.02	0.03
19	Yes	8.63	5.07	2.31	8.83	5.05	2.31	8.34	5.07	2.41	8.60	5.06	2.34	0.24	0.01	0.06
20	No	2.93	0.34	1.78	4.66	0.98	1.15	3.05	0.30	1.79	3.55	0.54	1.57	0.97	0.38	0.37
21	Yes	8.39	0.33	2.42	9.68	0.33	2.23	6.45	0.33	2.42	8.17	0.33	2.36	1.62	0.00	0.11
22	Yes	14.95	1.21	2.10	14.85	1.23	2.10	14.75	1.23	2.12	14.85	1.22	2.11	0.10	0.01	0.01
23	Yes	14.26	1.58	2.21	13.99	1.64	2.21	14.02	1.68	2.21	14.09	1.64	2.21	0.15	0.05	0.00
24	Yes	25.63	0.80	3.94	25.66	0.79	3.94	26.06	0.80	3.86	25.78	0.80	3.92	0.24	0.00	0.05
25	Yes	16.61	2.65	3.27	17.46	2.66	3.05	16.59	2.66	3.27	16.89	2.66	3.20	0.50	0.00	0.13
26	Yes	25.62	1.42	2.01	26.43	1.40	1.81	25.41	1.91	1.76	25.82	1.58	1.86	0.54	0.29	0.13
27	No	4.24	0.84	1.89	5.61	1.54	1.12	4.17	0.84	1.89	4.67	1.07	1.63	0.81	0.41	0.44
28	Yes	20.46	1.05	3.53	19.89	0.63	3.80	20.80	0.71	3.63	20.38	0.80	3.65	0.46	0.22	0.14
29	Yes	20.67	0.99	1.31	20.83	0.98	1.30	19.25	0.99	1.91	20.25	0.99	1.50	0.87	0.00	0.35
30	Yes	25.10	3.45	2.08	25.41	3.33	2.14	25.64	3.63	1.65	25.38	3.47	1.96	0.27	0.15	0.27
31	Yes	13.11	0.86	2.72	12.87	0.84	2.77	12.25	0.88	2.81	12.74	0.86	2.77	0.44	0.02	0.04
32	Yes	15.15	0.61	4.30	16.49	0.58	4.07	16.39	0.61	4.07	16.01	0.60	4.15	0.75	0.02	0.13
33	Yes	9.52	3.22	0.85	10.46	3.22	0.63	9.13	3.22	0.90	9.71	3.22	0.79	0.68	0.00	0.14
34	Yes	16.64	1.89	1.04	16.41	1.62	1.46	17.11	1.69	1.09	16.72	1.73	1.19	0.36	0.14	0.23
35	Yes	33.55	2.23	3.65	33.77	2.23	3.66	33.43	2.23	3.64	33.58	2.23	3.65	0.17	0.00	0.01
36	Yes	15.88	1.82	1.15	16.00	1.77	1.14	15.92	1.82	1.16	15.93	1.80	1.15	0.06	0.03	0.01
37	Yes	13.18	1.58	1.41	13.18	1.58	1.41	12.93	1.58	1.42	13.09	1.58	1.41	0.14	0.00	0.01
38	Yes	20.19	1.88	0.79	20.33	1.80	0.81	20.23	1.69	0.98	20.25	1.79	0.86	0.07	0.10	0.11
39	Yes	20.26	1.35	0.70	20.95	1.10	0.71	18.65	1.92	0.82	19.95	1.46	0.74	1.18	0.42	0.06
40	Yes	23.57	1.23	0.84	22.11	1.38	1.15	22.33	1.32	1.15	22.67	1.31	1.05	0.79	0.07	0.18

Table E.2 Continued: Scarp RMSE and Height calculations

Profile No./ Dist. along fault (km)	Repeat-able?	Run 1 H (m)	Run 1 RMSE LS (m)	Run 1 RMSE US (m)	Run 2 H (m)	Run 2 RMSE LS (m)	Run 2 RMSE US (m)	Run 3 H (m)	Run 3 RMSE LS (m)	Run 3 RMSE US (m)	Average H (m)	Average RMSE LS (m)	Average RMSE US (m)	Standard Deviation H (m)	Standard Deviation RMSE LS (m)	Standard Deviation RMSE US (m)
41	Yes	20.81	1.23	3.02	20.33	1.28	3.02	20.21	1.26	3.02	20.45	1.26	3.02	0.31	0.02	0.00
42	Yes	24.97	1.19	1.68	23.87	1.53	1.85	24.04	1.32	1.88	24.30	1.34	1.80	0.59	0.17	0.11
43	Yes	22.24	1.79	2.49	21.60	1.88	2.56	21.77	1.88	2.53	21.87	1.85	2.53	0.34	0.05	0.04
44	Yes	23.45	2.63	1.19	22.81	2.67	1.27	22.82	2.63	1.28	23.03	2.65	1.25	0.36	0.02	0.05
45	Yes	16.65	1.44	0.91	17.40	0.83	0.97	17.57	0.78	0.96	17.21	1.02	0.94	0.49	0.36	0.03
46	No	26.72	1.38	1.59	4.52	0.33	4.74	9.03	0.33	4.82	13.42	0.68	3.71	11.73	0.61	1.84
47	No	19.78	0.51	2.77	16.60	0.50	3.35	20.58	1.60	1.92	18.99	0.87	2.68	2.10	0.63	0.72
48	Yes	25.53	1.76	1.38	25.05	1.76	1.49	25.51	1.49	1.52	25.36	1.67	1.46	0.27	0.16	0.07
49	Yes	25.03	1.45	1.50	23.90	1.64	1.60	22.75	1.55	2.08	23.89	1.55	1.73	1.14	0.10	0.31
50	Yes	19.38	1.49	4.06	17.84	2.14	4.08	17.76	2.20	4.07	18.33	1.94	4.07	0.91	0.39	0.01
51	Yes	17.25	1.08	1.84	16.83	1.09	1.96	17.68	1.08	1.75	17.25	1.08	1.85	0.42	0.01	0.11
52	Yes	17.73	0.71	1.26	17.25	0.99	1.26	17.40	0.70	1.38	17.46	0.80	1.30	0.24	0.16	0.07
53	Yes	12.35	0.77	0.68	11.52	0.88	0.90	12.00	0.88	0.68	11.96	0.84	0.75	0.42	0.07	0.13
54	Yes	21.24	0.72	0.75	21.04	0.76	0.75	21.16	0.74	0.75	21.15	0.74	0.75	0.10	0.02	0.00
55	Yes	7.01	0.99	1.29	6.93	0.98	1.29	7.07	0.99	1.29	7.00	0.99	1.29	0.07	0.01	0.00
56	No	16.89	2.27	1.99	15.90	2.78	1.88	17.72	2.06	2.00	16.84	2.37	1.95	0.91	0.37	0.06
57	Yes	23.47	1.22	2.46	23.47	1.22	2.46	25.01	1.19	2.37	23.99	1.21	2.43	0.89	0.02	0.05
58	Yes	15.29	0.93	1.18	15.31	0.91	1.17	15.68	0.93	1.16	15.43	0.92	1.17	0.22	0.01	0.01
59	Yes	20.85	0.78	1.63	20.66	0.86	1.63	22.17	0.71	1.29	21.23	0.78	1.51	0.82	0.07	0.20
60	Yes	23.85	1.48	2.32	23.70	1.67	2.20	24.60	1.59	2.05	24.05	1.58	2.19	0.48	0.09	0.14
61	Yes	24.95	3.55	2.81	26.57	3.32	2.68	26.24	3.52	2.71	25.92	3.46	2.74	0.86	0.12	0.07
62	Yes	16.52	1.33	2.76	16.07	1.33	2.79	17.70	1.33	2.60	16.77	1.33	2.72	0.84	0.00	0.11
63	Yes	22.48	1.96	1.03	22.36	2.00	1.03	22.77	1.92	1.04	22.53	1.96	1.03	0.21	0.04	0.00
64	Yes	11.44	1.58	1.36	11.43	1.60	1.36	12.15	1.35	1.36	11.68	1.51	1.36	0.42	0.14	0.00
65	No	24.68	4.17	1.17	26.45	3.30	1.21	20.47	1.64	2.91	23.87	3.03	1.77	3.07	1.28	0.99
66	Yes	30.49	3.22	1.97	31.68	2.76	1.99	31.04	3.02	1.97	31.07	3.00	1.98	0.59	0.23	0.01
67	No	26.45	1.42	1.97	20.12	1.11	3.91	23.36	1.27	2.96	23.31	1.27	2.95	3.16	0.16	0.97
68	Yes	21.05	1.37	1.60	21.89	1.42	1.16	22.44	1.36	1.15	21.79	1.38	1.31	0.70	0.03	0.26
69	Yes	16.06	1.23	0.68	15.54	1.23	1.06	16.22	1.21	0.68	15.94	1.22	0.81	0.35	0.01	0.22
70	Yes	15.61	2.73	0.66	15.81	2.73	0.63	15.61	2.73	0.68	15.68	2.73	0.66	0.11	0.00	0.03
71	Yes	13.23	1.18	0.88	13.45	1.17	0.89	13.44	1.17	0.88	13.37	1.17	0.88	0.12	0.01	0.00
72	Yes	15.06	2.48	1.54	15.27	2.48	1.54	15.21	2.48	1.54	15.18	2.48	1.54	0.11	0.00	0.00
73	Yes	2.99	0.69	0.67	3.30	0.68	0.58	3.08	0.68	0.64	3.12	0.68	0.63	0.16	0.01	0.05
74	Yes	8.93	1.50	0.72	10.46	1.52	0.72	10.59	1.48	0.72	9.99	1.50	0.72	0.92	0.02	0.00
75	Yes	1.97	1.89	4.02	2.59	1.93	4.02	2.29	1.91	4.04	2.28	1.91	4.03	0.31	0.02	0.01
76	Yes	7.24	1.63	3.61	7.27	1.61	3.63	7.19	1.60	3.59	7.23	1.61	3.61	0.04	0.01	0.02
77	Yes	7.23	1.21	2.12	7.72	1.21	2.10	7.59	1.21	2.11	7.51	1.21	2.11	0.25	0.00	0.01
78	Yes	13.55	0.74	2.10	12.90	0.74	2.10	13.55	0.74	2.21	13.33	0.74	2.14	0.37	0.00	0.06
79	Yes	12.78	1.73	1.57	13.07	1.73	1.51	12.61	1.73	1.59	12.82	1.73	1.56	0.23	0.00	0.04
80	Yes	10.60	0.78	3.85	10.87	0.77	3.87	11.18	0.78	3.87	10.88	0.78	3.86	0.29	0.01	0.01

Table E.3 Continued: Scarp RMSE and Height calculations

Profile No./ Dist. along fault (km)	Repeat-able?	Run 1 H (m)	Run 1 RMSE LS (m)	Run 1 RMSE US (m)	Run 2 H (m)	Run 2 RMSE LS (m)	Run 2 RMSE US (m)	Run 3 H (m)	Run 3 RMSE LS (m)	Run 3 RMSE US (m)	Average H (m)	Average RMSE LS (m)	Average RMSE US (m)	Standard Deviation H (m)	Standard Deviation RMSE LS (m)	Standard Deviation RMSE US (m)
81	Yes	8.77	1.30	2.43	8.23	1.42	2.40	8.48	1.27	2.34	8.49	1.33	2.39	0.27	0.08	0.05
82	Yes	0.94	0.41	1.45	0.90	0.41	1.44	0.77	0.46	1.44	0.87	0.43	1.45	0.09	0.03	0.00
83	Yes	3.06	0.95	0.65	2.95	0.95	0.66	2.96	0.96	0.66	2.99	0.95	0.66	0.06	0.00	0.01
84	No	7.73	1.35	0.96	8.10	1.42	0.74	7.87	1.35	0.94	7.90	1.38	0.88	0.19	0.04	0.12
85	Yes	5.17	1.30	1.40	5.49	1.32	1.41	5.34	1.31	1.40	5.33	1.31	1.40	0.16	0.01	0.00
86	Yes	2.33	0.83	0.81	2.35	0.83	0.80	2.32	0.83	0.81	2.33	0.83	0.81	0.02	0.00	0.00
87	Yes	8.35	0.99	0.59	8.79	0.83	0.62	8.25	1.02	0.59	8.46	0.95	0.60	0.29	0.10	0.02
88	No	4.62	2.82	1.20	4.71	2.81	1.20	1.85	2.50	1.14	3.73	2.71	1.18	1.63	0.18	0.04
89	No	6.45	0.53	2.65	3.88	0.81	2.01	4.01	0.81	2.09	4.78	0.72	2.25	1.45	0.16	0.35
90	Yes	6.14	2.05	0.67	6.02	2.05	0.70	6.12	2.06	0.67	6.09	2.05	0.68	0.06	0.01	0.02
91	Yes	5.38	2.73	2.36	6.32	2.68	2.36	6.18	2.68	2.37	5.96	2.70	2.36	0.51	0.03	0.01
92	Yes	9.26	0.85	2.50	8.55	1.00	2.46	8.66	1.00	2.47	8.83	0.95	2.48	0.38	0.09	0.02
93	Yes	1.51	0.56	2.49	2.01	0.56	2.51	1.74	0.56	2.50	1.76	0.56	2.50	0.25	0.00	0.01
94	Yes	12.15	1.12	2.16	11.90	1.18	2.16	12.36	1.06	2.15	12.14	1.12	2.16	0.23	0.06	0.00
95	Yes	7.68	0.54	1.43	7.45	0.54	1.44	7.73	0.53	1.44	7.62	0.54	1.44	0.15	0.00	0.01
96	Yes	9.15	1.19	0.88	9.17	1.20	0.88	9.10	1.20	0.89	9.14	1.20	0.88	0.04	0.01	0.01
97	Yes	2.62	1.37	4.38	1.96	1.37	4.43	3.01	1.36	4.33	2.53	1.36	4.38	0.53	0.01	0.05
98	Yes	12.36	1.03	2.95	12.42	1.03	3.00	12.28	1.03	2.95	12.35	1.03	2.97	0.07	0.00	0.02
99	Yes	2.58	1.97	1.92	5.95	1.97	1.97	5.82	1.96	1.95	4.79	1.97	1.95	1.91	0.00	0.02
100	Yes	3.70	0.99	0.95	3.84	1.01	0.95	3.81	1.01	0.95	3.79	1.00	0.95	0.07	0.01	0.00
101	Yes	19.85	1.12	0.67	19.50	1.16	0.68	18.80	1.15	1.15	19.38	1.15	0.83	0.54	0.02	0.27
102	Yes	13.05	0.92	0.81	12.67	0.97	0.82	11.70	0.92	1.31	12.47	0.94	0.98	0.69	0.03	0.28
103	Yes	7.51	0.78	1.80	6.95	0.91	1.78	6.98	0.94	1.80	7.15	0.88	1.79	0.31	0.08	0.01
104	No	9.56	1.04	2.07	9.22	1.06	2.06	8.04	1.41	2.09	8.94	1.17	2.07	0.80	0.21	0.02
105	No	9.13	0.94	1.15	9.06	0.94	1.15	11.65	1.50	1.08	9.95	1.12	1.13	1.48	0.32	0.04
106	Yes	12.12	0.95	0.76	12.12	0.95	0.76	10.38	1.03	0.81	11.54	0.97	0.78	1.00	0.05	0.03
107	Yes	15.43	1.58	1.70	16.12	1.60	1.46	14.64	1.59	1.81	15.40	1.59	1.66	0.74	0.01	0.18
108	Yes	14.70	0.99	0.84	14.76	0.94	0.84	14.41	1.03	0.83	14.62	0.99	0.84	0.19	0.04	0.00
109	Yes	15.14	0.89	0.65	14.76	1.00	0.65	14.37	0.91	0.93	14.76	0.93	0.75	0.39	0.06	0.16
110	No	12.93	1.95	0.76	15.57	0.75	0.79	10.58	0.68	1.53	13.03	1.13	1.03	2.50	0.71	0.43
111	Yes	28.37	3.10	2.72	29.25	3.15	2.35	28.28	3.08	2.78	28.63	3.11	2.62	0.54	0.04	0.23
112	Yes	11.70	1.49	1.28	11.55	1.49	1.30	11.51	1.49	1.31	11.59	1.49	1.30	0.10	0.00	0.01
113	Yes	8.64	0.78	0.53	8.74	0.76	0.53	8.52	0.78	0.53	8.63	0.77	0.53	0.11	0.01	0.00
114	Yes	10.91	1.01	1.17	11.97	1.02	0.75	11.32	1.14	0.80	11.40	1.06	0.90	0.53	0.07	0.23
115	Yes	10.91	0.70	0.96	10.81	0.71	0.97	10.72	0.74	0.97	10.81	0.72	0.97	0.09	0.02	0.00
116	No	8.38	1.18	0.98	10.73	1.08	0.57	8.49	1.17	0.96	9.20	1.15	0.84	1.33	0.05	0.23
117	Yes	10.55	1.58	1.77	11.46	1.50	1.82	11.17	1.55	1.82	11.06	1.54	1.80	0.46	0.04	0.03
118	Yes	5.83	1.16	0.75	6.45	0.96	0.76	5.80	1.13	0.76	6.03	1.08	0.75	0.37	0.11	0.01
119	Yes	4.76	0.76	0.61	4.70	0.72	0.66	4.53	0.76	0.66	4.66	0.75	0.64	0.12	0.02	0.02
120	Yes	8.17	1.10	0.47	8.32	1.08	0.47	8.48	1.06	0.47	8.32	1.08	0.47	0.15	0.02	0.00

Table E.4 Continued: Scarp RMSE and Height calculations

Profile No./ Dist. along fault (km)	Repeat- able?	Run 1 H (m)	Run 1 RMSE LS (m)	Run 1 RMSE US (m)	Run 2 H (m)	Run 2 RMSE LS (m)	Run 2 RMSE US (m)	Run 3 H (m)	Run 3 RMSE LS (m)	Run 3 RMSE US (m)	Average H (m)	Average RMSE LS (m)	Average RMSE US (m)	Standard Deviation H (m)	Standard Deviation RMSE LS (m)	Standard Deviation RMSE US (m)
121	Yes	4.83	0.44	0.73	5.03	0.40	0.73	4.84	0.43	0.73	4.90	0.42	0.73	0.11	0.02	0.00
122	Yes	4.28	0.54	0.49	4.82	0.55	0.47	4.88	0.56	0.45	4.66	0.55	0.47	0.33	0.01	0.02
123	Yes	3.23	0.43	0.69	6.45	0.43	0.75	5.16	0.42	0.74	4.95	0.43	0.73	1.62	0.01	0.04
124	No	1.81	0.39	0.39	1.13	0.40	0.43	1.84	0.39	0.39	1.60	0.40	0.40	0.40	0.00	0.02
125	No	4.62	0.86	0.74	0.19	0.44	0.96	2.64	0.60	1.02	2.48	0.63	0.91	2.22	0.21	0.15
126	No	0.13	0.53	0.32	4.52	0.53	0.78	4.52	0.52	0.78	3.05	0.53	0.63	2.53	0.00	0.27
127	Yes	3.56	0.54	0.34	3.63	0.53	0.34	3.71	0.53	0.34	3.63	0.53	0.34	0.08	0.01	0.00
128	No	2.58	0.33	0.75	2.58	0.40	0.30	2.58	0.33	0.36	2.58	0.36	0.47	0.00	0.04	0.24

APPENDIX F

ALGORITHM PERFORMANCE FOR SYNTHETIC DATA

This Appendix contains results for the Chapter 4 algorithm applied to a range of synthetic catalogues. Figs. F.1 and F.2 are the misfit values for width and slope, respectively, using the noise free synthetic scarp catalogue. For the height misfit plot, please refer to the Chapter 4. Equally, figs. F.3 to F.4 show the algorithm misfit values (width and slope) for the noisy synthetic catalogue. All plots are for selected profiles, as the catalogues comprised over 1,000 profiles. The average height, width and misfit plots can be found in the original Chapter.

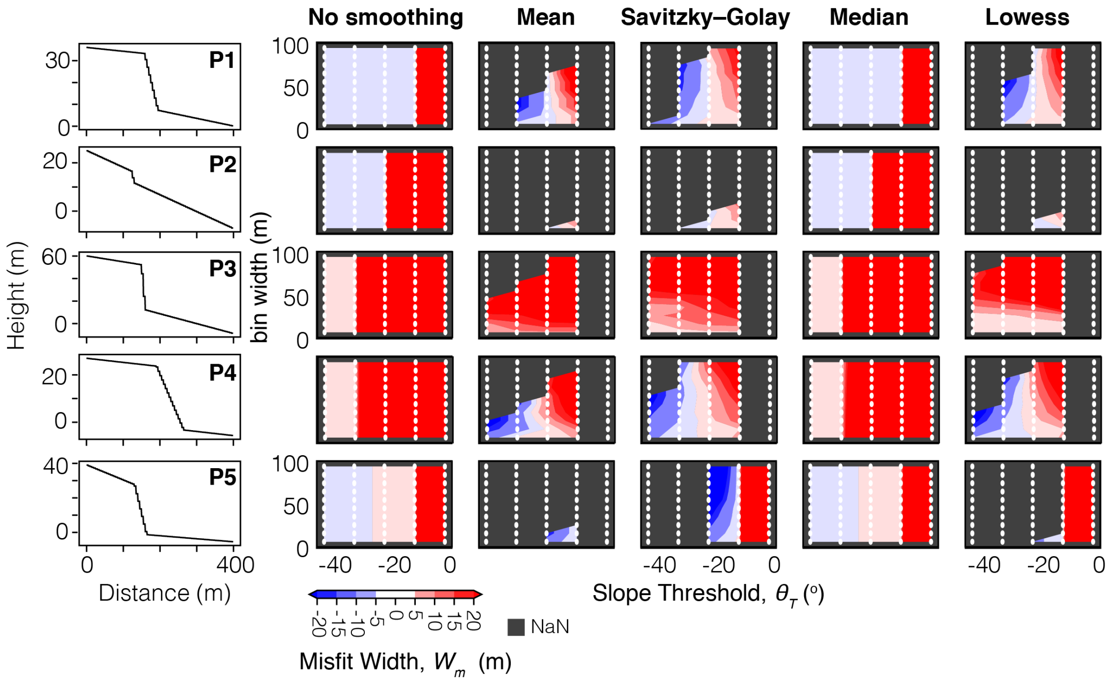

Fig. F.1 Scarp width misfit W_m for five noise-free synthetic catalogue examples: 1) randomly selected; 2) small scarp height; 3) steep, large scarp; 4) gentle original surfaces; and 5) variable original surfaces. See fig. 4.4 for scarp height H_m misfit results and fig. F.2 for scarp slope α_m misfit results.

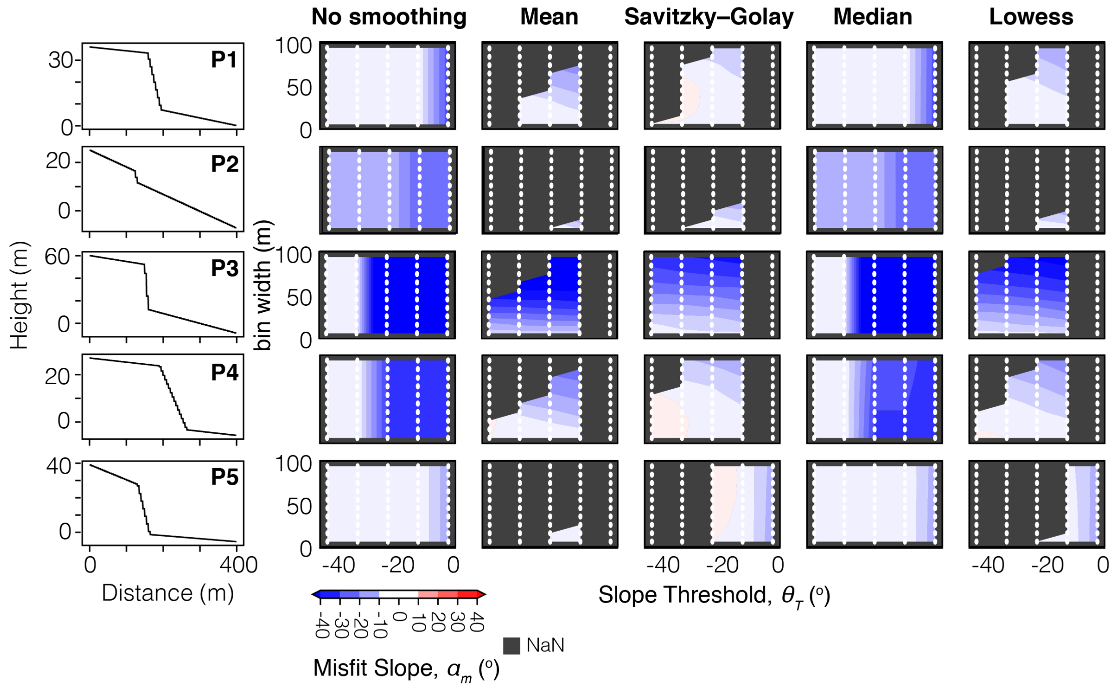

Fig. F.2 Scarp slope misfit W_m for five noise-free synthetic catalogue examples: 1) randomly selected; 2) small scarp height; 3) steep, large scarp; 4) gentle original surfaces; and 5) variable original surfaces. See fig. 4.4 for scarp height H_m misfit results and fig. F.1 for scarp width W_m misfit results.

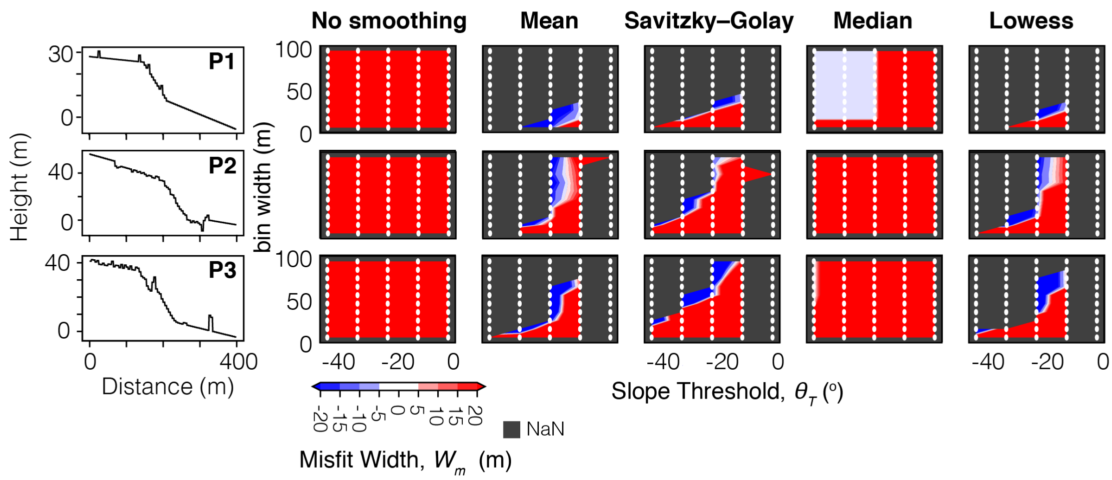

Fig. F.3 Scarp width misfit W_m for three noisy synthetic catalogue examples. See fig. 4.4 for scarp height H_m misfit results and fig. F.4 for scarp slope α_m misfit results.

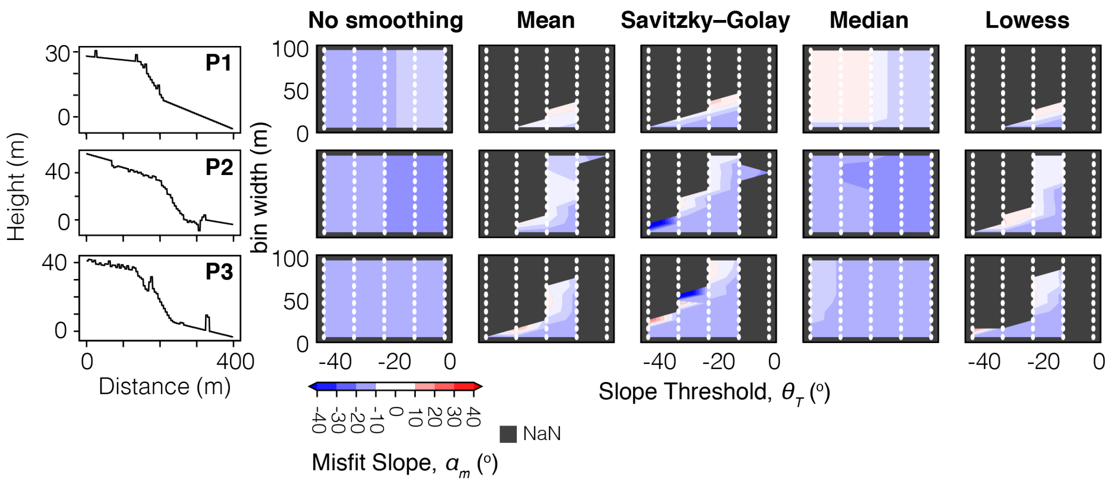

Fig. F.4 Scarp slope misfit α_m for three noisy synthetic catalogue examples. See fig. 4.4 for scarp height H_m misfit results and fig. F.3 for scarp width W_m misfit results.

Appendix G

Algorithm performance for southern Malawi faults

This Appendix presents algorithms results against a manual analysis (fig. G.1) for: the Thyolo fault (fig. G.2), the Muona fault (fig. G.3), and the Malombe fault scarps (figs. G.4 to G.6). The DEM used was a 12 m TanDEM-X DEM. The bottom plot shows the along-strike variation in scarp height, width and slope estimated by a manual analysis compared to the algorithm. The results for the algorithm are based on the best-fit parameter space for each fault. The best-fit parameter space can be found in the Chapter (4).

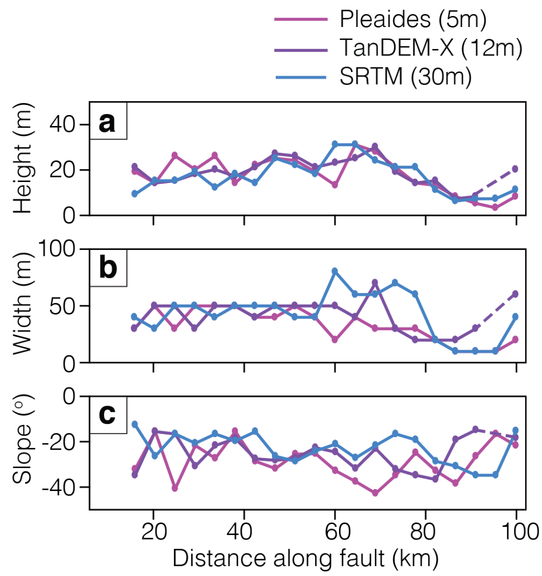

Fig. G.1 Manual along-strike Bilila-Mtakataka fault profile for scarp a) height H, b) width W and c) slope α. Profiles taken at ~ 5 km intervals using the Pleiades 5 m (pink), TanDEM-X 12 m (purple) and SRTM 30 m (blue) DEMs. For tabular results see Table H.2.

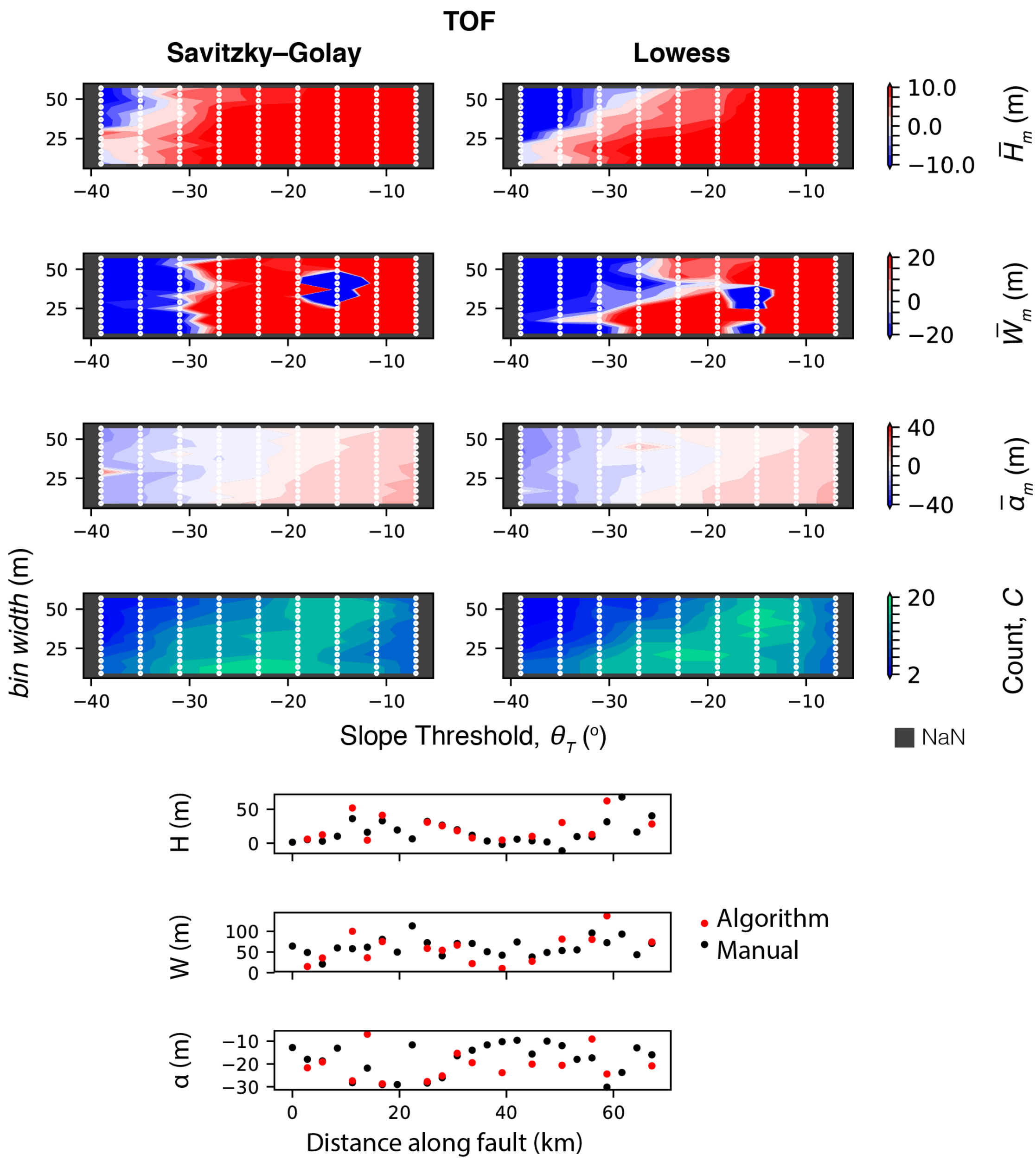

Fig. G.2 Top: The misfit analysis for the Thyolo fault (TOF). Bottom: The misfit between manual analysis and algorithm using the best performing parameters for twenty-five selected profiles.

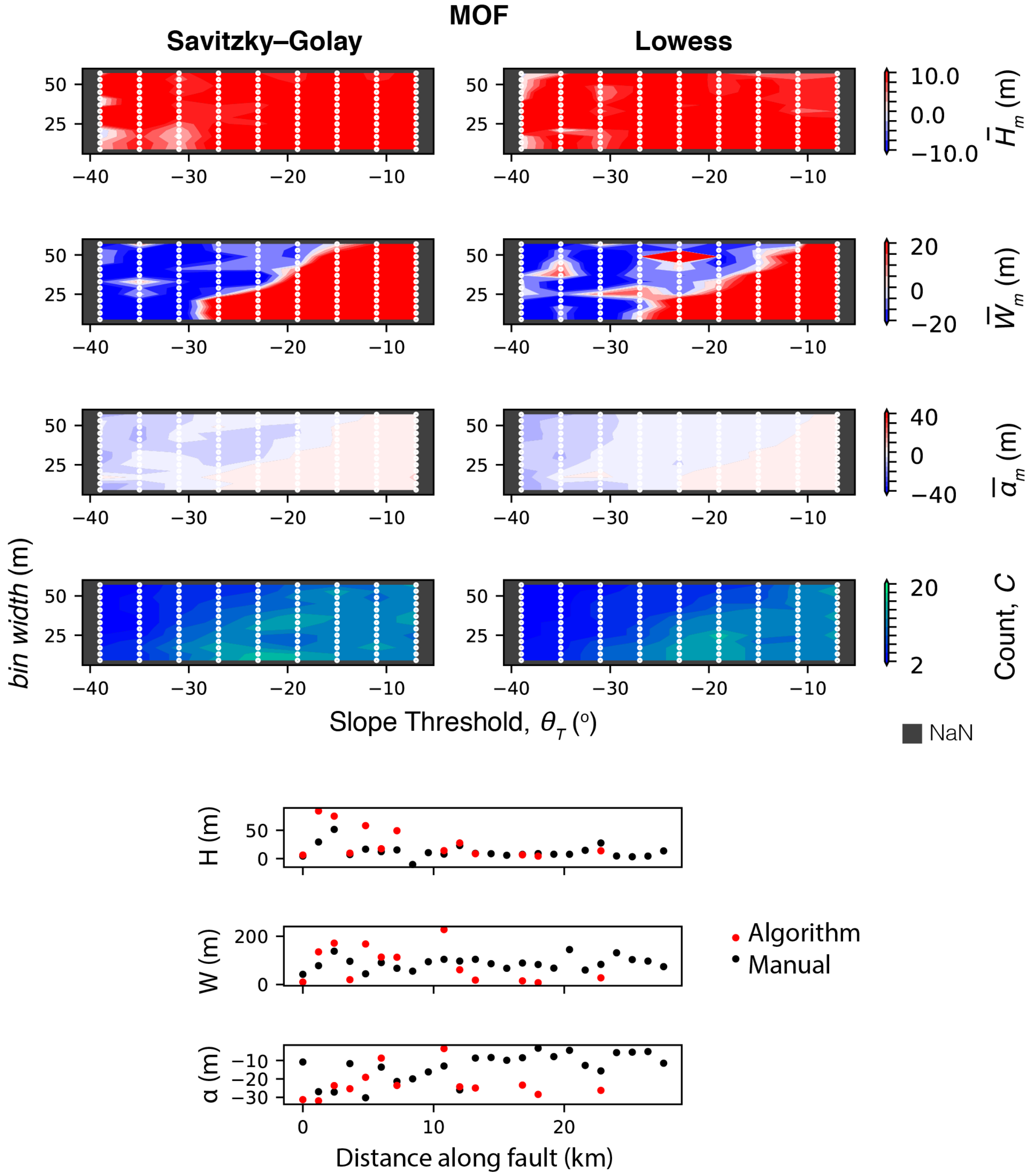

Fig. G.3 Top: The misfit analysis for the Muona fault (MOF). Bottom: The misfit between manual analysis and algorithm using the best performing parameters for twenty-five selected profiles.

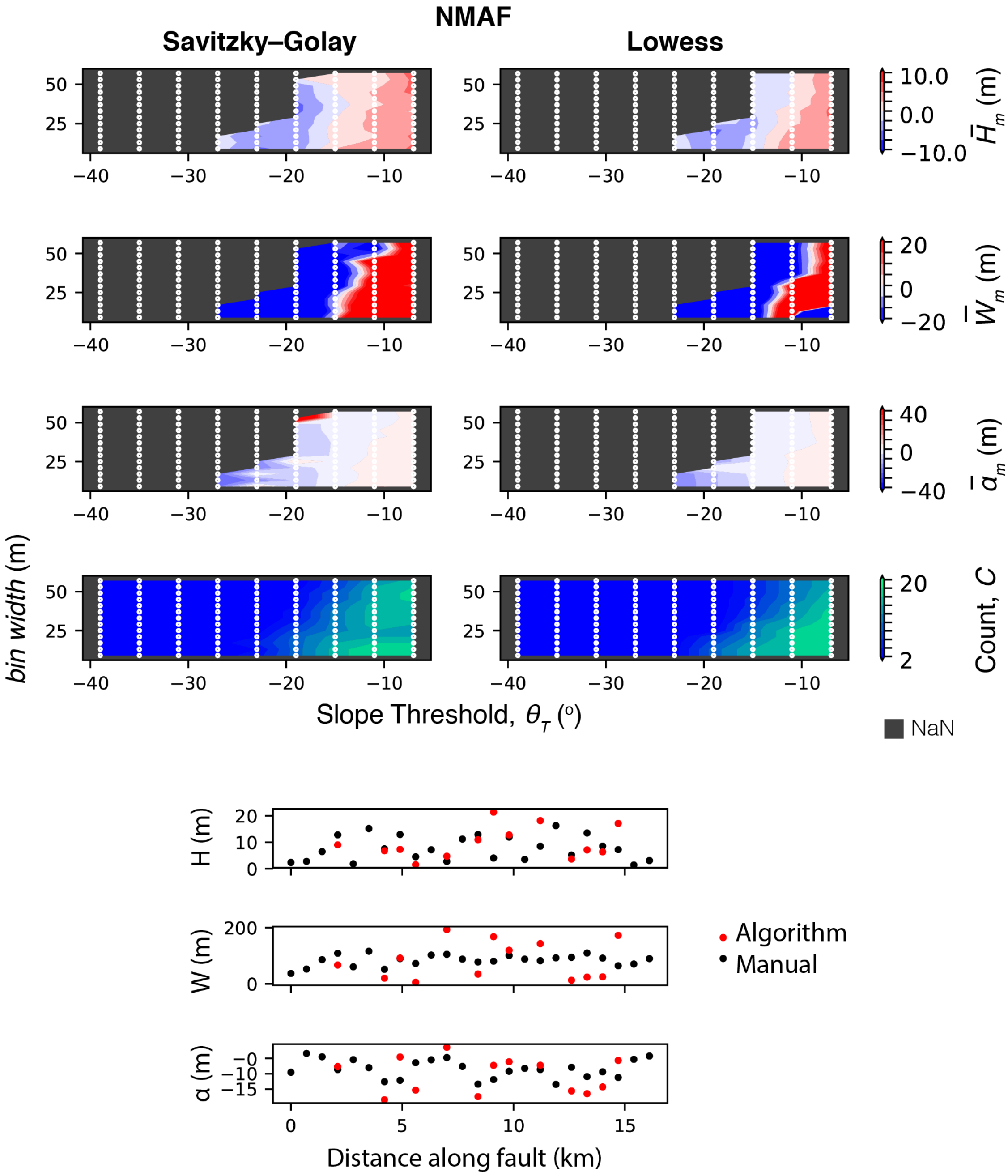

Fig. G.4 Top: The misfit analysis for the northern Malombe fault (NMAF). Bottom: The misfit between manual analysis and algorithm using the best performing parameters for twenty-five selected profiles.

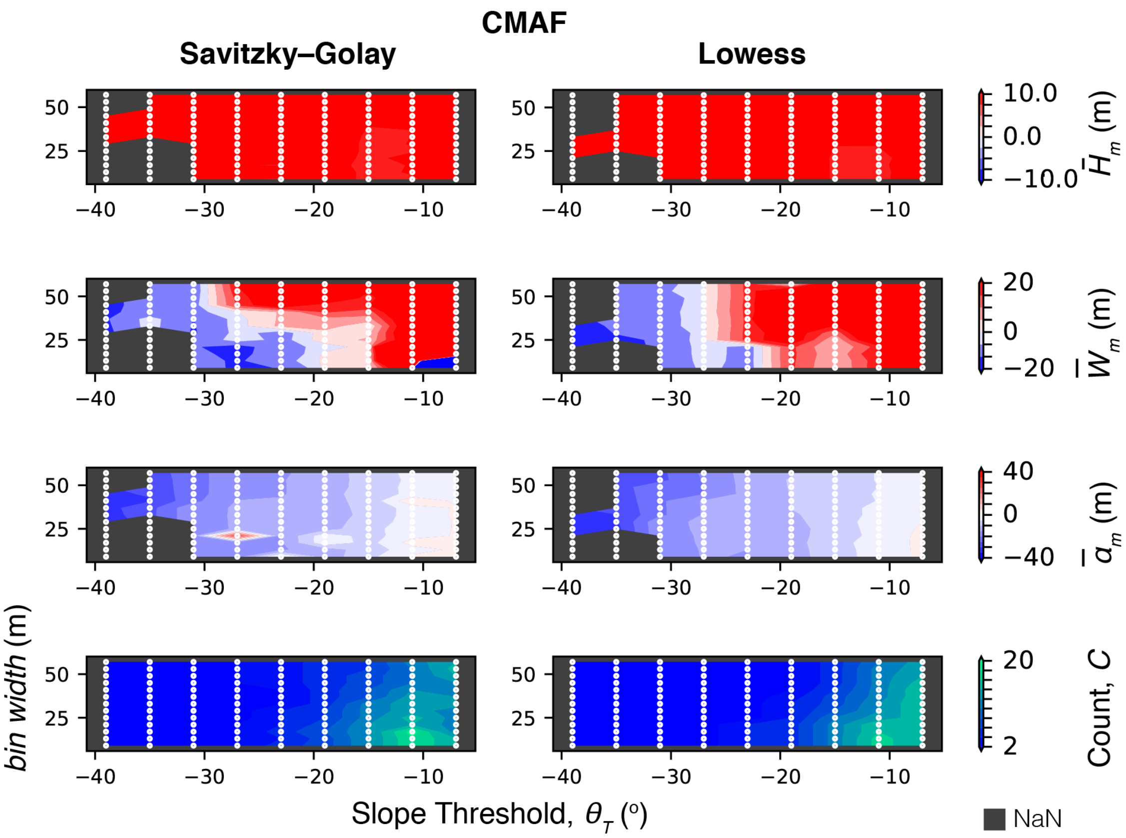

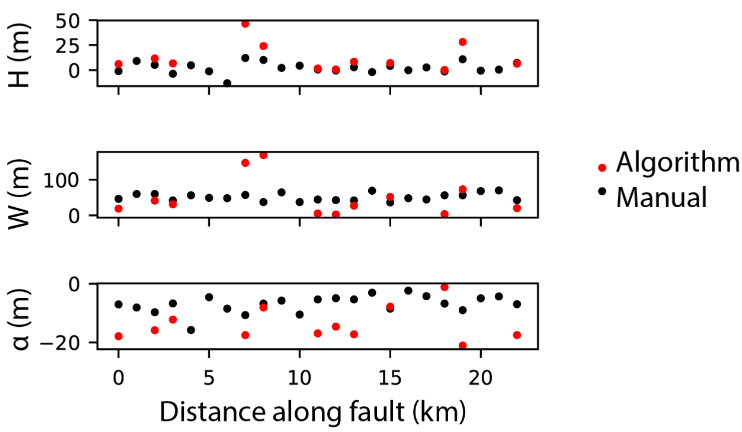

Fig. G.5 Top: The misfit analysis for the central Malombe fault (CMAF). Bottom: The misfit between manual analysis and algorithm using the best performing parameters for twenty-five selected profiles.

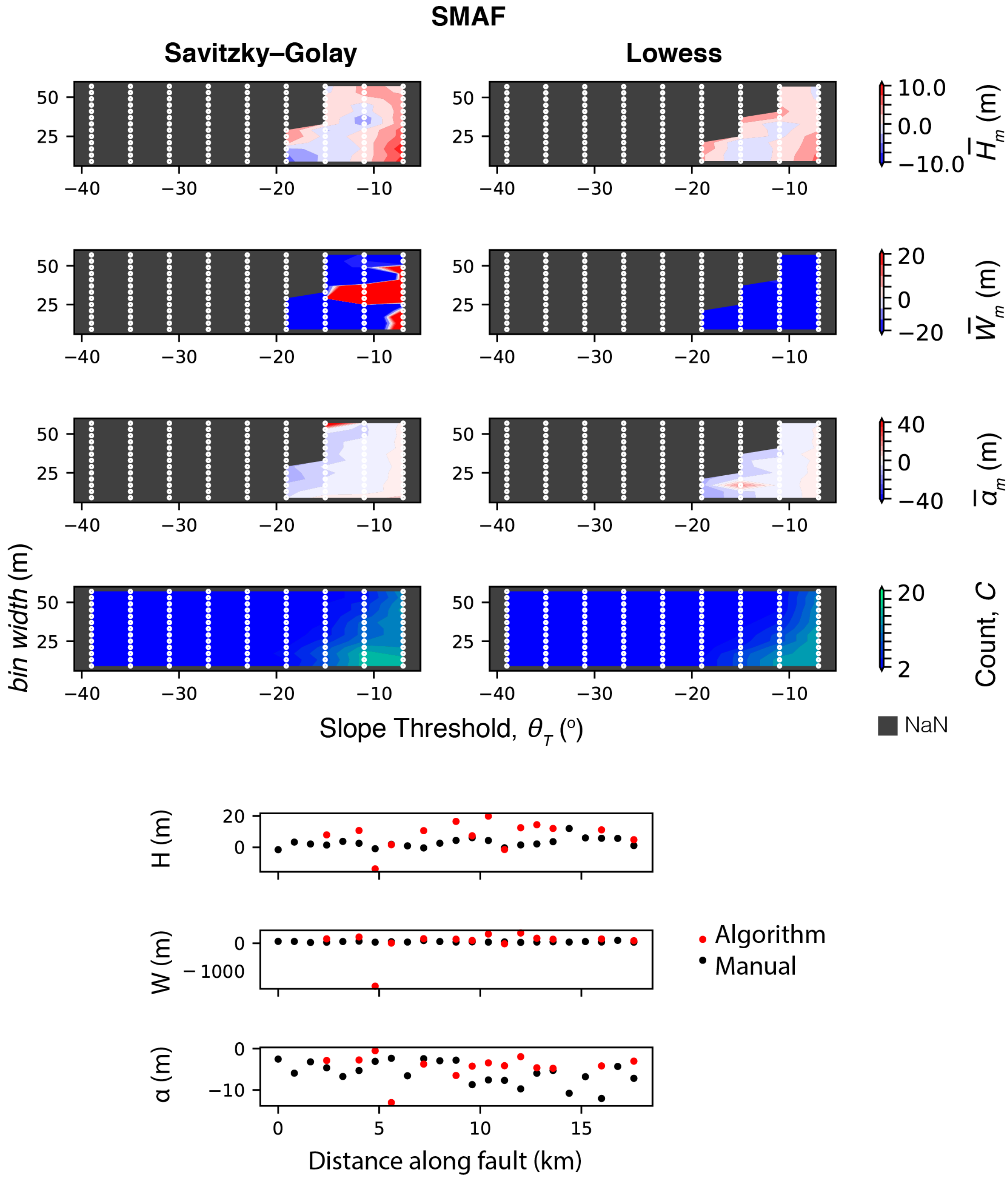

Fig. G.6 Top: The misfit analysis for the southern Malombe fault (SMAF). Bottom: The misfit between manual analysis and algorithm using the best performing parameters for twenty-five selected profiles.

APPENDIX H

RESOLUTION ANALYSIS FOR ALGORITHM

In this Appendix we explore whether DEM resolution affects the algorithm from Chapter 4 and/or the interpretation of structural segments. Here, we provide a resolution analysis. Figs. H.1 to H.3 show the average misfit for all 1,000 noisy catalogue scarps for resolutions of 5, 10 and 30 m, for three selected filter types from Table H.1. The plots show that a greater number of scarps were identified using the higher resolution data, especially those with gentle slopes. In addition, the misfit generally reduced with increasing resolution.

Figs. H.4 and H.5 show the misfit analysis for 12 and 30 m resolution profiles for the BMF, compared to the 5 m resolution used in Chapter 4 to infer structural segments along the fault. A tabular version of the manual anaysis is shown in Table H.2.The maximum scarp height, width and slope values calculated by the manual analysis is shown in Table H.3. Similar to the synthetic results, the higher the DEM resolution, the greater than number of scarps identified (Table H.4). A comparison between estimated scarp height, width and slope for each DEM resolution is shown in fig. H.6. The bottom panel (b) shows the results following the removal of outliers (for tabular form, see Table H.5).

The along-strike difference between DEM resolutions is shown in fig. H.7, prior to the removal of outliers, and fig. H.8 following their removal. It shows that the scarp height estimate is least influenced by the DEM resolution, and scarp width the most affected. A more detailed comparison for each scarp parameter, and the along-strike variation in scarp height is shown in fig. H.9.

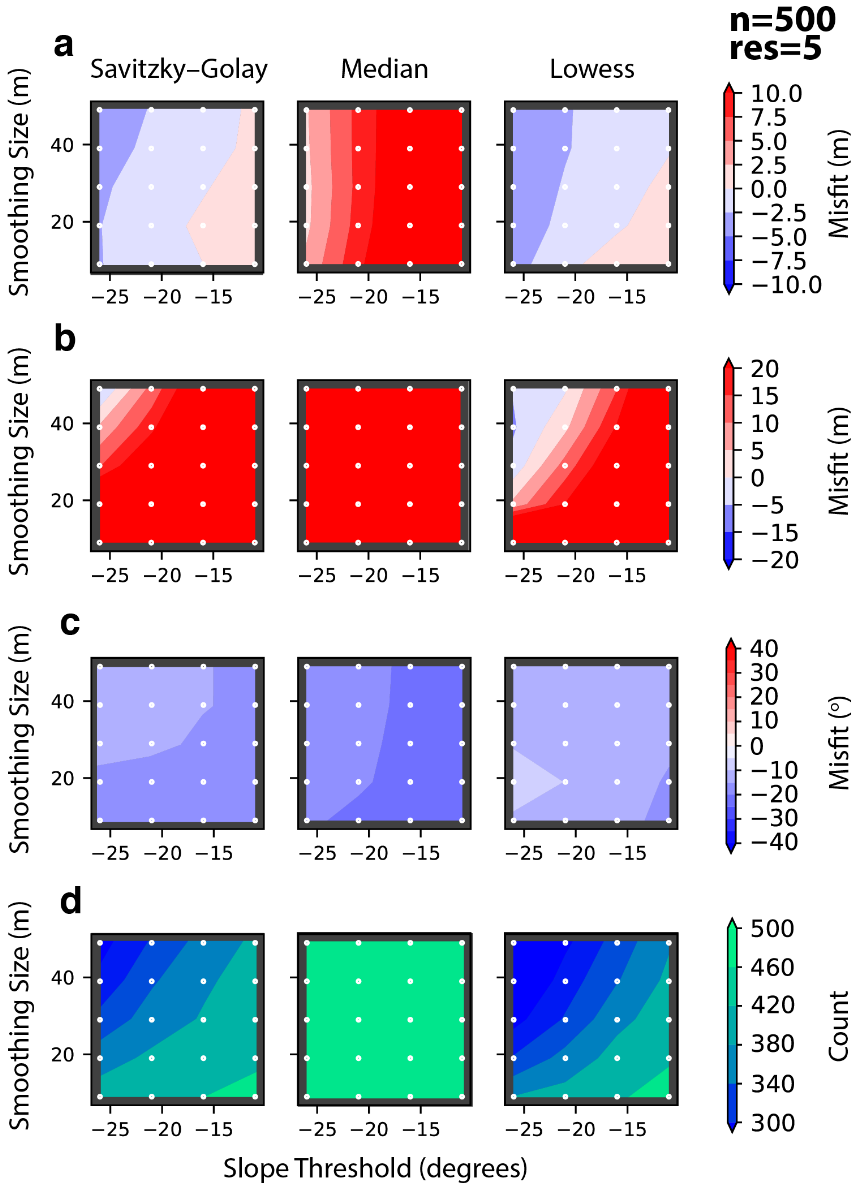

Fig. H.1 The average misfit and count for all 1,000 noisy synthetic catalogue fault scarps using a resolution of 5 m. a) Scarp height; b) Scarp width; c) Scarp slope; and d) Count. Grey values denote a NaN result was returned for all profiles.

Table H.1 A description of the digital filters used in this study.

	Filter Method	Description
1	No Smoothing	No Smoothing applied
2	Moving Mean (MME)	Uses the mean value in the window.
3	Moving Median (MMD)	Uses the median value in the window.
4	Savitzky-Golay (SG)	A least-squares polynomial filter.
5	Lowess (LW)	Locally weighted non-parametric regression.

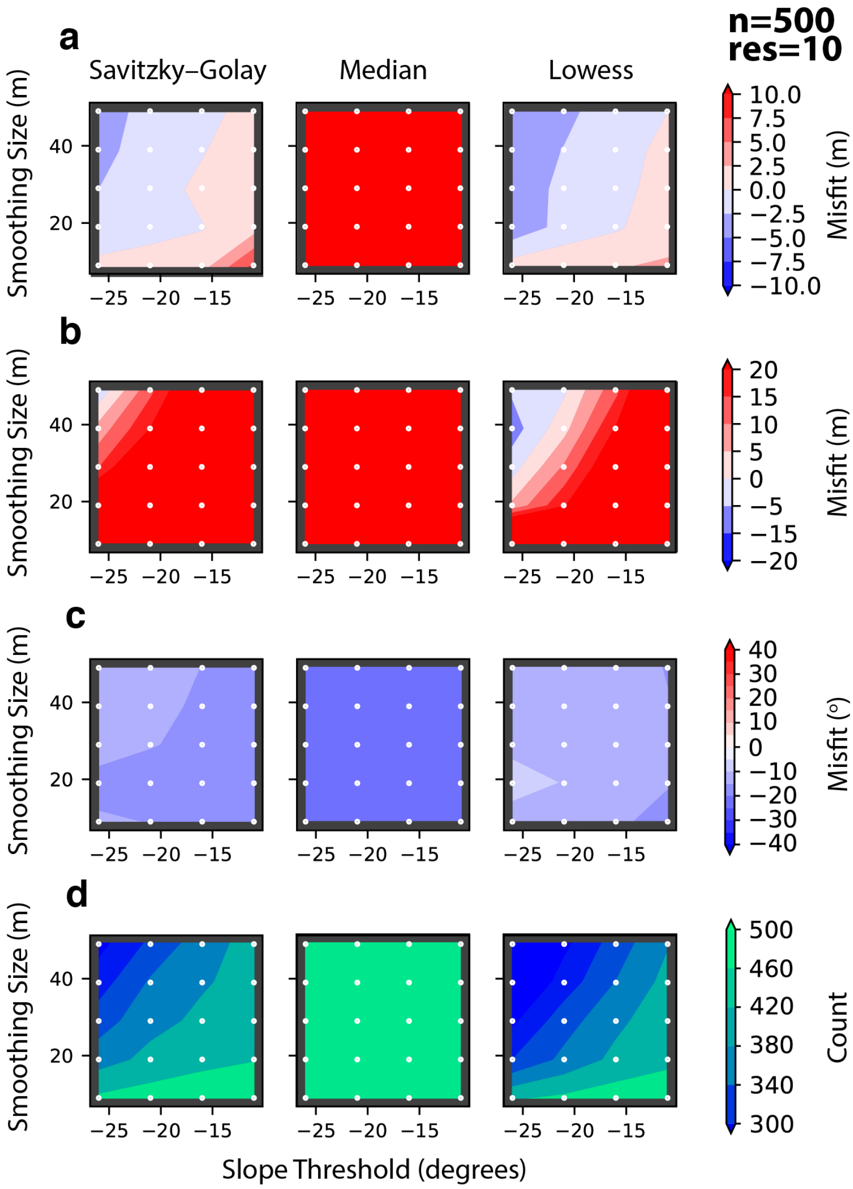

Fig. H.2 The average misfit and count for all 1,000 noisy synthetic catalogue fault scarps using a resolution of 10 m. a) Scarp height; b) Scarp width; c) Scarp slope; and d) Count. Grey values denote a NaN result was returned for all profiles.

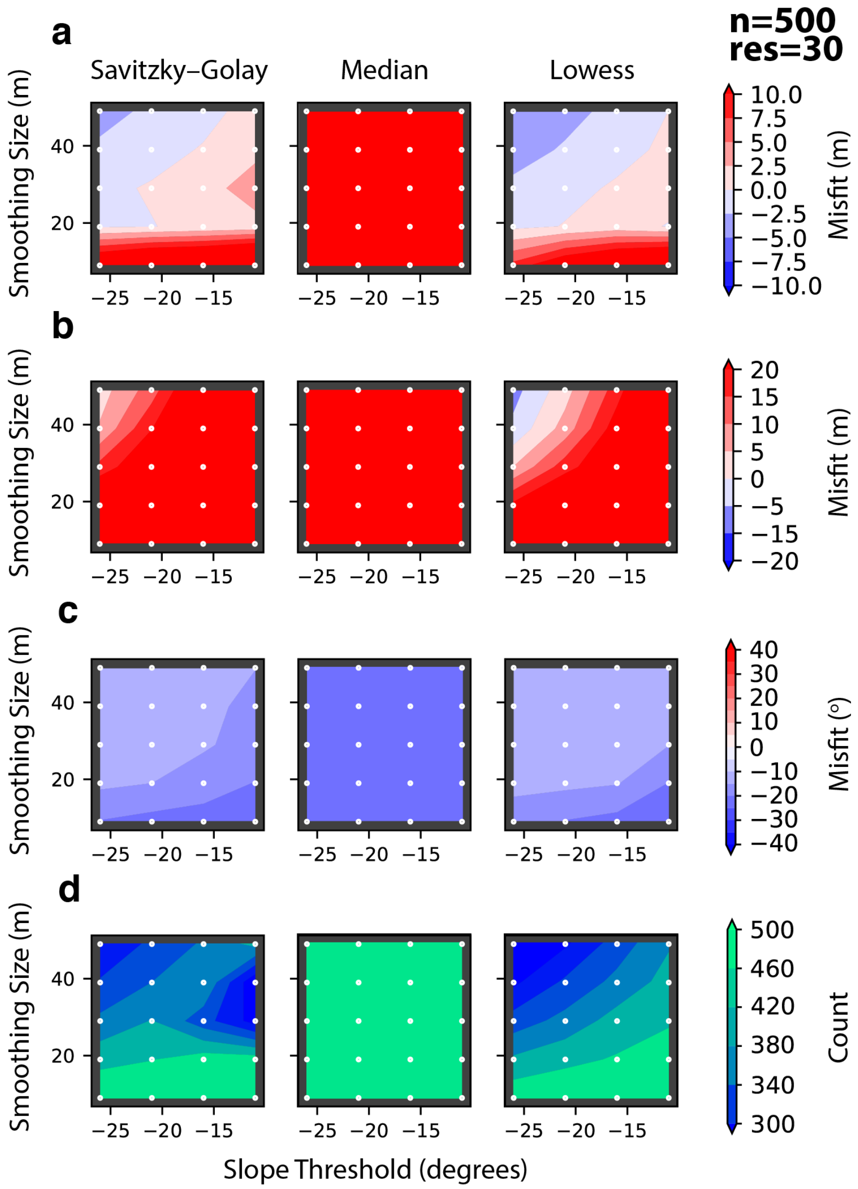

Fig. H.3 The average misfit and count for all 1,000 noisy synthetic catalogue fault scarps using a resolution of 30 m. a) Scarp height; b) Scarp width; c) Scarp slope; and d) Count. Grey values denote a NaN result was returned for all profiles.

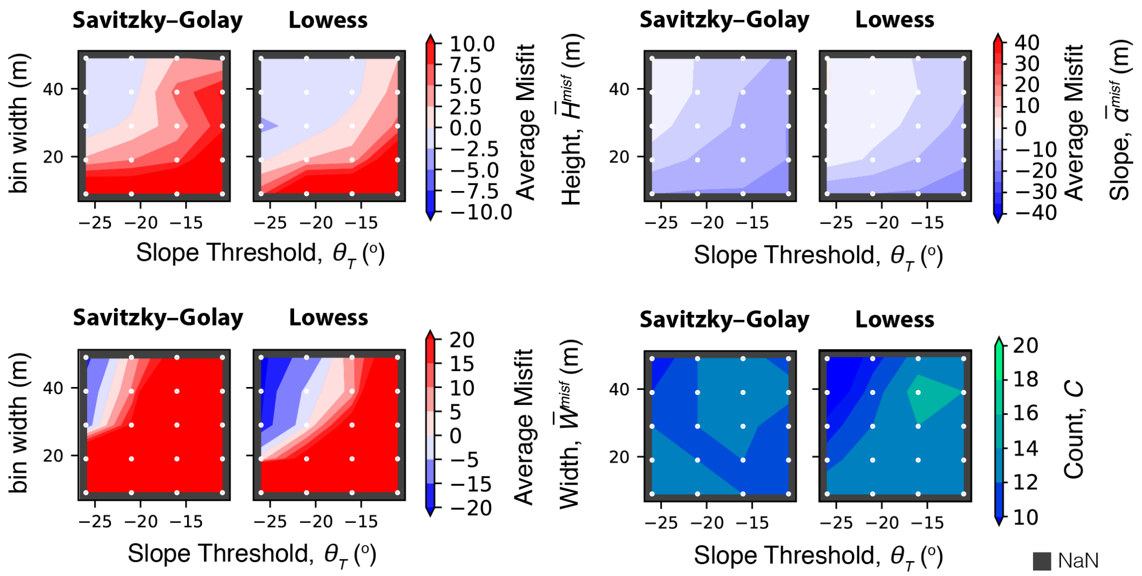

Fig. H.4 Average misfit values between algorithm and manual scarp parameters using the TanDEM-X 12 m DEM for: a) scarp height $\bar{H}^m$; b) scarp width $\bar{W}^m$; and c) scarp slope $\bar{\alpha}^m$. d) The count (C) of identified fault scarps.

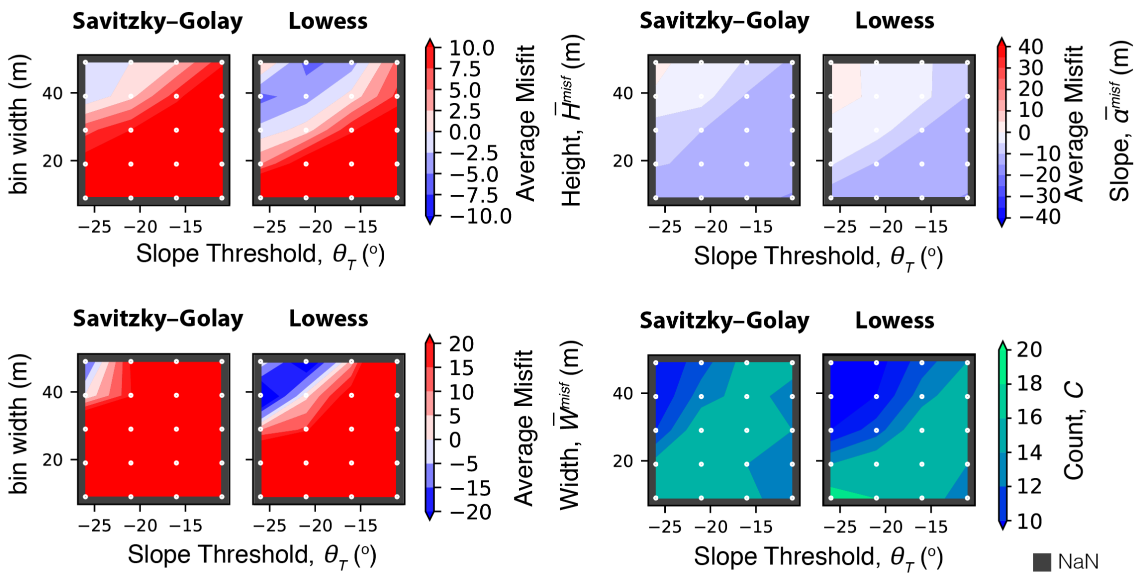

Fig. H.5 Average misfit values between algorithm and manual scarp parameters using the SRTM 30 m DEM for: a) scarp height $\bar{H}^m$; b) scarp width $\bar{W}^m$; and c) scarp slope $\bar{\alpha}^m$. d) The count (C) of identified fault scarps.

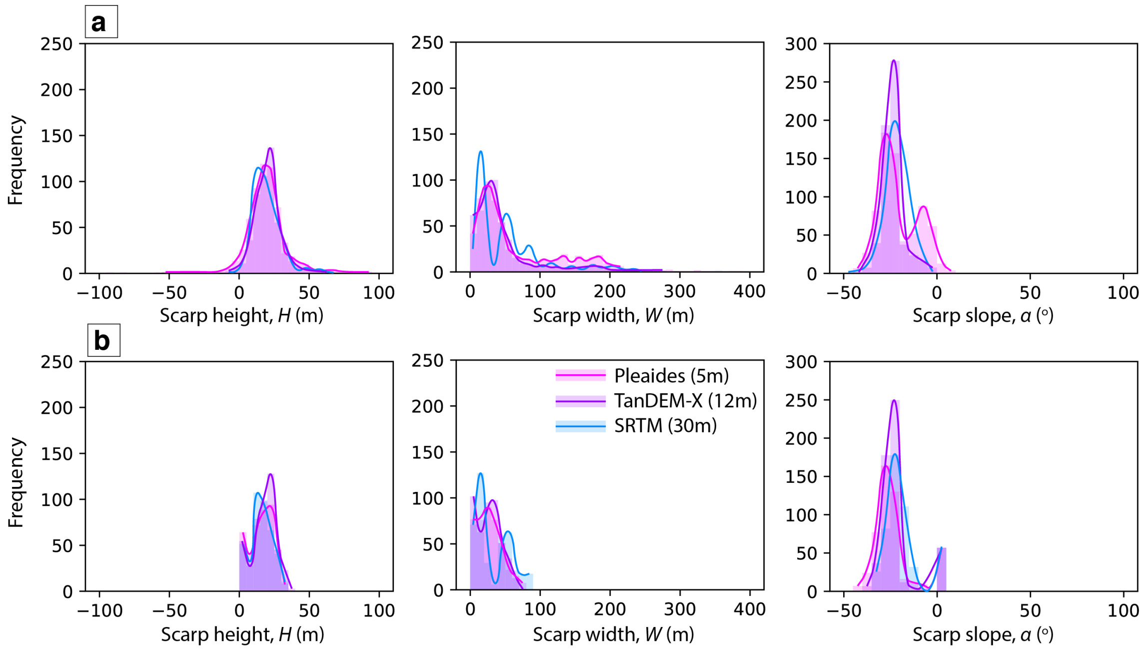

Fig. H.6 Histogram of the Bilila-Mtakataka fault scarp parameters using the algorithm for: a) all algorithm estimates (raw); and b) post-quality checked results. Pleiades 5 m (pink), TanDEM-X 12 m (purple) and SRTM 30 m (blue).

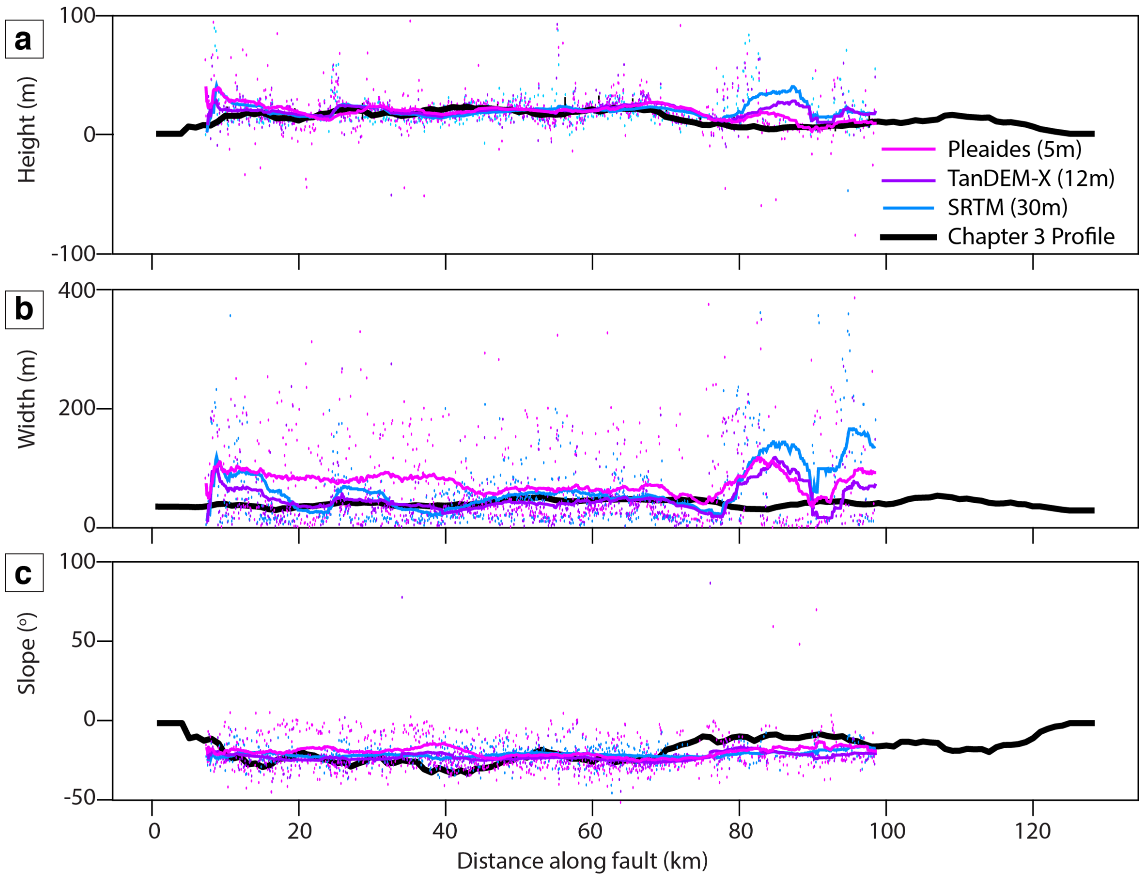

Fig. H.7 Height, width and slope profiles using the algorithm on Pleiades 5 m (pink), TanDEM-X 12 m (purple) and SRTM 30 m (blue) DEMs. A moving mean (window size of 7 km) is shown by a solid line coloured corresponding to the DEM used. The manually derived TanDEM-X moving mean (window size of 7 km) from chapter 3 is shown by a blacks line.

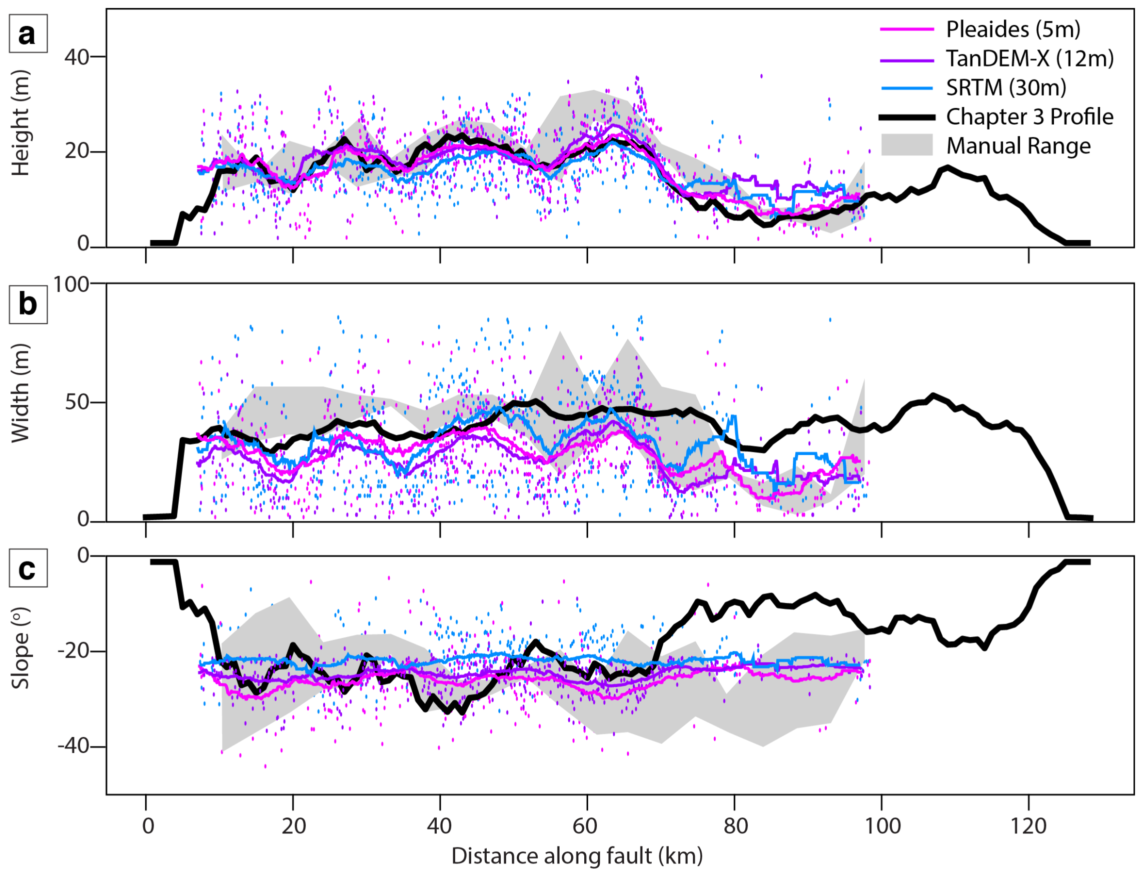

Fig. H.8 The quality checked height, width and slope profiles using the algorithm on Pleiades 5 m (pink), TanDEM-X 12 m (purple) and SRTM 30 m (blue) DEMs. A moving mean (window size of 7 km) is shown by a solid line coloured corresponding to the DEM used. The manually derived TanDEM-X moving mean (window size of 7 km) from chapter 3 is shown by a black line and the envelope of manual DEM results in this study is shown by the grey polygon.

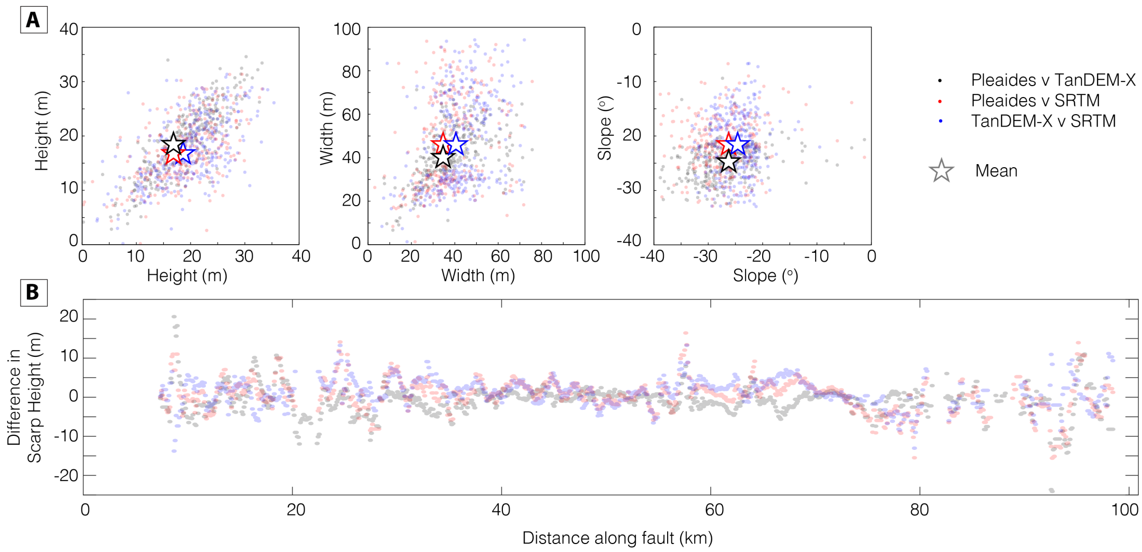

Fig. H.9 a) A comparison of algorithm scarp parameters for all DEMs (Pleiades, TanDEM-X and SRTM). b) The along-strike error between scarp height measurements for each DEM using the algorithm.

Table H.2 Manually derived scarp parameters for twenty Bilila-Mtakataka fault scarp profiles using the 5 m Pleiades, 12 m TanDEM-X and 30 m SRTM DEMs.

		Pleiades			TanDEM-X			SRTM		
	Dist (km)	H (m)	W (m)	α (^{o})	H (m)	W (m)	α (^{o})	H (m)	W (m)	α (^{o})
1	10.3	19	30	-32	21	30	-35	9	40	-13
2	14.9	14	50	-16	14	50	-16	15	30	-27
3	19.5	26	30	-41	15	50	-17	15	50	-17
4	24.1	20	50	-22	18	30	-31	19	50	-21
5	28.7	26	50	-27	20	50	-22	12	40	-17
6	33.3	14	50	-16	17	50	-19	18	50	-20
7	37.9	22	40	-29	21	40	-28	14	50	-16
8	42.5	25	40	-32	27	50	-28	25	50	-27
9	47.1	24	50	-26	26	50	-27	22	40	-29
10	51.7	19	40	-25	21	50	-23	18	40	-24
11	56.3	13	20	-33	23	50	-25	31	80	-21
12	60.9	31	40	-38	25	40	-32	31	60	-27
13	65.5	28	30	-43	30	70	-23	24	60	-22
14	70.1	21	30	-35	19	30	-32	21	70	-17
15	74.7	14	30	-25	14	20	-35	21	60	-19
16	79.3	13	20	-33	15	20	-37	11	20	-29
17	83.9	8	10	-39	7	20	-19	6	10	-31
18	88.5	5	10	-27	8	30	-15	7	10	-35
19	93.1	3	10	-17	-	-	-	7	10	-35
20	97.7	8	20	-22	20	60	-18	11	40	-15

Table H.3 The 2σ maximum and minimum values used in the algorithm quality check for the Bilila-Mtakataka fault.

Value	Pleiades	TanDEM-X	SRTM
Max Height (m)	37	35	33
Max Width (m)	77	71	88
Max Slope (°)	44	40	33

Table H.4 Algorithm scarp parameters for the Bilila-Mtakataka fault. Scarp height, width and slope are given as averages with an error of one standard deviation error.

Value	Pleiades	TanDEM-X	SRTM
Count, *C* (m)	719	610	581
Height (m)	19±17	21±11	21±13
Width (m)	73±71	46±48	61±63
Slope (°)	20±12	23±9	21±6

Table H.5 Quality checked (2σ of original data) algorithm scarp parameters for the Bilila-Mtakataka fault. Scarp height, width and slope are given as averages with an error of one standard deviation error.

Value	Pleiades	TanDEM-X	SRTM
Count, *C*	496	546	489
Height (m)	16±9	17±9	16±8
Width (m)	26±18	26±17	23±24
Slope (°)	23±10	22±8	19±8

APPENDIX I

SCARP DIFFUSION AGE MODELS

This Appendix describes the scarp diffusion age (κt) models developed in Chapter 5. Fig. I.1 shows how the diffusion constant κ alters the scarp profile after a 15,000 year period. This is a graphical representation of the core equation for scarp degradation (equation 5.2).

Fig. I.2 is a composite figure of the exploration of the model parameter space. Panel a shows the scarp degradation following a single event with slip u of 30 m, whereas panel b is a scarp formed by three u 10 m events. All other parameters are given at the top of the figure. Both scarp profiles degrade to the same shape after 15,000 years. All other panels are for multiple events, where certain parameters are altered: c) slip u per event is increased (6, 10, 14 m); d) slip u per event is decreased (14, 10, 6 m); e) slip rate r between events is increased (2, 4, 6 m/kyr); f) slip rate r between events is decreased (6, 4, 2 m/kyr); g) fault dip δ per event is increased (40°, 60°, 80°); h) fault dip δ per event is decreased (80°, 60°, 40°); i) the location of the fault crest x_s is moved toward the hanging-wall (HWM); j) the location of the fault crest x_s is moved toward the footwall (FWM); and k) the location of the fault crest x_s is alternated between two points. The scenarios that formed composite scarps were: changes in slip, changes in slip rate, and fault dip increase. The scenarios that formed multi-scarps were: fault dip decrease, movement of the scarp crest.

An underlying assumption in the Chapter was that the scarp and fault dip were equal (δ); however, in reality newly formed fault scarps comprise vertical to sub-vertical free faces at the top of the scarp. In Fig. I.3 we undertake a sensitivity test based on the initial scarp profile shape. We find that a free face rapidly smooths (within a hundred years) and does not affect the final profile after 15,000 years unless either the slip rate r is greater than 8 m/kyr (equivalent to 8 mm/yr) or the diffusion constant is less than 0.8 m^2/kyr. Diffusion constants this small are unlikely in rift environments, especially for southern Malawi. In addition, slow strain rifts will not have slip rates of 8 mm/yr, but this may be applicable for regions such as the Gulf of Corinth if all the extension is accommodated on a single fault.

The inverse solution to the scarp degradation model is shown for Mua in fig. I.4 and for Kasinje in fig. I.5. The best-fit diffusion age κt is given as the inverse solution with the smallest RMSE (marked by a circle in the plots). A uncertainty of 5 cm is applied to the RMSE to give diffusion age error bars (shown as vertical lines).

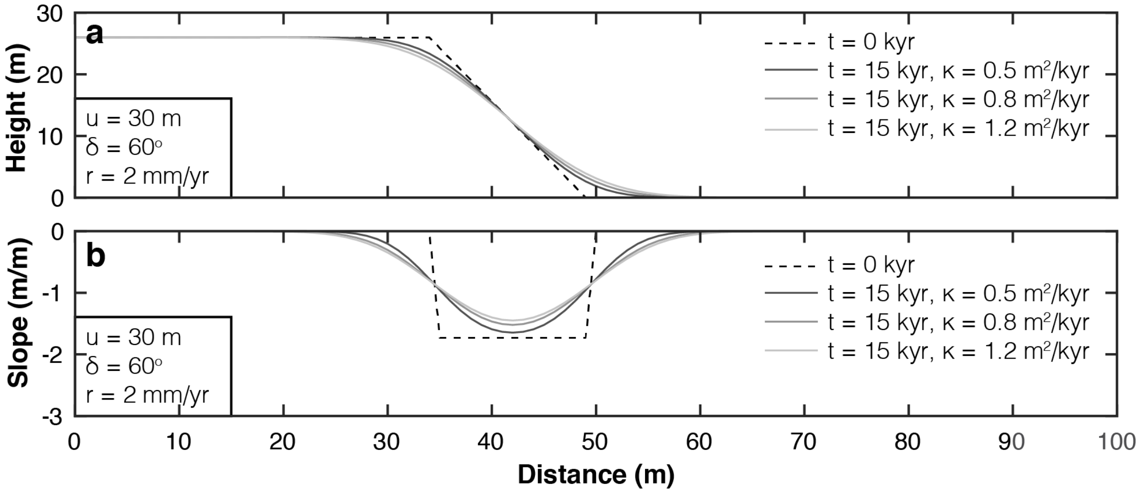

Fig. I.1 The response of varying diffusion constant κ on scarp degradation for a scarp formed by a single large slip u (30 m) event. a) Scarp profile. b) Slope profile.

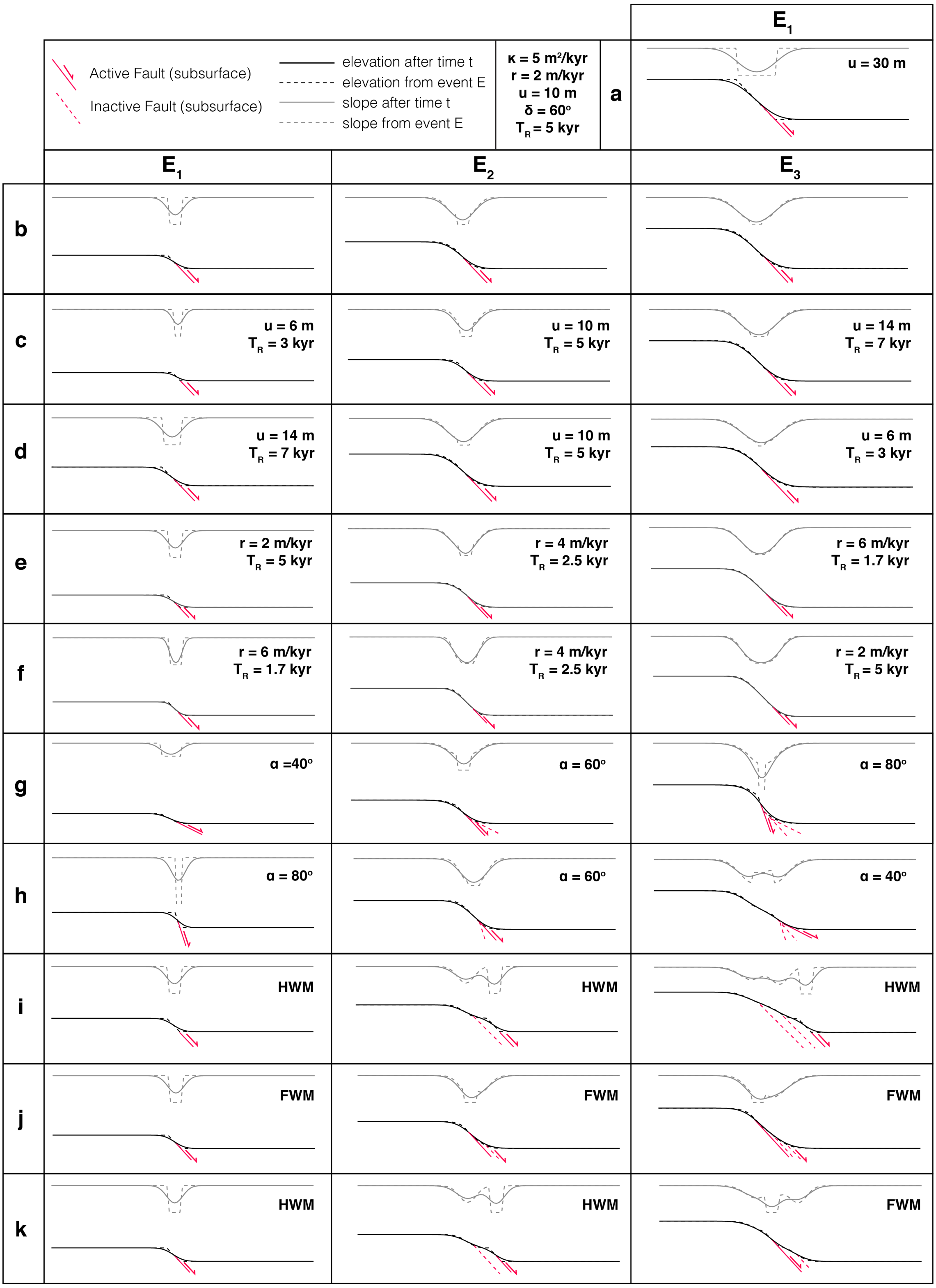

Fig. I.2 A composite figure for the scarp morphological response to scarp degradation for a: a) single and b) multiple events. For multiple events, simulation parameters are varied also: c) increasing slip per event; d) decreasing slip per event; e) increasing slip rate between events; f) decreasing slip rate between events; g) increasing fault dip per event; h) decreasing fault dip per event; i) moving the active fault surface toward the hanging-wall; j) moving the active fault surface toward the footwall; and k) alternating the active fault between two parallel faults.

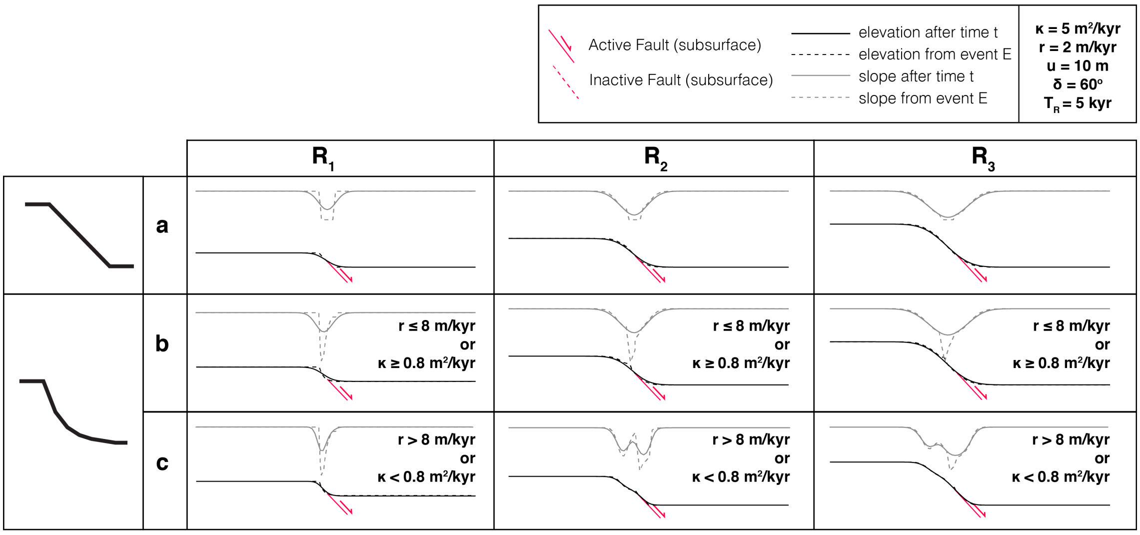

Fig. I.3 Comparing the morphological response to scarp degradation using: a) a simplified scarp that equals the fault dip; and b and c) a scarp with a steep fresh face at the top, for various values of slip rate and κ.

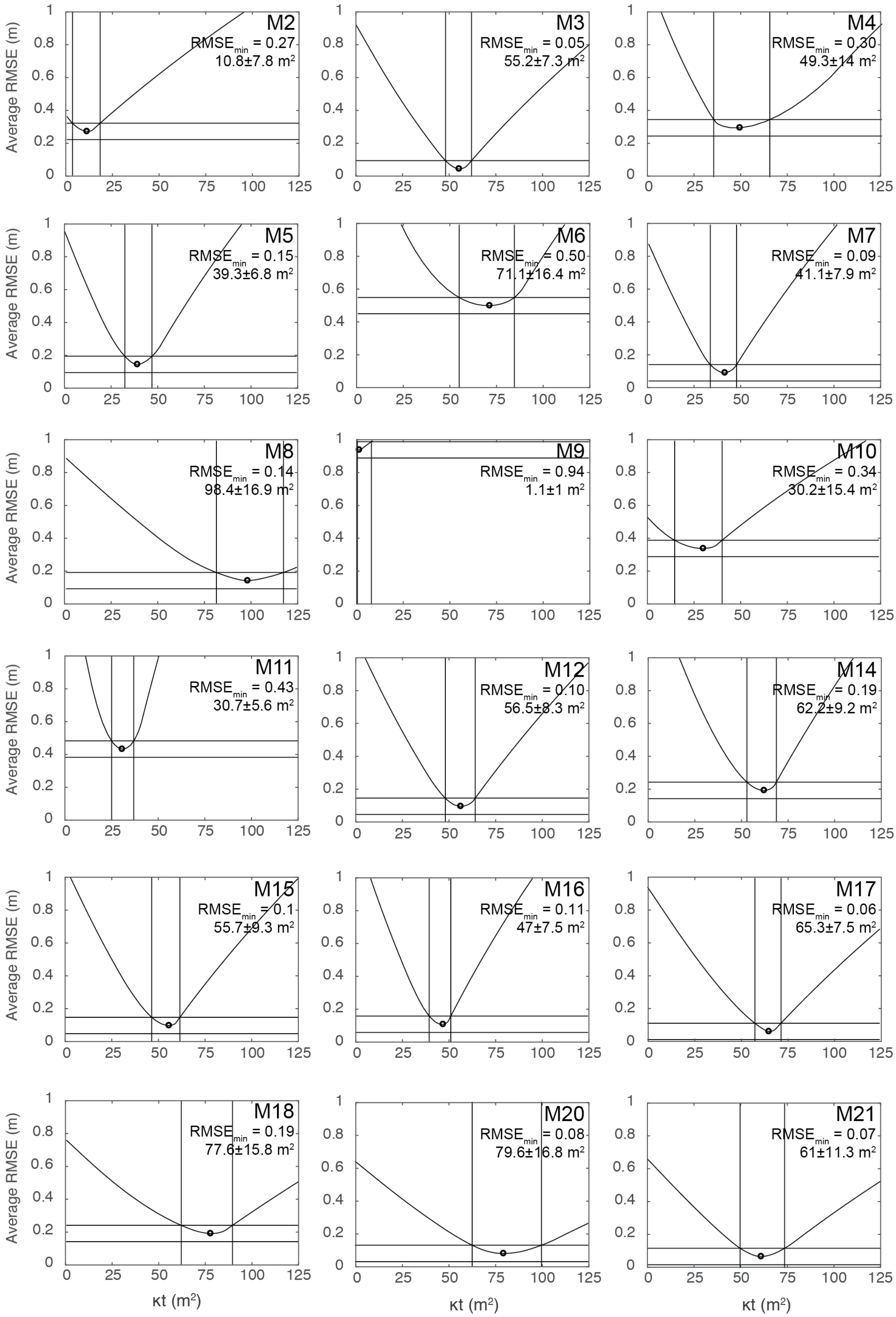

Fig. I.4 Forward model results for Mua profiles

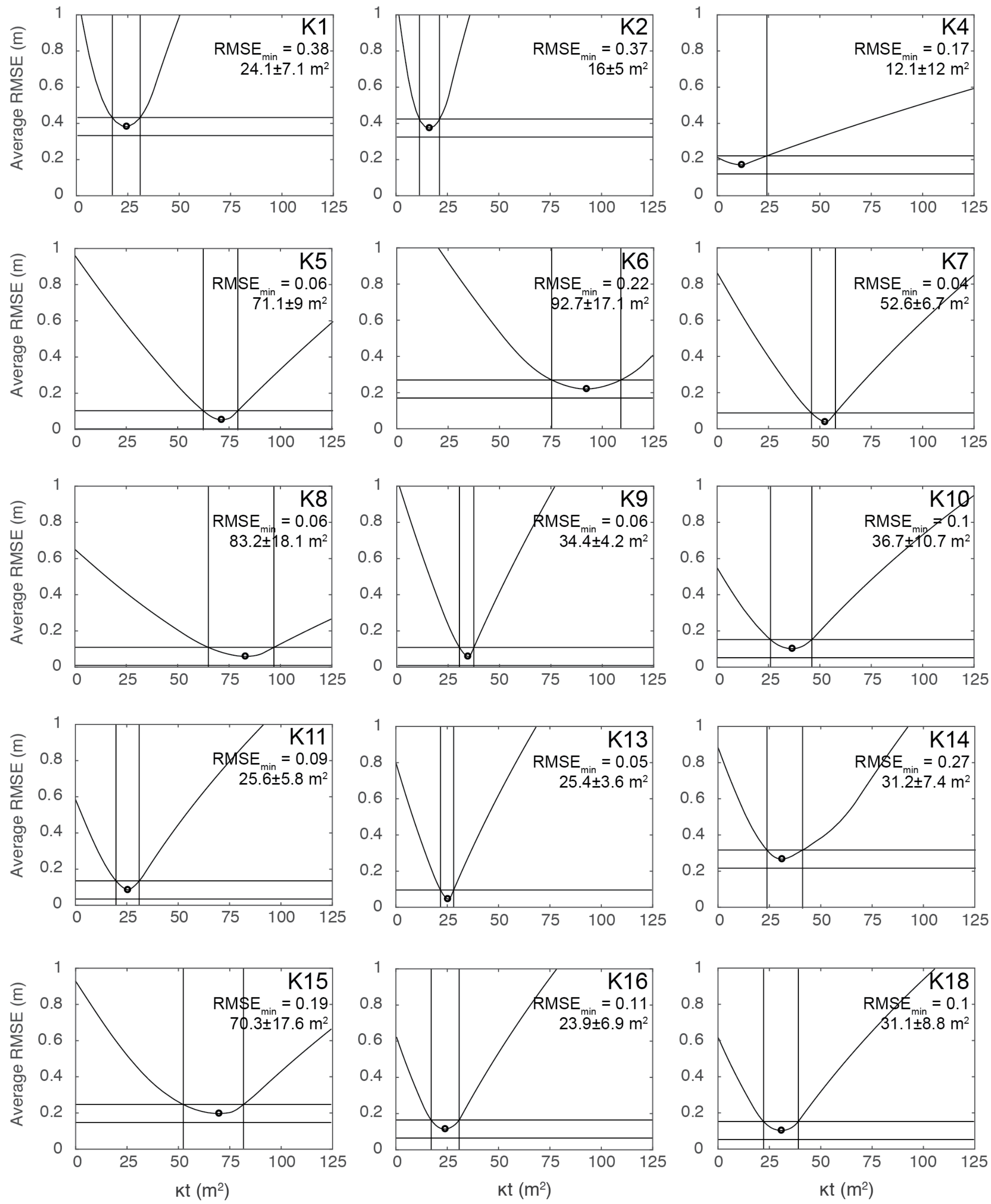

Fig. I.5 Forward model results for Kasinje profiles

Appendix J

Knickpoint analysis

This Appendix shows the river and stream profiles used in the knickpoint analysis in Chapter 5. Fig. J.1 shows a map-view of the seven rivers and streams used in the analysis: a) Naminkokwe River (Nm), b) Mua north stream (MsN), c) Mua south stream (MsS), d) Livelezi River (Lv), e) Kasinje north stream (KsN), f) Kasinje south stream (KsS), and g) Mtuta River (Mt). Fig. J.2 shows the location of the inferred knickpoints from the Chapter.

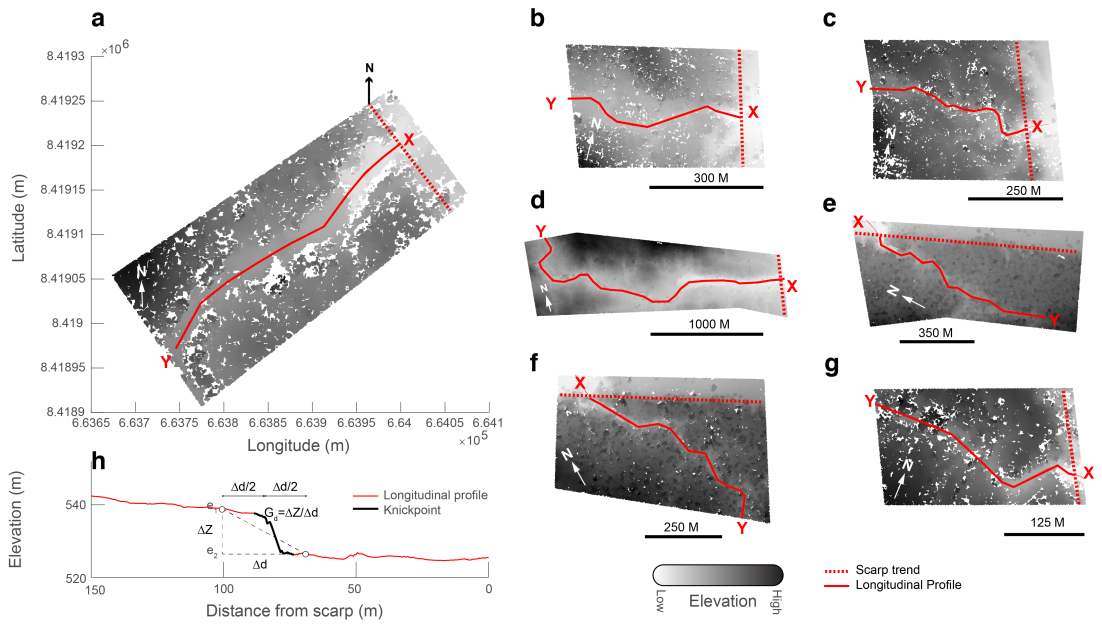

Fig. J.1 Panels a to g) Map-view image of the severn longitudinal profiles used in the knickpoint analysis: a) Naminkokwe River, b) Mua north stream, c) Mua south stream, d) Livelezi River, e) Kasinje north stream, f) Kasinje south stream, and g) Mtuta River. The red line shows the longitudinal profile, and the red dashed line the local scarp trend. h) The longitudinal river profile from the Naminkokwe River, showing the calculation method of the gradient G_d.

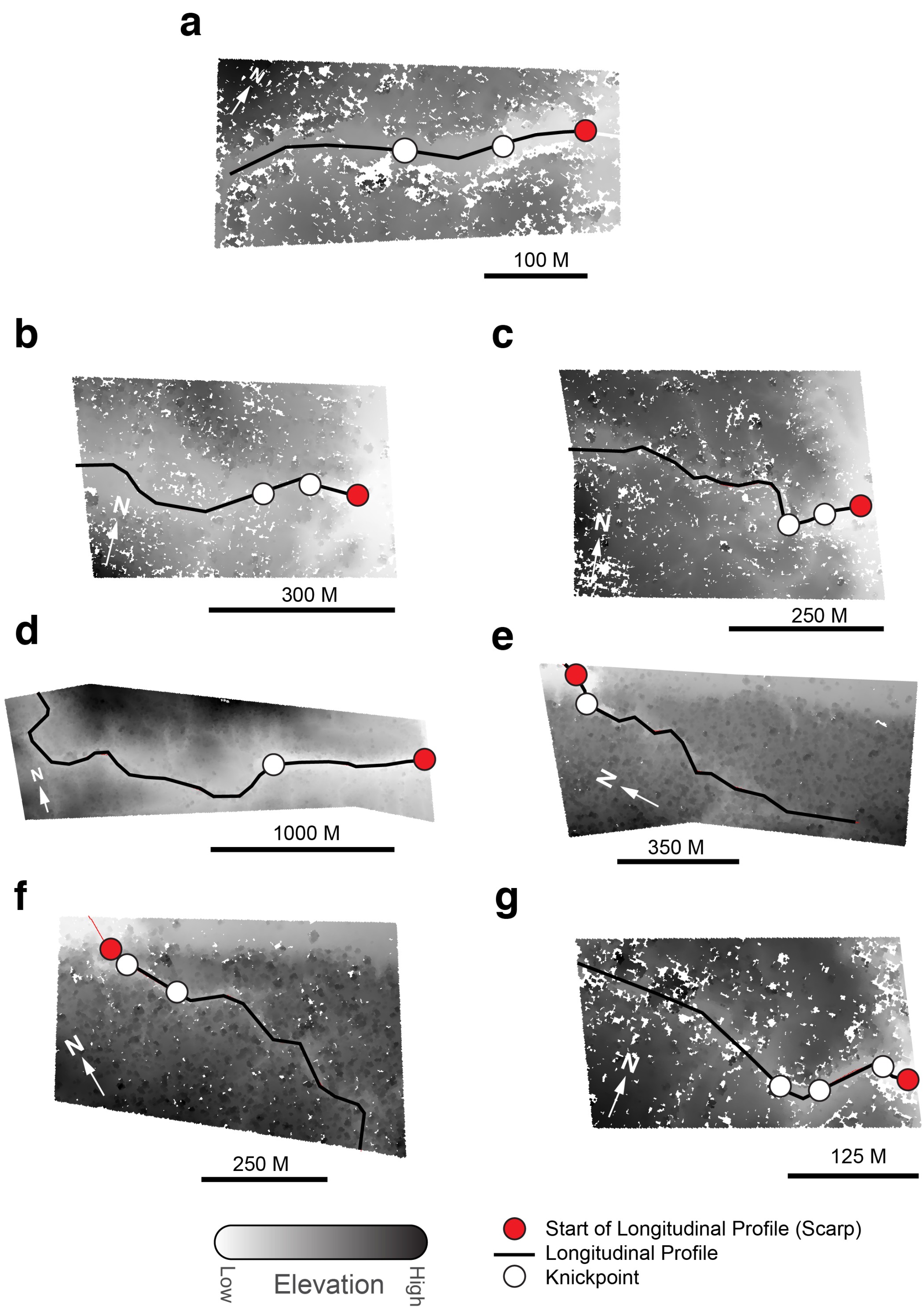

Fig. J.2 Location of knickpoints on rivers and streams: a) Naminkokwe River, b) Mua north stream, c) Mua south stream, d) Livelezi River, e) Kasinje north stream, f) Kasinje south stream, and g) Mtuta River.